Durham University

Durham E-Theses

Facies Control on Fluvial Reservoir Quality

ARO, OLUWAFEMI,EMMANUEL

How to cite:

ARO, OLUWAFEMI,EMMANUEL (2023) *Facies Control on Fluvial Reservoir Quality*, Durham theses, Durham University. Available at Durham E-Theses Online: http://etheses.dur.ac.uk/14934/

Use policy

The full-text may be used and/or reproduced, and given to third parties in any format or medium, without prior permission or charge, for personal research or study, educational, or not-for-profit purposes provided that:

- a full bibliographic reference is made to the original source
- a link is made to the metadata record in Durham E-Theses
- the full-text is not changed in any way

The full-text must not be sold in any format or medium without the formal permission of the copyright holders.

Please consult the full Durham E-Theses policy for further details.

Academic Support Office, The Palatine Centre, Durham University, Stockton Road, Durham, DH1 3LE
e-mail: e-theses.admin@durham.ac.uk Tel: +44 0191 334 6107
http://etheses.dur.ac.uk

Facies Control on Fluvial Reservoir Quality

Oluwafemi Emmanuel Aro

This thesis is submitted in partial fulfilment of the requirements for the degree of Doctor of Philosophy at Durham University

Department of Earth Sciences

Durham University

2023

Abstract

Fluvial sandstones form important hydrocarbon reservoirs and aquifers in many regions of the world and more recently been identified as potential sites for carbon dioxide and hydrogen subsurface storage. The characterization of fluvial reservoirs is however challenging due to the complex heterogeneities (internal and external) associated with the variable lithologies and sedimentary architecture. Understanding the main controls on the heterogeneities is essential for building accurate reservoir models. One of the main controls is depositional facies, which in turn has a major influence on early and late burial diagenesis. Although depositional facies is widely known to exert a primary control on fluvial lithological variability and heterogeneity, its role in clay-coat distribution and authigenesis remains poorly constrained. In this study, a multidisciplinary approach involving outcrop analogues, core analysis, petrography, electron microscopy, burial history/quartz cement modelling, clay coat and stable isotope analysis has been employed to understand the controls on fluvial reservoir quality and overall heterogeneity. A total of 293 samples comprising of core and outcrop samples from the Triassic Skagerrak Formation (UK Central North Sea), St Bees Sandstone Formation (West Cumbria, UK) and Buntsandstein facies (Central Iberian Basin, Spain) were investigated. This research clearly identifies that reservoir quality/heterogeneity is controlled by facies, grain size and clay/ductile grains content. Channel facies offer the best reservoir quality while floodplain facies offer poor quality. In the channel sandstones, porosity and permeability range from 0-24% and 0.01-1150 mD, respectively, while in the floodplain facies, they range from 0-7.3% and 0.004-0.51 mD, respectively. Grain size is a first order control on reservoir quality. Coarser-grained channel sandstones have a higher reservoir quality than finer-grained channel sandstones due to their lower clay and ductile grains content. This study reveals that within channel bodies, there is a significant variation in reservoir quality, with the channel centres having the best reservoir quality. Furthermore, this research reveals that the extent of coverage of clay coats governs its ability to effectively inhibit quartz cementation, and significantly correlates with grain size, clay content, and depositional energy. The most extensive clay coat coverage (70-98%) is associated with the finer-grained, low energy channel sandstones and possibly crevasse channel intervals containing between 5 and 10% clay coat by volume. The results of this study have significant implications for reservoir quality prediction and development of fluvial reservoir models especially in high pressure high temperature (HPHT) environments. Finer-grained, dirty sandstones that are often overlooked during exploration offer potentially better reservoir quality at depth and could provide better underground storage sites.

Declaration

I hereby declare that the work described in this thesis, which I submit for the degree of Doctor of Philosophy at Durham University, is my own work, except where acknowledgement is made in the text, and that it has not been submitted previously for a degree or any other qualifications at this or any other university.

May 2023

© Copyright, Oluwafemi Emmanuel Aro, 2023

The copyright of this thesis rests with the author. No quotation from it should be published in any form without the author's prior written consent. All information acquired from this thesis must be duly acknowledged.

Acknowledgements

First and foremost, I would like to thank the Almighty God, the King of kings and Lord of lords for his mercy, favour, and grace throughout my PhD programme. May His name be forever praised.

My sincere appreciation also goes to my excellent and amazing supervisory team: Stuart Jones, Neil Meadows, and Jon Gluyas for their guidance, assistance, and encouragement throughout my PhD programme. I cannot but say a special thank you to Stuart Jones for his immeasurable and invaluable support from the start of my PhD programme to the end. He provided critical advice in the course of acquiring data and writing up my thesis. Even when things did not go as planned, he was always looking for ways to keep me from feeling overwhelmed. Thank you so much and God bless you greatly.

I would like to specially appreciate the Petroleum Technology Development Fund (PTDF) and the Government of the Federal Republic of Nigeria for providing the funds for this research. The commencement and completion of this research work would not have been made possible without your financial support. God bless the Federal Republic of Nigeria.

My sincere appreciation also goes to Ian Chaplain and Sophie Edwards for preparation of numerous petrographic thin sections, Leon Bowen and Diana Alvarez-Ruiz for advice and assistance at the scanning electron microscope, and Joanne Peterkin for stable isotope analysis.

Special thanks to everyone in the Department of Earth Sciences, Durham University for making this journey so enjoyable and for being a part of my success story. I must not but mention the following people for their support during my PhD programme: Dimitrios Charlaftis, Chimaobi Nwachukwu, Abdulwahab Bello, Olakunle Oye, Ayodeji Jayeoba, and Franzel Maximilian. God bless you all.

Finally, I would like to appreciate my lovely wife, Oyinkansola, and my precious daughter, Oluwadarasimi, for their unwavering support, patience and understanding throughout this programme. I could not have achieved this success without you guys. To my mum, sisters, in-laws, friends, Pastor Olufemi Folorunso and the entire members of RCCG (Sanctuary of Power, Durham), I say a big thank you to you all for your support, encouragement, and prayers. God has used you all in making this journey a success. I pray that in your time of need, you will not lack help in Jesus name (Amen).

Table of Contents

Chapter 1: Introduction

1.1 Background

To meet the increasing demand for fossil energy, and boost hydrocarbon reserves globally, exploration companies are increasingly exploring deeper reservoir targets (Bloch et al. 2002) and focusing on maximizing recovery from mature oil and gas fields (Henares et al. 2014). A key factor for exploration success in these deeper settings is the accurate prediction of reservoir quality (i.e., porosity and permeability) ahead of the drill-bit, and more importantly, locating sandstone reservoirs with sufficient porosity and permeability (Taylor et al. 2010). In addition, the economic viability of a petroleum accumulation is largely influenced by reservoir quality. Therefore, in order to minimize exploration risk and optimize production, the accurate prediction of reservoir quality prior to drilling and throughout the entire lifecycle of a reservoir is essential (Kupecz et al. 1997; Ajdukiewicz and Lander 2010; Taylor et al. 2010; Worden et al. 2018a).

In deeply buried sandstones, the prediction of reservoir quality remains a major challenge due to the complex interrelated factors at depths (e.g., diagenesis, elevated temperatures and/or high effective stresses). The reservoir quality of deeply buried sandstones is the combined product of depositional, shallow- and deep-burial diagenetic processes (Ajdukiewicz and Lander 2010). Earlier predictive models in the 1980s relied on empirical correlations (i.e., porosity-depth trend driven by mechanical compaction), and the assumption that porosity in deeply buried sandstones was mainly due to dissolution from the interaction between unstable grains and migrating organic acids. These previous models have however, proven to be less effective due to the presence of preserved primary porosity in some deeply buried sandstones (>4 km). Current models are processed-oriented and are based on the concept of burial diagenesis. These new models have resulted in major improvements in reservoir quality prediction, but with varying degrees of success (Ajdukiewicz and Lander 2010). In the process-oriented diagenetic models, depositional elements are integrated with burial history elements (e.g., effective stress, thermal history, and fluid compositions) for the better understanding of controls on reservoir quality (Ajdukiewicz and Lander 2010; Worden et al. 2018a).

Reservoir quality generally decreases with increasing depth due to increasing vertical effective stress (VES) caused by sediment loading. However, deeply buried reservoirs with anomalously high porosity and permeability have been encountered in several hydrocarbon provinces (e.g., Central North Sea, UK and Gulf of Mexico) around the world (Bloch et al. 2002). Anomalously high porosity and permeability in these deeply buried sandstones has been linked to conditions that limit diagenesis (i.e., compaction and cementation) (Salem et al. 2000). These conditions include (1) overpressuring (Nguyen et al. 2013; Stricker and Jones 2016), (2) presence of clay coatings (Ehrenberg 1993; Nguyen et al. 2013; Stricker and Jones 2016), (3) early, evenly distributed, partial carbonate and quartz cementation (De Ros et al. 1994; Souza et al. 1995) and (4) shallow-burial oil emplacement (Marchand et al. 2001; Wilkinson and Haszeldine 2011). In deeply buried sandstones, quartz cement is a major and common porosity destroyer (McBride 1989; Walderhaug 1996; Worden and Morad 2000; Oye et al. 2018). Several studies have reported that the presence of clay minerals in form of clay coats can preserve reservoir quality in deeply buried sandstones by inhibiting quartz cementation (Heald and Larese 1974; Pittman et al. 1992; Ehrenberg 1993; Worden and Morad 2000; Bloch et al. 2002; Berger et al. 2009; Ajdukiewicz and Lander 2010; Taylor et al. 2010; Ajdukiewicz and Larese 2012; Nguyen et al. 2013; Stricker and Jones 2016; Stricker et al. 2016b; Tang et al. 2018; Worden et al. 2020).

Despite the ability of clay coats to inhibit quartz cementation, experimental and core-based studies have proven that the ability of clay coats to effectively inhibit quartz cementation is a function of its completeness (i.e. fraction of grain surface area covered by clay minerals) and not just its presence (Heald and Larese 1974; Ehrenberg 1993; Walderhaug 1996; Bloch et al. 2002; Billault et al. 2003; Lander et al. 2008; Ajdukiewicz and Larese 2012; Stricker and Jones 2016). Many studies have linked the completeness of clay coats on sand grain surfaces to grain size, sorting and clay volume; this has however, generated some controversies in the literature (Bloch et al. 2002; Ajdukiewicz et al. 2010; Dowey et al. 2017; Wooldridge et al. 2017b; Busch et al. 2020) and therefore needs further investigation. In some studies, a larger grain size (mean grain size >0.45mm) has been shown to offer better clay coat completeness with relatively minor amounts of clay (Bloch et al., 2002); while other studies claimed that a smaller grain size achieve better clay coat completeness than a larger grain size (Ajdukiewicz et al., 2010; Wooldridge et al., 2017). The work of Dowey et al. (2017) on modern-day estuarine sediments suggests that mean clay coat coverage is not controlled by grain size, but by sorting and skewness of grain size distribution (and clay volume). Their work suggests that the poorer the sorting, the higher the mean clay coat coverage, and the more negatively skewed the grain size distribution is towards fine and very-fine grain size, the higher the mean coat coverage. Of recent, the work of Busch et al. (2020) on fluvio-aeolian sandstones from wells in the Southern Permian Basin, suggests that there is no clear correlation between clay coat coverage and facies-controlled parameters (grain size and sorting). Grain size, sorting and clay content are facies-controlled parameters (Bloch and McGowen 1994; Bloch et al. 2002), which not only have a fundamental control on porosity and permeability at the time of deposition (Beard and Weyl 1973) but also maintain control on the evolution of sandstone porosity and permeability through burial (Akpokodje et al. 2017). Since depositional facies strongly influences the type/amount of early diagenetic attributes, which in turn control deep burial diagenesis (Morad et al. 2010), understanding the distribution of diagenetic processes as a function of depositional facies is critical for the accurate prediction of reservoir quality of deeply buried sandstones. Also, understanding the relationship between depositional (or facies-controlled) parameters and clay coat authigenesis/coverage is crucial for predicting clay-coat enhanced deep reservoir quality.

Furthermore, to maximize potential from a sandstone reservoir, it is essential to understand and model the spatial distribution of diagenetic alterations and rock properties (i.e., heterogeneity) within sandstone bodies. Reservoir heterogeneity strongly influences reservoir performance by controlling fluid flow and recovery factors (Miall 1988; Tyler and Finley 1991; Sharp et al. 2003; Morad et al. 2010). Fluvial reservoirs, in particular, are highly heterogeneous and thus difficult to characterise and model, despite the fact that they form important hydrocarbon reservoirs, groundwater aquifers and potential sites for CO_2 sequestration in many parts of the world (Bridge 2001; Keogh et al. 2007; Issautier et al. 2014). The characterisation of subsurface fluvial reservoirs/systems is challenging with subsurface datasets, due to inter-well spacing and lateral changes in facies. As a result, fluvial outcrops are often used as analogues for subsurface fluvial reservoirs and to characterise sandstone body geometry/architecture, an essential requirement for subsurface reservoir modelling (Howell et al. 2014; Franzel et al. 2019; Franzel 2022). However, the inherent heterogeneity associated with different geometries has received less attention and therefore needs further investigation. In general, to maximize hydrocarbon recovery in fluvial sandstones and evaluate their CO_2 storage potential, the key controls on reservoir quality and heterogeneity must be adequately understood.

1.2 Research aim and objectives.

The main aim of this research is to have a better understanding of the controls on reservoir quality evolution in Triassic fluvial sandstone reservoirs. To accomplish this, core and outcrop samples of Triassic fluvial sandstones were collected and studied using a multidisciplinary approach involving core and outcrop analysis, light and scanning electron microscopy, stable isotope analysis, burial history, clay-coat quantification technique and quartz cementation modelling to investigate the facies, petrography and diagenesis.

The main objectives of this research are as follows:

- To describe the core and outcrop samples of Triassic fluvial sandstones and identify the lithofacies within them.
- To determine the mineralogical composition (detrital and authigenic) of the sandstones in order to understand the diagenetic processes, reconstruct the diagenetic sequence and identify factors that govern the reservoir quality.
- To determine the role played by depositional facies in controlling diagenesis/clay-coat authigenesis and reservoir quality in fluvial sandstones.
- To determine the function of clay coatings in the evolution of reservoir quality in HPHT sandstones, quantify clay-coating coverage, and identify the primary controls.
- To investigate the heterogeneity within fluvial channel bodies and the main controls.
- To compare cross-section and longitudinal profiles of fluvial channel bodies in order to determine any similarities or differences in terms of petrography, mineralogy (detrital and diagenetic), reservoir quality and stacking patterns.

1.3 Thesis structure

This thesis contains six chapters.

- Chapter 1 gives a general background of the research topic and a brief overview of the aims and objectives of the research. It also summarizes the current state of the literature regarding reservoir quality of siliciclastic reservoirs and discusses the impacts of factors such as depositional facies, grain-coating clays, quartz cementation and carbonate cementation on reservoir quality.
- Chapter 2 gives a detailed description of the methodology and techniques utilised to achieve the aim of this study.
- Chapter 3 presents and discusses the importance of facies, grain size, and clay content in controlling fluvial reservoir quality, using the Triassic Skagerrak Formation, Central North Sea, UK as a case study. Special attention was given to the impacts of grain size, clay content and depositional energy on quartz cementation, clay coverage, and their overall implications for reservoir quality prediction in high pressure high temperature

(HPHT) environments. *This chapter has been published in the Petroleum Geoscience journal*, doi.org/10.1144/petgeo2022-043.

- Chapter 4: presents and discusses the diagenesis and reservoir quality/heterogeneity of a Triassic braided fluvial system, the controls, and implications for reservoir modelling. This chapter focuses on the outcropping St Bees Sandstone in West Cumbria, UK, which has been interpreted as an analogue for the Sherwood Sandstone Group in the Corrib gas field, offshore west of Ireland. *This chapter has been written in a paper format and will be submitted for publication to a peer-reviewed journal.*
- Chapter 5 presents and discusses facies and reservoir heterogeneity in low net-to-gross fluvial systems. Using the outcropping Buntsandstein facies at Riba De Santiuste in the Central Iberian Basin, Spain as a case study, this chapter discusses the heterogeneity within channelized sandstone bodies and the main controls.
- Chapter 6 elaborates on the discussion sections from preceding chapters while using an integrated approach to summarize and discuss the wider implications of depositional facies and reservoir heterogeneity for sandstone reservoir quality, modelling, and CCS. Conclusions reached throughout the body of the thesis are summarized. This chapter also identifies future research areas that could expand on the themes discussed in this thesis.

1.4 Reservoir quality of sandstones and the controls: a review

1.4.1 Introduction

Reservoir quality (i.e., porosity and permeability) exerts a fundamental control, not only on the economic viability of a petroleum accumulation, but also on the success of carbon capture and storage technology, and geothermal energy exploration. The porosity of a reservoir determines the volume of oil and gas in place while permeability determines the flow rate of oil and gas from the reservoir to the wellbore (Worden et al. 2018a). Reservoir quality of sandstones is primarily a function of both depositional and diagenetic processes (Fig. 1.1) (Kupecz et al. 1997; Schmid et al. 2004; Ajdukiewicz and Lander 2010; McKinley et al. 2011; Stricker et al. 2016a). Thus, adequate understanding of these processes is essential for predicting good quality hydrocarbon reservoirs. Similarly, the increased emphasis on carbon capture and storage (CCS) in an effort to mitigate climate change and the global demand for clean energy (e.g., geothermal energy) necessitates a better understanding of the controls on subsurface reservoir quality. These controlling factors have been extensively discussed in the literature and are only briefly reviewed in this section.

1.4.2. Depositional facies

Depositional facies play a very important role in the reservoir quality of siliciclastic deposits. It controls (1) grain size distribution and sorting, (2) primary porosity and permeability, (3) sand body architecture/geometry, (4) pore-water chemistry and (5) near-surface eodiagenesis (Bloch and McGowen 1994; Morad et al. 2000). Depositionally-controlled parameters exert a major control on the distribution of eodiagenetic alterations, which in turn influence deep-burial, mesodiagenetic evolution of sandstones (Bloch and McGowen 1994; Morad et al. 2000; Morad et al. 2010). Due to the strong relationship between depositional facies and diagenesis, depositionally-controlled parameters are commonly employed to predict present-day reservoir quality quantitatively or qualitatively, provided a calibration data set is available. In relatively shallow reservoirs (diagenetically-simple rocks), the impact of depositional facies on reservoir quality is most pronounced, making quantitative reservoir quality prediction very possible. This is because reservoir quality in such rocks is primarily controlled by lithofacies (Weber 1980), and have not yet undergone complex diagenetic alterations (Bloch and McGowen 1994). Conversely, in deeply buried reservoirs (>2.5 km), quantitative reservoir quality prediction is less accurate due to the exposure to elevated temperature and prolonged interactions with pore fluids. However, even in such diagenetically-complex rocks, the original fabric does not change considerably and still maintains control on the diagenetic and reservoir quality evolution of the rock, allowing for qualitative reservoir quality prediction (Bloch and McGowen 1994).

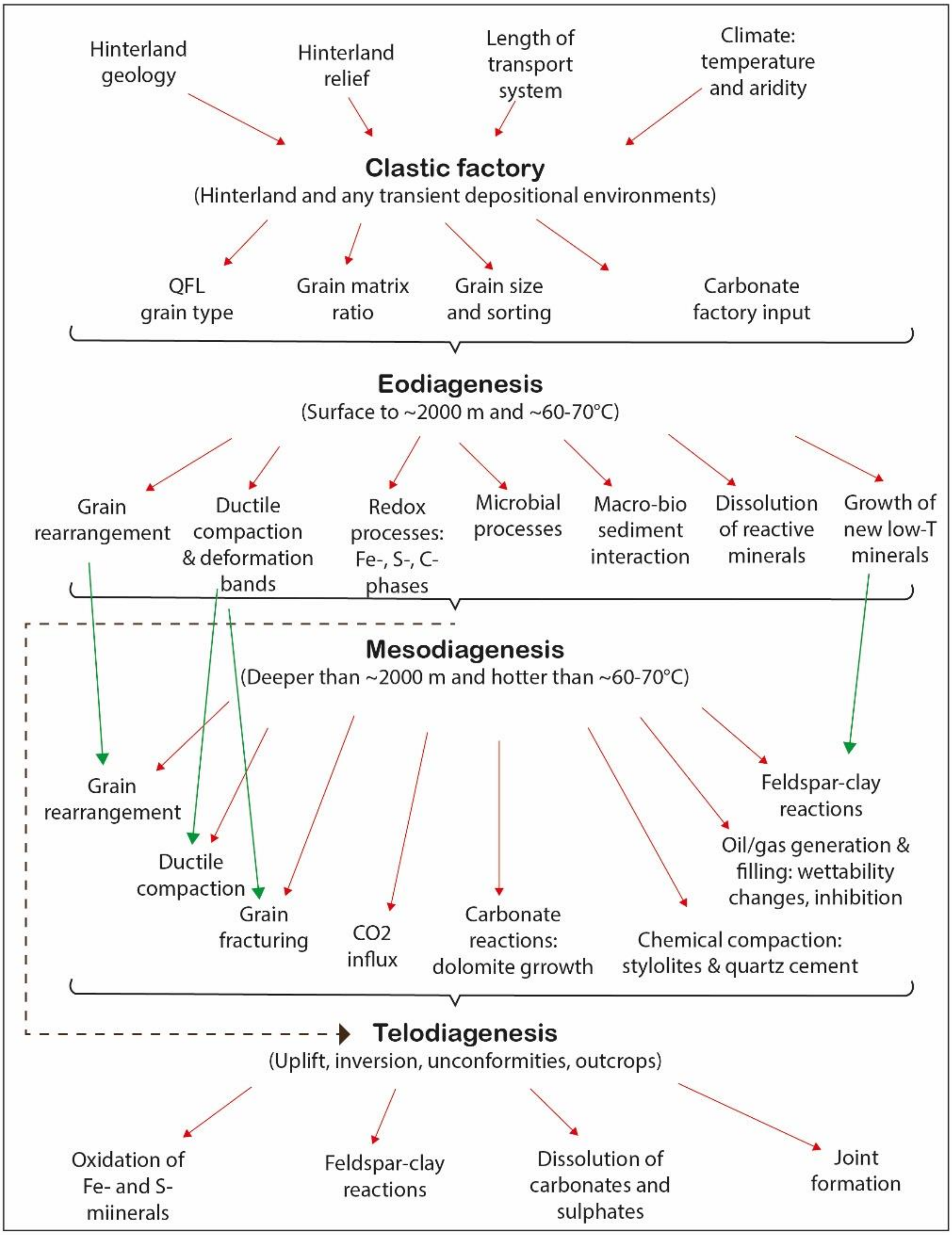

Figure 1.1. Controls on sandstone reservoir quality split between the major controls on clastic grains: the 'clastic factory', eodiagenetic (early/shallow burial diagenetic) controls, mesodiagenetic (burial diagenetic) controls, and even telodiagenetic (uplift-related) influences. The clastic factory is controlled by geology in the source area, climate, relief and length of the sediment transport systems. Together these control the composition of the sand (QFL), the amount of matrix, sediment texture and the extent of in-situ (autochthonous) carbonate generation (modified after Worden et al., 2018a).

1.4.3 Detrital composition

Sandstone detrital composition is controlled mainly by provenance, paleoclimatic conditions, and tectonics (De Ros et al. 1994; Morad et al. 2010). The type and relative abundance of detrital components in sand can greatly influence both physical and chemical diagenesis and reservoir quality (Bloch 1994; Morad et al. 2010; Dutton et al. 2012; Bjørlykke 2014). Mature sandstones (quartz arenite) are mechanically and chemically stable and have the potential to form good reservoirs when deeply buried (Bloch and Helmold 1995; Primmer et al. 1997; Warren and Pulham 2001; Bloch et al. 2002; Morad et al. 2010). Feldspar-rich sandstones (arkoses) are mechanically stable but can become chemically unstable and undergo dissolution and kaolinization when subjected to prolonged interaction with acidic-rich pore water (McKay et al. 1995; Worden and Morad 2003; Morad et al. 2010). Ductile-grain sandstones (litharenite) are generally mechanically and/or chemically unstable, and experience rapid loss of porosity and permeability during burial (Burns and Ethridge 1979; Pittman and Larese 1991; Bloch 1994; Rezaee and Lemon 1996; Worden et al. 2000; Paxton et al. 2002; Morad et al. 2010; Rahman and Worden 2016; Li et al. 2019; Wang et al. 2020). An adequate understanding of detrital composition and the controlling factors is a vital tool for predicting reservoir quality and compaction processes during progressive burial (Bjørlykke 2014). The impact of detrital grain types on the diagenetic evolution and reservoir heterogeneity of sandstones is presented below (Table 2.1).

1.4.4 Diagenesis

Diagenesis refers to the physical and chemical changes that alter the textural and mineralogical characteristics of sediments after deposition. These processes which result in the lithification of sediments occur at relatively low temperatures (<250°C) and prior to metamorphism which occurs at temperatures >250°C (Nichols 2009). During the deposition, burial and uplift cycle of basin history, these processes (physical, chemical and biological) are continually active as the ambient environment changes in terms of temperature, pressure and pore-fluid chemistry (Worden and Burley 2003).

Diagenesis can be divided into three conceptual regimes: eodiagenesis, mesodiagenesis and telodiagenesis (Fig 1.1).

Table 1.1. Impact of framework grain types on the diagenetic and reservoir quality and heterogeneity evolution of sandstones (after Morad et al. 2010)

Type of framework grains	Common related diagenetic alterations	Impact on reservoir quality	Depositional/Tectonic setting
Quartz	Mesodiagenetic pressure dissolution (silica exporters) and/or quartz cementation (silica importers)	Preservation of reservoir porosity and permeability to depth of about 3 km. Substantial loss of reservoir porosity and permeability at depths greater than 3 km	Intracratonic basins, wet climate, granitic, felsic gneissic, and quartzitic source rocks; more common in eolian, fluvial, and shallow-marine facies
Feldspars and plutonic rock fragments	Eo- and mesodiagenetic dissolution, resulting in the formation of intragranular and moldic pores. Eodiagenetic kaolinization, Mesodiagenetic albitization	Creation of secondary porosity Mesodiagenetic K-feldspar albitization promotes illite authigenesis and permeability deterioration	Rifts and pull-apart basins adjacent to uplifted basement rocks; common in all facies
Lithic: ductile (e.g., mud intraclasts, glaucony, mudrocks, low-grade metamorphic)	Mechanical compaction and formation of pseudomatrix	Severe loss of porosity and permeability	Orogenic settings; intrabasinal reworking
Lithic: chemically unstable (e.g., volcanics)	Formation of smectite, chlorite, zeolites, calcite, microquartz, and opal	Severe loss of permeability	Basins adjacent to volcanic arcs or plateaus
Lithic: chemically and mechanically stable (e.g., chert, quartzite)	No significant alterations; chert may be subjected to partial dissolution	Preservation of reservoir porosity and permeability	Basins adjacent to uplifted continental crust, or subduction complexes
Micas	Enhanced pressure dissolution	Reduction of porosity and permeability by chemical compaction	Basins adjacent to uplifted continental crust, or orogenic arcs
Extrabasinal and intrabasinal carbonate grains	Extensive carbonate cementation and chemical compaction	Deterioration of reservoir porosity and permeability	Orogenic settings (extrabasinal) or passive margins (intrabasinal)
Intrabasinal siliceous bioclasts	Eodiagenetic dissolution resulting in formation of microquartz rims	Preservation of reservoir porosity-permeability to depth of about 3 km	Shallow- and deep-marine sandstones

Eodiagenesis: refers all processes that take place at or near the surface of the sediments where the chemistry of the interstitial waters is primarily controlled by the depositional environment. Eodiagenesis occurs at depths of about 1-2 km and at temperatures <60-70°C. Eodiagenetic processes include meteoric infiltration, groundwater flow, weathering and soil development, bioturbation, microbial activity and precipitation of dolomite and anhydrite arising from seawater reflux. The role of eodiagenesis in sandstone reservoir quality is becoming more recognised due to its influence on the creation of clay coats that may inhibit later quartz cement (Dowey et al. 2017; Wooldridge et al. 2017b). Eodiagenesis can result in the early formation of carbonate and sulphate cements, which may either prevent compaction or be extensively distributed, resulting in loss of porosity. Eodiagenesis can also result in the partial or complete alteration of unstable detrital grains due to interaction with groundwater (Worden et al. 2018a). The main eodiagenetic clay minerals are kaolinite, glauconite, berthierine, verdine, di-and trioctahedral smectite, illite/smectite (I/S), chlorite/smectite (C/S) and Mg-clay minerals (palygorskite). In the eodiagenetic realm, the formation of diagenetic clay minerals in sands is strongly influenced by depositional facies, detrital composition of the sandstones and climatic conditions (Worden and Morad 2003).

Mesodiagenesis: This regime includes the physical, chemical, and biological processes that act upon a sediment during burial as it is gradually removed from the influence of the depositional environment and persists until the onset of metamorphism, or structural uplift and exposure to meteoric water (cf. Worden and Burley 2003). The main factors that control mesodiagenesis are the time-temperature history, primary mineralogy, fabric, local eodiagenetic modifications, material loss and gain to neighbouring lithologies, the geochemistry of the pore water and the presence of petroleum-related fluids (Worden and Burley 2003). Mesodiagenetic processes include, but not limited to, clay-mineral transformation reactions, albitization and dissolution of feldspar, quartz cementation and development of K-feldspar overgrowths. These processes commence at depths ≥2 km and temperatures ≥60-70°C, where the sediments are physically free from atmospherically influenced water (Morad et al. 2000).

Telodiagenesis: Telodiagenesis occurs in uplifted and exhumed rocks that have been exposed to the influx of meteoric water that is unconnected to the depositional environment of the host sediment. The water-rock interaction commonly results in the dissolution of minerals (e.g., feldspars, carbonates, and sulphates), alteration of feldspar to clay minerals, and the oxidation of reduced phases such as pyrite, Fe-clay minerals, and Fe-carbonates (Worden and Burley 2003; Worden et al. 2018a).

The diagenetic processes controlling reservoir quality are: (1) compaction, (2) cementation, (3) dissolution, and (4) recrystallization. These processes are primarily influenced by depositional facies, and other factors which include temperature, burial depth, and pressure (Bloch and McGowen 1994; Morad et al. 2010; Nguyen et al. 2013; Bjørlykke 2014; Stricker and Jones 2016).

1.4.5 Compaction

There are two types of compaction: (1) mechanical compaction and (2) chemical compaction (or pressure dissolution). Both involve porosity loss during sediment burial and compactional effects. Mechanical compaction begins during shallow burial (eodiagenesis) and continues into the mesodiagenetic realm. Mechanical compaction occurs as a result of the progressive increase in vertical effective stress caused by increasing overburden thickness (Bjørlykke 2014; Worden et al. 2018a). Evidence of mechanical compaction includes the re-orientation and re-packing of grains, deformation of ductile grains, brittle grain fracture and ultimately, loss of porosity. Porosity loss due to mechanical compaction is a function of the effective overburden stress and the initial sediment composition (Bjørlykke 2014) (Fig. 1.2). The work of Paxton et al. (2002) on the effect of compaction on porosity loss shows that rigid-grain sandstones decline from about 40-45% primary porosity at deposition (Beard and Weyl 1973) to 26% porosity at ~2500 m burial depth because of mechanical compaction. From ~2500 m, rigid framework grains stabilize, and below this depth, further porosity loss is no longer by mechanical compaction but by chemical compaction (Fig. 1.3a-c). Ductile-rich sandstones, commonly loose porosity at a faster rate by mechanical compaction at relatively shallow depths compared to rigid-grain sandstones with little or no ductile grains (Fig. 1.3d-e) (Bloch 1994; Gluyas and Cade 1997; Paxton et al. 2002). Ductile grains deform more easily and rapidly than rigid grains during mechanical compaction, hence the reason for the quicker and severe porosity loss in rocks containing them (Gluyas and Cade 1997).

Chemical compaction (or pressure dissolution) occurs during mesodiagenesis at depths >2 km and temperatures >70-80°C (Morad et al. 2000; Worden and Morad 2000; Bjørlykke 2014). Chemical compaction involves the dissolution of grains at intergranular contacts and re-precipitation of the dissolved material on grain surfaces adjacent open pores (Sheldon et al. 2003; Worden and Burley 2003). The main drivers of chemical compaction are temperature, vertical effective stress, and the pore fluid/mineral composition (Sheldon et al. 2003). Earlier studies have claimed that chemical compaction (and related quartz cementation) is primarily influenced by temperature and largely independent of vertical effective stress (Bjorkum 1996; Walderhaug 1996; Bjørkum et al. 1998; Lander and Walderhaug 1999; Bjørlykke 2014). Recent studies, have however, shown that chemical compaction and the supply of silica through quartz dissolution at grain contacts are primarily driven by vertical effective stress rather than temperature (Oye et al. 2018; Oye et al. 2020). In other studies, the presence of sheet silicates (such as clays and micas) along quartz grain contacts has been suggested to promote chemical compaction without the application of stress (Bjorkum 1996; Oelkers et al. 1996). This claim has been refuted by Sheldon et al. (2003). According to Sheldon et al. (2003), silica dissolution promoted by sheet silicates at quartz grain contacts is unlikely to occur without the application of stress at grain contacts. The presence of sheet silicates along grain contacts only act to increase the rate of dissolution and diffusion in the grain contact zone. In general, the process of compaction (mechanical and chemical) is an irreversible process that commonly result in the loss of porosity. However, the development of pore fluid overpressure can limit or slow down the rate of compaction by reducing the vertical effective stress during progressive burial and help preserve porosity (Stricker and Jones 2016; Stricker et al. 2016a).

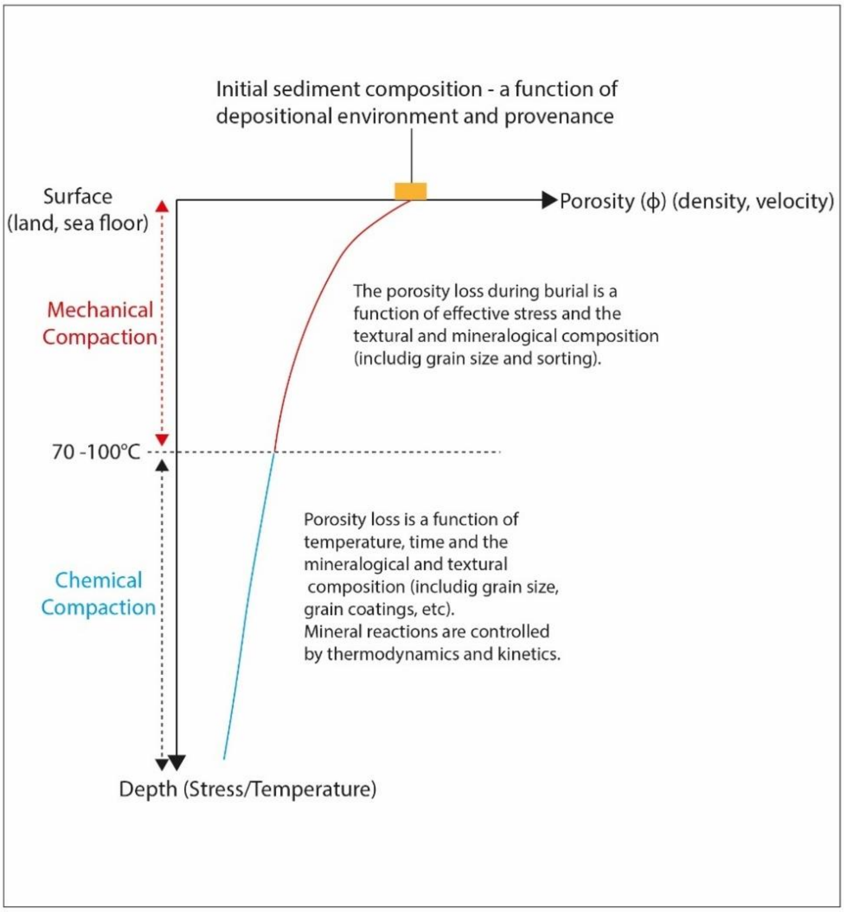

Figure 1.2. Diagram illustrating the principal aspects of siliceous sediment compaction during burial in sedimentary basins (after Bjørlykke 2014).

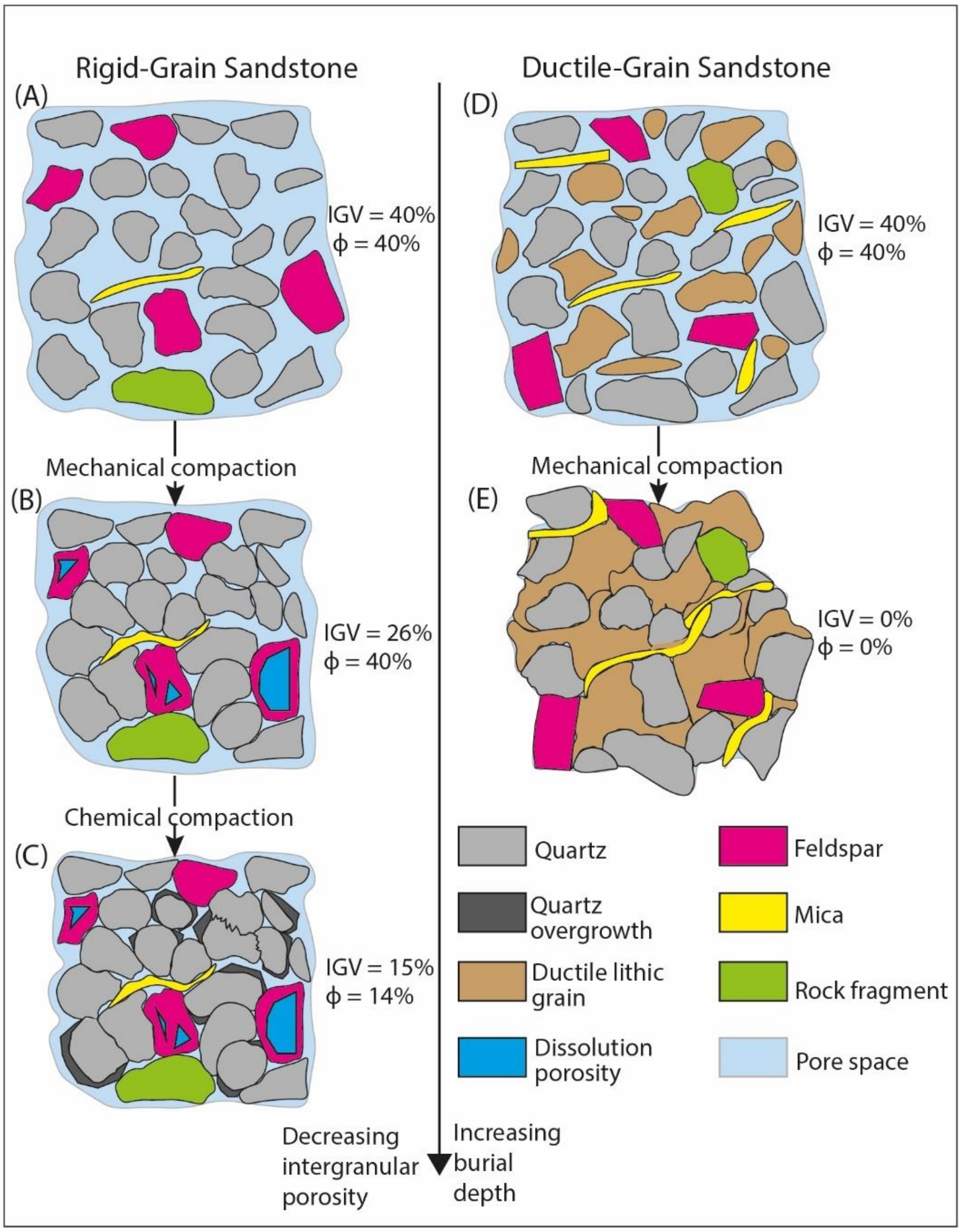

Figure 1.3. Schematic illustration of progressive compaction of a rigid-grain sandstone versus ductile-grain sandstone (modified after Paxton et al. 2002). IGV = intergranular volume; ϕ = intergranular porosity.

1.4.6 Cementation

Cementation refers to the process by which minerals are chemically precipitated within the pore spaces of sediment during diagenesis. Cementation transforms the sediment into a rock, and as it does, porosity and permeability are reduced (Nichols 2009). Although cementation generally reduces porosity and permeability, the early precipitation of framework-supporting cements (e.g., quartz, carbonates, and anhydrite) can prevent further compaction, and thereby preserve porosity to considerable depths (Paxton et al. 2002; Ali et al. 2010). Several minerals can form diagenetic cements in a body of sediments, however, the type of cements formed depends on the chemical composition, acidity, and temperature of the pore waters.

1.4.6.1 Quartz cement

Quartz is the most abundant and main porosity destroying cement in deeply buried sandstones (>2500m) exposed to temperatures >70-80°C (McBride 1989; Bjørlykke and Egeberg 1993; Walderhaug 1996; Worden and Morad 2000; Harwood et al. 2013; Wells et al. 2015; Stricker and Jones 2016; Oye et al. 2018; Worden et al. 2018b). Quartz overgrowth is the commonest form of quartz cement in sandstones and usually develops on detrital quartz grains when silica directly precipitates from aqueous solution (McBride 1989). Where the overgrowth is in optical continuity with its host, it is termed syntaxial, but where it is not, it is referred to as epitaxial (Worden and Burley 2003). Different sources of silica for quartz cement have been proposed in the literature by numerous workers (Heald 1955; Houseknecht 1988; McBride 1989; Walderhaug 1996; Giles et al. 2000; Sheldon et al. 2003; Kim and Lee 2004; Harwood et al. 2013). However, it is worth noting that the silica in quartz cement has no single source that can be predicted universally in sandstones (Worden and Morad 2000). The different silica sources have been classified into two major groups: internal and external sources (Worden and Morad 2000). The internal sources (those derived from within the sandbody) include: (1) pressure dissolution at grain contacts and in stylolites, (2) alterations of feldspar, (3) illitization and chloritization of smectite, and (4) dissolution of biogenic silica and volcanic fragments. Externally sourced silica includes (1) those incorporated via diffusion into the sandstones from nearby shales and (2) those imported during episodes of fluid flow from deeper sections of the basin along faults. Quartz cementation is controlled by several factors; these are grain size, detrital mineralogy, clay coats, temperature history (Walderhaug 1996), residence time in the silica mobility window, fluid composition, flow volume and pathways (McBride 1989). In deeply buried sandstone reservoirs, certain factors have been reported to inhibit the growth of quartz cement and help preserve reservoir quality. These are overpressure, early emplacement of hydrocarbon, and presence of clay and microquartz coats (Ehrenberg 1993; Aase et al. 1996; Aase and Walderhaug 2005; Wilkinson and Haszeldine 2011; Nguyen et al. 2013; Sathar and Jones 2016; Stricker and Jones 2016; Stricker et al. 2016a; Stricker et al. 2016b; Worden et al. 2018b).

1.4.6.2 Carbonate cements

Carbonate cements are among the most important authigenic cements in sandstones (Carvalho et al. 1995; Wang et al. 2016). They have an important influence on sandstone reservoir quality and heterogeneity, hence, understanding their distribution patterns and geochemical evolution is essential for predicting sandstone reservoir quality (Morad 1998; Morad et al. 1998; Taylor et al. 2000; Dutton 2008; Taylor and Machent 2011; Wang et al. 2016; Cui et al. 2017). Major carbonate cements found in clastic rocks are calcite ($CaCO_3$), dolomite ($MgCa(CO_3)_2$) and siderite ($FeCO_3$); these three can form during eodiagenesis and mesodiagenesis (Worden and Burley 2003; Morad et al. 2010). In fluvial environments, near-surface eodiagenetic carbonate cements are typically low-Mg calcite, siderite, and dolomite cements (occurring as caliche crusts, calcretes and dolocretes) and are usually precipitated under semiarid climatic conditions (Dutta and Suttner 1986; Mozley 1989; Garcia et al. 1998; Morad 1998; Morad et al. 1998; Morad et al. 2000; Morad et al. 2010). During mesodiagenesis, earlier formed eodiagenetic carbonate cements transform to more stable forms (Mazzullo 1992), while some undergo dissolution and are re-precipitated as ferroan carbonates (ferroan calcite, ferroan dolomite, ankerite, and siderite) with more coarsely crystalline fabric (poikilotopic) than early formed equivalents (Saigal and Bjørlykke 1987; Girard 1998). The presence of small volumes of early carbonate cements in sandstones can inhibit mechanical compaction by strengthening the grain framework, and thus preserve porosity (Burley 1984; Souza et al. 1995; Salem et al. 2005; Mahmic et al. 2018; Worden et al. 2018a; Busch et al. 2022). On the other hand, larger volumes of early carbonate cements are typically harmful to reservoir properties, unless leached during the later stages of burial diagenesis (Amthor and Okkerman 1998; Ulmer-Scholle et al. 2014). Both eodiagenetic and mesodiagenetic carbonate cements locally fill pores and preferentially occlude pore throats, which consequently result in reservoir heterogeneity (Worden and Burley 2003; Morad et al. 2010).

1.4.6.3 Clay minerals

The presence of authigenic clay minerals in sandstones can have a major impact on reservoir quality and other rock properties such as density, natural radioactivity, electrical conductivity, and water saturation of oil reservoirs (Worden and Morad 2003). From the diagenetic point of view, clay minerals can be subdivided into two types: eodiagenetic and mesodiagenetic clay minerals. Eodiagenetic (or detrital) clays are formed at near surface conditions and during shallow burial. Their formation occurs under a wide range of conditions (e.g., temperature, pressure, and pore water chemistry) and is controlled by depositional facies, detrital composition, and climatic conditions. They are generally stable or metastable and are usually transformed into more stable forms as temperature (the principal control) increases and pore water chemistry changes. The most common eodiagenetic clay minerals in sandstones are kaolinite, smectite, glauconite and berthierine. Mesodiagenetic clay minerals, on the other hand, are formed during burial diagenesis under a wide range of physical and chemical conditions different to those of eodiagenesis. During mesodiagenesis, earlier formed eodiagenetic clays are transformed, due to increasing temperature, into more stable clay minerals such as dickite, illite and chlorite (Worden and Morad 2003). Common pathways for the transformation of clay minerals during burial diagenesis are shown in figure 1.4. During burial, mesodiagenesis commonly results in the development of a simplified clay mineral assemblage that is commonly dominated by illite and chlorite (Worden et al. 2018a).

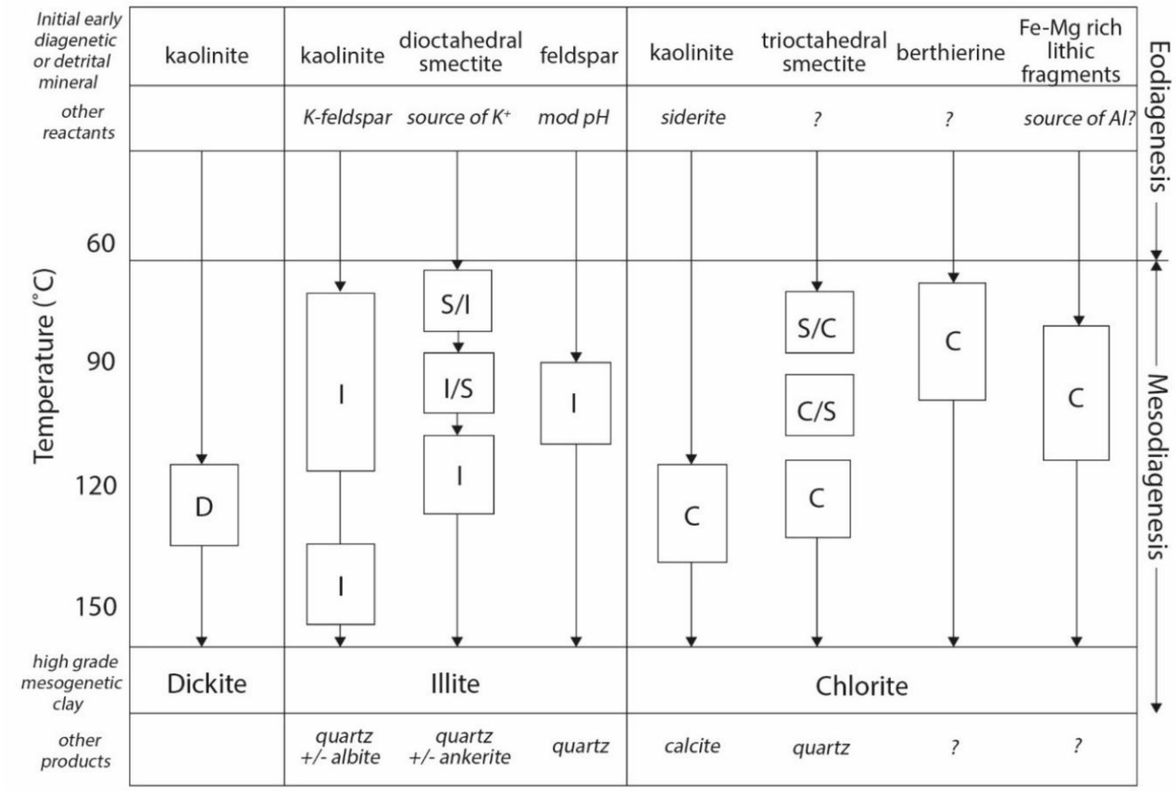

Figure 1.4. Common mesodiagenetic pathways for clay minerals in sandstones, where D is dickite, S is smectite, I is illite and C is chlorite. Randomly interstratified mixed-layer clay minerals are named according to the types of layers involved, with the most abundant layer type listed first: S/I is mixed-layer smectite-illite dominated by smectite; I/S is the same mineral mixture dominated by illite. The same naming rules apply for interlayered smectite-chlorite. High grade diagenesis leads to dickite, illite, and chlorite minerals in sandstones. Kaolinite forms predominantly during eodiagenesis and can be cannibalized to form dickite, illite or even chlorite during mesodiagenesis. Illite forms by at least three main routes during mesodiagenesis. Although it can be a detrital clay (following incomplete weathering), it does not form during eodiagenesis. Chlorite also seems to unlikely form during eodiagenesis and forms by at least four main pathways (after Worden and Morad, 2003).

1.4.6.4 Smectite

Smectites are 2:1 layered silicates in which one octahedral layer is sandwiched between two tetrahedral layers. They are commonly found in sandstones and have the general formular: $(0.5Ca,Na)_{0.7}(Al,Mg,Fe)_4(Si,Al)_8O_{20}(OH)_4$. nH_2O. Smectites can be classified into two types: dioctahedral and trioctahedral smectites. They are dioctahedral smectites when the octahedral sites are occupied mainly by trivalent cations (e.g., Al^{3+} or Fe^{3+}) and trioctahedral smectites when all or most octahedral units are occupied by divalent cations (e.g., Fe^{2+}, Mg^{2+}, Ca^{2+}) (Mckinley et al. 2003; Worden and Morad 2003). The type, occurrence, and abundance of smectite in sandstones is controlled by several factors. These include provenance, climate, depositional environment, and diagenesis. In terms of provenance, dioctahedral smectites form predominantly from the weathering of acid and intermediate igneous rocks and more silicic metamorphic rocks while trioctahedral smectites tend to form from more mafic-rich basaltic volcanics and volcaniclastics, metabasites, impure marbles, metapelites, mudstones and lithic sandstones (Mckinley et al. 2003). Climate exerts a major influence on smectite occurrence. Smectite is preferentially formed during weathering under arid climatic conditions. Intense weathering requires the loss of a significant proportion of cations by percolating or flowing fresh water. However, under arid conditions, there is minimal amount of percolating or flowing fresh water, and therefore limited ability to lose cations. These in turn, result in mineralogically immature sediment that enhances the retention of smectite in the resulting rock (Mckinley et al. 2003). Detrital smectite can be found in any depositional environment (such as fluvial, aeolian, lacustrine and marine), but rarely found in beach sands due to the continuous high energy (wave action/tidal currents) that result in the winnowing of fine-grained clays from the sand and silt-grade material in such environments. Sands deposited in fluvial and lacustrine environments tend to have more smectite than those deposited further basinward (e.g., shallow-marine environments). This is because fluvial and lacustrine sands, and the correlative clay minerals in the mud layers tend to be more mineralogically immature, reflecting the lesser degree of reworking and chemical weathering. Smectites are predominantly formed during eodiagenesis under oxidizing conditions in alkaline waters. Due to their finer-grained size, they are usually not co-deposited with non-marine or shallow marine sand-grade sediment but are incorporated by mechanical infiltration, bioturbation, and soft-sediment deformation. Smectite is generally unstable and commonly transforms to illite or chlorite via mixed-clay intermediates during progressive burial or diagenesis (Fig. 1.4). Grain-coating smectite usually occurs as clay particles oriented parallel to the grain surfaces, with curled edges (Matlack et al. 1989; Pittman et al. 1992; Mckinley et al. 2003; Worden and Morad 2003). Pittman et al. (1992), through hydrothermal reactor experiments identified four stages of development for smectite clay coats (Fig. 1.5 and 1.6). The growth sequence starts with the development of clay wisps (stage 1), followed by clay platelets forming a "root zone" (stage 2), then polygonal boxwork (stage 3) and finally denser

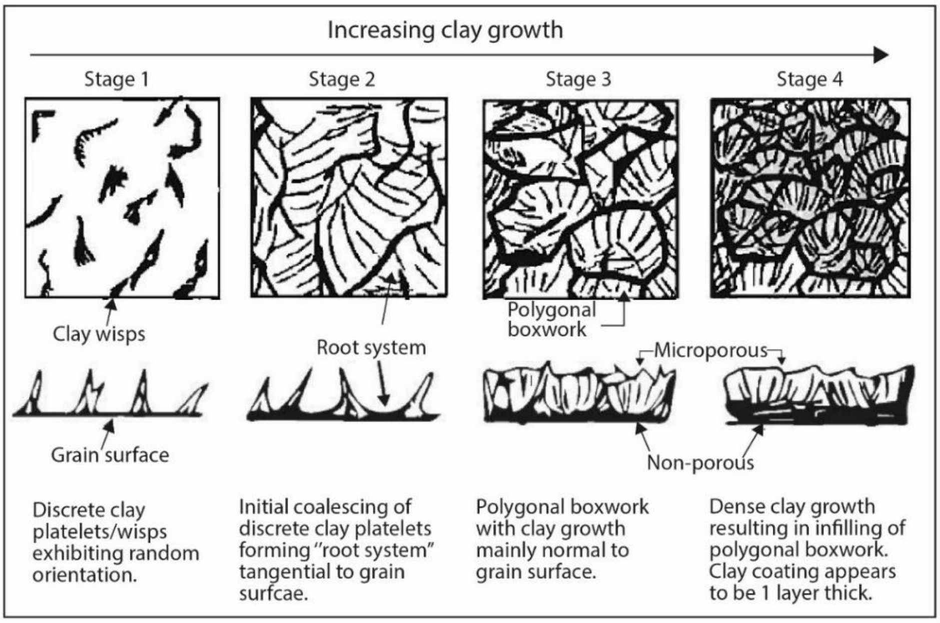

Figure 1.5. Schematic diagram of the four stages of smectite clay coat development from hydrothermal reactor experiments (modified after Pittman et al. 1992).

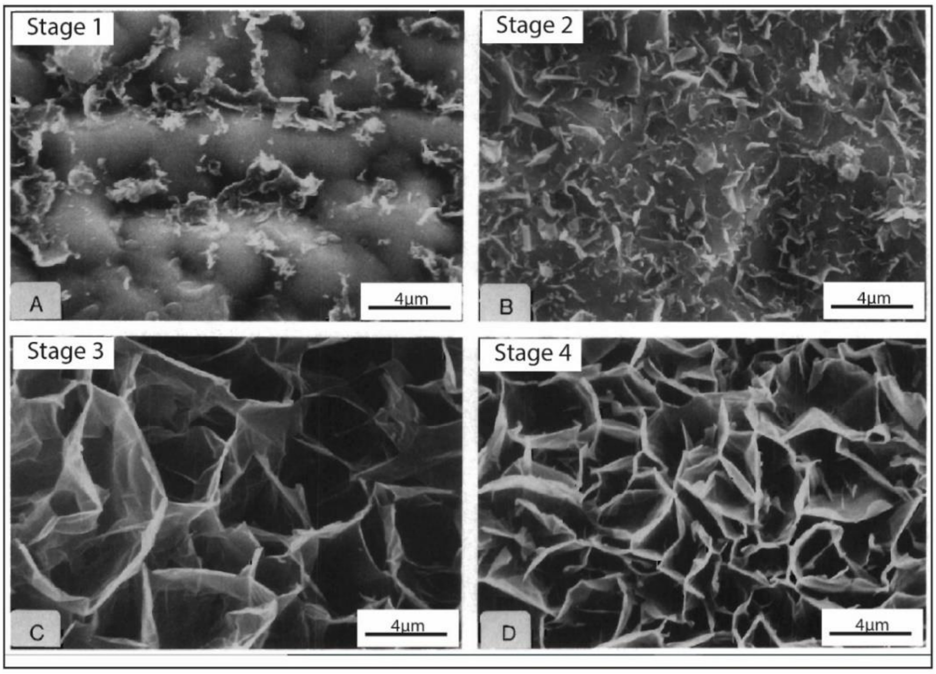

Figure 1.6. SEM images of the four growth stages of smectite clay coats from hydrothermal reactor experiments (modified after Pittman et al. 1992).

polygonal boxwork (stage 4). The experiments further revealed that the flatly attached, root zone is especially effective at blocking the nucleation of quartz overgrowths on detrital quartz grains.

1.4.6.5 Mixed-layer clay minerals

Mixed-layer clay minerals are composed of interstratified layers of different clay minerals in a single structure (Środoń 1999). According to Środoń (1999), they are intermediate products of reactions involving pure end-member clays and are formed by two mechanisms: (1) solid state transformation and (2) dissolution/crystallization. Mixed-layer clays can occur as grain-coats and also as pore-filling clays in sandstones. Various types of mixed-layer clay minerals have been reported in the literature. Examples of these are: chlorite/illite (Humphreys et al. 1994; Storvoll et al. 2002; Ajdukiewicz et al. 2010; Chen et al. 2011), illite/smectite (Kazerouni et al. 2013; Tang et al. 2018; Miruo et al. 2020; Sayem et al. 2022), smectite/chlorite, chlorite/smectite (Worden and Morad 2003; Chen et al. 2011; Beaufort et al. 2015), illite/kaolinite (Han et al. 2014; Bauluz et al. 2021), chlorite/kaolinite, dickite/kaolinite and kaolinite/smectite. Most mixed-layer clay minerals contain smectite as a swelling component (e.g., illite/smectite and chlorite/smectite). During progressive burial diagenesis, illite/smectite (I/S) becomes illite-rich while chlorite/smectite (C/S) becomes chlorite-rich (Worden and Morad 2003). Mixed-layer clay minerals play an important role in controlling reservoir quality. Also, because they are products of reactions involving discrete, end-member clay minerals, they are commonly used as tools for assessing maximum burial and thermal evolution in sedimentary basins (McIntosh et al. 2021).

1.4.6.6 Illite

Illite is a potassium-rich dioctahedral 2:1 clay mineral with layers consisting of one octahedral sheet sandwiched between two tetrahedral sheets. Illite is structurally related to muscovite since their principal interlayer cation is potassium; however, it differs from muscovite chemically in having more silica and less potassium, and physically in having clay size (<2μm) particles. The general formula for illite is: $K_{1.5-1.0}Al_4[Si_{6.5-7.0}Al_{1.5-1.0}O_{20}](OH)4$ (Deer et al. 2013). Illite is one of the most common authigenic clay minerals in sandstone reservoirs. It is primarily a grain-coating and pore-bridging clay, which in some instances, completely fills pores (Fig. 1.7). Illite often displays a fibrous morphology (Fig. 1.7c-f) which has a detrimental effect on the porosity and permeability of sandstone reservoirs and hydrocarbon production (Güven 2001; Wilkinson and Haszeldine 2002; Lander and Bonnell 2010). Normally, illite fibres grow as separate thin strands and extend farther into the pore spaces of the host sandstone than other authigenic clays. As a result, they greatly enhance flow-path tortuosity and decrease permeability (Lander and Bonnell 2010). Authigenic illite develops from and through a variety of precursors and pathways; these include alteration of kaolinite to illite, dickite to illite, muscovite to illite, K-feldspar to illite and dioctahedral smectite to illite (Fig. 1.4) (Storvoll et al. 2002; Mckinley et al. 2003; Worden and Morad 2003). The illitization of smectite normally begins around 70°C (Abercrombie et al. 1994; Storvoll et al. 2002), but this process has also been observed at very low temperatures of 50°C and at high temperatures around 120°C for very slow or rapid burial conditions, respectively (Abercrombie et al. 1994).

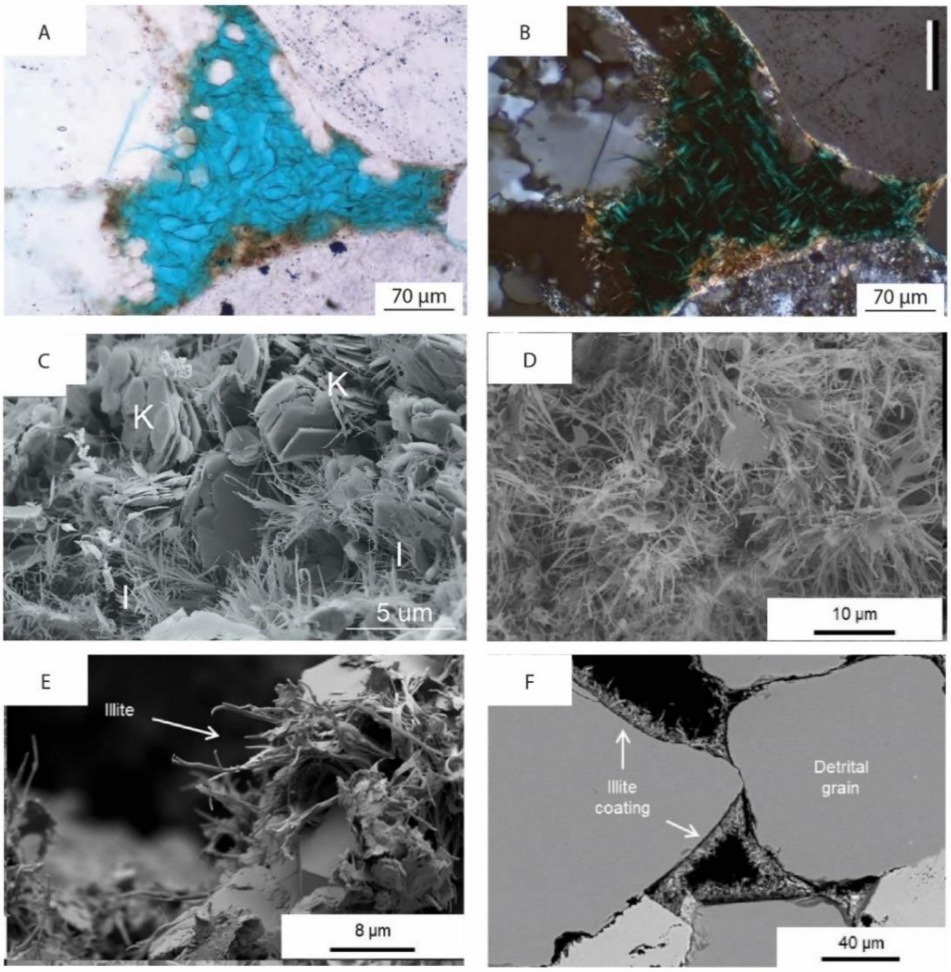

Figure 1.7. (A-B) Thin section photomicrographs of pore-filling illite under plane polarized light and cross polar (Ulmer-Scholle et al. 2014). (C) SEM image of fibrous/hairy authigenic illite based on kaolinite (Tang et al. 2018). (D) SEM image of fibrous illite. (E) Long illite fibres filling pore space. (F) Cross section of illite-coated quartz grains (Stricker 2016).

1.4.6.7 Berthierine

Berthierine is an aluminous Fe^{2+}-rich 1:1 clay belonging to the kaolinite-serpentine series of minerals. Berthierine forms during eodiagenesis and occurs as small (<5 μm), lath-shaped grain coats (fringes or tangentially arranged), pellets, ooids and void fillings or as replacements of detrital grains (Odin and Matter 1981; Worden and Morad 2003). It is commonly found in marginal marine sediments such as deltaic and estuarine deposits and Fe-rich sedimentary rocks (Hornibrook and Longstaffe 1996). The predominance of ferrous iron in berthierine suggests that it formed under strongly reducing conditions. Authigenesis of berthierine occurs prior to the burial depths in sediments where bacterial sulphate reduction dominates, and where Fe^{2+} becomes incorporated preferentially in sulphide minerals (Worden and Morad 2003). Berthierine authigenesis is favoured in volcanogenic sediments deposited in estuarine-coastal-plain environments (Jeans et al. 2000) During mesodiagenesis, berthierine is transformed into Fe-chlorite, which in turn helps to preserve reservoir quality by inhibiting quartz cementation and possibly because of its tendency to be oil wet (Morad et al. 2010). Berthierine and chlorite have similar chemical composition and this has been confirmed through experimental studies (Aagaard et al. 2000). Temperature plays an important role in the rate of authigenic chlorite precipitation. Berthierine to chlorite transformation has been proposed to occur at temperatures greater than 60°C (Jahren and Aagaard 1989; Aagaard et al. 2000; Worden and Morad 2003). However, recent hydrothermal experiments on berthierine-bearing sandstone samples from the Lower Jurassic Cook Formation, Norway revealed that the main temperature window of berthierine to chlorite conversion lies between 100°C and 175°C, with chlorite becoming the dominant phase at about 150°C (Charlaftis et al. 2021).

1.4.6.8 Kaolinite

Kaolinite is an aluminosilicate clay mineral with a book-like or vermicular habit. It is typically formed during eodiagenesis under humid climatic conditions in continental sediments through the interaction of low-pH groundwaters with aluminosilicate minerals such as feldspars, mica, rock fragments, mud intraclasts and heavy minerals (Emery et al. 1990). The amount and distribution pattern of kaolinite is controlled by various factors; these include the amount of unstable detrital silicates, annual precipitation, hydraulic conductivity, and rate of fluid flow in the sand body. During eodiagenesis, grain dissolution is most common in permeable sediments, such as channel sand deposits. Thus, under humid conditions, the production of eodiagenetic kaolinite is facilitated due to the availability of greater amounts of meteoric waters (Worden and Morad 2003). Kaolinite typically forms patchy, pore-filling cement and acts as precursors for authigenic clays. With increasing burial depth and temperatures, kaolinite transforms into dickite, illite or chlorite (Fig. 1.4 and 1.8). Dickite, a high temperature equivalent of kaolinite forms at temperatures between 70°C and 130°C. Compared to kaolinite, dickite is more stable and less susceptible to illitization due to its better ordered crystal structure (Fig. 1.8) (Morad et al. 1994).

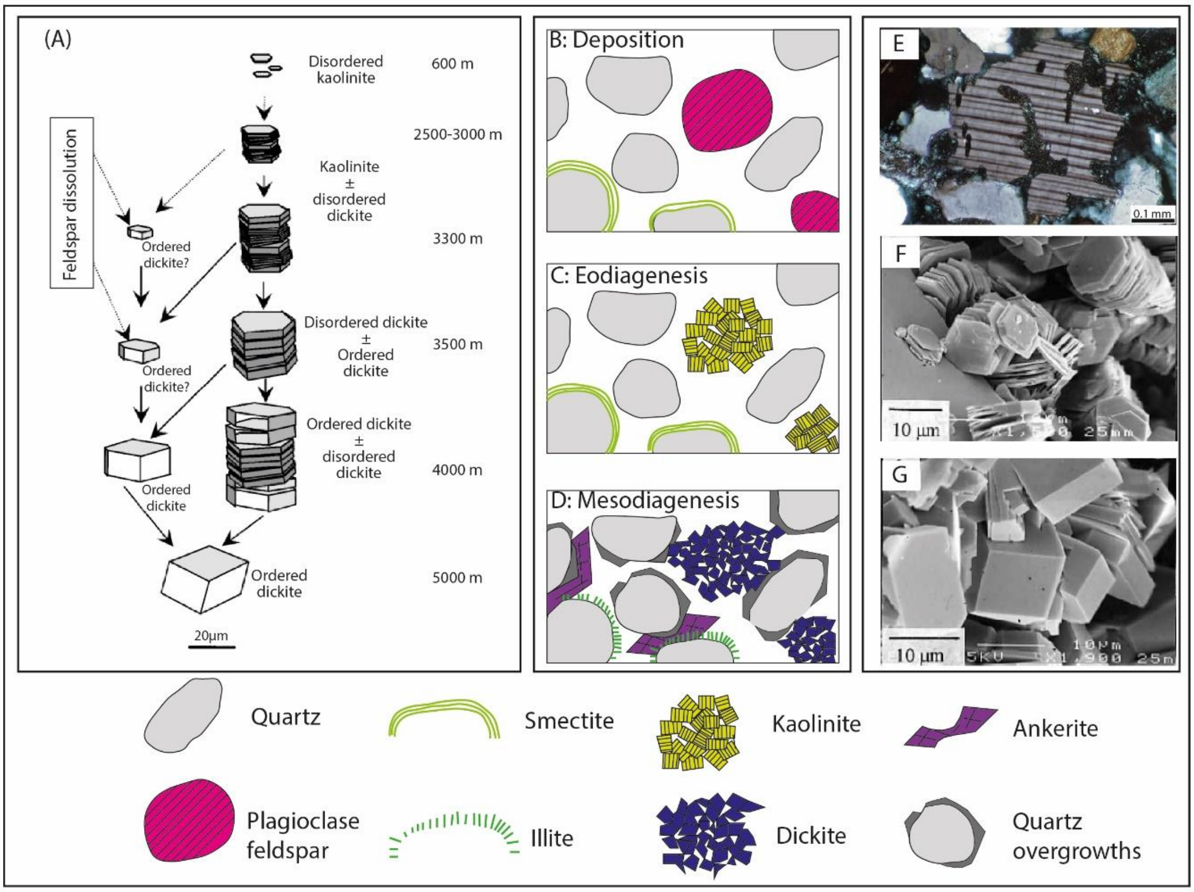

Figure 1.8. (A) Schematic model of kaolinite-to-dickite reaction involving both morphological and structural changes due to water-rock interaction for increasing burial depths of sandstone reservoirs. Arrows indicate the transfer of matter due to material redistribution involved in the dissolution-crystallization processes (Beaufort et al. 1998). (B-D) Schematic representation of the development of kaolinite from feldspar and dickite from kaolinite (modified after Worden and Morad 2003). (E) A plagioclase feldspar grain (cross polar). (F) SEM image of kaolinite with a book-like or vermicular habit. (G) SEM image of blocky and well-ordered dickite buried at 5000 m (Beaufort et al. 1998).

Kaolinite to dickite transformation is kinetically controlled and usually more prevalent in high permeability sandstones than in low permeability sandstones (Cassagnabere 1998). This transformation is possibly assisted by an increase in acidity of formation waters or a decrease in aK^+/aH^+ ratio. The origin of the fluids involved in kaolinite to dickite transformation has been discussed by some authors (Lanson et al. 2002). Given the substantial depths at which dickite forms, kaolinite to dickite transformation is probably caused by the invasion by organic acids or source-rock-derived CO_2, rather than meteoric-water incursion (Morad et al. 1994; Lanson et al. 2002; Worden and Morad 2003).

1.4.6.9 Chlorite

Chlorite (general formula: $(Mg,Al,Fe)_{12}$ $[(Si,Al)_8O_{20}](OH)_{16}$) is the most common authigenic clay mineral in clastic reservoirs. It is a 2:1:1 clay mineral with crystal structure is composed of tetrahedral-octahedral-tetrahedral layers interlayered with an octahedral sheet composed of cations and hydroxyls. Due to the variability in the chemical composition of chlorite minerals, several classifications exist (Bayliss 1975; Hillier 1994; Deer et al. 2013). However, the most common ones are the Fe-rich types (chamosite) and Mg-rich types (clinochlore) (Hillier 1994; Dowey et al. 2012). In sandstones, chlorite can be either detrital or authigenic. Detrital chlorite includes mineral grains, components of lithic grains, matrix and detrital grain coats. Authigenic chlorite can occur as grain-coats (Fig. 1.9), pore-filling, grain-replacing or as a replacement product of detrital or earlier authigenic clay (Worden et al. 2020). Grain-coating chlorite has been shown to be effective in inhibiting the growth of quartz cements, and preserving primary intergranular porosity in amounts that are anomalously high for the depths to which the sandstones are buried (Heald and Larese 1974; Pittman et al. 1992; Ehrenberg 1993; Berger et al. 2009; Ajdukiewicz et al. 2010; Stricker and Jones 2016; Stricker et al. 2016b; Dutton et al. 2018). The process of formation of chlorite and grain-coating chlorite in sandstone reservoirs has previously been investigated and reviewed (Pittman et al. 1992; Ehrenberg 1993; Hillier 1994; Bloch et al. 2002; Anjos et al. 2003; Worden and Morad 2003; Worden and Burley 2003; Dowey et al. 2012; Bahlis and De Ros 2013; Cao et al. 2018; Worden et al. 2020). These studies revealed that authigenic chlorite can be formed by two processes: (1) the diagenetic transformation of precursor clay minerals and (2) dissolution of detrital grains. The main clay mineral precursors for authigenic chlorite are berthierine, smectite and kaolinite (Aagaard et al. 2000; Worden and Morad 2003; Dowey et al. 2012; Haile et al. 2015). The dissolution of Fe-and Mg-rich detrital grains, volcanic rock fragments (VRFs) and mud intraclasts during diagenesis can also lead to the development of authigenic chlorite. Several studies have shown that a positive relationship exists between chlorite coatings and detrital grains (Thomson 1979; Thomson and Stancliffe 1990). For example, a study on the Tuscaloosa Formation, Gulf Coast, USA by Thomson (1979) identified a positive relationship between chlorite coatings and VRFs. Thompson and Stancliffe (1990) claimed that VRFs provided the magnesium for chlorite in the Norphlet Formation of the Central Graben in the UK North Sea. Other examples where dissolution of detrital grans may have played an important role in chlorite formation are the

Lower Clair Group (Pay et al. 2000), Taranaki Basin, New Zealand (Martin et al. 1994), Santos Basin, Brazil (Anjos et al. 2003). Chlorite-coats can be found in all depositional environments; they are most prevalent in estuarine and deltaic environments, but they have also been found in turbidites and fluvial-alluvial deposits (Dowey et al. 2012; Worden et al. 2020). Fe-rich chlorites occur predominantly in coastal environments, while mixed Fe- and Mg-rich chlorites are mostly found in marine and terrestrial environments (Dowey et al. 2012). According to Dowey et al. (2012), rivers play an important role in the formation of chlorite because they supply the precursor material that is used to generate chlorite during mesodiagenesis. Common pathways for chlorite formation during mesodiagenesis are shown in figure 1.4.

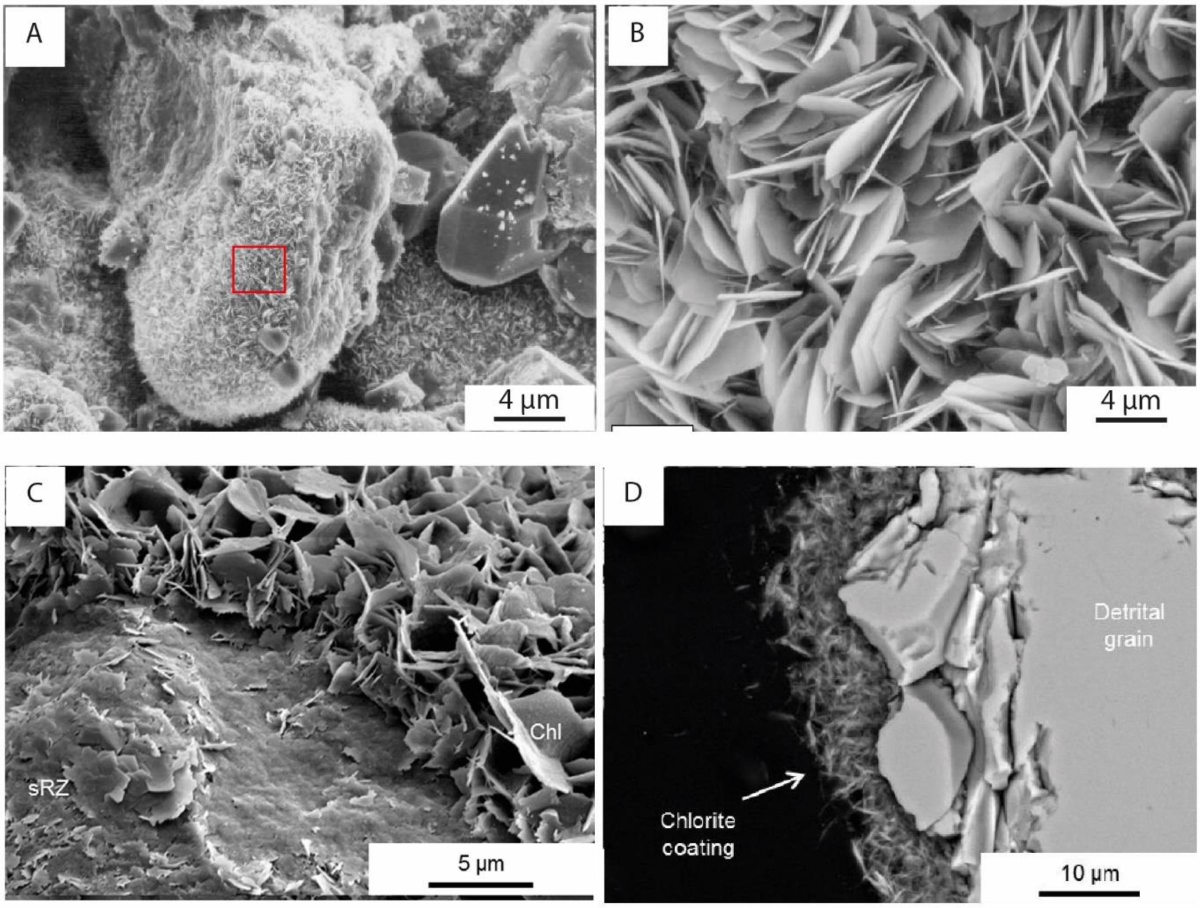

Figure 1.9. SEM photomicrographs of grain-coating authigenic chlorite. (A) Low magnification view revealing near continuous chlorite coats on detrital quartz grains. (B) Higher magnification view corresponding to the box in panel A ((Taylor et al. 2010). (C) Well developed authigenic chlorite (chl) coatings with a sutured root zone (sRZ) ((Stricker et al. 2016b). (D) A cross section of a well-developed chlorite coating with crystals oriented randomly (Stricker 2016).

1.4.7 Dissolution

Dissolution of framework grains and cements commonly creates secondary porosity during burial diagenesis, which in turn improves reservoir quality (Schmidt and McDonald 1979; Ehrenberg and Jakobsen 2001; Boggs 2006). Dissolution can occur during any stage of diagenesis. The two principal factors governing the process are: detrital composition and the chemistry of the pore waters. During diagenesis, the mineral grains within the sediments are subjected to varied temperature and pressure conditions, and water chemistries different to those under which they were formed, and this results in their dissolution. The most common detrital minerals that commonly undergo dissolution are feldspars (whether as isolated grains or as constituents of rock fragments), carbonate cements and evaporites (Ulmer-Scholle et al. 2014). Dissolution of quartz and silica (Bjorkum 1996), siderite and dolomite (Burley and Kantorowicz 1986) and zeolites (Tang et al. 1997; Bernet and Gaupp 2005) may be locally important. The anomalously high porosity in some oil fields has been attributed to secondary porosity (Schmidt and McDonald 1979; Surdam et al. 1984; Burley and Kantorowicz 1986; Harris 1989; Wilkinson et al. 1997; Wilkinson et al. 2014; Nguyen et al. 2018; Gordon et al. 2022). Furthermore, the volume of secondary porosity in many sedimentary basin sandstones is reportedly equal to or greater than that of primary porosity (Schmidt and McDonald 1979). However, the supposedly important contribution of secondary porosity to the total porosity in many deeply buried reservoirs has generated diverse views in the literature. This controversy is focused on whether there is an open or closed geochemical system for the development of secondary porosity during burial diagenesis. While some workers (Gluyas and Coleman 1992; Land 1997; Land and Milliken 2000; Day-Stirrat et al. 2010, 2011) are supportive of an open geochemical system during burial diagenesis, others support the hypothesis that deeply buried sediments represent a closed geochemical system, and not an open system (Bjørlykke and Jahren 2012; Yuan et al. 2015; Lai et al. 2016).

1.4.8 Recrystallization

Recrystallization refers to the in-situ formation of new crystal structures (size and shape) without any change in the mineralogy or chemical composition (Nichols 2009). It commonly occurs in carbonates and clay minerals, such as formation of low magnesium calcite from high magnesium calcite, dickite from kaolinite, and illite from Kaolinite and smectite. This process is completely different from replacement whereby an authigenic mineral takes the place of another former mineral through a dissolution-precipitation process. The process of recrystallization requires an aqueous medium and is always preceded by the dissolution of the precursor mineral, followed by precipitation (Worden and Burley 2003). Other essential controlling factors are temperature and pressure. As temperature and pressure increases with burial depth, micro-granular and fine minerals transform into coarse textures, while retaining their chemical composition. Continuous recrystallization generally leads to an increase in crystal grain size, which consequently reduces porosity and permeability (Baiyegunhi et al. 2017).

1.5 Other reservoir quality controlling factors

1.5.1 Overpressure

Overpressure (also referred to as geopressure) occurs when pore fluid pressure exceeds the calculated hydrostatic gradient at a specific depth (Osborne and Swarbrick 1997). Several mechanisms have been put forward for the generation of overpressure in sedimentary basins. These mechanisms are divided into four categories: (1) increase in compressive stress (pore volume reduction) initiated by disequilibrium compaction and tectonic compression; (2) fluid volume change generated by temperature increase (i.e., aquathermal pressuring), diagenetic reactions (e.g., clay mineral transformations), hydrocarbon generation and cracking to gas; (3) lateral transfer and drainage of pore fluid pressure and (4) fluid movement and other processes such as buoyancy and osmosis (Osborne and Swarbrick 1997; Yardley and Swarbrick 2000; O'Neill et al. 2018).

Several studies have shown that the presence of overpressure in reservoir sandstones during burial can inhibit mechanical compaction and pressure solution, retard quartz cementation, and help to preserve porosity (Osborne and Swarbrick 1999; Nguyen et al. 2013; Grant et al. 2014; Stricker et al. 2016a; Stricker et al. 2016b). Studies by Osborne and Swarbrick (1999) on the deeply buried Fulmar reservoirs in the UK Central North Sea concluded that the anomalously high porosity characterizing these reservoirs is partly due to overpressure, which is mostly generated by disequilibrium compaction. Other workers (e.g., Nguyen et al., 2013; Grant et al., 2014; Stricker et al., 2016a; and Stricker et al., 2016b) on UK Central North Sea deeply buried sandstones (Triassic Skagerrak Formation in particular) also reported that overpressure amidst other several factors, is responsible for the anomalously high porosity in these sandstones. According to these workers, the effectiveness of overpressure in preserving porosity is dependent on the timing of its generation during burial, and not just its magnitude. For overpressure to effectively preserve porosity to great depth, it must be generated early enough after sediment burial and maintained during progressive burial. Conversely, late development of overpressure at depth can no longer preserve porosity because most of the porosity would have been lost to mechanical compaction.

The role of vertical effective stress (VES) in reservoir quality evolution has been documented in the literature (Stricker et al. 2016a; Oye et al. 2018). Vertical effective stress is the pressure exerted on a layer of rock by the weight of the overlying formations and is the main driver of mechanical compaction and pressure solution (chemical compaction) and in turn porosity loss during sediment burial. High vertical effective stress increases the rate of compaction and in turn, the rate of quartz overgrowth precipitation via pressure solution (Osborne and Swarbrick 1999). On the other hand, low vertical effective stress arising from overpressure development inhibits mechanical compaction and pressure solution and helps preserve porosity during deep burial (Osborne and Swarbrick 1999; Sheldon et al. 2003; Stricker et al. 2016a).

1.5.2 Early emplacement of oil

The role of early oil emplacement in the prevention of quartz cementation and preservation of porosity has been a subject of controversy in the literature for many decades. While some studies claim that early oil emplacement can prevent quartz cementation (Gluyas et al. 1993; Marchand et al. 2000; Marchand et al. 2001; Marchand et al. 2002; Wilkinson and Haszeldine 2011; Sathar et al. 2012; Worden et al. 2018b), others claim that early oil emplacement has no effect on quartz cementation and that quartz cement precipitation may proceed even after oil emplacement (Walderhaug 1990, 1994a, 1994b; Aase and Walderhaug 2005; Bonnell et al. 2006a; Bonnell et al. 2006b; Molenaar et al. 2008; Taylor et al. 2010; Maast et al. 2011). Aase and Walderhaug (2005) and Bonnell et al. (2006a, b), using datasets from the Miller field, North Sea, studied the effect of pore fluid on quartz cementation by measuring volume of quartz cement in sandstone samples taken from the oil leg and water leg. They reported that samples from both oil and water legs showed similar average volume of quartz cement. Based on their findings, they concluded that the presence of oil in sandstone reservoirs does not in any way inhibit quartz cementation. Taylor et al. (2010) analysed the same data and found that quartz cementation occurs in both the oil and water legs. They concluded that there is no relationship between pore fluid type and quartz cement volume, and that the popular belief that hydrocarbon pore fluids preserve porosity by inhibiting the growth of quartz cements does not represent a viable predictive model.

Many studies suggest that the inhibition of quartz cementation by oil emplacement is a function of reservoir wettability (Barclay and Worden 2000; Maast et al. 2011). Wettability describes the preference of a rock to be in contact with one type of fluid over another (Worden and Morad 2003). The wetting state of a rock containing two immiscible fluids dictates which fluid is in contact with grain surfaces. For example, a water-wet petroleum reservoir is one where sands grains are coated with water, and where petroleum finds it difficult to come into contact with the grain surfaces, and vice versa (cf. Worden and Morad 2003). The works of Barclay and Worden (2000) and Maast et al. (2011) revealed that oil emplacement is only effective at inhibiting quartz cementation when the reservoirs are oil-wet and ineffective when water-wet. A more recent study of the role of petroleum emplacement in the inhibition of quartz cementation and preservation of porosity in deeply buried sandstones was conducted by Xia et al. (2020) on reservoirs from the Kessog Field in the Central North Sea. They concluded that the high porosity in the Kessog Field is mainly influenced by petroleum emplacement which inhibited quartz cementation. The impact of other factors such as overpressure, grain coats, and secondary porosity were reported to be insignificant. In general, the role of oil emplacement in porosity preservation and quartz cement inhibition remains controversial, hence the need for further and detailed studies.

1.5.3 Structural deformation

Structural features such as fractures, faults, deformation bands and disaggregation bands, can have an impact (positive or negative) on reservoir quality and even cause significant reservoir heterogeneity. (Lianbo and Xiang-Yang 2009; Morad et al. 2010; Stricker et al. 2018; Worden et al. 2018a; Awdal et al. 2020; Alkhasli et al. 2022). For instance, open fractures or faults can enhance porosity and permeability while mineral-filled fractures reduce porosity and permeability and form flow barriers in an aquifer or a hydrocarbon field. In highly porous sandstones and sediments, the most common stress-related structural features are strain localization features known as deformation bands. Deformation bands are strictly restricted to porous granular rocks. They typically occur as small or micro faults and often serve as precursors for larger faults in sedimentary basins (Aydin 1978; Antonellini et al. 1994; Antonellini and Aydin 1995; Fossen and Hesthammer 1997; Du Bernard et al. 2002; Aydin et al. 2006; Fossen and Bale 2007; Fossen et al. 2007; Stricker et al. 2018; Awdal et al. 2020). According to Du Bernard et al. (2002) and Stricker et al. (2018), disaggregation bands and fractures are ideal pathways for meteoric fluids and therefore can enhance the infiltration of clay minerals, which can subsequently lead to porosity reduction in sandstones. The effects of structural deformation on reservoir quality are not the focus of this research, and therefore will not be discussed further.

1.6 Clay mineral grain coats and reservoir quality

Clay minerals are commonly thought to be detrimental to sandstone reservoir quality due to their ability to plug pore throats and promote chemical compaction (Worden and Morad 2003). However, not all clay minerals are detrimental to sandstone reservoir quality. Several studies have reported that the presence of clay minerals in form of clay coats (Fig. 1.9) can preserve reservoir quality in deeply buried sandstones by inhibiting quartz cementation (Heald and Larese 1974; Pittman et al. 1992; Ehrenberg 1993; Worden and Morad 2000; Bloch et al. 2002; Berger et al. 2009; Ajdukiewicz and Lander 2010; Taylor et al. 2010; Ajdukiewicz and Larese 2012; Nguyen et al. 2013; Stricker and Jones 2016; Stricker et al. 2016b; Tang et al. 2018; Worden et al. 2020). Clay coats on sand grains could be formed either by allogenic processes (detrital clay coats), or authigenic processes (diagenetic clay coats) (Pittman et al. 1992; Wilson 1992). Detrital clay coats are commonly formed before or immediately after deposition through multiple processes such as inherited clay coats (Wilson 1992), mechanical infiltration of clays (Matlack et al. 1989; Houseknecht and Ross Jr 1992; Worden and Morad 2003; Ajdukiewicz and Larese 2012), flocculation of mud (Worden and Morad 2003), bioturbation (Needham et al. 2005; Worden et al. 2006) and attachment through cohesive biofilms (Wooldridge et al. 2017a). Diagenetic clay coats, on the other hand, form by the thermally driven recrystallization of low temperature precursor detrital clay coats, or via *in situ* growth from authigenic alteration of precursor and early diagenetic minerals (Wilson and Pittman 1977; Wilson 1982; Worden and Morad 2003; Ajdukiewicz and Larese 2012; Ulmer-Scholle et al. 2014; Griffiths et al. 2018). The most common and widely reported clay mineral coats that effectively preserve porosity in deeply buried sandstone reservoirs is chlorite. Studies have shown that chlorite is more effective at retarding quartz cementation than illite (Pittman et al. 1992; Dowey et al. 2012; Verhagen et al. 2020; Worden et al. 2020). Although illite coats may retard quartz cementation, it could also enhance pressure solution when under stress along quartz grain contacts (Heald and Larese 1974; Pittman et al. 1992; Bjorkum 1996; Harris 2006; Ajdukiewicz et al. 2010; Busch et al. 2018).

Numerous studies have demonstrated that the ability of clay coats to effectively inhibit quartz cementation and preserve porosity is a function of its completeness (i.e., extent of coverage) (Heald and Larese 1974; Ehrenberg 1993; Walderhaug 1996; Bloch et al. 2002; Billault et al. 2003; Lander et al. 2008; Ajdukiewicz and Larese 2012; Stricker and Jones 2016; Wooldridge et al. 2017b, 2019b; Busch 2020; Busch et al. 2020; Verhagen et al. 2020). However, the main controls on clay coat coverage remains controversial and thus requires further investigations.

The prediction of clay-coat enhanced reservoir quality in deeply buried sandstones requires an understanding of the origin, spatial distribution, and extent of coverage of detrital clay coats since they are precursors of diagenetic clay coats. In an attempt to develop predictive models for clay coat distribution in deeply buried sandstones, modern analogue studies have linked the distribution of detrital clay coated grains and extent of coverage of clay coats to sedimentary processes, depositionally-controlled parameters (e.g., grain size, sorting, skewness, and clay content) and biological processes (bioturbation) (Dowey et al. 2017; Wooldridge et al. 2017b; Griffiths et al. 2018; Virolle et al. 2019; Verhagen et al. 2020; Virolle et al. 2020). Core-based studies of deeply buried sandstones have also attributed the extent of clay coat coverage to depositional environment, grain size and clay volume (Bloch et al. 2002). It should be noted that the modern analogue approach for predicting clay coat distribution and deep sandstone reservoir quality is based on shallowly buried sediments that have not yet undergone burial diagenesis, casting doubts on its applicability in deeply buried settings.

1.7 Fluvial architecture, sand-body geometries and reservoir modelling

The development of fluvial reservoir models requires an accurate geological description of reservoir properties, particularly architecture, geometry, size, heterogeneity, and porosity and permeability distribution (Ramón and Cross 1997; Keogh et al. 2007). Different fluvial systems produce significant variations in sand-body architecture and geometry (Einsele 2000; Morad et al. 2010). In fluvial systems, sandstone bodies commonly occur as “ribbon” or “sheet” sandstones, and each of these can occur as isolated and/or amalgamated bodies (Fig. 1.10) (Friend et al. 1979; Hirst 1992; Gibling 2006; Pranter et al. 2014).

<u>Ribbon sandstones</u>: are formed when paleochannels become plugged with sediment prior to any major lateral migration of the original scour. They generally have a width/thickness ratio (W/T) of <15 with wings attached to each side of the central body (Fig. 1.10a). These wings are often referred to as the coarse, overbank deposits (levees) within the fluvial system (Hirst, 1992).

<u>Sheet sandstones:</u> unlike ribbon sandstones, sheet sandstones have width/thickness ratios >15 and oftentimes >100 (Fig. 1.10b-e). Depending on the form of basal erosion surface and the development of cutbanks, they may be subdivided into three main types: (1) channelised flow, (2) Poorly channelized flow, and (3) unconfined or overbank flow sheet sandstones.

- Channelised flow sheet sandstones are marked by well-developed cutbanks, indicating channelized flow deposition. The associated channels are laterally unstable, hence the reason for the deposition of these broader units (Fig. 1.10b-c).
- Poorly channelised flow sheet sandstones are flow deposits within a course with poorly defined banks. Due to the absence of clear cutbanks, the sandstone bodies wedge out laterally and internally display structureless to horizontally laminated beds (Fig. 1.10d).
- The unconfined, overbank flow sheet sandstones, on the other hand, generally lack cutbanks and have a large width relative to their thickness (Fig. 1.10e). Thicknesses could range from <0.5m to <1.5m. Types of unconfined flow sheet sandstones include channel levees, and distal parts of terminal and crevasse splays (Hirst, 1992; Gibling, 2006).

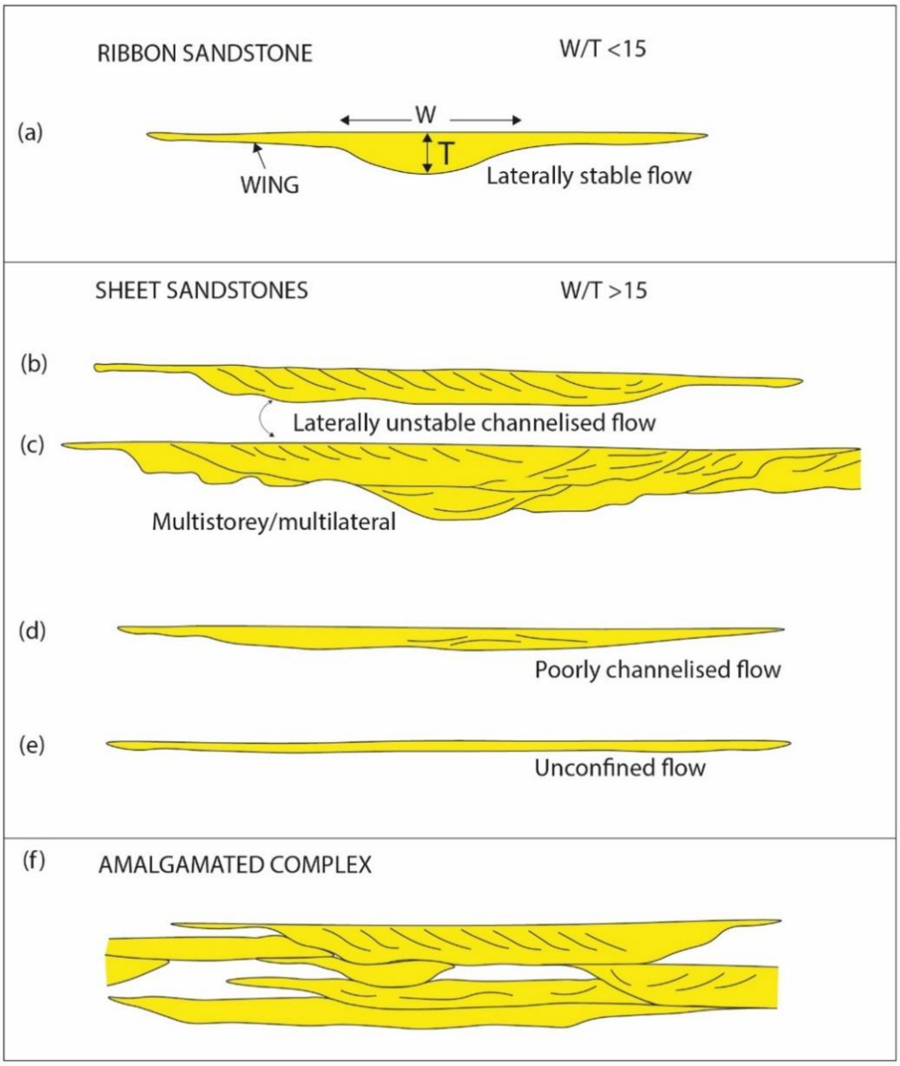

Figure 1.10. Schematic illustration of a range of sand body geometries. (a) ribbon sandstone; (b-c) channelised (or confined flow) sheet sandstones; (d) poorly channelised flow sheet sandstone; (e) unconfined flow sheet sandstone and (f) amalgamated sandstones.

Over the past decades, the architecture, geometry, size and internal sedimentology of fluvial systems/channel sandstone bodies have received much attention compared to their internal heterogeneity (in terms of porosity and permeability distribution). Sandstone bodies are not homogeneous with respect to porosity and permeability but contain internal heterogeneities and discontinuities. The internal variations may result from the inherent sediment variability of depositional processes, subsequent localisation of diagenetic effects, and deformation during burial (Alexander 1993). These heterogeneities influence fluid flow, sweep and recovery efficiencies (Morad et al. 2010). To appreciate the intricacies of fluid flow through sand bodies, it is necessary to understand the scale, density, distribution, geometry and interdependence of the various heterogeneities, so that their relative importance to hydrocarbon accumulation, distribution and recovery, as well as CO_2 injection can be assessed (Alexander 1993). In general, understanding and quantifying the characteristics and distribution of the reservoir rock properties is an evaluation step that needs to be performed before starting any reservoir model (Pacheco et al. 2019).

In reservoir modelling, outcrop analogues are commonly used to quantify heterogeneities and geometries of fluvial channels. This is owing to the inability of well data to fully capture the widespread spatial heterogeneities and facies variations resulting from the inherent geological complexity of fluvial systems. It is worth noting that while these observations from outcrop analogues help to describe two-dimensional fluvial channel shapes, particularly width-to-thickness ratios and stacking configurations, they often lack a description of the length scale or three-dimensional aspect due to outcrop limitations (Franzel 2022). Therefore, to build more accurate fluvial reservoir models, the use of outcrop analogues that provide the opportunity to quantify spatial heterogeneities in both cross-section and longitudinal/reach length profiles is crucial.

1.8 Summary

The accurate prediction of favourable reservoir quality in deep HPHT environments requires an understanding of the controls on reservoir quality. As stated earlier, sandstone reservoir quality is influenced by several combination of factors such as depositional facies, diagenesis (e.g., compaction, cementation and dissolution), overpressure, early emplacement of oil, and structural deformation. Of particular importance in this research is the role of depositional facies in controlling diagenesis, clay-coat authigenesis and overall reservoir quality of fluvial sandstone reservoirs. In sandstones buried to >3000 m and heated to >80-100°C, porosity can be at least 10% higher than expected due to the presence of abundant clay coats (Ehrenberg 1993; Worden et al. 2020). The ability of clay coats to effectively inhibit quartz cementation and preserve porosity is a function of its completeness (i.e., extent of coverage) and not just its presence (Heald and Larese 1974; Ehrenberg 1993; Walderhaug 1996; Bloch et al. 2002; Billault et al. 2003; Lander et al. 2008; Ajdukiewicz and Larese 2012; Stricker and Jones 2016; Wooldridge et al. 2017b, 2019b; Busch 2020; Busch et al. 2020; Verhagen et al. 2020; Worden et al. 2020). A small break in the continuity of clay coats on detrital quartz grains could result in quartz cementation and porosity reduction. The completeness of clay coats on detrital grain surfaces has been linked to facies-controlled parameters (such as grain size, sorting and clay fraction), however, these have been controversially discussed in the literature. For example, while some models attribute higher clay coat coverage to coarse grains, others claim a more complete coating coverage is found in finer grain size (Bloch et al. 2002; Ajdukiewicz et al. 2010; Shammari et al. 2011; Wooldridge et al. 2017b). It is worth noting that most of the studies on the controls on clay coat coverage have largely focused on aeolian, estuarine and marine deposits with little attention on fluvial deposits. Fluvial reservoirs serve as a major host for groundwater, hydrocarbon and geothermal resources, as well as potential sites for subsurface storage operations in many parts of the world. Thus, understanding the impact of facies, grain size and other facies-controlled parameters on clay coat coverage is essential for predicting clay-coat enhanced deep reservoir quality in fluvial sandstones.

In addition, the three-dimensional geometry of fluvial channel sand bodies and their internal sedimentology have received much attention in the literature (Miall 1985; Labourdette and Jones 2007; Mitten et al. 2020; Korus and Joeckel 2022). However, less attention has been given to the heterogeneity/petrographic variations within channel sand bodies and the different geometries (e.g., isolated ribbon and sheet sandstones) despite their strong impact on fluid flow. Understanding these heterogeneities and the key controls will enhance the construction of more robust fluvial reservoir models and simulation of fluid flow.

This research focuses on three Triassic reservoirs of fluvial origin from different basins: (1) the Skagerrak Formation (Central North Sea, UK), (2) St Bees Sandstone Formation (Sherwood Sandstone Group, West Cumbria, UK) and (3) Buntsandstein facies (Central Iberian Basin, Spain). The Triassic successions of the Central North Sea, East Irish Sea and Southern North Sea basins, in recent years, have attracted a renewed interest as hydrocarbon production targets and potential targets for CO_2 storage. Thus, a better understanding of the controls on reservoir quality in Triassic successions is key for maximizing hydrocarbon recovery and ensuring safe storage operations. As stated in the aim and objectives (see section 1.2), this study integrates subsurface core and outcrop samples to investigate the facies, petrography and diagenesis of fluvial sandstones in order to better understand the controls on fluvial reservoir quality which will aid in the development of more accurate predictive models.

Chapter 2: Methodology

2.1 Introduction

This chapter introduces the datasets and methodology applied in this research. To achieve the aim and objectives of this study (see chapter 1), two types of datasets were carefully acquired. The first set of data are subsurface core data/samples while the second set of data are outcrop data/samples. The key methods used are presented below.

2.2 Outcrop data acquisition (Fieldwork)

Understanding reservoir architectures and how reservoir properties vary spatially within fluvial sand bodies is key to building fluvial reservoir models. This is, however, difficult to achieve via subsurface data sets due to inter-well spacing and lateral changes in facies, hence, outcrop analogues which provide information on geobody size, geometry, and potential connectivity (Howell et al. 2014) are commonly employed. In this research, two fluvial outcrops were investigated: (1) the Buntsandstein facies at Riba de Santiuste, Central Iberian Basin, Spain and (2) St Bees Sandstone Formation along the coast of West Cumbria, UK. The Buntsandstein facies has been proposed as an excellent analogue for the subsurface Triassic Skagerrak Formation in the Central North Sea (Morgan et al. 2010), while the St Bees Sandstone Formation outcrop has been reported as a suitable analogue for the fluvial reservoir sandstones in the Corrib Gas Field, offshore west of Ireland (Dancer et al. 2005). The two outcrops were chosen due to the following reasons: they are of similar age (i.e., Triassic) and have similar depositional style/distribution patterns which are controlled by climate variations and tectonics. During the field campaign, graphic logs of the outcrops at each location were drawn, to understand facies architecture and distribution. Bed thicknesses and contacts, grain size, colour, sedimentary structures and geometries were also noted. To understand the spatial and temporal distribution of reservoir properties, samples were taken at strategic points within the sandstone bodies for petrographic analysis. For example, within the channel sandstone bodies, samples were picked from the base, middle, top and wing sections. Where possible, sampling was done both along the cross section and longitudinal section of the outcrops.

2.3 Core sampling

Core sampling was carried out at the British Geological Survey (BGS) core store, Keyworth, UK. Core samples examined in this study are from the Joanne and Judy sandstone members of the

Triassic Skagerrak Formation encountered in wells 30/07a-7 (Judy field) and 30/2c-4 (Jade field) in the North Sea Central Graben (see chapter 3). The two wells were selected because they contain a good variety of facies with different reservoir properties. The sampled sandstone members (Joanne and Judy) are composed of highly heterogeneous fluvial reservoirs. They are presently at their maximum burial depths and form important hydrocarbon reservoirs in several high-pressure high-temperature (HPHT) fields in the North Sea Central Graben, UK. A total of 116 core samples, covering the main depositional facies were collected from well 30/07a-7 (56 samples) at depths between 11291 and 11548 ft, MD (3441 to 3519 m) and well 30/2c-4 (60 samples) at depths between 15, 585 and 15793ft, MD (4750 to 4813m) for petrographic studies.

2.4 Thin section petrography

2.4.1 Sample preparation

Two sets of samples were prepared for petrographic analysis: unpolished and polished sections. Thin section slabs (rock slices) were cut from all the rock samples (cores) using a slab saw. These were further reduced to smaller sizes (or chips) using a diamond trim saw. To enhance the identification of porosity, the chips were impregnated with blue epoxy dye before being glued to a glass slide. After attaching the rock chip to a glass slide, most of the chip was cut off with a cut-off saw leaving a thin slice attached. The produced thin section slides were then carefully ground to a standard thickness of 30 microns. The first set of samples (i.e., unpolished thin sections) were partly stained with alizarin red-S and potassium ferricyanide to facilitate the identification of carbonate cement types and then cover slipped for standard petrographic study. The second sets of thin section samples were polished and carbon-coated for Scanning Electron Microscopy.

2.4.2 Standard Petrography

The blue-epoxy impregnated thin sections from the core samples were analysed using transmitted-light microscopy. Detailed petrographic analysis was carried out on all produced thin sections using a Leica DM2500P microscope. Mineralogical composition, porosity, grain contact relationship, matrix and cement types were estimated and observed by point counting technique (300 counts per thin section), using an automated point-counting stepping stage (PETROG System, Conwy Valley Systems Limited, UK). The automated stepping stage is controlled by a software that stores, collates, and analyses point-counted petrographic data. Grain size and sorting were determined by measuring the long axis of 200 grains (quartz and feldspar) per thin section using the grain size analysis tool in the Petrog software. Thin section photomicrographs were captured using a LEICA DFC420C digital camera attached to the Leica petrographic microscope.

2.4.3 Scanning Electron Microscopy (SEM) equipped with Energy Dispersive X-ray (EDX)

The Scanning electron microscopy (SEM) is often used to generate high-resolution images of shapes of objects and show spatial variations in chemical compositions. The SEM, unlike conventional light microscopy, produces images by recording various signals resulting from interactions of an electron beam with the sample as it is scanned in a raster pattern across the sample surface (Huang et al., 2013). In this study, carefully selected polished and carbon-coated thin sections were examined with a Hitachi SU-70 field emission gun Scanning Electron Microscope (SEM) equipped with an energy-dispersive X-ray (EDX) detector at an accelerating voltage of 10-15kV and working distance of 15mm. The SEM-EDX system was used to identify the chemical compositions of clay minerals and other minerals in the samples, and their orientation. The imaging of the SEM samples was done in secondary electron (SE) and back-scattered electron (BSE) modes. Large area maps were generated for each of the analysed samples using an area dimension of 2.5mm by 2.5mm, and a magnification of x150 and x300 depending on grain size. To enhance the quality of acquired EDX map data, a process and pixel dwell time of 2 and 300 µs respectively were used. Each area map generated contains about 24 to 70 frames (depending on the sample grain size). These were montaged into one single image and converted to phase maps for the purpose of mineral quantification. All SEM-EDX map data processing was carried out using the Aztec software developed by Oxford Instruments.

2.4.4 Clay-coat quantification technique: coverage and thickness measurement

To quantify the fraction of grain surface area covered by clay coats (i.e., clay-coat coverage), two quantitative techniques were considered and compared, with the aim of choosing an appropriate technique for our study. The first technique (Wooldridge et al. 2019b) employs the cross-sectional perimeter length method, using the perimeter tool in Petrog software. This method involves (1) importing any pre-existing image, of appropriate resolution of clay-coated sand grains (e.g., light optical, SEM, or SEM-EDS) into the software, (2) defining the total perimeter length of a grain, (3) manually selecting the length that is covered by attached clay-coating material, and (4) calculating the percentage perimeter of the grain covered by clay-coat material.

The second technique (Dutton et al. 2018) is like the first technique, but with a slight difference in the procedure, and software used. In this technique, the program JMicroVision (v. 1.27) for measuring and quantifying components of high-definition images was employed using the following procedure: (1) measurement of the grain circumference, (2) measurement of the lengths of any parts of the grain that are in contact with other grains and thus are not available for clay-coatings and (3) measurement of the lengths of clay coatings on the grain surface. The clay-coat coverage was then calculated using the equation below:

*Clay coat coverage (%) = (Sum of clay-coated lengths) / (Grain circumference – Sum of grain contact lengths) *100* *Equation 1.1*

In this research, the second technique was employed due to its suitability for deeply buried sandstones that have experienced compaction (i.e., grain-grain contacts). The first technique was developed for clay-coat coverage measurement in modern-day sediments or loose sands with minimal grain-grain contacts and so the impact of compaction on reservoir quality was not taken into consideration. Unlike the first technique, the second technique excludes grain contacts, which are not available for quartz cement/clay-coats and focuses only on the exposed surface area of detrital quartz grains in contact with the intergranular volume (IGV) or pore space. To quantify clay coat coverage in the studied samples, few high-resolution backscattered electron images were taken at different areas in each thin section sample. For each sample, about 150 quartz grains were analysed in the BSE images acquired from them. To enhance consistency in the identification of clay coats on detrital quartz grain surfaces (especially where they are thin), and better quantify clay coat coverage, an Fe/Mg/Al elemental maps were generated for each image and integrated with their corresponding BSE image.

2.5 Stable isotope analysis

Stable isotope analysis was conducted on selected samples with considerable amounts of carbonate cements to determine their possible sources and formation temperature. All stable isotope analyses were performed at the Stable Isotope Biogeochemistry Laboratory at Durham University. Prior to analysis, small amounts of the selected whole rock samples were cut and ground in a ball mill. Based on carbonate content, each sample was weighed out to give a CO_2 signal of 12mV, and then transferred into individual exetainer vials. Vials were afterwards flushed with helium (grade 4.5) and CO_2 was liberated by reaction with 99% ortho-phosphoric acid for two hours at 70°C. The resultant gas mix of helium and CO_2 was transferred through a Thermo Fisher Scientific GasBench II in which a gas chromatographic column separated the CO_2 from the gas mixture, and then passed into a Thermo Scientific MAT 253 stable isotope ratio mass spectrometer. The following international reference materials were analysed within each batch of samples: NBS-18 (calcite, n=3), IAEA-CO-1 (marble, n=3) and LSVEC (Lithium Carbonate, n=3). In addition, an internal standard, DCS01 (calcium carbonate, n=7) was also analysed. Repeated analysis of both international and internal standards yielded an analytical precision better than ±0.1‰ for $d_{13}C$ and ±0.2‰ for $d_{18}O$. Duplicate analyses of two of the samples yielded a good precision with a mean difference of ±0.2‰ for both $d_{13}C$ and $d_{18}O$. Normalisations and corrections were made using IAEA-CO-1 and LSVEC, with all $d_{13}C$ and $d_{18}O$ values reported relative to the Vienna Pee Dee Belemnite (VPDB) standard. $d_{18}O$ was additionally reported to the Vienna Standard Mean Ocean Water (VSMOW) standard for comparison purposes.

2.6 Burial-thermal history modelling

The burial-thermal history of the Skagerrak Formation sandstones in the studied wells was modelled in one dimension using the Schlumberger's PetroMod software (V.2014.2). The one-dimensional basin modelling software utilizes a forward-modelling approach to re-construct the geological evolution of sedimentary basins and burial history of the associated reservoirs. It also has the capability to provide insight into the evolution of temperature, and pore pressure generated by disequilibrium compaction and pore fluid expansion due to temperatures increase. However, the one-dimensional modelling software is incapable of modelling pore pressure arising from lateral fluid flow, diagenetic processes, and hydrocarbon charging or generation. The data used to construct the models were obtained from well composite logs, geological well reports, core analysis reports, and other published materials such as Millennium Atlas (Knox and Holloway 1992; Cameron 1993; Johnson and Lott 1993; Richards et al. 1993; Evans et al. 2003; Goldsmith et al. 2003). The main geological inputs for the burial history models include stratigraphic layers, layer thicknesses, lithologies, erosion and depositional events. The lithological units used in the burial-thermal history models are primarily PetroMod (V.2014.2) default lithology types, selected based on well log descriptions and core analysis reports of the studied wells, except for the Hod and Skagerrak Formations. The Hod Formation (i.e., chalk unit) is a laterally extensive, low-permeability, non-reservoir rock that acts as a major vertical fluid flow barrier in the Central North

Sea (Mallon and Swarbrick 2008). The Hod chalk unit was modified to match the compaction trend and permeability trend proposed by Mallon and Swarbrick (2002, 2008) for the North Sea. Due to the heterogeneous nature of the Triassic Skagerrak Formation sandstones, the sandstones of the Joanne and Judy Sandstone members were simulated by a mix of PetroMod default lithologies (70% sandstone, 30% shale) in combination with a regional compaction trend for shaly sandstones given by Sclater and Christie (1980).

In addition, the construction of an ideal one-dimensional model requires accurate palaeo-heat flow models. Several heat-flow models have been published for the North Sea, especially for the Central Graben. These models can be subdivided into two main types: constant heat flow (Schneider and Wolf 2000) and thermal upwelling models (Swarbrick et al. 2000; Carr 2003; Allen and Allen 2005; di Primio and Neumann 2008). In this study, we used the thermal upwelling basement palaeo-heat flow model of Allen and Allen (2005) with 63-110 Mw/m2 (average: 80 mW/m2) during syn-rift phases and 37-66 mW/m2 (average: 50 mW/m2) during post-rift phases, coupled with the palaeo-surface temperature history published by Swarbrick et al. (2000). The burial-thermal history models were then calibrated against present-day RFT temperature measurements (corrected after Andrew-Speed et al., 1984), measured Triassic sandstone porosities and carefully adjusted towards present-day RFT formation pressure measurements by taken into consideration late stage, high temperature overpressure mechanisms (Osborne and Swarbrick 1997; Isaksen 2004).

2.7 Kinetic modelling of quartz cementation

The precipitation of authigenic quartz cement is one of the important factors that cause the degradation of sandstone reservoir quality. The volume of precipitated quartz cement and the resulting porosity loss in a sandstone can be calculated from the temperature history of the sandstone based on an equation relating the quartz precipitation rate per unit surface area and per unit time to temperature (Walderhaug 1994a, 1994b, 1996; Walderhaug et al. 2000). This precipitation algorithm developed by Walderhaug (1994a) and Walderhaug (1994b) forms the basis of many commercially available diagenetic modelling software packages for predicting reservoir quality. According to Walderhaug's kinetic model, the barriers to quartz precipitation kinetics are overcome at temperatures around 80C and rate of quartz cementation increases exponentially with increasing temperature during burial. This quartz cementation threshold temperature corresponds to burial depths of about 2.5 km, which is often referred to as the onset of chemical compaction (Taylor et al. 2010; Bjørlykke 2014). At this depth, intergranular volume (IGV) is reduced to about 26% via mechanical compaction. Under hydrostatic pressure, this IGV is assumed to be the porosity at the start of quartz cementation (Ajdukiewicz and Lander 2010).

Walderhaug's (1994b) model is based on the observation that there is a logarithmic relationship between the rate of quartz precipitation and temperature. At constant temperature, the volume of quartz cement, V_q (cm^3), precipitated in a 1-cm^3 volume of sandstone with quartz surface area A (cm^2) during time t (s) can be calculated as:

$$V_q = MrAt/\rho \qquad \textit{Equation 1.2}$$

where M is the molar mass of quartz (60.09 g/mole), r is the rate of quartz precipitation (moles/cm^2s), and ρ is the density of quartz (2.65 g/cm^3).

Quartz precipitation rate (r) can further be expressed as a logarithmic function of temperature based on experimental data and studies of quartz-cemented sandstones (Walderhaug 1994b):

$$r = a10^{bT} \qquad \textit{Equation 1.3}$$

where T is temperature (°C) and a and b are constants with units of moles/cm^2s and 1/°C, respectively. In basin modelling, the temperature history of a sandstone is commonly given as a series of time-temperature points linked by linear functions, hence, T can be replaced by linear time functions, and equation 1.3 rewritten as

$$r = a10^{b(c_n t + d_n)} \qquad \textit{Equation 1.4}$$

where c_n is heating rate (°C/s), d_n is the initial temperature (°C), and the index n refers to the relevant segment of the temperature history curve. By combining equations 1.2 and 1.4, Walderhaug (1996) derived an expression for predicting the volume of quartz cement (V_q) precipitated in a volume of sandstone at a particular time interval:

$$V_{q2} = \phi_o - (\phi_o - V_{q1}) \exp - MaA_0 / \rho\phi_0 bc \ln 10(10^{bT_2} - 10^{bT_1}) \qquad \textit{Equation 1.5}$$

where V_{q2} is the amount of quartz cement (cm^3) precipitated from time T_1 to T_2, V_{q1} is the amount of quartz cement present at time T_1 and A_0 (cm^2) is initial quartz surface area.

According to Lasaga (1984), initial quartz surface area, A_0, is calculated as the cumulative surface area of spheres with a diameter, D, equal to the grain size and with total volume equal to the fraction of detrital quartz, f, in a unit volume, V, of the sandstone. A_0 can therefore expressed as:

$$A_0 = 6\, fV / D \qquad \textit{Equation 1.6}$$

The change in quartz surface area caused by quartz cement precipitation is commonly assumed to be proportional to the porosity loss caused by quartz precipitation. Hence, the quartz surface area, A, when an amount of quartz cement, Vq, has precipitated can be expressed as:

$$A = A_0\, (\phi_0 - V_q) / \phi_0 \qquad \textit{Equation 1.7}$$

where ϕ_0 is the porosity when quartz cement precipitation commences.

Equation 1.5 is Walderhaug (1996) model for quartz cementation and was used in this study to model quartz cement in the Skagerrak Formation sandstones from the Judy and Jade fields.

2.7.1 Modelling parameters/inputs

Quartz cementation models were built using the approach of Walderhaug (1996). As earlier stated, this kinetic model calculates the rate of quartz cementation using a logarithmic function and assumes that compaction terminates at the onset of quartz cementation and stabilization of framework grains (Walderhaug 1996, 2000). The model incorporated grain size, percentage of grain coatings (i.e., coverage), detrital mineralogy (i.e., detrital quartz fraction), and available quartz surface area, all of which were quantified from petrographic analysis. Other input parameters were temperature and burial histories; these were generated using Petromod (V. 2012.2). Time-temperature histories generated were used to calculate the heating rates incorporated in the cementation models. In order to incorporate grain-coat data into the model, the initial quartz surface area was reduced using the clay coat coverage data. The kinetic model was generated using Walderhaug's (1996) standard parameters on 1cm3 of sandstone, with an 80°C threshold temperature for quartz cementation and a starting porosity of 26% at the onset of quartz cementation. A value of 1.98×10^{-22} moles/cm^{2}s was used for the pre-exponential a, and 0.022/°C for the exponential constant b, as calculated by Walderhaug (1994b) for some North Sea sandstones. Calculations of quartz cement volume were performed with a time step of 1 m.y.

Chapter 3: The importance of facies, grain size, and clay content in controlling fluvial reservoir quality – An example from the Triassic Skagerrak Formation, Central North Sea, UK

This chapter has been published in the Petroleum Geoscience journal

(https://doi.org/10.1144/petgeo2022-043)

3.1 Summary

Clay-coated grains play an important role in preserving reservoir quality in high-pressure high-temperature (HPHT) sandstone reservoirs. Previous studies have shown that the completeness of coverage of clay coats effectively inhibits quartz cementation. However, the main factors controlling the extent of coverage remain controversial. This research sheds light on the influence of different depositional processes and hydrodynamics on clay coat coverage and reservoir quality evolution. Detailed petrographic analysis of core samples from the Triassic fluvial Skagerrak Formation, Central North Sea, identified that channel facies offer the best reservoir quality; however, this varies as a function of depositional energy, grain size and clay content. Due to their coarser grain size and lower clay content, high energy channel sandstones have higher permeabilities (100-1150 mD) than low energy channel sandstones (<100 mD). Porosity is preserved due to grain-coating clays, with clay coat coverage correlating with grain size, clay coat volume and quartz cement. Higher coverage (70-98%) occurs in finer-grained, low energy channel sandstones. In contrast, lower coverage (<50%) occurs in coarser-grained, high energy channel sandstones. Quartz cement modelling showed a clear correlation between available quartz surface area and quartz cement volume. Although high energy channel sandstones have better reservoir quality, they present moderate quartz overgrowths due to lesser coat coverage, thus prone to allowing further quartz cementation and porosity loss in ultra-deep HPHT settings. Conversely, low energy channel sandstones containing moderate amounts of clay occurring as clay coats are more likely to preserve porosity in ultra-deep HPHT settings and form viable reservoirs for exploration.

3.2 Introduction

The Triassic Skagerrak Formation sandstones are important hydrocarbon-producing reservoirs in the High-Pressure High-Temperature (HPHT) section of the UK North Sea Central Graben, with present-day pore pressure and temperature exceeding 80 MPa and 150°C, respectively (Stricker and Jones 2016; Stricker et al. 2016b). They exhibit varying degrees of heterogeneity and contain anomalously high porosity (up to 35%) and permeability (up to 3000 mD), despite their present-day burial depth of 3442 to 5100 m (11,291-16,732 ft) below rotary table and temperature of over 150°C (Smith et al. 1993; Nguyen et al. 2013; Akpokodje et al. 2017). Previous studies have attributed the anomalously high porosity and permeability in the Skagerrak sandstones to the shallow onset and continuous increase of overpressure, which limited mechanical compaction, and the presence of chlorite coats, which inhibited quartz cementation during burial diagenesis (Nguyen et al. 2013; Stricker and Jones 2016; Stricker et al. 2016b). However, only a few studies have been published on the distribution of clay coatings as a function of depositional facies (i.e., grain size, sorting, and clay content) in these deeply buried sandstones. The HPHT hydrocarbon reservoirs of the UKCS Triassic successions are increasingly becoming attractive for further exploration (McKie and Audretsch 2005; Burgess et al. 2020). They are also potential targets for geothermal energy and carbon capture and storage (CCS). Thus, understanding the controls on reservoir quality, and most importantly clay coating effectiveness, is crucial for finding good quality reservoirs.

The reservoir quality (i.e., porosity and permeability) of deeply buried sandstones is mainly dictated by the combined effect of depositional facies, burial compaction and diagenetic processes (Ajdukiewicz and Lander 2010). Depositional factors (such as grain size, sorting, clay content and detrital composition have a considerable influence on sandstone initial depositional porosity and permeability, as well as the extent and distribution of subsequent diagenesis (Baker 1991; Smith et al. 1993; Morad et al. 2000; Ajdukiewicz and Lander 2010; Morad et al. 2010). Diagenetic processes that control reservoir quality include compaction, cementation (mainly by quartz, clay minerals and carbonates), and dissolution of framework grains and cements. In general, with increasing burial depth, sandstones progressively lose porosity via mechanical compaction. At greater depth, chemical compaction (pressure dissolution) becomes active, resulting in further porosity reduction via quartz cementation (Bjørlykke 2014). Quartz is volumetrically the most important pore-occluding diagenetic cement in deeply buried clean sandstone reservoirs (McBride 1989; Ehrenberg 1990; Walderhaug 1996; Worden and Morad 2000; Molenaar et al. 2007; Gier et al. 2008; Worden et al. 2018a; Worden et al. 2018b). Quartz cementation starts at around 70-80°C (McBride 1989; Bjørlykke and Egeberg 1993; Walderhaug 1994a; Storvoll et al. 2002; Lander et al. 2008; Ajdukiewicz and Lander 2010; Taylor et al. 2010; Oye et al. 2018). The presence of early-formed clay coats (e.g., chlorite) can inhibit quartz cementation by blocking nucleation sites and making the surface area unavailable for pore-occluding quartz overgrowths, thereby preserving anomalously high porosity in deeply buried sandstones (Worden and Morad 2000; Bloch et al. 2002; Ajdukiewicz and Larese 2012; Nguyen et al. 2013; Stricker and Jones 2016; Worden et al. 2020; Xia et al. 2020).

The ability of clay coats to effectively inhibit quartz cementation is primarily a function of its completeness or coverage (i.e., fraction of surface area of grains covered by clay minerals) and not just its presence (Ehrenberg 1993; Walderhaug 1996; Bloch et al. 2002; Billault et al. 2003; Lander et al. 2008; Ajdukiewicz and Larese 2012; Stricker and Jones 2016; Charlaftis et al. 2021). Detrital clay coats are often interpreted as precursors for authigenic clay coats in deeply buried sandstone reservoirs (Bahlis and De Ros 2013; Verhagen et al. 2020). In fluvial settings, the most common ways by which detrital clay minerals (e.g., smectite) are incorporated into fluvial sandstones either as clay-coatings or pore-filling clays are by mechanical infiltration of clay-rich waters and inherited grain-coating clays (Matlack et al. 1989; Worden and Morad 2003; Dowey et al. 2012). With increasing burial, detrital clays are recrystallized to authigenic clays which could either have a positive or negative impact on deep reservoir quality (Morad et al. 2010; Mahmic et al. 2018; Virolle et al. 2019). In general, the distribution of detrital clay minerals, which are precursors for authigenic clay minerals, has been reported to be controlled by depositional processes, at least in shallow marine (estuarine) depositional environments (Dowey et al. 2012; Dowey et al. 2017; Wooldridge et al. 2017b). Therefore, understanding how the completeness of clay coats is changing as a function of depositional processes (e.g., grain size, sorting, and clay content) is crucial for the prediction of quality reservoirs in deeply buried sandstones.

In this study, we investigate the impact of depositional facies, grain size, clay content and clay coverage on sandstone reservoir quality in two deeply buried sandstone members (Joanne and Judy) of the Triassic Skagerrak Formation, UKCS Central Graben. Additionally, we model quartz cement using burial-thermal history to understand quartz cement evolution through time and its relationship with clay coat coverage and then compare it with measured quartz cement in the studied sandstones. The sandstone members examined in this study are from wells 30/7a-7 (Judy field) and 30/2c-4 (Jade field) in Quadrant 30. They form the main producing intervals in the UKCS Skagerrak Formation; however, they exhibit different reservoir qualities. This study also aims to ascertain whether grain size and clay content are viable tools for predicting clay-coat-enhanced reservoir quality in deeply buried and diagenetically complex sandstone reservoirs.

3.3 Geological setting

The Central Graben is the southern arm of a northwest-southeast-trending trilete rift system in the North Sea, with the Viking Graben (VG) as the northern arm and the Moray Firth Basin (MFB) as the western arm (Fig. 3.1a). At least two major rifting phases led to the development of the Central Graben, one during the Permian-Triassic (290-210 Ma) and the other during the Upper Jurassic (155-140 Ma), the latter being the main rifting episode. The Central Graben is divided into the West and East Central Graben by two main horst blocks: Forties-Montrose high and the Josephine Ridge (Fig. 3.1b) and is flanked by the Norwegian basement in the East and UK continental shelf in the West (Gowers and Sæbøe 1985; Glennie 1998; di Primio and Neumann 2008). The main graben system and the medial horst blocks are presently deeply buried due to subsequent post-rift thermal subsidence and sediment inundation that began at the end of the Jurassic rift episode. Today, they are overlain by a 3-4 km thick sequence of Cretaceous and Cenozoic strata (Grant et al. 2014).

The Triassic sediments of the CNS were deposited in a variety of dryland terminal fluvial settings, ranging from relatively arid terminal splay and playa to more vegetated, confined-channel systems with associated floodplain facies (McKie et al. 2010). Palaeocurrent data reveal that the fluvial drainage pattern was in a North-South direction towards the Southern North Sea, with sediments input from the Fennoscandian Shield to the east and the Scottish Highlands to the west (McKie 2011) (Fig. 3.1a). The deposition of the Triassic sediments occurred directly above an extensive and relatively thick Permian Zechstein salt layer in a series of fault- and salt-controlled mini-basins (pods). Early Triassic rifting coupled with sediment loading initiated a widespread syn-depositional movement of the underlying Zechstein salt, and this led to the creation of salt withdrawal mini-basins or pods, in which the contemporaneous Triassic sediments accumulated

(Hodgson et al. 1992; Smith et al. 1993). The progressive withdrawal of the salt from beneath the pods into the adjacent salt walls resulted in the continued subsidence of the pods, until they grounded on the underlying Lower Permian Rotliegend faulted basement. The overall thickness of the pods and the rate at which they became grounded vary across the basin and were strongly controlled by the salt thickness. In areas where the salt was initially thin (on basin flanks), the sediment pods grounded early and thus prevented further intra-pod deposition and preservation of sediments. In the East and West Central Graben, the salt layer was relatively thick, and the sediment pods did not become grounded until Late Cretaceous. This allowed the accumulation and preservation of thick sedimentary successions within the pods relative to the inter-pod areas (Smith et al. 1993; Nguyen et al. 2013).

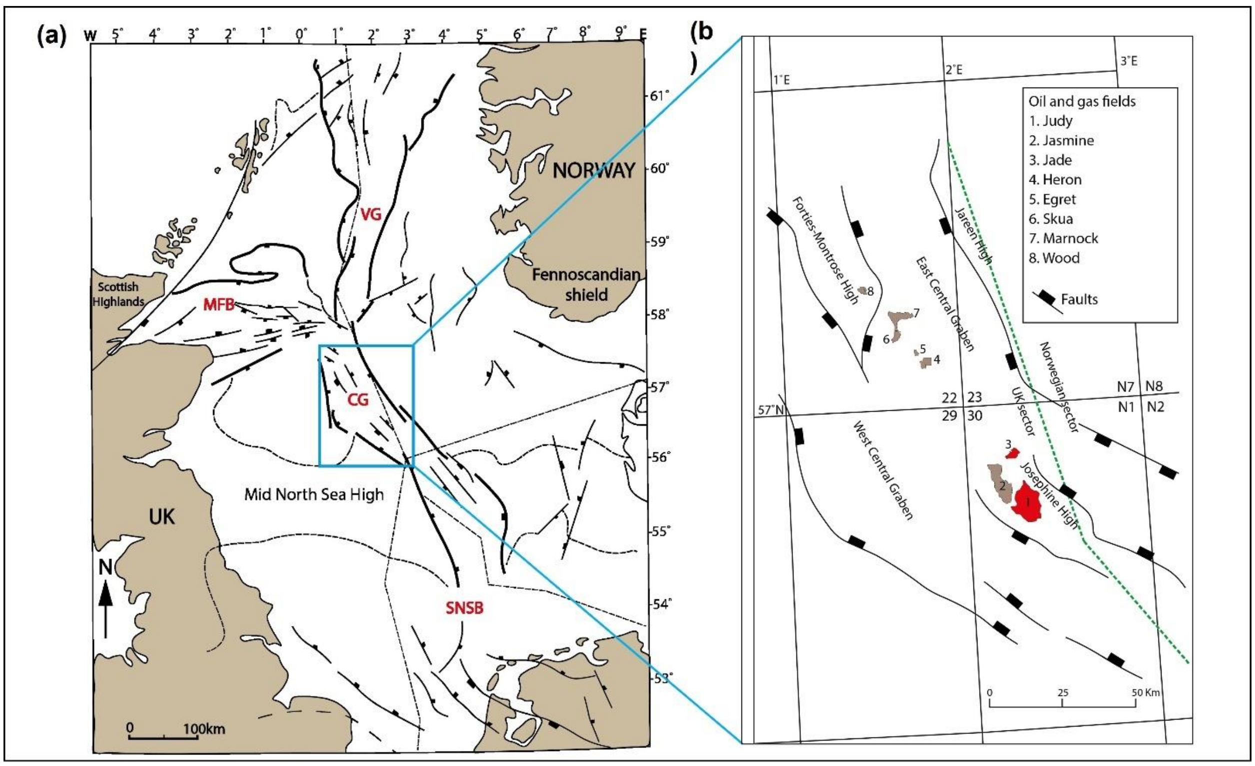

Figure 3.1: Location map showing (a) the North Sea rift system and its structural elements with Moray Firth Basin (MFB), Viking Graben (VG), Central Graben (CG) and Southern North Sea Basin (SNSB) (modified after Brown, 1991) and (b) the study area (blue box on the structural map), with the Forties-Montrose High (to the Northwest) & Josephine Ridge horst blocks (to the Southeast) dividing the Central Graben into East Central Graben & West Central Graben. The wells selected for this study are from the fields highlighted in red (Judy and Jade).

The stratigraphic division and nomenclature for the Triassic sequences in Central North Sea was defined based on detailed biostratigraphic and lithostratigraphic correlation of wells within the J-Ridge area in the South Central Graben (Goldsmith et al. 1995; Goldsmith et al. 2003). This stratigraphic correlation has been extended to other areas of the CNS (UKCS Quads 29 & 22; NCS Quads 7, 15 & 16) through the integration of heavy mineral stratigraphy, seismic and well log correlation, and high-quality biostratigraphic data (McKie and Audretsch 2005; McKie et al. 2010; McKie 2014; Mouritzen et al. 2017; Burgess et al. 2020). The Triassic of the CNS is divided into two distinct lithostratigraphic units (or Formations): Early Triassic Smith Bank Formation and Middle to Late Triassic Skagerrak Formation (Fig. 3.2). The Smith Bank Formation (lower unit), consisting of shales, evaporites and thin sandstones, forms the bulk of the pod infill. The overlying Skagerrak Formation (alternating sandstones and mudstones) occupies the upper section of the pods and the interpod areas. The Skagerrak Formation is further subdivided into three sandstone-dominated members (Judy, Joanne, Josephine) and three mudstone-dominated members (Julius, Jonathan, Joshua) (Goldsmith et al. 1995, 2003). The mud-dominated members are thick and laterally extensive within Quadrant 30 but thin northwards and are commonly used as the primary correlation markers for the Skagerrak Formation (McKie and Audretsch 2005). Recent studies of the Triassic stratigraphic framework have however proposed a new correlation scheme for the Triassic successions based on the results from high-resolution biostratigraphy and heavy mineral stratigraphy (Mouritzen et al. 2017; Burgess et al. 2020).

The Triassic Skagerrak Formation underwent a prolonged shallow burial phase (about 150 Ma) followed by a rapid burial phase from 90 Ma onwards to their present-day maximum burial depth (Fig. 3.3). The phase of rapid burial was accompanied by a significant increase in pore pressure and temperature (Stricker et al. 2016b). The study area (J-Block, UK quadrant 30) is situated in the southern part of the UK Central Graben (Fig. 3.1). Throughout the Triassic, this area was at the distal end of a continental clastic (fluvial distributive) system, with sediment originating mainly from the Norwegian mainland, but with additional source areas in the Scottish Highlands and Fladen Ground Spur (Steel and Ryseth 1990; Goldsmith et al. 1995; Gray et al. 2019). The focus of this study is on the Judy and Joanne sandstone members of the Skagerrak Formation in wells 30/07a-7 (Judy field) and 30/2c-4 (Jade field). These sandstone members form the main hydrocarbon reservoirs in the Skagerrak Formation and occur in an HPHT environment. In the upper part of the Skagerrak Formation, especially at depths of 4000 to 5000 m (13,123-16,404 ft) below sea floor, pore pressures and temperatures exceed 11,603 psi (80 MPa) and 166°C, respectively (Swarbrick et al. 2000; di Primio and Neumann 2008; Nguyen et al. 2013). Present-day overpressures in Judy and Jade fields are 3250 psi (22.4 MPa) and 3950 psi (27.2 MPa), respectively (Grant et al. 2014) (Table 3.1).

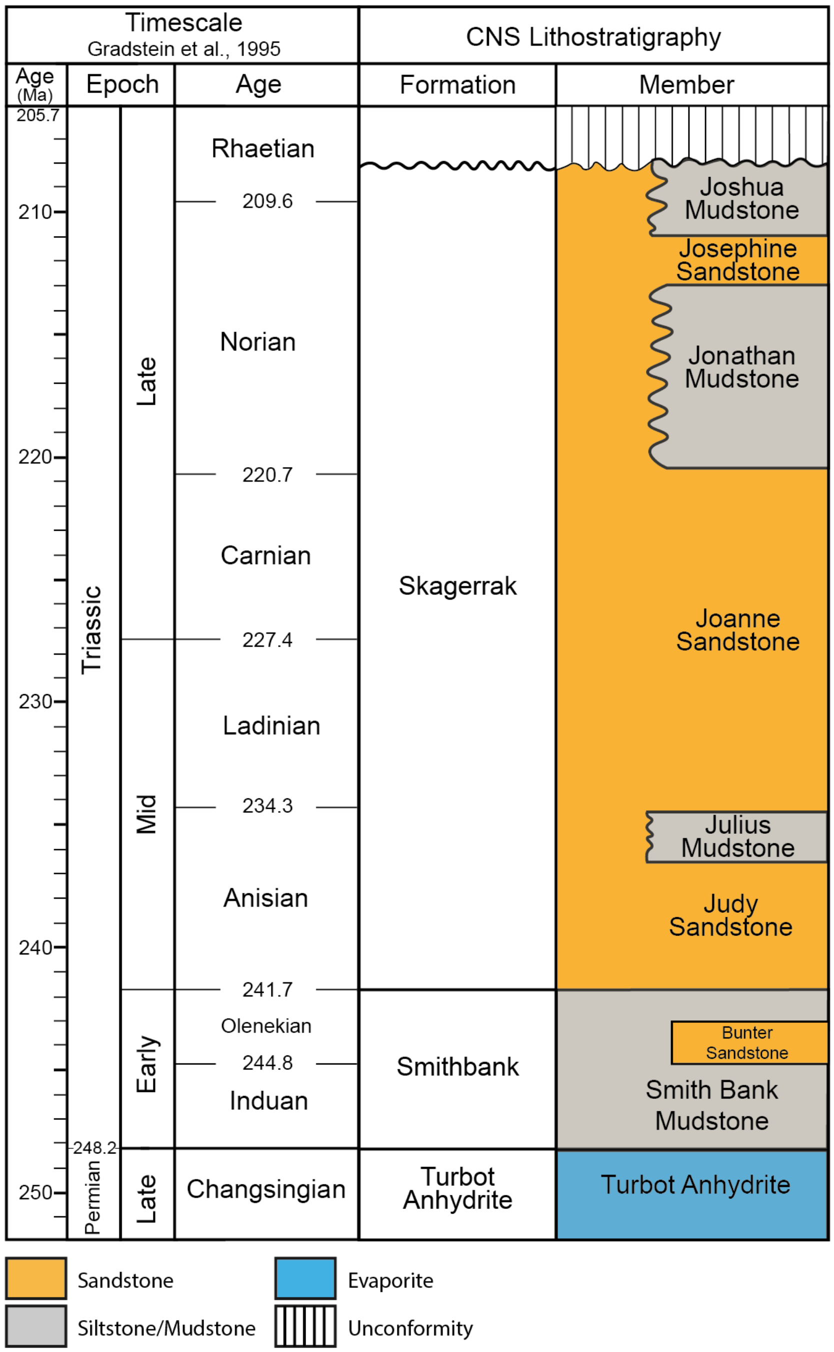

Figure 3.2: Central North Sea (CNS) Triassic stratigraphic column showing the six lithostratigraphic members of the Skagerrak Formation (after Goldsmith et al., 2003) and their respective ages (after Gradstein et al., 1995).

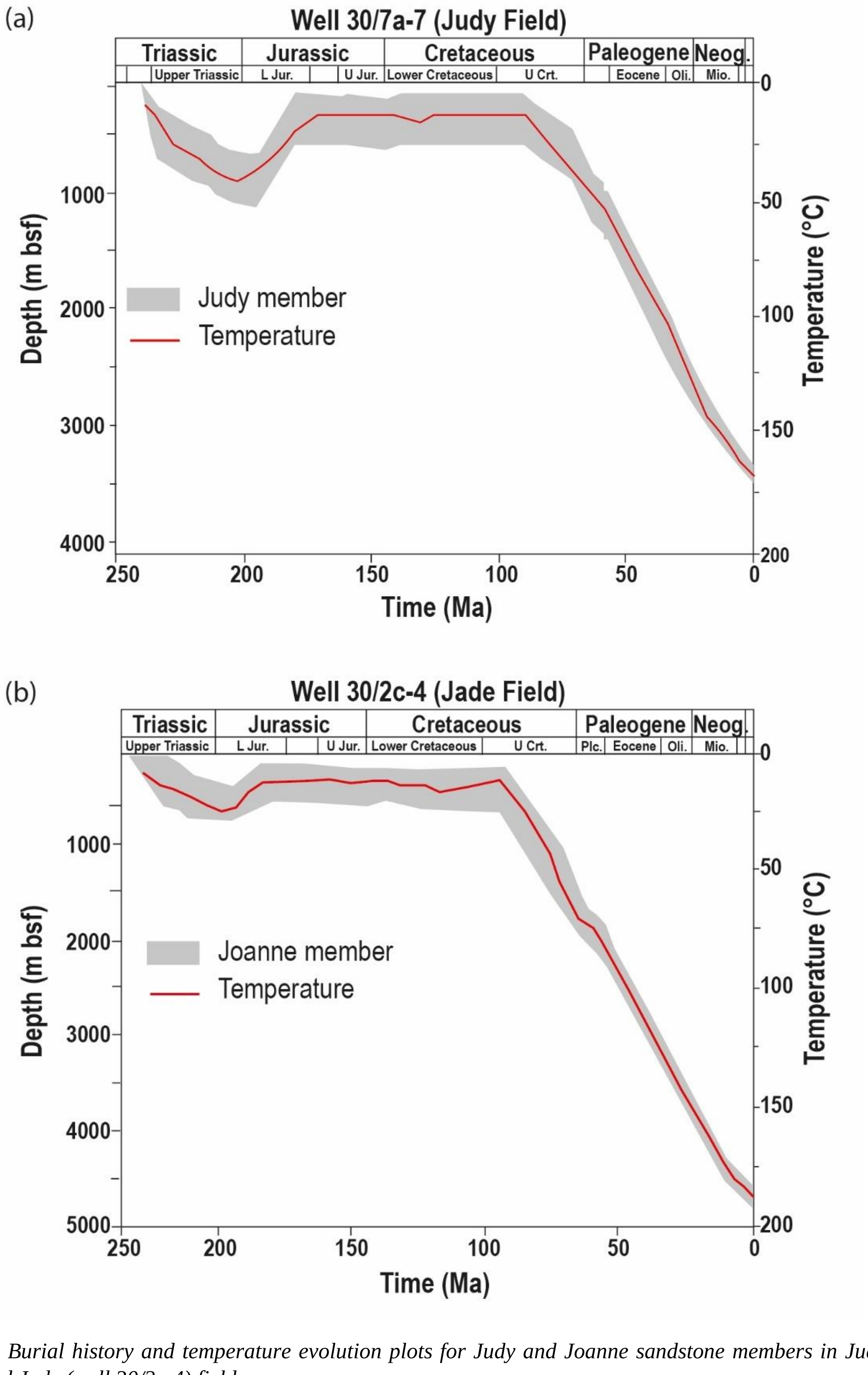

Figure 3.3: Burial history and temperature evolution plots for Judy and Joanne sandstone members in Judy (well 30/7a-7) and Jade (well 30/2c-4) fields.

Table 3.1: Well data of 30/7a-7 (Judy field) and 30/2c-4 (Jade field) used in this study. Included are water depth, top reservoir depth, overpressure, and repeat formation tester (RFT) temperatures based on Grant et al. (2014).

Field			Judy	Jade
Well			30/7a-7	30/2c-4
Depth interval		(ft)	11291 - 12655	15354 - 16675
		(m)	3441 - 3857	4680 – 5083
		(TVDSS ft)	11219 - 12572	14964 - 16276
		(TVDSS m)	3420 - 3832	4561 - 4961
Water depth		(ft)	249	262
		(m)	76	80
Top Reservoir		(TVDSS ft)	11219	14964
		(TVDSS m)	3420	4561
Overpressure		(psi)	3250	3950
		(MPa)	22.4	27.2
RFT-Temperature	Measured	(°C)	143.3	163.8
	Corrected	(°C)	164.1	187.7
	Depth	(TVDSS ft)	12572	15566
		(TVDSS m)	3832	4745
Number of core samples			56	60
Sandstone member			Judy	Joanne

3.4 Methodology

The core samples investigated in this study were chosen from the Judy and Joanne sandstone members of the Triassic Skagerrak Formation in wells 30/7a-7 (Judy field) and 30/2c-4 (Jade field), respectively. These two wells were chosen because they contain a variety of fluvial facies with different reservoir properties. A total of 116 core samples (in form of chips) covering the main depositional facies (Table 3.2) were chosen from well 30/7a-7 (56 samples) at depths between 11,291 and 11,548 ft, (Measured Depth: 3441 and 3519 m) and well 30/2c-4 (60 samples) at depths between 15,585 and 15793 ft (Measured Depth: 4750 and 4813 m). The samples were selected at depths that had previously measured porosity and permeability data.

All core samples were vacuum-impregnated with blue-dyed epoxy resin to enhance porosity identification and then made into thin-sections. The thin sections were partly stained with alizarin red-S and potassium ferricyanide to facilitate the determination of carbonate cement types. Detailed petrographic analysis was conducted on all prepared thin sections, using a Leica DM2500P microscope coupled with a Leica DFC420C digital camera. Thin sections were point-counted to determine the percentage of detrital grains, clay matrix, pore-filling and grain-coating cements, and porosity, using an automated point-counting stepping stage (PETROG System, Conwy Valley Systems Limited, UK) attached to the Leica petrographic microscope. Modal point count analysis of the mineral components and porosity was based on 300-point counts per section. Grain size was determined by measuring the long axis of 200 grains (quartz and feldspar) per thin section using the Petrog petrographic software package. Sorting was determined from grain size measurements using the formula proposed by Folk and Ward (1957). To understand how grain size relates to permeability, the Kozeny equation for estimating permeability from grain size and total porosity (Kozeny 1927; Walderhaug et al. 2012) was employed. Measured porosity and permeability data from core analysis were provided by UK Common Data Access (CDA). Core plug porosity measurements were made using a Boyles Law Helium Porosimeter. Air permeability measurements were performed using nitrogen gas as a flowing fluid at a confining Hassler pressure of 250 psi. The term "thin-section porosity" (also known as macroporosity or visible porosity) used in this study is derived from point counting and refers to the sum of intergranular porosity and intragranular porosity. Helium porosity (i.e., measured/core plug porosity), on the other hand, is the sum of macroporosity and microporosity. In this study, microporosity is estimated by subtracting thin-section porosity from helium porosity. Data from point count analysis was used to calculate Intergranular volume (IGV). This is defined as the sum of intergranular porosity, depositional matrix, and intergranular cement in sandstone samples, and is used to measure compaction in sandstones. Porosity loss due to compaction (COPL) and porosity loss due to cementation (CEPL) was calculated following the methodology described by Lundegard (1992):

$$\mathrm{COPL} = P_{\mathrm{initial}} - \{[(100 - P_{\mathrm{initial}}) \times \mathrm{IGV}] / (100 - \mathrm{IGV})\}$$

$$\mathrm{CEPL} = (P_{\mathrm{initial}} - \mathrm{COPL}) \times (\mathrm{C} / \mathrm{IGV})$$

(Where $P_{initial}$ = initial depositional porosity, assumed as 45%; IGV = Intergranular volume; C = Intergranular cement).

The detailed point count results, petrographic information (including IGV, COPL and CEPL), and laboratory measured porosity and permeability are presented in Appendix A.

To determine the source of carbonate cement in the sandstones, 19 samples with variable amounts of carbonate cements were selected for stable isotope analysis using CO_2 liberation method. The detailed stable isotope analytical technique employed is discussed in chapter 1. To investigate the occurrence and morphology of clay minerals in the studied sandstones, 23 sandstone samples with clay volume between 1% and 11% (based on point counting) were selected from both wells for SEM analysis.

Table 3.2: Classification and description of identified facies in the Judy and Joanne sandstone members from wells 30/7a-7 (Judy field) and 30/2c-4 (Jade field).

Code	Facies	Description
S1	Parallel laminated/current rippled sandstones	Very fine to fine-grained sandstones with planar parallel lamination and well-defined current ripples with thin silty drapes defining laminae. Rippled bed sets define a low angle cross stratification parallel to sparse planar lamination.
S2	Massive sandstone	Moderately well sorted to well sorted, fine to medium-grained massive sandstones with thickness ranging from 0.3m to 2.5m
S3	Cross laminated/bedded sandstones	Very fine to medium grained, moderately to well sorted sandstones forming stacked decimetre to metre scale cross stratified sets with planar erosive set boundaries.
S4	Mottled, bioturbated and pedoturbated sandstones	Very fine to fine grained mottled sandstones with evidence of bioturbation resulting in disrupted bedding. Composed of localized dolocrete nodules and dolomite cements.
C	Intraformational conglomerate and gravelly sandstone (dolocrete pebbles-D; mudclast pebbles-M)	Poorly sorted sandstones containing pebble-sized clasts with size ranging from 2 mm to 8 mm. The pebbles are primarily composed of dolocrete and mudclasts and are often occur in channel bases.
M1	Mottled and bioturbated mudstone	Grey or green/red coloured bioturbated silty mudstone facies with frequent mottling.
M2	Pedoturbated mudstones and siltstones	Silty mudstones with pervasive carbonate nodules. Commonly mottled, greenish in colour, locally reddened, frequently bioturbated and rootletted with occasional preservation of current rippling and planar parallel lamination.
M3	Laminated mudstone	Mid to dark grey finely laminated argillaceous siltstone/mudstone with thin laminae and lenses of laminated or current rippled very fine sandstone.

The selected samples were polished to 30 µm, carbon-coated and examined under a Hitachi SU-70 Scanning Electron Microscope (SEM) equipped with backscatter (BSE) and an Energy-Dispersive X-ray (EDX) spectrometer at an accelerating voltage of 10-15 kV and working distance of 15 mm. The EDX system was used to identify the chemical compositions and distribution of the clays and other minerals in the samples. Furthermore, using montaged SEM/BSE images and high-resolution photomicrographs of the 23 selected sandstone samples, two major clay coat properties affecting reservoir quality (i.e., clay coat coverage and thickness) were measured on

150 quartz grains per sample using JMicroVision software. Clay-coat coverage (i.e., fraction of surface area of grains covered by clay minerals) on detrital quartz grains was measured using the perimeter tool in the JMicroVision software, following the procedure proposed by Dutton et al. (2018) (Appendix B). Also, clay-coat thickness was measured using the line selection tool in the software. Where clay coat thickness varies along a grain surface, several thickness measurements were taken, and an average thickness value was calculated.

The burial-thermal history curves of the two wells (30/7a-7 - Judy field and 30/2c-4 - Jade field) were constructed using Schlumberger's Petromod (V. 2012.2) one-dimensional basin modelling software. The software uses a forward modelling approach to calculate the geological evolution of a basin and burial history of a reservoir, especially the temperature and pore fluid pressure evolution of the reservoir. Although the technique is limited in its ability to model overpressure generation from the effect of lateral fluid flow, diagenetic processes, and hydrocarbon charging, it can effectively simulate overpressure generation from disequilibrium compaction and pore fluid expansion. Present-day stratigraphy, well log lithology and lithological descriptions were used to set the one-dimensional burial models (Knox and Holloway 1992; Cameron 1993; Johnson and Lott 1993; Richards et al. 1993; Goldsmith et al. 1995; Goldsmith et al. 2003). Palaeo-basement heat flow was assumed according to Allen and Allen (2005) with 63-110 mW/m^2 (avg. 80 mW/m^2) during syn-rift phases and 37-66 mW/m^2 (avg. 50 mW/m^2) during post-rift phases. The burial history models were calibrated against present-day RFT temperature measurements corrected after Andrews-Speed et al. (1984), and measured Skagerrak Formation porosities. They were then carefully adjusted to present-day formation pressure measurements, taking into account late stage, high-temperature overpressure mechanisms (i.e., disequilibrium compaction and pore fluid expansion) (Osborne and Swarbrick 1997; Isaksen 2004).

Quartz cementation models for the Judy and Jade field sandstones (Judy and Joanne) were built using the approach of Walderhaug (1996). This mathematical kinetic model calculates the rate of quartz cementation using a logarithmic function and assumes that compaction terminates at the onset of quartz cementation and stabilization of framework grains (Walderhaug 1996, 2000). The model incorporates grain size, percentage of grain coatings (i.e., coverage), detrital mineralogy (i.e., detrital quartz fraction), and available quartz surface area, all of which were quantified using the acquired petrographic data. The model also incorporates temperature and burial history, both of which were modelled using Petromod (V. 2012.2). Time-temperature histories generated were used to calculate the heating rates incorporated in the cementation models. In order to incorporate grain-coat data into the model, the initial quartz surface area was reduced using the clay coat coverage data from the samples. The kinetic model was generated using Walderhaug's (1996) standard parameters on $1cm^3$ of sandstone, with an 80°C threshold temperature for quartz cementation and a starting porosity of 26% at the onset of quartz cementation. A value of 1.98×10^{-22} mol/cm^2s was used for the pre-exponential *a*, and 0.022°C for the exponential constant *b*, as calculated by Walderhaug (1994b) for some North Sea sandstones. Twenty-one (21) samples of similar facies (i.e., channel sandstones) were used in the model; eight samples from the Judy sandstone member (well 30/7a07 - Judy field) and 13 samples from the Joanne sandstone member (well 30/2c-4 - Jade field) (see Appendix C).

Table 3.3: Facies association scheme used in this study and their colour codes.

Facies association	End members	Facies code	Colour code
Confined fluvial channel (FC)	High energy fluvial channel (HEFC)	S1, S2, S3, S4, C	
	Low energy fluvial channel (LEFC)	S1, S2, S3, S4, C	
Unconfined fluvial splays and sheetfloods (SF)	–	S1, S2, S4, M1, M2, C	
Floodplain, palaeosols and lakes (FL)	–	S4, M1, M2, M3	

3.5 Results

3.5.1 Facies description and classification

Eight sedimentary facies were identified in the studied cored intervals from the Judy (well 30/7a-7) and Joanne (well 30/2c-4) sandstone members of the Skagerrak Formation based on grain size, lithology, and sedimentary structures (Table 3.2). These facies types have been classified into three main facies associations comprising: (1) confined fluvial channels (FC), (2) unconfined fluvial splays and sheetfloods (SF), and (3) floodplain, palaeosols and lakes (FL) (Table 3.3). A schematic fluvial depositional model illustrating the sub-environments and different facies associations identified is shown in figure 3.4. Figures 3.5-3.8 show the sedimentary logs for the two wells, representative cores, and thin section images of the identified sedimentary facies, respectively.

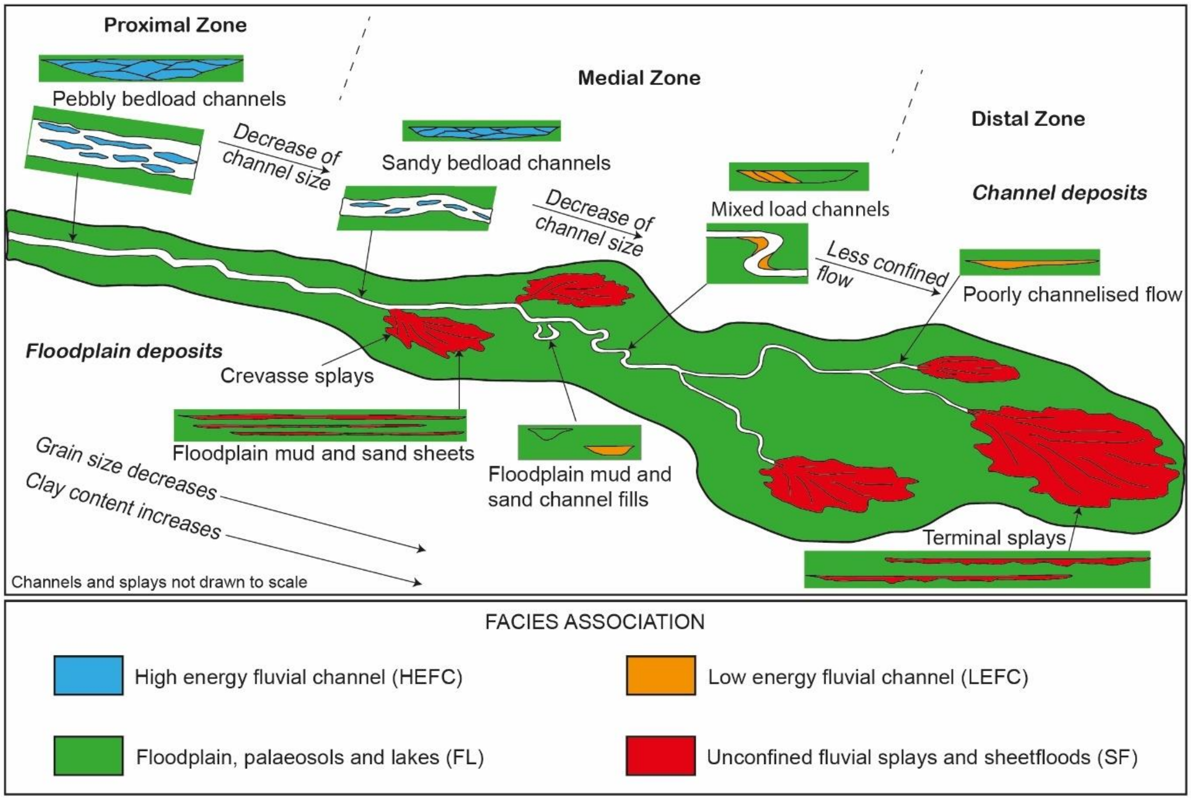

Figure 3.4: A schematic fluvial depositional model illustrating the sub-environments and different facies associations identified in this study (modified after Nichols and Fisher, 2007).

3.5.1.1 Confined fluvial channel (FC)

Sandstone sequences representing the fill of fluvial channels are highly variable but range between distinctive end members (i.e., high and low energy) based on grain size and bedform scale, all of which overlie sharp-based erosional surfaces commonly defined by intraformational conglomerates (C). The more abundant of these types comprise moderately to well sorted, fine to medium grained sandstones, forming decimetre to metre scale, high to moderate angle cross-stratified beds (S3) (Fig. 3.7). These are often stacked, forming channel-filling sequences of up to more than 23 ft (7 m) in thickness. Channel-fills of this type are more common in the Joanne Sandstone and rare in the Judy Sandstone Member. Both the dominant grain size (fine sand) and the scale of the bedforms suggest that most of these channel filling sandstones were deposited under conditions of high flow competence in active streams and represent bar scale bedforms.

Similar characteristics have been ascribed to deposition within low to moderate sinuosity channels (Bridge and Lunt 2006) but for the purposes of this paper, they are referred to as high energy fluvial channel (HEFC) sandstones.

At the opposite end of the spectrum of channel fills are sequences that commonly exhibit a marked upwards fining. They similarly tend to overlie intraclastic conglomerates (C) resting on sharply erosive channel bases but are dominated by very fine to fine sandstones forming low angle decimetre scale beds, planar lamination, current and wave rippling (S1) (Fig. 3.7). Where complete, the channel filling sequences can equally range up to more than 23 ft (7 m) in total thickness but commonly pass upwards into highly argillaceous very fine sandstones and siltstones that are locally disrupted by either or both bioturbation and pedoturbation. The finer grain sizes (i.e., very fine sand) and a range of sedimentary structures indicate lower energy levels and stream competence at the time of deposition. While sandstone sequences of the corresponding type have been interpreted to represent higher sinuosity channels (Leeder 1973; Bridge et al. 1995; Wu et al. 2015; Wu et al. 2016), in this paper, they are referred to as low energy fluvial channel (LEFC) sandstones.

The channel filling sandstone sequences occurring within the Joanne and Judy Sandstone Members are intermediate in character between the two end members described above. However, the samples used in this study can be assigned with confidence to the two end members. It is therefore proposed that the terms high energy fluvial channels (HEFC) and low energy fluvial channels (LEFC) best serve the purposes of the assessments of reservoir quality within the present contribution (Figs. 3.5 and 3.6).

3.5.1.2 Unconfined fluvial splays and sheetfloods (SF)

This facies association mainly comprises very fine to fine-grained, variably argillaceous, and micaceous sandstones, and silty mudstones (Figs. 3.5, 3.6, 3.8e & f). The sandstone components are characterised by planar lamination and current ripples with thin silty/mica drapes (S1). The sandstone units of this facies association commonly occur as weakly defined coarsening-upward sequences or upward-fining packages that are less than 1 ft (0.3 m) and up to 7 ft (2 m) thick. They are usually interbedded with argillaceous silty mudstones of facies M1-M3. The splay facies of the Skagerrak Formation have been interpreted as unconfined sheetflood deposits, which either

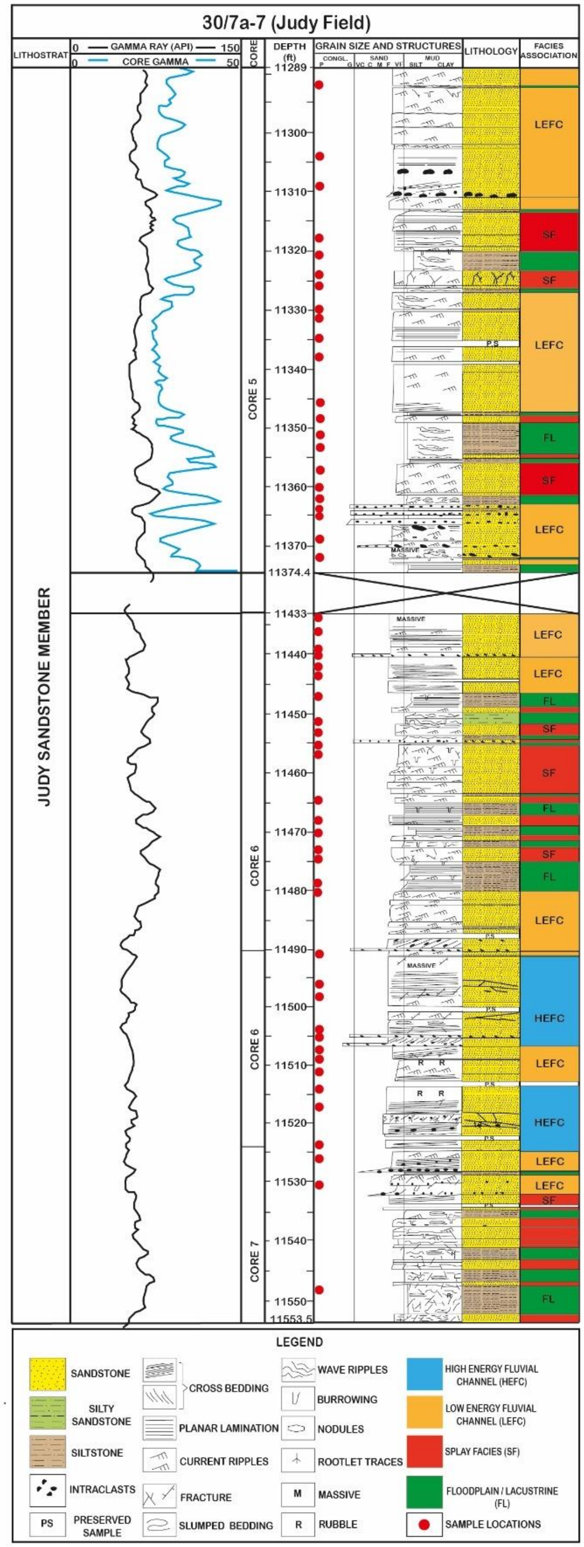

Figure 3.5: Sedimentary log of well 30/7a-7 (Judy Field) showing the interpreted facies association based on lithology, grain size and sedimentary structures. Corresponding gamma ray logs of the cored intervals and core sample locations are also shown.

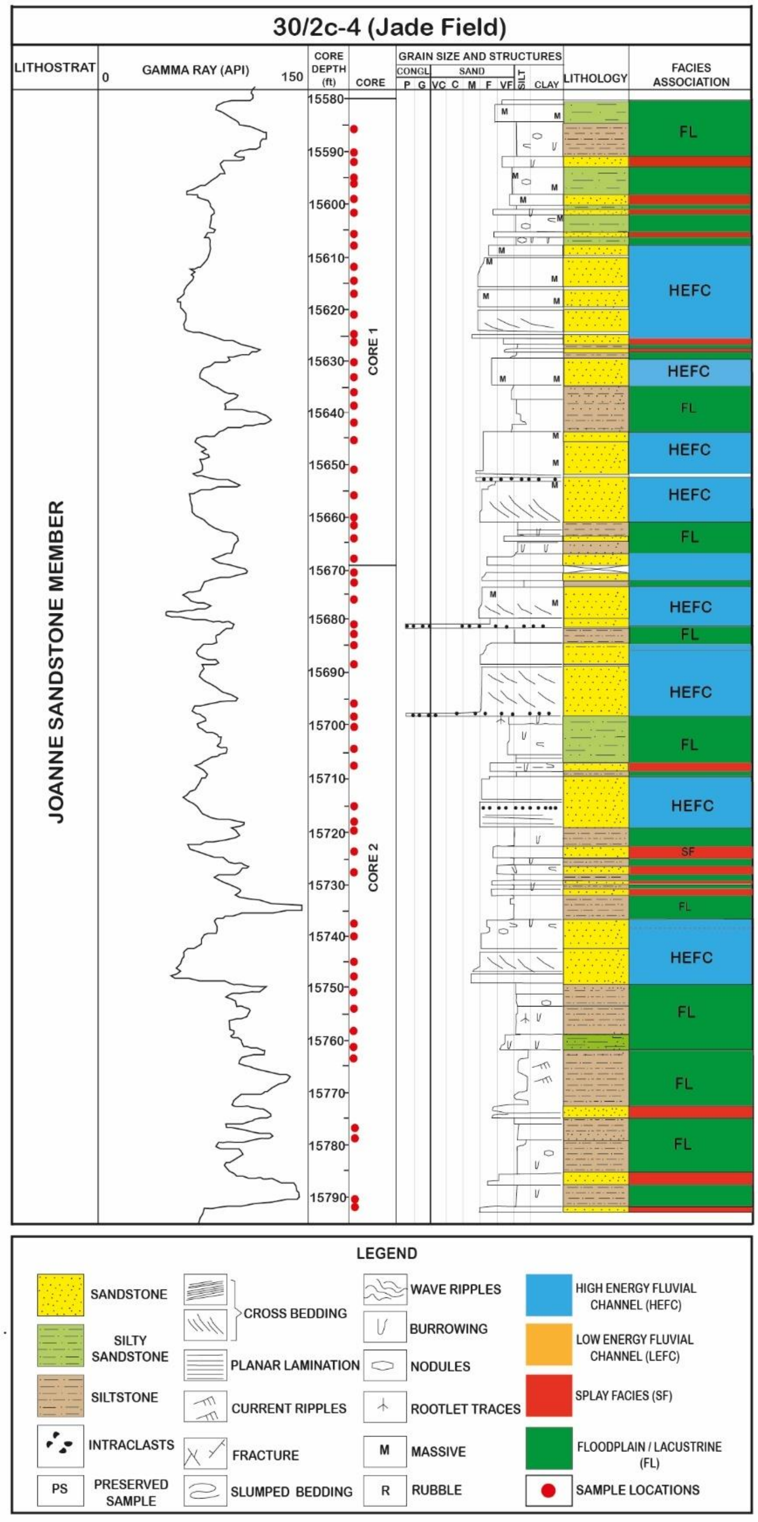

Figure 3.6: Sedimentary log of well 30/2c-4 (Jade Field) showing the interpreted facies association based on lithology, grain size and sedimentary structures. Corresponding gamma ray logs of the cored intervals and core sample locations are also shown.

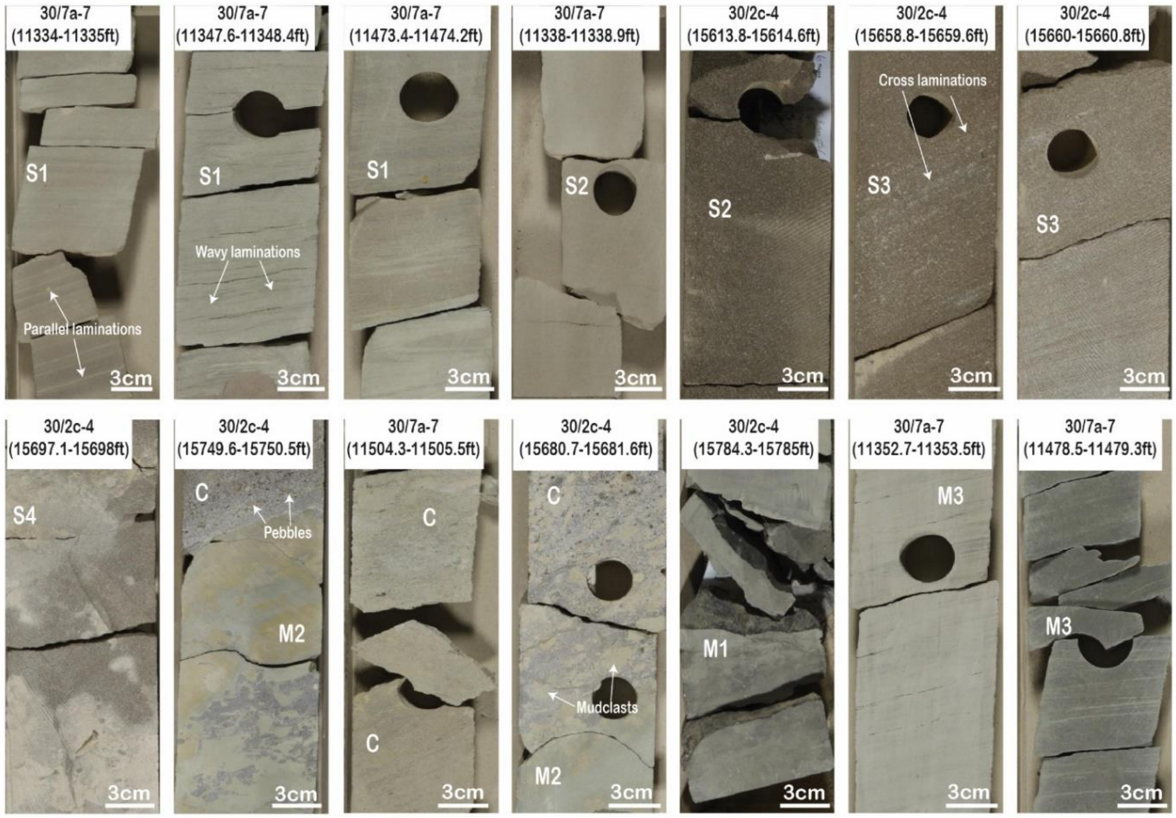

Figure 3.7: Representative core photographs of the identified facies. S1: Parallel laminated/current rippled sandstones; S2: massive sandstones; S3: cross laminated/bedded sandstones; S4: mottled, bioturbated and pedoturbated sandstones; C: intraformational conglomerates and gravelly sandstones. The dark green pebbles represent reworked dolocretes nodules sourced from adjacent floodplain facies (M2); M1: mottled and bioturbated mudstone; M2: pedoturbated mudstones and siltstones; M3: laminated mudstone.

form as crevasse (adjacent to river channels) or terminal splay (McKie and Audretsch 2005; McKie 2011; Akpokodje et al. 2017; Gray et al. 2019). The micaceous splay sandstone facies are interpreted to depict more proximal sheetflood deposits while the argillaceous and highly micaceous splay sandstones correspond to more distal sedimentation.

3.5.1.3 Floodplain, palaeosols and lakes (FL)

The sediment packages characterising this facies association generally include silt to clay grain-sized siltstones and mudstones (Figs. 3.5, 3.6 and 3.8j-l). They mostly contain pedogenic carbonate nodules (e.g., dolocrete), suggested to be reworked as clasts within channel bases, influencing the distribution of carbonate cements. They are usually mottled, bioturbated and pedoturbated. Common sedimentary structures include current or wave ripples, and parallel laminations, where not overprinted by bioturbation and pedoturbation. The sediments of this facies association are generally associated with fluvial channel and splay facies and can form thicker units up to 27 ft (8 m). The floodplain facies (M1 and M2; Fig. 3.7) represent sediments deposited in low energy

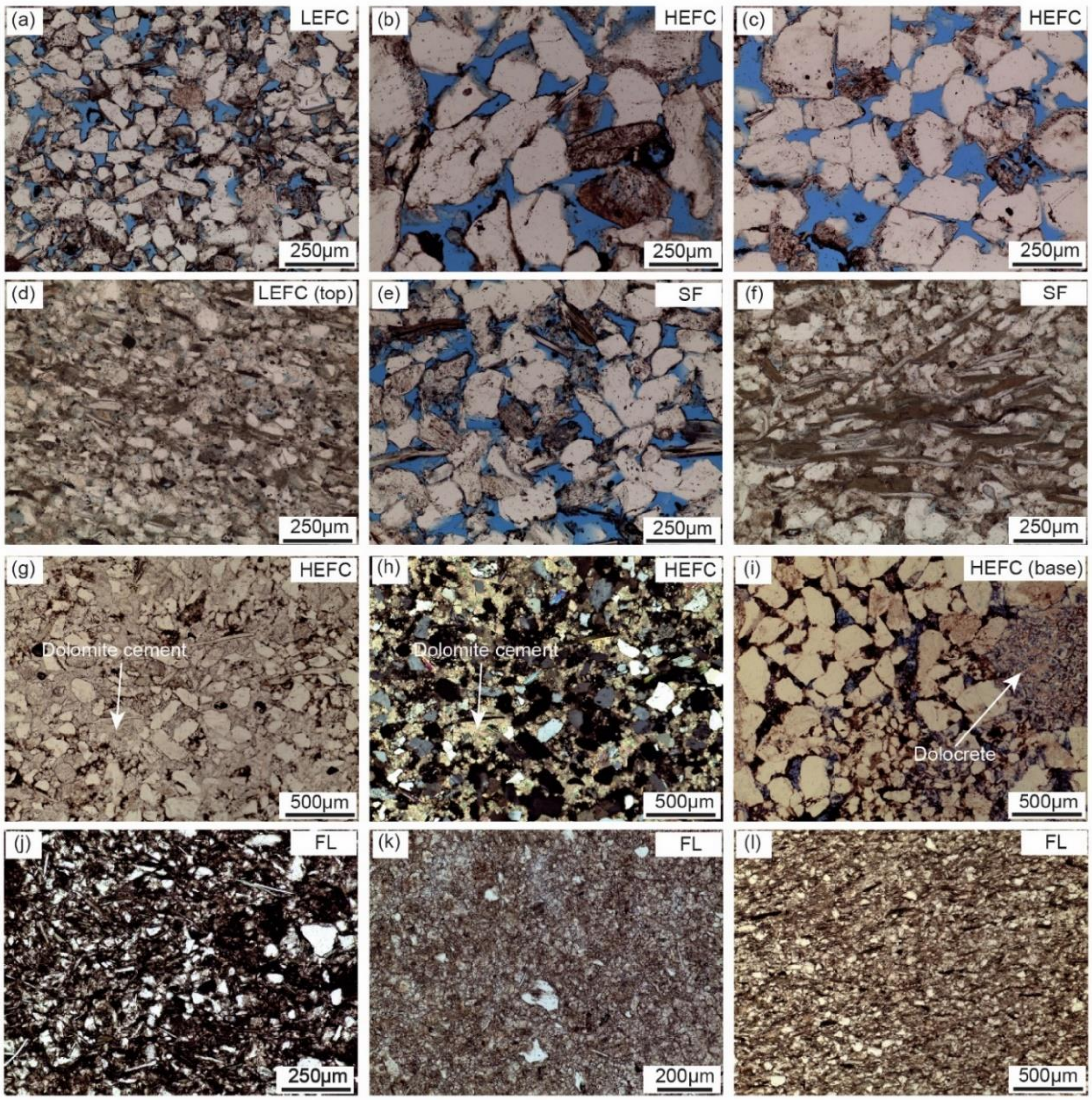

Figure 3.8: Representative thin section photomicrographs of the various facies and their reservoir properties (ϕ: porosity; Kh: permeability; PPL: plane polarized light; XPL: Cross polarized light; n/a: not applicable). (a) Facies S1: very fine-grained sandstone (30/7a-7), ϕ: 25.7%, Kh: 45 mD, depth: 11335 ft (3454.9 m); (b) Facies S2: medium-grained sandstone (30/2c-4), ϕ: 25.4%, Kh: 890 mD, depth: 15614.17 ft (4759.2 m); (c) Facies S3: upper fine-grained sandstone (30/2c-4) ϕ: 23%, Kh: 1050 mD; Depth: 15660 ft (4773.2 m); (d) Facies S1: very fine-grained current rippled sandstone (30/7a-7), ϕ: 18.1%, Kh: 3.1 mD; depth: 11480 ft (3499.1 m); (e) Facies S1: lower fine-grained sandstone (30/7a-7), ϕ: 23.5%, Kh: 166 mD, depth: 11468.3ft (3495.6m); (f) Facies S1: very fine-grained current rippled sandstone (30/7a-7), ϕ: 6.9%, Kh: 0.01 mD, depth: 11360.1ft (3462.6 m); (g) Facies S4: upper fine-grained pedoturbated sandstone - PPL (30/02c-4), ϕ: 13.3%, Kh: 2.6 mD, depth: 15697 ft (4784.5 m); (h) Facies S4: upper fine-grained pedoturbated sandstone - XPL (30/2c-4), ϕ: 13.3%, Kh: 2.6 mD, depth: 15697 ft (4784.5 m); (i) Facies C. ϕ: 4.9%, Kh: 0.04 mD, depth: 15681 ft (4779 m) - 30/2c-4; (j) Facies M1. ϕ: 6.3%, Kh: 0.014 mD, depth: 15778 ft (4809 m) - 30/2c-4; (k) Facies M2. ϕ: 6.7%, Kh: 0.017mD, depth: 15682 ft (4780 m) - 30/2c-4; (l) Facies M3. ϕ: 10.5%, Kh: 0.11mD, depth: 11479 ft (3498.8 m) - 30/7a-7. (LEFC: Low energy fluvial channel; HEFC: High energy fluvial channel; SF: Splay/sheetflood) and FL: Floodplain/lake facies).

environments and/or distal parts of sheetflood and splay facies. The lacustrine facies (M3; Fig. 3.7) represent depositions within abandoned channels or lakes created by salt tectonic subsidence. The presence of dolocrete nodules in these deposits is indicative of pedogenesis resulting from lowering of the water table and prolonged sub-aerial exposure in an arid setting (Akpokodje et al. 2017; Gray et al. 2019).

3.5.2 Detrital texture and composition

The Skagerrak sandstones are very fine- to medium-grained (Fig. 3.9) and moderately well sorted (0.5-0.71) to very well sorted (<0.35) according to the classification of sorting degree proposed by Folk and Ward (1957). The sandstones are subarkosic to lithic arkosic in composition (Folk 1980) (Fig. 3.10). Compositionally, the sandstones (i.e., Judy and Joanne) are immature and have an average composition of 55% quartz, 39% feldspar, and 6% rock fragments. Quartz grains comprise both monocrystalline and polycrystalline quartz but are mostly monocrystalline. The feldspar grains include K-feldspar, plagioclase (of an albitic composition), and trace amounts of microcline. Associated rock fragments include igneous and metamorphic rocks. Intrabasinal mudclasts and dolocrete nodules are also common and more abundant at channel bases (Fig. 3.8i). Detrital micas (muscovite and biotite) range from 0.7% to 19.6% (avg. 6.2%) and 0.3% to 8.3% (avg. 2.7%) in the sandstones of the Judy and Joanne member, respectively. They are, however, more abundant in SF sandstones than in HEFC and LEFC sandstones in both members (Tables 3.4 and 3.5). In addition to detrital micas, other accessory minerals recognised during SEM analysis include rutile, apatite, and zircon, but these occur in trace amounts within the samples.

Both sandstone members (Judy and Joanne) are compositionally similar. However, they have different average grain size and total amount of clay (detrital/authigenic). Sandstones from the Joanne member are on average, coarser compared to those from the Judy member (Table 3.6 and Fig. 3.9). Judy member sandstones are made up of LEFC, HEFC and SF sandstone facies, and have an average grain size of 0.102 mm (upper very fine sand). Joanne member sandstones, on the other hand, are composed of HEFC and SF sandstone facies, and have an average grain size of 0.19 mm (upper fine sand) (Tables 3.4-3.6). The detrital clay matrix consists of clay minerals mixed with silt-sized quartz and feldspar. The clays consist of chlorite and illite, with moderately high birefringence and greenish to brown colour. In this study, it is sometimes difficult to distinguish detrital clays from authigenic clays due to their diagenetic recrystallization. Thus, for simplicity, the clays have been classified into pore-filling and grain-coating clays. Total clay content varies from 5.6% to 46.9% in the Judy sandstones and 1.3% to 36.2% in the Joanne sandstones, based on point count data (Table 3.6). Pore-filling clays vary from 0% to 37.6% (avg. 9.7%) and 0% to 33.6% (avg. 8.9%) in the Judy and Joanne sandstones, respectively. Grain-coating clays vary from 0.3% to 17.4% (avg. 6.6%) in the Judy sandstones and 0.3% to 8.3% (avg. 3.6%) in the Joanne sandstones (Table 3.6). Generally, the HEFC and LEFC sandstones in both members have a lower average clay content than their SF counterparts. In addition, the LEFC sandstones, on average, have a higher total clay content compared to the HEFC sandstones (Tables 3.4 and 3.5).

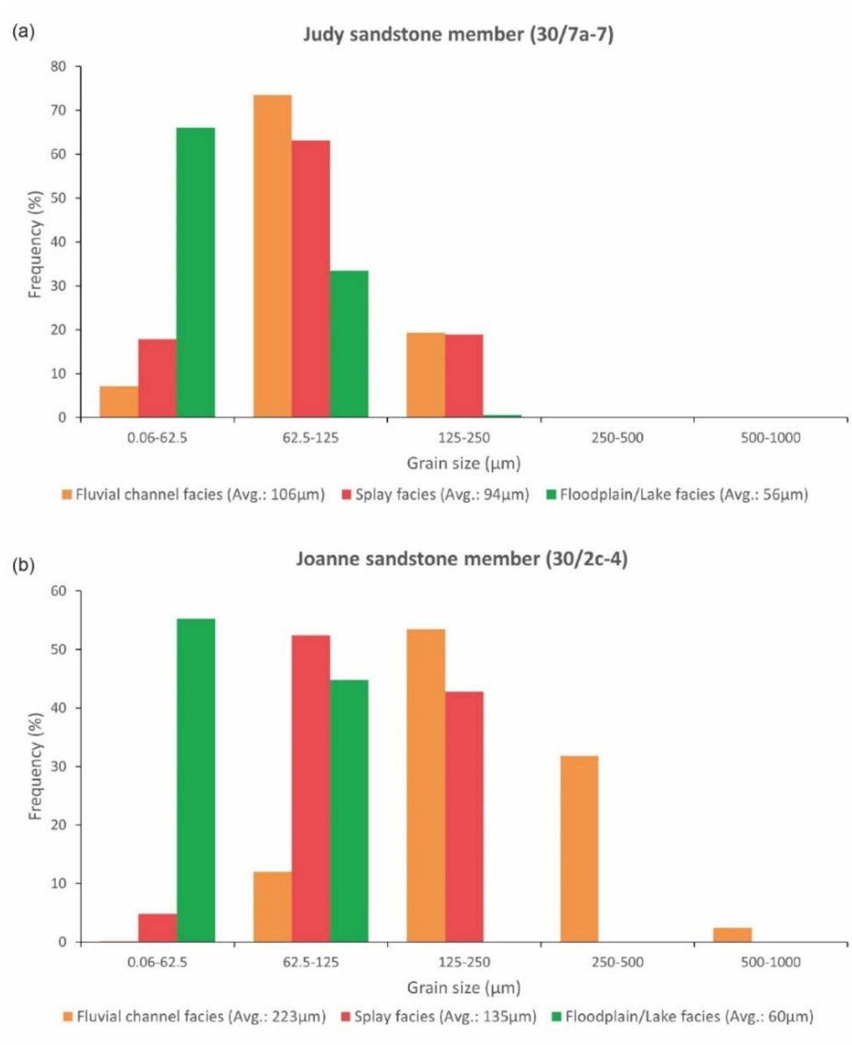

Figure 3.9: Grain size distribution by facies for (a) Judy and (b) Joanne sandstone members.

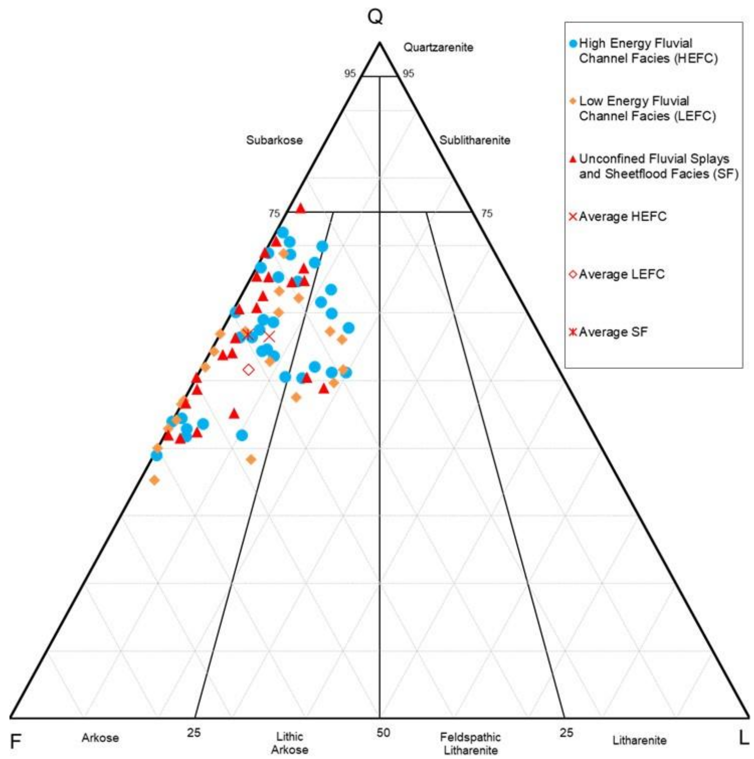

Figure 3.10: QFL plot showing the classification of the Skagerrak Formation sandstones in this study (after Folks, 1980).

3.5.3 Diagenesis

A summary of the paragenesis of the Triassic Skagerrak Formation sandstones is shown in figure 3.16.

3.5.3.1 Compaction

Skagerrak Formation sandstones exhibit different degrees of mechanical compaction, with minimal input from chemical compaction. Evidence of mechanical compaction in the studied sandstones include grain re-arrangement, grain deformation, bending of mica grains (Fig. 3.11a), point and long grain contacts between grains (Fig. 3.11b and c). Chemical compaction (or pressure solution) features include concave-convex and sutured grain contacts, and these occur between some detrital quartz grains (Fig. 3.11b and d). An important parameter for measuring the degree of mechanical compaction is intergranular volume (IGV), which is the sum of intergranular porosity, intergranular cement, and depositional matrix (Houseknecht 1987, 1988; Paxton et al. 2002).

Table 3.4: Summary of petrographic data for the Skagerrak Judy sandstones in the Judy field (well 30/7a-7) by facies (LEFC: Low energy fluvial channel; HEFC: High energy fluvial channel; SF: Unconfined fluvial splays and sheetfloods). More detailed data are reported in Appendix A.

Judy sandstones (30/7a-7)												
	LEFC				HEFC				SF			
	Min	*Max*	*Avg.*	*N*	*Min*	*Max*	*Avg.*	*N*	*Min*	*Max*	*Avg.*	*N*
Quartz (%)	20	45	33.8	22	30	42.7	35.3	8	25.7	44.7	33.2	12
Feldspar (%)	17.7	42.7	28.2	22	15	46.7	23.8	8	10.7	41.6	23.9	12
Total lithic fragments (%)	0.3	13.6	6.1	22	0.3	12.6	7.7	8	0.3	11	3.6	12
Total mica (%)	0.7	13.6	6	22	1.3	9.3	4.1	8	1.3	19.6	8	12
Quartz cement (%)	0.3	4.7	1.5	22	0.7	4.3	3.1	8	0	3.8	0.8	8
K-feldspar cement (%)	0	0.7	0.4	22	0	0.7	0.2	8	-	-	-	
Carbonate cement (%)	0	30	1.4	22	0	8.3	1.8	8	0.7	-	-	
Helium porosity (%)	2.3	26.7	22.3	22	17.9	26.0	23.8	8	6.9	23.5	17.5	12
Permeability (mD)	0.01	141	41.2	22	14.0	539	155.9	8	0.01	166	17.3	12
Grain size (mm)	0.07	0.13	0.09	22	0.12	0.17	0.14	8	0.07	0.14	0.09	12
Sorting (F & W)	0.30	0.61	0.38	22	0.36	0.43	0.38	8	0.32	0.45	0.39	12
Pore-filling clay (%)	0.7	32.7	6.8	22	0	19.6	3.9	8	0	37.6	18.9	12
Grain-coating clay (%)	0.3	17.4	7.5	22	2.7	8.3	5.8	8	0.3	9.7	5.4	12
Total clay (%)	6.3	33	14.3	22	5.6	22.3	9.7	8	6.6	46.9	24.2	12
Intergranular porosity (%)	0.3	13.6	8.4	22	2.4	17.0	9.7	8	0	18.7	4.2	12
Dissolution porosity (%)	0.3	5.6	2.3	22	1.0	6.0	3.7	8	0	5.0	1.4	12
Microporosity (%)	2.3	18.5	11.8	21	2.6	15	9.4	7	2.5	17.8	12.0	12
Total thin section porosity (%)	0.3	16.6	10.2	22	6.1	19.4	13.4	8	0.7	21	5.5	12
IGV (%)	18.6	31.3	24.3	21	16.3	30.9	25.4	8	18.2	38.1	28.5	11

Table 3.5: Summary of petrographic data for the Skagerrak Joanne sandstones in the Jade field (well 30/2c-4) by facies (LEFC: Low energy fluvial channel; HEFC: High energy fluvial channel; SF: Unconfined fluvial splays and sheetfloods). More detailed data are reported in Appendix A.

Joanne sandstones (30/2c-4)												
	LEFC				HEFC				SF			
	Min	*Max*	*Avg.*	*N*	***Min***	***Max***	***Avg.***	***N***	***Min***	***Max***	***Avg.***	***N***
Quartz (%)	-	-	-	-	19.3	54.7	37.7	26	27.6	40	32.9	11
Feldspar (%)	-	-	-	-	6.3	39.3	24.5	26	12	42.3	23.7	11
Total lithic fragments (%)	-	-	-	-	0.3	11.7	3.4	26	0.3	3.6	1.4	11
Total mica (%)	-	-	-	-	0.3	8.3	2.5	26	0.3	6.3	3.0	11
Quartz cement (%)	-	-	-	-	0.3	7.3	3.8	26	0	4.3	0.9	11
K-feldspar cement (%)	-	-	-	-	0	1.3	0.2	26	0	0.3	0.1	11
Carbonate cement (%)	-	-	-	-	0	42.7	8.1	26	0	36.3	8.5	11
Helium porosity (%)	-	-	-	-	4.9	25.9	19.2	24	6.5	16.0	11.4	11
Permeability (mD)	-	-	-	-	0.038	1150	394.7	24	0.004	2.35	0.41	11
Grain size (mm)	-	-	-	-	0.13	0.33	0.21	26	0.063	0.19	0.12	11
Sorting (F & W)	-	-	-	-	0.36	0.71	0.5	26				
Pore-filling clay (%)	-	-	-	-	0	27.9	2.9	26	3.6	33.6	23.3	11
Grain-coating clay (%)	-	-	-	-	0.3	8.3	3.5	26	0.7	7.0	3.8	11
Total clay (%)	-	-	-	-	1.3	29.2	6.4	26	7.6	36.2	27.1	11
Intergranular porosity (%)	-	-	-	-	0	21.3	9.3	26	0	3.0	0.7	11
Dissolution porosity (%)	-	-	-	-	0	5.7	1.9	26	0	2.0	0.7	11
Microporosity (%)	-	-	-	-	1.4	19.8	7.4	24	6.5	15.7	10.1	11
Total thin section porosity (%)	-	-	-	-	0	23.9	11.2	26	0	4.3	1.4	11
IGV (%)	-	-	-	-	16.9	37.6	27.1	24	12.5	42.8	32.3	8

Table 3.6: Distribution of grain size, porosity, permeability, and other measured parameters for the Judy and Joanne sandstones in wells 30/7a-7 (Judy field) and 30/2c-4 (Jade field).

Formation /well		**Grain size (mm)**	**Thin section porosity (%)**	**Helium porosity (%)**	**Permeability (mD)**	**Total clay (%)**	**Pore-filling clay (%)**	**Grain-coating clay (%)**	**Microporosity (%)**	**IGV (%)**	**COPL (%)**	**CEPL (%)**
Judy sandstones (30/7a-7)	Minimum	0.065	0	2.3	0.01	5.6	0	0.3	2.3	16.3	20.4	3.8
	Maximum	0.165	21.0	26.7	539.0	46.9	37.6	17.4	18.5	38.1	34.3	13.8
	Average	0.102	9.5	21.1	54.1	16.2	9.7	6.6	11.4	25.7	27.8	8.0
Joanne sandstones (30/2c-4)	Minimum	0.063	0	4.9	0.004	1.3	0	0.3	1.4	12.5	11.9	4.7
	Maximum	0.33	23.9	25.9	1150	36.2	33.6	8.3	19.8	42.8	37.1	31.6
	Average	0.19	8.3	16.8	270.8	12.5	8.9	3.6	8.3	28.4	24.7	11.6

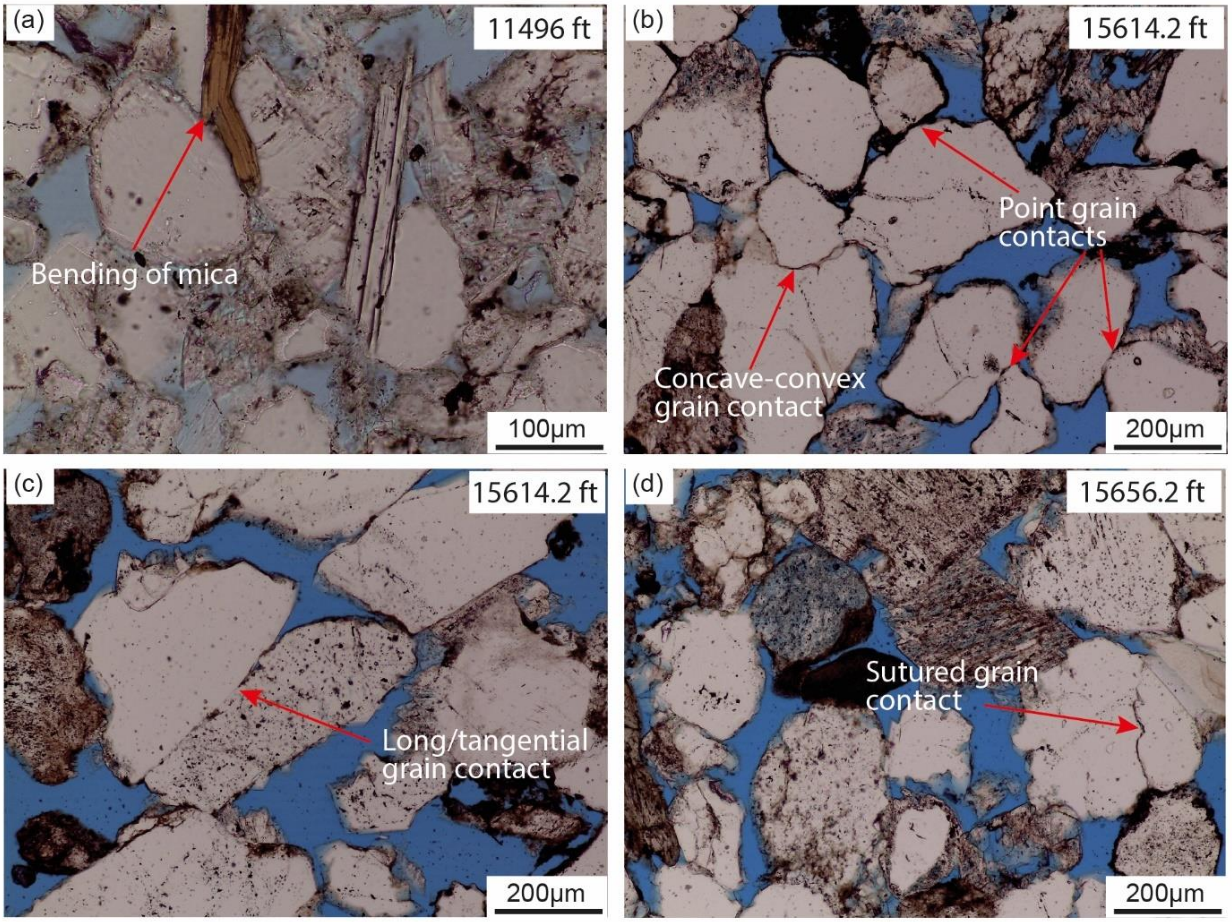

Figure 3.11: Thin-section photomicrographs showing different compaction features - (a) Bending of mica; (b) Point and concave-convex grain contacts; (c) Long grain contact; and (d) Sutured grain contact.

The calculated IGV values range from 16.3% to 38.1% (avg. 25.7%) and 12.5% to 42.8% (avg. 28.4%) in wells 30/7a-7 and 30/2c-4, respectively (Table 3.6). The wide range in IGV values indicates variations in the degree of compaction between the samples. Cross plots of COPL and CEPL for the studied sandstone samples are shown in figure 3.12a and b. Sandstone samples with clay matrix >10% were not included in the cross plots to avoid overestimation of compactional porosity loss due to abundant clay matrix (Lundegard 1992). In Judy well (30/7a-7), COPL and CEPL values range from 20.4% to 34.3% (avg. 27.8%) and 3.8% to 13.8% (avg. 8%), respectively, while in Jade well (30/2c-4), COPL and CEPL range from 11.9% to 37.1% (avg. 24.7%) and 4.7% to 31.6% (avg. 11.6%), respectively (Table 3.6). In well 30/7a-7, 11% of the samples fall between the 0% and 10% intergranular porosity line while the remaining 89% fall within 10 to 20% intergranular porosity lines. In well 30/2c-4, 40% of the samples fall within 0% to 10% intergranular porosity lines, 52% fall between 10% and 20% lines, while the remaining 8% fall between 20% to 30% intergranular porosity lines. The significance of the COPL versus CEPL plot is highlighted in the discussion section.

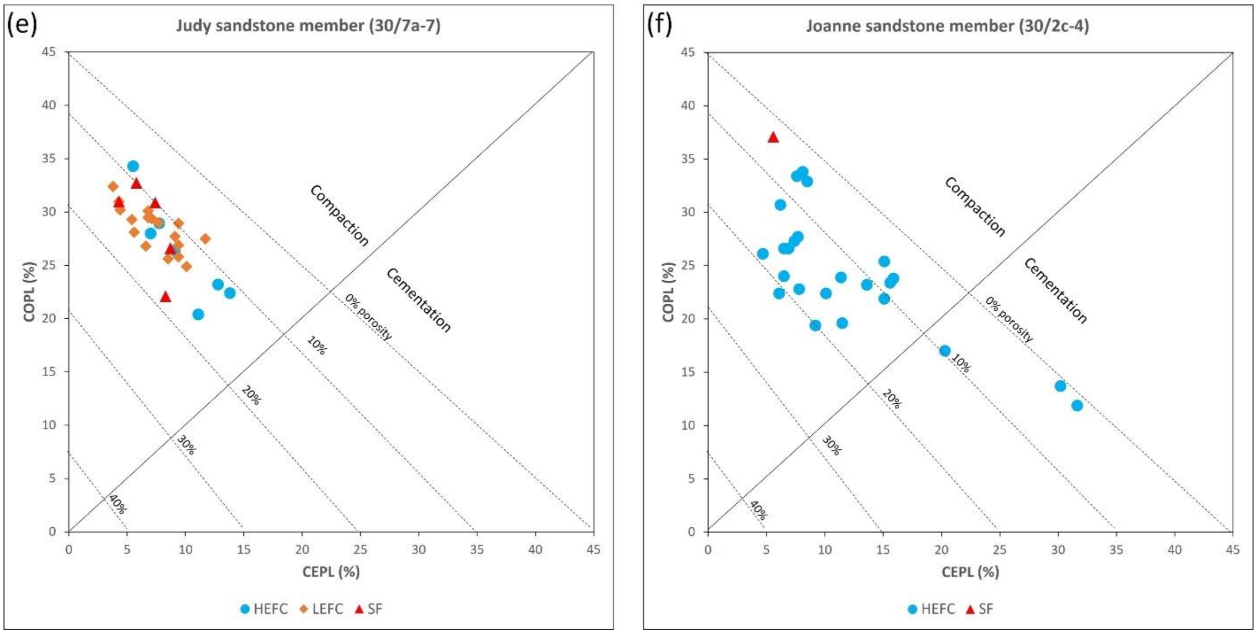

Figure 3.12: Plots of porosity loss due to compaction (COPL) and porosity loss due to cementation (CEPL) for the Judy and Joanne sandstones. Sandstones samples with more than 10% clay matrix were not included to avoid the overestimation of compactional porosity loss. (LEFC: Low energy fluvial channel; HEFC: High energy fluvial channel; SF: Splay/sheetflood) facies).

3.5.3.2 Diagenetic minerals

3.5.3.2.1 Quartz cement

In the studied sandstone samples, quartz cement occurs mainly as synataxial quartz overgrowths on detrital quartz grains. They typically occur on non-clay coated quartz grain surfaces or at breaks within clay coatings. Where present, they partially or fully cover detrital quartz grains and encroach into the available pore spaces (Figs. 3.13a-d). Quartz cement thickness ranges from 2.3 µm to 100 µm with an average of 14 µm. Based on point counting, quartz cement volume ranges from 0.3% to 4.7% (avg. 1.7%) in the Judy sandstone member, and from 0.3% to 7.3% (avg. 3.2%) in the Joanne sandstone member (see Appendix A). Microquartz cement has been reported for the Skagerrak Formation sandstones (Nguyen et al. 2013; Stricker and Jones 2016), but was not observed in the analysed samples.

3.5.3.2.2 Clay minerals

Diagenetic clay minerals are common in all the sandstones studied. Detailed petrographic and SEM-EDX analysis revealed that the diagenetic clay minerals are predominantly chlorite and, to a lesser extent, a mixture of illite and chlorite (Figs. 3.13d-j and 3.14). Kaolin was not observed in the studied samples. The diagenetic clays occur in variable amounts and in three principal forms: grain-coating, pore-filling, and grain-replacing. The diagenetic grain-coating clays are mainly chlorite, but in some samples, they coexist with illite; they occur on the surfaces of the detrital grains (e.g., quartz and feldspar, Figs. 3.13a-h) and are in some instances enclosed by the pore-filling clays making their identification challenging. The diagenetic pore-filling clays are mostly chlorite (Fig. 3.13i); however, a mixture of densely packed illite and chlorite, occurring as pore-filling clay is also observed in some samples (Fig. 3.13j).

Chlorite coat properties (coverage and thickness) – As revealed by SEM-EDX analysis, the chlorite coats in the studied sandstones are Fe- and Mg-rich (Fig. 3.14 and Table 3.7). In few samples, the chlorite coats commonly display two layers, each exhibiting different morphology and orientation (Pittman et al. 1992; Stricker and Jones 2016; Stricker et al. 2018). Layer 1 (or root zone) is made up of densely packed, laminated, and poorly crystallized sheets, oriented parallel to the detrital quartz grain surface (Fig. 3.14). Layer 2 (outer layer) contains well-defined crystals that are parallel but sometimes near perpendicular to the grain surface (Fig. 3.14). Layer 1 comprises a mixture of illite and chlorite, whereas layer 2 is mainly chlorite. The chlorite coats are less developed and discontinuous on some grains, but well developed and continuous on others. Where they are absent or discontinuous, quartz overgrowth cements were observed (Figs. 3.13a-c). In samples where chlorite coats are well-developed and continuous, the development of quartz overgrowth cements was inhibited (Figs. 3.13d-h). Chlorite coat coverage and thicknesses on the measured grains range from 1.2% to 100% and 0.5 μm to 16 μm, respectively. Average chlorite coat coverage in the Joanne sandstone member samples ranges from 15.9% to 69%, with 69% of the samples having <40% average chlorite coat coverage. In the Judy sandstone samples, average chlorite coat coverage is higher, ranging from 70% to 98%. 98% of the coating thickness values are <10 μm while the remaining 2% are within the range of 10 μm to 16 μm. Coating thickness values >10 μm are commonly found in grain embayments (Figs. 3.13f and h). Average chlorite coat thickness ranges from 4.2 μm to 7.2 μm in the Joanne samples, whereas in the Judy samples, it ranges from 3.5 µm to 6.2 µm. Coating thickness is generally not uniform on the grain surfaces; they are often thicker in grain embayments (i.e., grain indentations) (Fig. 3.13h). A summary of chlorite coat coverage and thickness measurements is presented in table 3.8.

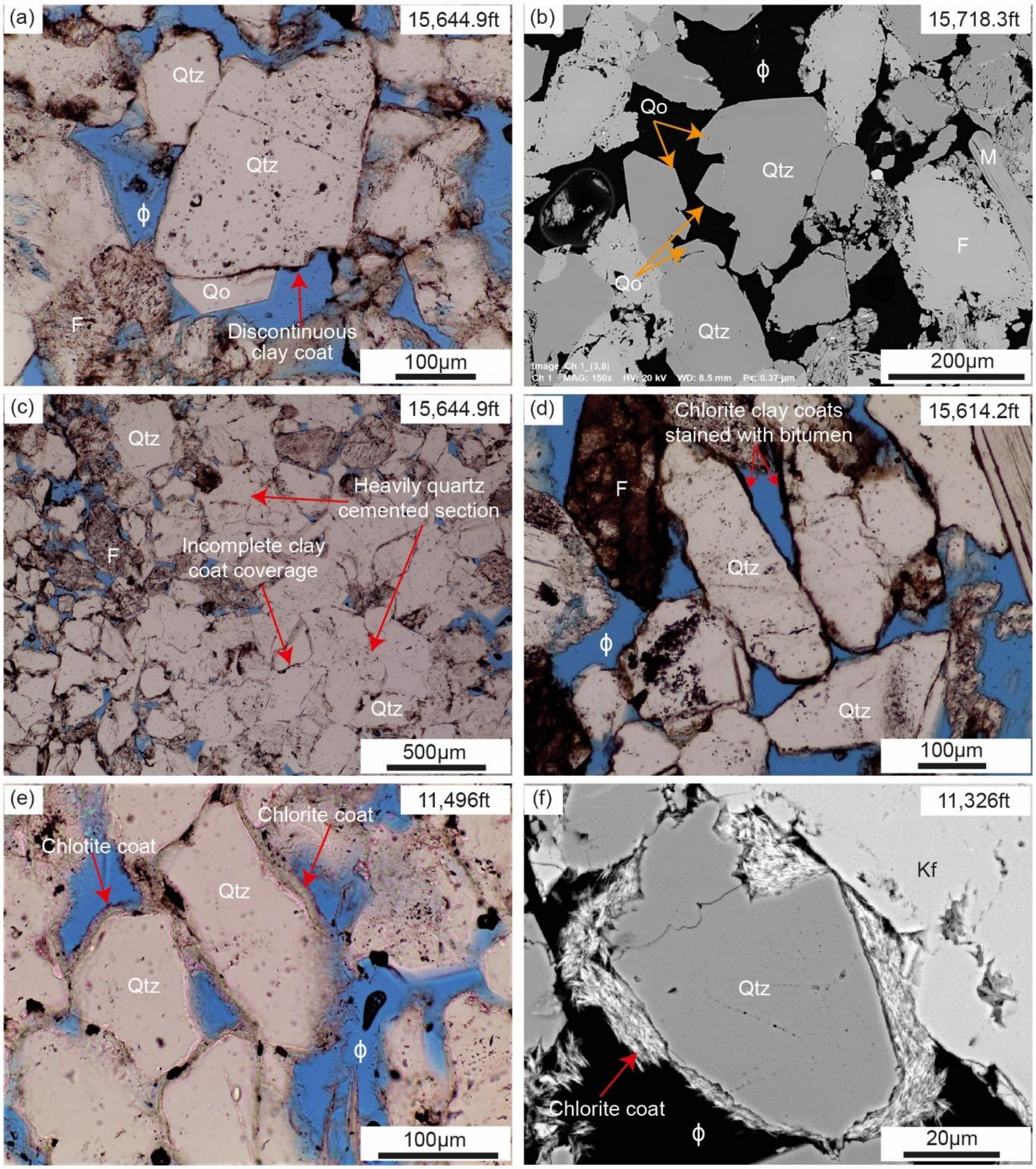

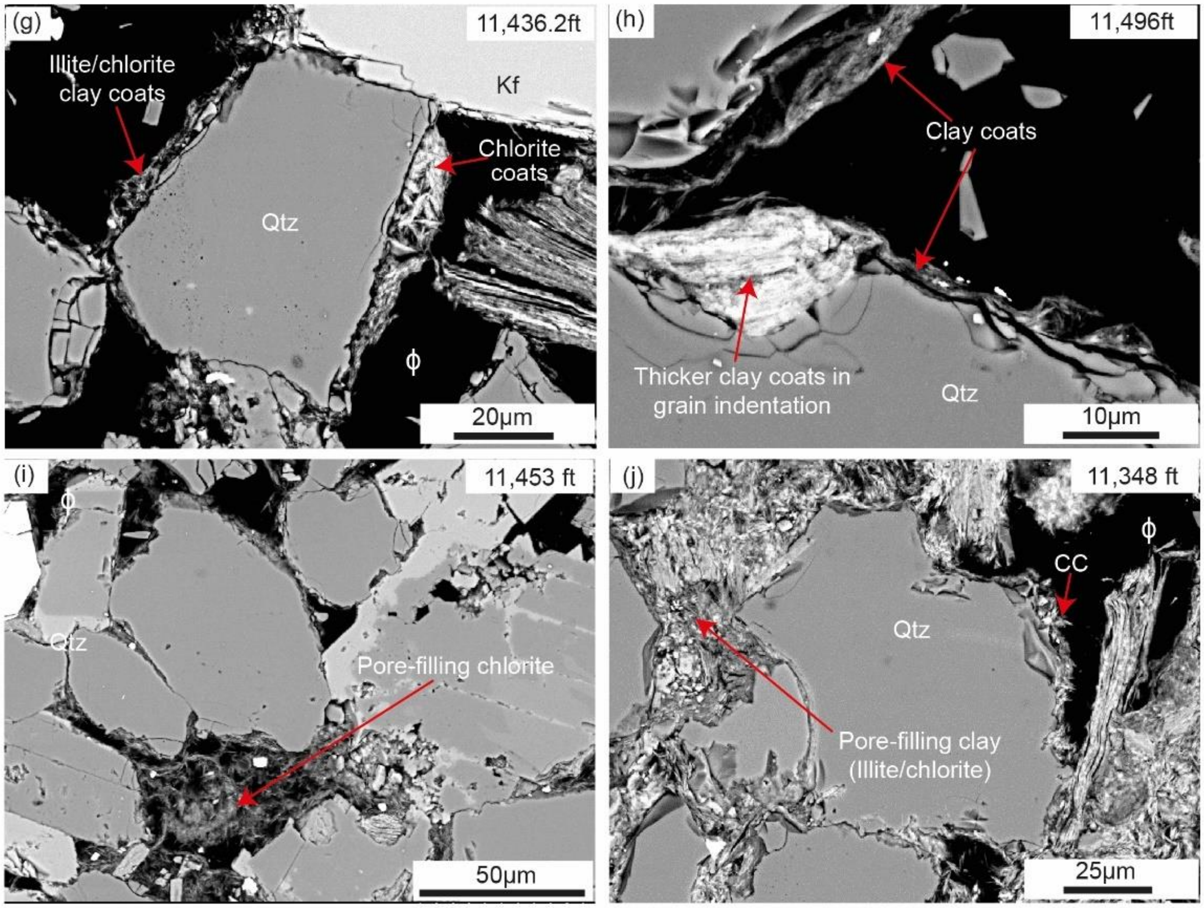

Figure 3.13: Thin section photomicrographs and BSE images showing detrital quartz (Qtz), feldspar (F), mica (M), quartz overgrowth (Qo), clay coats, pore-filling clays, and porosity (ϕ). (a-c) Thin section photomicrographs showing quartz overgrowth (Qo) and discontinuous clay coats on detrital quartz grains; (d-e) Thin section photomicrographs showing well-developed and continuous clay coats; (f-g) BSE images showing well-developed clay coats; (h) BSE image showing thicker clay coats in grain indentation; and (i-j) BSE images showing pore-filling clays occluding pore space.

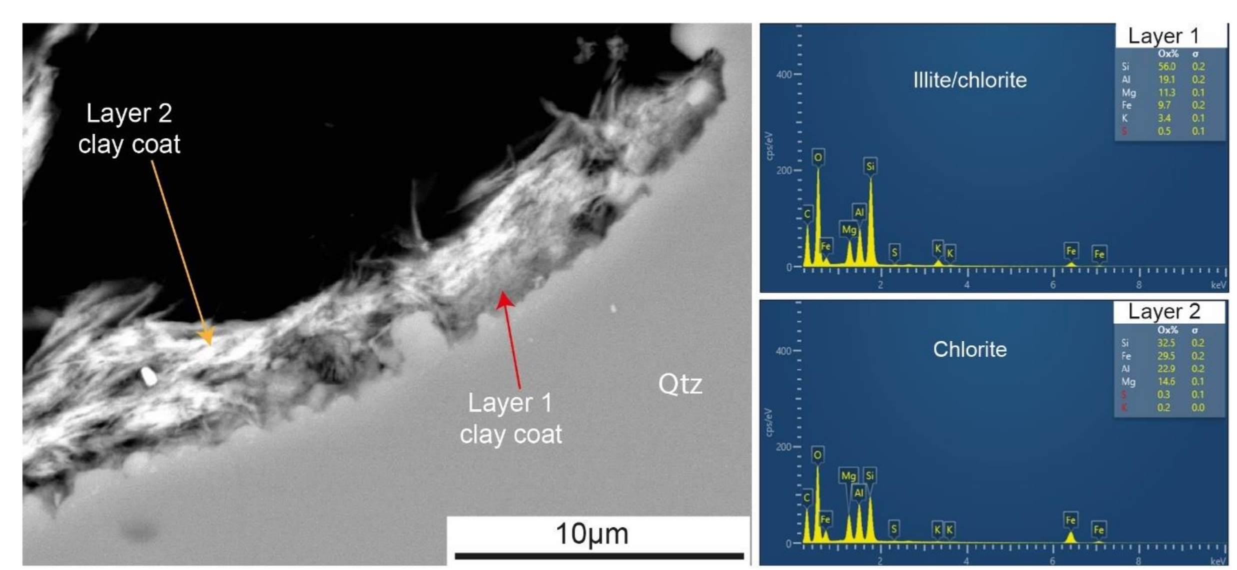

Figure 3.14: BSE image and EDX spectra of a sample at 11,348 ft (well 30/7a-7), showing a two-layered clay coats. The EDX spectra on the right show changes in clay coat chemistry from the root zone to the outer layer. The root zone (layer 1) is a mixture of illite and chlorite, while layer 2 is pure chlorite.

Table 3.1: Result of a spot SEM-EDX spectral analysis conducted on a two layered clay coats on a detrital quartz grain (shown in figure 3.14).

	Layer 1			**Layer 2**		
Elements	Wt (%)	Oxide	Oxide (%)	Wt (%)	Oxide	Oxide (%)
O	42.7			40.7		
Si	26.3	SiO_2	56.3	15.3	SiO_2	32.7
Al	13.7	Al_2O_3	19.2	12.2	Al_2O_3	23.1
Fe	7.6	FeO	9.7	22.9	FeO	29.5
Mg	6.9	MgO	11.4	8.9	MgO	14.7
K	2.8	K_2O	3.4	0	K_2O	0
Total	100		100	100		100
Clay type	***Illite-chlorite***			***Chlorite***		

3.5.3.2.3 Carbonate cements

Dolomite is the principal carbonate cement in the studied samples (Figs. 3.15a and b). Dolomite cements are found in all the facies identified, however, in variable amounts. Volumetrically, they range from 0% to 42.7% with an average value of 11.1%. They are locally distributed and occur mainly as pore-filling and, in some cases, infilling of partly dissolved grains. Dolocrete clasts deposited simultaneously with mud intraclasts were also recognized but are restricted to channel bases (Fig. 3.8i – facies C). Petrographic and SEM-EDX analysis revealed two types of dolomite cements: non-ferroan (nFe-D) and ferroan dolomite (Fe-D) cements. Based on petrographic light microscopy analysis, the nFe-D shows no stain, while the Fe-D was identified by its characteristic pale turquoise blue stain with potassium ferricyanide (Fig. 3.15a). Both types exhibit a rhombic crystal structure with compositional zonation in some places. The ferroan dolomite cements were observed to enclose the non-ferroan phase (Figs. 3.15a and b), indicating that they formed during late-stage diagenesis (i.e., mesodiagenesis). The carbon and oxygen isotope data for the carbonate cemented sandstones show that the $\delta^{13}C$ values for the carbonate cements vary between -16.17‰ and -8.13‰, and $\delta^{18}O$ values from -7.60‰ to +0.50‰ (Table 3.9).

Table 3.8: Summary of clay coat coverage measurements made on 23 sandstone samples from the Skagerrak Formation. Also included are measured textural parameters, quartz cement and clay coat volume derived from point counting, and their corresponding reservoir properties.

Well name	Sandstone member	Depth (ft)	Facies	Avg. grain size (µm)	Sorting	Clay coat coverage (%)	Clay coat volume_point count (%)	Clay coat thickness (µm)	Quartz cement volume (%)	Temp. (°C)	Thin-section porosity (%)	Helium Porosity (%)	Permeability (mD)
30/07a-7	Judy	11291.3	LEFC	98.3	0.44	78.5	7.3	3.7	1.8	164.0	9.7	24.1	43
30/07a-7	Judy	11303.8	LEFC	88.9	0.40	95.3	10	6.2	1.6	164.0	12	25.7	18
30/07a-7	Judy	11309.8	LEFC	93.3	0.44	96	6	4.9	0.5	164.0	14.4	21.5	27
30/07a-7	Judy	11335.1	LEFC	91.7	0.38	93	6.7	3.5	1.7	164.0	14	25.7	45
30/07a-7	Judy	11338.4	LEFC	96.8	0.34	91	5	4.9	1.3	164.0	13.3	26.2	53
30/07a-7	Judy	11433	SF	96.5	0.37	82	8	3.6	4.7	164.0	13.7	25	48
30/07a-7	Judy	11442	LEFC	101.4	0.40	98	5.6	5	2.7	164.0	14.7	25.9	85
30/07a-7	Judy	11468.3	SF	143.6	0.42	70	7	4.5	3.8	164.0	21	23.5	166
30/07a-7	Judy	11490.9	LEFC	135.2	0.50	92.7	5.2	4.7	4.2	164.0	16.6	21.9	52
30/07a-7	Judy	11496	HEFC	144.5	0.40	80.4	8.3	5	4	164.0	19.4	25.3	269
30/02c-4	Joanne	15612	HEFC	151.5	0.51	69	6.3	4.5	2.3	187.7	13	23.3	124
30/02c-4	Joanne	15614.2	HEFC	259.2	0.56	50	4.8	4.6	6	187.7	21	25.4	890
30/02c-4	Joanne	15617.1	HEFC	244.7	0.59	36.2	2.3	5.9	5	187.7	20.3	22	692
30/02c-4	Joanne	15621.1	HEFC	319.5	0.60	30.2	1.7	5	4.3	187.7	19.7	23.4	842
30/02c-4	Joanne	15625	HEFC	244.9	0.71	40	3.7	6.6	6	187.7	14.3	19.9	355
30/02c-4	Joanne	15644.9	HEFC	219.5	0.44	60	5.3	7.2	4.5	187.7	19.6	24.4	670
30/02c-4	Joanne	15650.1	HEFC	216.2	0.59	17	2.3	4.2	7.3	187.7	16.7	19.9	279
30/02c-4	Joanne	15656.2	HEFC	211.4	0.55	36.8	3.3	6	4.2	187.7	23.9	25.3	1150
30/02c-4	Joanne	15660	HEFC	220.7	0.52	27	1.3	6.2	6.2	187.7	19.7	23	1050
30/02c-4	Joanne	15671	HEFC	145.2	0.60	60.2	8.3	5.3	2.7	187.7	13.7	25.9	167
30/02c-4	Joanne	15676.2	HEFC	163.3	0.64	36	2.7	5.2	6.3	187.7	17.7	23.3	529
30/02c-4	Joanne	15718.3	HEFC	183.0	0.55	17.3	2.7	5.3	6	187.7	21.1	24.7	614
30/02c-4	Joanne	15748.2	HEFC	273.8	0.64	15.9	4	4.9	7	187.7	20	23	1134

Table 3.9: Stable carbon and oxygen isotopes data for carbonate cements in the Triassic Skagerrak Formation.

Field	Well name	Depth (ft)	Carbonate cement type	$\delta^{13}C_{V\text{-}PDB}$	$\delta^{18}O_{V\text{-}PDB}$	$\delta^{18}O_{V\text{-}SMOW}$
Judy	30/7a-7	11328.68	Dolomite	-11.90	-6.56	24.15
Judy	30/7a-7	11363.5	Dolomite	-9.95	-2.85	27.97
Judy	30/7a-7	11440.2	Dolomite	-8.13	-2.88	27.94
Judy	30/7a-7	11517	Dolomite	-10.32	-4.64	26.13
Judy	30/7a-7	11531.57	Dolomite	-16.17	-7.60	23.08
Jade	30/2c-4	15596.08	Dolomite	-9.48	-1.85	29.00
Jade	30/2c-4	15599	Dolomite	-9.03	-3.57	27.23
Jade	30/2c-4	15606	Dolomite	-9.37	-1.73	29.12
Jade	30/2c-4	15626	Dolomite	-8.69	0.50	31.43
Jade	30/2c-4	15636	Dolomite	-9.09	-2.37	28.46
Jade	30/2c-4	15638.33	Dolomite	-9.44	-0.95	29.93
Jade	30/2c-4	15661	Dolomite	-9.02	-1.00	29.88
Jade	30/2c-4	15681	Dolomite	-8.38	-4.01	26.78
Jade	30/2c-4	15697.17	Dolomite	-9.28	-4.03	26.76
Jade	30/2c-4	15706.08	Dolomite	-9.80	-1.52	29.34
Jade	30/2c-4	15714.95	Dolomite	-8.80	-1.37	29.50
Jade	30/2c-4	15745.08	Dolomite	-8.24	-5.42	25.33
Jade	30/2c-4	15750.5	Dolomite	-10.71	-3.56	27.24
Jade	30/2c-4	15781.92	Dolomite	-8.86	-2.26	28.58

3.5.4 Porosity and permeability distribution

Thin-section and helium porosity of samples from the Judy sandstone member (30/7a-7) range from 0% to 21% (avg. 7.3%) and 2.3% to 26.7% (avg. 19.1%), respectively, while the Joanne sandstone member samples (30/2c-4) have thin-section and helium porosity values in the range of 0% to 23.9% (avg. 5.1%) and 3.7% to 25.9% (avg. 13.7%), respectively. Core permeability ranges from 0.055 mD to 539 mD (avg. 40.9 mD) in the Judy sandstone member and from 0.004 mD to 1150 mD (avg. 197.4 mD) in the Joanne sandstone member (Appendix A). Cross plots of helium porosity and permeability show a strong positive correlation (R = 0.9) in both sandstone members (Fig. 3.18a and b). Also, thin-section porosity strongly correlates with permeability (Fig. 3.18c and d). Pore types identified in the studied samples include primary (intergranular), secondary (dissolution), and micro-pores, with intergranular pores dominating the pore system. Intergranular porosity ranges from 0.3% to 18.7% (avg. 7.8%) in the Judy sandstones and from 0% to 21.3% (avg. 8.8%) in the Joanne sandstones. Secondary porosity in the Judy and Joanne sandstones ranges from 0.3% to 6% (avg. 2.3%) and 0% to 5.7% (1.7%), respectively. The secondary pores were created by partial to complete dissolution of detrital grains (feldspars and rock fragments) (Figs. 3.15c and d). The micropores are not visible under the microscope. They are associated with the clay minerals in the studied sandstone samples and are responsible for the higher helium porosities compared to the thin-section porosities (Fig. 3.18e and f). Microporosity ranges from 2.3% to 18.5% (avg. 11.4%) in the Judy sandstones and 1.4% to 19.8% (avg. 8.3%) in the Joanne sandstones (Table 3.6). Cross plots of microporosity against total clay and grain-coating clay estimated from point counting show that microporosity generally increases with increasing clay content (Fig. 3.18g and h).

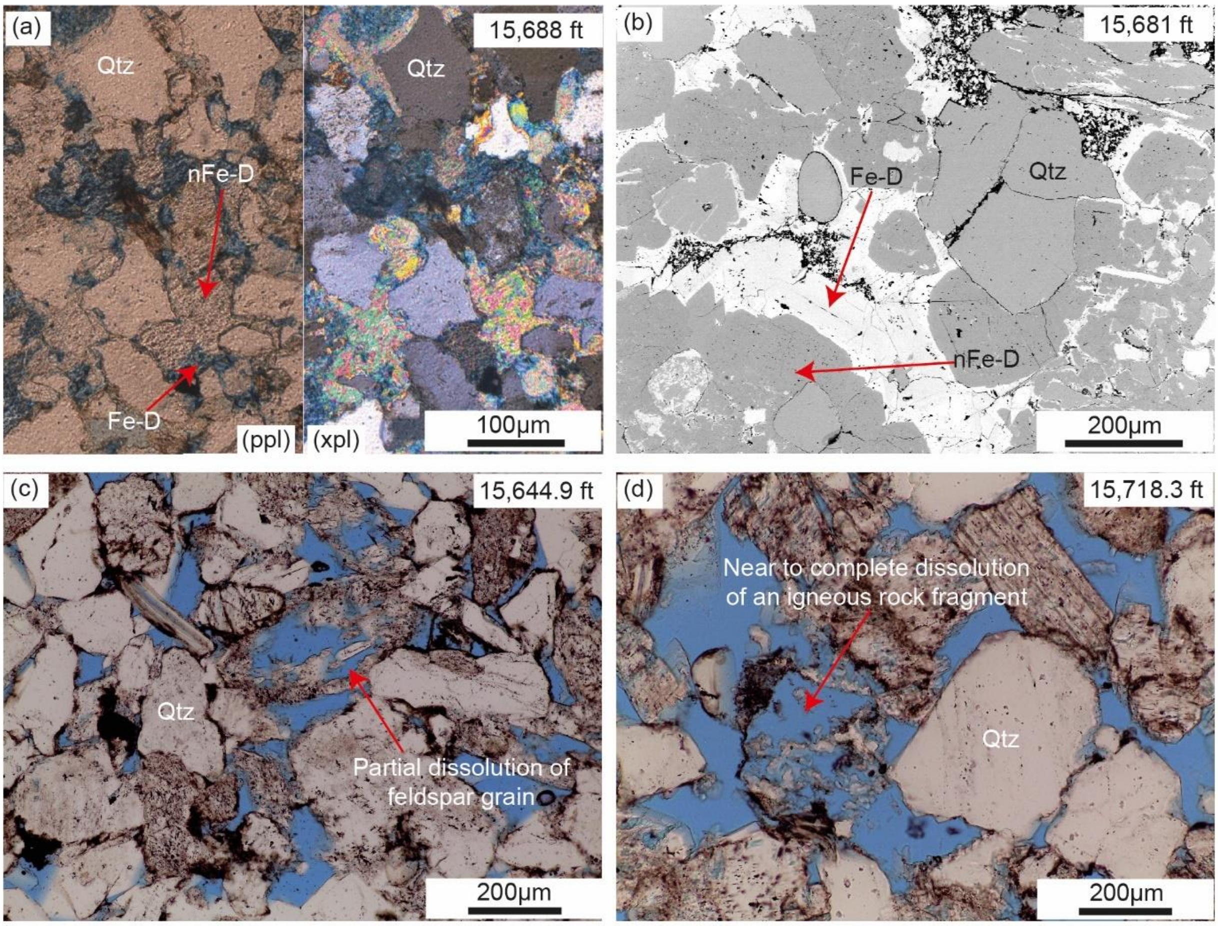

Figure 3.15: Thin section photomicrograph showing non-ferroan (nFe-D) and ferroan dolomite (Fe-D) under plane polarized (ppl) and cross polarized light (xpl); (b) BSE image showing non-ferroan (nFe-D) and ferroan dolomite (Fe-D). Both dolomite types exhibit a rhombic crystal structure with compositional zonation. The ferroan dolomite encloses the non-ferroan phase indicating that the ferroan dolomite was formed during late-stage diagenesis; (c-d) Thin section photomicrographs showing secondary porosity created by partial and near to complete dissolution of feldspar grain (c) and igneous rock fragment (d).

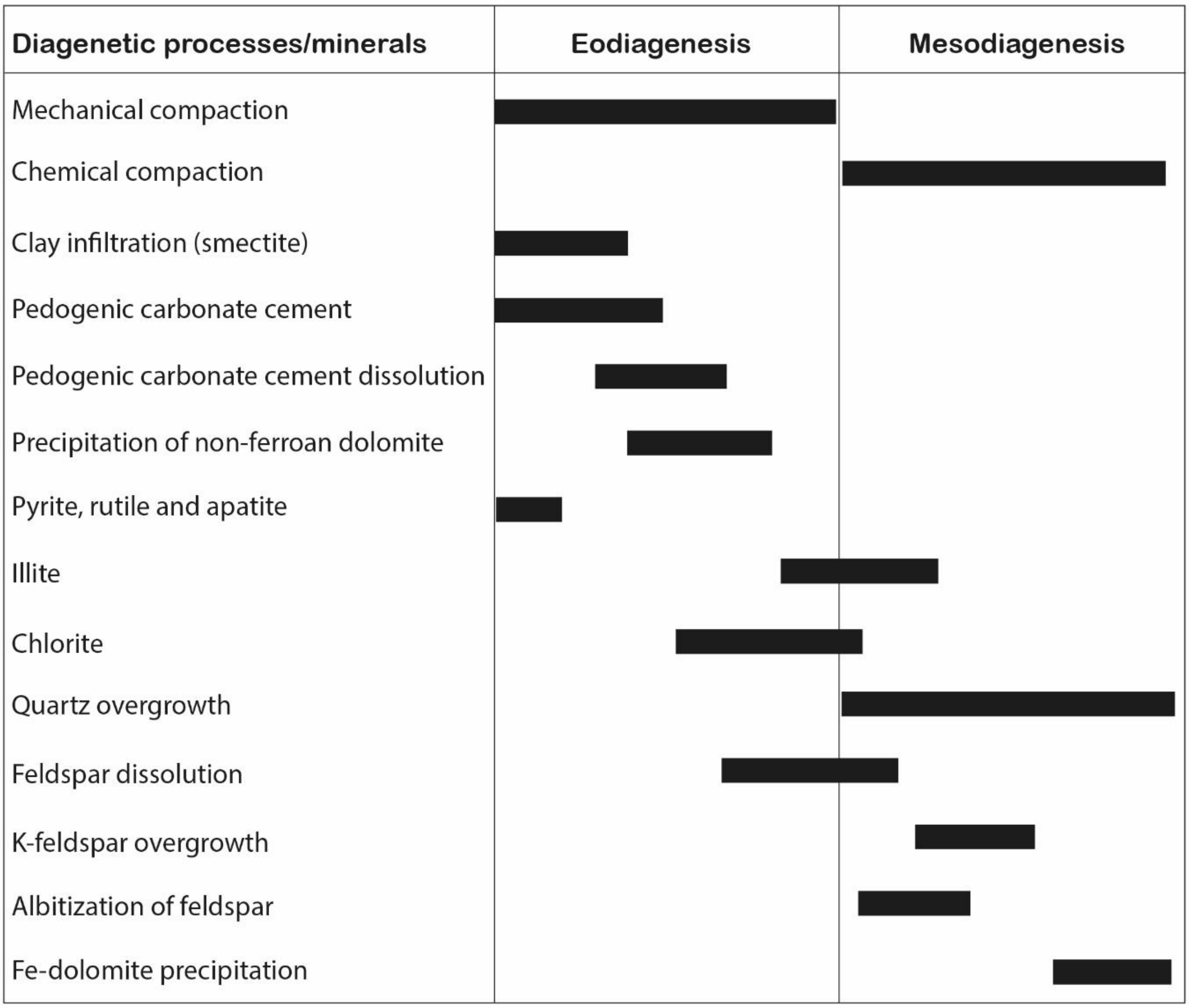

Figure 3.16: Paragenetic sequence of the diagenetic processes in the studied Skagerrak Formation sandstones based on petrographic relationships.

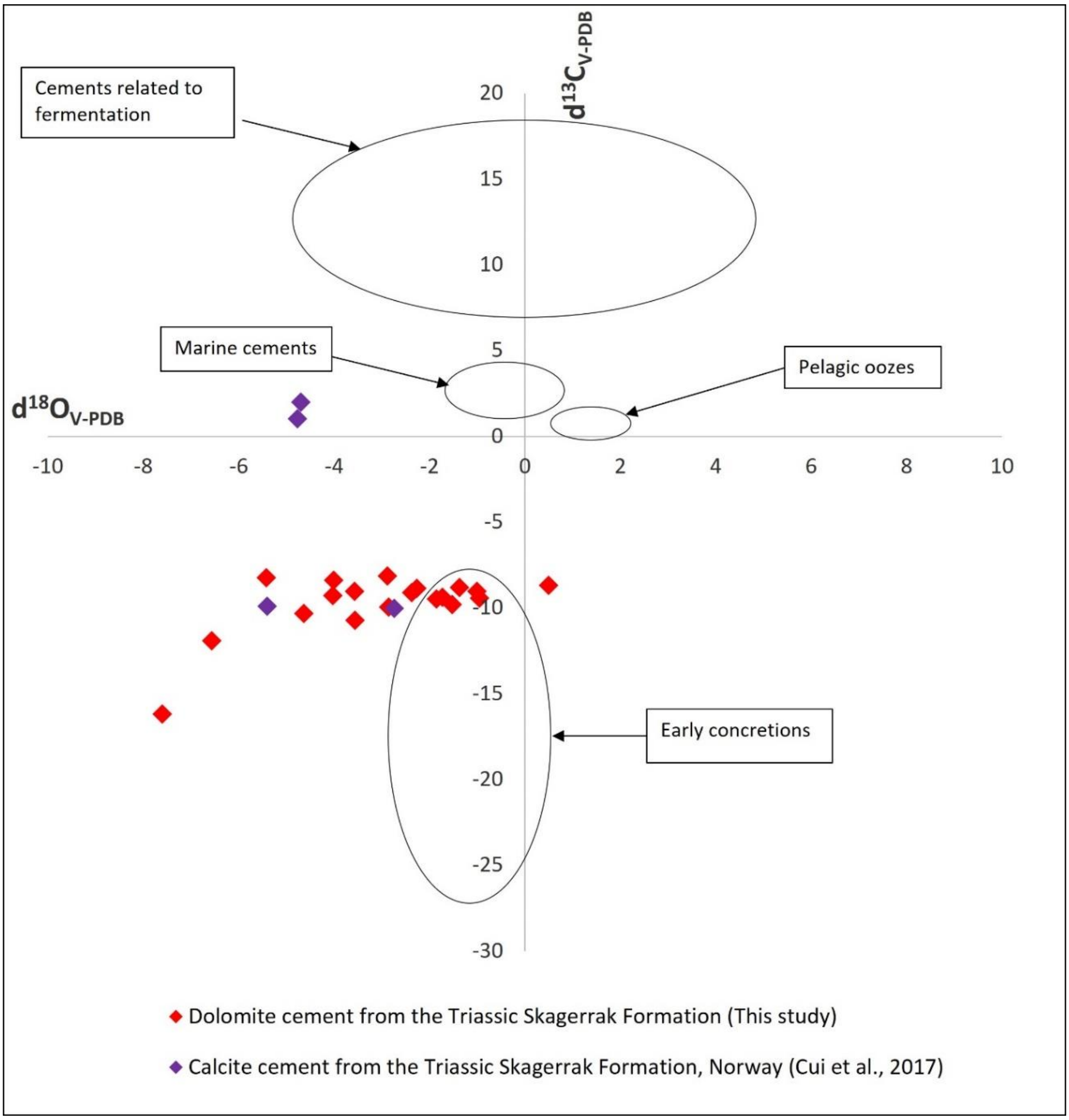

Figure 3.17: Cross plot of stable isotope analysis on selected Skagerrak Formation sandstone samples (axes and compositional fields after Moore, 1989).

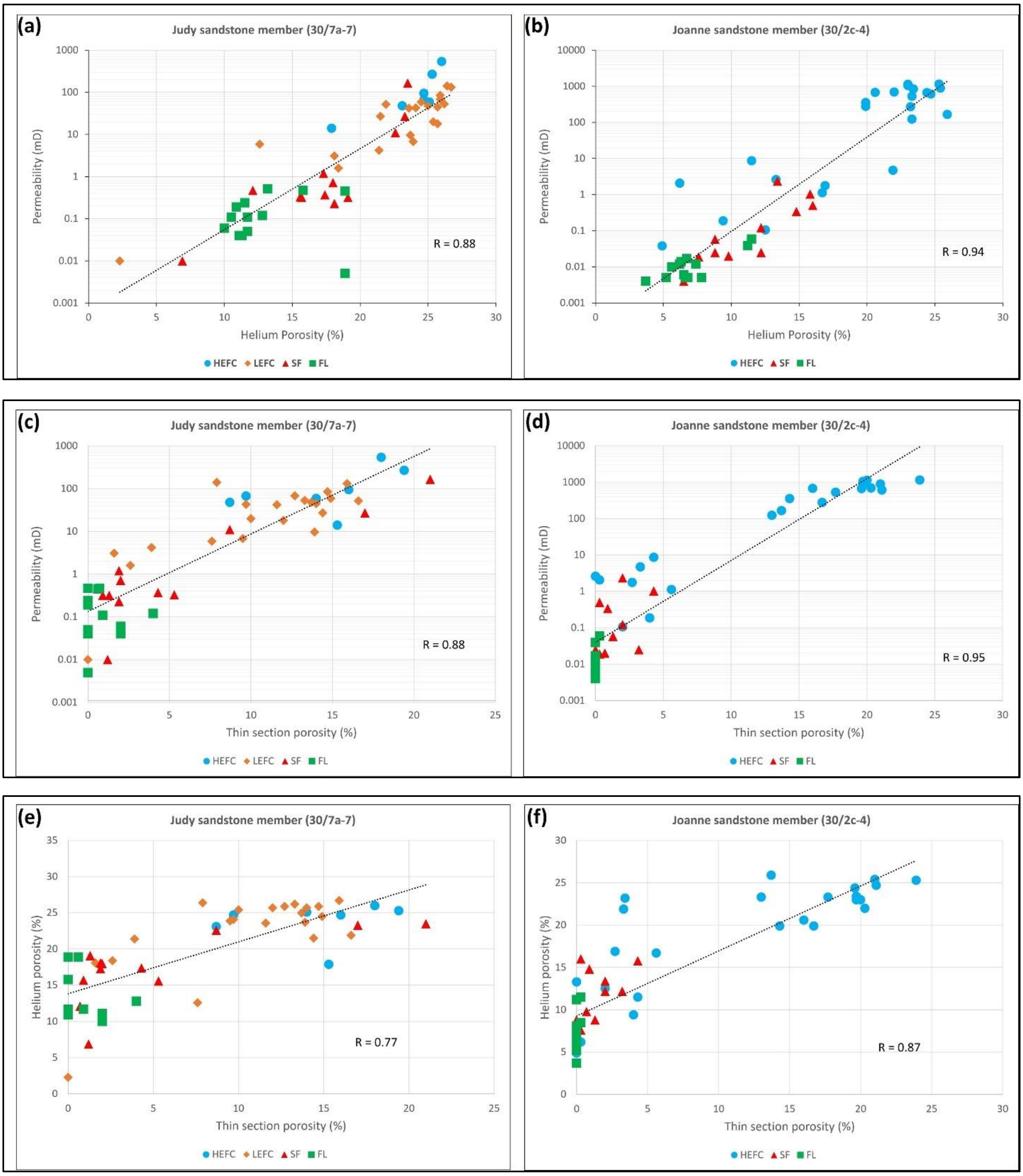
(a)
Judy sandstone member (30/7a-7)
Permeability (mD)
Helium Porosity (%)
R = 0.88
HEFC LEFC SF FL
(b)
Joanne sandstone member (30/2c-4)
Permeability (mD)
Helium Porosity (%)
R = 0.94
HEFC SF FL
(c)
Judy sandstone member (30/7a-7)
Permeability (mD)
Thin section porosity (%)
R = 0.88
HEFC LEFC SF FL
(d)
Joanne sandstone member (30/2c-4)
Permeability (mD)
Thin section porosity (%)
R = 0.95
HEFC SF FL
(e)
Judy sandstone member (30/7a-7)
Helium porosity (%)
Thin section porosity (%)
R = 0.77
HEFC LEFC SF FL
(f)
Joanne sandstone member (30/2c-4)
Helium porosity (%)
Thin section porosity (%)
R = 0.87
HEFC SF FL

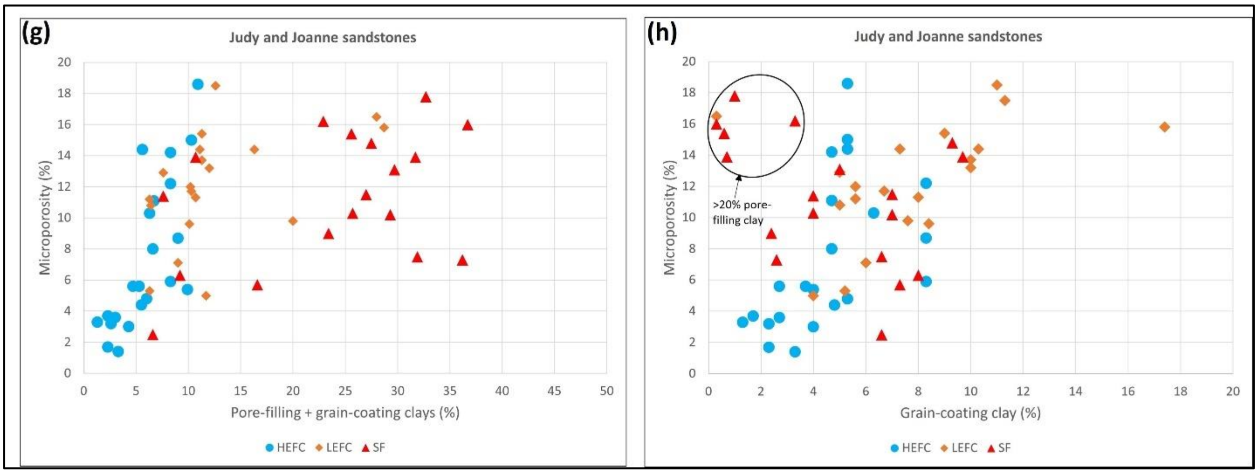

Figure 3.18: (a-b) Cross plots of helium porosity and permeability for the Judy and Joanne sandstones; (c-d) Cross plots of thin section porosity and permeability; (e-f) Cross plots of helium porosity and thin section porosity; (g) Cross plot of clay microporosity and total clay (pore-filling and grain-coating clays); (h) Cross plot of clay microporosity and grain-coating clay.

3.6 Discussion

3.6.1 Facies/depositional control on reservoir quality

Reservoir quality (i.e., porosity and permeability) of the Triassic Skagerrak Formation is primarily controlled by depositional processes, facies, grain size and clay content (Figs. 3.18-3.20). The best quality reservoirs are associated with fluvial channel facies (HEFC and LEFC); however, some splay facies (SF) also retain good reservoir quality. Lacustrine and floodplain facies (FL) constitute non-reservoirs; although they have 5 to 18.9% helium porosity (Fig. 3.18a and b), permeability is less than 1 mD and could thus act as barriers or baffles to fluid flow. Within the channel facies, HEFC sandstones have better reservoir quality (in terms of permeability) than the LEFC sandstones (Fig. 3.18a and b). Cross plots of petrographic data show that the main facies elements controlling reservoir quality distribution are grain size and clay content, both of which are influenced by depositional processes (Figs. 3.19 and 3.20).

The impact of grain size on the porosity and permeability of the studied Skagerrak Formation sandstones is shown in figures 3.19a-f. As grain size increases, there is a general increase in porosity (thin section/helium) and permeability in the Judy and Joanne sandstones. With the exception of a few isolated points, permeability values in the range of 100 mD to 1150 mD are generally restricted to the fine- to medium-grained HEFC sandstones with an average grain size of >0.15 mm (lower fine sand to lower medium sand), while permeability values of <100 mD are restricted to the very fine-grained LEFC sandstones and very fine to fine-grained SF sandstones with an average grain size of <0.15 mm (lower very fine sand to lower fine sand) (Fig. 3.19e and f). Furthermore, cross plots of grain size and calculated permeability using the

Kozeny equation (Kozeny 1927; Walderhaug et al. 2012) show a positive correlation, with calculated permeability increasing as grain size increases (Fig.3.19g and h). Although the Kozeny equation overestimates permeability for most of the samples (Appendix D), it does demonstrate that grain size has a strong influence on permeability. The HEFC sandstones, are on average, coarser-grained (upper fine sand), whereas the LEFC sandstones are, on average, finer-grained (upper very fine sand). An important parameter controlling permeability is pore-throat size, which is a function of grain size (Bloch et al. 2002; Nelson 2009; Lala and El-Sayed 2017; Lai et al. 2018). In this study, higher permeability in the fine- to medium-grained HEFC sandstones is associated with larger pore-throat sizes, while lower permeability in the very fine-grained LEFC and SF sandstones is associated with smaller pore-throat sizes (Figs. 3.8a-c).

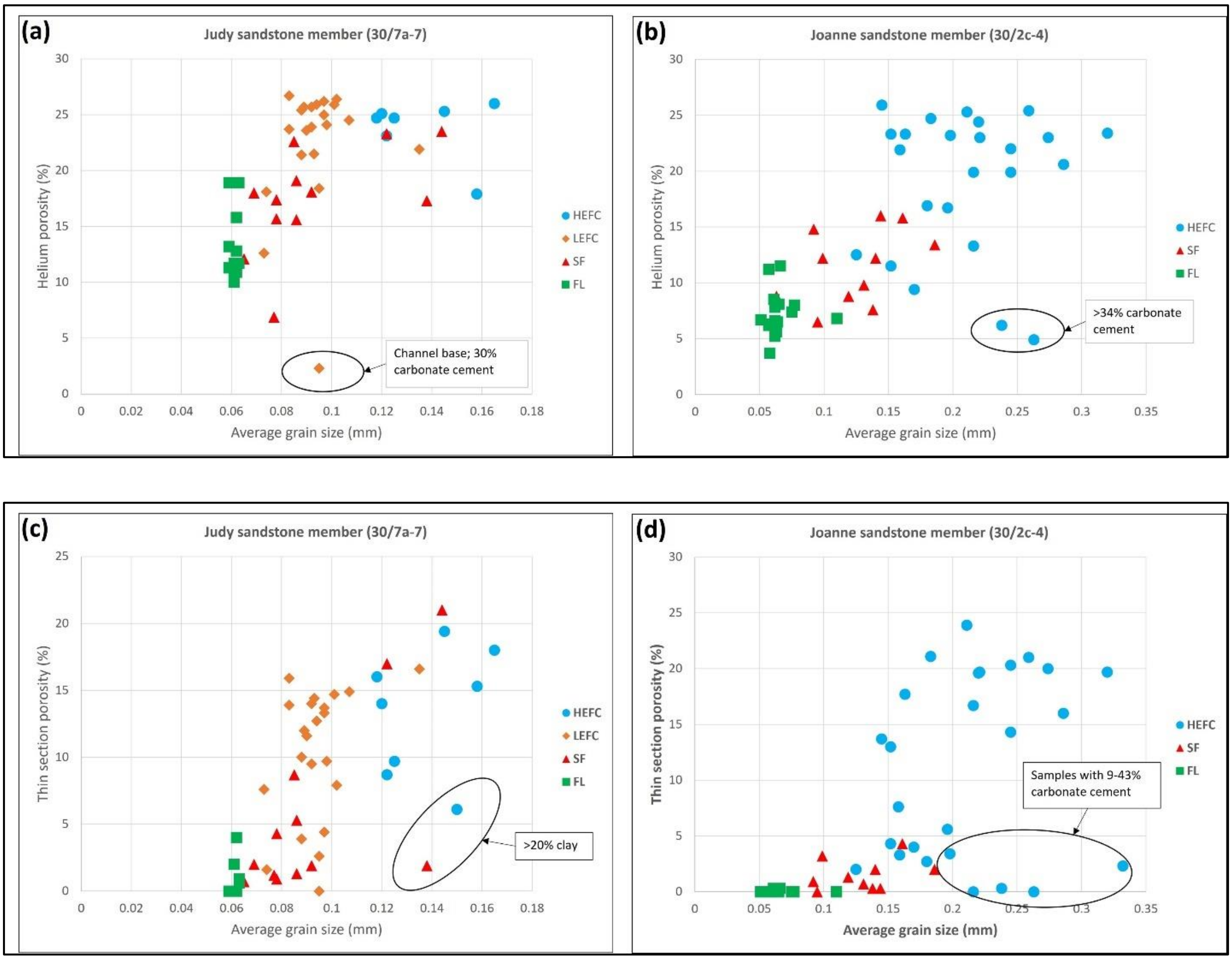

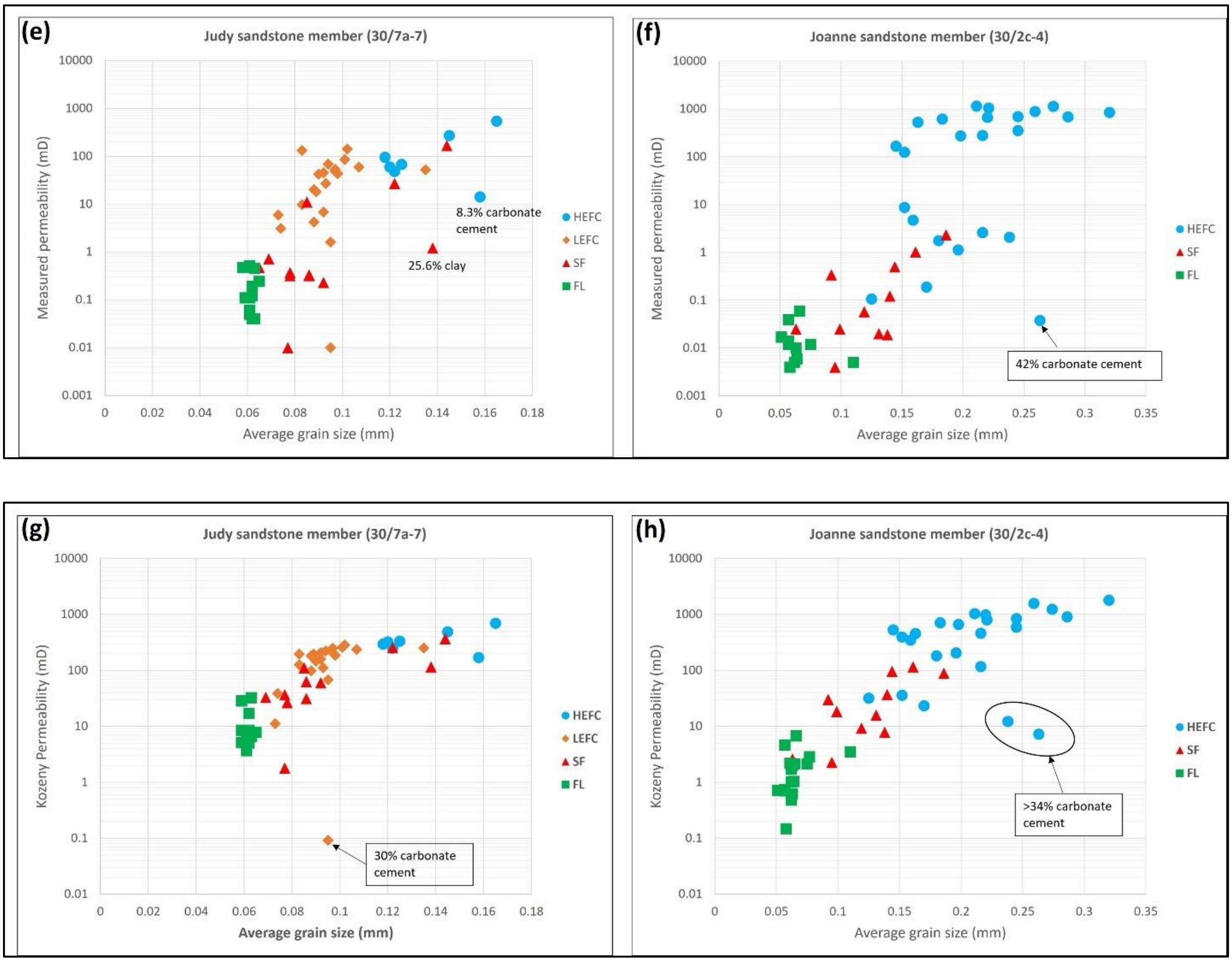

Figure 3.19: Relationship between grain size, clay content and reservoir properties of the studied Skagerrak sandstones (HEFC: High energy fluvial channel sandstones; LEFC: Low energy fluvial channel sandstones; SF: Splay facies). (a-b) Cross plots of helium porosity and average grain size; (c-d) Cross plots of thin section porosity and average grain size. The cross plots show that porosity increases with increasing grain size; (e-f) Cross plots of measured permeability and average grain size; (g-h) Cross plots of Kozeny permeability (calculated) and average grain size. The cross plots show that permeability generally increases with increasing grain size.

The impact of clay content on the reservoir quality of the investigated Skagerrak Formation sandstones (channel and splay/sheetflood) is shown in figures 3.20a-c. The figures show an inverse correlation between clay content and porosity/permeability. As clay content increases, there is a general decrease in porosity and permeability. In this study, sandstones with <16% total clay generally have better reservoir quality (>10 mD), while those with >16% total clay have lower to poor reservoir quality (<10 mD) (Fig. 3.20c). According to Worden and Morad (2003), the amount, distribution pattern and morphology of clay minerals have a major impact on the porosity and permeability of sandstones. Clay minerals in the form of grain coats (Figs. 3.13d-h) can preserve porosity by reducing nucleation sites available for the growth of quartz cements (Walderhaug 1996; Stricker and Jones 2016; Tang et al. 2018). Pore-filling clays (Fig. 3.13i and j), on the other hand, can degrade reservoir quality by enhancing mechanical compaction and blocking pore throats (Schmid et al. 2004; Olivarius et al. 2015; Oluwadebi et al. 2018; Barshep and Worden 2021; Bello et al. 2021; Bukar et al. 2021). In this study, porosity and permeability decrease with increasing volume of pore-filling clay (Fig. 3.20e and f). Generally, sandstones with >9% pore-filling clay have lower permeabilities (<10 mD), while those with <9% pore-filling clay have higher permeabilities (>10 mD).

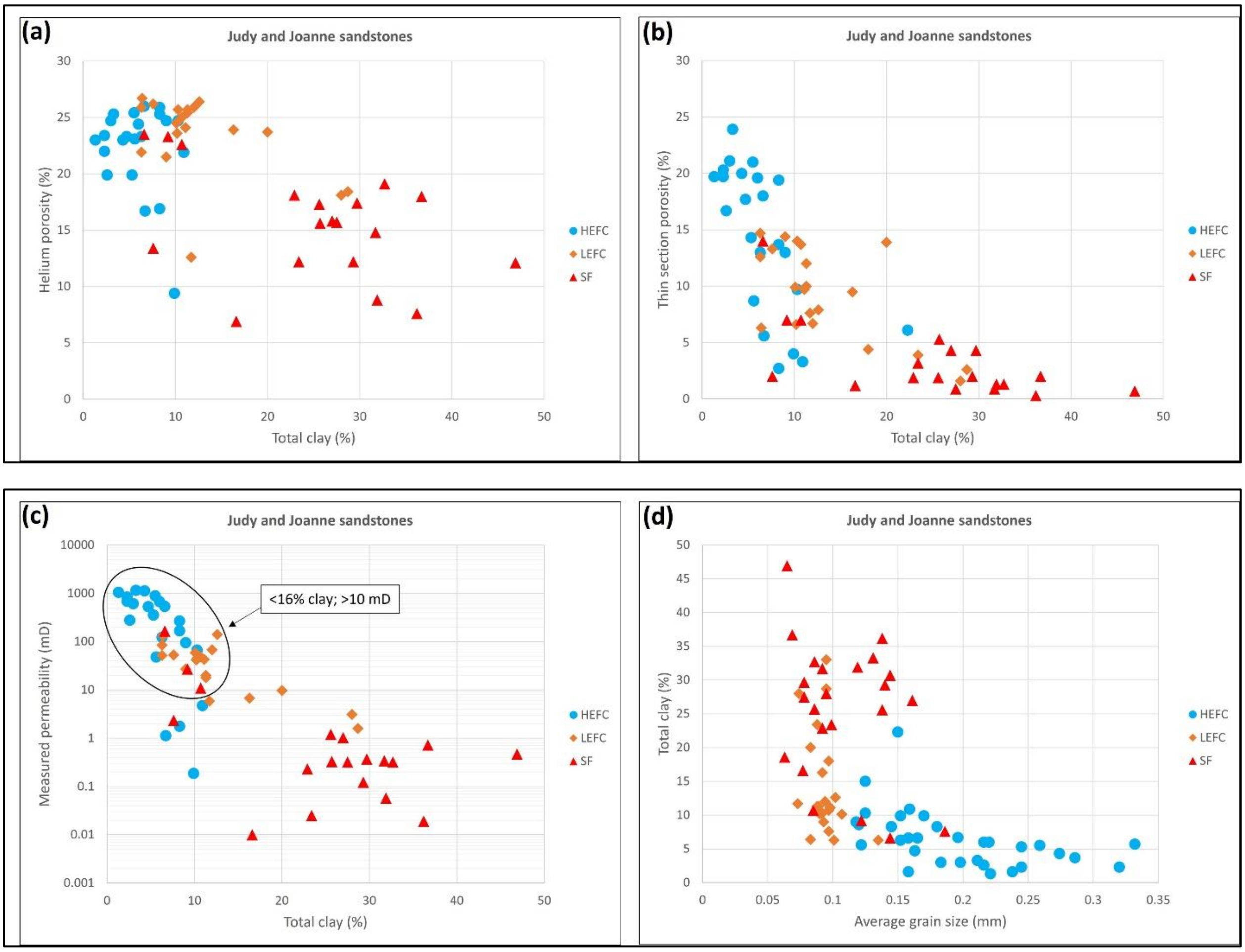

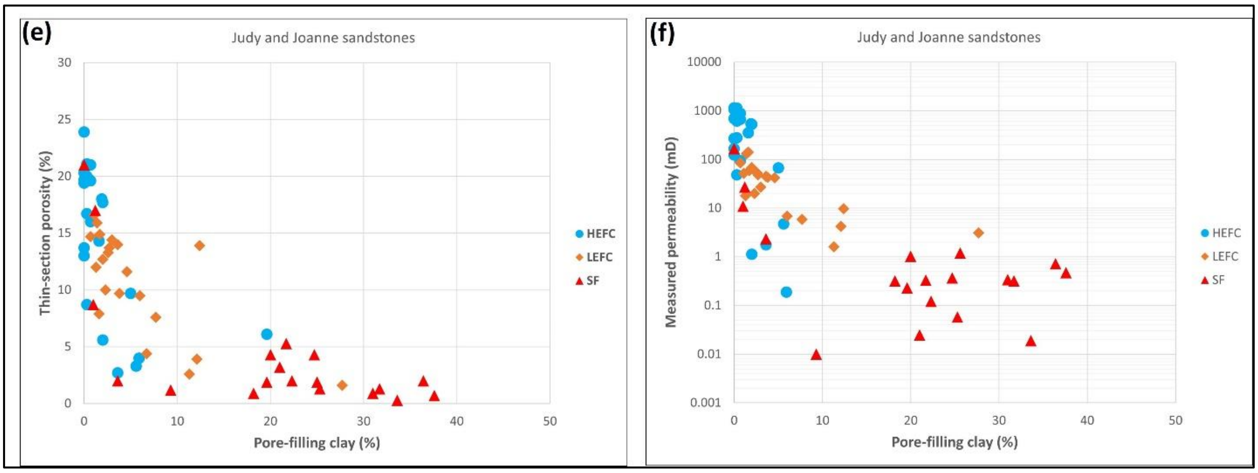

Figure 3.20: (a) Cross plot of helium porosity and total clay; (b) Cross plot of thin section porosity and total clay. The cross plots show that porosity decreases with increasing total clay; (c) Cross plot of measured permeability and total clay. Permeability decreases with increasing total clay. With few exceptions, sandstones with less than 16% total clay (circled) have better reservoir quality (>10 mD); (d) Cross plot of total clay and average grain size. Increase in grain size results in a decrease in total clay; (e) Cross plot of porosity and pore-filling clay (f) Plot of permeability against pore-filling clay.

The variations in sand grain size and clay content between/within the channel (i.e., HEFC and LEFC) and splay/sheetflood facies associations could be attributed to variations in depositional energy. The very fine-grained, clay-rich LEFC sandstones are suggestive of deposition in a lower energy environment, while the fine to medium-grained, relatively clean HEFC sandstones are suggestive of deposition in a higher energy environment. Our study shows that as you move from a high energy environment to a low energy environment, there is a general decrease in grain size and an overall increase in clay content (Fig. 3.20d), hence, an overall reduction in reservoir quality. The ratio of HEFC to LEFC sandstones varies between the Joanne and Judy sandstone members. In the Joanne sandstone member, the fluvial channel facies are predominantly HEFCs. In the Judy sandstone member, 15% of the fluvial channels are HEFCs, while the remaining 85% are LEFCs. In general, channel sandstones from the Joanne member have better permeabilities (up to 1150 mD) due to their coarser grain size (fine to medium-grained) and lower total clay content (avg. 6.4%), which are related to their higher depositional energy. Conversely, channel sandstones from the Judy member have lower permeabilities due to their finer grain size (very fine-grained) and higher clay content (avg. 13.1%), which are indicative of their lower depositional energy. The above findings are similar to those of previous research in the Judy and Jade fields, where depositional facies has been identified as the primary control on reservoir quality (Jones et al. 2005; Keller et al. 2005).

3.6.2 Diagenesis and reservoir quality evolution

During burial diagenesis, compaction and cementation are the two main processes reducing reservoir quality (Houseknecht 1987; Gluyas and Cade 1997; Wolela and Gierlowski-Kordesch 2007; Tang et al. 2018a). Cross plots of porosity loss due to compaction (COPL) and cementation (CEPL) show that porosity loss in the majority of studied sandstones is mainly due to compaction (Fig. 3.12a and b). However, a few HEFC data points in figure 3.12b suggest that cementation also plays an important role in porosity loss. These data points (or samples) are mainly from channel bases and pedoturbated sandstones containing a high volume of dolomite cement (10%-42.7%). Based on petrographic textural observations, compaction is primarily mechanical and largely influenced by depositional facies. According to Paxton et al. (2002), sandstones with a high proportion of ductile grains such as mudclasts or mica, exhibit higher levels of porosity loss by mechanical compaction at relatively shallow depths of burial. In this study, channel sandstones (HEFC and LEFC) have relatively lower degree of compaction (Figs. 3.8a-c) due to the absence or lesser amount of detrital clay and mica. Unconfined splay/sheetflood (SF) sandstones have a greater degree of compaction (Fig. 3.8f) due to higher amounts of detrital clay and mica content. Very few SF sandstone samples were observed to have undergone lesser compaction due to minimal amount of clay/mica, thus retaining good porosity and moderate permeability (Fig. 3.8e). In addition to depositional facies having a substantial influence on differences in compaction state, several studies have identified low vertical effective stress (VES) as a critical factor for reduced state of compaction and reservoir quality preservation (Grant et al. 2014; Stricker et al. 2016a).

Apart from carbonate cements, other important diagenetic cements in the studied sandstones are chlorite, mixture of chlorite and illite, and quartz. The diagenetic clays occur mainly as pore-filling and coatings and predates quartz cements. Where they occur as pore-filling, pore spaces and pore throats are occluded, thus reducing reservoir quality (Fig. 3.13i and j). On the other hand, where they occur as coatings (mainly chlorite), quartz cementation is inhibited and porosity is preserved (Figs. 3.13d-h). Quartz cement is variable (generally $<8\%$) and localized (Fig. 3.13c) and has had minimal or no effect on the overall porosity and permeability, due to the inhibiting effect of pore-filling clays and chlorite clay coats (Figs. 3.13d-j and 3.14).

3.6.2.1 Origin of carbonate cement

Stable carbon and oxygen isotope data can help to unravel the origin of carbonate cements and the precipitation temperature (Naylor et al. 1989; Morad et al. 1998; Ma et al. 2017; Mao et al.

2019). The carbonate cements (primarily dolomite) in the studied Skagerrak sandstones have $\delta^{13}C$ values that range from -16.17‰ to -8.13‰ and $\delta^{18}O$ values between -7.60‰ and +0.50‰ (Table 3.9). Due to the various controls on the isotopic composition of carbon and oxygen such as latitude, elevation, temperature, vegetation type, isotopic composition of the rainfall, degree of evaporation, to mention a few (Cui et al. 2017) and challenges associated with the interpretation of dolomite stable isotope data (Land 1980), the acquired isotope data were plotted and compared with previous studies (Cui et al. 2017) for simplicity (Fig. 3.17). According to figure 3.17, the range in $\delta^{13}C$ values (-16.17‰ to -8.13‰) suggest that the carbonate cements were derived from early concretions in adjacent floodplain sediments (Moore 1989). Carbonate concretions are early diagenetic structures, that form primarily in the first few metres below the sediment/water interface, and sometimes continues to grow at a much slower rate thereafter (Nelson and Smith 1996). The derivation of the carbonate cements from early concretions as shown in figure 3.17 agrees with the proposition of Cui et al (2017). According to Cui et al (2017), the carbonate cements in the Skagerrak Formation sandstones formed from the reprecipitation of intra-Skagerrak Formation calcretes which could be sourced from reworked rhizoliths, pedogenic nodules, groundwater calcretes and fluvial sediments (Morad 1998; McKie 2014).

3.6.3 Clay coats and reservoir quality

3.6.3.1 Origin of chlorite coats

The chlorite coats in the studied Skagerrak Formation sandstones, as revealed by SEM analysis, are mostly oriented parallel to detrital grain surfaces (Figs. 3.13f-h), indicating a detrital origin and emplacement by mechanical infiltration process (Matlack et al. 1989; Pittman et al. 1992). In addition, the presence of thicker chlorite coats within the embayments on detrital grain surfaces (Fig. 3.13h) and wide variations in rim thickness point to a detrital origin (Pittman et al. 1992; Wilson 1992). Several studies have shown that chlorite-coat formation in sandstones takes place during diagenesis through precursor phases such as berthierine, odinite, kaolinite and smectite (Moraes and De Ros 1992; Mckinley et al. 2003; Dowey et al. 2012; Charlaftis et al. 2021). As revealed by SEM-EDX analysis, the chlorite coats in the studied sandstones are Fe- and Mg-rich (Fig. 3.14 and table 3.7), suggesting a detrital smectite precursor clay mineral. This agrees with earlier interpretations where chlorite coats in the Skagerrak sandstones have been interpreted to form by thermally driven recrystallization of precursor detrital smectite coats (Stricker et al. 2016b). The recrystallization of smectite to chlorite occurs via a mixed-layer chlorite-smectite at around 120°C (Worden and Morad 2003; Worden et al. 2020).

Present-day reservoir temperature of the studied Skagerrak sandstones is >160°C (Fig. 3.3). This implies that any smectite precursor clays would have been fully recrystallized to chlorite at this temperature. As earlier mentioned, the clay coatings on some of the detrital quartz grains exhibit two layers: inner (layer 1/root zone) and outer layer (layer 2) (Fig. 3.14). As shown in Figure 3.14, the root zone directly overlying the detrital quartz grain surface is densely packed, poorly crystallized and composed of a mixture of illite and chlorite, which we believe is the product of the diagenetic recrystallization of detrital smectite coats. The presence of potassium in the root zone or layer1 suggests the presence of small amounts of illite or mica as a contaminant within the chlorite structure (Humphreys et al. 1994; Shelukhina et al. 2021). The outer layer is well-crystalized and purely chlorite. We hypothesize that the outer layer is younger and was formed by the interaction of the root zone's outermost part with adjacent pore waters during burial (due to increasing temperature and pressure); hence, the reason for changes in the chemistry and increased crystallinity of the clay coats from the root zone to the outer layer.

Smectite minerals preferentially form during weathering in arid climates (Mckinley et al. 2003). In arid environments, evaporation frequently exceeds meteoric influx resulting in an upward flow of groundwater, evaporation, and the formation of various smectitic clays and magnesium-rich clay minerals (Worden and Morad 2003). The Skagerrak Formation sandstones were deposited in an arid to semi-arid environment (McKie 2011, 2014), therefore supporting the assumption that the precursor clay mineral for the chlorite coats is smectite. In addition to smectite acting as a precursor for chlorite in the studied sandstones, the dissolution of igneous rock fragments (Fig. 3.15d) observed in some samples may have aided the formation of chlorite. According to Dowey et al. (2012), authigenic chlorite can also form during diagenesis from the dissolution of Fe- and Mg-rich detrital grains and volcanic rock fragments. Thus, this observation likely supports the interpretations of Humphreys et al. (1989) that authigenic chlorite in late Triassic sandstones from the North Sea Central Graben, developed from a potential smectite precursor and aided by detrital grain dissolution.

3.6.3.2 Chlorite coats and quartz cementation

Quartz cementation is the dominant mechanism for porosity loss in deeply buried sandstones, especially those with prolonged exposure to elevated temperatures (Worden and Morad 2000; Taylor et al. 2010; Xia et al. 2020). In this study, the modelled burial-thermal history (Fig. 3.3) reveals that the Triassic Skagerrak Formation is at its maximum burial depth (>3400 m) and temperature (> 160°C) at the present day. Considering the temperature history, quartz cement, which commonly forms at around 70-80°C (Walderhaug 2000; Worden and Morad 2000; Bjørlykke 2014; Xi et al. 2015), is expected to have pervasively developed in the studied samples, occluding the entire pore spaces. However, this is not the case, as the quartz cement volume recorded is generally <8%. Petrographic examination reveals that the presence of early formed chlorite coats has significantly inhibited the growth of quartz cement and therefore contributed to preservation of reservoir quality (Figs. 3.13d-h). However, in few samples, quartz cementation is observed to be pervasive and locally distributed due to the absence or lack of continuous chlorite coats (Figs. 3.13a-c). In the studied sandstones, detrital quartz grains with continuous chlorite coats have minimal or no quartz cements, while those with discontinuous or no chlorite coats have moderate quartz cements. This implies that discontinuous clay coats on detrital quartz grain surfaces promote quartz cementation. Figure 3.21a shows the relationship between chlorite coat coverage (i.e., continuity/discontinuity) and quartz cement volume for 23 of the investigated samples. As illustrated in figure 3.21a, there is an inverse relationship between chlorite coat coverage and quartz cement, with quartz cement volume generally increasing as chlorite coat coverage decreases. With few exceptions, sandstones with lower average chlorite coat coverage (<50%) have higher quartz cement volume (4.2%-7.3%), while those with higher average chlorite coat coverage ranging from 60% to 98% have lesser quartz cement volume (0.5% to 4.2%). This finding is similar to those of previous studies where an inverse correlation between clay coat coverage and quartz cement volume has been identified (Bloch et al. 2002; Taylor et al. 2015; Dutton et al. 2018). In addition, this finding supports the claim that the completeness of clay coats and not just its presence is the most important factor governing its ability to effectively inhibit quartz cementation (Heald and Larese 1974; Ehrenberg 1993; Walderhaug 1996; Bloch et al. 2002; Billault et al. 2003; Lander et al. 2008; Ajdukiewicz and Larese 2012).

To further test the impact of the continuity or discontinuity of clay coats on quartz cementation and reservoir quality, clay coat coverage data of 21 fluvial channel sandstone samples (Table 3.8) was incorporated into the quartz cementation model developed for this study (Fig. 3.21b and c). The sandstones of the Judy and Joanne member are currently buried to temperatures >160°C and have stayed in the quartz cementation window (above 80°C) for about 41 Ma and 45 Ma, respectively (Fig. 3.3). The model shows that with 50% clay coat coverage in both Judy and Joanne sandstones, there is minimal or no effect on quartz cementation, however, increasing the clay coat coverage to 90% results in a significant impact on quartz cementation.

At 90-91% clay coat coverage, the modelled quartz cement volume is 9.1% (after 41 Ma in the quartz cementation window) and 15% (after 45 Ma in the quartz cementation window) for the Judy and Joanne channel sandstones, respectively (Fig. 3.21b and c). Based on point counting, the average measured quartz cement volume for the modelled Judy and Joanne channel sandstones is 2.2 and 5.2%, respectively (Appendix C). The concurrence between measured and modelled quartz cement volume for the Judy and Joanne channel sandstones was achieved at 98% and 97% clay coat coverage, respectively (Fig. 3.21b and c). This implies that to limit the average quartz cement volume to the observed value of 2.2% and 5.2%, each detrital quartz grain must be 97-98% coated.

Chlorite coat coverage ranges from 78% to 98% in the Judy channel sandstones and 15.9% to 69% in the Joanne channel sandstones (Table 3.8). In the Judy channel sandstones, the average chlorite coat coverage is 91% and this gives an average measured quartz cement volume of 2.2% (see Appendix C), which is lower than the modelled volume (9.1%; after 41 Ma in the quartz cementation window), using similar coating coverage of 91% (Fig. 3.21b). Also, in the Joanne channel sandstones, the average chlorite coat coverage is 38% and this gives an average measured quartz cement volume of 5.2% (see Appendix C), which is far lower than the modelled volume (25.9%; after 41 Ma in the quartz cementation window) using similar coating coverage of 38% (Fig. 3.21c). The lower measured quartz cement volume compared to the modelled volume in both sandstones can be attributed to the additional impacts of high pore fluid pressure and low vertical effective stress (VES), which inhibited mechanical compaction and quartz cementation in the Skagerrak Formation sandstones (Nguyen et al. 2013; Grant et al. 2014; Stricker and Jones 2016; Stricker et al. 2016a). In general, chlorite clay coats have inhibited quartz cementation in the studied Skagerrak Formation sandstones; however, its effectiveness is dependent on its extent of coverage (or continuity) on the detrital grain surfaces.

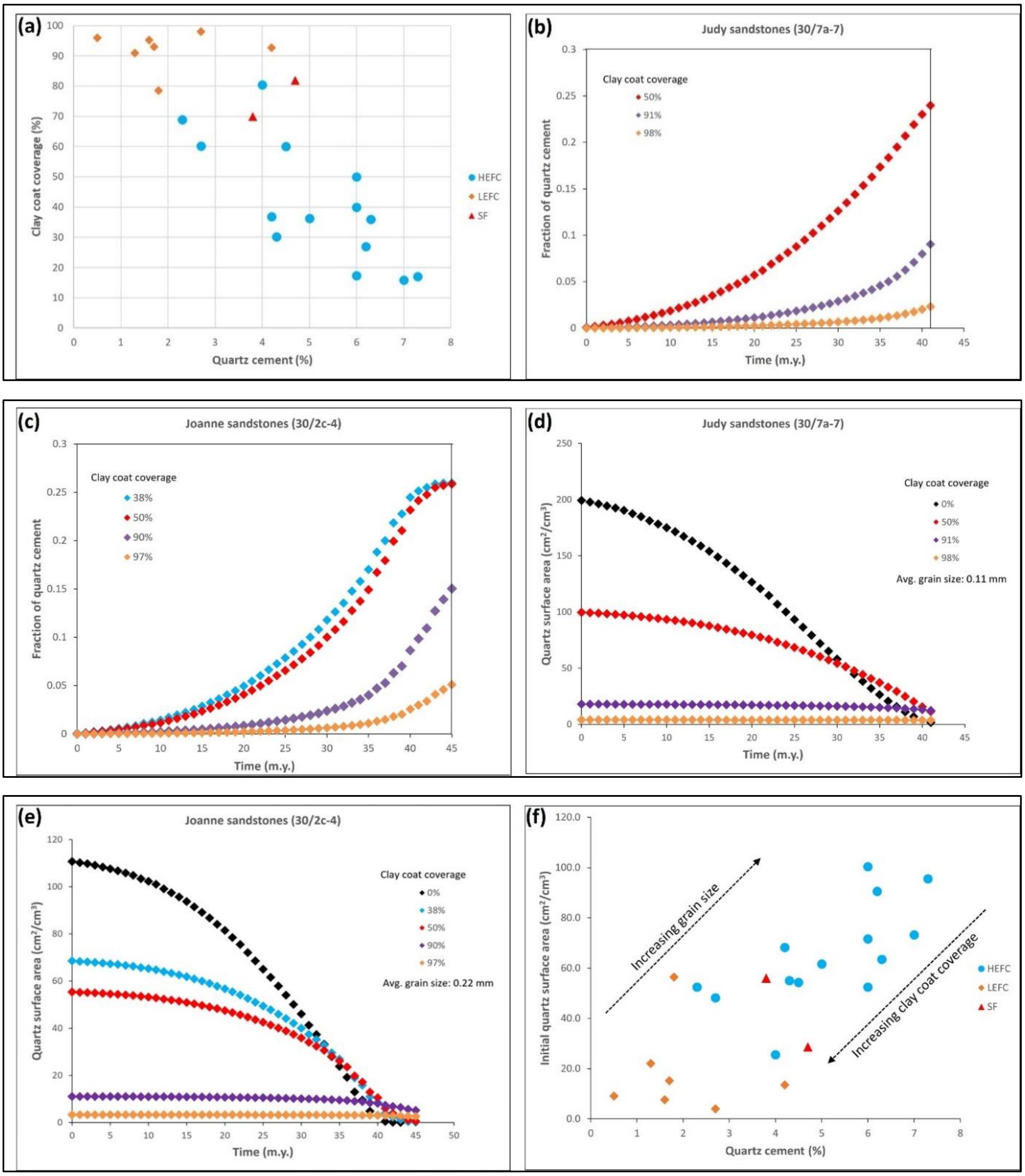

Figure 3.21: (a) Inverse relationship between clay-coat coverage and quartz cement volume; (b-c) Quartz cementation model output for the Judy sandstones (Judy field) and Joanne sandstones (Jade field) showing the effect of varying clay coat coverage on quartz cement evolution through geologic time. Increasing clay coat coverage results in the reduction of quartz cement volume. Average measured clay coat coverage in the Judy and Joanne sandstones is 91% and 38%, respectively. The model output indicate that the Judy and Joanne sandstones would require around 97% to 98% clay coat coverage for their current average quartz cement volumes of 2.2% and 5.2%, respectively; (d-e) Quartz surface area versus time for the Judy and Joanne sandstones. The plots show the effect of varying clay coat coverage on quartz surface area and its evolution through time. Generally, increasing clay coat coverage results in the reduction of initial quartz surface area available for quartz cement precipitation; (f) Cross plot of point-counted quartz cement and initial quartz surface area per cubic centimeter of sandstone. The positive correlation suggests that available quartz surface area (and extent of clay coat coverage) have a profound influence on quartz cementation.

3.6.3.3 Grain size and quartz cementation

In addition to clay coats, grain size has also been reported to have an impact on quartz cementation (Walderhaug 1996; Bloch et al. 2002). According to Walderhaug (1996), the surface area available for quartz cementation is a function of grain size. Finer grain sizes have a higher surface area than coarser grain sizes. As a result, finer-grained sandstones are likely to be more quartz cemented than coarser-grained sandstones (Walderhaug 1996; Bloch et al. 2002). In this study, however, very fine-grained sandstones contain less quartz cement than fine to medium-grained sandstones. This could be attributed to the higher clay coat coverage in the very fine-grained sandstones, which resulted in the reduction of available quartz grain surface area for quartz precipitation. The quartz cementation model shows that prior to clay coating (0% coating coverage), the very fine-grained Judy sandstones (avg. grain size: 0.11 mm) have a higher quartz surface area (199 cm^2/cm^3) than the fine-grained Joanne sandstones (110.7 cm^2/cm^3) with an average grain size of 0.22 mm (Fig. 3.21d and e). Increasing chlorite coat coverage to 91% and 38% (average measured values) in the Judy and Joanne channel sandstones, respectively, reduces the quartz surface area available for quartz precipitation to 17.9 cm^2/cm^3 in the Judy channel sandstones and 68.5 cm^2/cm^3 in the Joanne channel sandstones. This implies that finer-grained sandstones with extensive clay coat coverage can become less quartz cemented (due to reduced quartz surface area) than coarser-grained ones with lesser clay coat coverage. In general, the positive correlation between initial quartz surface area and quartz cement volume, as shown in figure 3.21f, suggests that available quartz surface area is a primary control on quartz cementation. In addition, clay coatings can inhibit quartz cementation by reducing quartz surface area available for quartz precipitation (Walderhaug 1996, 2000).

3.6.3.4 Correlation between grain size and clay coat coverage

In the studied datasets, a strong correlation exists between grain size and clay coat coverage, with clay coat coverage increasing with decreasing grain size (Fig. 3.22a and 3.23). Average clay coat coverage ranges from 78.5% to 98% in the finer-grained LEFC sandstones (avg. grain size: <0.15 mm), whereas it ranges from 15.9% to 69% in their coarser-grained HEFC counterparts (avg. grain size: >0.15 mm). This observation is consistent with those of previous studies, where clay coat coverage has been reported to increase with decreasing grain size (Wilson 1992; Ajdukiewicz et al. 2010; Wooldridge et al. 2017b). Furthermore, the lower clay coat coverage characterizing the HEFC sandstones could be linked to the high degree of abrasion or reworking they were subjected to during sediment transport. During sediment transport, coarser grains experience a high degree of abrasive transport than finer grains. As a result, clay coats can be more completely abraded on coarser grains than finer grains (Wilson 1992; Ajdukiewicz et al. 2010; Wooldridge et al. 2019a; Verhagen et al. 2020).

3.6.3.5 Correlation between clay volume and clay coat coverage

Increased clay mineral volume (occurring mainly as coats) has been widely reported to enhance clay coat coverage (Pittman et al. 1992; Wooldridge et al. 2019b; Charlaftis et al. 2022). In this study, a positive correlation exists between clay coat coverage and clay coat volume derived from point counting (R = 0.77) (Fig. 3.22b). Sandstones with >60% average clay coat coverage contain clay coat volumes in the range of 5% to 10%, while sandstones with ≤50% clay coat coverage have <5% clay coat volume (Fig. 3.22b; table 3.8). With few exceptions, sandstones with >60% average clay coat coverage and 5% to 10% clay coat volume are restricted to the LEFC sandstone facies, while those with <50% clay coat coverage and <5% clay coat volume are restricted to the HEFC sandstone facies. This implies that variations in depositional energy have a major influence on the volume of detrital clay distributed as clay coats prior final burial. This observation supports the assertion of Wooldridge et al. (2019a) that lower energy environments generally have a greater volume of clay available for infiltration and higher degrees of clay coat coverage than high energy environments.

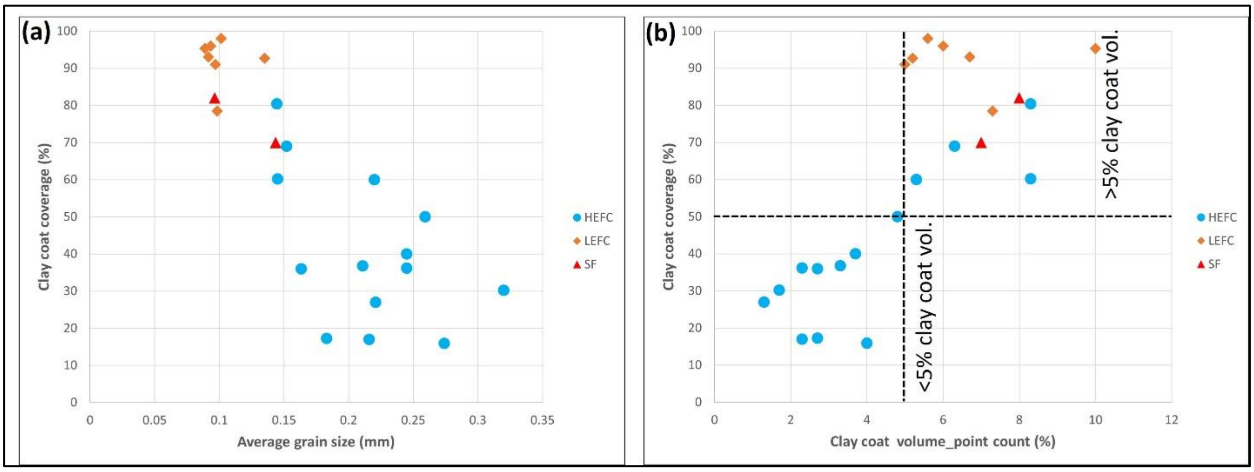

Figure 3.22: (a) Correlation between clay-coat coverage and grain size. Clay coat coverage increases with decreasing grain size and is influenced by depositional energy. Low energy fluvial channel (LEFC) sandstones have better clay coat coverage than their high energy fluvial channel (HEFC) sandstone counterparts; (b) A positive correlation between clay coat coverage and volume of clay coats. Clay coat coverage increases with increasing clay coat volume.

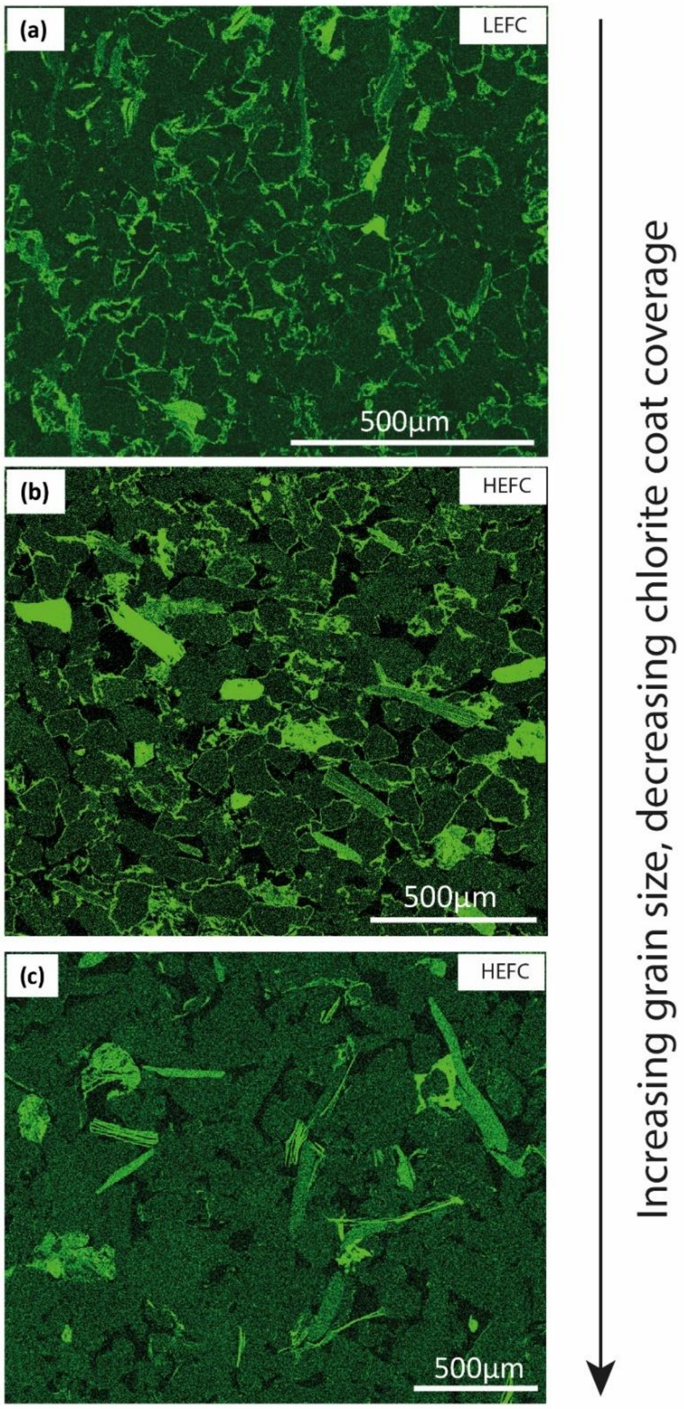

Figure 3.23: Grain-coating phase maps of three representative chlorite-coated Skagerrak Formation sandstones showing the relationship between clay coat coverage and grain size. (a) Low energy fluvial channel (LEFC) sandstone. Depth: 11309.8 ft, avg. grain size: 93.3 µm (0.093 mm), avg. clay coat coverage: 96%; (b) High energy fluvial channel (HEFC) sandstone. Depth: 11496 ft, avg. grain size: 145 µm (0.145 mm), avg. clay coat coverage: 80.4%; (c) High energy fluvial channel (HEFC) sandstone. Depth: 15650.1 ft, avg. grain size: 216 µm (0.216 mm), avg. clay coat coverage: 17%. Generally, average clay coat coverage reduces with increasing average grain size.

3.6.3.6 Microporosity and chlorite coats

Clay minerals in sandstones often contain considerable microporosity, which contributes to the total porosity from core analysis and wireline-log data (Hurst and Nadeau 1995). However, clay microporosity can introduce high irreducible water saturation, lowering effective porosity and permeability (Hurst and Nadeau 1995; Xia et al. 2020). This study shows a positive correlation between microporosity and volume of chlorite coats, as well as a positive correlation between microporosity and chlorite coat coverage (Fig. 3.24a and b). Sandstones with >6% microporosity have higher clay coat volume (5% to 10%) and clay coat coverage (60% to 98%). Conversely, those containing <6% microporosity have lower clay coat volume (1.3% to 5%) and clay coat coverage (15.9% to 60%). In general, clay microporosity increases with increasing clay coat volume and coverage.

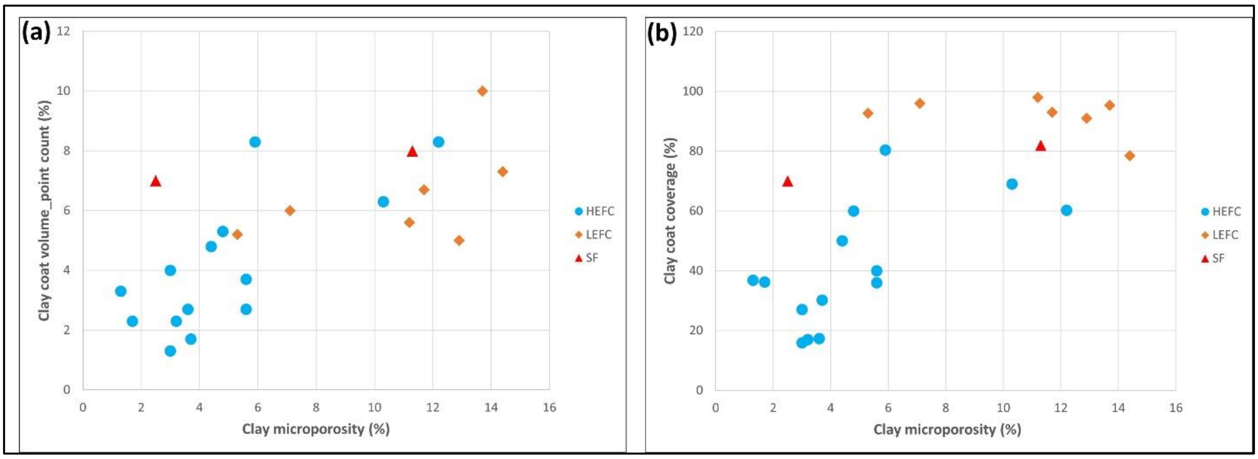

Figure 3.24: Relationship between clay coat volume and clay coat coverage for 23 of the studied sandstone samples from the Skagerrak Formation (see Table 3.8). (a) Cross plot of clay coat volume and microporosity; (b) Cross plot of clay coat coverage and microporosity.

3.6.3.7 Correlation between clay coat coverage and porosity-permeability

Previous studies (Dutton et al. 2018; Bello et al. 2021) have established a positive correlation between clay coat coverage and porosity/permeability. These studies showed that porosity and permeability increase with increasing clay coat coverage. However, in this study, such a positive correlation could not be established (Figs. 3.25a-c). In this study, sandstones with lower clay coat coverage (HEFC) have higher porosity (thin section) and permeability than those with higher clay coat coverage (LEFC). The porosity and permeability of the sandstones are primarily influenced by depositional processes/energy of the system, which in turn control the distribution of grain size and clay content. The high porosity (thin section) and permeability exhibited by the HEFC sandstones, despite their low clay coat coverage and greater quartz cement volume, is due to their coarser grain sizes (fine- to medium-grained) and absence or minimal amounts of clays (Figs. 3.25d-g). On the other hand, the low porosity (thin section) and permeability characterising the LEFC sandstones, despite their higher clay coat coverage, is due to their finer grain sizes (very fine- to fine-grained) and the relatively higher amounts of clay (Figs. 3.25d-g). It is worth noting that the cross plot of measured permeability and helium porosity for the selected sandstones in figure 3.25h shows a poor correlation, in contrast to figures 3.18a and b, which include all of the investigated samples. This is due to the effect of clay microporosity on helium porosity. However, a strong positive correlation occurs when plotted with thin section porosity (Fig. 3.25i).

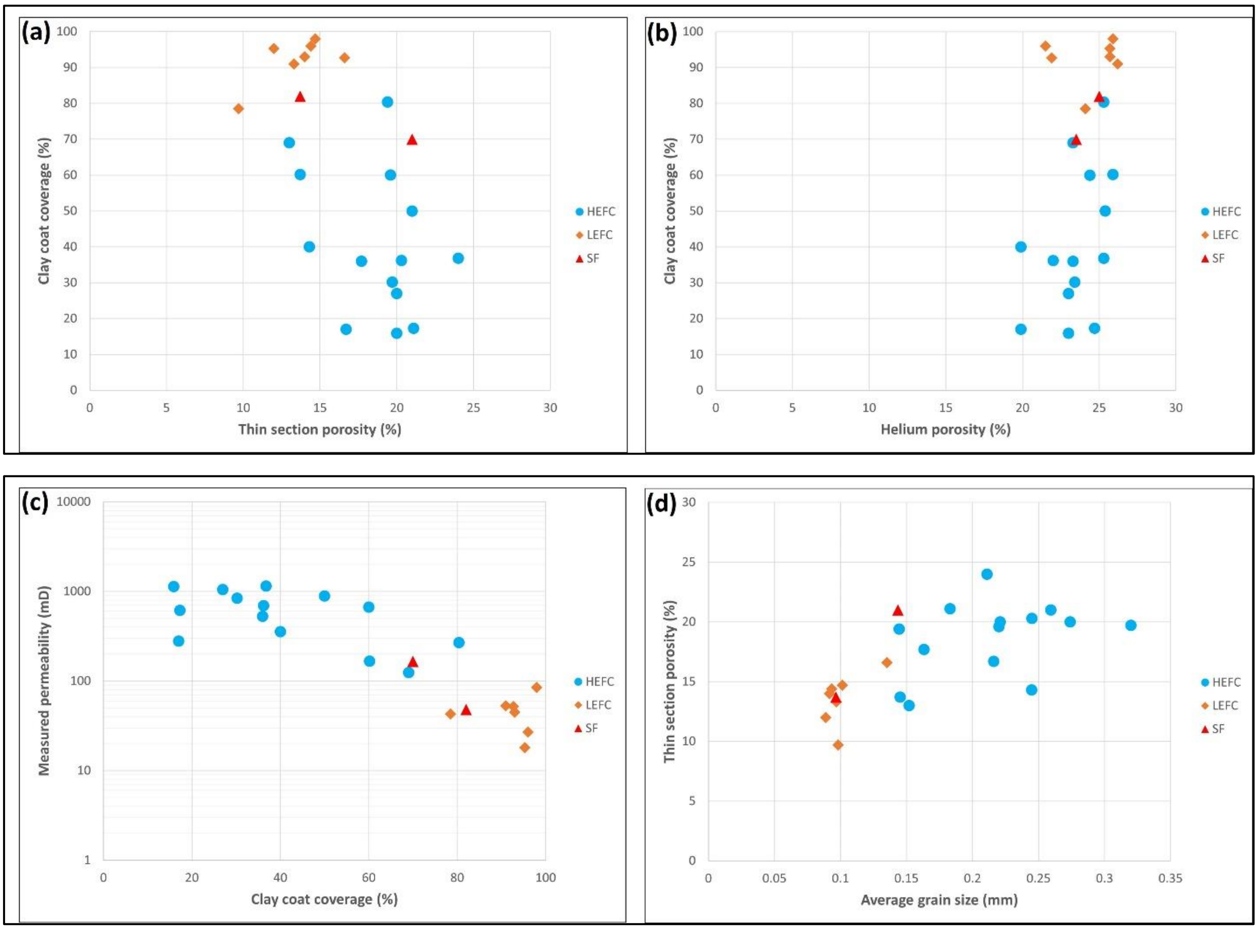

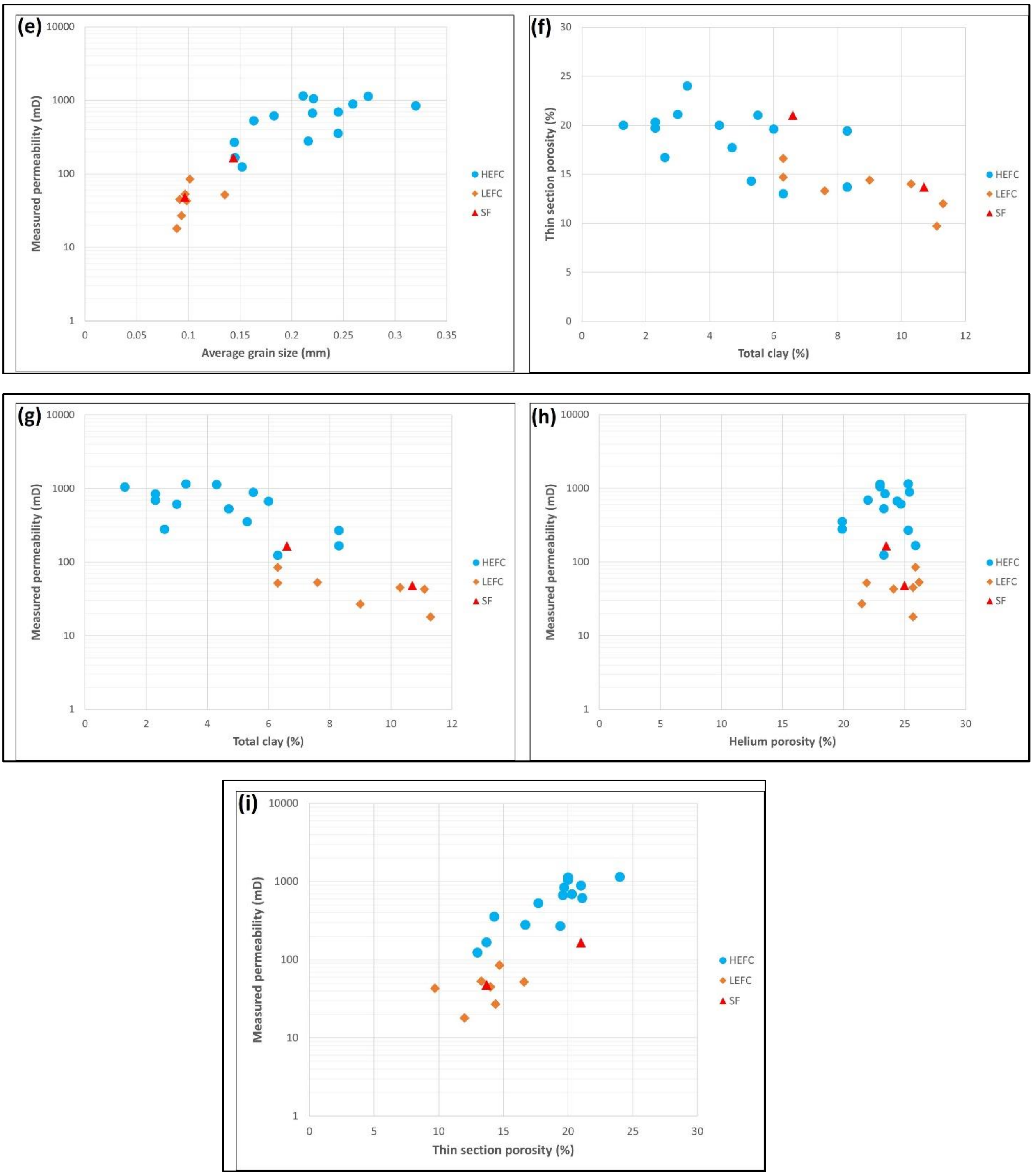

Figure 3.25: (a-b) Cross plots of clay coat coverage versus thin section and helium porosity; (c) Cross plot of measured permeability and clay coat coverage; (d-e) Cross plots of thin section porosity and measured permeability versus grain size; (f-g) Cross plots of thin section porosity and permeability versus total clay; (h) Cross plot of helium porosity and measured permeability (Note: Unlike figure 3.18a and b, the plot does not show any clear correlation due to the effect of clay microporosity on helium porosity); (i) Cross plot of permeability and thin section porosity showing a good correlation.

3.6.4 Implications for reservoir quality prediction

It is a common practice to target clean (clay-free) sandstones and ignore their relatively clay-rich counterparts (Wooldridge et al. 2017b). This is due to the general belief that the best reservoir quality occurs in clean and coarser-grained sandstones. As demonstrated in this study, cleaner and coarser-grained channel sandstones have better reservoir quality than finer-grained, clay-rich channel sandstones. However, the cleaner and coarser-grained channel sandstones (HEFC) have greater quartz cement volume due to lesser clay coat coverage (<50%) on the detrital quartz grain surfaces. Continuous burial of these coarser-grained and less-coated sandstones into ultra-deep HPHT settings (>20,000 psi; >200°C) (Smithson 2016) may result in further quartz cementation and severe porosity/permeability loss. Conversely, the higher clay coat coverage (70-98%) in the finer-grained, slightly dirty channel sandstones (LEFC) will inhibit further quartz cementation and help preserve good porosity and moderate permeability, when buried in ultra-deep HPHT settings (Fig. 3.26).

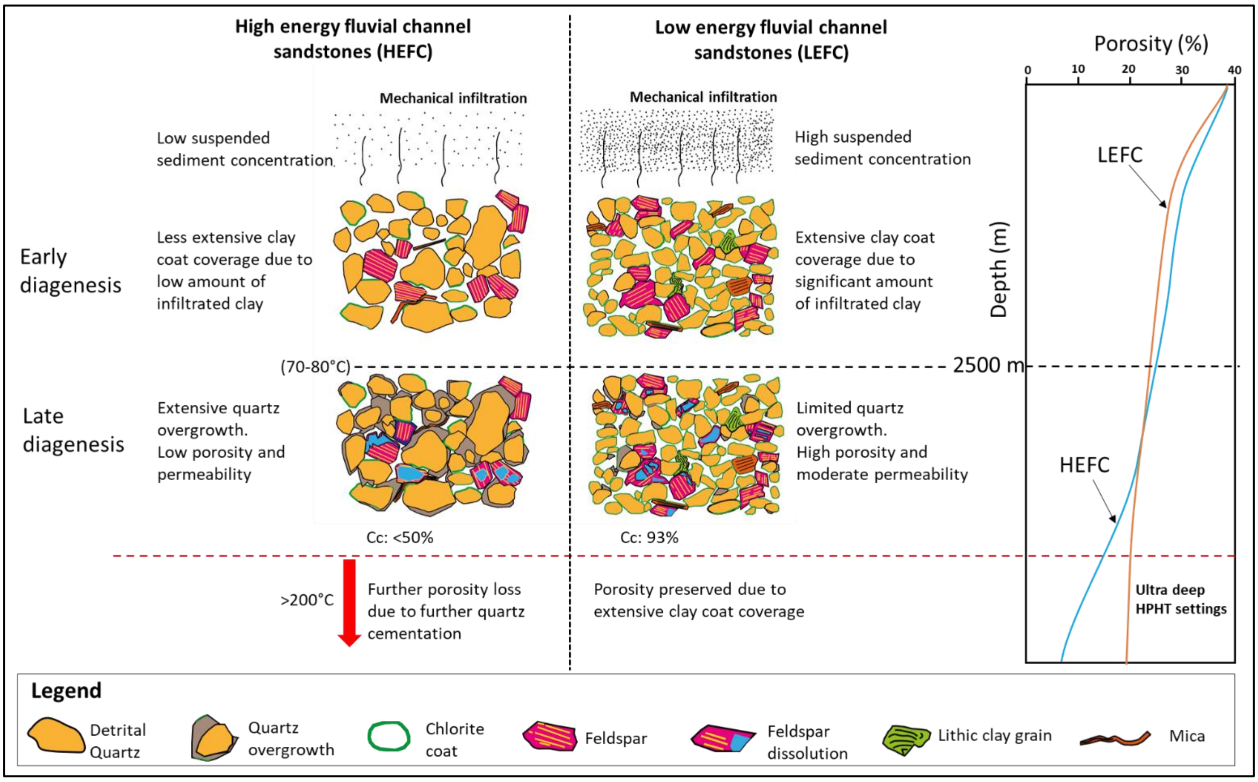

Figure 3.26: Schematic illustration of diagenetic and related reservoir quality evolution pathways in high and low energy fluvial channel sandstone reservoirs (Cc: average clay coat coverage).

It is also worth noting that increased clay content and clay coat thickness in sandstones can have negative impacts on reservoir quality. Our study suggests that between 5 to 10% clay fraction (occurring primarily as clay coats) is required to form adequate clay coat coverage that can effectively inhibit quartz cementation and preserve favourable reservoir quality in deeply buried fluvial sandstones. This range is within the optimum range (5-13%) proposed by Pittman et al. (1992) for the Tuscaloosa Formation. Depending on pore-throat size, thicker clay coats can block pore throats and consequently inhibit fluid flow (Worden et al. 2020). Clay coat thickness in this study ranges from 0.5 µm to 10 µm (except in embayed surfaces where it is up to 16 um) and has not resulted in blockage of pore throats. These thickness values are within the 5 µm to 10 µm range reported as beneficial for reservoir quality preservation (Anjos et al. 2003; Sun et al. 2014; Charlaftis et al. 2021).

The impacts of authigenic chlorite on wireline logs (particularly neutron and resistivity logs) have been highlighted in the literature (Nadeau 2000; Bloch et al. 2002; Worden et al. 2020; Azzam et al. 2022). Chlorite, unlike illite, contains more hydrogen atoms, and therefore gives rise to high neutron responses and ultimately additional porosity. The presence of microporous grain-coating or pore-filling chlorite in sandstones commonly results in anomalously high-water saturation. Consequently, low resistivity can result even in oil-bearing sandstones (Anjos et al. 1999; Xia et al. 2020). Ultimately, this can lead to underestimating the recoverable hydrocarbon resources during field appraisal and development. This implies that low reservoir quality intervals (dirty sandstones), previously regarded as non-productive zones in ageing and matured fields, need to be re-evaluated. This can help to replenish reserves and increase production/recovery.

3.7 Conclusions

1. The reservoir quality (porosity and permeability) of the deeply buried HPHT Triassic Skagerrak fluvial sandstones is primarily controlled by depositional facies/processes, grain size and clay content.
2. The confined fluvial channel facies constitute the best reservoirs, while the floodplain, palaeosols and lake facies form poor to non-reservoirs. However, within the channel facies, there is a variation in reservoir quality. The high energy channel sandstones have higher reservoir quality (100-1150 mD), due to their coarser grain size and lower clay content. The low energy channel sandstones, on the other hand, have lower reservoir quality (<100 mD) due to their finer grain size and slightly higher clay content.

3. Petrographic and SEM analysis revealed that the preservation of good reservoir quality in these channel sandstones is also partly due to the presence of grain-coating chlorite which inhibited the extensive growth of quartz cement.
4. In this study, clay coat coverage (the principal factor controlling the ability of grain-coating clays to effectively inhibit quartz cementation) can be linked to depositional facies, grain size, clay coat volume and depositional energy. Higher clay coat coverage (70-98%) occurs in finer-grained, low energy channel sandstones containing between 5% to 10% clay coat volume, while lesser clay coat coverage (<50%) is found in coarser-grained, high energy channel sandstones containing <5% clay coat volume.

5. Clean sands have been highlighted as being the best starting material for good reservoir quality at depth. This study demonstrates that clay-rich fluvial channel and crevasse splay sandstones with moderate amounts of clay, mostly in the form of clay coats, could equally offer good reservoir quality.

Chapter 4: Diagenesis and Reservoir heterogeneity of a Triassic braided fluvial system

4.1 Summary

Deposits of braided fluvial systems are generally known to possess excellent reservoir qualities. The reservoirs are typically very thick and laterally continuous, and highly connected due to their high net to gross (>80%). However, pore to small scale heterogeneities caused by subtle variations in depositionally controlled parameters and diagenetic alterations can have a major influence on their reservoir quality and consequently, reservoir performance (e.g., injection and recovery rates). An understanding of these controls is essential for developing robust reservoir models for hydrocarbon exploration and storage operations. Furthermore, understanding the distribution of depositional and diagenetic alterations in the cross section and longitudinal profiles of channel bodies is critical for accurate three-dimensional reservoir modelling. Here, we employed an integrated approach including outcrop studies, optical and scanning electron microscopy to investigate the main controls on diagenesis and reservoir heterogeneity in the St Bees Sandstone Formation (SBSF), West Cumbria, UK. The SBSF is a braided fluvial reservoir composed of laterally and vertically stacked channel sandstone bodies. Its exposure on the Cumbrian coast provides an excellent opportunity to investigate reservoir quality/heterogeneity in fluvial channel bodies in both cross-section and longitudinal profiles. This study reveals that the SBSF has excellent reservoir quality with porosity as high as 24%. Reservoir quality and heterogeneity of the SBSF are controlled by a combination of grain size, ductile grains content, carbonate cement and variable degrees of compaction. Furthermore, this study reveals that in the SBSF, there is no major difference between the cross section and longitudinal profiles in terms of petrography, mineralogy (detrital and diagenetic), porosity and stacking patterns for a preserved length of 7 km. This suggests that during modelling of braided fluvial sandstones, reservoir parameters derived from the cross-sectional areas of channel bodies could also be used to model the longitudinal sections, depending on the preserved reach length. The high porosity and potentially good permeability, favourable detrital/authigenic mineralogy coupled with the high net to gross (NTG) of the SBSF suggest its suitability for further hydrocarbon exploration and potential subsurface storage operations.

4.2 Introduction

Braided fluvial deposits form major aquifers and hydrocarbon reservoirs in many parts of the world (Bridge 2001) and have recently become potential targets for CO_2 storage in some basins such as the East Irish Sea, Central North Sea and Southern North Sea basins. However, due to the variable scales of internal and external heterogeneities associated with fluvial deposits, they are generally difficult to characterize and develop. Although heterogeneity in fluvial deposits has long been known to have a major impact on fluid flow (Miall 1988; Tyler and Finley 1991; Sharp et al. 2003; Morad et al. 2010), its representation in three-dimensional aquifer/reservoir models remains a major challenge. Currently, fluvial reservoir models are built using stochastic techniques that employ different algorithms (Seifert and Jensen 2000; Deutsch and Tran 2002; Huffman et al. 2005; Keogh et al. 2007; Pyrcz et al. 2009; Koneshloo et al. 2018; Vevle et al. 2018; Puig et al. 2019; Mitten et al. 2020; Thanh and Sugai 2021). An important factor in these models is the definition of sand body geometry and spatial distribution of reservoir properties (e.g., porosity and permeability) and sedimentary heterogeneities. This is however not possible to achieve with well data due to inter-well spacing. To overcome this challenge, outcrop analogues are commonly employed to define sand body geometries, predict geometries of barriers/baffles and finally understand how reservoir properties/heterogeneities are spatially distributed within sandstone bodies (Howell et al. 2014; Newell and Shariatipour 2016).

Previous outcrop studies and inferences on ancient fluvial channel deposits have been mainly on/from cross-sectional areas of channel bodies with little/no description of their corresponding longitudinal profiles (or reach lengths). This is primarily due to the lack of proper exposure of the longitudinal profiles of most channel bodies. As a result, the characterization of longitudinal profiles of channel bodies remains a major challenge for reservoir modellers. The main aim of this chapter is to investigate the diagenetic history of a Triassic braided fluvial succession, the associated heterogeneity (in both cross section and longitudinal profiles) and the main controls, using the St Bees Head, West Cumbria, UK as an example. Also, this chapter aims to test whether variations in reservoir properties and diagenetic features observed in cross-sectional profiles of braided channels can be used to model their longitudinal profiles. The outcropping St Bees Sandstone Formation (SBSF), the main focus of this chapter, provides an excellent opportunity to study reservoir quality/heterogeneity in braided fluvial successions in both the cross-section and longitudinal profiles. Furthermore, the St Bees Sandstone Formation outcrop on the West Cumbrian coast has been reported as a suitable analogue for the fluvial reservoir sandstones in the Corrib Gas Field, offshore west of Ireland (Dancer et al., 2005). It is also a major aquifer in the UK and one of the prime targets for CO_2 storage in the East Irish Sea Basin. Therefore, understanding the main controls on reservoir quality and heterogeneity in this sandstone is essential .

In particular, this chapter aims to answer the following questions: (1) What is the depositional and authigenic mineralogy of the St Bees Sandstone Formation? (2) What was the environment of deposition of the St Bees Sandstone Formation? (3) What are the main controls on the porosity of this regional sandstone reservoir? (4) How do porosity and diagenetic features vary in the cross-section and longitudinal profiles/reach length of braided channel bodies? (4) What are the similarities or differences between cross-section and longitudinal profiles of braided channel bodies, and implications for subsurface reservoir models and CO_2 storage? The overall aim of this research is to identify the main controls on sample-scale reservoir quality and heterogeneity in these rocks.

4.3 Geological setting

The Permo-Triassic outcrops around St Bees Head, West Cumbria, UK, lie within the north-east margin of the East Irish Sea Basin (EISB), an essentially post-Variscan structure, lying predominantly offshore between mainland Britain to the east and south and the Isle of Man to the west (Fig. 4.1). During the Permo-Triassic, several basins and structural highs in Britain and NW Europe developed in response to the E-W rifting phase associated with the post-Variscan break-up of Pangea and early Atlantic opening (Jackson and Mulholland 1993; Meadows and Beach 1993a; McKie and Williams 2009). The structural highs served as the main source of sediments in these basins (McKie and Williams 2009; McKie and Shannon 2011; Medici et al. 2015; Medici et al. 2019). In NW England, the Permo-Triassic basins are fault-controlled and generally served as conduits for the extensive Budleighensis fluvial systems that deposited the Permo-Triassic Sherwood Sandstone Group (SSG) (Newell 2018; Marsh et al. 2022). These basins (both onshore and offshore) which are reportedly linked include the Worcester, Stafford, Needwood, Cheshire, East Irish Sea, North Channel, and Solway Basins. The EISB forms the central part of this array of basins (Hardman et al. 1993; Knipe et al. 1993) and extends onshore in West Cumbria, where it is bounded at its eastern margin by normal faults that divide it from the Lake District morpho-structural high (Akhurst et al., 1998). Structurally, the EISB can be divided into two distinct provinces: a northern province and a southern province. The northern province is dominated by NW-SE and NE-SW trending extensional faults while the southern province is dominated by N-S- trending extensional faults affected by closely spaced minor faults. Seismic data revealed that majority of the principal faults in the EISB are listric faults with evidence of rotation and sedimentary growth in their hanging walls, indicating intermittent activity during the Permo-Triassic (Knipe et al. 1993; Meadows and Beach 1993a). Generally, both the Permian and Triassic sediments thicken into the hanging walls of these major faults whilst present-day normal faults displacements of the top of the SSG across these major faults can reach up to 4000 ft (cf. Hardman et al., 1993).

St Bees Head, the main focus of this study, lies close to the southern margin of the NE-SW trending Ramsey-Whitehaven Ridge that separates the EISB from the similarly Permo-Triassic Solway Basin to the north (see Figs. 4.1 and 4.2). The St Bees sandstone is widely interpreted to be deposited by low sinuosity, braided fluvial systems in a semi-arid environment (Jones and Ambrose 1994; Yaliz and Chapman 2003; Medici et al. 2015). Palaeocurrent data revealed that this braided fluvial system flowed in a north, north-west direction (Jones and Ambrose 1994; Medici et al. 2015) and formed part of a major, northwards flowing channel belt derived from a sediment source (the Armorican Massif) south of the UK (Fitch et al. 1966; Audley-Charles 1970).

4.3.1 Stratigraphy

A generalized lithostratigraphy and chronostratigraphy of the East Irish Sea Basin is shown in figure 4.3. The stratigraphic record of the Permo-Triassic East Irish Sea Basin consists of five depositional sequences comprising: the Appleby Group (Lower Permian), Cumbrian Coast Group (Upper Permian), Sherwood Sandstone Group (Lower Triassic), Mercia Mudstone Group (Upper Triassic) and Penarth Group. These depositional sequences are separated by major sequence boundaries or disconformities (Jackson et al. 1987; Jackson et al. 1997). The Appleby Group forms the lowermost sequence and unconformably overlies a previously uplifted, folded, and eroded sequence of Carboniferous rocks. The Cumbrian Coast Group which overlies the Appleby Group is divided into the St Bees Evaporite Formation and Barrowmouth mudstone Formation. The Barrowmouth mudstone Formation is the offshore equivalence of the St Bees Shales that overlies the St Bees Evaporite Formation at St Bees Head in West Cumbria (Arthurton and Hemingway 1972; Jackson et al. 1997). The Sherwood Sandstone Group (SSG), which contains the Formation of interest in this study, overlies the Cumbrian Coast Group and mainly consists of sandstones, siltstones, and mudstones. The SSG is divided into two distinct Formations: the upper Ormskirk Sandstone Formation (age: earliest

Anisian) and the lower St Bees Sandstone Formation (age: Scythian) (e.g., Jackson et al., 1997; Fig. 4.3). The upper Ormskirk Sandstone Formation comprises mainly sandstones of mixed fluvial, aeolian and sheetflood origin (e.g., Meadows and Beach, 1993). The lower St Bees Sandstone Formation is subdivided into two members: (1) an upper Calder Sandstone Member, containing sandstones of mixed fluvial-aeolian origin, and (2) a lower Rottington Sandstone Member, comprising sandstones of fluvial origin (Jackson et al. 1997). The SSG is overlain by the Mercia Mudstone Group (MMG). The MMG is made up of thick alternating units of silty mudstone and halite (about 3,025 m thick) and forms a regional seal in the EISB (Jackson et al. 1997; Seedhouse and Racey 1997).

The area of study is the West Cumbrian coast around St Bees village (Fig. 4.1 & 4.2). At this location, the SSG is well exposed in several sea cliff and cliff top quarry sections around St Bees Head, thus giving the opportunity to study the sections in three-dimensions. Albeit the exposed SSG in this area comprises only the SBSF, as younger sediments are not preserved. Underlying the St Bees Sandstone Formation (SBSF) is the St Bees Shale Formation (onshore equivalence of the Barrowmouth mudstone Formation) outcropping at Saltom Bay.

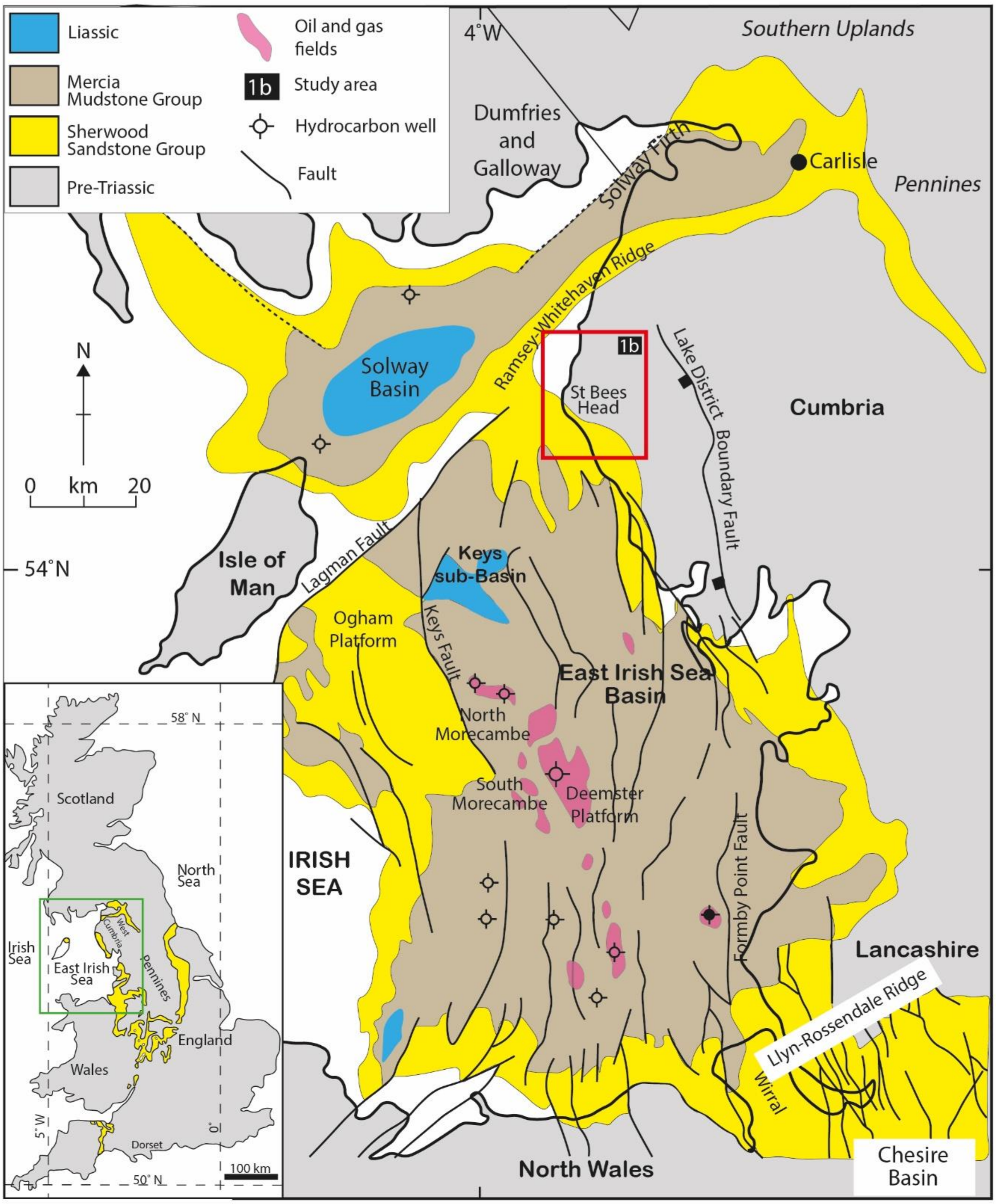

Figure 4.1: Location map and structural configuration of the East Irish Sea Basin (EISB) and surrounding areas (modified from Marsh et al., 2022 and Meadows and Beach, 1993a). The study area (Fig 1b) is indicated by the red box.

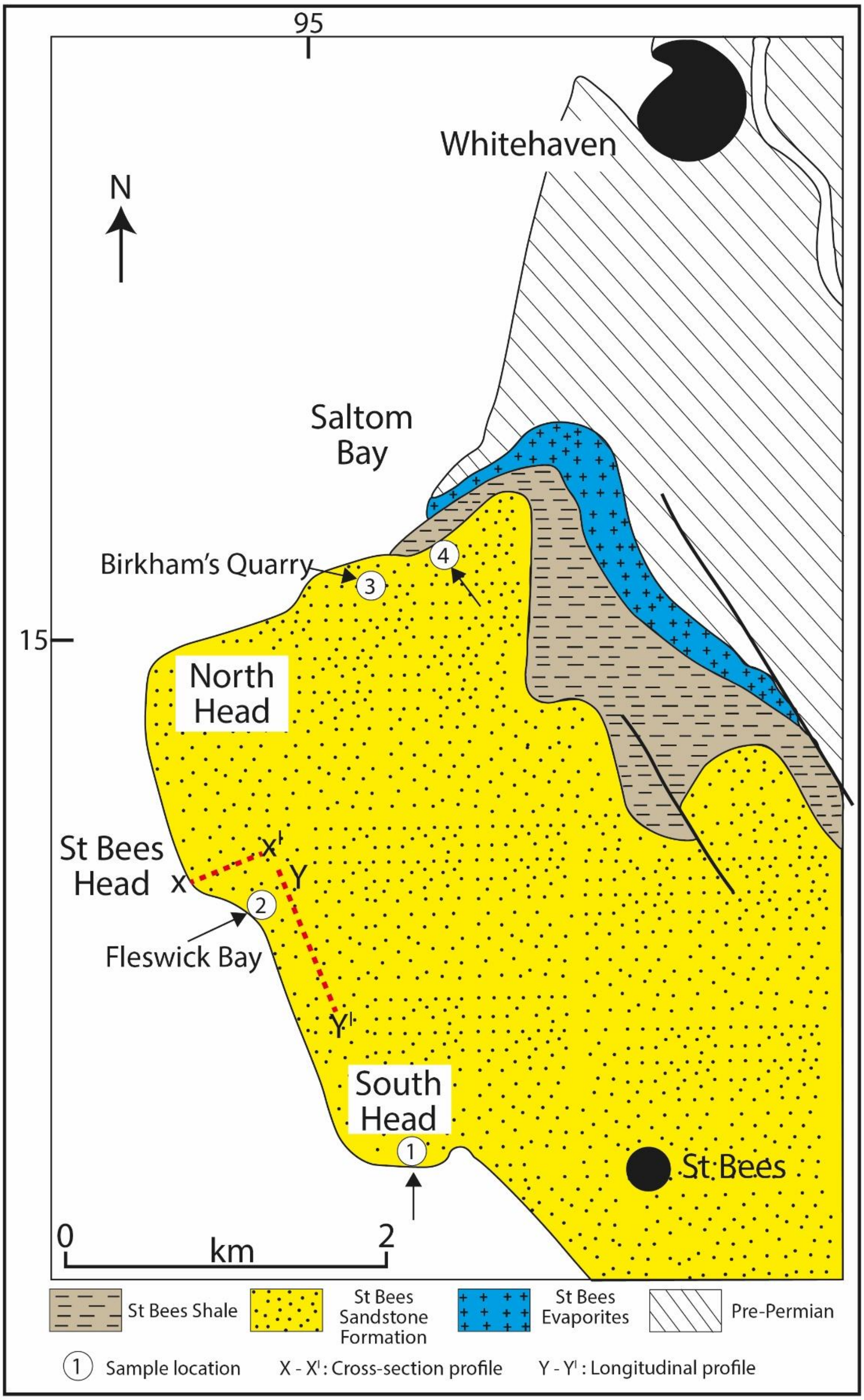

Figure 4.2: Locality map of part of West Cumbria showing the simplified distribution of Permo-Triassic strata (Modified from Macchi, 1981).

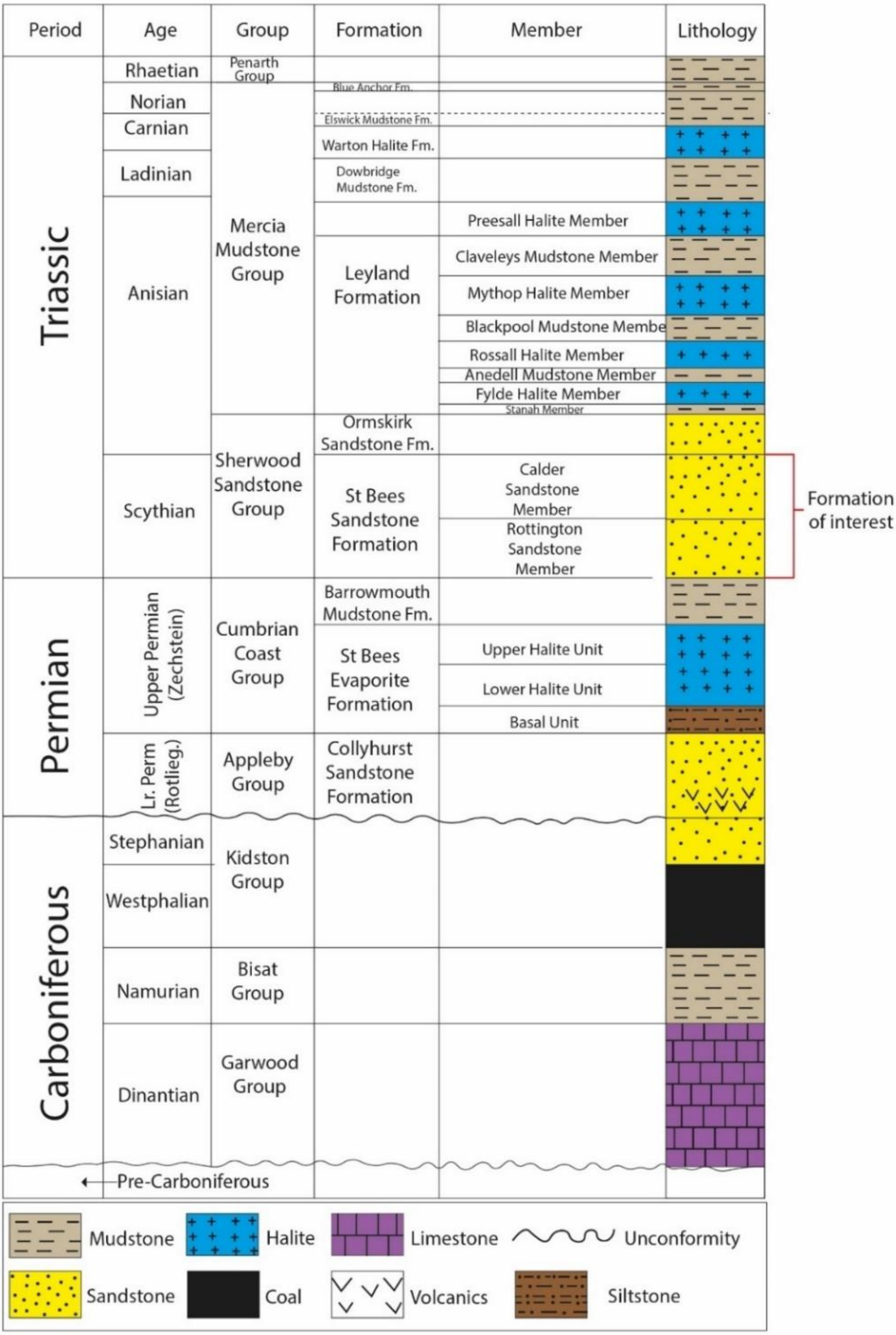

Figure 4.3: Stratigraphic sequence of the EISB (modified after Jackson et al., 1997).

4.4 Methodology

In order to investigate the St Bees Sandstone Formation at West Cumbria, UK and characterize the associated channel architecture, well exposed outcrop sections along the Cumbrian coast were targeted. The study area covers four main locations between Whitehaven and St Bees including: South Head, Fleswick Bay, Birkham's Quarry and Saltom Bay (Fig. 4.2). Along the Cumbrian coast, the SBSF outcrop spans approximately 7km in length from St Bees to Saltom Bay, near Whitehaven (Fig. 4.2). It is important to note that the limited amounts of Triassic outcrops in onshore UK and wider Northwest Europe means that the 7 km longitudinal section of the St Bees outcrop investigated in this study provides one of the best representations as an analogue for offshore exploration. The SBSF outcrop contains mainly stacked channel bodies bounded by laterally continuous erosional surfaces which can be traced for 100s of metres at both Fleswick Bay and St Bees South Head. Fleswick Bay lying between St Bees North and St Bees South Heads (Fig. 4.2) provides at least 500 m of laterally continuous exposure of stacked channel sandstones. The cliff along this section rises from approximately 20 m in height at the northern end of the bay to over 100 m at the southern end. Sedimentary graphic logs were created at each location with each log starting from the base to the top of the section (Fig. 4.4). Bed thicknesses, contacts, grain sizes, sedimentary structures, colour, architecture, and geometries of sandstone bodies were recorded. A series of photomontage images traversing the cliff sections have provided an understanding of the style and dimensions of the channel cross-sections and channel length geometries. For petrographic analysis, a total of 157 rock samples were collected from fluvial channel bodies (St bees: 41; Fleswick Bay: 90; Birkham's quarry: 26; Saltom Bay: 25 samples). The samples were strategically collected from the top, middle and base of the channel bodies, and from less weathered surfaces, in order to investigate any inherent petrographic variations. It is worth noting that the petrographic data collected from the outcrop samples may not represent subsurface conditions as the studied samples might have additional diagenetic features due to weathering (such as dissolution).

A detailed petrographic examination was carried for all 157 samples by using light microscopy and scanning electron microscope (SEM) equipped with an energy-dispersive x-ray analyser (SEM-EDX). The composition and porosity were determined by standard point-count (300 points) analysis after the specimens had been impregnated with blue epoxy resin to highlight their porosity. Grain size was estimated by measuring the long axis of 100 grains per thin section using the grain size measurement tool in PETROG^{TM} software. Sorting was estimated by comparison with published sorting comparators (Beard and Weyl 1973; Longiaru 1987). To estimate reservoir quality, reservoir parameters from the point count analysis such as mean grain size, total porosity and cement content were used. Data from the point count analysis was used to calculate IGV (Intergranular volume). IGV (sum of intergranular porosity, detrital matrix, and intergranular cement) is used to measure compaction in sandstones. The degree of compaction and cementation in the sandstones were determined by measuring the porosity loss due to compaction (COPL) and porosity loss due to cementation respectively, following established criteria (Lundegard 1992; Ehrenberg 1995):

$$COPL = P_{initial} - \{[(100 - P_{initial}) \times IGV] / (100 - IGV)\}5$$

$$CEPL = (P_{initial} - COPL) \times (C / IGV)$$

(Where $P_{initial}$ = initial depositional porosity, assumed as 45%; IGV = Intergranular volume; C = Intergranular cement).

To investigate the clay minerals (i.e., their composition, morphology, and distribution) present within the sandstone samples, 25 carbon-coated thin sections were selected and studied using an Oxford instrument Hitachi SU70 scanning electron microscope (SEM), equipped with a backscatter electron (BSE) and an energy dispersive x-ray (EDS) detector, at an acceleration voltage of 15 kV.

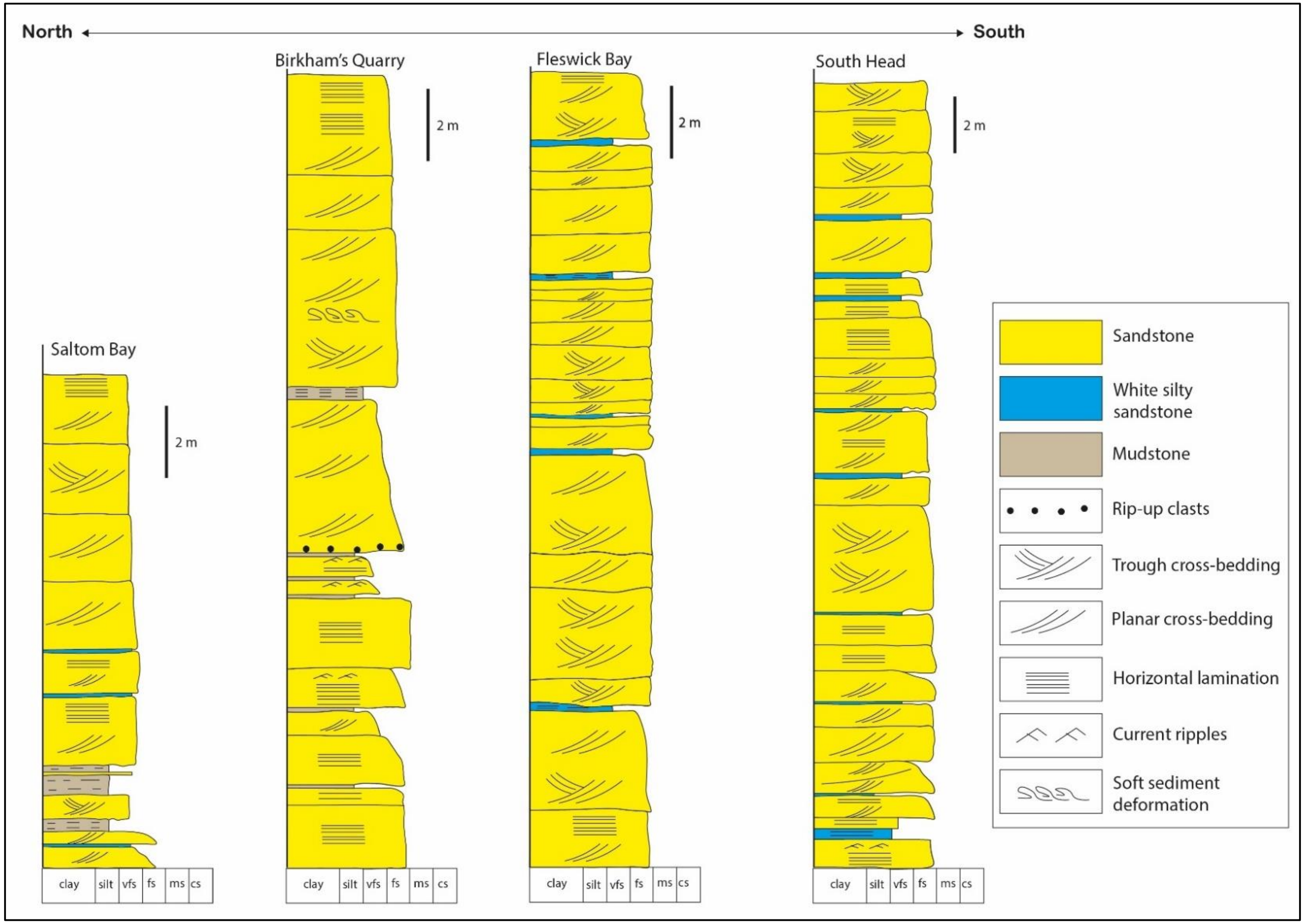

Figure 4.4: Graphic logs of the St Bees Sandstone Formation at the studied locations.

4.5 Results

4.5.1 Facies analysis

Detailed facies analysis of the Sherwood Sandstone Group (subsurface and outcrop) has been previously conducted by several authors (Meadows and Beach 1993; Meadows and Beach 1993a; Dancer et al. 2005; Medici et al. 2015). Facies analysis of the Lower SBSF outcrop (the main focus of this research) from St Bees South Head to Saltom Bay (Fig. 4.2) revealed seven facies types (Table 1 and fig. 4.5) which have been grouped into three main facies associations namely: fluvial channel, sheetflood and floodplain facies. The fluvial channel facies represent deposits of confined fluvial deposition, while the sheetflood and floodplain facies represent deposits of unconfined fluvial deposition. These facies associations are described briefly below; however, the main focus of this research are the fluvial channel facies.

4.5.1.1 Fluvial channel facies association (FCA)

Fluvial channel facies dominate the fluvial succession (about 80-95%) of the SBSF from St Bees South Head to Saltom Bay (Fig. 4.2). This facies association is made up of laterally and vertically stacked (or multistorey/multilateral) channel sandstones that are bounded by laterally continuous erosional surfaces which can be traced for hundreds of metres along the cliff sections (Fig. 4.6a). At St Bees South Head and Fleswick Bay, 98-100% of the outcrop is made up of stacked channel sandstones. At Saltom Bay, this is not the case. Here, the upper section of the Saltom Bay cliff is comprised of stacked channel sandstones, while the lower section is comprised of interbedded sheetflood and floodplain facies (see fig. 4.6b & c). The interbedded sheetflood and floodplain units at the lower section of Saltom Bay indicate the transition from unconfined fluvial deposition to fully confined channel deposition (i.e., near 100% stacked channels) in the fluvial succession. The channel sandstone bodies are mainly sheet sandstones, based on Hirst (1992) sandbody classification. Five main facies types were identified within the channel facies association based on lithology and sedimentary structures: (1) cross-bedded sandstones (Sp and St), (2) horizontally laminated sandstones (Sh), (3) rippled laminated sandstones (Sr), (4) deformed sandstones (Sdf) and (5) finely laminated siltstones and very fine silty sandstones (Sws) (see Table 1 and Fig. 4.5). These main facies types correspond to the four main sub-facies described by Dancer et al (2005) for the channel facies of the SSG in the Corrib Field, offshore west of Ireland. These main sub-facies are:- high-stage bars, low-stage bars, inter-bar channels, and channel abandonment fines, and can all be ascribed to variations in the flow regime within a low-sinuosity fluvial channel system. According to these workers, the high-stage bars are interpreted as major compound bars that would have migrated only during episodes of peak discharge and bank-full conditions; these are represented by large scale (>0.5 m) sets and co-sets of cross-bedded clean sandstones. The low-stage bars are minor bars that represent bedforms within an anastomosing network of anabranches diverted around the major bars as flow waned. They are represented by smaller-scale sets and co-sets of cross-bedded sandstones. The inter-bar channel components are made up of sandstones with plane-bed and current ripple laminations formed at the lowest flow stage in response to flow acceleration between bars as individual channels formed a pool and riffle system. The channel abandonment fines form a minor component of the channel deposits due to extensive reworking attested to by the abundance of mudstone intraclasts within the high-stage bar bedforms (cf. Dancer et al., 2005). The channel abandonment deposits are mostly made up of finely laminated siltstones and very fine-grained silty sandstones with silty drapes (facies Sws) indicating very low energy traction carpet sedimentation alternating with near stagnation that allowed the deposition of some suspension fines (N. Meadows, personal communication). Facies Sws is whitish in colour and commonly found towards the top of the channel deposits. It ranges in thickness from 0.1 m to 0.2 m and is laterally restricted (2 to 50 m) in the fluvial succession.

4.5.1.2 Sheetflood facies association (SFA)

This facies association is strictly comprised of thin tabular, lenticular or sheet-like sandstones and is commonly interbedded with floodplain red-mudstone and stacked channel facies (Fig. 4.6c). The SFA is present in the lower section of the cliff at Saltom Bay, where it underlies the FCA. It extends laterally over hundreds of meters and range in thickness from 0.1 m to 0.4 m. Associated lithofacies include horizontally laminated and current-rippled sandstones. The sediments of this facies association could be ascribed to the deposition by unconfined fluvial processes, which occur when a river channel overflows its banks (crevasse splays) or towards the terminal end of the channel (terminal splays).

Table 1. Summary of lithofacies identified in the St Bees Sandstone Formation of the Sherwood Sandstone Group at West Cumbria (based on lithology, grain size and sedimentary structures; Miall, 1985).

Facies code	Sedimentary structures	Description	Interpretation
Sp	Planar cross-bedding	Fine-grained, moderately to well-sorted sandstones with solitary or grouped planar cross-beds. Individual bed thickness ranges from 0.7-1.5 m.	Deposits of migration of 2D subaqueous sandy dunes (lower flow regime) of transverse and linguoid bars in braided channels
Sh	Horizontal lamination	Very fine to fine-grained, moderately to well sorted sandstones with horizontal or parallel laminations.	Deposits of planar bed flow (upper flow regime).
St	Trough cross-bedding	Fine-grained sandstones with grouped sets of trough cross-bedding. Individual bed ranges in thickness from 0.5-1.5 m. This lithofacies passes upwards into lithofacies Sp and Sh.	Deposits of downstream migration of sinuous-crested dunes in high energy braided fluvial channels under lower flow regime.
Sr	Ripple marks	Very fine to fine-grained, moderately sorted, climbing ripple laminated sandstone.	Ripples (lower flow regime).
Sws	Fine lamination	Finely laminated siltstone and very fine-grained silty sandstones interbedded with cross-bedded and horizontally laminated sandstone. Bed thickness ranges from 0.1-0.3 m. They are typically white in colour and laterally restricted in the fluvial succession.	Drapes that overlie bedform deposits; records deposition during relatively low-energy flow conditions (Medici et al. 2015).
Sdf	Deformation structure	Fine-grained sandstones with soft-sediment deformation structures in form of over steepened and slumped cross beds.	Insitu deformation produced by liquefaction and/or fluidization of unconsolidated sediments during rapid deposition and burial, slumping or seismic shock (Lowe 1975; Nichols 2009; Owen and Moretti 2011).
Fm	Massive, horizontal lamination	Red to reddish-brown finely laminated or massive mudstone with thickness ranging from 0.1-1.2 m.	Overbank or waning flood deposits.

4.5.1.3 Floodplain facies association (FFA)

This facies association is common at the lower section of Saltom Bay cliff, but generally absent at St Bees South Head and Fleswick Bay. It is composed of laterally extensive red mudstones (Fm) and are commonly interbedded with ephemeral fluvial channel and sheetflood facies (Fig 5b & c). This facies association represents products of deposition from suspension as flow velocity progressively decreases to zero during overbank flooding events (Medici et al. 2015).

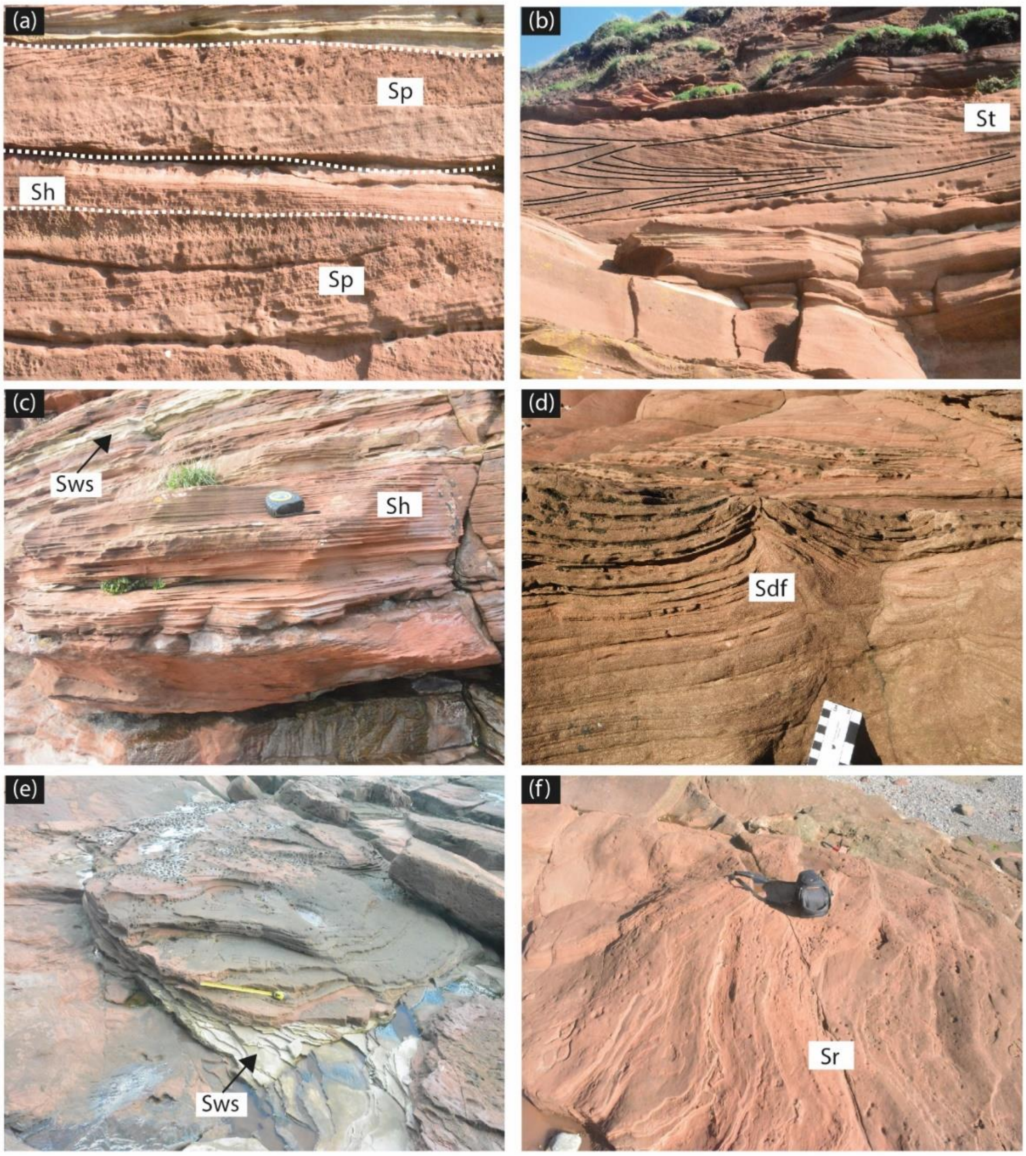

Figure 4.5: Representative lithofacies of the Sherwood Sandstone Group at west Cumbria. (a) Image showing superimposition of planar cross-bedded sandstone (Sp) and horizontally laminated sandstone (Fh) at Fleswick Bay (location 2). (b) Image of trough cross-bedded sandstone (St) at Fleswick Bay. (c) Horizontally laminated sandstone (Sh) interbedded with very fine- to fine-grained, white siltstone/silty sandstone (Sws). (d) Sandstone showing soft sediment deformation (Sdf). (e-f) Rippled laminated sandstone interbedded with white fine-grained siltstone/silty sandstone (Sws). Figures 4.5c-f are from South Head (location 1).

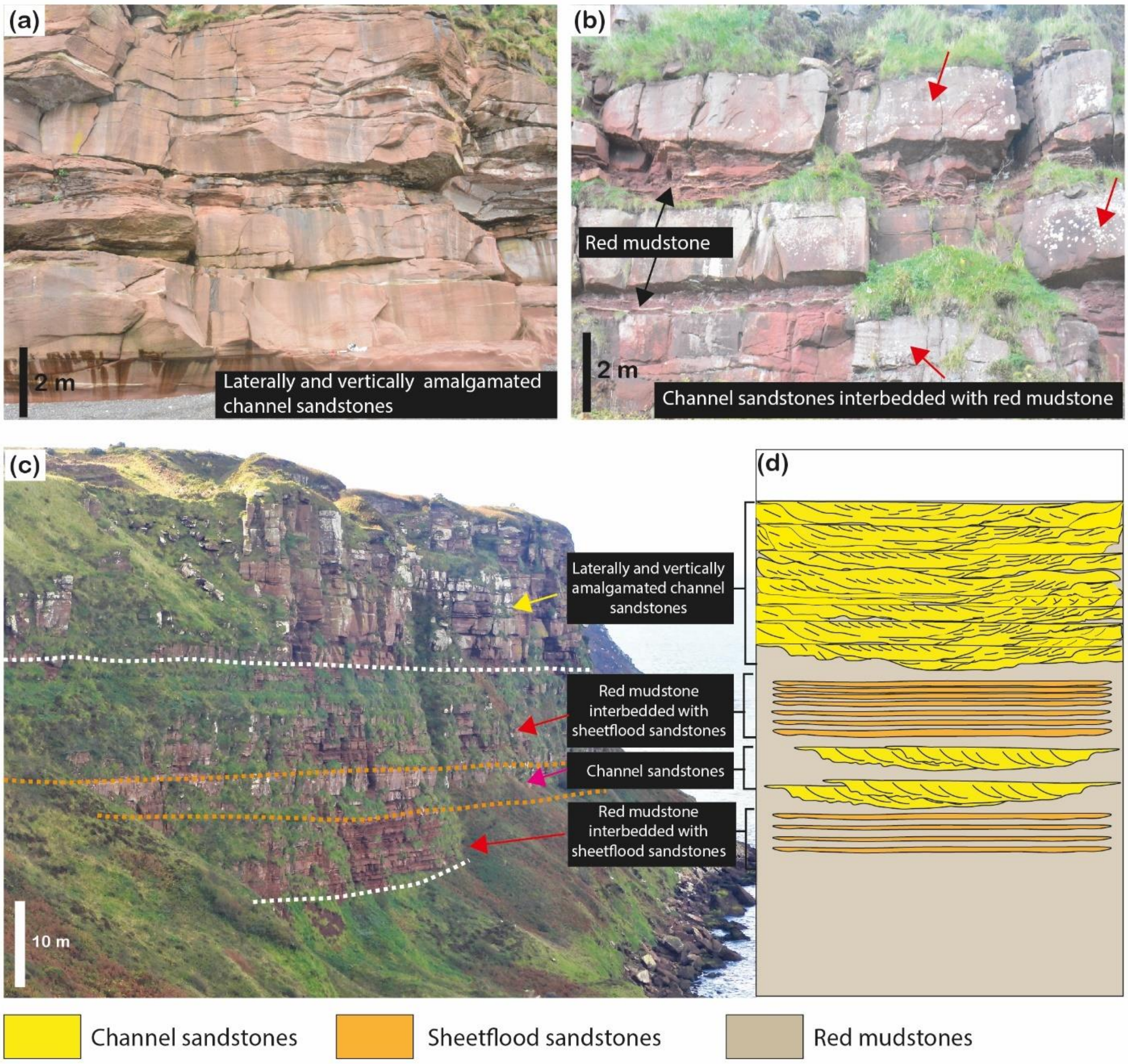

Figure 4.6: Outcrop images of fluvial architecture characterizing the St Bees Sandstone Formation at West Cumbria. (a) Laterally and vertically stacked channel sandstones at Fleswick Bay. (b) Channel sandstones interbedded with red mudstone at Saltom Bay. (c) North Head Member of the St Bees Sandstone Formation outcropping at Saltom Bay. (d) A summary of the style of fluvial architecture up section through the St Bees Sandstone Formation at Saltom Bay. The interbedded red mudstone and sheetflood sandstones mark the transition from the St Bees Shales underlying the St Bees Sandstone Formation but become less abundant and thinner upwards through the succession.

4.5.2 Petrography and diagenesis

4.5.2.1 Detrital mineralogy and texture

Petrographic analysis of samples from the SBSF show that the sandstones are very fine- to fine-grained, sub-angular to sub-rounded and moderately to poorly sorted. Compositionally, the sandstones are predominantly arkosic, with few samples classifying as lithic arkosic (Folk 1980) (Fig. 4.7). The detrital mineralogy is dominated by quartz, K-feldspar, plagioclase and lithic fragments. Other detrital minerals present are muscovite, biotite and clay; however, these occur in relatively low amounts in most of the studied samples. Pseudomatrix derived from the deformation of ductile grains (such as mudclasts, schist rock fragments, and illitized detrital feldspars) are also common, and frequently mistaken for true matrix (Fig. 4.8c-d, 4.8f & 9b).

The stacked channel sandstones of the SBSF are on average, fine-grained while the sheetflood sandstones mostly occurring at the base of the Formation, are on average, very fine-grained. A common sedimentary feature in the studied sandstones is the presence of parallel and cross laminations. In some of the sandstones, the laminae show a fine to slightly coarser grain size alternation, with the finer grained laminae containing a higher concentration of clay-rich and silt-sized matrix, coupled with micas and Fe-oxide cements (Fig. 4.8e). All petrographic data are reported in Appendix E.

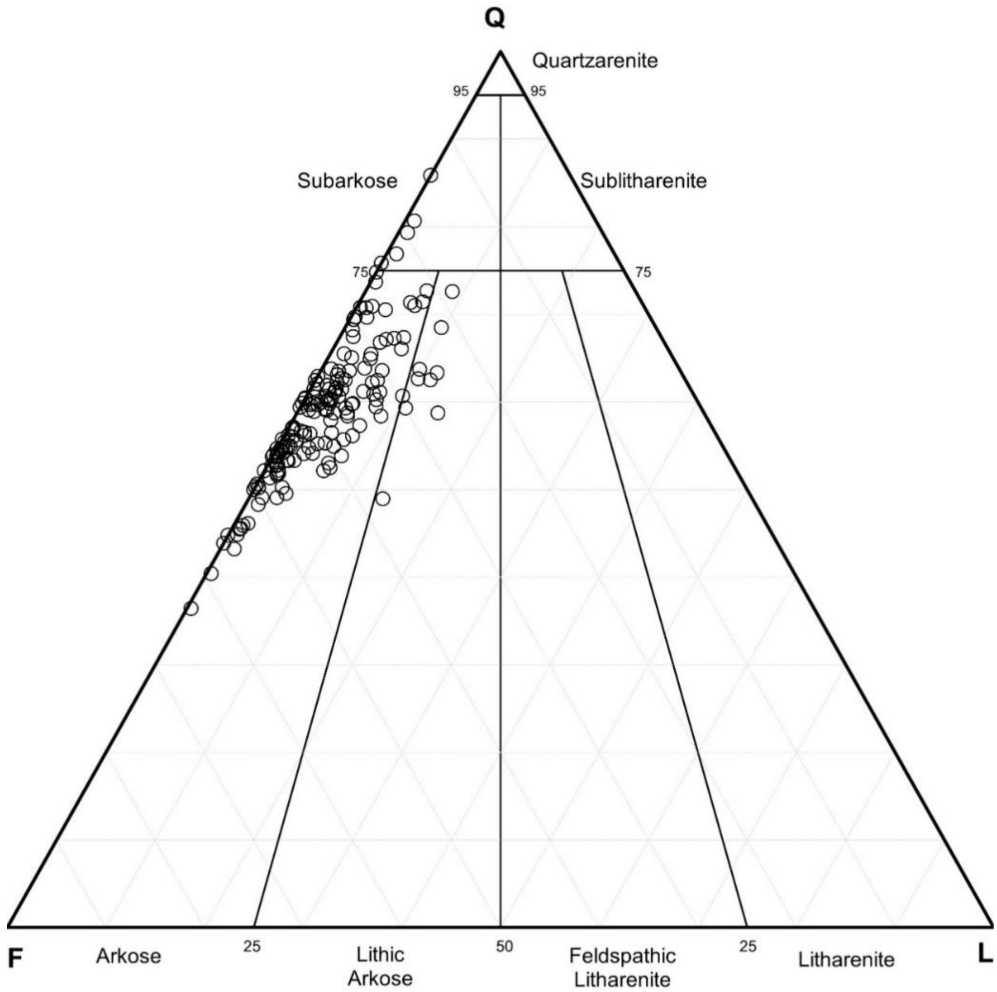

Figure 4.7: Classification of St Bees Sandstone Formation based on Folk's classification (Folk 1980) (Q: Quartz, F: Feldspar, L: Lithic rock fragment).

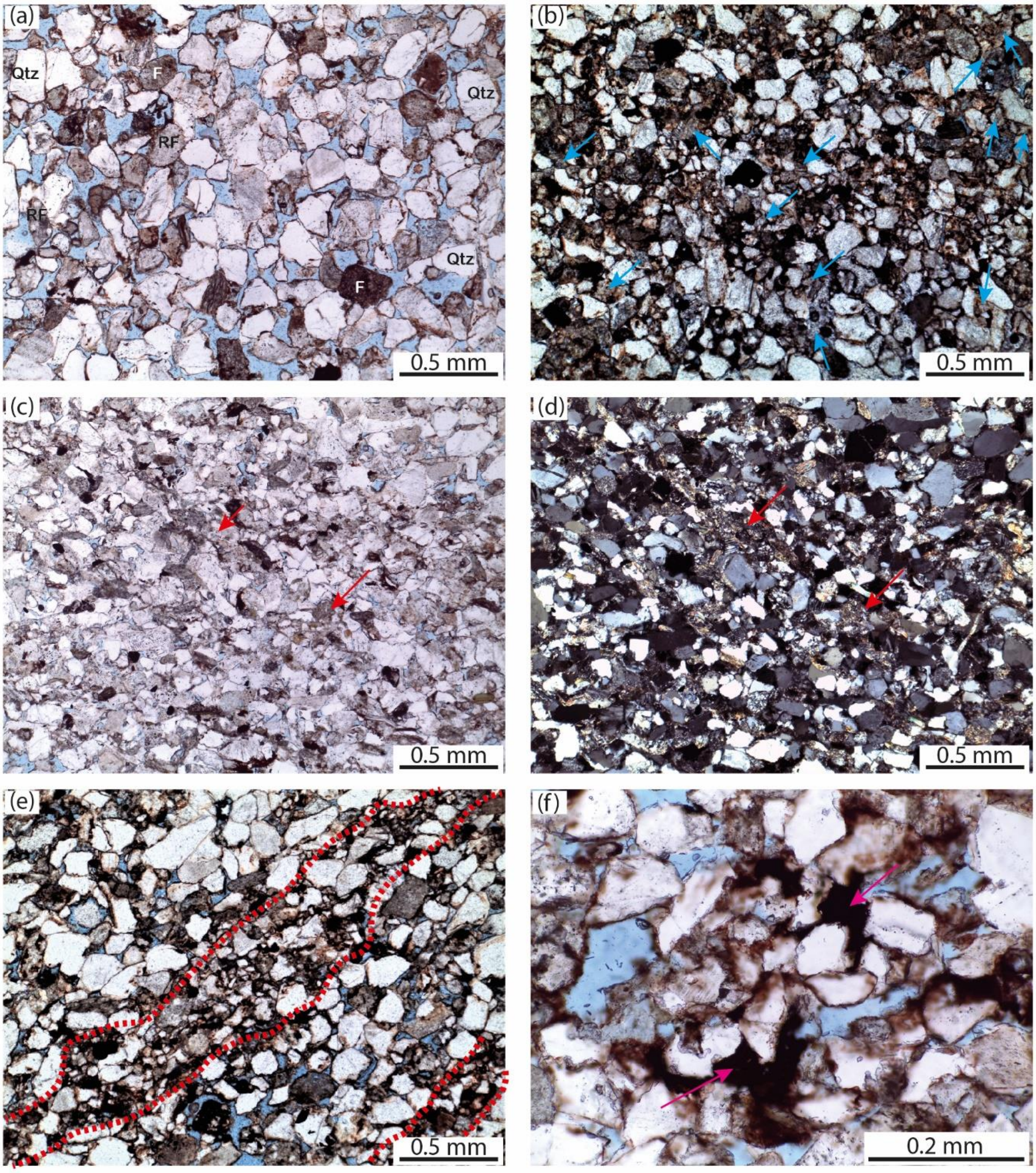

Figure 4.8: Photomicrographs of selected sandstones from the St Bees Sandstone Formation, West Cumbria. The sandstones were selected from different parts of the channel sandstone bodies (see the appendix for the sample numbers and their corresponding point count data). (a) Clean, fine-grained, and well sorted sandstone with well-preserved porosity (channel centre: Fleswick Bay, sample A2X). (b) Fine-grained sandstone with carbonate cement (blue arrow) and clay minerals (channel base: Fleswick Bay, sample X10). (c) Photomicrograph (plane-polarized light: PPL) showing sandstone with abundant ductile grains and pseudomatrix (red arrow) (channel top: South Head, sample LS45). (d) Cross polarized (XPL) version of photomicrograph in figure 4.8c. (e). Alternation of coarser- and finer-grained laminae in sandstone (channel top: Fleswick Bay, sample F1T). Note the presence of clay-rich and silt-sized matrix in the finer-grained lamina (delineated by dashed red lines) at the centre and bottom right of the photomicrograph. (f) Photomicrograph showing the presence of pseudomatrix (pink arrow) due to the deformation of illitic mud clast. The dark colouration is due to iron oxide staining (channel centre: Birkham's Quarry, sample S19).

4.5.2.2 Compaction

Evidence of mechanical compaction includes rearrangement and close packing of mechanically stable grains (quartz and feldspar), bending of mica grains (Fig. 4.10a) and deformation of ductile lithic grains (mud clasts and schistose rock fragments) into pseudomatrix (Figs. 4.8c-d, 4.8f, & 4.10b). Chemical compaction features (e.g., elongate/concavo-convex contacts) arising from local intergranular pressure dissolution were also identified between some detrital quartz grains (Fig. 4.9b). Using the method described by Lundegard (1992) to assess the relative importance of compaction and cementation to porosity loss in the studied sandstones, plot of porosity loss due to compaction (COPL) against porosity loss due to cementation (CEPL) shows that porosity loss is mainly by compaction (Fig. 4.13a).

4.5.2.3 Quartz cement

Quartz cement occurs as syntaxial overgrowths around detrital quartz grains (Fig. 4.9b & 4.10c). Quartz overgrowths develop where grain-coating clays are discontinuous or absent on detrital quartz grains. They occur either as incomplete or complete rims around detrital quartz grains and partially or completely occlude adjacent pore spaces. As shown in figure 4.9b, the boundaries between detrital quartz grains and quartz overgrowths are easily identified by the presence of dust rims or lines of impurities around the original quartz grain. Quartz cement volume (based on point-counting) varies from 0.3 to 9.3% (avg. 3%). Average volume of quartz cement in the channel sandstones and sheetflood sandstones is 2.9% and 2.4% respectively.

4.5.2.4 Clay minerals

Based on petrographic and SEM-EDX analyses, the diagenetic clay minerals in the studied St Bees sandstones include illite and chlorite. They occur as grain-coats (Fig. 4.9a & 4.10d) and pore-filling cement (Fig. 4.11a) (see also Appendix F). Where they occur as grain coats, they are oriented parallel or sub-parallel to detrital grain surfaces and commonly absent at grain contacts (Fig. 4.10d). The grain-coating clays are irregular and anisopachous, tangentially arranged and generally show features typical of mechanical infiltration (Matlack et al. 1989; Moraes and De Ros 1990). The grain-coating clays are in some instances partially engulfed by quartz overgrowths, especially where the clay coatings are discontinuous around detrital grains (Fig. 4.9b). Where grain-coating clays are well developed, quartz overgrowths are inhibited (Fig. 4.9a).

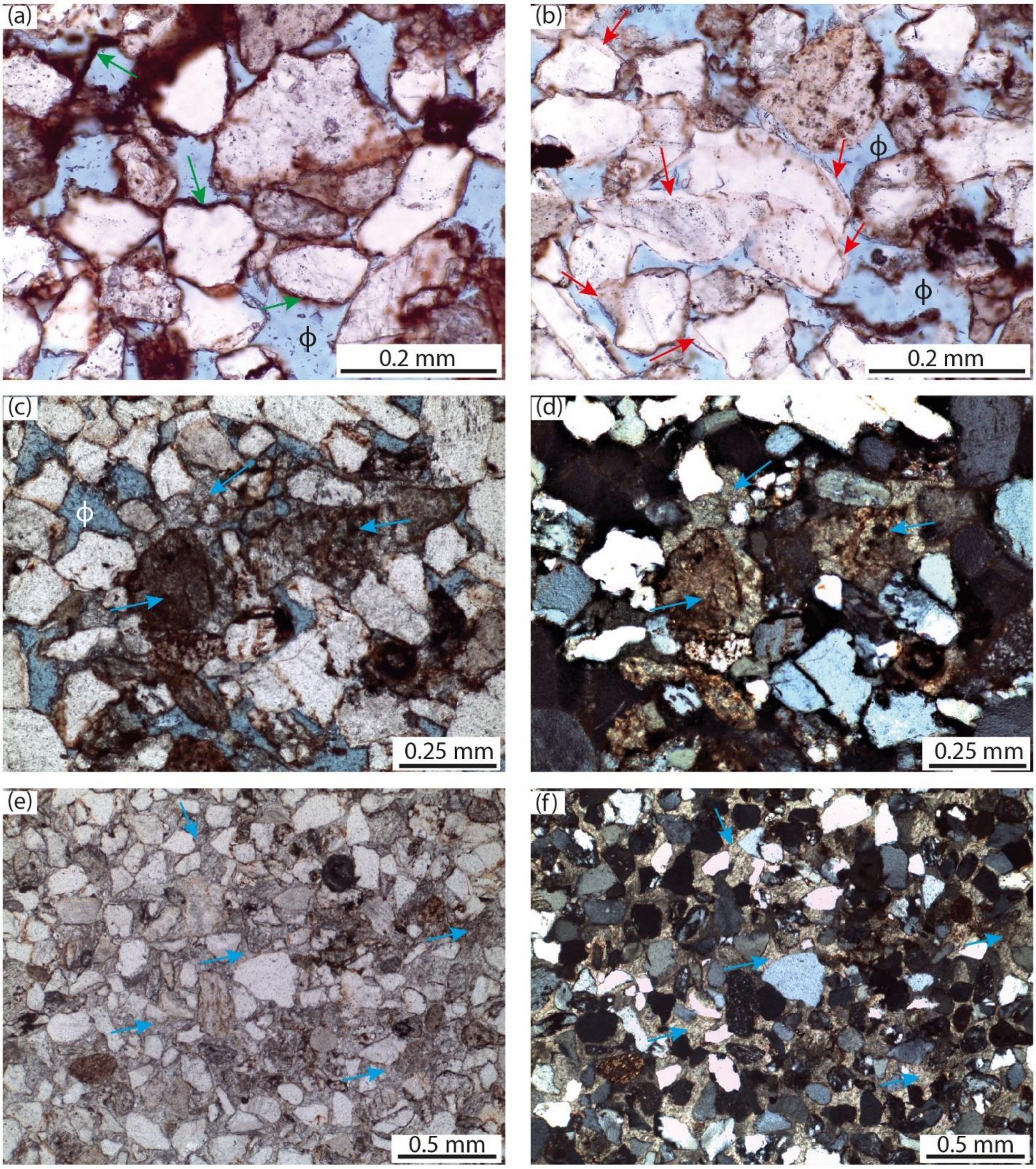

Figure 4.9: (a) Thin section photomicrograph of sample A1 showing Fe-oxide stained illite coats (green arrows) and intergranular porosity (ϕ). (b) Quartz cements (red arrows) around detrital quartz grains due to the absence or lack of complete illite coats (Sample S19). (c-d) Photomicrographs of sample E7 showing patchy and discrete carbonate cement (blue arrows) filling pore spaces and in close contact with detrital grains under plane polarized light (fig. 4.9c) and cross polarized light (fig. 4.9d). (e-f) Photomicrographs of another section of sample E7 showing porosity destruction by dolomite cement (blue arrows) under plane polarized (fig. 4.9e) and cross polarized (fig. 4.9f) light. Based on textural relationship, the detrital grains in figure 4.9e and f are enclosed within dolomite cement and completely lack quartz cement overgrowth, suggesting that dolomite cement predates quartz cement in the sandstones (Image locations – a: Fleswick Bay; b: Birkham's Quarry; c-f: Fleswick Bay).

4.5.2.5 Carbonate cement

Based on point-counting and SEM-EDX analyses, non-ferroan dolomite is the most abundant carbonate cement in the studied samples (Figs. 4.9c-f, 4.11b-c and Appendix F), however, non-ferroan calcite was also identified in few samples (Fig. 4.11c). The carbonate cements are patchily distributed and primarily occur as blocky, poikilotopic and pore-filling cements, and secondarily, as grain replacements of unstable grains (mostly feldspars). As determined by point counting, total carbonate cement volume varies from 0 to 21% with an average of 3.2%. The highest volume of carbonate cement (>10%) within the channel sandstones is generally found at the base of the channel.

4.5.2.6 Fe-oxide and Ti-oxide cements

Fe-oxide cement occurs in low amounts (0-8.7%; avg. 1.1%) in all the samples investigated. It occurs as coatings around detrital grains and as dispersed patches of pore filling cement. Ti-oxides occur in trace amounts and as microcrystalline cements within the pores. They are often associated with pore filling clays in the studied samples. Based on SEM analysis, the Fe-oxide cement is interpreted to be hematite, while the Ti-oxide cement is interpreted to be rutile. The red colour of the sandstones in this study reflects the presence of hematite cement.

4.5.2.7 Porosity distribution

The porosity of the St Bees sandstones is dominated by primary intergranular porosity. Total thin section porosity ranges from 0 to 24% (avg. 11.4%). Primary porosity varies from 0 to 22% (avg. 9.5%) while secondary porosity varies from 0 to 4.7% (avg. 2%). The secondary pores are products of grain dissolution mainly feldspars (Fig. 4.11d). Average porosity at the sampled locations (location 1 to 5; Fig. 4.13b) varies from 8.9% to 12.7%. Location 1 to 3 have comparable average porosity, despite being about 2.1 km apart. Samples at locations 1 and 3 were taken across the cross-sections while samples at location 2 were taken along the longitudinal section of the outcrop. Generally, the channel and sheet-like sandstones stand out as having high porosity (up to 24%), while the floodplain facies (i.e., the red mudstones) have very low porosity (<2%), therefore constituting poor or non-reservoirs. It is worth noting that porosity distribution in the channel sandstone bodies is not uniform. Higher porosity is generally associated with the channel centre while the top and base of the channels have lower porosity. Figures 4.14b, 4.15b, 4.16c-e and 4.18a-f show the porosity distribution within the channel sandstone bodies.

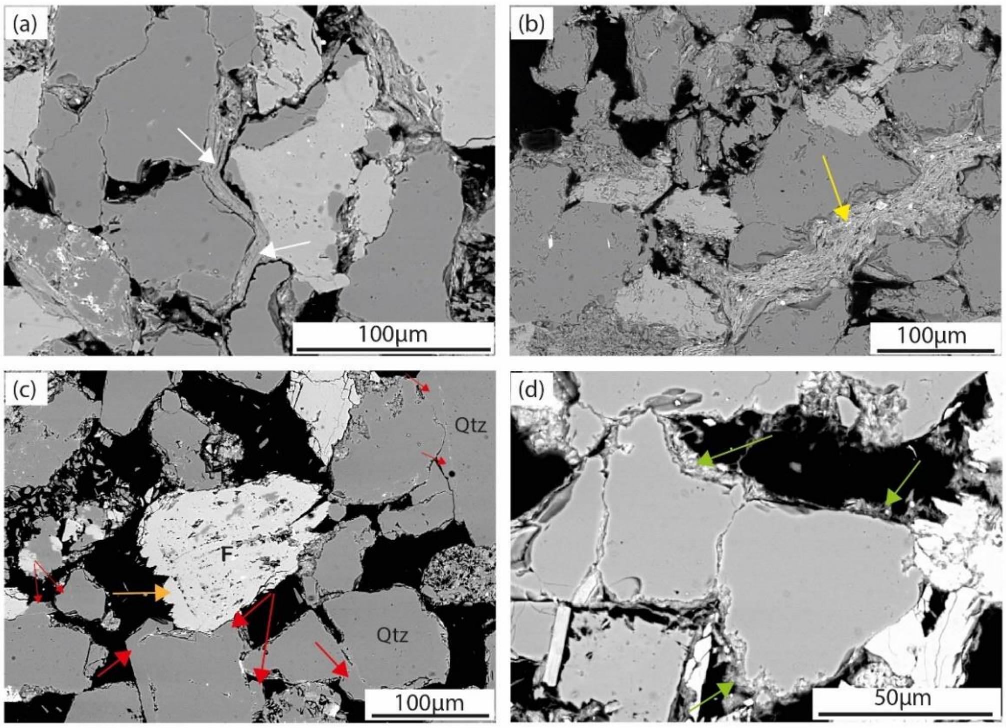

Figure 4.10: BSE images showing (a) mechanical compaction, evidenced by bending of mica grain (white arrow), point and long (or tangential) grain contacts (Sample SC6, Saltom Bay); (b) pseudoplastic deformation of mudclast (yellow arrow) in sample SC7 at Saltom Bay; (c) quartz (red arrows) and K-feldspar (orange arrow) overgrowths (Sample SC8, Saltom Bay) and (d) authigenic illite coats (green arrows) on detrital quartz grains (Sample SC6, Saltom Bay).

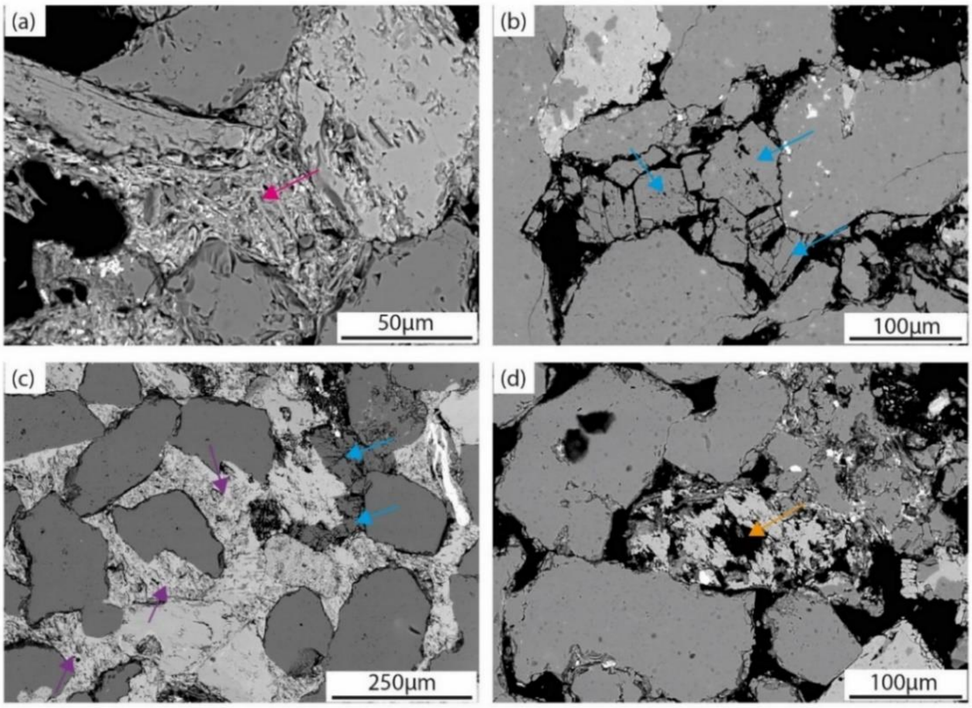

Figure 4.11: BSE images of (a) sample SC7 (Saltom Bay) showing pore-filling illitic clay (pink arrow); (b) sample A2 (Fleswick Bay) showing pore-filling non-ferroan dolomite cement (blue arrows); (c) sample E7 (Fleswick Bay) showing pore filling non-ferroan calcite (purple arrows) and non-ferroan dolomite cement (blue arrows); and (d) sample A2X (Fleswick Bay) showing the development of secondary porosity due to feldspar grain dissolution (orange arrow).

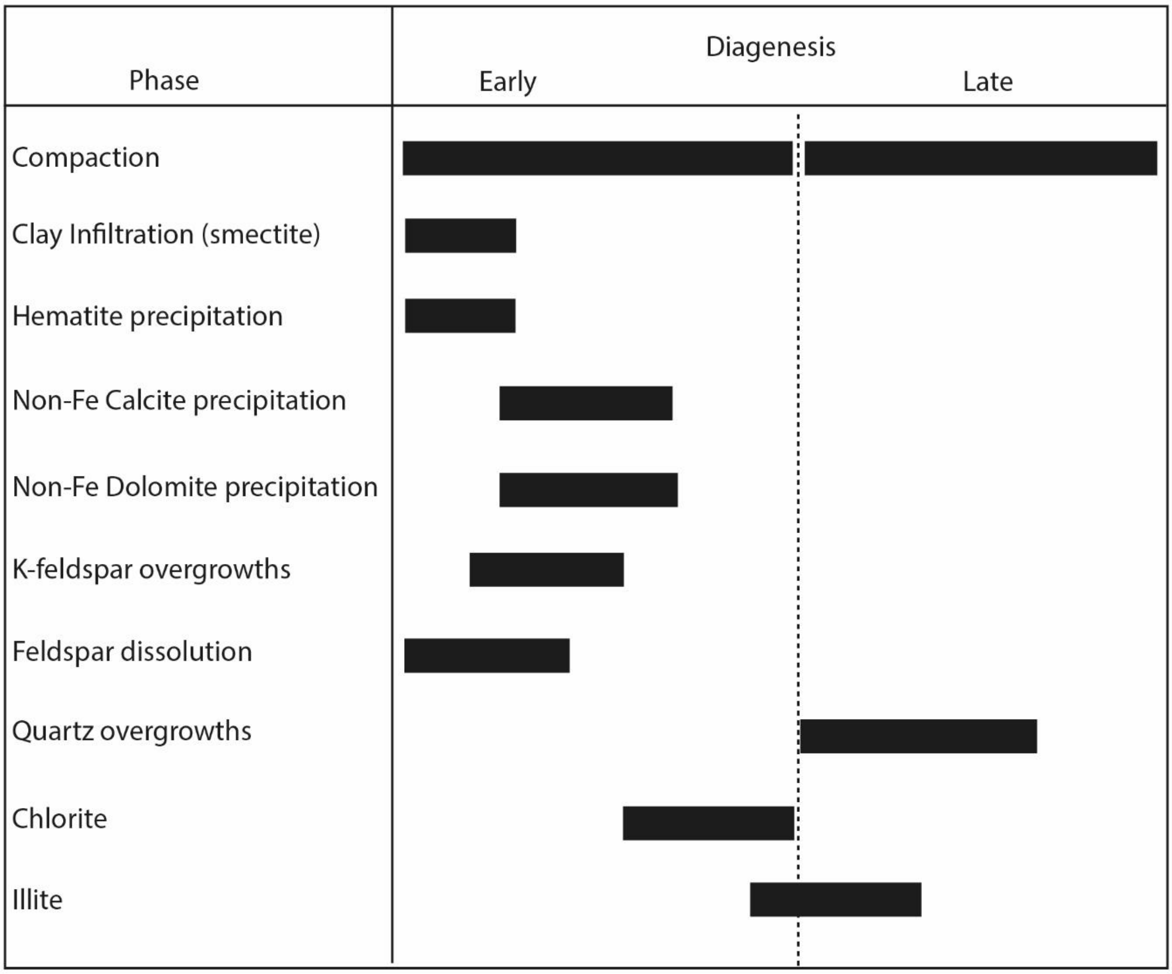

Figure 4.12: Schematic diagram of the sequence of diagenetic events in the St Bees Sandstone Formation at West Cumbria.

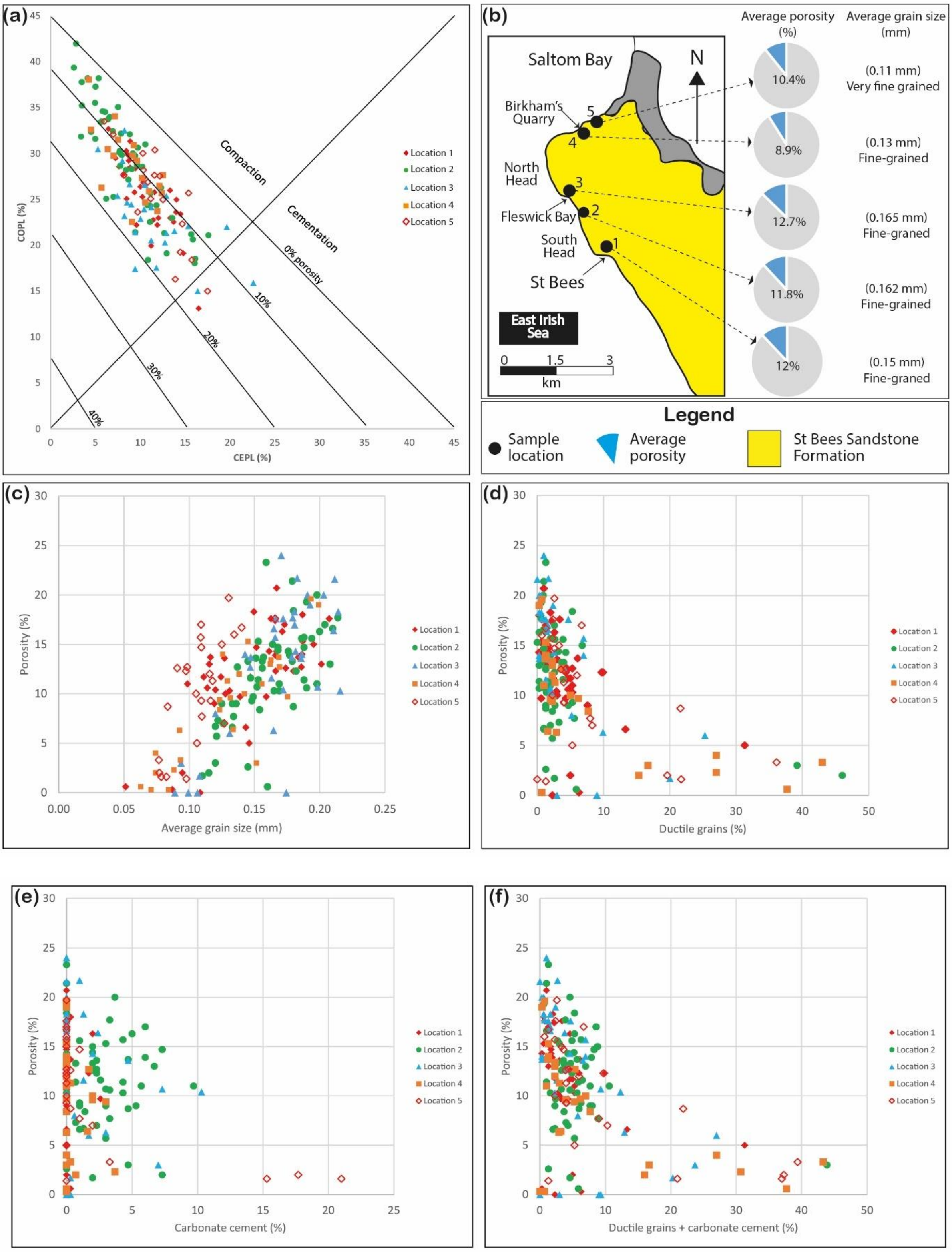

(a)
COPL (%)
CEPL (%)
Compaction
Cementation
0% porosity
10%
20%
30%
40%
Location 1
Location 2
Location 3
Location 4
Location 5
(b)
Average porosity (%)
Average grain size (mm)
Saltom Bay
N
Birkham's Quarry
North Head
Fleswick Bay
South Head
St Bees
East Irish Sea
0 1.5 3
km
10.4%
8.9%
12.7%
11.8%
12%
(0.11 mm) Very fine grained
(0.13 mm) Fine-grained
(0.165 mm) Fine-graned
(0.162 mm) Fine-grained
(0.15 mm) Fine-graned
Legend
Sample location
Average porosity
St Bees Sandstone Formation
(c)
Porosity (%)
Average grain size (mm)
(d)
Ductile grains (%)
(e)
Carbonate cement (%)
(f)
Ductile grains + carbonate cement (%)

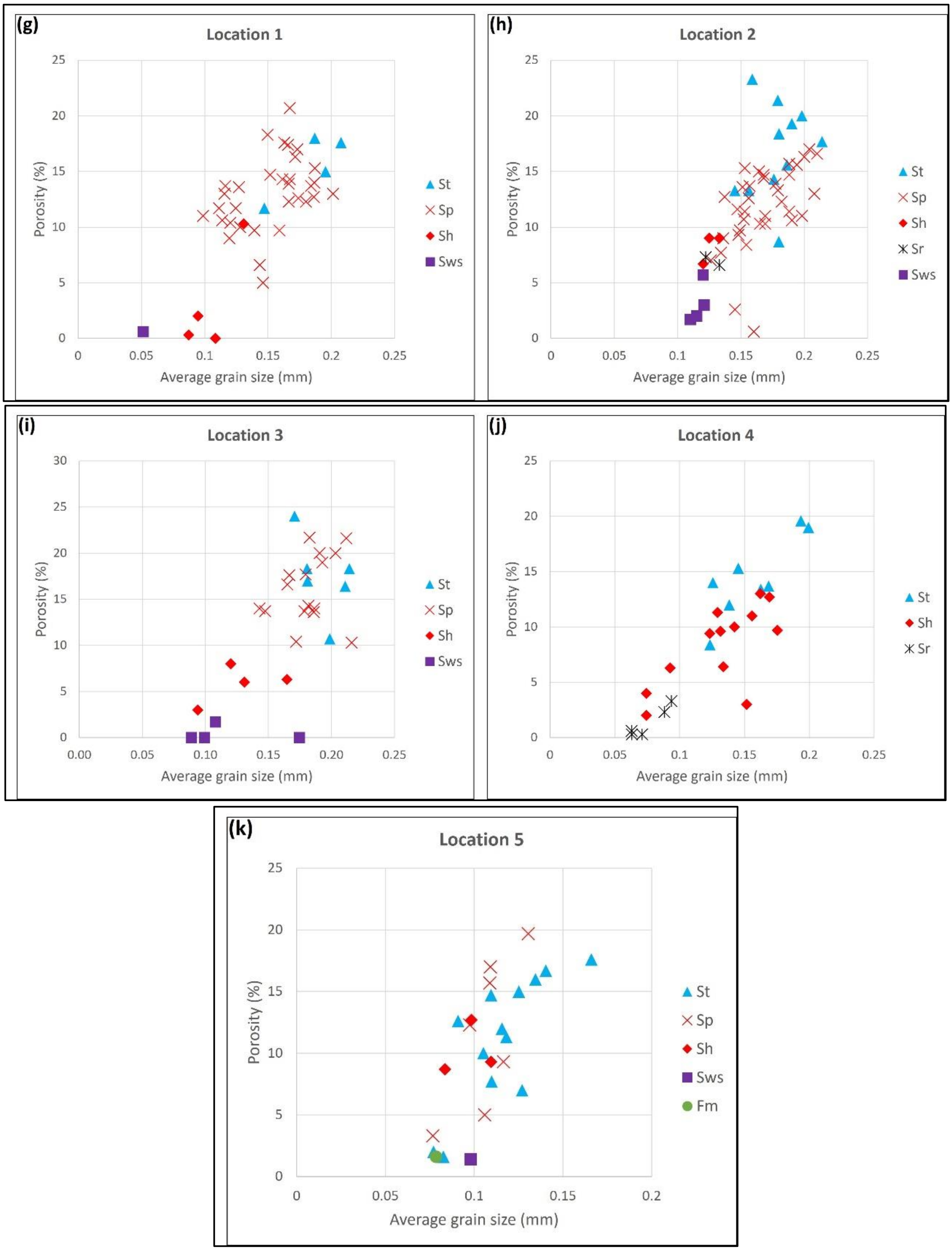

Figure 4.13: (a) Cross plot of compactional porosity loss (COPL) versus cementational porosity loss (CEPL). The plot shows that porosity loss in the sandstones is mainly driven by compaction. (b) Average porosity distribution from location 1 to 5 (total distance is about 7 km). (c) Cross plot of porosity and average grain size showing that porosity increases with increasing grain size. (d) Cross plot of porosity and ductile grains. Increase in ductile grain content leads to a decrease in porosity. (e) Cross plot of porosity and carbonate cement. (f) Cross plot of porosity against ductile grains and carbonate cement. (g-k) Cross plots of porosity and average grain size by sedimentary structures (Location 1: South Head; Location 2: Fleswick Bay longitudinal profile; Location 3: Fleswick Bay cross section; Location 4: Birkham's quarry; Location 5: Saltom Bay; St: Red sandstone with trough cross beddings; Sp: Red sandstone with planar cross beddings; Sh: Red sandstone with horizontal laminations; Sr: Red sandstone with ripple marks; Sws: Whitish silty sandstone with fine laminations; Fm: mudstone with horizontal laminations).


(a)
0.5 m

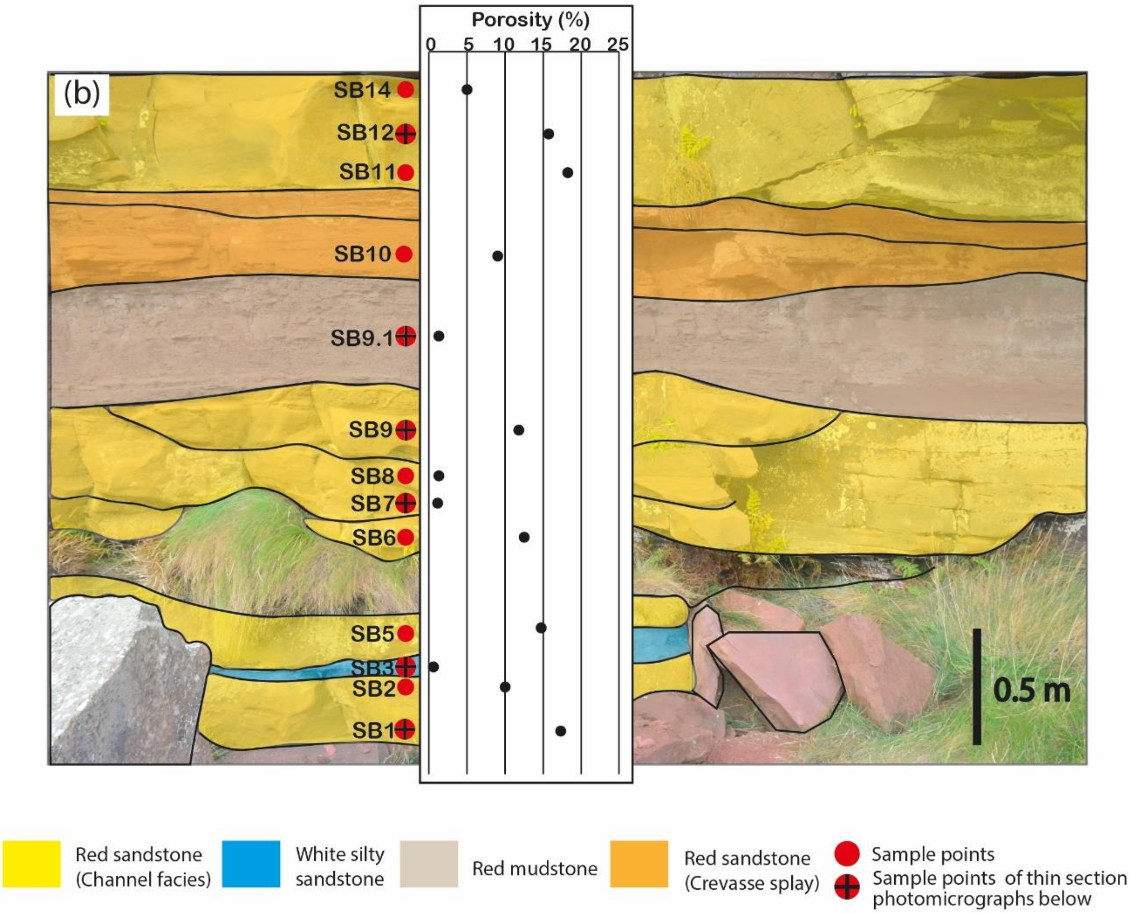
Porosity (%)
0
5
10
15
20
25
(b)
SB14
SB12
SB11
SB10
SB9.1
SB9
SB8
SB7
SB6
SB5
SB3
SB2
SB1
0.5 m
Red sandstone (Channel facies)
White silty sandstone
Red mudstone
Red sandstone (Crevasse splay)
Sample points
Sample points of thin section photomicrographs below

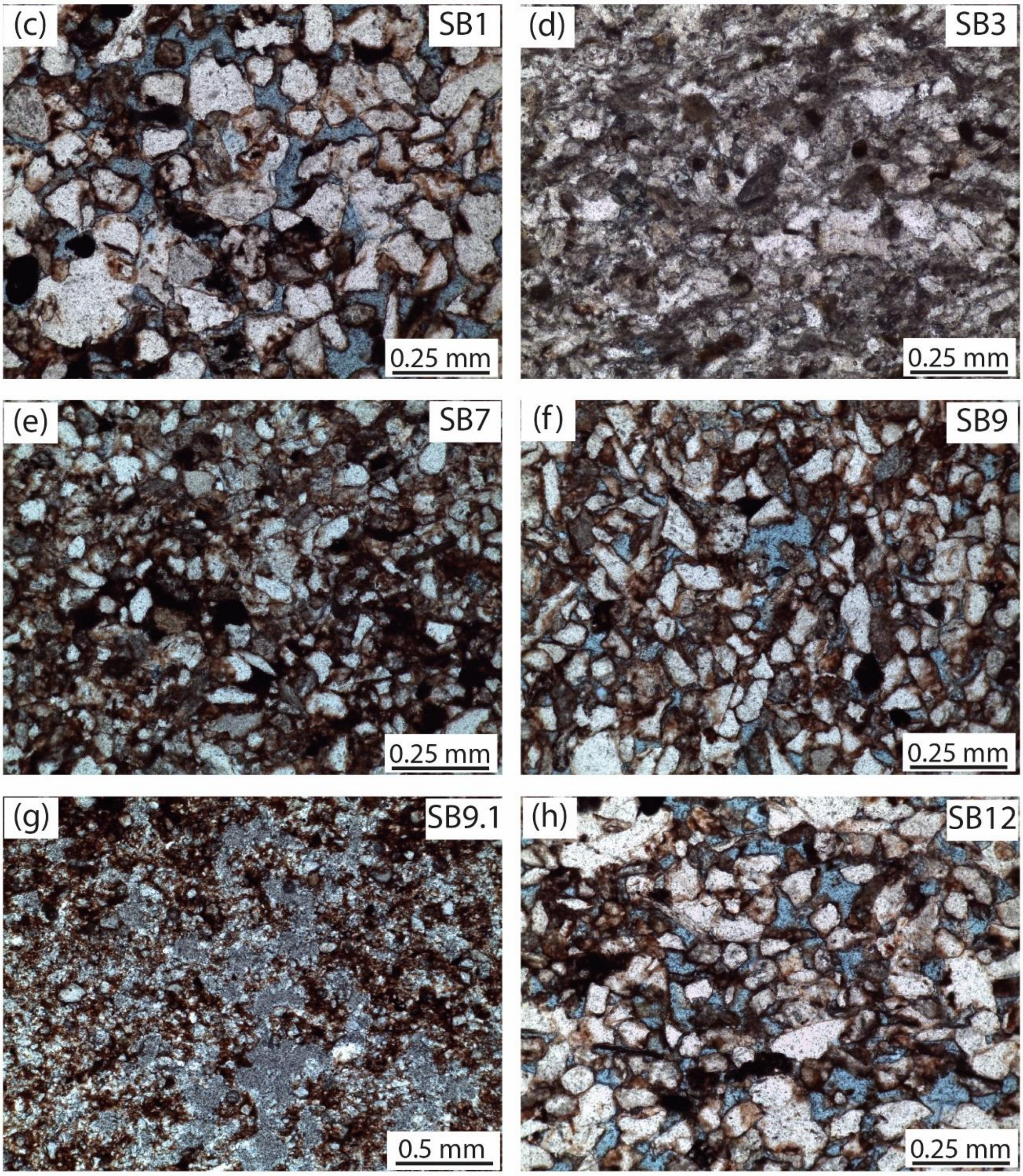

*Figure 4.14: (**a**) Outcrop photo of channel sandstones interbedded with mudstone and sheetflood (crevasse splay) sandstones at Saltom Bay. (b) Porosity curve superimposed on the outcrop photo in figure 4.14a showing the vertical variation in porosity and the sampled points. (c-h) Photomicrographs of samples SB1, SB3, SB7, SB9, SB9.1, and SB12.*


(a)
1 m

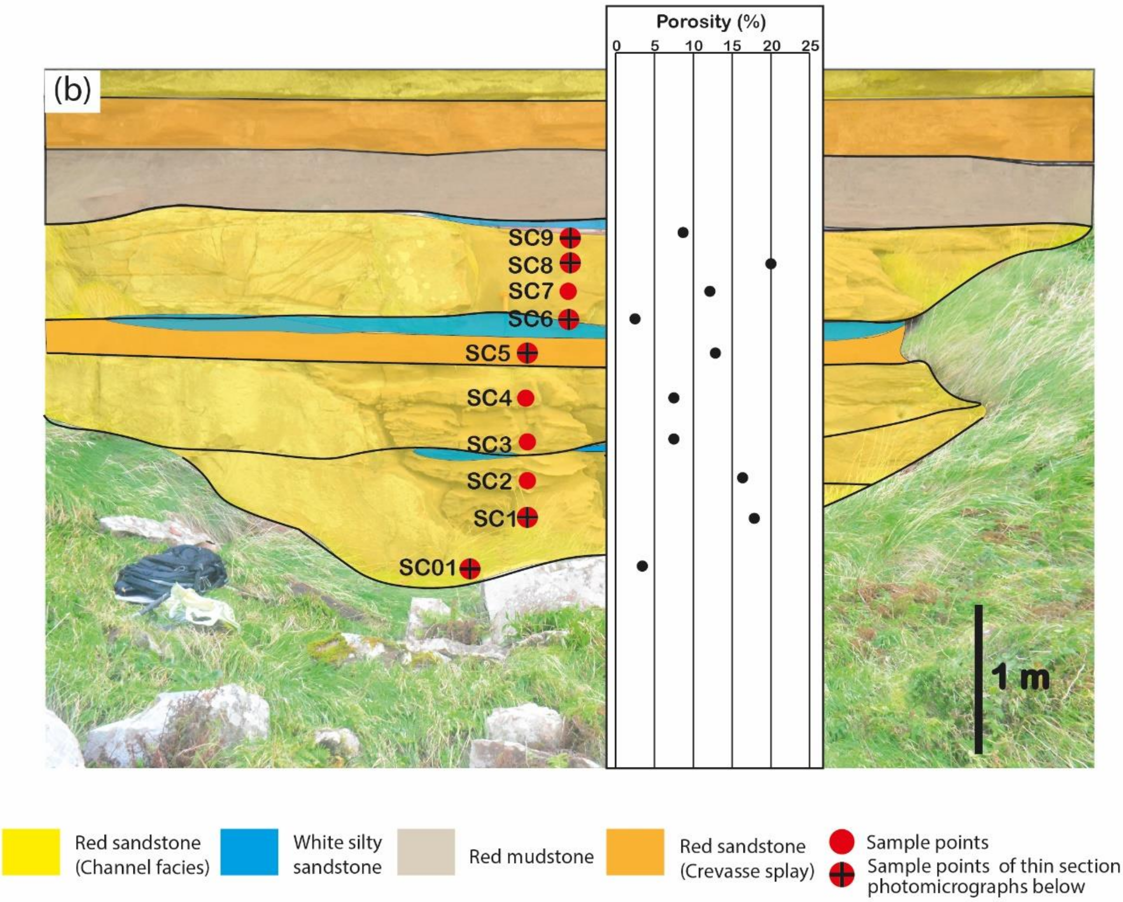
(b)
Porosity (%)
0
5
10
15
20
25
SC9
SC8
SC7
SC6
SC5
SC4
SC3
SC2
SC1
SC01
1 m
Red sandstone (Channel facies)
White silty sandstone
Red mudstone
Red sandstone (Crevasse splay)
Sample points
Sample points of thin section photomicrographs below

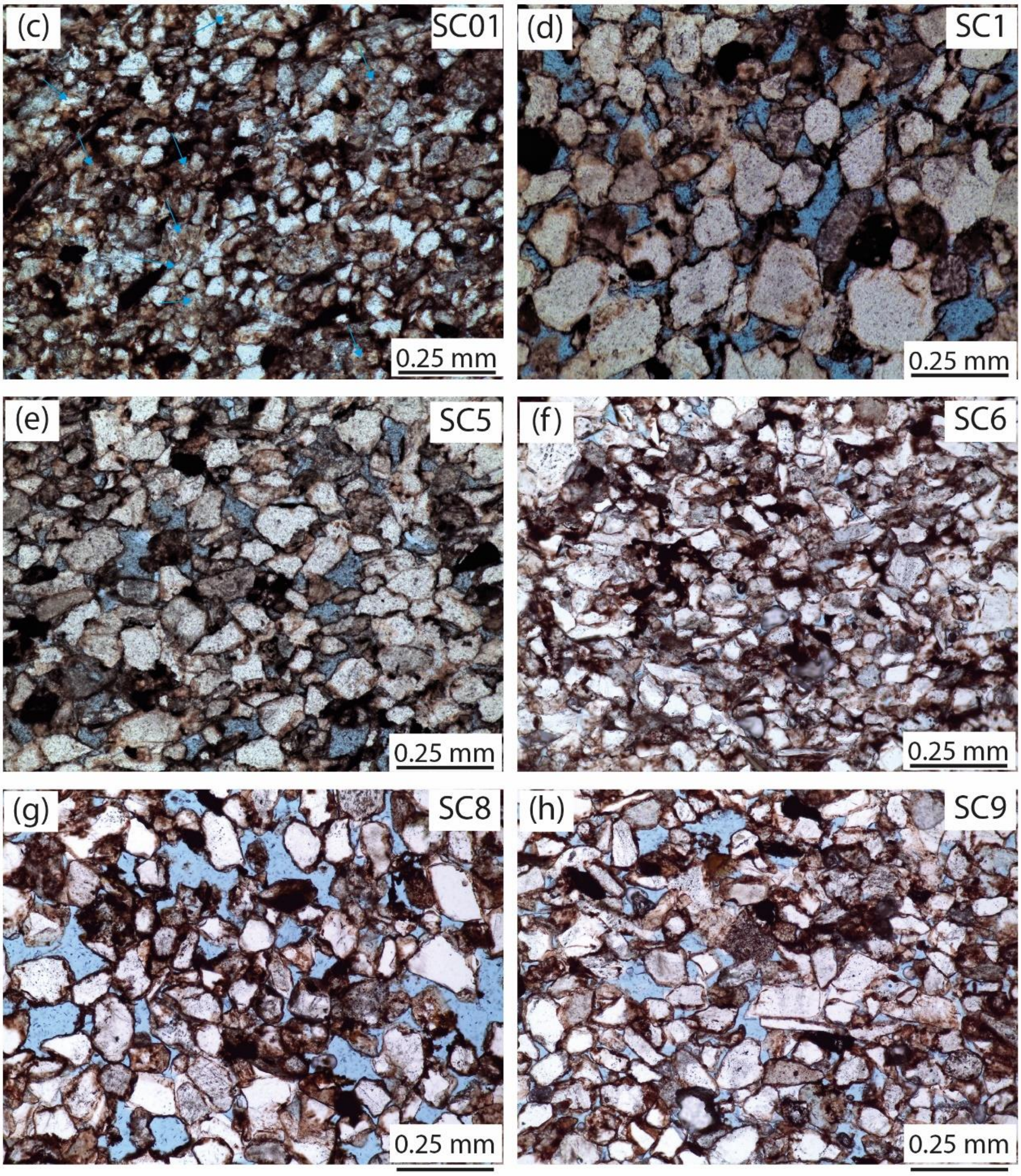

Figure 4.15: (a) Outcrop photo of another channel sandstones (to the right of figure 4.14) at Saltom Bay. The red mudstone here is correlatable to the one in figure 4.14; (b) Porosity curve superimposed on the outcrop photo in figure 4.15a showing the vertical variation in porosity and the sampled points. (c-h) Photomicrographs of samples from different parts of the channel: SC01 (channel base; the blue arrows point to carbonate cement), SC1 (channel centre), SC5, SC6 (channel base), SC8 (channel centre) and SC9 (channel top).

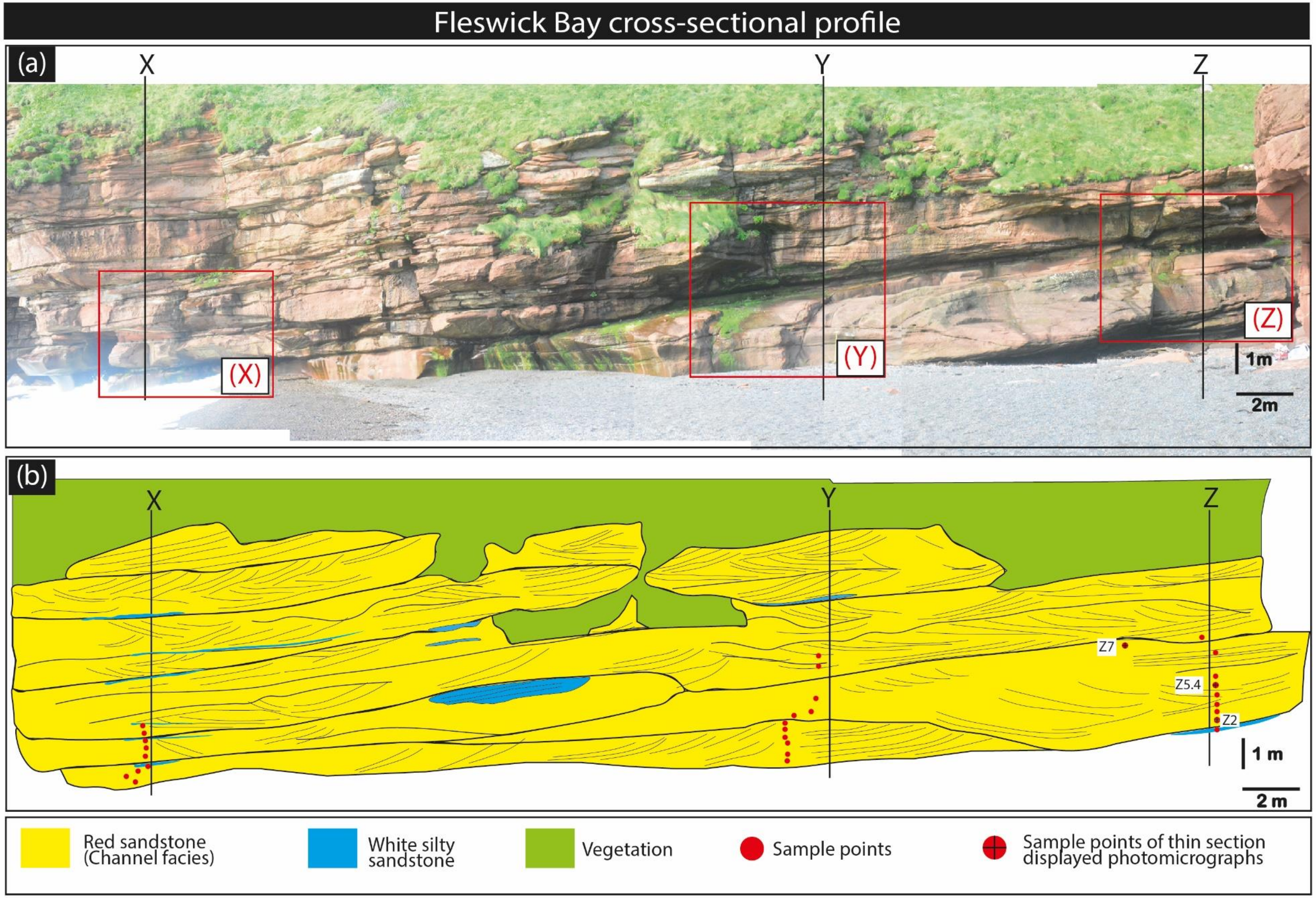
Fleswick Bay cross-sectional profile
(a)
X
Y
Z
(X)
(Y)
(Z)
1m
2m
(b)
X
Y
Z
Z7
Z5.4
Z2
1 m
2 m
Red sandstone
(Channel facies)
White silty
sandstone
Vegetation
Sample points
Sample points of thin section
displayed photomicrographs

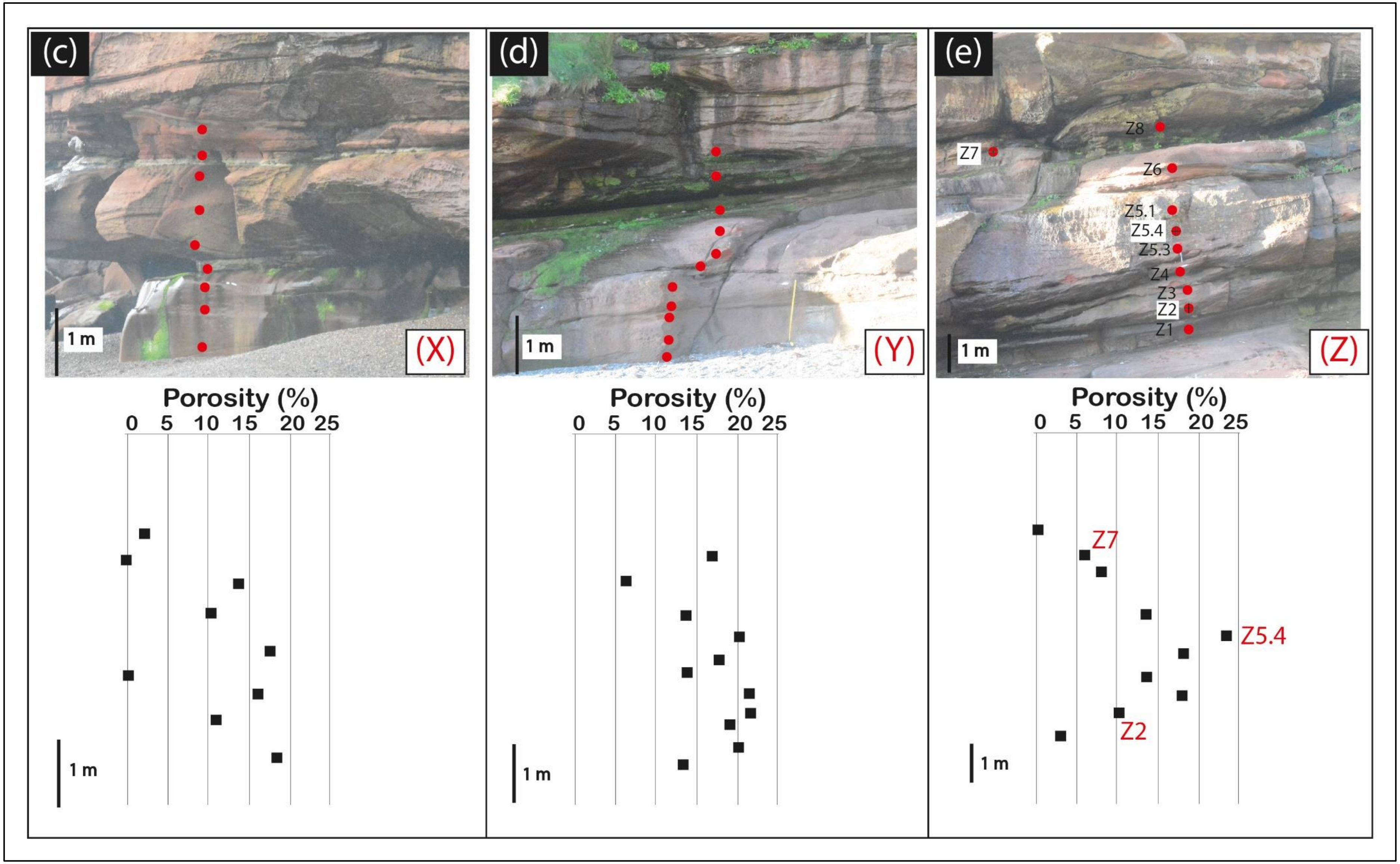
(c)
1 m
(X)
Porosity (%)
0 5 10 15 20 25
1 m
(d)
1 m
(Y)
Porosity (%)
0 5 10 15 20 25
1 m
(e)
Z8
Z7
Z6
Z5.1
Z5.4
Z5.3
Z4
Z3
Z2
Z1
1 m
(Z)
Porosity (%)
0 5 10 15 20 25
Z7
Z5.4
Z2
1 m

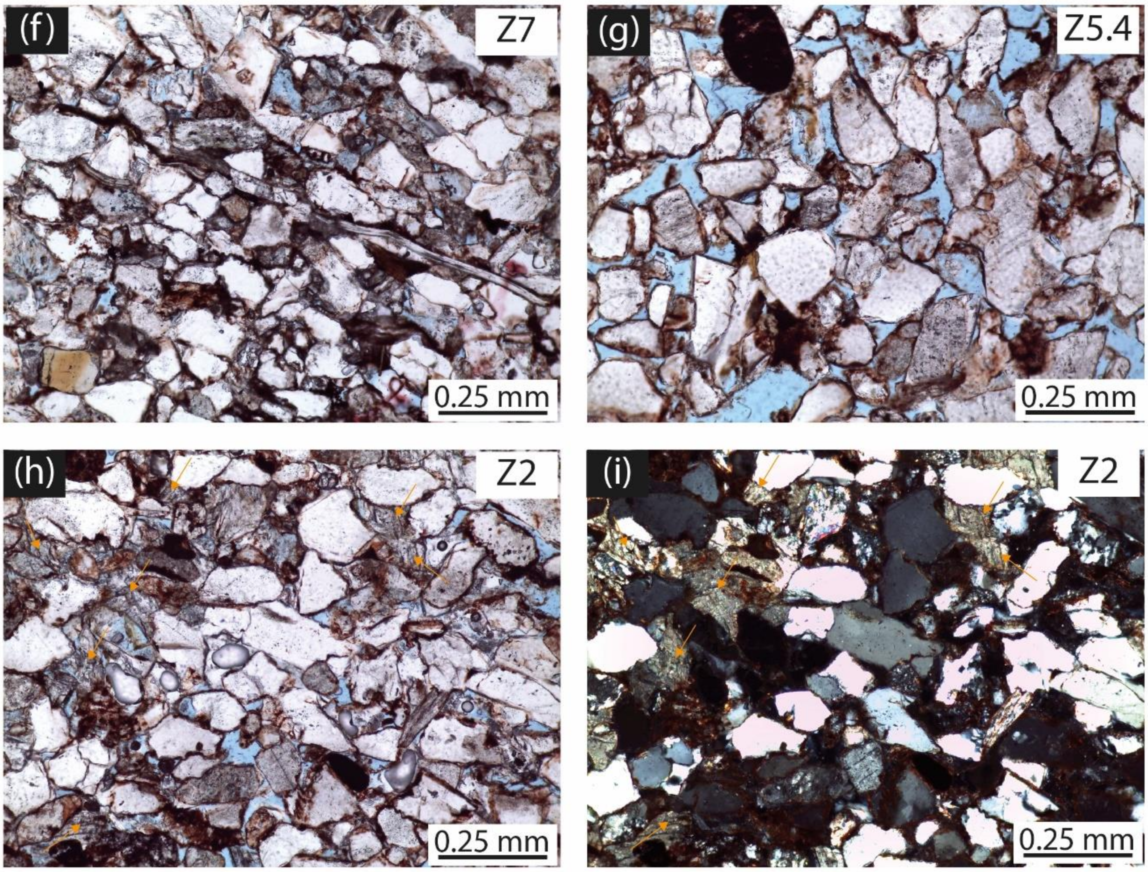

Figure 4.16: (a) Cross-sectional view (profile X-X' in fig. 4.2) of the laterally and vertically stacked channel sandstones at Fleswick Bay. Sampled sections in red boxes. (b) Digitized version of figure 4.16a showing the interpreted architecture and lithologies. (c-e) Zoomed-in versions of the sampled sections in red boxes in figure 4.16a and the corresponding porosity curves. The porosity curves show that there are vertical and lateral variations in porosity within the channel bodies. (f-i) Photomicrographs of samples Z7 (channel top), Z5.4 (channel centre), and Z2 (channel base) in figure 4.16b and e. The orange arrows in figure 4.16h-i point to the carbonate cement within the sample (channel base).

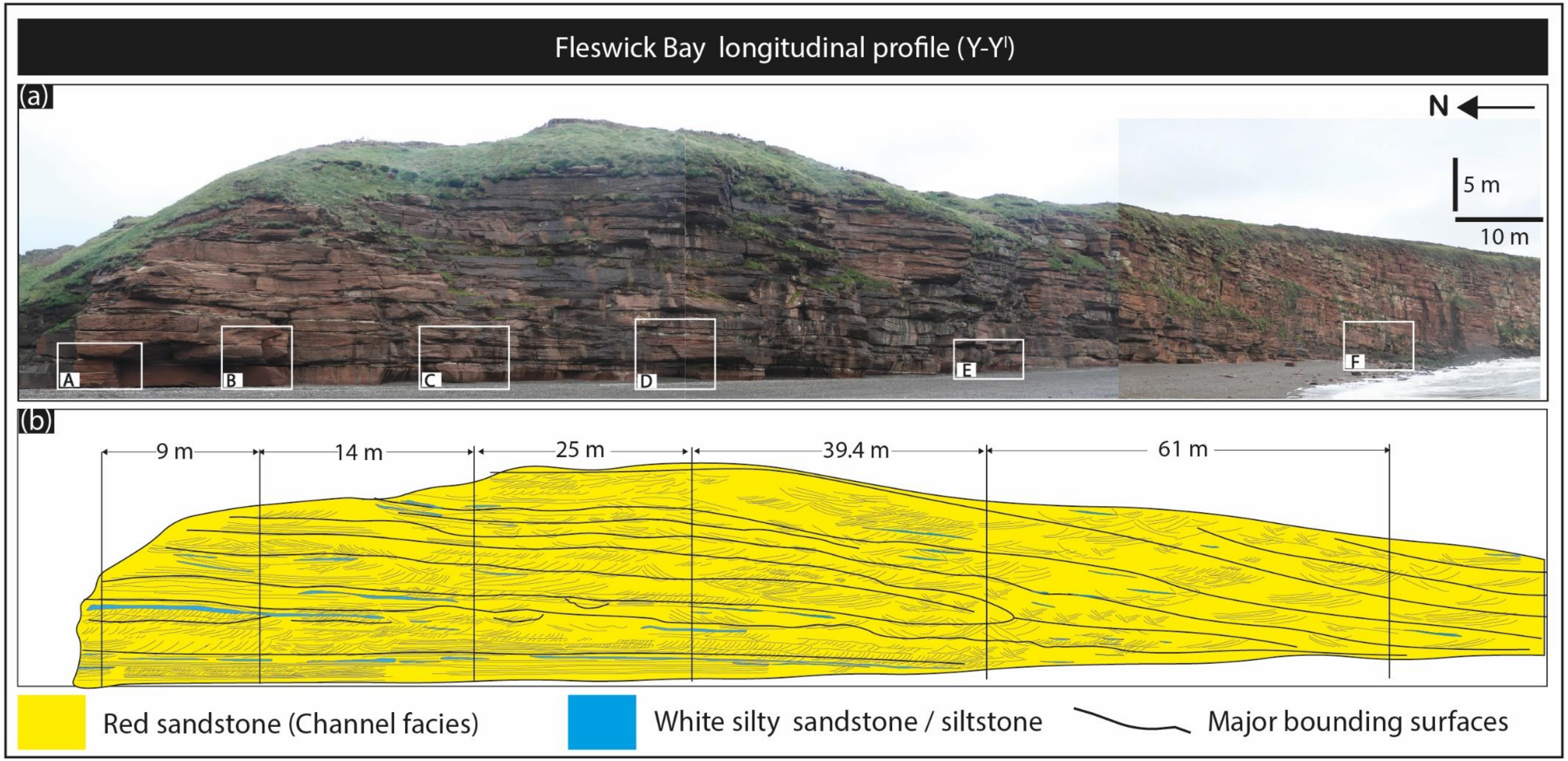

Figure 4.17: (a) A montaged outcrop photo of the longitudinal section (profile Y-Y': fig. 4.2) of the laterally and vertically stacked, multistorey channel sandstones at Fleswick Bay. Sampled sections are depicted by the white boxes; (b) Digitized version of figure 4.17a showing the interpreted architecture and lithologies. The white silty sandstones/siltstone are laterally restricted and therefore represent potential baffles within the stacked channel bodies.

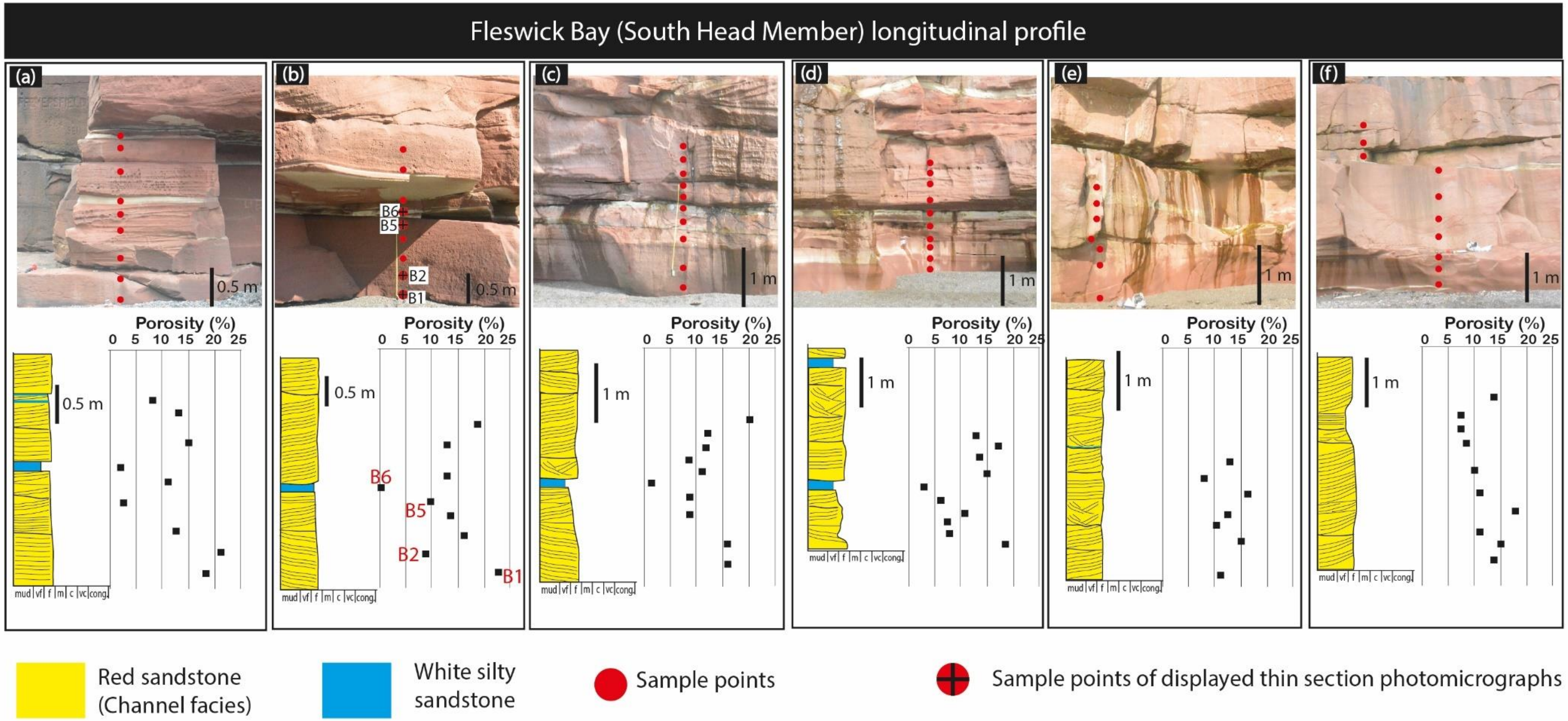

Fleswick Bay (South Head Member) longitudinal profile
(a)
(b)
(c)
(d)
(e)
(f)
0.5 m
1 m
B6
B5
B2
B1
Porosity (%)
0 5 10 15 20 25
mud vf f m c vc cong.
Red sandstone (Channel facies)
White silty sandstone
Sample points
Sample points of displayed thin section photomicrographs

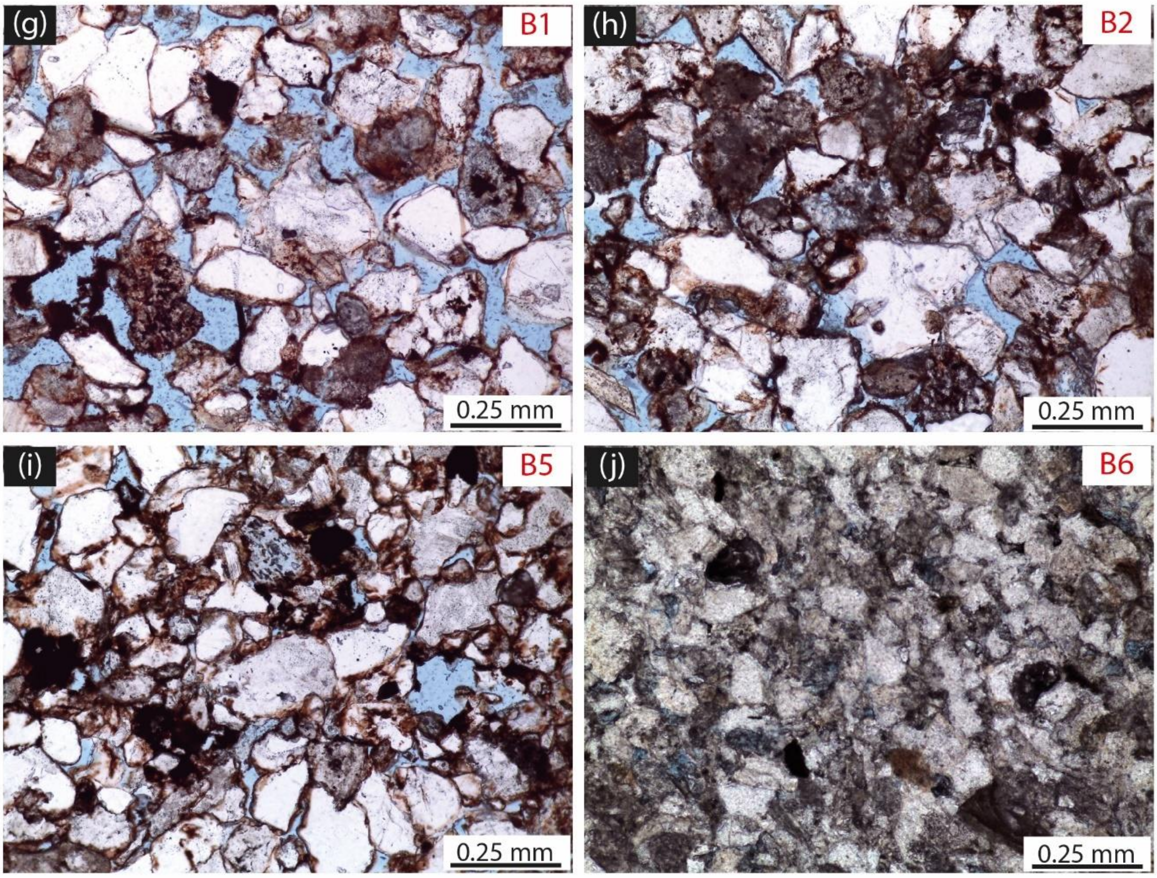

Figure 4.18: (a-f) Zoomed-in versions of the sampled sections of the outcrop shown in white boxes in figure 4.17a and the corresponding sedimentary logs and porosity curves. The porosity curves show that there are vertical and lateral variations in porosity within and along the channel bodies. (g-j) Photomicrographs of samples B1, B2, B5 and B6 in figure 4.18b.

4.6 Discussion

4.6.1 Environment of deposition

Field observations, facies and petrographic analysis all suggest that the St Bees Sandstone Formation (SBSF) was deposited by a low-sinuosity, braided fluvial channel system in a semi-arid environment. The SBSF is mainly characterized by highly interconnected, high net-to-gross, laterally and vertically stacked channels, with high width-to-thickness (W/T) ratios. In addition, there is general scarcity of channel abandonment fines and floodplain deposits within the multi-stacked channel sequences (see Figs. 4.4, 4.6a, 4.16b and 4.17). These characteristics are typical of depositions in braided fluvial channel systems (Jones and Ambrose 1994; Medici et al. 2015). The presence of sedimentary structures such as trough cross-bedding, upper flow regime horizontal laminations, ripple-marked surfaces, and the subtle fining upward grain size, with the presence of calcrete/dolocrete intraclasts all suggest that the SBSF was deposited in a fluvial environment under semi-arid climatic conditions (Schmid et al., 2006). A schematic block diagram illustrating the depositional environments and channel stacking geometry for the SBSF in the Sherwood Sandstone Group is shown in figure 4.19.

4.6.2 Paragenetic sequence

The relative timing of the diagenetic processes that have modified the porosity of the investigated St Bees sandstones, based on petrographic observations, is presented in figure 4.12. The sequence of events is comparable to what has been interpreted in the earlier studies of the Sherwood Sandstone Group diagenesis (Schmid et al. 2004). The diagenetic processes are divided into early and late diagenesis and are discussed in detail below.

Early diagenesis - encompasses all processes that occur at or close to the sediment surface, where the chemistry of the pore waters is controlled largely by the depositional environment (Worden and Morad 2003). Infiltration of detrital clays (smectite) occur after deposition and were deposited mostly as coatings on detrital grain surfaces. Partial dissolution of feldspar and rock fragments also occur during this stage. However, the secondary porosity generated is relatively minor and does not contribute significantly to the overall porosity. Based on textural relationships between detrital framework grains and authigenic minerals, one of the earliest authigenic minerals to be precipitated was hematite. This is indicated by the occurrence of hematite coatings (red stains) around detrital grains beneath quartz overgrowths (Fig. 4.9a & b). Sandstones formed in hot, arid or semi-arid environments such as the SBSF, are typically characterised by early precipitation of hematite, an authigenic cement commonly believed to form from the oxidation of ferrous iron released by dissolution of unstable ferromagnesian minerals during early burial (Walker et al. 1978; Burley et al. 1985; Morad et al. 1995; Chan et al. 2005; Aretz et al. 2016; Oluwadebi et al. 2018; Al-Juboury et al. 2020). Non-ferroan dolomite and partly non-ferroan calcite are the main carbonate cements in the studied sandstones. They are patchily distributed and occur mainly as pore-filling cement (Fig. 4.9c-f, 4.11b-c). Their textural relationships with quartz cement and detrital grains indicate an early precipitation. For example, in figures 4.9e and 4.11c, carbonate cements fully enclose the detrital grains and are in direct contact with them, suggesting that the precipitation of carbonate cements preceded quartz cementation. Early diagenetic carbonate cements comparable to those in this study have been reported in some of the sandstones of the Triassic SSG in the EISB by various authors (Burley 1984; Strong and Pearce 1995; Greenwood and Habesch 1997). Greenwood and Habesch (1997) identified and described three phases of calcite (calcite I, II, and III). Calcite I is interpreted as an early diagenetic phase due to its micronodular form and caliche fabrics. Calcite II is a burial phase and calcite III is a late inversion phase. Calcite I cement has been described as carbonate spheroids by Strong and Pearce (1995), who also presumed they were early diagenetic and possibly biologically generated or reworked caliche. Non-ferroan dolomite nodules, interpreted as incipient caliche precipitates have also been described by Burley (1984). These were found at the tops of the fluvial units in the Triassic sequence of the SSG. In this study, the carbonate cement shown in figure 4.9c forms groups of coalesced crystals, which are comparable to the spheroids and calcite I of caliche origin, previously described by these authors. The absence of iron in the calcite and dolomite cement as revealed by SEM-EDX is suggestive of precipitation in an O_2-rich water (Schmid et al. 2004; Oluwadebi et al. 2018).

Late (Burial) diagenesis - includes to all physical, chemical, and biological processes that act upon a sediment during burial away from the influence of depositional environment and surface waters (Schmid et al. 2004). Late diagenetic minerals in the studied St Bees sandstones include illite, chlorite and quartz. Based on SEM-EDX observations, the diagenetic (or authigenic) illite and chlorite clays occur primarily as grain coats and are oftentimes partially engulfed by quartz overgrowths, indicating that the latter postdates authigenic illite and chlorite clay coats (Fig. 4.9b). Numerous studies have suggested that authigenic clays could be formed in several ways (Chang et al. 1986; Bloch et al. 2002; Storvoll et al. 2002; Worden and Morad 2003; Ajdukiewicz and Larese 2012; Dowey et al. 2012; Haile et al. 2015; Charlaftis et al. 2021). These include the alteration of unstable silicate minerals (e.g., feldspars), dissolution of Fe-and Mg-rich detrital grains and volcanic fragments, and pseudomorphic transformation of detrital or precursor diagenetic clays (e.g., smectite, kaolinite, berthierine and odinite). The authigenic clays in the studied St Bees sandstones are believed to have formed from the recrystallization of smectitic detrital clays, emplaced by mechanical infiltration immediately after deposition. Smectite formation is a common occurrence in arid or semiarid environments (Worden and Morad 2003). Based on SEM-EDX analysis, the clay coats are a mixture of illite and chlorite (Appendix F) . They are irregular and anisopachous and generally show features typical of mechanically infiltrated clays (Matlack et al. 1989; Moraes and De Ros 1990). These evidence support the assumption that the authigenic illite and chlorite coats in the studied St Bees sandstones were formed from the recrystallization of infiltrated smectite and predates the quartz cements.

4.6.3 Depositional and diagenetic controls on porosity of the St Bees Sandstone Formation (SBSF)

Understanding the controls on porosity and permeability (i.e., reservoir quality) in geological formations is essential for the success of any hydrocarbon exploration, aquifer development, and carbon capture and storage (CCS) projects. Porosity and permeability is a function of the combination of various interrelated depositional (grain size, sorting, detrital composition/clay matrix) and diagenetic (compaction, cementation, and dissolution) factors (Salem et al. 2000; Baiyegunhi et al. 2017; Worden et al. 2018a; Lawan et al. 2021). Depositional facies exert the greatest control on reservoir quality in the SBSF, with channel facies having the best reservoir quality and floodplain facies having poor reservoir quality. The focus of this study is, however, on channel facies, which is the dominant facies in the SBSF.

As revealed by petrographic data, the main controls on porosity of the investigated sandstones are the grain size and ductile grain content (mica and pseudomatrix). Average grain size of the sandstones varies from very fine to fine sand. Generally, sandstones with average grain size greater than 0.125 mm (fine-grained) have higher porosity while those with average grain size less than 0.125 mm (very fine-grained) have lower porosity (Fig. 4.13c). Also, sandstones with higher amounts of ductile grains (>10%) have lower porosity while those with lower amounts of ductile grains (<10%) have higher porosity (Fig. 4.13d). The finer-grained sandstones have higher amounts of ductile grains than their coarser-grained counterparts. The variations in grain size and amounts of ductile grains could be attributed to variations in depositional energy or hydrodynamic conditions at the time of deposition. The finer-grained, ductile-rich sandstones are interpreted as deposits of low energy or weak hydrodynamic conditions, while their coarser-grained counterparts with lower amounts of ductile grains are interpreted as deposits of high energy or strong hydrodynamic conditions (Li et al. 2017; Okunuwadje et al. 2020). It is worth noting that apart from the grain size and ductile grain content, sedimentary structures also have considerable impact on porosity. Sandstones with trough and planar cross beddings have higher porosity than those with parallel laminations, ripple marks and fine laminations (Fig. 4.13g-k). In general, the different grain size, ductile grain content and sedimentary structures are all facies-related (i.e., depositionally-controlled) and therefore constitute the major controls on the porosity of the SBSF.

Compaction and cementation are the main diagenetic factors controlling porosity loss in the channel sandstones of the SBSF. However, the plot of compactional porosity loss (COPL) against cementational porosity loss (CEPL) shows that compaction rather than cementation is the main driver of porosity loss in the sandstones after deposition (Fig. 4.13a). Numerous studies have shown that compaction (mechanical compaction in particular), results in the severe loss of porosity and permeability and is commonly enhanced by the presence of clay and ductile grains (Pittman and Larese 1991; Paxton et al. 2002; Makowitz and Milliken 2003; Morad et al. 2010; Bello et al. 2021; Lawan et al. 2021; Yan et al. 2022). In the studied sandstones, petrographic analysis shows evidence of compaction such as point, long and concavo-convex grain contacts (Fig. 4.9a-c), and deformation of ductile grains around rigid grains (Fig. 4.8f and 4.10a-b). The degree of compaction is generally higher in the very fine-grained sandstones (Fig. 4.8c) than the fine-grained sandstones (Fig. 4.8a); this is due to the greater amounts of ductile grains in the former. Apart from compaction, cementation played an important, but secondary role in the porosity evolution of the sandstones. The main authigenic cements are carbonate, quartz overgrowths, Fe-oxide (hematite), illite and chlorite. Of all the authigenic cements, carbonate cement has the greatest impact on the porosity of the sandstones. Carbonate cements, mostly non-ferroan dolomite, are patchily distributed and occur mainly as pore-filling cements. Their patchy distribution resulted in local reduction of porosity in some of the sandstones (Fig. 4.9c & d). A plot of porosity against carbonate cement shows that there is no clear relationship between the two parameters (see Fig. 4.13e). This is likely due to the patchy distribution of the carbonate cements in the analysed samples. However, a plot of porosity against the sum of carbonate cement and ductile grains shows an inverse relationship, indicating that these two jointly influence the porosity of the St Bees sandstones (Fig. 4.13f). Quartz is a major porosity reducing cement in deep sandstones (Worden and Morad 2000; Wells et al. 2015; Oye et al. 2018; Worden et al. 2018a; Worden et al. 2018b). However, the volume of quartz cement in the studied sandstones is generally low and has no major impact on the overall porosity. The low amounts of quartz cement in the sandstones is probably due to their shallow depth of burial before uplift or the widespread occurrence of grain-coating clays which inhibited quartz cement development (Bjørlykke and Egeberg 1993; Ajdukiewicz and Larese 2012; Hansen et al. 2017; Wooldridge et al. 2017a; Wooldridge et al. 2017b; Worden et al. 2020). The authigenic clays (i.e., illite, chlorite and Fe-oxide) occur primarily as grain-coating and pore-lining clays (Fig. 4.9a & 4.10d), rather than pore-filling cements, and therefore has minimal impact on the overall porosity.

4.6.4 Cross versus longitudinal (or reach length) sections of channels – implications for sand body modelling

Understanding the spatial distribution of porosity, permeability, depositional and diagenetic features/cements (i.e., heterogeneity) in the cross-sectional and longitudinal profiles of fluvial channel bodies is important for three-dimensional (3-D) modelling of reservoirs and aquifers. Currently, reservoir modellers are of the opinion that there is a huge petrographic difference between the cross-section and longitudinal profiles (also known as reach lengths) of channel sandstone bodies. However, a critical look at about 7 km long reach of an outcropping braided fluvial channel succession at St Bees Head reveals that there is no major difference between the cross-section (X-X^1) and longitudinal profiles (Y-Y^1) in terms of sedimentology, stacking patterns and petrography. Also, the sedimentology, stacking pattern and petrography of the channel sandstones along the 7 km longitudinal profile is uniform (see Figs. 4.17-4.19). The similarities between the cross-section and longitudinal profiles of the studied channel bodies are discussed below.

First, the sandstones in both profiles occur as laterally and vertically stacked channel bodies, with a general absence of mud and floodplain deposits. The general absence of mud deposits indicates strong connectivity between the channel bodies. One of the key factors governing the degree of connectivity of channel sandstone bodies is channel deposits proportion (CDP), also known as net-to-gross ratio. Channel belts are unconnected if CDP is less than 0.4 and connected if it is greater than 0.75 (Bridge and Mackey, 1993; Bridge 1993; Bridge and Tye, 2000; Allen 1978; Bridge, 2001). In the studied fluvial channel succession, the CDP is almost 100% in both the cross-section and longitudinal profiles (Fig. 4.16b and 4.17b). This indicates that in both profiles, there is potentially a high degree of vertical and lateral connectivity (in three dimensions) between the channel bodies, and the connectivity seems to be consistent along the longitudinal profile (for about 7 km).

Second, the sandstones in both profiles are compositionally the same; they are mainly arkosic (Fig. 4.7). Texturally, grain size distribution is also comparable. Average grain size in the cross-section profile is 0.165 mm (lower fine sand) and in the longitudinal profile, it is 0.162 mm (lower fine sand). In both profiles, a subtle variation in grain size is observed, and this in turn controls the porosity of the sandstone (Fig. 4.13h and i). In both profiles, although subtle, the channel sandstone bodies generally show fining-upward cycles. Each cycle begins with coarser-grained lithofacies St at the base, followed by lithofacies Sp and Sh in the middle and finally by very fine-grained lithofacies Sws at the top of the cycle. Facies Sws, as previously mentioned, occurs as white silty sandstones in the fluvial succession and are mainly characterised by finer grain size, high matrix/ductile grains and low to negligible porosity. In both profiles, they commonly occur at the top of the individual channel bodies, or as bar tops and are laterally restricted (< 10 m?) (Figs. 4.16-4.18). Their lateral restriction in the fluvial succession shows that they are baffles, and hence would not obstruct fluid (e.g., oil and gas) flow.

Third, the porosity distribution in both profiles is comparable (Figs. 4.13h-i). At Fleswick Bay, porosity varies from 0% to 24% (avg. 12.7%) in the cross-section profile, and from 0.6% to 23.3% (avg. 12%) in the longitudinal profile. The sweet spot (i.e., highest porosity) is generally found at the centre of the channel in both profiles. This is due to the lesser degree of compaction caused by lower amounts of matrix and ductile grains characterising this section of the channel (e.g., Figs. 4.15d, 4.15g and 4.16g). In contrast, the top and base of the channels have lower porosity due to the greater degree of compaction caused by higher amounts of clay matrix and ductile grains (Figs. 4.14e, 4.15f, 4.15h and 4.16f). It is also worth noting that, along the longitudinal profile, that is from log a-f (Figs. 4.17 and 4.18a-f), there is no drastic reduction in average porosity. Average porosity varies from 11.8% (Log A) to 12.3% (Log F)

As previously mentioned, carbonate cements are the most important authigenic cements in the St Bees Sandstone Formation. The distribution of carbonate cements in the cross-section and longitudinal profiles of the fluvial channel bodies is the same. They are patchily distributed, but essentially, are more abundant at the base of the channels (>10% by volume) in both profiles (e.g., Figure 4.16h and 4.19b). The preferential abundance of carbonate cement at the base of the studied channels is another reason for the lower porosity in this section of the channel. The abundance of carbonate cements at the base of fluvial channels has equally been reported in other studies (Taylor et al. 2000; Morad et al. 2010). In fluvial channel sandstones, carbonate cements form mostly from dissolution of carbonate intraclasts, derived from the erosion of floodplain pedogenic calcretes or cemented layers of vadose and phreatic calcrete and dolocrete deposits by avulsing rivers and episodic floods (Morad 1998; Morad et al. 2010). In braided fluvial deposits which develop in semi-arid settings, carbonate concretions mostly phreatic calcretes and dolocretes are very common. They are preferentially deposited as channel lags or at the base of mid-channel bars. Also, they occur as scattered concretions that might be elongated in the direction of regional groundwater flow (McBride et al. 1994; Mozley and Davis 1996; Cavazza et al. 2009; Henares et al. 2020). According to Henares et al (2020), the preferential occurrence of carbonate intraclasts at the basal part of channels and mid-channel bars in a braided river environment leads to extensively carbonate-cemented sandstone layers that may extend parallel to the flow direction for several metres to kilometres. In this study, the lateral continuity of carbonate cements at the base of the channel bodies in the longitudinal profile could not be ascertained due to the wide sampling spacing.

4.6.5 Implication for Reservoir modelling

The similarity in stacking pattern, mineralogy, texture, and distribution of diagenetic alterations of the studied channel sandstones in the cross-section and longitudinal profiles suggests that the channel sandstones in both profiles have the same style of sedimentation and provenance. In addition, the similarity in the grain size distribution along the reach length (about 7 km) also suggests that the depositional energy within the channel is uniform throughout that length. Generally, in the high net-to-gross, multi-stacked braided fluvial channel sequences at West Cumbria (e.g., Fleswick Bay), other than at the bounding surfaces, there is no major difference in the grain size, diagenetic alterations, cement types and overall porosity, whether you are looking at the cross-section or longitudinal profiles (Fig. 4.19). This implies that in braided fluvial reservoir models, reservoir parameters derived from the cross-sectional areas of channel bodies could also be used to model the longitudinal sections, depending on the preserved reach length of the sandstone bodies.

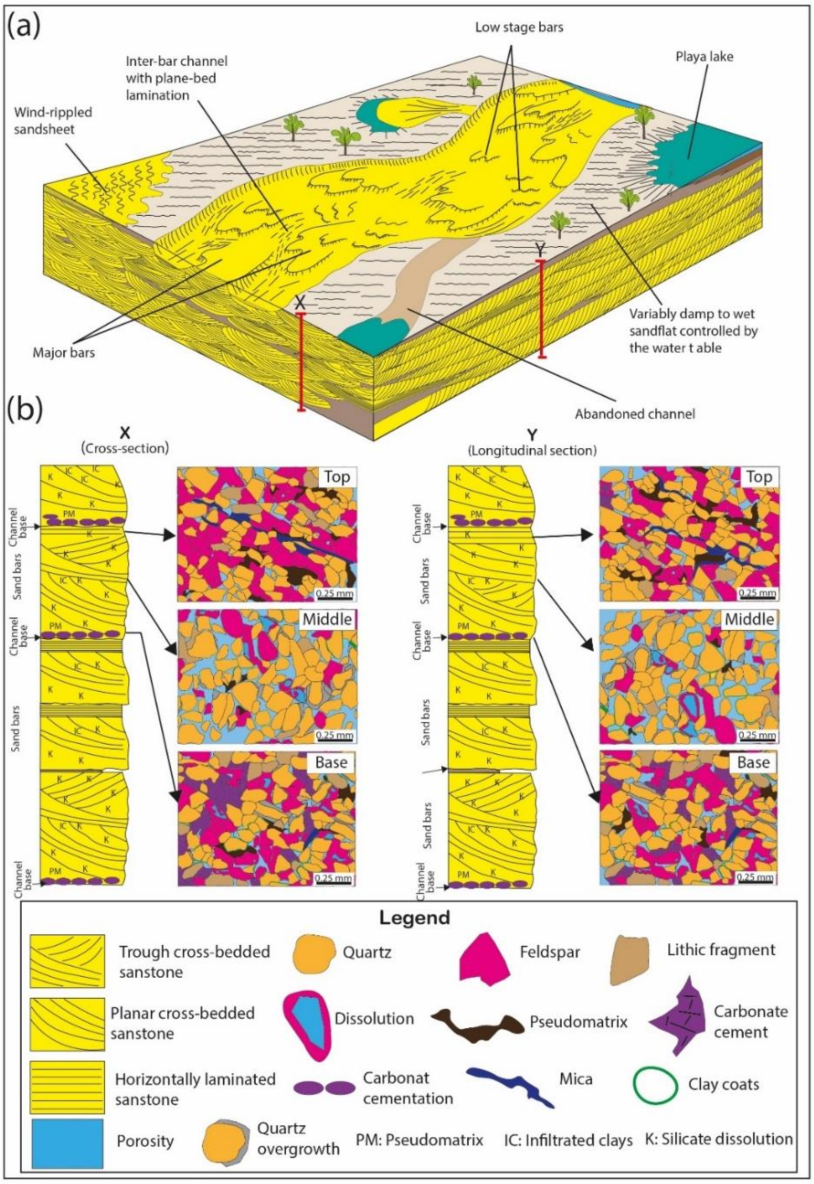

Figure 4.19: Schematic model showing (a) the depositional environments and channel stacking geometry in the Sherwood Sandstone Group (modified from Dancer et al., 2005) and (b) the petrography and distribution of diagenetic alterations in the channel sandstones in the cross-section and longitudinal section.

4.6.6 Implications for CO_2 storage

The Triassic is already one of the main targets for CCS development in the UK. A suitable site for CO_2 storage in subsurface formations must have sufficient porosity and permeability, and a good containment system (Rochelle et al. 2004; Raza et al. 2016; Ajayi et al. 2019; Alcalde et al. 2021). In this study, a detailed sedimentological and petrographic analysis of the Triassic SBSF, a major aquifer and hydrocarbon reservoir in the UK, has provided an insight into its suitability as a CO_2 storage site. Based on petrographic observations, the St Bees sandstones have good porosity (up to 24%), and potentially good permeability, thus, making them potential storage sites for CO_2. The high net to gross and amalgamation of the channel sandstone bodies indicate good vertical and lateral connectivity. However, the main heterogeneities within the stacked (or amalgamated) channel sandstones that dominate the SBSF are represented by (1) the white silty sandstones towards the top of individual channel bodies, (2) subtle variations in grain size, (3) bimodal grain-size and sorting distribution in the cross-bedded sandstones, and (4) carbonate cements within the fluvial channel sequences. The white silty sandstones are characterised by finer grain size, high matrix, and ductile grains and very low to negligible porosity. They are laterally restricted (< 10 m?) and thus, represent baffles, which would not pose significant hinderance to fluid flow (e.g., CO_2). The subtle changes in grain size between (or within) the channel sandstones and the bimodal grain-size and sorting distribution in the cross-bedded channel sandstone facies would result in porosity and permeability variations at the architectural and pore scale. Variations in vertical permeability is an important feature in braided fluvial deposits. High permeabilities in the coarsest sections can act as thief zones during fluid injection (Shepherd 2009). This means that during CO_2 injection, greater volume of CO_2 will be channelled through the high permeability zones, and consequently bypass the less permeable zones. In addition, the finer-grained laminae in cross-bedded sandstones (Fig. 4.8e) can act as small-scale local baffles for fluid migration perpendicular to the bedding, due to the high amount of silt/clay matrix associated with them (Henares et al. 2020).

Carbonate cements (predominantly non-ferroan dolomite) are preferentially concentrated at channel bases within the fluvial succession. The preferential and pervasive cementation of channel lags by carbonate cements can induce strong heterogeneity and constitute barriers to fluid flow (e.g., CO_2) in channel sandstone bodies (Morad et al. 2010; De Ros and Scherer 2012), particularly in laterally and vertically stacked channel sandstones. Although the early precipitation of pore-filling carbonate cements commonly results in the destruction of original porosity, it could also increase the pressure resistance of reservoir sandstones, prevents further mechanical compaction, and thus create a chance for subsequent dissolution (Morad 1998; Salem et al. 2000; Chi et al. 2003; Morad et al. 2010; Cui et al. 2017). Several experimental and field-based studies have shown that the injection of CO_2 into reservoir rocks will dissolve carbonate cements and create secondary pores which can increase the permeability (Worden and Smith 2004; Farquhar et al. 2015; Cao et al. 2016). In essence, the dissolution of carbonate cements by CO_2 in the St Bees sandstones will increase the storage capacity of injected CO_2 and enhance its flow in the reservoir or aquifer. In addition, the dissolved carbonate cements could be redistributed and reprecipitated within the pore spaces, and thus lead to the permanent trapping of the injected CO_2.

Furthermore, the presence of feldspars, clays, micas, and hematite in the St Bees sandstones has strong implications for the sequestration of CO_2. The carbonate ions ($CO3^{2-}$) derived from the dissolution of CO_2 in formation water will react with these minerals to precipitate secondary carbonate minerals and other clay minerals. For example, Na-rich plagioclase feldspar (albite) could react with the dissolved CO_2 in the formation water to precipitate a relatively uncommon carbonate mineral, dawsonite (Worden 2006; Gaus 2010; Yu et al. 2020). Likewise, K- feldspar in the presence of excess aqueous Na (i.e., saline solutions) and CO_2 will dissolve to precipitate dawsonite (Johnson et al. 2001; Rochelle et al. 2004; Yu et al. 2020). Chlorite has the capability of trapping CO_2 permanently in the form of siderite and dolomite where iron and magnesium are the donor cations (Gaus 2010). Fe-oxide cement, such as the hematite cement in the studied St Bees Formation sandstones is also capable of trapping CO_2 to precipitate siderite, provided a reducing agent (e.g., sulphur dioxide, SO_2) is co-injected with the CO_2 (Palandri and Kharaka 2005; Palandri et al. 2005; Garcia et al. 2012; Kampman et al. 2014). The aforementioned chemical reactions between CO_2 and mineral grains, known as mineral trapping, is an effective method of locking up CO_2 (in solid form) permanently in subsurface reservoirs and saline aquifers (Lu et al. 2011).

4.7 Conclusion

- Petrographic and sedimentological analysis of the Triassic fluvial outcrop at West Cumbria, NW England reveal that the St Bees Sandstone Formation was deposited in a braided fluvial environment under semi-arid climatic conditions and is dominated by laterally and vertically stacked sheet channel sandstones.
- Petrographic and outcrop/facies analysis reveal that the St Bees Sandstone Formation possess excellent reservoir quality, however they exhibit internal heterogeneities.
- The reservoir quality and heterogeneity of the channel sandstones are controlled by a combination of grain size, ductile grain content, carbonate cement and variable degrees of compaction. The sandstones are very fine- to fine-grained, with porosity ranging from 0 to 24%. The coarser-grained (i.e., fine-grained) sandstones have higher porosity (avg. 13.5%), whereas the finer-grained (i.e., very fine-grained) sandstones have lower porosity (avg. 6.5%). Within the channel bodies, the channel centre is the sweet spot, with the highest porosity (24%). This is due to the low compaction and lack or lesser

amounts of clay/ductile grains and carbonate cements characterising this section of the channel compared to the top and base.

- This study reveals that there is a close match between the cross-sectional area and longitudinal length (about 7 km long) of the investigated braided channel sandstone bodies, in terms of petrographic properties (e.g., grain size, porosity and mineralogy), and distribution of diagenetic features. This suggests that in braided fluvial reservoir models, reservoir parameters derived from the cross-sectional areas of channel bodies could also be used to model the longitudinal sections, depending on the preserved reach length and net-to- gross (NTG) of the fluvial system. High NTG in this study reveals little variability in the character of the sandstones.
- The heterogeneity associated with the braided channel sandstone bodies in this study indicates that the conventional approach to estimating hydrocarbon or injectable CO_2 volume from average petrophysical values is likely to result in an overestimation of hydrocarbon/injectable CO_2 volumes. To better estimate hydrocarbon volumes and CO_2 storage potential, small-scale petrographic variations/heterogeneities in channel bodies must be carefully integrated into 3-D fluvial reservoir models.
- The outcropping St Bees Sandstone Formation is as an analogue for the subsurface hydrocarbon-bearing fluvial reservoirs in the East Irish Sea Basin. The results of this study suggest that the sandstone is a potential CO_2 storage sites, due to its considerable thickness, high NTG, connectivity, and favourable porosity (up to 24%; avg. 11.4%) and mineralogy (detrital and authigenic).

Chapter 5: Facies and petrographic assessment of low net-to-gross fluvial reservoirs

5.1 Summary

Low net-to-gross fluvial reservoirs (or systems) are becoming increasingly important prospects in many matured oil and gas fields. Their significance for CO_2 storage is also gaining attention. Understanding the different facies and heterogeneity within and/or between different fluvial facies in low net-to-gross fluvial systems is therefore essential for maximizing production and ensuring safe storage operations. In this study, a combination of field-based and laboratory-based (petrographic) techniques is used to characterize the different facies within the low net-to-gross, Mid-Triassic Buntsandstein fluvial deposits at Riba de Santiuste, Central Iberian Basin, Spain. Three main facies associations were identified; these include channel, crevasse splay and floodplain facies. The channel facies occurs as single storey and multistorey ribbon-shaped sand bodies and constitutes the best reservoir in the fluvial succession. However, petrographic analysis reveals that a considerable heterogeneity occurs within the ribbon-shaped channel bodies. The highest porosity occurs in the centre of the channel, while the top, base, left wing and right-wing sections have lower porosity. The internal heterogeneity could be linked to the variations in clay/ductile grains content and degree of compaction/cementation within the channel bodies. The crevasse splay facies, on the other hand, occurs as sheet-like sandstone bodies, whilst the floodplain facies occurs as background sediments (mostly mudstones/siltstones) and encases the channel and crevasse splay facies. Both facies (crevasse splay and floodplain) have poor reservoir quality due to higher amounts of clay/ductile grains and carbonate cements, and therefore constitute baffles or barriers to fluid flow.

5.2 Introduction

Fluvial reservoirs commonly display a high degree of heterogeneity, internal geometries and complex architecture, making them particularly difficult to develop (Nguyen et al. 2013). Heterogeneity (i.e., lateral and vertical variations in porosity and permeability) in these reservoirs exists at various scales ranging from the laminae to the basin fill (Fig. 5.1), with the architectural element scale typically posing the most challenges (Keogh et al. 2007). Fluvial architecture describes the stacking of channel and overbank sandbodies, as well as their geometry and interconnectedness (Allen 1978). Channelized fluvial deposits, which comprise channel fills, the aggradation of channel belts, or part or all of the infill of valleys, are the principal components of most fluvial reservoirs and aquifers because they typically contain the majority of the potentially producible volumes (Colombera et al. 2019). To date, the majority of studies have focused on the stacking of channel bodies, their geometry, interconnectedness and internal sedimentology, with little attention on the petrographic variations within the channel bodies. The aspect ratio (width/thickness) of fluvial channels is commonly used to characterize their geometry, with end members of ‘ribbon sandstone and ‘sheet sandstone’ (Friend et al. 1979; Hirst 1992; Gibling 2006) (see Fig. 5.2). Understanding the heterogeneity within these two end members is crucial for optimizing hydrocarbon production in fluvial reservoirs, and more importantly for CO_2 storage.

In this study, outcrop analogues of well exposed fluvial deposits of the Triassic Buntsandstein Formation (or facies) (Age: Olenekian) at Riba De Santiuste, Central Iberian Basin, Spain were investigated. The Triassic Buntsandstein facies at Riba De Santiuste is characterised by low net-to-gross fluvial reservoirs and provides an excellent opportunity to evaluate sand body geometries. While this outcrop section has previously been studied from a sedimentological, stratigraphic, and architectural standpoint (Franzel et al. 2021), the main aim of this study is to investigate the petrography of the different facies and heterogeneity (i.e., porosity variations) within the associated channel sandstone bodies and the implications for CO_2 storage. The key question to be answered in study is: how does porosity varies within channelized sandstone bodies and what are the main controls? The understanding derived from this study will enhance the appraisal of fluvial sandstone reservoirs and building of more accurate predictive models for subsurface reservoirs.

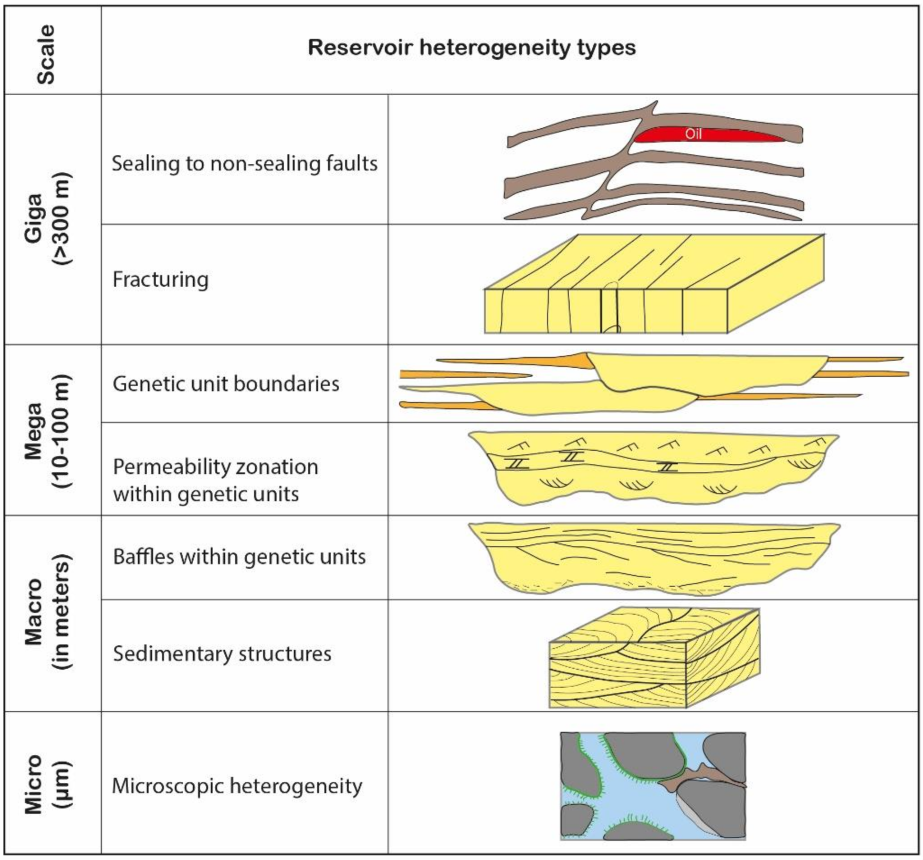

Figure 5.1:Classification of reservoir heterogeneity types and scales. Reservoir heterogeneity is commonly attributed to variations in depositional, diagenetic evolution pathways and structural features (e.g., fractures and faults) (modified from Morad et al. 2010).

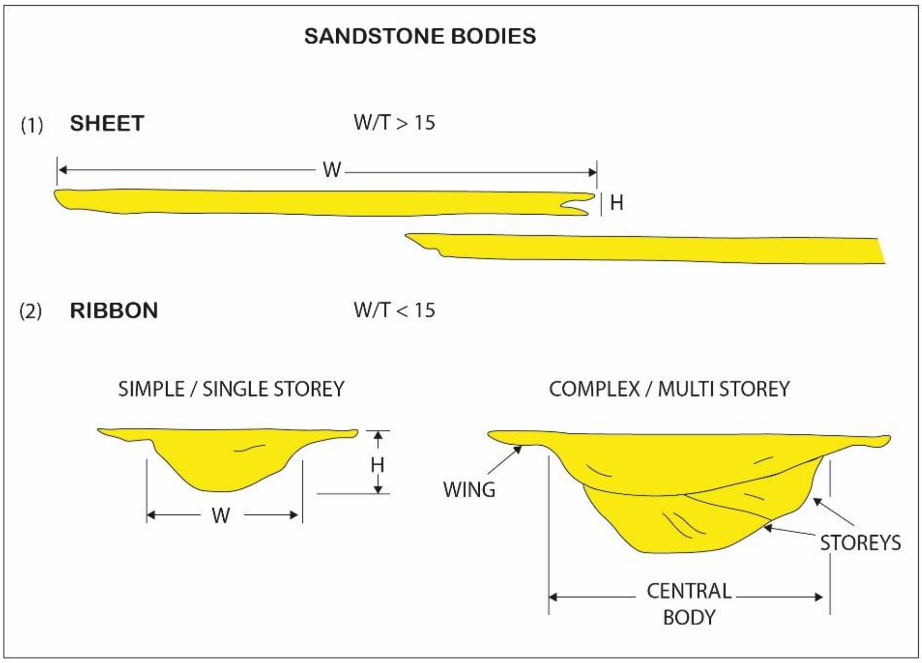

Figure 5.2: Range of fluvial sandstone body geometries based on width/thickness ratios (after Friend et al. 1979)

5.3 Geological setting and stratigraphy of the Central Iberian Basin

The Iberian basin (Ranges) was an intracratonic rift basin in Central Spain trending NW-SE in the northeast edge of the Iberian Microplate (Fig. 5.3). During the Late Carboniferous and Early Permian (that is at the end of the Hercynian orogeny), the Iberian plate, which was a suture zone between Africa and Laurasia, experienced a complex strike-slip movement along the two major faults bounding it: the Bay of Biscay-Pyrenees fracture zone and the Gibraltar fracture zone (Arthaud and Matte 1977). This movement resulted in the creation of major NW-SE and NE-SW faults within the plate coupled with the deposition of continental sediments and volcanic rocks in the basins created. During the Late Permian-Triassic, the older strike-slip faults were reactivated as normal faults and this led to the creation of different rift basins in the Iberian plate (Sopeña et al. 1988) with the Iberian basin occupying an interior position (Fig. 5.3). According to López-Gómez and Arche (1993), the first extensional tectonic event that occurred during the development of the Iberian basin occurred in two major phases: (1) the Late Permian-Early Triassic rifting phase and (2) a thermal subsidence phase extending till Late Jurassic.

The Central Iberian Basin (CIB) is predominantly made up of Permian and Mesozoic sediments that unconformably overlie the Hercynian basement (metamorphic). The Buntsandstein Facies which is the unit of interest in this study was deposited during the first phase of rifting and is composed of breccias, conglomerates, sandstones, and mudstones of continental (fluvial) origin. Overlying the Buntsandstein fluvial facies, are shallow marine carbonates (the Röt and Muschelkalk facies). These marine facies comprising of clay, mudstones, marls, dolomites, and gypsum were deposited during the second phase that began as a slow and widespread thermal subsidence of the basin resulting in marine transgression of the Tethys Sea. The uppermost section of the Buntsandstein facies is composed of shallow marine siliciclastics, an equivalence of the Röt Facies, northern Europe (López-Gómez and Arche 1992) and it marked the onset of marine transgression in the Southeast. Succeeding the Röt facies is the Muschelkalk Facies (Fig. 5.4). However, during the Cenozoic times (that is, Early Cretaceous and Oligocene-Early Miocene), two major episodes of compressional events occurred, and this led to folding, fracturing and tectonic inversion in the Iberian basin (present-day Iberian Ranges), along the NW-SE fault systems (Arche and López-Gómez 1996; Salas et al. 2001).

The study area for this study is Riba de Santiuste in Central Spain. It is located in the north-western part of the Central Iberian range and the CIB (Fig. 5.3) and has excellent fluvial outcrop exposures of the Triassic Buntsandstein Facies which is the main focus of this research.

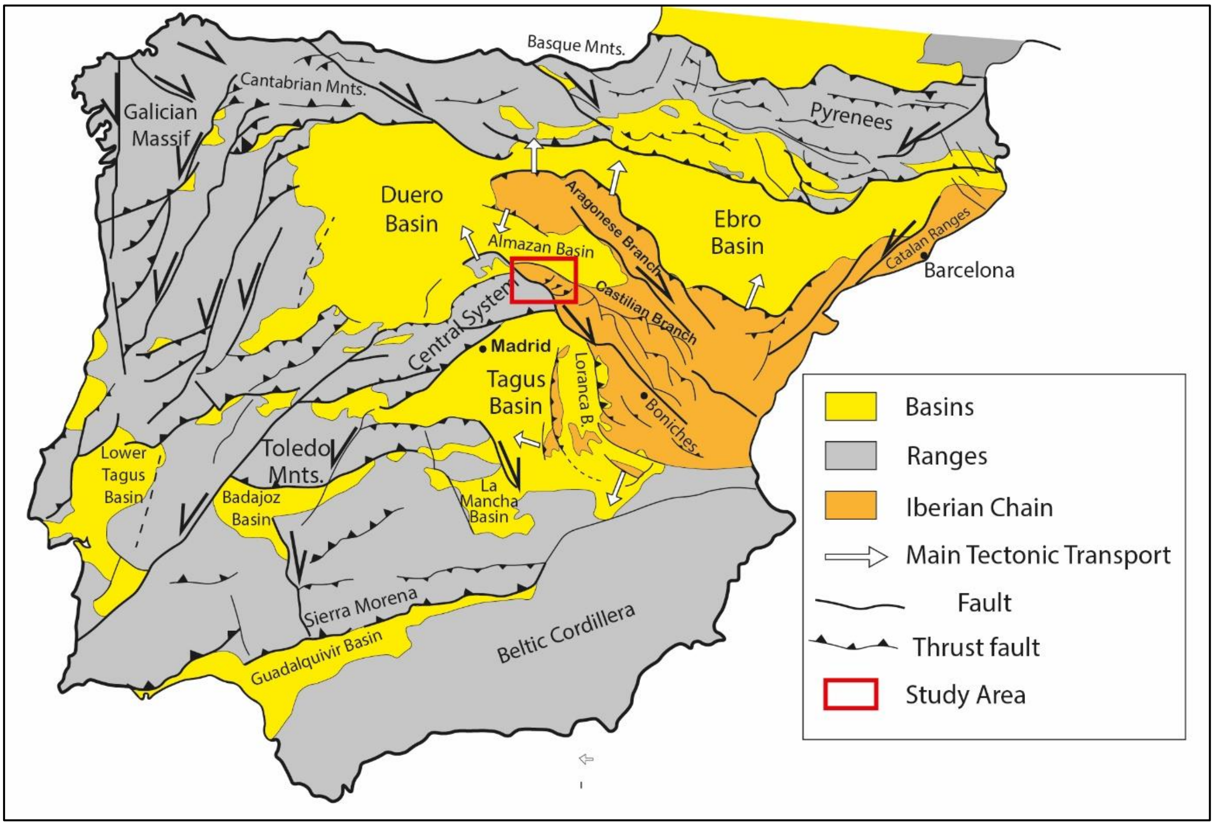

Figure 5.3: Simplified tectonic map of the Iberian Peninsula showing the Central Iberian Basin (highlighted in orange). The study area (Riba de Santiuste) is shown in red box (map after De Vicente et al., 2009).

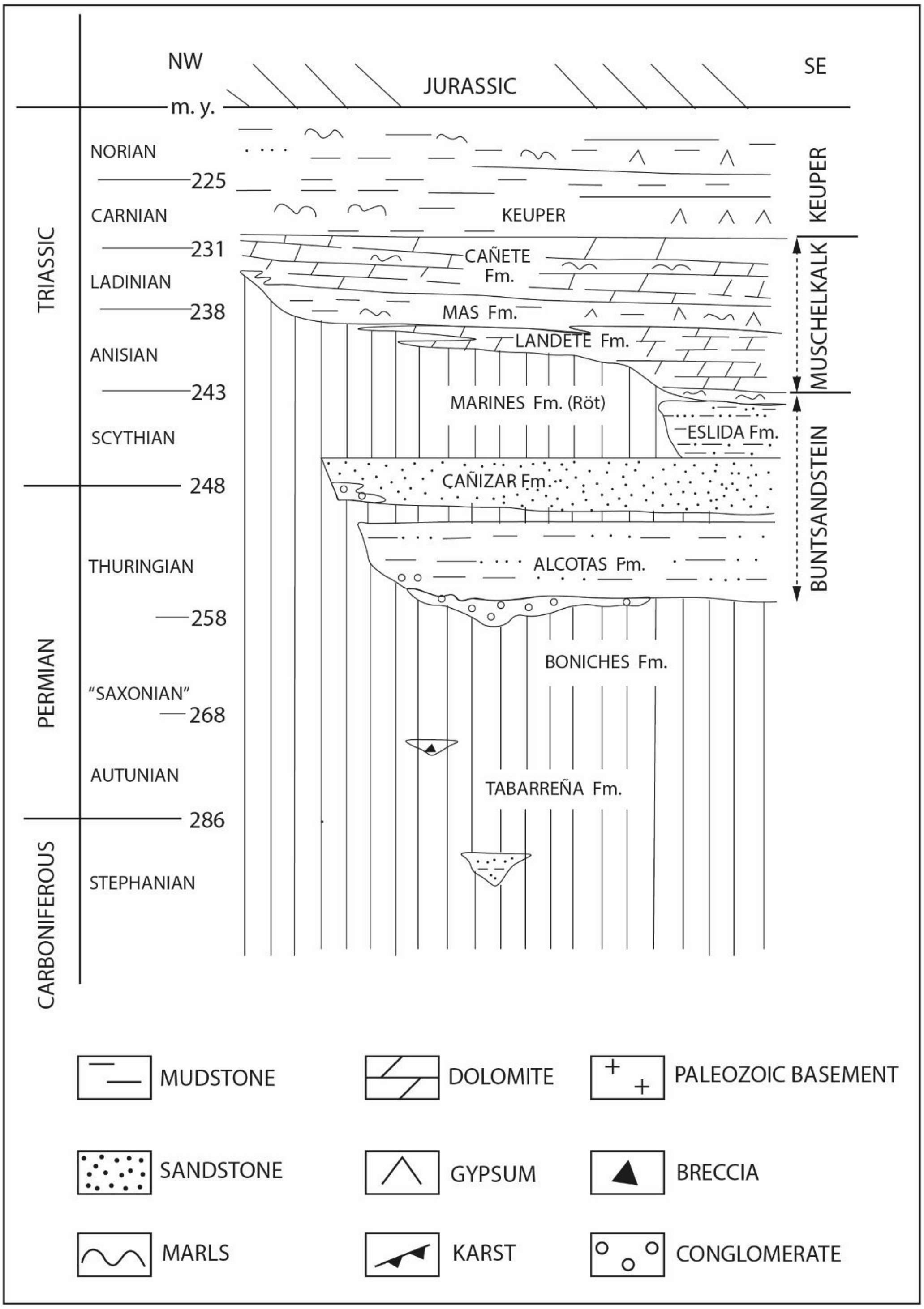

Figure 5.4: A generalized stratigraphy of the Permian and Triassic Formations in the Iberian Ranges showing the Buntsandstein facies (after López-Gómez & Arche, 1993).

Figure 5.5: Cross-sectional view of fluvial exposures at Riba de Santiuste (Figure 5a: courtesy of Max Franzel).

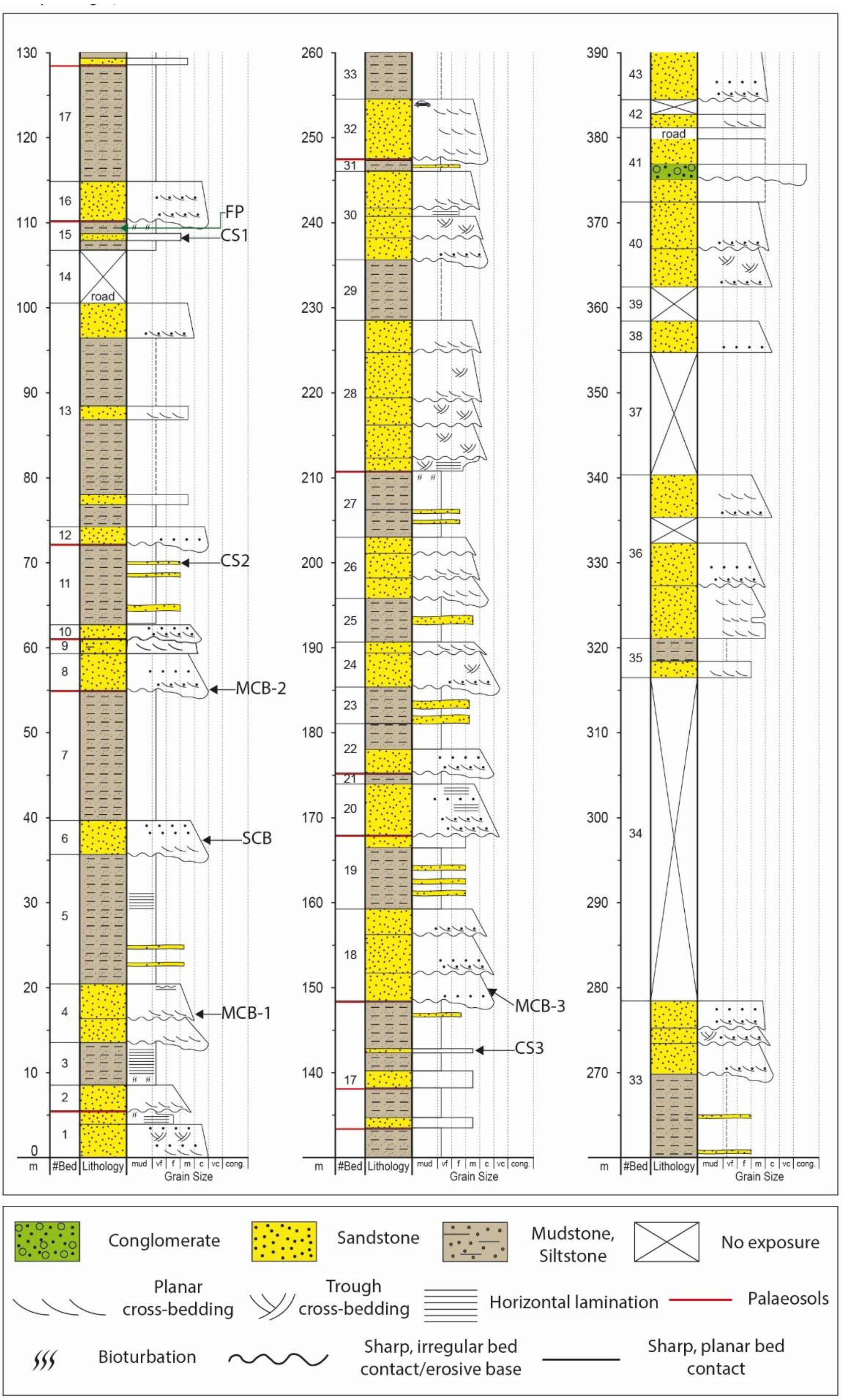

Figure 5.6: Graphic log of location B from which samples investigated in this study were taken (SCB: Single storey channel body, MCB: Multistorey channel bodies, CS: Crevasse splay and FP: Floodplain fines).

5.4 Methodology

A combination of field-based and laboratory techniques were employed in this study. A field work was carried out in June 2018 at Riba De Santiuste in the Central Iberian Basin, Spain (Fig. 5.3) for the purpose of collecting outcrop data. Sedimentary graphic logs were created from the base of the outcropping Buntsandstein sequence to the top of the Muschelkalk facies (Fig. 5.6). Bed thicknesses/contacts, grain sizes, sedimentary structures, colour, and key fluvial structures were noted. The identified sandstone bodies were classified on the basis of geometry using the classification schemes of Friend et al. (1979) (see Fig. 5.2).

A total of 20 rock samples were taken across these facies for detailed petrographic studies. To understand how reservoir properties vary within the sandstone bodies, especially channelised sandstone bodies, samples were taken from the base, middle, top and wing sections of the sampled channel bodies. It is important to note that the petrographic data acquired from outcrop samples may not represent subsurface conditions because the investigated samples may have extra diagenetic characteristics owing to weathering (such as dissolution). Thin sections were prepared from the 20 samples, and these constitute the petrographic data base for this study. The thin sections were impregnated with blue dye to aid the identification of porosity (i.e., macroporosity). They were also stained with Alizarin Red-S and potassium ferricyanide for easy identification of carbonate cement. The mineral composition was determined by standard point counts (300 points) of thin sections using Leica DM2500P polarizing microscope. Optical porosity, grain size and sorting were also determined by point counting. To characterise the intensity of compaction and cementation in the studied sandstone samples, the point-count data was used to quantitatively estimate the compactional porosity loss (COPL) and cementational porosity loss (CEPL) using the formula proposed by Ehrenberg (1995) and Lundegard (1992):

$$COPL = Pi - [(100 - Pi) \times IGV] / (100 - IGV)$$

$$CEPL = (Pi - COPL) \times (C/IGV)$$

where Pi is the initial sandstone porosity, which is assumed to be 45% for the calculations, C is the volume of intergranular cement, and IGV is the percentage of intergranular volume to rock volume, which is calculated using the sum of depositional matrix, intergranular porosity, and the volume of intergranular cement.

5.5 Results

5.5.1 Facies analysis

Facies analysis of the Buntsandstein facies at Riba de Santiuste was carried out using Miall's (1988, 1996) and Franzel et al's (2021) lithofacies classification scheme. The lithofacies identified in the study area are described and summarised in table 5.1, figures 5.7 and 5.8, and have further been grouped into three main facies associations namely: fluvial channel, crevasse splay and floodplain fines (with palaeosols). The texture, composition (detrital/authigenic) and porosity distribution within these facies associations are discussed below. Previous workers (e.g., Friend et al., 1979 and Hirst, 1992) have classified channel sandstone bodies into two main end members: ribbon and sheet sandstones (Fig. 5.2). In this study, the identified channel sandstone bodies are mainly ribbon-shaped and are therefore the main focus of this study.

5.5.1.1 Fluvial channel sandstones

The channel sandstones in the study area occur as both single storey and multistorey (i.e., vertically stacked) channels, separated by floodplain mudstones and siltstones (Fig. 5.6). They are recognised by the presence of concave-up erosional bases (Fig. 5.7a and 5.8b-d). Where they occur as multistorey channel sandstones, the younger unit is observed to erode into the older unit (e.g., fig. 5.8c). Associated lithofacies include: Sp, Sh, Ss, Sr and St (Table 5.1). The sandstones are primarily arkosic in composition, with an average framework composition of $Q_{48}F_{22}L_5$ (Fig. 5.9). Quartz grains are mainly monocrystalline; feldspar is dominated by K-feldspars, and rock fragments are mainly of igneous and metamorphic origin. Detrital clay matrix varies from 0.3 to 28.3% (avg. 8.9%). The detrital clay matrix occurs as homogeneous silt (quartz and feldspar) and clay sized particles, and as pseudomatrix. The sandstones are moderately to poorly sorted, fine to coarse-grained (avg. grain size: 0.125-0.67 mm) with a fining upward sequence. Identified authigenic cements include quartz, feldspar, carbonate, and clays (frequently reddish-stained by adsorption of Fe-oxide). Quartz cement is generally <4% and occurs mainly as syntaxial overgrowths around detrital quartz grains. The authigenic clays are presumably illite or smectite/illite and occur mainly as grain-coats. Carbonate cement is a major cement in the channel sandstones but was only observed at the base of one of the channel bodies. Fe-oxide cement (possibly hematite) is also common and occurs as both grain coatings and pore filling cement. The modal compositions of the channel sandstones are presented in table 5.2.

Table 5.1: Facies description and interpretation (after Miall, 1988, 1996 and Franzel et al., 2021).

Lithofacies	**Facies code**	**Description**	**Sedimentary structures**	**Interpretation**
Gravelly facies	Gp	Clast or matrix supported, red gravel with clasts up to 10 cm in diameter. Bed thickness: 0.5-1.5 m	Planar cross-bedding	Gravel bars
	Gt	Clast or matrix supported, red gravel with clasts up to 10 cm in diameter. Bed thickness: 0.5-1.0 m	Trough cross-bedding	Minor channel fills
	Gms	Massive, red gravel with clasts up to 25 cm in diameter. Bed thickness: 0.3-5 m	Horizontal bedding	Longitudinal bars, lag deposits
Sandy facies *(Sandstone)*	St	Medium- to very coarse-grained sandstone, usually contains pebble layers and may contain rip-up clasts. Bed thickness: 1.0-3.0 m	Trough cross-bedding	Sinuous crested and linguoid type sand dunes, deposited during lower flow regime
	Sp	Medium- to very coarse-grained sandstone, usually contains pebble layers and may contain rip-up clasts. Bed thickness: 1.0-3.0 m	Planar cross-bedding	Linguoid, transverse bars, sand waves (lower flow regime)
	Sh	Fine- to coarse-grained sandstone, may be pebbly. Bed thickness: 0.5-2.5 m	Horizontal lamination	Planar bed flow (upper flow regime)
	Sr	Fine- to coarse-grained sandstone, may be pebbly. Bed thickness: 1.0-5.0 m	Ripple marks	Ripples (lower flow regime)
	Ss	Fine- to coarse-grained sandstone, may be pebbly. Bed thickness: 1.0-3.0 m	Broad, shallow scours and/or low angle cross bedding	Scour fills
Muddy facies *(Siltstone, mudstone)*	Fl	Highly micaceous siltstone and mudstone with minor sand content, may be interbedded with fine-grained sandstone lenses. Bed thickness ranges from 0.2-10.0 m	Fine lamination, very small ripples	Overbank or waning flood deposits
	Fm	Mudstone and siltstone with minor sand content, may show palaeosol development and colour mottling. Bed thickness: 0.2-2.0 m	Massive, dessication cracks, bioturbation	Overbank, abandoned channel or drape deposits
	Fr	Mudstone and siltstone with minor sand content. Shows palaeosol development with rhizoliths, may show calcareous glæbules. Bed thickness: 0.2-0.5 m	Massive, roots, bioturbation	Near channel depsoits, vegetaton cover, increased maturity

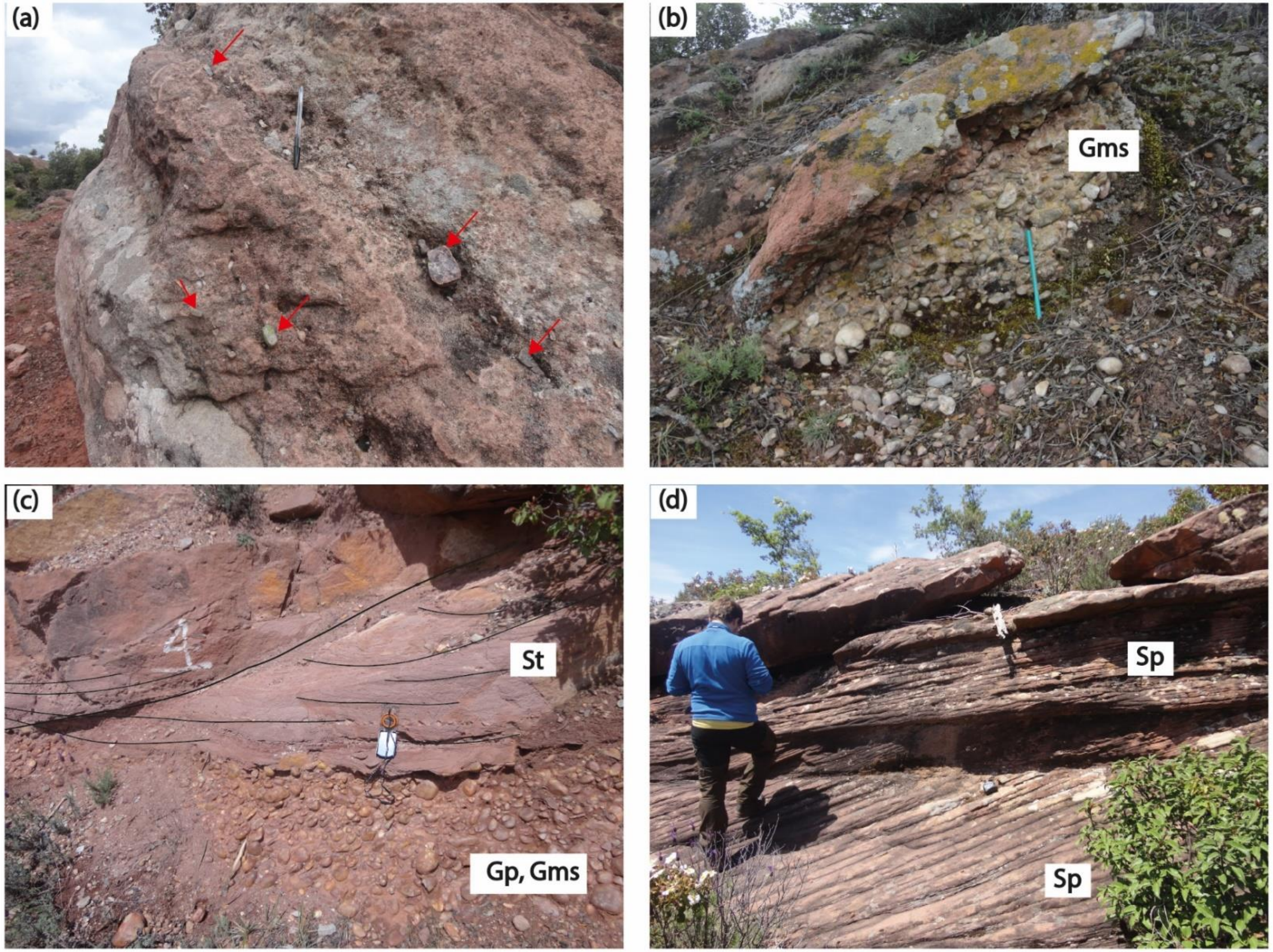

Figure 5.7: Photographs showing (a) Channel sandstone body with pebbles (red arrows) at the basal section, (b) Sandstone underlain by conglomerates (facies: Gms), (c) Trough- cross bedded sandstone and (d) Planar cross bedded fluvial sandstone.

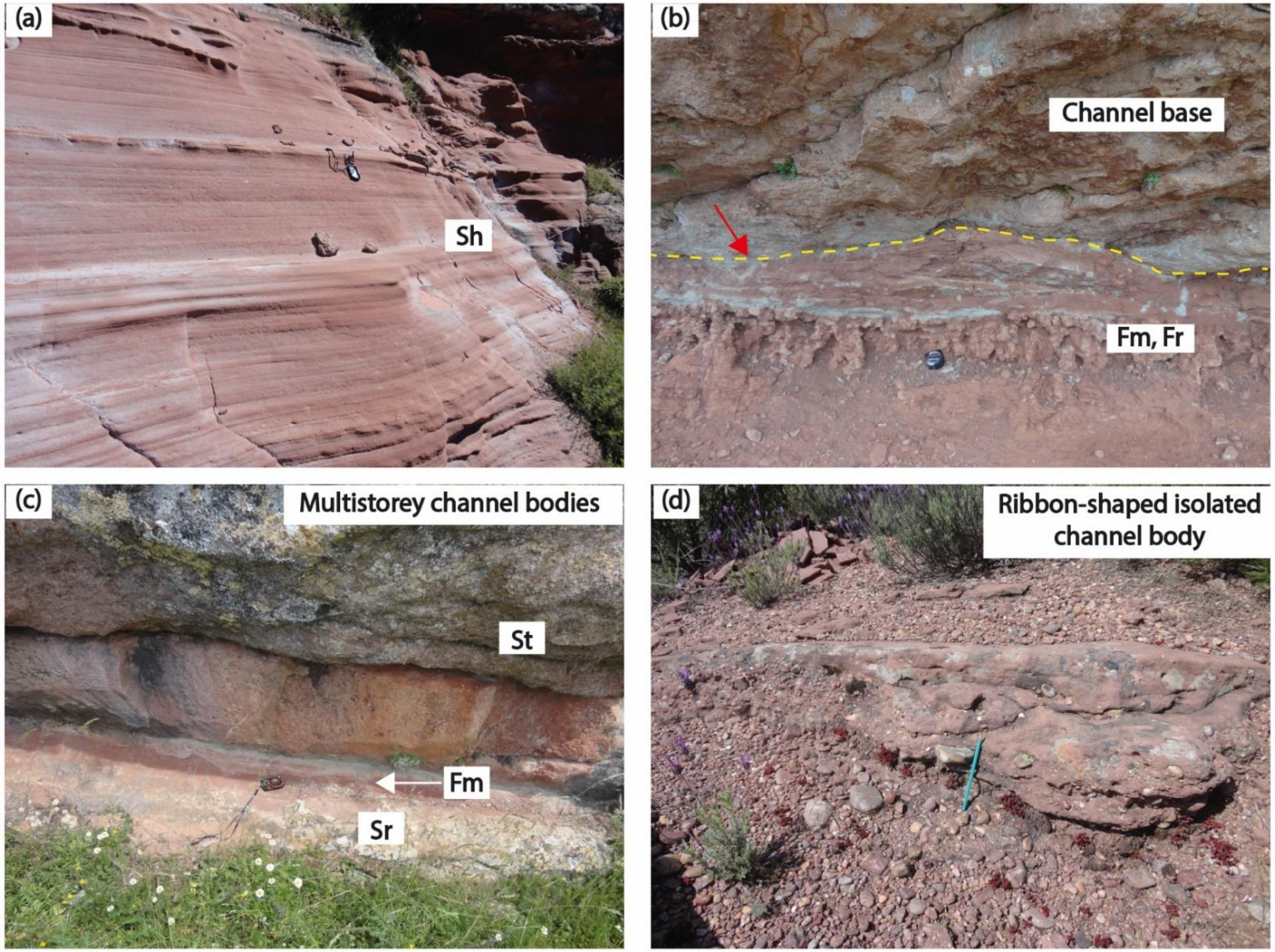

Figure 5.8: Photographs showing different sediments and associated facies at Riba de Santiuste. (a) Channel sandstone with horizontal laminations (b) Floodplain facies (Fm and Fr) overlain by a channel sandstone body. The red arrow shows the erosional contact between the two facies. (c) Multistorey channel sandstone bodies with trough cross bedding (St). The upper channel body is seen to erode into the one below it. (d) Ribbon-shaped fluvial sandstone body encased in floodplain sediments.

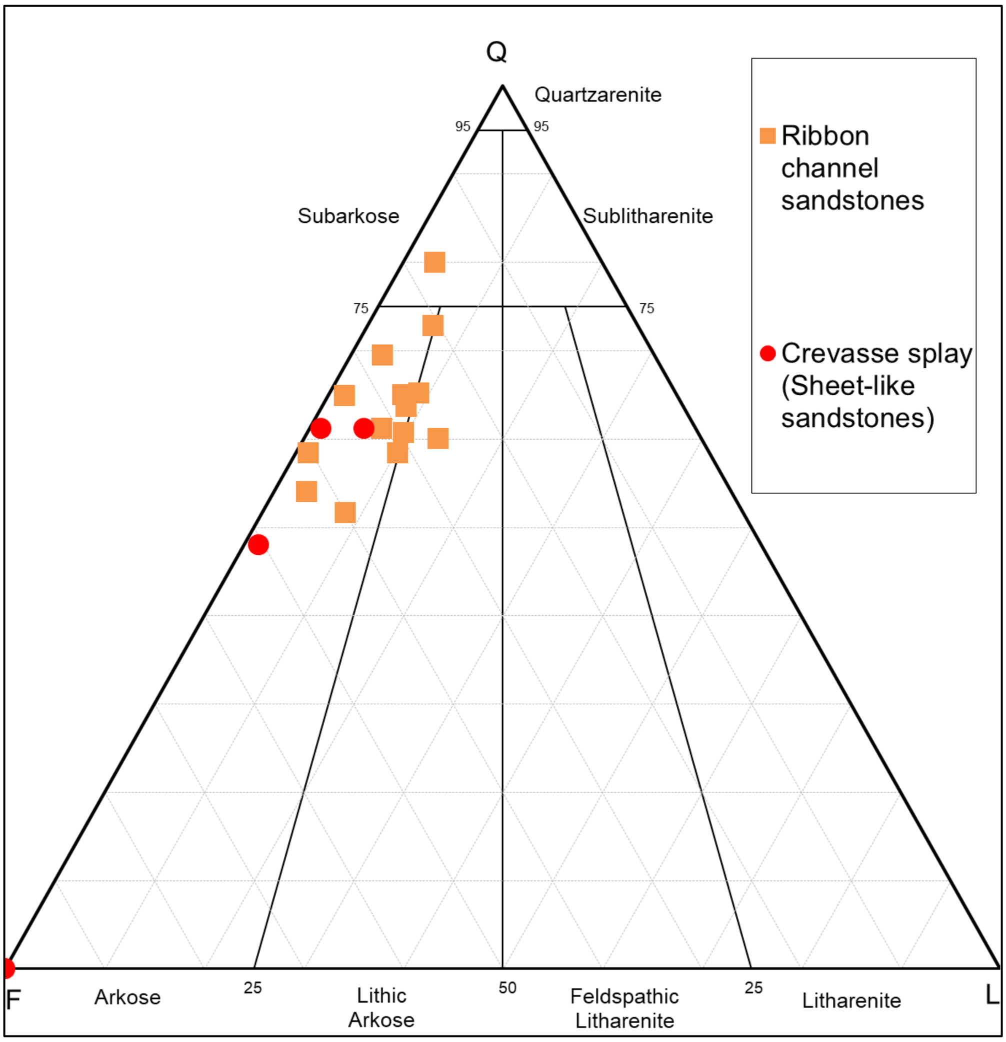

Figure 5.9: Classification of sandstones at Riba de Santiuste (after Folk 1980).

5.5.1.1.1 Single storey channel bodies: SCB

Figure 5.10 shows a typical single storey channel body (SCB) in the study area, with the photomicrographs of the sampled points (top, middle, base, and right wing). The left wing could not be sampled due to lack of proper exposure. Grain size within the SCB varies from medium to coarse sand with a fining upward trend. Likewise, porosity is variably distributed within the channel with the middle section having the highest porosity (Table 5.2). The top section of the channel (Fig. 5.10B & C) is finer-grained, moderately sorted and has a porosity of 5.8%. The photomicrograph of the channel top (Fig. 5.10C) shows that the pore spaces are filled with dark brown muddy matrix in some places. The middle of the channel (Fig. 5.10B & D) has the highest porosity (19%); it is cleaner and better sorted than the other parts of the channel.

Table 5.2: Petrographic data of the studied channel sandstones (ribbon-shaped), crevasse splays and floodplain fines at Riba de Santiuste.

Facies association		Sample points	Q (%)	F (%)	L (%)		M (%)	Clay Matrix (%)	Cal/ Dol (%)	I/S (%)	Fe-oxide (%)	Qo (%)	Fo (%)	Avg. grain size (mm)	Total clay matrix + ductile grains (%)	Porosity (%)	IGV	COPL	CEPL
					Rigid	Ductile													
Single storey channel (Ribbon)	SCB	Top	47	20.7	5.5	5.1	0.3	10.3		4	0.3	1		0.26	15.7	5.8	20.6	30.7	3.7
		Middle	50.3	14.2	3.1	1.5		0.3		7	1	3.6		0.42	1.8	19	29.6	21.9	9.1
		Base	49.6	21	4.7	1		5.6		7.3		2.7		0.53	6.6	8.1	23.1	28.5	7.2
		Right wing	54	11.3	2.2			15		8		3.3		0.64	15.0	6.2	30.7		
Multistorey channel (Ribbon)	MCB-1	Top	45	19.7	4	2	0.7	14.8		5.8	5			0.34	17.5	3.0	27.9		
		Middle	55	21.6	2	0.6	3	1.8		2.3	1	0.7		0.37	5.4	12	16.8	33.9	2.6
		Base	51.3	20.3	3.9	3.2	0.7	8.3		5.0	4.0			0.44	12.2	3.3	20.6	30.7	6.2
		Left wing	38.7	30	3.3	3	1.4	9.5		3.0	3.1	1.0	0.7	0.30	13.9	6.3	21.6	29.8	5.5
		Right wing	49.3	24	3.9	4	1	4.3		4.7	2	1.3		0.34	9.3	5.5	17.8	33.1	5.4
Multistorey channel (Ribbon)	MCB-2	Top	46	24.7	3.1	5	1	8.7		3.0	1.0	1.7		0.37	14.7	5.7	19.6	31.6	3.9
		Middle	48.6	25	1.3			1.3		4.8		1.0	0.7	0.59	1.3	17.3	22.5	29.0	4.6
		Base	47.1	24.3	1.3	4.3	0.3	6.0		3.3	1.1	2.7		0.67	10.6	9.6	18.7	32.3	4.8
		Left wing	44.6	30.7	1		1.7	5.7		5.9		2.3	0.7	0.48	7.4	7.3	20.6	30.7	6.2
		Right wing	39.2	31	1.7	0.7	1	13.7		1.3	3.8	1.6	0.7	0.37	15.4	5.3	26.1		
Multistorey channel (Ribbon)	MCB-3	Base	47	10.7	0.3		0.7	28.3	6.7	3.7	0.3	1		0.125	29	1.3	41.3		
Crevasse splay	CS1	-	35.4	19.3	2	1.2	5.7	2.3	28.4	2.3	1.5	0.3	0.3	0.242	9.2	1.7	36.8	13	28.5
	CS2	-	35.5	21.8	0.7		5.9	22.5		7.5	0.3	4.2		0.123	28.4	1.7	35.5		
	CS3	-	33	34.7	1		1	4.3	8	0.4	7.3	5.3	2.7	0.272	5.3	2.3	30.3	21.1	18.7
Floodplain fines	FP	-	36	18.7	1.7		2.3	36.3	0.3	3.5	1.2			0.063	38.6	0	42		
Palaeosols	P	-																	

Figure 5.10E shows the photomicrograph of the base of the channel. Although the base is coarser-grained compared to the middle section, it has a lower porosity (8.1%) and some dark brown muddy matrix within its pores. The right wing of the channel is the coarsest section of the channel with an average grain size of 0.64 mm (Fig. 5.10F; Table 5.2). It has a porosity of 6.2% and considerable amount of pore-filling matrix and ductile grains (15%).

5.5.1.1.2 Multistorey channel bodies: MCB-1

Figure 5.11 shows an example of a multistorey channel, made up of two vertically stacked channel bodies in the study area. Grain size analysis of samples taken from the top, middle, base, left, and right wing shows that the sandstone is medium-grained throughout the channel body. However, there is a subtle variation in grain size with a fining upward trend. Also, moving away from the channel centre and base towards the wings of the channel body, there is a subtle reduction in grain size (Table 5.2). Point count data shows that the middle section of this channel is more porous than the other sections. The middle section has a porosity of 12%, while the top and base have porosities of 3% and 3.3% respectively. The left wing has a porosity of 6.3% while the right wing has a porosity of 5.5%. Clay matrix and ductile grains content also vary throughout the channel. From the point count data, the total amounts of clay matrix and ductile grains in the middle of the channel is 5.4%, while it varies from 9.3-17.5% in the other sections (top, base, left and right wing). Thin section photomicrographs of the different sections are shown in figures 5.11E to 5.11I.

5.5.1.1.3 Multistorey channel bodies: MCB-2

Figure 5.12 shows another example of a multistorey channel sandstone body (MCB-2) in the study area. In this example, there is a considerable variation in grain size across the channel body, unlike MCB-1. Grain size varies from coarse sand to medium sand, with a general upward fining trend. In this example the base of the multistorey channel is coarse-grained while the other sections are medium-grained (Table 5.2). The highest porosity (17.3%) is found in the channel centre, while the right wing has the lowest porosity (5.3%). Total clay matrix and ductile grains components vary from 1.3 to 15.4% (avg. 9.9%), with the channel centre having the lowest amounts (1.3%; Table 5.2).

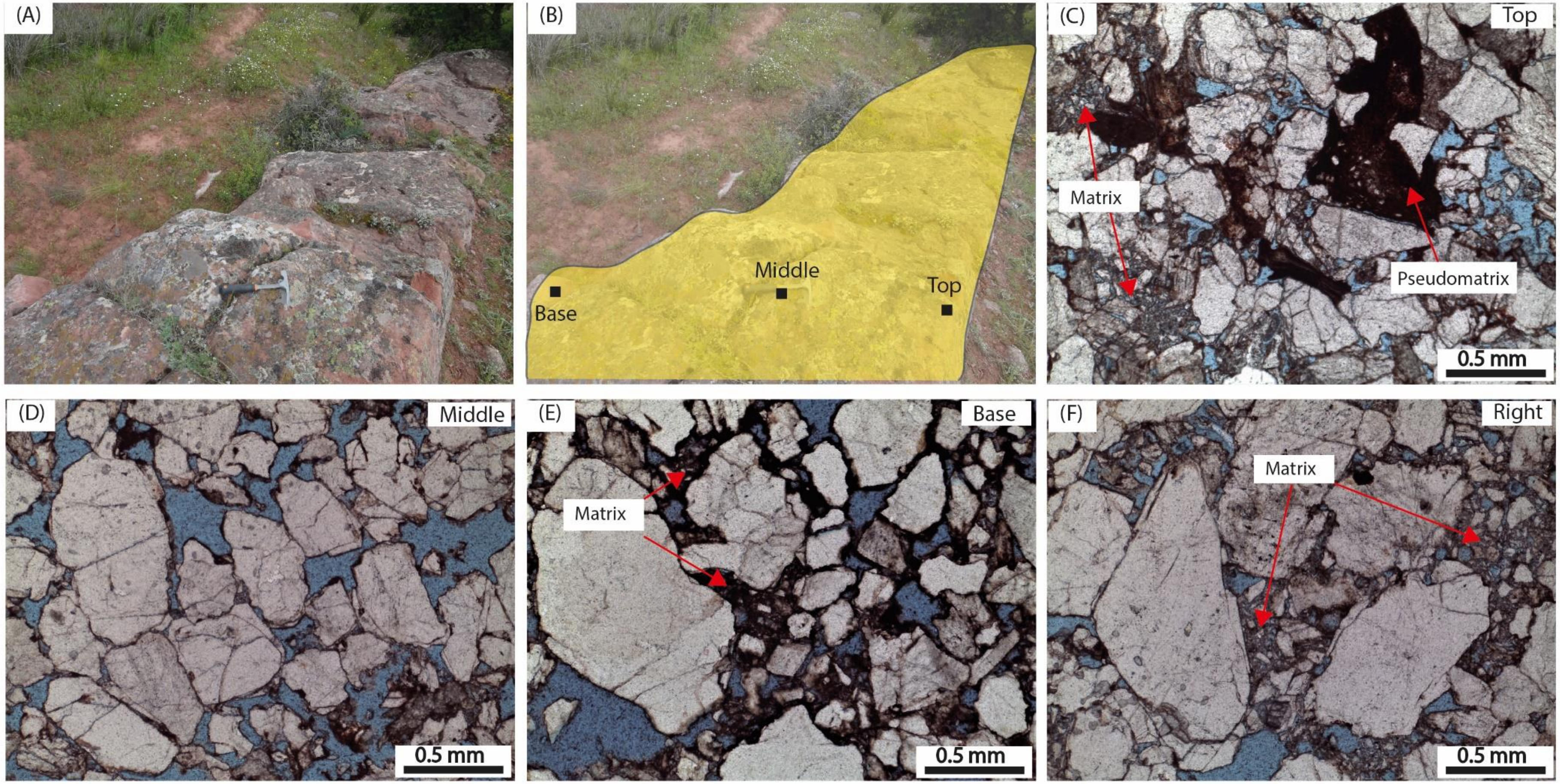

Figure 5.10: Photograph of a single storey channel sandstone body (SCB) at Riba de Santiuste and the thin section photomicrographs of the top (C), middle (D), base (E), and right wing (F).

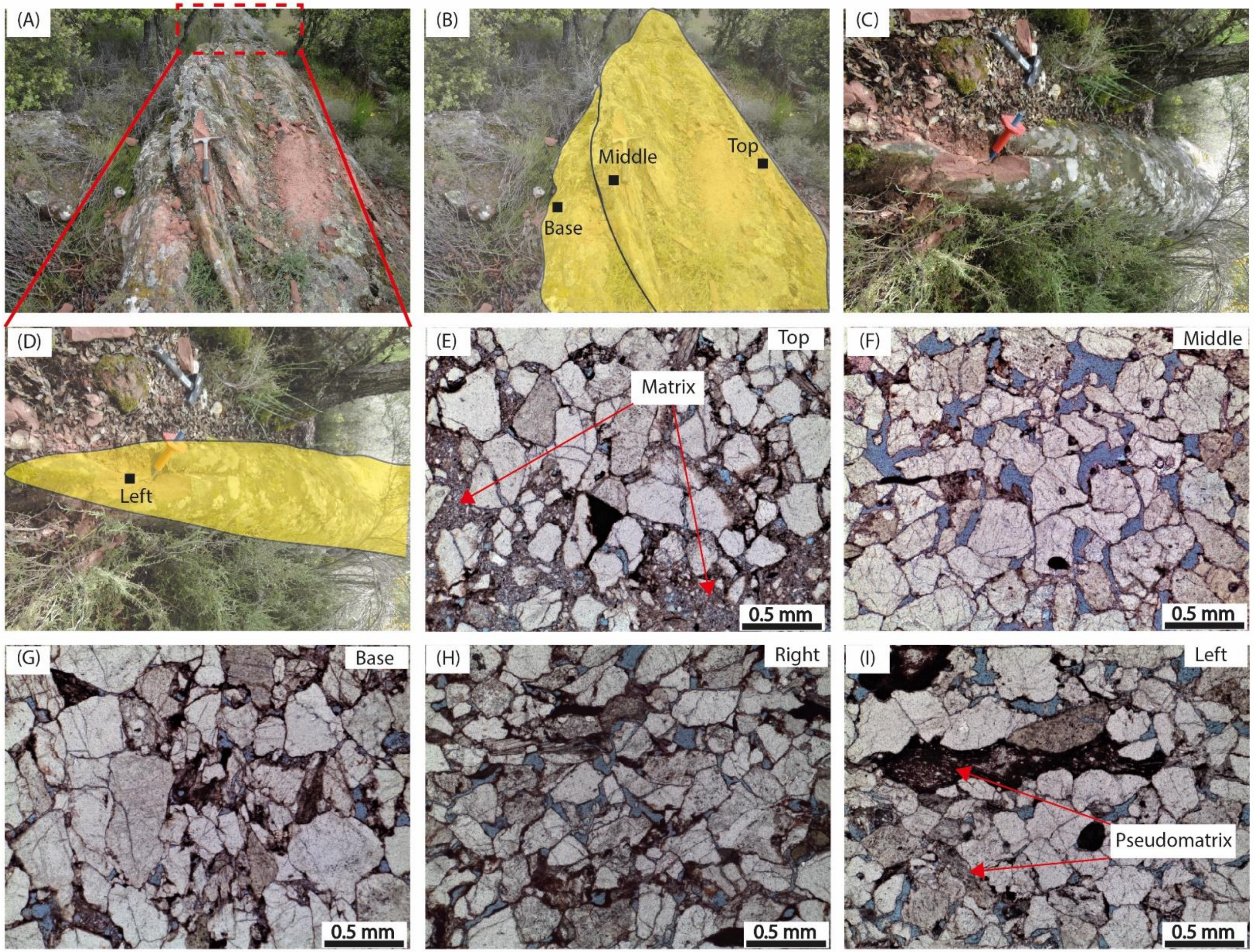

Figure 5.11: Photograph of a multistorey channel sandstone body (MCB-1) at Riba de Santiuste and the thin section photomicrographs of the sampled points: top (E), middle (F), base (G), right (H) and left wing (I).

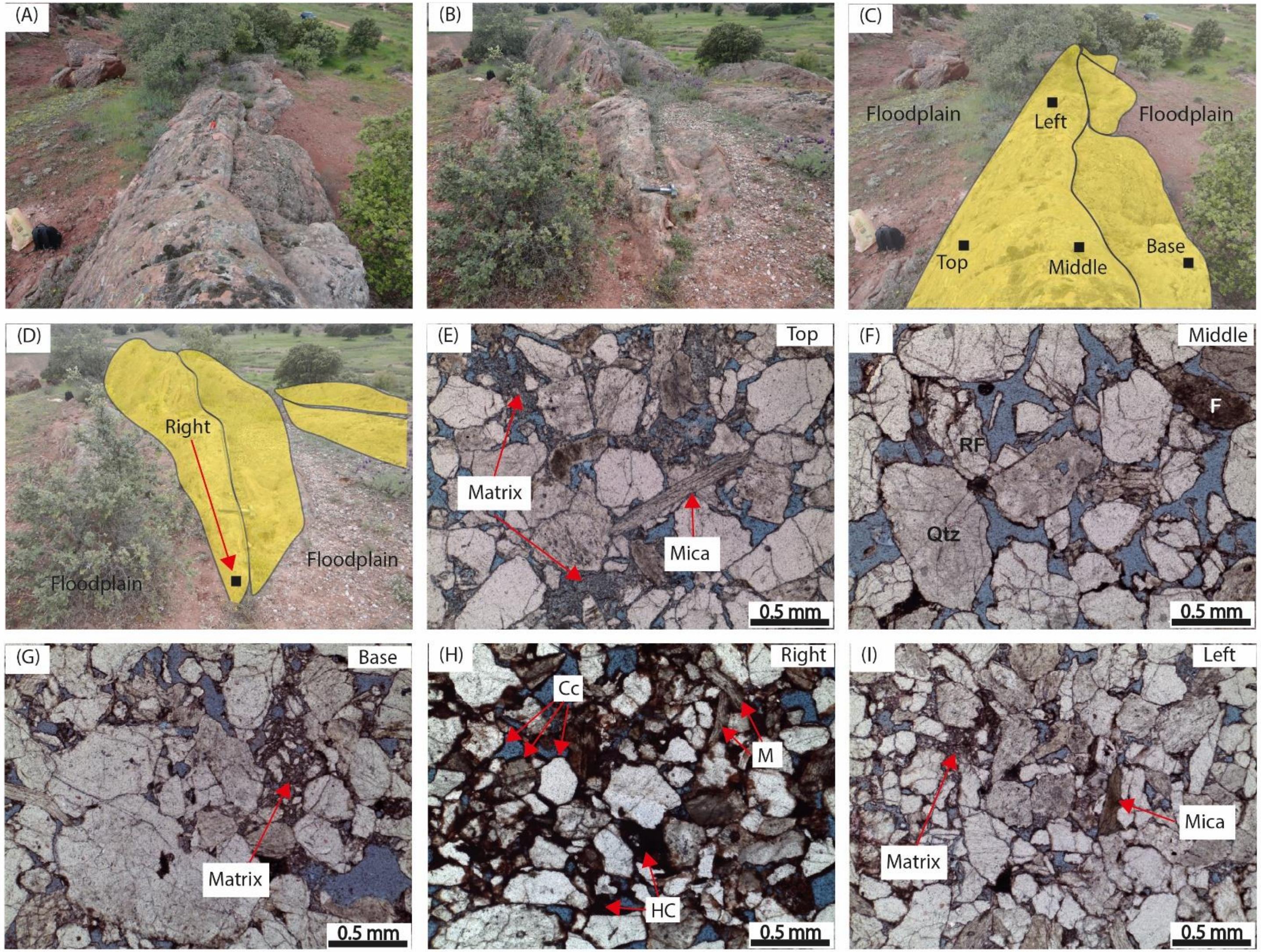

Figure 5.12: Photograph of a multistorey channel sandstone body (MCB-2) and thin section photomicrographs of the top (E), middle (F), base (G), right (H) and left wing (I).

5.5.1.1.4 Multistorey channel bodies: MCB-3

Figure 5.13a shows another multistorey channel body. Here, only the base of the channel was sampled. The thin section photomicrograph (Fig. 5.13b) of the channel base in figure 5.13a shows the presence of carbonate intraclast and abundant muddy matrix, typical of channel bases. From the point count data, porosity of this channel base is 1.3% and is governed by the abundant muddy matrix and carbonate cement which is about 28.3% and 6.7%, respectively (Table 5.2a).

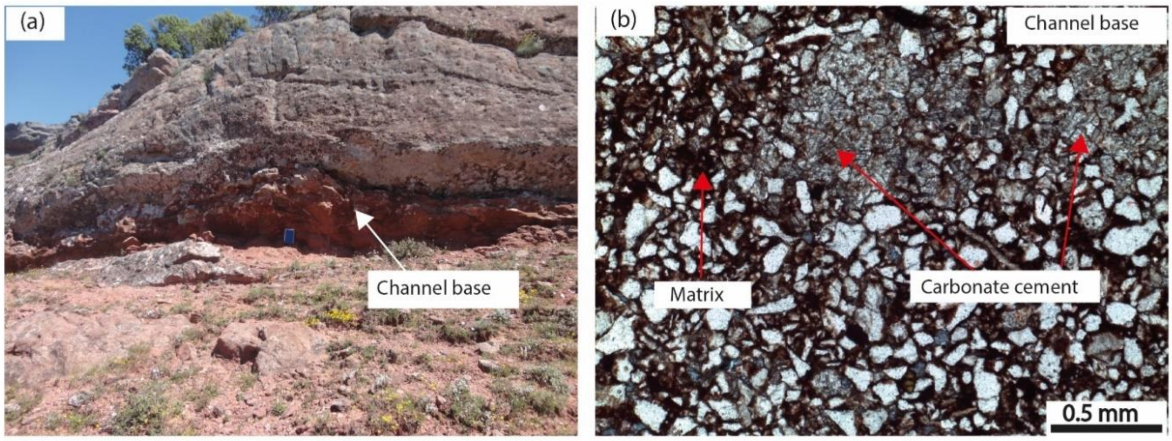

Figure 5.13: Photograph of a multistorey channel sandstone body (MCB-3) and photomicrograph of the basal section.

5.5.1.2 Crevasse splays

Crevasse splays occur as sheet-like sandstone bodies embedded within floodplain facies (Fig. 5.14) They range in thickness from 10 to 50 cm and extend laterally up to 50 m. Associated lithofacies include facies Sh, Sr, Fl, Fm and Fr (Table 5.1). The sandstones of this facies association are arkosic in composition using Folk (1980) classification (Fig. 5.9); they are very fine- to fine-grained and moderately sorted. Clay matrix varies from 2.3 to 22.5% with an average of 9.7%. Diagenetic cements include quartz, feldspar, carbonate, clay minerals and hematite. The main diagenetic cement with a major impact on the porosity of the associated sandstones is carbonate. Carbonate cement varies from 0 to 28.4%. Samples CS1 and CS3 are more tightly carbonate cemented compared to CS2. Porosity is very low to negligible in the crevasse splay sandstones sampled with values ranging from 1.7 to 2.3% (avg. 1.9%) (Table

5.2). Photographs of the sampled crevasse splay sandstones and their corresponding thin section photomicrographs are shown in figure 5.14.

5.5.1.3 Floodplain fines

Floodplain facies are common in the entire fluvial succession at Riba de Santiuste. They are commonly interbedded with the channel and crevasse splay facies (Fig. 5.15). They separate the sandstone beds and could reach up to 20 m in thickness They are dark red in colour, finely laminated and highly micaceous. Associated lithofacies include Fl, Fm and Fr (Table 5.1). The top of this facies commonly shows evidence of palaeosols with calcretised rhizoliths, colour mottling from dark red to medium grey and trace fossils (e.g., Franzel et al., 2021). The floodplain facies have a higher amount of clay matrix and ductile grains (38.6%) than their channel and crevasse splays counterparts. Average grain size is 0.63 mm (i.e., coarse silt), and porosity is zero or negligible (Table 5.2). Figures 5.15a and b show the photograph and thin-section photomicrograph of the sampled floodplain fines while figures 5.15c and d show the photograph and thin section photomicrograph of a sampled palaeosol.

5.5.2 Summary of petrographic results

A comparison of the different facies associations shows that average grain size, clay matrix/ductile grains and porosity vary between them. Texturally, the channel facies are coarser than the crevasse splay and floodplain fines and contain lower amounts of clay matrix and ductile grains. Average grain size varies from 0.125-0.67 mm in the channel facies, 0.123-0.272 mm in the crevasse splays and is 0.063 mm in the floodplain fines. Plot of grain size distribution for the different facies is shown in figure 5.16. Cross plots of average porosity against average grain size and clay matrix/ductile grains content reveals that that channel facies have a higher porosity than the crevasse splay and floodplain facies (Fig. 5.17). Figure 5.17a shows a positive relationship between average grain size and porosity. As grain size increases, porosity increases. Fig. 5.17b shows an inverse relationship between average porosity and average detrital clay matrix/ductile grains content, with porosity reducing with increasing clay matrix and ductile grains content. Furthermore, petrographic observations show that the degree of compaction varies between the facies. The crevasse splays and floodplain facies are more compacted than the channel facies. This is supported by the cross plot of porosity loss due to compaction (COPL) and porosity loss due to cementation (CEPL) (Fig. 5.20).

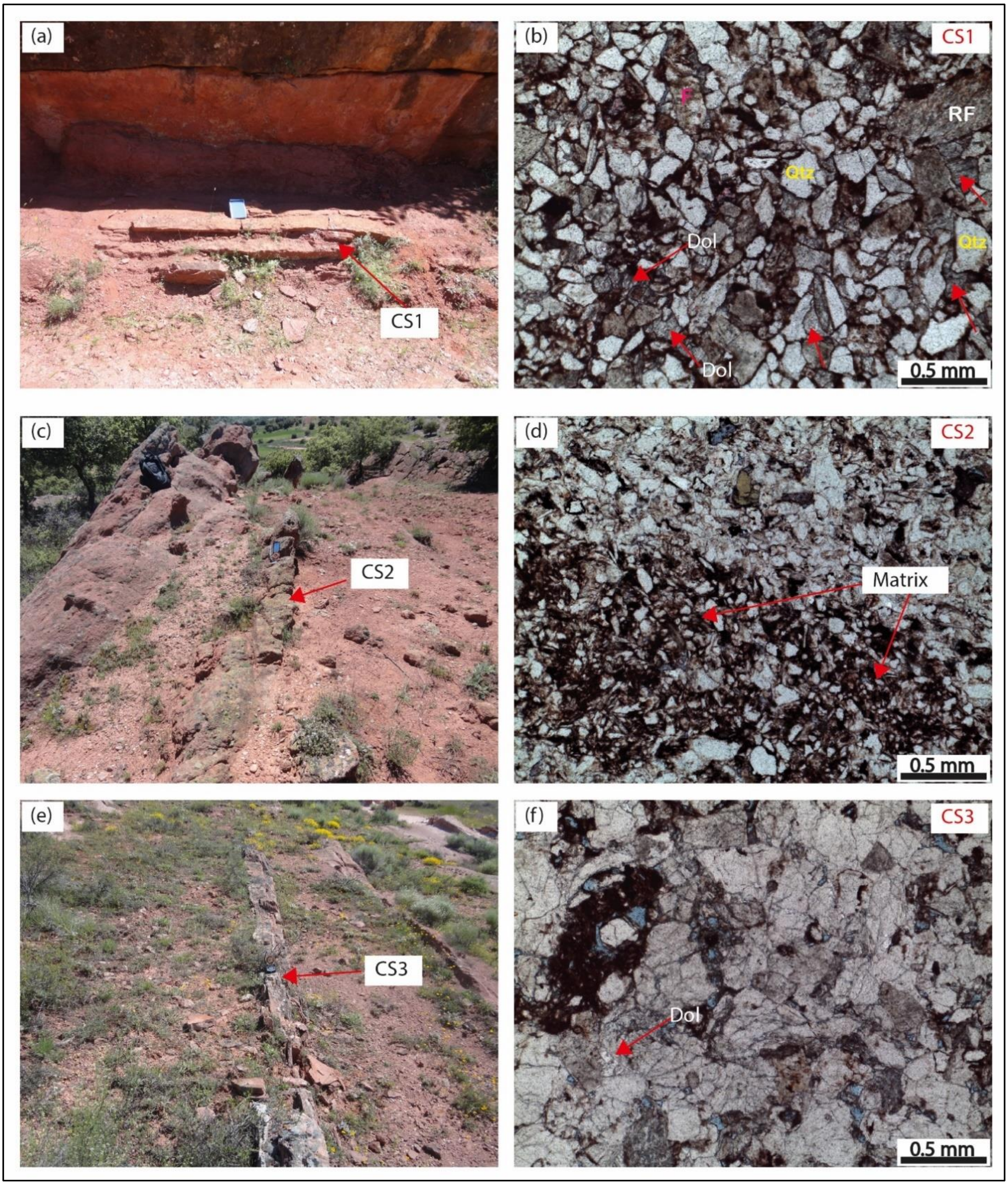

Figure 5.14: Photographs of crevasse splay sandstones encased in floodplain sediments, with their corresponding thin section photomicrographs.

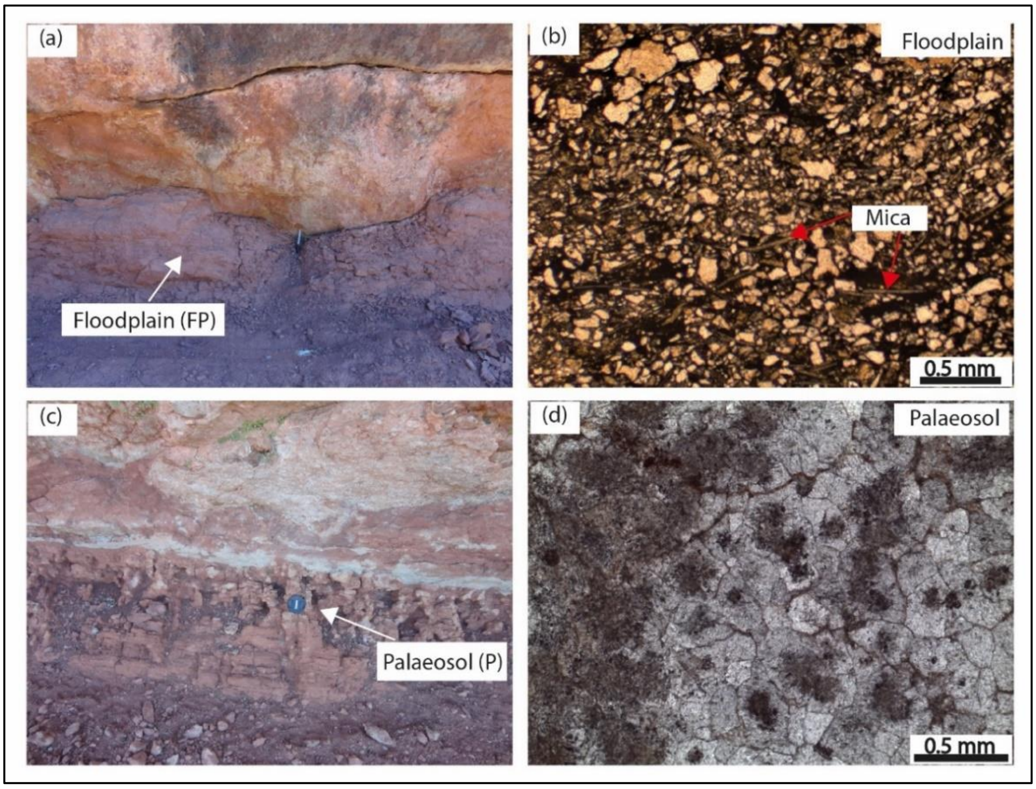

Figure 5.15: Photographs of floodplain sediments and palaeosols, with their corresponding thin section photomicrographs. Overlying the floodplain fines and palaeosol are channel bodies depicted by their concave-up erosional bases.

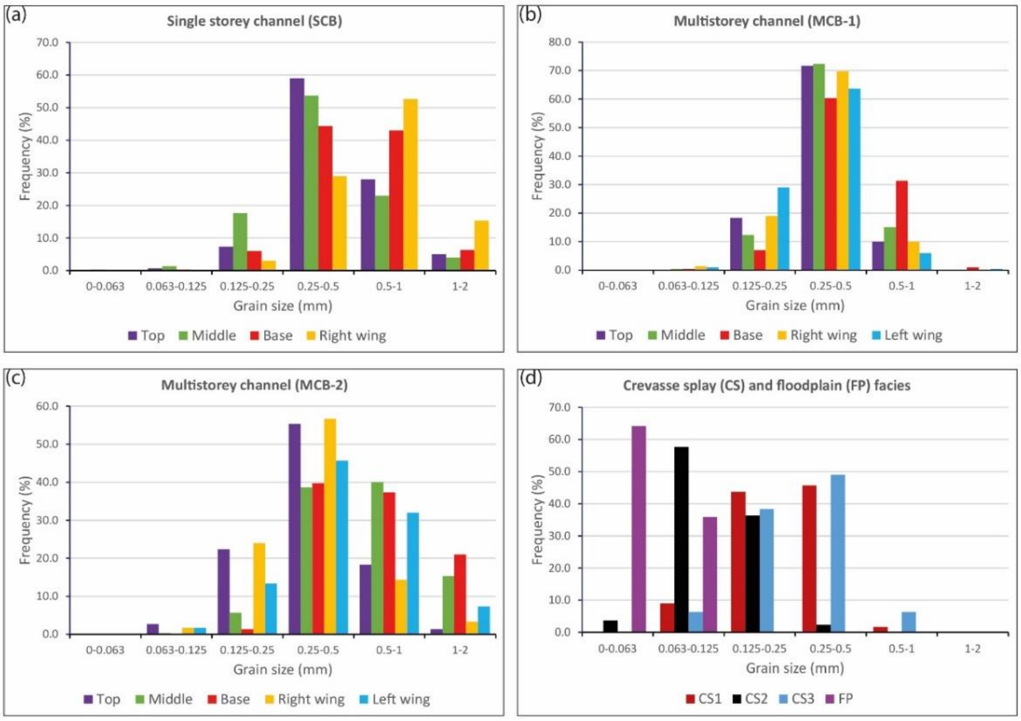

Figure 5.16: Grain size distribution of (a) single storey channel sandstone; (b-c) multistorey channel sandstones; and (d) crevasse splay/floodplain facies.

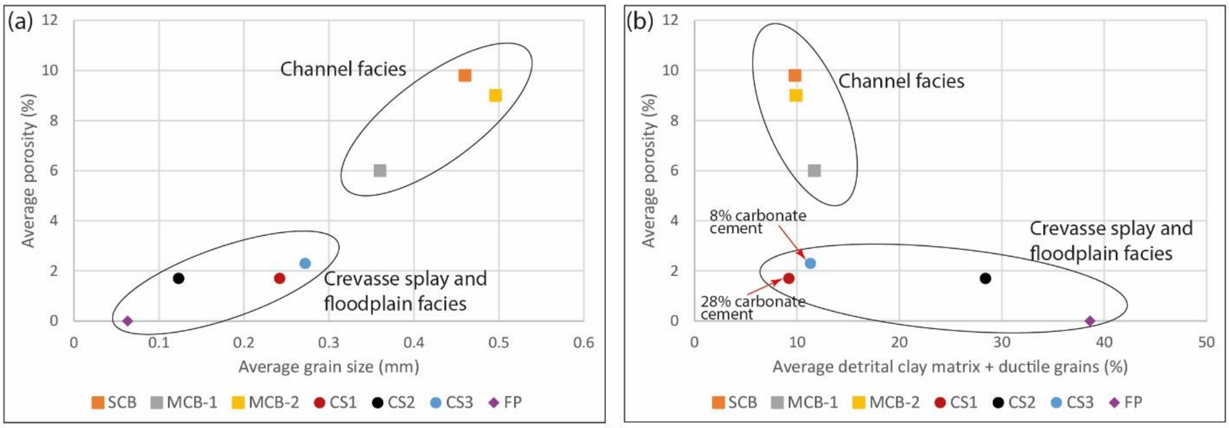

Figure 5.17: Cross plots of average porosity against average grain size and detrital clay matrix/ductile grain content for single storey channel sandstone (SCB), multistorey channel sandstones (MCB-1 and MCB-2), crevasse splay sandstones (CS1, CS2, CS3) and floodplain fines (FP). The average value for each of the channel bodies in the plot (i.e., SCB, MCB-1 and MCB-2) is the average of the top, middle, base, left wing and right wing for each body (see table 5.2). The plot shows that channel facies have better porosity than the crevasse splay and floodplain facies. It also shows that porosity increases with increasing grain size and decreases with increasing clay matrix/ductile grains content. As shown in the plot, channel facies have better porosity due to their coarser grain size and lesser amounts of clay matrix/ductile grains.

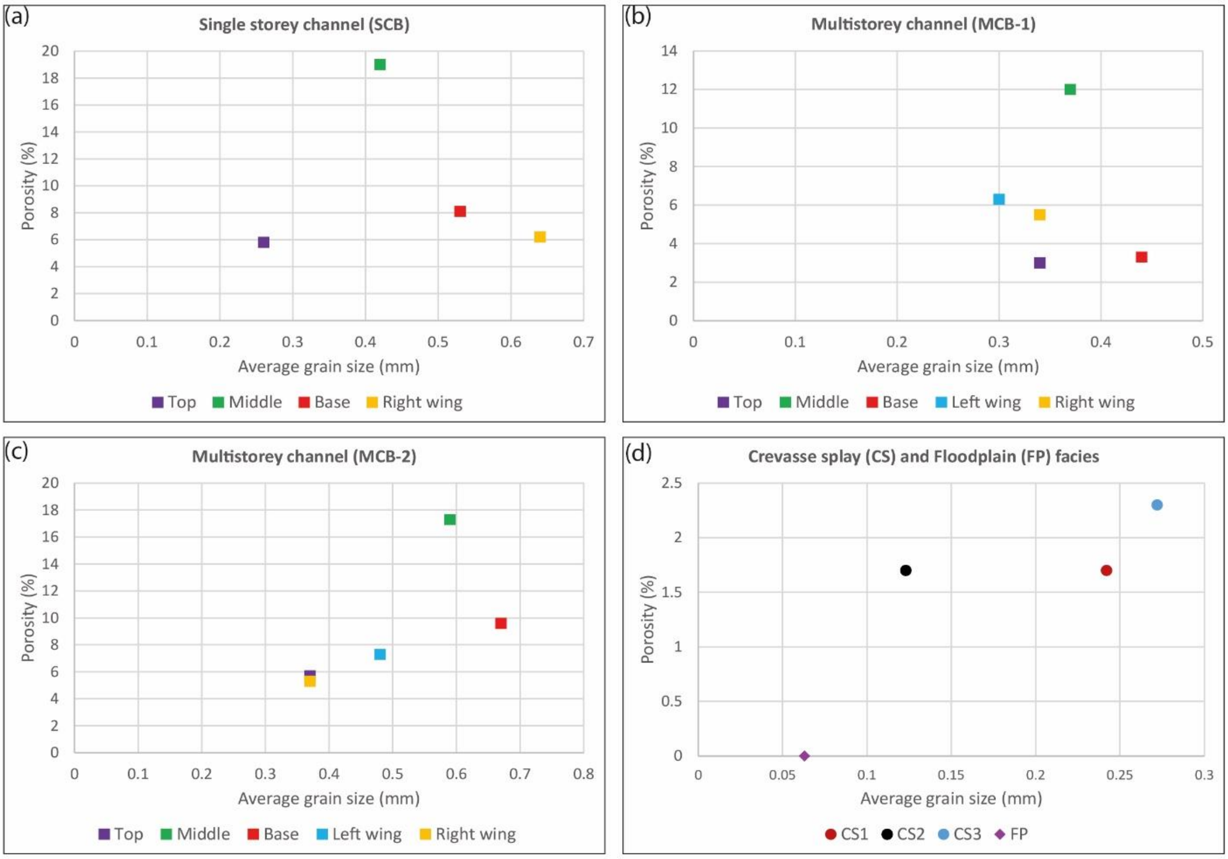

Figure 5.18: Cross plots of grain size and porosity for (a-c) the different sections of the studied channel sandstone bodies (SCB, MCB-1 and MCB-2) and (d) crevasse splay sandstones and floodplain fines. The cross plots (a-c) show that porosity varies within the channel bodies. Also from the plot, it appears that porosity variation within the channel bodies is not influenced by grain size.

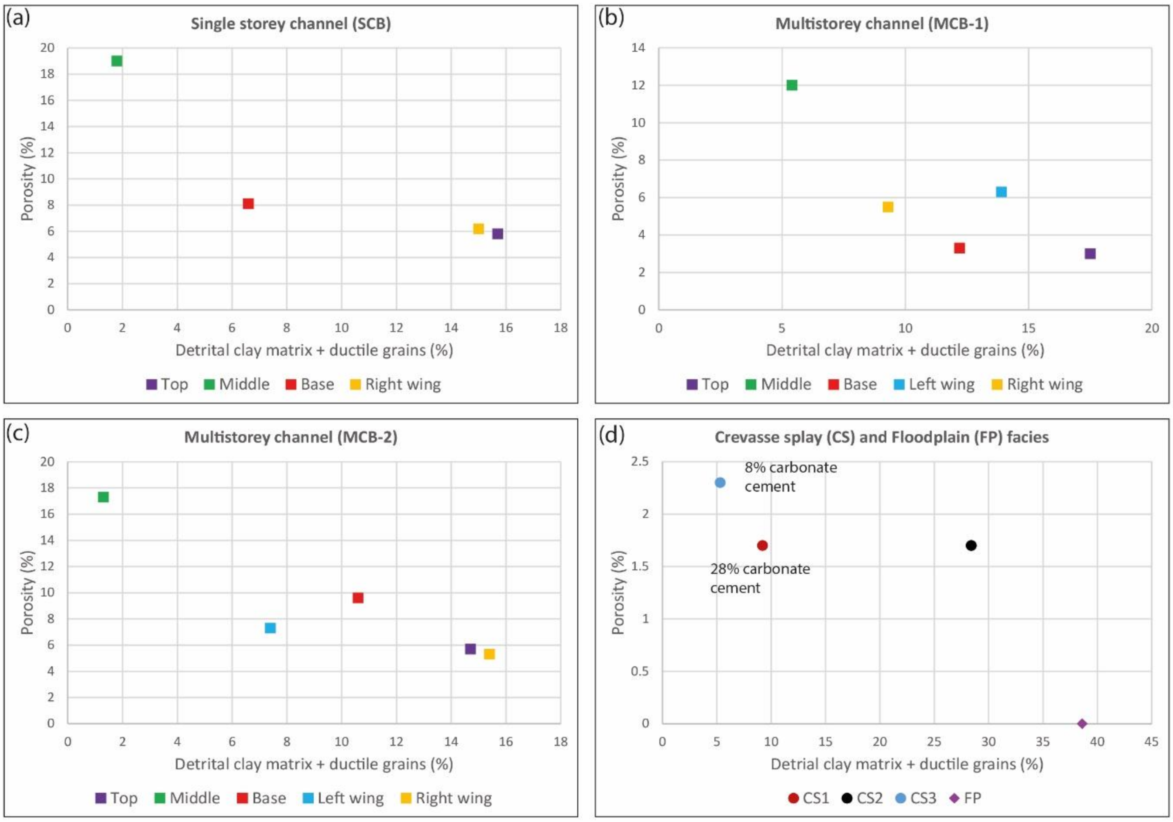

Figure 5.19: Cross plots of porosity and total detrital clay matrix/ductile grains for (a-c) the different sections of the studied channel sandstone bodies (SCB, MCB-1 and MCB-2) and (d) crevasse splay sandstones and floodplain fines. The cross plots show that porosity variation is strongly controlled by detrital clay matrix and ductile grains.

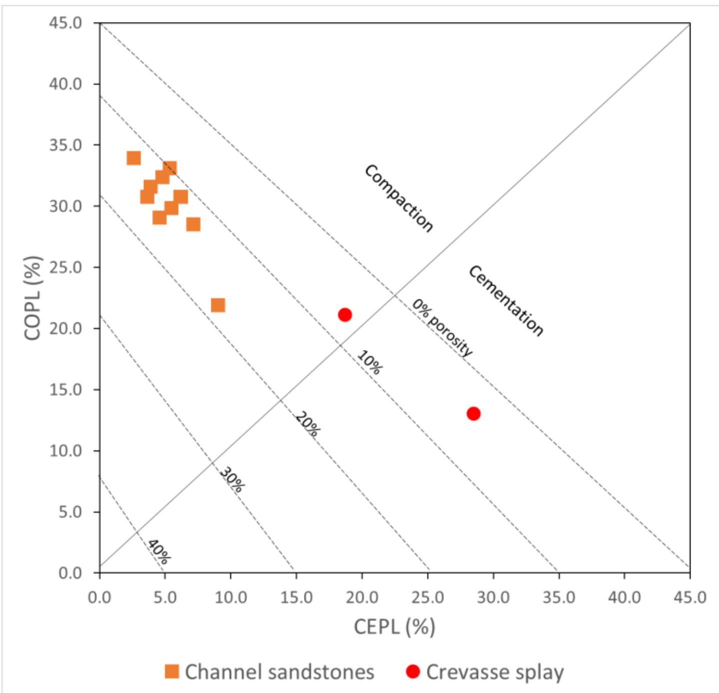

Figure 5.20: Cross plot of porosity loss due to compaction (COPL) and porosity loss due to cementation (CEPL) for the studied sandstones. The plot shows that porosity loss in majority of the sandstones is due to compaction.

5.6 Discussion

5.6.1 Controls on reservoir quality

Petrographic study of the different fluvial facies at Riba de Santiuste clearly shows that the reservoir quality (i.e., porosity) of these facies is primarily controlled by grain size, clay matrix/ductile grain content and carbonate cement, all of which are facies related. The channel facies (single storey and multistorey) has better porosity (up to 19%) than their crevasse splay and floodplain fines counterparts which have low to negligible porosity (<3%). The good porosity in the channel facies (comprising mainly sandstone) could be attributed to their coarser grain size and lesser amounts of clay matrix/ductile grains (Fig. 5.17). On the other hand, the poor to negligible porosity in the crevasse splay and floodplain fines could be linked to their finer grain size, higher clay matrix/ductile grains and considerable presence of carbonate cement (Fig. 5.17).

Porosity loss in the different fluvial facies is controlled by compaction and cementation. In the channel facies, porosity loss is mainly driven by compaction, whereas in the crevasse splay and floodplain facies, it is a combination of compaction and cementation (particularly carbonate cement). This is demonstrated by the plot of porosity loss due to compaction (COPL) versus porosity loss due to cementation (CEPL) (Fig. 5.20). Petrographic observations of thin sections reveal evidence of mechanical compaction such as point grain contact and formation of pseudomatrix (Fig. 5.10C and 5.11I). Mechanical compaction in sandstones is enhanced by clay and ductile fragments . Based on this study, sandstones with greater amounts of clay matrix and ductile grains have a higher degree of compaction than those with lesser amounts. The effect of clay matrix and ductile grains on porosity, as observed in this study, agrees with other studies which have shown that abundant clay matrix and ductile grains can greatly enhance compaction and porosity loss in sandstones (Paxton et al. 2002; Henares et al. 2016; Li et al. 2017; Wang et al. 2019).

5.6.2 Petrography of channel geometries and reservoir heterogeneity

Understanding the lateral and vertical variations in porosity and permeability (i.e., reservoir heterogeneity) within different sandstone body geometries and the main controls is important for accurate reservoir modelling. As previously stated, the channel sandstones (single storey and multistorey) which constitute the main reservoirs in the study area are ribbon-shaped. However, despite having the best reservoir quality, they generally exhibit considerable internal heterogeneities with respect to porosity distribution. As shown in table 5.2 and figures 5.18a-c, the highest porosity in the channel sandstone bodies (SCB, MCB-1 and MCB-2) is found at the centre of the channel (i.e., middle section). Although grain size controls the porosity variations between the different facies as shown in figure 5.17a, this is not the case within the channel bodies (Fig. 5.18a-c). Petrographic and statistical analysis revealed that the main control on porosity heterogeneities within the ribbon channel sandstone bodies is the variations in the total amounts of ductile grains and clay matrix (Table 5.2 and figs. 5.19a-c). As shown in figures 5.19a-c, there is an inverse relationship between porosity and total clay matrix/ductile grains. Higher porosity at the channel centre, compared to the other sections is due to lesser amounts of clay matrix and ductile grains. As you move towards the top, base and wings of the channel bodies, porosity gradually reduces due to increasing amounts of clay matrix and ductile grains. A summary diagram showing the distribution of porosity in a typical ribbon-shaped channel sandstone bodies is shown in figure 5.21. Variable amounts of clay matrix and ductile grains within channel bodies could be attributed to variations in depositional energy/hydrodynamic conditions in the channel system. Lower amounts of clay matrix/ductile grains at the channel centre corresponds to a higher energy while the higher clay matrix/ductile grains at the top, base and wings corresponds to a lower energy.

In addition, the lower porosity at the base of the channel in the model (Fig. 5.21) could also be attributed to the presence of carbonate cement in this section of the channel. A typical example is figure 5.13 which shows the thin section photomicrograph of a sample from the base of channel MCB-3. Here, the point-counted carbonate cement is about 7% and the porosity is 1.3%. The carbonate cement in the channel base of MCB-3 is believed to originate from the dissolution and reprecipitation of carbonate intraclasts derived from the erosion of adjacent floodplain pedogenic calcretes during the formation of the channel (e.g., Morad et al., 2009). Although the channel sandstones (or facies) form the main reservoirs in the study area, the multistorey channel sandstones are better reservoirs (due to their greater thickness) compared to the single storey channel sandstones (Fig. 5.6)

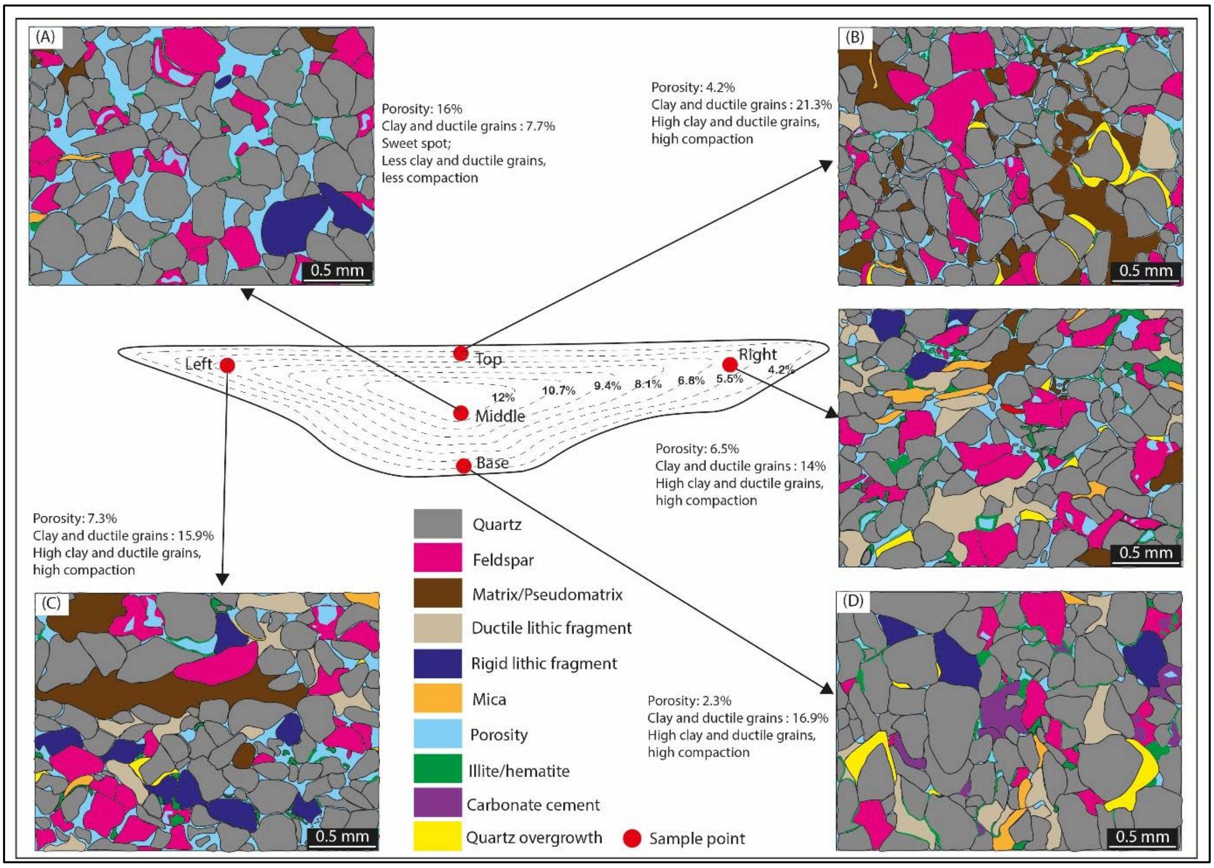

Figure 5.21: A model summarizing the distribution of porosity and diagenetic alterations in a typical ribbon-shaped channel sandstone body at Riba de Santiuste, Central Spain. The porosity distribution pattern is depicted by the contour map.

5.6.3 Implications for carbon capture and storage (CCS)

Reservoir heterogeneity strongly influences reservoir performance by controlling fluid flow and recovery factors (Morad et al. 2010). It also has an impact on sequestration capacity and effectiveness. Several studies have shown that geologic or reservoir heterogeneity can increase or enhance sequestration capacity and its effectiveness (Hovorka et al. 2004; Bryant et al. 2006; Ambrose et al. 2008; Singh et al. 2021). Reservoir heterogeneity can be defined as the vertical and lateral variations in porosity and permeability. The heterogeneity patterns of sandstone reservoirs are controlled by the geometry and internal structures of sand bodies, grain size, sorting, degree of bioturbation, provenance, and by the types, volumes, and distribution of diagenetic alterations (Morad et al. 2010).

Based on the findings of this study, the heterogeneity within ribbon-shaped channel sandstone bodies and between different facies in a low net-to-gross fluvial system has strong implications for CCS. The reduction in porosity, and potentially permeability, as you move away from the channel centre towards the top due to decreasing grain size and increasing muddy matrix/ductile grains may inhibit the upward migration of injected CO_2, thus dispersing flow paths and providing a larger percentage of the rock volume that could be contacted by the injected CO_2 (e.g., Ambrose et al., 2008). A suite of simulation models constructed by Flett et al. (2007) showed that heterogeneous reservoirs are more effective in containing CO_2 compared to homogeneous reservoirs. Their work showed that a decrease in reservoir quality, would increase the tortuosity of the vertical migration path of the injected CO_2 plume (i.e., inhibit its vertical flow) and promotes its lateral migration. According to Flett et al. (2007), the increased lateral migration of the CO_2 plume will enhance an overall reservoir contact between the plume and the formation, and ultimately a larger dissolution of the injected CO_2. Other studies (e.g., Bryant et al., 2006) have also shown that as the heterogeneity of aquifer hydraulic conductivity increases, capillary effects become more prevalent during the buoyant movement of CO_2, therefore resulting in enhanced dissolution and residual trapping of the injected CO_2. Reservoir heterogeneity also limits the reliance on the formation seal (i.e., overlying seal) as the only mechanism for CO_2 containment (Flett et al. 2007).

The importance of sandstone body connectivity for fluid flow and reservoir performance has been highlighted in the literature (Larue and Hovadik 2006; Donselaar and Overeem 2008; Pranter and Sommer 2011; Miall 2014; Xue et al. 2021). According to Miall (2014), the most important control on reservoir performance is not reservoir architecture, but sandstone body connectivity which loosely depends on reservoir architecture. In a stratigraphic interval, one of the key factors governing the degree of connectedness of channelized sandstone bodies is channel-deposits proportion (CDP), also known as net to gross ratio (NTG). Channel belts are unconnected if CDP is less than 0.4 and connected if it is greater than 0.75 (Bridge et al. 2000; Bridge and Tye 2000). The channel-deposit proportion at Riba De Santiuste is less than 0.4; this indicates that the interconnection of the channel belts is generally low. The low lateral and vertical interconnection of these channel bodies could be attributed to the high A/S conditions under which they were deposited, which resulted in their isolated nature, and the thick/areally extensive floodplain mudstones associated with them . In general, high A/S channel sandstones are more heterogeneous, discontinuous and have lower net to gross ratios (Ramón and Cross 1997). We infer from this study that the low connectivity between the Riba de Santiuste channel sandstone bodies has a positive implication for CCS. Although they form smaller reservoir compartments, any injected CO_2 will be securely trapped without any concerns of leakage or migration into adjacent sandstone bodies. Furthermore, the associated floodplain facies are very thick and laterally extensive. They are poor/non-reservoirs, due to their negligible porosity and thus constitute potential barriers to fluid flow.

The importance of crevasse splay deposits as viable production units in hydrocarbon reservoirs and as a vital component of fluvial overbank successions have been discussed in several studies (Colombera et al. 2013; Stuart et al. 2014; Van Toorenenburg et al. 2016; Burns et al. 2017). Their presence in fluvial successions could potentially increase the lateral connectivity of sandstone bodies by acting as conduits that connect larger channel sandstone bodies (Mjøs et al. 1993; Hornung and Aigner 1999; Larue and Hovadik 2006; Bos and Stouthamer 2011; Van Toorenenburg et al. 2016; Burns et al. 2017; Yeste et al. 2020), thus increasing overall reservoir performance (Colombera and Mountney 2021). However, the crevasse splay deposits in this study have very low porosity (avg. 1.9%) due to the high amounts of detrital clay matrix and carbonate cement, thus making them poor reservoirs and potential barriers/baffles to fluid flow.

5.7 Conclusion

- The Triassic Buntsandstein Formation at Riba de Santiuste consists of three main facies associations namely: (1) channel facies (single-storey and multistorey/multilateral channel bodies; (2) crevasse splays; and (3) floodplain fines and palaeosols.
- Petrographic studies of samples from the different facies show that the single-storey and multistorey/multilateral channel sandstone bodies form the main reservoirs with porosity values ranging from 1.3%-19%. However, the multistorey channels form better reservoirs, due to their greater thickness.
- Our study also shows that despite the channel facies constituting the main reservoirs, there are petrographic/reservoir quality variations within the individual channel bodies. The centre of the channel bodies has higher porosities (ranging from 12%-19%), due to their lower clay matrix and ductile grain content, and lower degree of compaction. Conversely, the top, base, and wings of the individual channel bodies have greater amounts of matrix and ductile grains, and consequently, higher degree of compaction and lower porosities (1.3%-9.6%). Also, the channel base is carbonate cemented, thus contributing to its lower porosity.
- The heterogeneity within the channel facies and between the different facies at Riba de Santiuste has strong implications for CO_2 storage. The higher porosity (and potentially higher permeability) at the centre of the channel bodies compared to other parts of the

channel suggests that during CO_2 injection, the channel centre would act as thief zones allowing the channelling of greater volume of CO_2.

- Furthermore, heterogeneous reservoirs increases sequestration capacity by enhancing the dispersion of flow paths. The lower porosity and potentially lower permeability at the upper part of the channel sandstone bodies (i.e., channel top) may prevent injected CO_2, from moving upward, causing it to move laterally. This, in turn, will improve the overall reservoir contact between the CO_2 plume and the formation, and ultimately enhance dissolution and residual trapping of injected CO_2.
- The crevasse splay facies, on the other hand, form poor reservoirs due to their low porosity (ranging from 1.7%-2.3%). The low porosity is due to their higher amounts of clay/ductile grains and carbonate cement with values ranging from 5.3%-28.4% and 8%-28.4%, respectively. The associated floodplain facies are non-reservoirs and occur as laterally extensive element within the fluvial succession. This suggests that during CO_2 injection, the floodplain facies would act as barriers to fluid flow and as internal seals.

Chapter 6: Discussion, conclusion, and future work

6.1 Discussion

This chapter aims to synthesise the main findings of this thesis. Chapter specific discussions of the main findings are contained within chapter 3, 4 and 5. Here, a general overview of the main findings addressing the main aim and objectives of the research is provided. The key findings of this research are summarised in figures 6.1 and 6.2.

6.1.1 Facies control on fluvial reservoir quality

As demonstrated in chapters 3 to 5, the fundamental factor controlling reservoir quality in the Skagerrak Formation, St Bees Sandstone Formation and Buntsandstein facies is depositional facies. The main lithologies in these Formations are sandstones and mudstones; these comprise of seven to eleven lithofacies which are grouped into three facies associations: (1) fluvial channel, (2) splay (or sheetflood) and (3) floodplain, palaeosols or lake facies associations. Of the three facies associations, the channel facies which is predominantly sandstone, has the best reservoir quality, while floodplain/lake facies have poor reservoir quality (Table 6.1 and figure 6.1).

The main depositional parameters that have influenced the reservoir quality of the sandstones are grain size, clay content and amounts of ductile grains. In all the Formations, coarser-grained sandstones have better reservoir quality due to lower amounts of clay and ductile grains, while finer-grained sandstones have lower reservoir quality due to higher amounts of clay and ductile grains. The variations in grain size, clay content and amounts of ductile grains that resulted in the differences in reservoir quality could be attributed to the variations in depositional energy. The coarser-grained sandstones are interpreted as deposits of a high-energy environment, while the finer-grained sandstones are interpreted as deposits of a low-energy environment (Fig. 6.1).

It is worth noting that the occurrence of better reservoir quality in the channel sandstones of the deeply buried and diagenetically complex Skagerrak Formation compared to other facies in the same Formation, indicates that depositional facies maintains a primary control on the evolution of reservoir quality from deposition through burial (Bloch and McGowen 1994; Akpokodje et al. 2017).

Table 6.1: Comparison of porosity and permeability data for the Skagerrak, Buntsandstein facies (Riba de Santiuste) and St Bees Sandstone Formations based on facies associations. Values in black are thin section (or optical) porosities; values in red are helium porosities.

	Facies associations								
Triassic Formations	**Channel**			**Splay/sheetflood**			**Floodplain, lakes and palaeosol**		
		Por (%)	Kh (mD)		Por (%)	Kh (mD)		Por (%)	Kh (mD)
Skagerrak Fm. (*Age: Anisian-Carnian*)	min	0 (2.3)	0.01	min	0 (6.5)	0.004	min	0 (3.7)	0.004
	max	23.9 (26.7)	1150	max	21 (23.5)	166	max	4 (11.5)	0.51
	avg.	**11.5 (21.6)**	**219.8**	avg.	**3.5 (14.6)**	**9.2**	avg.	0.4 **(7.3)**	**0.1**
Riba de Santiuste Sst. (*Age: Olenekian*)	min	1.3	-	min	1.7	-	min	0	-
	max	19.0	-	max	2.3	-	max	0	-
	avg.	**7.7**	-	avg.	**1.9**	-	avg.	**0**	-
St Bees Sandstone Fm. (*Age: Induan-Smithian*)	min	0.3	-	min	0.3	-	min	0	-
	max	24	-	max	8.7	-	max	1.6	-
	avg.	**12.2**	-	avg.	**2.4**	-	avg.	**0.7**	-

6.1.2 Diagenetic control on fluvial reservoir quality

Another important control on reservoir quality of fluvial sandstones in this study is diagenesis. The main diagenetic processes in the investigated sandstones are compaction and cementation. However, petrographic observations and plots of porosity loss due to compaction (COPL) and cementation (CEPL) showed that mechanical compaction is the main driver for porosity loss in the sandstones (Fig. 3.12, 4.12a and 5.20). It is worth noting that depositional facies play a fundamental role in the diagenetic evolution of the sandstones. Sandstones with higher amounts of clays and ductile grains have a higher degree of compaction, while those containing lower amounts of clays and ductile grains have a lower degree of compaction, and consequently better reservoir quality than the former. This supports the assertion of other workers that clay and ductile grains enhance compaction and porosity loss in sandstones during burial (Paxton et al. 2002; Morad et al. 2010; Lawan et al. 2021; Yan et al. 2022).

The most common and important diagenetic cements in all the investigated sandstones are quartz and carbonate cements. Quartz cement degrades reservoir quality by occluding pore spaces and is commonly formed during mesodiagenesis at around 70-80°C as a result of chemical compaction (or pressure dissolution) along grain contacts (Bjørlykke and Egeberg 1993; Walderhaug 1994a; Ajdukiewicz and Lander 2010; Oye et al. 2018). In this study, quartz cement volume from thin-section point counts is <10% with an average value of 1.7-3.2% in all the investigated sandstones. This could be attributed to the presence of clay (and hematite) coats that inhibited quartz cementation. Based on petrographic and SEM-EDX observations, the authigenic clay coat in the Skagerrak Formation sandstones is mainly chlorite, whereas illite and mixed-layer illite/smectite are dominant in the St Bees and Riba De Santiuste sandstones. The clay coats have a tangentially arranged root zone that is overlain by a layer that is occasionally perpendicular or near-perpendicular to the grain surface (Fig. 3.13f- h). The tangential morphology of the clay coats indicates that the clay coats were emplaced by mechanical infiltration and are of detrital origin (Matlack et al. 1989; Moraes and De Ros 1990). Detrital clay coats are often interpreted as precursors of authigenic clay coats in deeply buried sandstones. During burial diagenesis, increase in temperature results in recrystallization of detrital clays to authigenic clays. SEM-EDX analysis suggests that the authigenic clay coats in the investigated sandstones from the Skagerrak Formation, St Bees and Riba De Santiuste originated from the diagenetic transformation of smectite which is a common detrital clay in fluvial sands deposited in arid to semi-arid environments. Carbonate cement also degrades the reservoir quality of the sandstones by filling pore spaces. However, they are localized and tend to the more abundant in channel bases (Fig. 6.2) and some crevasse splay sandstones.

6.1.3 Clay coatings and deep reservoir quality: controls on clay coat effectiveness

In the studied Skagerrak Formation sandstones, chlorite clay coats played an important role in porosity preservation through the inhibition of quartz cementation (chapter 3). Despite their great burial depths and temperatures of over 3200 m and 150°C respectively, the sandstones have porosity and permeability as high as 26% and 1150 mD, respectively. Although clay coats inhibit quartz cementation and help preserve reservoir quality in deeply buried sandstones, its effectiveness is a function of its completeness of coverage on detrital grain surfaces. Accurate prediction of clay coat enhanced deep reservoir quality requires an understanding of the controls on clay coat coverage. In this research, detailed quantification of clay coats coverage in 23 selected Skagerrak Formation sandstones, suggest that grain size and clay volume, both of which are controlled by facies and depositional energy, have a major effect on clay coat coverage. Bloch et al. (2002), in their study of marine sandstones, ascribed higher clay coat coverage to coarser-grained sandstones and lesser clay coat coverage to finer-grained sandstones. On the contrary, our study of fluvial Skagerrak sandstones shows that finer-grained sandstones have better clay coat coverage than coarser-grained sandstones. This observation is consistent with those of other studies where clay coat coverage has been shown to increase with decreasing grain size (Ajdukiewicz et al. 2010; Wooldridge et al. 2017b). Furthermore, our study reveals a positive correlation between the volume of clay (mostly in form of coatings) and clay coat coverage. Sandstones with 5 to 10% clay coat volume have higher clay coat coverage (>50% and up to 98%) while sandstones with <5% clay coat volume have lesser clay coat coverage (<50%). Variations in grain size and clay coat volume in these sandstones could be linked to the depositional energy of the fluvial environment. Low energy fluvial channel environments are characterised by finer sand grains and high volume of suspended clays that infiltrates sand deposits to form clay coats. On the other hand, high energy environments are characterised by coarser grains and lesser volume of suspended sediments. This implies that the finer-grained, channel sandstones containing higher clay coat volume (5-10%) in the Skagerrak Formation were deposited in a low energy environment, while the coarser-grained channel sandstones containing lower clay coat volume (<5%) were deposited in a high energy environment (Fig. 6.1). Also, the lower clay coat coverage in the coarser-grained, high-energy channel sandstones may be due to the high degree of abrasion coarser grains are exposed to during transport, leading to the near or complete removal of clay coats (Ajdukiewicz et al. 2010; Wooldridge et al. 2019a; Verhagen et al. 2020).

In summary, our study shows that in fluvial environment, clay coat coverage increases with decreasing grain size, and increases with increasing clay coat volume. Finer-grained, low-energy fluvial channel (LEFC) sandstones of the Skagerrak Formation have better clay coat coverage than the coarser-grained, high-energy fluvial channel (HEFC) sandstones (Fig. 6.1). The higher clay coat coverage in the finer-grained Skagerrak sandstones resulted in less quartz cement volume, whereas the lower coverage in their coarser-grained counterparts resulted in greater quartz cement volume. Although the coarser-grained sandstones have better reservoir quality than the finer-grained sandstones despite their lower clay coverage, they are susceptible to further quartz cementation and porosity loss when buried to ultra-deep HPHT environments. On the other hand, the finer-grained sandstones with higher clay coverage stand a better chance of preserving porosity in ultra-deep HPHT environments (Fig. 3.24).

6.1.4 Reservoir quality distribution in fluvial channel bodies and the main controls.

As revealed in this study and other previous works, channel sandstones constitute the best reservoirs in fluvial environments. Defining channel body geometries and understanding how reservoir properties vary within them, as well as the main controls are essential for developing robust three-dimensional (3D) fluvial reservoir models. In this research, two end members of channel sandstone bodies, as described by Hirst (1992) and Friend et al. (1979) were identified from outcrops: ribbon-shaped and sheet sandstones.

The sandstones of Riba de Santiuste are dominated by ribbon-shaped channel sandstones, while the St Bees sandstones are dominated by channelised sheet sandstones. In both end members, reservoir quality (in this case, porosity) varies across the channel bodies, with the channel centre having the highest porosity and other sections (top, base and wings) having lower porosity. Our study shows that the variations in reservoir quality in the channel bodies is due to variations in the distribution of facies-controlled parameters (i.e., grain size, clay content and ductile grains) and diagenetic alterations (mainly compaction and carbonate cementation). The highest porosity (i.e., sweet spot) at the centre of the channel bodies is due to the lower amounts of clay/matrix and ductile grains which resulted in lesser compaction. Conversely, the lower porosity at the top, base and wings of the channel bodies is due to the greater compaction caused by higher amounts of clay and ductile grains characterising these sections (e.g., Figs 4.19, 5.21 and 6.2).

Another factor responsible for the variations in reservoir quality in the fluvial channel bodies is carbonate cements. In fluvial channels, carbonate intraclasts from the erosion of floodplain calcretes or dolocretes are preferentially deposited at the base as channel lags. The dissolution of these carbonate intraclasts and their re-precipitation as carbonate cements commonly result in their abundance in this part of the channel compared to other parts. Thus, the abundance of carbonate cements in the basal part of the studied channel bodies is also responsible for the lower porosity recorded in this section (e.g., Figs 4.19, 5.21 and 6.2).

6.1.5 Cross versus longitudinal fluvial channel sections

Very few outcrops allow for the investigation of spatial variations in porosity and permeability in fluvial channel bodies in both cross-section and longitudinal profiles. Unlike channel cross-sections, the longitudinal sections (also known as reach lengths) are rarely exposed. As a result, the majority of fluvial outcrop studies rely on channel cross-sections. Furthermore, the majority of fluvial outcrop data are derived from channel cross-sections, making it difficult to accurately model channel reach lengths in subsurface reservoirs. In this study (chapter 4), the outcropping St Bees Sandstone Formation along the coast of West Cumbria, UK provided an excellent opportunity to study the spatial variations in reservoir properties and the main controls in both cross-section and longitudinal profiles. Reservoir modellers currently believe that there is a big reservoir property difference between the cross-section and longitudinal profiles of channel sandstone bodies. However, in this study, a comparison of the cross-section and longitudinal profiles (~7 km long) of the multi-stacked braided fluvial channel succession at St Bees Head has revealed that in a braided fluvial system, there is no major difference between the cross-section and longitudinal profiles of channel sandstone bodies in terms of sedimentology, stacking patterns, mineralogy, texture, and distribution of diagenetic alterations. First, in both profiles, the sandstones are laterally and vertically stacked with a general lack of mud and floodplain fines. Second, the sandstones in both profiles are similar in composition; they are mostly arkosic. Third, the distribution of grain size in both profiles is comparable. The average grain size in the cross-section profile is 0.165 mm (lower fine sand) and 0.162 mm (lower fine sand) in the longitudinal profile. Fourth, porosity distribution is comparable in both profiles. Porosity varies from 0% to 24% (avg. 12.7%) in the cross-section profile, and from 0.6% to 23.3% (avg. 12%) in the longitudinal profile. In both profiles, the sweet spot (i.e., highest porosity) is at the centre of the channel. Fifth, carbonate cements are preferentially abundant at the base of the channel in both profiles, and therefore contribute to the lower porosity in this section of the channel. In addition, the occurrence of white siltstones/silty sandstones (facies Sws) interpreted as deposits of low energy or channel abandonment is a common feature in both profiles, especially at the top of individual channel bodies. This facies is laterally restricted in both profiles and is distinguished by finer grain size, high matrix/ductile grains and very low to negligible porosity.

The similarity in stacking pattern, mineralogy, texture, porosity, and distribution of diagenetic alterations in the cross-section and longitudinal profiles suggests that the channel sandstones in both profiles have the same style of sedimentation and provenance. In addition, the similarity in the grain size distribution along the reach length (about 7 km) suggests that the depositional energy within the channel is uniform throughout that length. Generally, in the high net to gross, multi-stacked braided fluvial channel sequences at West Cumbria (e.g., Fleswick Bay), other than at the bounding surfaces, there is no major difference in grain size, diagenetic alterations, cement types and overall porosity, whether you are looking at the cross-section or longitudinal profiles. This therefore implies that during the modelling of braided fluvial reservoirs, reservoir properties (i.e., porosity and permeability) derived from channel cross-sections can also be used to model longitudinal sections, depending on the preserved reach length and net-to-gross of the fluvial system (Fig. 4.19).

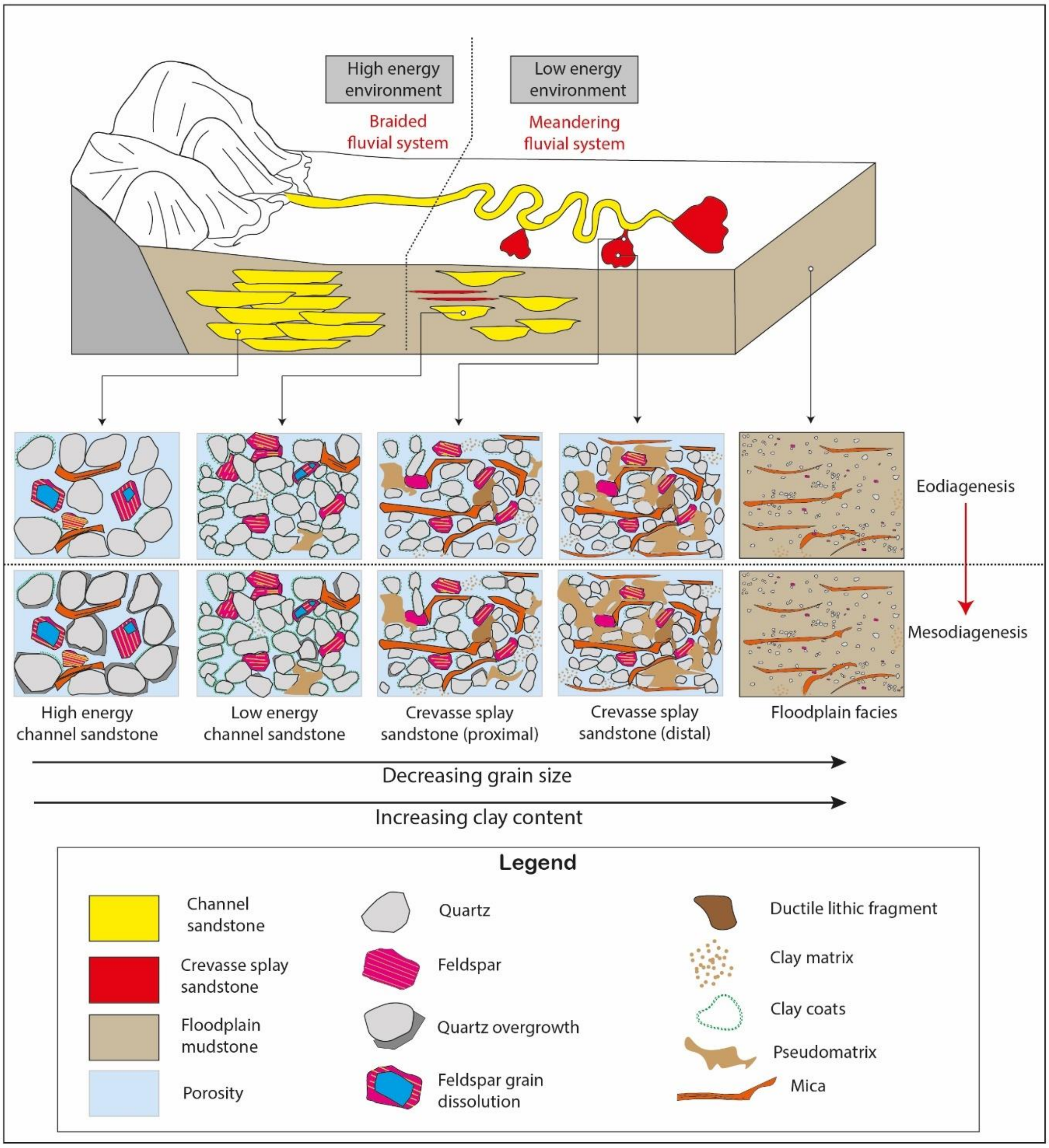

Figure 6.1: Schematic summary diagram showing the influence of depositional facies (including grain size and clay content) on reservoir quality and diagenetic evolution of fluvial deposits. The diagram illustrates that channel sandstone facies constitute the best reservoirs in a fluvial environment (due to their coarser grain size and lower clay content), while floodplain facies (mudstone) are poor reservoirs. As you move from high energy environment to low energy environment in a fluvial system, there is a general decrease in grain size and increase in clay content, and consequently, overall reduction in reservoir quality. However, within the channel facies, reservoir quality varies as a function of grain size and clay content. Generally, high energy channel sandstones have better reservoir quality than low energy channel sandstones due to their coarser grain sizes and minimal or lack of clay minerals. It is worth noting that some crevasse splay sandstones could also form good reservoirs. The diagram demonstrates that as you transit from the proximal section of crevasse splays towards the distal section, there is a degradation in reservoir quality (resulting from decreasing grain size and increasing clay content). The good to moderate reservoir quality found in some crevasse splay sandstones in this study could be linked to the proximal section, while those with poorer reservoir quality could be linked to the distal section. In addition, the diagram demonstrates the importance of the extent of clay coat coverage in inhibiting quartz cementation. Higher clay content/clay coat coverage results in low quartz cement and is found to be associated with low energy channel sandstone and some crevasse splay sandstones.

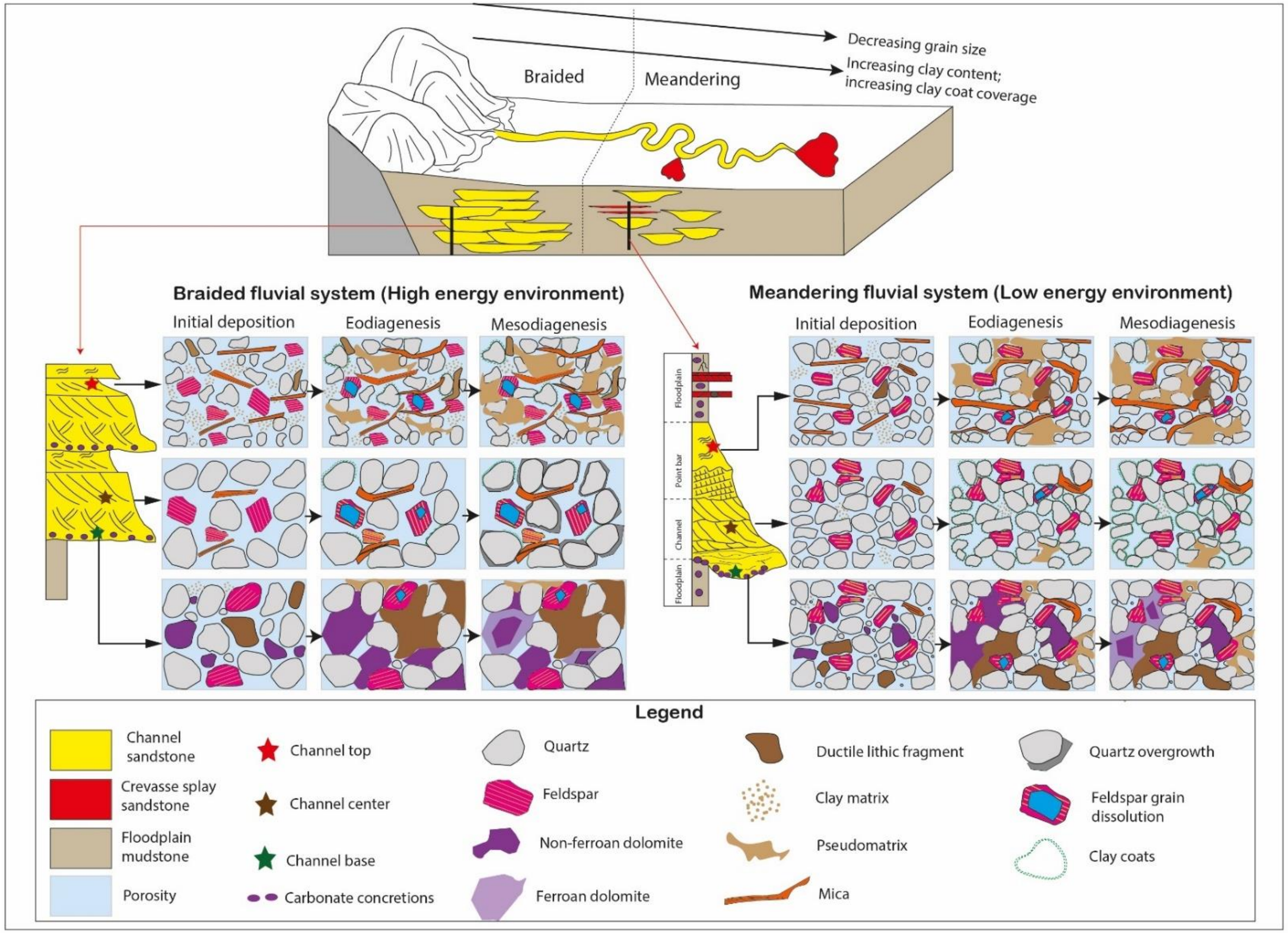

Figure 6.2: Schematic summary diagram illustrating the petrography and distribution of diagenetic alterations within channel sandstone bodies in a high energy and low energy environment. In addition, the diagram shows that the sweet spot (i.e., highest porosity) in channel bodies is found in channel centres due to lesser amounts of clays and ductile grains. It also shows that carbonate cement is preferentially abundant at the base of channels, thus contributing to the lower porosity or total destruction of porosity in the part of the channel.

6.2 Wider implications for carbon capture and storage (CCS)

The storage of CO_2 in subsurface formations has been recognised as one of the most effective ways of reducing greenhouse gas emissions (Metz et al. 2005; Bui et al. 2018; Ali et al. 2022). Potential storage sites are depleted oil and gas fields, deep saline aquifers and unmineable coal beds. While some of these storage sites are already being used for CCS (e.g., Utsira Formation) (Ringrose 2018; Raza et al. 2019), others are under appraisal (e.g., Sherwood Sandstone Group and Bunter Sandstone Formation) (Gluyas and Bagudu 2020; Alshakri et al. 2022; Marsh et al. 2022). A suitable site for CCS must be deeper than 800 m to keep the injected CO_2 in a supercritical state, have adequate porosity and permeability and an effective containment system (i.e., trap or seal) to prevent leakage. At depths > ~800 m, CO_2 forms a supercritical fluid phase (>7.38 MPa and >31.1°C). In this phase, it becomes much denser than gaseous CO_2 but less dense than water, allowing for more efficient use of underground storage space and improved storage security (Bachu 2000; Shafeen et al. 2004; van der Meer et al. 2009). Another important factor to consider when selecting a suitable site for CCS is the feasibility of long-term storage of CO_2 in geological formations over hundreds of thousands of years (Lu et al. 2011; Ajayi et al. 2019). CO_2 can be stored in geological formations via a combination of physical (structural, stratigraphic, and residual) and geochemical (solubility and mineral) trapping mechanisms (Gilfillan et al. 2009; Han et al. 2010; Ajayi et al. 2019; Yanzhong et al. 2020). Several experimental studies have shown that mineral trapping is the most effective mechanism of permanently storing large volumes of CO_2 in the subsurface (Matter and Kelemen 2009; Luquot et al. 2012). In mineral trapping mechanism, the dissolution of CO_2 turns the formation water into a weak acid, triggering a series of chemical reactions with certain minerals in the geologic formation, and converting a fraction of the injected CO_2 to solid carbonate minerals.

The Triassic is one of the main targets for CCS development in several basins around the world. As revealed in this study, the fluvial sandstones of the Triassic Skagerrak Formation, St Bees Sandstone Formation and Buntsandstein facies possess the essential criteria for a safe, long-term storage of CO_2.

<u>Skagerrak Formation</u>: The Skagerrak Formation in the UK Central North Sea is a proven and mature hydrocarbon reservoir, with excellent reservoir quality and a good containment system, making it a suitable candidate for CO_2 storage. In addition, the reservoirs are situated at depths >800 m, the preferable depth to ensure supercritical CO_2 conditions. The Skagerrak Formation

is highly heterogeneous due to the variations in depositional facies and diagenetic alterations (see chapter 3). This heterogeneity has important implications for CCS because it may provide additional trapping capacity to the reservoir. Heterogeneous reservoirs are more effective than homogeneous reservoirs at containing CO_2 (Flett et al. 2007). According to Flett et al. (2007), as heterogeneity increases, the vertical migration of injected CO_2 is inhibited, resulting in increased lateral migration and overall reservoir contact between the plume and the formation. Furthermore, as heterogeneity increases, capillary effects become more prevalent during the buoyant movement of CO_2, resulting in increased dissolution and residual trapping of the injected CO_2 (Bryant et al. 2006). The interbedded mudstone members (Julius, Jonathan, and Joshua) in the Skagerrak Formation could also act as local or internal seals for injected CO_2 and improve its lateral distribution.

St Bees Sandstone Formation: The St Bees Sandstone Formation (SBSF) is the lowermost unit of the Triassic Sherwood Sandstone Group (SSG), an important host to major hydrocarbon reservoirs in the East Irish Sea Basin (EISB), and a major groundwater aquifer in the UK (Yaliz and Chapman 2003; Medici et al. 2018; Scorgie et al. 2021). The studied SBSF outcrop along the Cumbrian coast, NW England is primarily made up of high net-to-gross, vertically, and laterally amalgamated channel sandstone bodies deposited in a braided fluvial environment. From petrographic analysis, the outcrop sandstone samples have good porosity as high as 24%, making it a potential candidate for CO_2 storage. A subsurface equivalent/analogue of the SBSF outcrop is found in the Corrib gas Field, Slyne Basin, offshore west of Ireland (Dancer et al. 2005). In the Corrib Field, the SSG is dominated by high net to gross channel sandstones of braided fluvial origin with average porosities ranging from 4.9% to16.9% (per well). Typical average permeability is 15.2 mD but could be as high as 736 mD in some places (Dancer et al. 2005). The occurrence of favourable porosity and permeability and accumulation of hydrocarbon in the SSG of the EISB and other Irish Basins indicates that the SSG is a potential CO_2 storage site. In addition to the favourable reservoir quality of the SSG, the thick and very fine-grained Mercia Mudstone Group (MMG) overlying the SSG could serve as a potential seal or trap for injected CO_2.

As observed in the studied SBSF outcrop, the main heterogeneities with possible implications for subsurface storage of CO_2 are represented by: (1) subtle variations in grain size, (2) presence of laterally restricted, less porous white siltstone/silty sandstone at the top of individual channel bodies and (3) abundance of carbonate cements at the base of channel bodies within the fluvial succession. The variation in grain size within and between the sandstone bodies would result in porosity and permeability variations and in turn, uneven injection of CO_2 in the reservoir (Shepherd 2009). The high permeability zones within the fluvial succession would act as thief zones, allowing CO_2 to migrate quickly and preferentially along these zones during injection. The laterally restricted, less porous white siltstones/silty sandstones distributed spatially and temporally in the fluvial succession may act as flow baffles, preventing or slowing vertical migration and encouraging injected CO_2 to migrate laterally within the sandstone reservoir. This, in turn, would improve the retention, residual trapping, and dissolution of CO_2 plumes in the reservoir (Gibson-Poole et al. 2008; Teletzke and Lu 2013; Wethington et al. 2022). The abundance of carbonate cements at the base of the individual channel bodies within the fluvial succession could constitute baffles or barriers to fluid flow or even compartmentalise the reservoirs if they are laterally extensive.

Buntsandstein facies: The outcropping fluvial sandstones at Riba de Santiuste is part of the Buntsandstein facies, which has been identified as one of the promising sites for CO_2 storage in the Spanish Basins (Suárez et al. 2009; Pueyo et al. 2012; Mediato et al. 2017). As revealed in this study (chapter 5), the Riba de Santiuste sandstones have good porosity ranging from 3% to 19% (avg.: 8.9%) and potentially good permeability, making the Buntsandstein facies a potential site for CO_2 storage. Overlying the Buntsandstein facies are the Muschelkalk and Keuper facies which serve as regional seals in the basins. The presence of a regional seal or cap rock also makes the Buntsandstein facies a potential reservoir for CO_2 storage. The fluvial architecture at Riba de Santiuste has a major implication for CO_2 storage. The studied section which falls within the Mid Triassic Buntsandstein facies comprises of low net-to-gross fluvial reservoirs. The reservoirs are made up of ribbon-shaped channel bodies (single-storey and multistorey/multilateral) which are interbedded with crevasse splays and thick floodplain fines (mudstone/siltstone). The isolated and low net-to-gross nature of the channel bodies suggests a lack of or low degree of connectivity between the channel bodies in the area. As a result, a large number of injection wells may be required for large-scale CO_2 geological storage in low net-to-gross fluvial systems. However, the positive implication is that the thick, interbedded floodplain mudstone/siltstone may act as flow barriers, allowing a large volume of injected CO_2 to be trapped (via residual trapping mechanism) before reaching the main reservoir-seal interface (i.e., the Muschelkalk facies).

Mineral trapping is the most secure and stable mechanism for ensuring long-term geological storage of CO_2 (Munz et al. 2012; Yang et al. 2017). Understanding the detrital and diagenetic mineralogy of the geological formation is critical, as it has a substantial impact on the long-term fate of injected CO_2 (Rochelle et al. 2004). For example, Ca-rich feldspars could react with dissolved CO_2 to precipitate calcite (Gaus 2010; Yanzhong et al. 2020) while K- and Na-rich feldspar could react with injected CO_2 to form dawsonite (Johnson et al. 2001; Rochelle et al. 2004; Worden 2006; Gaus 2010; Yu et al. 2020). Furthermore, the dissolution of chlorite in sandstones can result in the permanent trapping of CO_2 by releasing cations (iron and magnesium) that would react with dissolved CO_2 to precipitate siderite and dolomite (Gaus 2010). In general, the sandstones of the Triassic Skagerrak Formation, St Bees Sandstone Formation and Riba de Santiuste are arkosic in composition and contain Fe- and Mg-rich diagenetic clay minerals such as chlorite and illite-smectite, making them potential sites for mineral trapping, and as a result, CO_2 storage.

6.3 Conclusions

1. The reservoir quality of the fluvial sandstones from the Triassic Skagerrak Formation, St Bees Sandstone Formation, and Buntsandstein facies (Riba de Santiuste) is primarily controlled by depositional facies and its associated parameters (e.g., grain size and clay content/ductile grains), and secondarily by diagenesis (compaction and cementation).
2. Channel facies constitute the best reservoirs due to their coarser grain sizes and lower clay content. Floodplain facies constitute poor to non-reservoirs and represent baffles or barriers to fluid flow.
3. Although channel facies (or bodies) form the best reservoir, reservoir quality varies between and within the channel sandstone bodies, due to differences in grain size, clay content and diagenetic alterations. The highest porosity (and permeability) is generally associated with the channel centre due to the lower amounts of clay and ductile grains compared to other sections (i.e., top, base and wings).
4. Porosity loss in the sandstones is primarily due to mechanical compaction, which can be linked to depositional facies. Sandstones with greater amounts of clay/ductile grains have higher compaction while those with lesser amounts of clay/ductile grains have lesser compaction.
5. Carbonate cements (predominantly dolomite) of early diagenetic origin, are important cement in all the sandstones analysed. In the channel sandstone bodies, they are more abundant at the basal section and contributed to the low or near destruction of porosity in this part of the channel.
6. The presence of authigenic clay coatings (such as chlorite, illite, and illite-smectite) has inhibited quartz cementation and helped preserve reservoir quality in all the sandstones

analysed. For example, in the Skagerrak Formation sandstones, chlorite clay coats have inhibited extensive quartz cementation and helped preserve exceptional reservoir quality despite burial depths and temperatures of over 3200 m and 150°C, respectively.

7. As observed in the Skagerrak Formation sandstones, the extent of clay coat coverage, which is the primary determinant of clay coat effectiveness is related to depositional facies, grain size and clay coat volume. Higher clay coat coverage (70-98%) is generally associated with finer-grained sandstones containing 5-10% clay (in form of coatings) while lesser clay coat coverage (<50%) is found in coarser-grained sandstones with less than 5% clay (in form of coatings).
8. As carbon capture and storage (CCS) technology becomes more widely accepted as a viable tool for mitigating climate change and transitioning to a low-carbon economy, the importance of accurately characterising subsurface reservoirs cannot be overstated. As revealed in this study, the finding of suitable reservoirs for the subsurface storage of CO_2 requires an adequate understanding of depositional facies including grain size, clay content and detrital/diagenetic composition, as they have a major impact on the diagenesis and reservoir quality of sandstones, and long-term fate of CO_2 storage.

6.4 Suggestions for future work.

Source (s) of chlorite coats in the Skagerrak Formation sandstones

In this study, the chlorite coats in the Skagerrak Formation sandstones are interpreted to form from the recrystallization of detrital smectite clay emplaced via mechanical infiltration. However, some samples with dissolved igneous lithic grains were also observed. If these grains were mafic volcanics, then they may have in addition to smectite clays served as a possible source of early diagenetic chlorite. Detailed study on relationship between igneous lithic fragments and chlorite clay coats should be conducted to further affirm the possible sources of chlorite clay coats in the Skagerrak Formation sandstones.

Quantification of flow characteristics

This study has shown that outcrop-based study can be used to understand porosity distribution in deeply buried sandstone bodies. However, lack of permeability data has hindered the understanding of fluid flow in these outcrop data. It is therefore suggested that permeability data should be collected and incorporated into future work. This can be done using a portable hand-held mechanical mini permeameter for rapid in-situ permeability measurement at outcrop and on fresh hand specimens (Chandler et al. 1989). The inclusion of permeability data will help us understand how permeability varies spatially in channel sandstone bodies and further confirm the connectivity of some the sandstone bodies.

Geochemical and storage modelling

The Triassic Skagerrak Formation, St Bees Sandstone Formation, and Buntsandstein facies (Riba de Santiuste) have been identified as potential targets for carbon capture and storage. The next critical step is to experimentally investigate or simulate the potential mineralogical evolution of the sandstones upon injection with brine saturated with supercritical CO_2 at in situ HPHT reservoir conditions. The results will help us understand or predict the long-term CO_2 storage potential of these sandstones.

Roles of microbes and biofilms in Triassic reservoirs and potential implications for injectivity

As demonstrated in this study and other studies, clay coats play a critical role in the preservation of reservoir quality by inhibiting quartz cementation. The processes of adhesion between sand and silt/clay-grade particles, however, remain uncertain. Recent studies have demonstrated that the attachment of clay materials to sand grain surfaces can be linked to microbial activity (Wooldridge et al. 2017a; Duteil et al. 2020; Charlaftis 2021). Microorganisms can form supracellular structures, called biofilms, that aid in the adhesion of sand and clay minerals in sedimentary environments. These biofilms are made up of surface-associated microbial cells embedded in hydrated extracellular polymeric substances (EPS). Experimental studies have shown that the interaction of EPS with the basal surface and particle edge sites of clay mineral platelets can result in the formation of detrital clay coats which are precursors for authigenic clay coats. Microbial activity occurs in all near-surface sediment (Worden et al. 2018a). However, recent investigations of biofilm-mediated clay-coat formation have often focused on modern marginal marine/estuary sediments, with no major focus on fluvial sediments, despite their importance as major hosts of hydrocarbon/groundwater resources and potential storage sites for CO_2. Experimental modelling and laboratory experiments using hydrothermal reactors to model the roles of microbes and biofilms in fluvial sediments can expand our knowledge of fluvial diagenesis and clay coat authigenesis/distribution, and lead to better developed reservoir quality predictive models. In addition, several studies have reported that microbial activity in subsurface reservoirs can influence storage by lowering injectivity (due to the pore-clogging tendency of biofilms), or precipitating carbonate and/or other minerals such as framboidal pyrite (Worden et al. 2018a; Heinemann et al. 2021). Understanding the impact of microbes and biofilms on injectivity in fluvial reservoirs is thus crucial for the effective storage of CO_2.

Geomechanical assessment

The injection of large amounts of CO_2 into subsurface geological formations (e.g., depleted oil and gas reservoirs, and deep saline aquifers) may pose a number of geomechanical risks (due to the unavoidable pore pressure build up), including caprock failure, reactivation of existing faults, poroelastic response of rock and well integrity loss (Goodarzi et al. 2015; Bai et al. 2016; Pan et al. 2016; Song et al. 2022). The pressure build up within the reservoir/aquifer might lead to slip and dilation along pre-existing faults and fracture zones. In addition, CO_2 injection may introduce new hydraulic fractures within or near the injection zone. These fractures may propagate upwards into the lower caprock and may propagate further through the upper caprock (Ringrose et al. 2013; Pan et al. 2016). The aforementioned risks may lead to undesirable environmental concerns such as CO_2 leakage to the surface, induced seismicity, surface uplift and contamination of shallow drinking water (Keating et al. 2010; Rutqvist et al. 2010). Depleted hydrocarbon reservoirs are more prone to CO_2 leakage than saline aquifers. This is because the latter possess wells whose structural integrity might have deteriorated over time (Ajayi et al. 2019). As revealed in this research, the studied Triassic fluvial sandstones are potential sites for CO_2 storage due to their favourable reservoir quality and the presence of overlying seal or caprock. However, a detailed geomechanical assessment of the reservoirs/aquifers and the associated seal/caprock prior to CO_2 injection is suggested to ensure optimal design of the CCS process, safe operation and long-term storage.

References

Aagaard, P., Jahren, J., Harstad, A., Nilsen, O., and Ramm, M. 2000. Formation of grain-coating chlorite in sandstones. Laboratory synthesized vs. natural occurrences. *Clay Minerals*, ***35***(1), 261-269.

Aase, N.E., Bjørkum, P.A., and Nadeau, P.H. 1996. The effect of grain-coating microquartz on preservation of reservoir porosity. *AAPG Bulletin*, ***80***, 1654-1673.

Aase, N.E., and Walderhaug, O. 2005. The effect of hydrocarbons on quartz cementation: diagenesis in the Upper Jurassic sandstones of the Miller Field, North Sea, revisited. *Petroleum Geoscience*, ***11***, 215-223.

Abercrombie, H.J., Hutcheon, I.E., Bloch, J.D., and Caritat, P.d. 1994. Silica activity and the smectite-illite reaction. *Geology*, ***22***(6), 539-542.

Ajayi, T., Gomes, J.S., and Bera, A. 2019. A review of CO2 storage in geological formations emphasizing modeling, monitoring and capacity estimation approaches. *Petroleum Science*, ***16***(5), 1028-1063.

Ajdukiewicz, J.M., and Lander, R.H. 2010. Sandstone reservoir quality prediction: The state of the art. *AAPG Bulletin*, ***94***, 1083-1091, https://doi.org/10.1306/intro060110.

Ajdukiewicz, J.M., and Larese, R.E. 2012. How clay grain coats inhibit quartz cement and preserve porosity in deeply buried sandstones: Observations and experiments. *AAPG Bulletin*, ***96***, 2091-2119, https://doi.org/10.1306/02211211075.

Ajdukiewicz, J.M., Nicholson, P.H., and Esch, W.L. 2010. Prediction of deep reservoir quality using early diagenetic process models in the Jurassic Norphlet Formation, Gulf of Mexico. *AAPG Bulletin*, ***94***, 1189-1227, https://doi.org/10.1306/04211009152.

Akpokodje, M., Melvin, A., Churchill, J., Burns, S., Morris, J., Kape, S., Wakefield, M., and Ameerali, R. 2017. Regional study of controls on reservoir quality in the Triassic Skagerrak Formation of the Central North Sea. *Geological Society, London, Petroleum Geology Conference series*, ***8***, 125-146, https://doi.org/10.1144/PGC8.29.

Al-Juboury, A.I., Hussain, S.H., McCann, T., and Aghwan, T.A. 2020. Clay mineral diagenesis and red bed colouration: A SEM study of the Gercus Formation (Middle Eocene), northern Iraq. *Geological Journal*, ***55***(12), 7977-7997.

Alcalde, J., Heinemann, N., James, A., Bond, C.E., Ghanbari, S., Mackay, E.J., Haszeldine, R.S., Faulkner, D.R., Worden, R.H., and Allen, M.J. 2021. A criteria-driven approach to the CO2 storage site selection of East Mey for the acorn project in the North Sea. *Marine and Petroleum Geology*, ***133***, 105309.

Alexander, J. 1993. A discussion on the use of analogues for reservoir geology. *Geological Society, London, Special Publications*, ***69***(1), 175-194.

Ali, M., Jha, N.K., Pal, N., Keshavarz, A., Hoteit, H., and Sarmadivaleh, M. 2022. Recent advances in carbon dioxide geological storage, experimental procedures, influencing parameters, and future outlook. *Earth-Science Reviews*, ***225***, 103895, https://doi.org/10.1016/j.earscirev.2021.103895.

Ali, S.A., Clark, W.J., Moore, W.R., and Dribus, J.R. 2010. Diagenesis and reservoir quality. *Oilfield Review*, ***22***, 14-27.

Alkhasli, S., Zeynalov, G., and Shahtakhtinskiy, A. 2022. Quantifying occurrence of deformation bands in sandstone as a function of structural and petrophysical factors and their impact on reservoir quality: an example from outcrop analog of Productive Series (Pliocene), South Caspian Basin. *Journal of Petroleum Exploration and Production Technology*, 1-19.

Allen, J. 1978. Studies in fluviatile sedimentation: an exploratory quantitative model for the architecture of avulsion-controlled alluvial suites. *Sedimentary Geology*, ***21***(2), 129-147.

Allen, P.A., and Allen, J.R. 2005. *Basin Analysis: Principles and Applications, 2nd edn.* Blackwell Publising, Oxford.

Alshakri, J., Hampson, G.J., Jacquemyn, C., Jackson, M.D., Petrovskyy, D., Geiger, S., Silva, J.D.M., Judice, S., Rahman, F., and Costa Sousa, M. 2022. A Screening Assessment of the Impact of Sedimentological Heterogeneity on CO2 Migration and Stratigraphic-Baffling Potential: Sherwood and Bunter Sandstones, UK. *Geological Society, London, Special Publications*, ***528***(1), SP528-2022-2034, https://doi.org/10.1144/SP528-2022-34.

Ambrose, W., Lakshminarasimhan, S., Holtz, M., Núñez-López, V., Hovorka, S.D., and Duncan, I. 2008. Geologic factors controlling CO2 storage capacity and permanence: case studies based on experience with heterogeneity in oil and gas reservoirs applied to CO2 storage. *Environmental Geology*, ***54***(8), 1619-1633, https://doi.org/10.1007/s00254-007-0940-2.

Amthor, J.E., and Okkerman, J. 1998. Influence of early diagenesis on reservoir quality of Rotliegende sandstones, northern Netherlands. *AAPG Bulletin*, ***82***(12), 2246-2265, https://doi.org/10.1306/00AA7F04-1730-11D7-8645000102C1865D.

Andrews-Speed, C., Oxburgh, E.R., and Cooper, B. 1984. Temperatures and depth-dependent heat flow in western North Sea. *AAPG Bulletin*, ***68***, 1764-1781, https://doi.org/10.1306/AD461999-16F7-11D7-8645000102C1865D.

Anjos, S., De Ros, L., and Silva, C. 1999. Chlorite authigenesis and porosity preservation in the Upper Cretaceous marine sandstones of the Santos Basin, offshore eastern Brazil. *Clay mineral cements in sandstones*, 289-316, https://doi.org/10.1002/9781444304336.ch13.

Anjos, S., De Ros, L., and Silva, C. 2003. Chlorite authigenesis and porosity preservation in the Upper Cretaceous marine sandstones of the Santos Basin, offshore eastern Brazil. In Worden, R.H. and Morad, S. (eds) Clay Mineral Cement in Sandstones, Int. Assoc. Sedimentol. Spec. Publ, **34**, 291-316.

Antonellini, M., and Aydin, A. 1995. Effect of faulting on fluid flow in porous sandstones: geometry and spatial distribution. *AAPG Bulletin*, ***79***(5), 642-671, https://doi.org/10.1306/8D2B1B60-171E-11D7-8645000102C1865D.

Antonellini, M.A., Aydin, A., and Pollard, D.D. 1994. Microstructure of deformation bands in porous sandstones at Arches National Park, Utah. *Journal of structural geology*, ***16***(7), 941-959, https://doi.org/10.1016/0191-8141(94)90077-9.

Arche, A., and López-Gómez, J. 1996. Origin of the Permian-Triassic Iberian basin, central-eastern Spain. *Tectonophysics*, ***266***(1-4), 443-464, https://doi.org/10.1016/S0040-1951(96)00202-8.

Aretz, A., Bär, K., Götz, A.E., and Sass, I. 2016. Outcrop analogue study of Permocarboniferous geothermal sandstone reservoir formations (northern Upper Rhine Graben, Germany): impact of mineral content, depositional environment and diagenesis on petrophysical properties. *International Journal of Earth Sciences*, ***105***(5), 1431-1452.

Arthaud, F., and Matte, P. 1977. Late Paleozoic strike-slip faulting in southern Europe and northern Africa: Result of a right-lateral shear zone between the Appalachians and the Urals. *Geological Society of America Bulletin*, ***88***(9), 1305-1320, https://doi.org/10.1130/0016-7606(1977)88<1305:LPSFIS>2.0.CO;2

Arthurton, R., and Hemingway, J. 1972. The St. Bees Evaporites—a carbonate-evaporite formation of Upper Permian age in West Cumberland, England. *Proceedings of the Yorkshire Geological Society*, ***38***(4), 565-592.

Audley-Charles, M.G. 1970. Stratigraphical correlation of the Triassic rocks of the British Isles. *Quarterly Journal of the Geological Society*, ***126***(1-4), 19-46.

Awdal, A., Suramairy, R., Singh, K., Fabre, G., and Alsop, G.I. 2020. Deformation bands and their impact on fluid flow: Insights from geometrical modelling and multi-scale flow simulations in sandstones. *Journal of structural geology*, ***141***, 104215, https://doi.org/10.1016/j.jsg.2020.104215.

Aydin, A. 1978. Small faults formed as deformation bands in sandstone. *pure and applied geophysics*, ***116***, 913-930.

Aydin, A., Borja, R.I., and Eichhubl, P. 2006. Geological and mathematical framework for failure modes in granular rock. *Journal of structural geology*, ***28***(1), 83-98, https://doi.org/10.1016/j.jsg.2005.07.008.

Azzam, F., Blaise, T., Patrier, P., Abd Elmola, A., Beaufort, D., Portier, E., Brigaud, B., Barbarand, J., and Clerc, S. 2022. Diagenesis and reservoir quality evolution of the Lower Cretaceous turbidite sandstones of the Agat Formation (Norwegian North Sea): Impact of clay grain coating and carbonate cement. *Marine and Petroleum Geology*, 105768, https://doi.org/10.1016/j.marpetgeo.2022.105768.

Bachu, S. 2000. Sequestration of CO2 in geological media: criteria and approach for site selection in response to climate change. *Energy conversion and management*, ***41***(9), 953-970, https://doi.org/10.1016/S0196-8904(99)00149-1.

Bahlis, A.B., and De Ros, L.F. 2013. Origin and impact of authigenic chlorite in the Upper Cretaceous sandstone reservoirs of the Santos Basin, eastern Brazil. *Petroleum Geoscience*, ***19***(2), 185-199, https://doi.org/10.1144/petgeo2011-007.

Bai, M., Zhang, Z., and Fu, X. 2016. A review on well integrity issues for CO2 geological storage and enhanced gas recovery. *Renewable and Sustainable Energy Reviews*, ***59***, 920-926, https://doi.org/10.1016/j.rser.2016.01.043.

Baiyegunhi, C., Liu, K., and Gwavava, O. 2017. Diagenesis and Reservoir Properties of the Permian Ecca Group Sandstones and Mudrocks in the Eastern Cape Province, South Africa. *Minerals*, ***7***, 88, https://www.mdpi.com/2075-163X/7/6/88.

Baker, J.C. 1991. Diagenesis and reservoir quality of the Aldebaran Sandstone, Denison Trough, east-central Queensland, Australia. *Sedimentology*, ***38***, 819-838, https://doi.org/10.1111/j.1365-3091.1991.tb01874.x.

Barclay, S., and Worden, R. 2000. Effects of reservoir wettability on quartz cementation in oil fields. In Worden, R.H. and Morad, S. (eds) Quartz cementation in sandstones: Oxford, Blackwell Science, International Association of Sedimentologists Special Publication, **29**, 103-117.

Barshep, D.V., and Worden, R.H. 2021. Reservoir Quality of Upper Jurassic Corallian Sandstones, Weald Basin, UK. *Geosciences*, ***11***(11), 446, https://doi.org/10.3390/geosciences11110446.

Bauluz, B., Mayayo, M.J., Laita, E., and Yuste, A. 2021. Micro-and Nanotexture and Genesis of Ball Clays in the Lower Cretaceous (SE Iberian Range, NE Spain). *Minerals*, ***11***(12), 1339.

Bayliss, P. 1975. Nomenclature of the trioctahedral chlorites. *The Canadian Mineralogist*, ***13***(2), 178-180.

Beard, D.C., and Weyl, P.K. 1973. Influence of texture on porosity and permeability of unconsolidated sand. *AAPG Bulletin*, ***57***, 349-369.

Beaufort, D., Cassagnabere, A., Petit, S., Lanson, B., Berger, G., Lacharpagne, J., and Johansen, H. 1998. Kaolinite-to-dickite reaction in sandstone reservoirs. *Clay Minerals*, ***33***(2), 297-316.

Beaufort, D., Rigault, C., Billon, S., Billault, V., Inoue, A., Inoué, S., Patrier, P., and Ferrage, E. 2015. Chlorite and chloritization processes through mixed-layer mineral series in low-temperature geological systems–a review. *Clay Minerals*, ***50***, 497-523, https://doi.org/10.1180/claymin.2015.050.4.06.

Bello, A.M., Jones, S., Gluyas, J., Acikalin, S., and Cartigny, M. 2021. Role played by clay content in controlling reservoir quality of submarine fan system, Forties Sandstone Member, Central Graben, North Sea. *Marine and Petroleum Geology*, ***128***, 105058, https://doi.org/10.1016/j.marpetgeo.2021.105058.

Berger, A., Gier, S., and Krois, P. 2009. Porosity-preserving chlorite cements in shallow-marine volcaniclastic sandstones: Evidence from Cretaceous sandstones of the Sawan gas field, Pakistan. *AAPG Bulletin*, ***93***, 595-615, https://doi.org/10.1306/01300908096.

Bernet, M., and Gaupp, R. 2005. Diagenetic history of Triassic sandstone from the Beacon Supergroup in central Victoria Land, Antarctica. *New Zealand Journal of Geology and Geophysics*, ***48***(3), 447-458, https://doi.org/10.1080/00288306.2005.9515125.

Billault, V., Beaufort, D., Baronnet, A., and Lacharpagne, J.-C. 2003. A nanopetrographic and textural study of grain-coating chlorites in sandstone reservoirs. *Clay Minerals*, ***38***, 315-328, https://doi.org/10.1180/0009855033830098.

Bjorkum, P.A. 1996. How important is pressure in causing dissolution of quartz in sandstones? *Journal of Sedimentary Research*, ***66***(1), 147-154, https://doi.org/10.1306/D42682DE-2B26-11D7-8648000102C1865D.

Bjørkum, P.A., Oelkers, E.H., Nadeau, P.H., Walderhaug, O., and Murphy, W.M. 1998. Porosity prediction in quartzose sandstones as a function of time, temperature, depth, stylolite frequency, and hydrocarbon saturation. *AAPG Bulletin*, ***82***(4), 637-648, https://doi.org/10.1306/1D9BC5CF-172D-11D7-8645000102C1865D.

Bjørlykke, K. 2014. Relationships between depositional environments, burial history and rock properties. Some principal aspects of diagenetic process in sedimentary basins. *Sedimentary Geology*, ***301***, 1-14, https://doi.org/10.1016/j.sedgeo.2013.12.002.

Bjørlykke, K., and Egeberg, P. 1993. Quartz cementation in sedimentary basins. *AAPG Bulletin*, ***77***, 1538-1548, https://doi.org/10.1306/BDFF8EE8-1718-11D7-8645000102C1865D.

Bjørlykke, K., and Jahren, J. 2012. Open or closed geochemical systems during diagenesis in sedimentary basins: Constraints on mass transfer during diagenesis and the prediction of porosity in sandstone and carbonate reservoirs. *AAPG Bulletin*, ***96***(12), 2193-2214.

Bloch, S. 1994. Effect of detrital mineral composition on reservoir quality. In Wilson, M.D. (eds) Reservoir quality assessment and prediction in clastic rocks: SEPM Short Course, **30**, 161-182.

Bloch, S., and Helmold, K. 1995. Approaches to predicting reservoir quality in sandstones. *AAPG Bulletin*, ***79***, 97-114.

Bloch, S., Lander, R.H., and Bonnell, L. 2002. Anomalously high porosity and permeability in deeply buried sandstone reservoirs: Origin and predictability. *AAPG Bulletin*, ***86***, 301-328, https://doi.org/10.1306/61EEDABC-173E-11D7-8645000102C1865D.

Bloch, S., and McGowen, J. 1994. Influence of depositional environment on reservoir quality prediction.

Boggs, S. 2006. Principles of sedimentology and stratigraphy: Pearson Prentice Hall. *Upper Saddle River, New Jersey*.

Bonnell, L., Larese, R.E., and Lander, R. 2006b. Porosity preservation by inhibition of quartz cementation: Microquartz versus hydrocarbons. *AAPG Search and Discovery Article #90061*.

Bonnell, L.M., Larese, R.E., and Lander, R.H. 2006a. Hydrocarbon versus microquartz inhibition of quartz cementation in North Sea sandstones: Empirical and experimental evidence (abs.): Annual AAPG Convention Abstracts. ***15***, 12.

Bos, I.J., and Stouthamer, E. 2011. Spatial and temporal distribution of sand-containing basin fills in the Holocene Rhine-Meuse delta, the Netherlands. *The journal of geology*, ***119***(6), 641-660.

Bridge, J., and Lunt, I. 2006. Depostional models of braided rivers. In Sambrook Smith, G.H., Best, J. L., Bristow, C. S. and Petts, G.E. (eds) Braided Rivers: Process, Deposits, Ecology and Management. Special Publication International Association of Sedimentologists, **36**, 11-50 https://doi.org/10.1002/9781444304374.ch2.

Bridge, J.S. 2001. Characterization of fluvial hydrocarbon reservoirs and aquifers: problems and solutions. *Revista de la Asociación Argentina de Sedimentología*, ***8***(2), 87-114.

Bridge, J.S., Alexander, J., Collier, R.E.L., Gawthorpe, R.L., and Jarvis, J. 1995. Ground-penetrating radar and coring used to study the large-scale structure of point-bar deposits in three dimensions. *Sedimentology*, ***42***, 839-852, https://doi.org/10.1111/j.1365-3091.1995.tb00413.x.

Bridge, J.S., Jalfin, G.A., and Georgieff, S.M. 2000. Geometry, lithofacies, and spatial distribution of Cretaceous fluvial sandstone bodies, San Jorge Basin, Argentina: outcrop analog for the hydrocarbon-bearing Chubut Group. *Journal of Sedimentary Research*, ***70***(2), 341-359, https://doi.org/10.1306/2DC40915-0E47-11D7-8643000102C1865D.

Bridge, J.S., and Tye, R.S. 2000. Interpreting the dimensions of ancient fluvial channel bars, channels, and channel belts from wireline-logs and cores. *AAPG Bulletin*, ***84***(8), 1205-1228, https://doi.org/10.1306/A9673C84-1738-11D7-8645000102C1865D.

Bryant, S.L., Lakshminarasimhan, S., and Pope, G.A. (2006). Buoyancy-Dominated Multiphase Flow and Its Impact on Geological Sequestration of CO2. SPE/DOE Symposium on Improved Oil Recovery, Tulsa, April 22-26.

Bui, M., Adjiman, C.S., Bardow, A., Anthony, E.J., Boston, A., Brown, S., Fennell, P.S., Fuss, S., Galindo, A., and Hackett, L.A. 2018. Carbon capture and storage (CCS): the way forward. *Energy & Environmental Science*, ***11***(5), 1062-1176.

Bukar, M., Worden, R.H., Bukar, S., and Shell, P. 2021. Diagenesis and its controls on reservoir quality of the Tambar oil field, Norwegian North Sea. *Energy Geoscience*, ***2***(1), 10-31, https://doi.org/10.1016/j.engeos.2020.07.002.

Burgess, R., Jolley, D., and Hartley, A. 2020. Stratigraphic palynology of the Middle–Late Triassic successions of the Central North Sea. *Petroleum Geoscience*, https://doi.org/10.1144/petgeo2019-128.

Burley, S. 1984. Patterns of diagenesis in the Sherwood Sandstone Group (Triassic), United Kingdom. *Clay Minerals*, ***19***, 403-440.

Burley, S., and Kantorowicz, J. 1986. Thin section and SEM textural criteria for the recognition of cement-dissolution porosity in sandstones. *Sedimentology*, ***33***(4), 587-604, https://doi.org/10.1111/j.1365-3091.1986.tb00763.x.

Burley, S., Kantorowicz, J., and Waugh, B. 1985. Clastic diagenesis. *Geological Society, London, Special Publications*, ***18***(1), 189-226.

Burns, C.E., Mountney, N., Hodgson, D., and Colombera, L. 2017. Anatomy and dimensions of fluvial crevasse-splay deposits: Examples from the Cretaceous Castlegate Sandstone and Neslen Formation, Utah, USA. *Sedimentary Geology*, ***351***, 21-35.

Burns, L.K., and Ethridge, F.G. 1979. Petrology and Diagenetic Effects of Lithic Sandstones Paleocene and Eocene Umpqua Formation Southwest Oregon.

Busch, B. 2020. Pilot study on provenance and depositional controls on clay mineral coatings in active fluvio-eolian systems, western USA. *Sedimentary Geology*, ***406***, 105721, https://doi.org/10.1016/j.sedgeo.2020.105721.

Busch, B., Adelmann, D., Herrmann, R., and Hilgers, C. 2022. Controls on compactional behavior and reservoir quality in a Triassic Buntsandstein reservoir, Upper Rhine Graben, SW Germany. *Marine and Petroleum Geology*, ***136***, 105437, https://doi.org/10.1016/j.marpetgeo.2021.105437.

Busch, B., Hilgers, C., and Adelmann, D. 2018. Reservoir quality modelling in deeply-buried Permian Rotliegendes sandstones, N-Germany: Impact of illite textures. *EAGE Conference and Exhibition, Copenhagen*, 1-5, https://doi.org/10.3997/2214-4609.201801135.

Busch, B., Hilgers, C., and Adelmann, D. 2020. Reservoir quality controls on Rotliegend fluvio-aeolian wells in Germany and the Netherlands, Southern Permian Basin – Impact of grain coatings and cements. *Marine and Petroleum Geology*, ***112***, 104075, https://doi.org/10.1016/j.marpetgeo.2019.104075.

Cameron, T.D.J. 1993. *4. Triassic, Permian and pre-Permian of the central and northern North Sea.* In: Knox, R. W. O'B. & Cordey, W. G. (eds) Lithostratigraphic nomenclature of the UK North Sea. British Geological Survey, Nottingham.

Cao, P., Karpyn, Z.T., and Li, L. 2016. The role of host rock properties in determining potential CO2 migration pathways. *International Journal of Greenhouse Gas Control*, ***45***, 18-26.

Cao, Z., Liu, G., Meng, W., Wang, P., and Yang, C. 2018. Origin of different chlorite occurrences and their effects on tight clastic reservoir porosity. *Journal of Petroleum Science and Engineering*, ***160***, 384-392, https://doi.org/10.1016/j.petrol.2017.10.080.

Carr, A. 2003. Thermal history model for the South Central Graben, North Sea, derived using both tectonics and maturation. *International Journal of Coal Geology*, ***54***(1-2), 3-19, https://doi.org/10.1016/S0166-5162(03)00017-X.

Carvalho, M.V., De Ros, L.F., and Gomes, N.S. 1995. Carbonate cementation patterns and diagenetic reservoir facies in the Campos Basin Cretaceous turbidites, offshore eastern Brazil. *Marine and Petroleum Geology*, ***12***(7), 741-758, https://doi.org/10.1016/0264-8172(95)93599-Y.

Cassagnabere, A. (1998). *Caractérisation et interprétation de la transition kaolinite-dickite dans les réservoirs à hydrocarbures de Froy et Rind (Mer du Nord, Norvège)* Poitiers.

Cavazza, W., Braga, R., Reinhardt, E.G., and Zanotti, C. 2009. Influence of host-rock texture on the morphology of carbonate concretions in a meteoric diagenetic environment. *Journal of Sedimentary Research*, ***79***(6), 377-388.

Chan, M.A., Bowen, B.B., Parry, W., Ormö, J., and Komatsu, G. 2005. Red rock and red planet diagenesis. *GSA today*, ***15***, 4-10.

Chandler, M.A., Goggin, D.J., and Lake, L.W. 1989. A mechanical field permeameter for making rapid, non-destructive, permeability measurements. *Journal of Sedimentary Research*, ***59***(4).

Chang, H.K., Mackenzie, F.T., and Schoonmaker, J. 1986. Comparisons between the diagenesis of dioctahedral and trioctahedral smectite, Brazilian offshore basins. *Clays and Clay Minerals*, ***34***(4), 407-423.

Charlaftis, D. (2021). *Assessing sandstone reservoir quality: identifying the reality. PhD dissertation, Durham University.*

Charlaftis, D., Dobson, K., Jones, S.J., Lakshtanov, D., Crouch, J., and Cook, J. 2022. Experimental simulation of burial diagenesis and subsequent 2D-3D characterization of sandstone reservoir quality. *Frontiers in Earth Science*, https://doi.org/10.3389/feart.2022.766145.

Charlaftis, D., Jones, S.J., Dobson, K.J., Crouch, J., and Acikalin, S. 2021. Experimental study of chlorite authigenesis and influence on porosity maintenance in sandstones. *Journal of Sedimentary Research*, ***91***(2), 197-212, https://doi.org/10.2110/jsr.2020.122.

Chen, G., Du, G., Zhang, G., Wang, Q., Lv, C., and Chen, J. 2011. Chlorite cement and its effect on the reservoir quality of sandstones from the Panyu low-uplift, Pearl River Mouth Basin. *Petroleum Science*, ***8***(2), 143-150.

Chi, G., Giles, P., Williamson, M., Lavoie, D., and Bertrand, R. 2003. Diagenetic history and porosity evolution of Upper Carboniferous sandstones from the Spring Valley# 1 well, Maritimes Basin, Canada–implications for reservoir development. *Journal of Geochemical Exploration*, ***80***(2-3), 171-191.

Colombera, L., and Mountney, N.P. 2021. Influence of fluvial crevasse-splay deposits on sandbody connectivity: Lessons from geological analogues and stochastic modelling. *Marine and Petroleum Geology*, ***128***, 105060, https://doi.org/10.1016/j.marpetgeo.2021.105060.

Colombera, L., Mountney, N.P., and McCaffrey, W.D. 2013. A quantitative approach to fluvial facies models: Methods and example results. *Sedimentology*, ***60***, 1526-1558, https://doi.org/10.1111/sed.12050.

Colombera, L., Mountney, N.P., Medici, G., and West, L.J. 2019. The geometry of fluvial channel bodies: Empirical characterization and implications for object-based models of the subsurface. *AAPG Bulletin*, ***103***(4), 905-929, https://doi.org/10.1306/10031817417.

Cui, Y., Jones, S.J., Saville, C., Stricker, S., Wang, G., Tang, L., Fan, X., and Chen, J. 2017. The role played by carbonate cementation in controlling reservoir quality of the Triassic Skagerrak Formation, Norway. *Marine and Petroleum Geology*, ***85***, 316-331, https://doi.org/10.1016/j.marpetgeo.2017.05.020.

Dancer, P., Kenyon-Roberts, S., Downey, J., Baillie, J., Meadows, N., and Maguire, K. 2005. The Corrib gas field, offshore west of Ireland. *Geological Society, London, Petroleum Geology Conference Series*, ***6***(1), 1035-1046, https://doi.org/https://doi.org/10.1144/0061035.

Day-Stirrat, R.J., Milliken, K.L., Dutton, S.P., Loucks, R.G., Hillier, S., Aplin, A.C., and Schleicher, A.M. 2010. Open-system chemical behavior in deep Wilcox Group mudstones, Texas Gulf Coast, USA. *Marine and Petroleum Geology*, ***27***(9), 1804-1818, https://doi.org/10.1016/j.marpetgeo.2010.08.006.

Day-Stirrat, R.J., Milliken, K.L., Dutton, S.P., Loucks, R.G., Hillier, S., Aplin, A.C., and Schleicher, A.M. 2011. Discussion in response to Knut Bjørlykke regarding JMPG_1376" Open-System Chemical Behavior In Deep Wilcox Group Mudstones, Texas Gulf Coast, USA". *Marine and Petroleum Geology*, ***28***(7), 1383-1384, https://doi.org/10.1016/j.marpetgeo.2011.01.010.

De Ros, L.F., Morad, S., and Paim, P.S. 1994. The role of detrital composition and climate on the diagenetic evolution of continental molasses: evidence from the Cambro—Ordovician guaritas sequence, southern Brazil. *Sedimentary Geology*, ***92***(3-4), 197-228, https://doi.org/10.1016/0037-0738(94)90106-6.

De Ros, L.F., and Scherer, C.M. 2012. Stratigraphic controls on the distribution of diagenetic processes, quality and heterogeneity of fluvial-aeolian reservoirs from the Recôncavo Basin, Brazil. *Int. Assoc. Sedimentol. Spec. Publ*, ***45***, 105-132.

De Vicente, G., Vegas, R., Muñoz-Martín, A., Van Wees, J., Casas-Sáinz, A., Sopeña, A., Sánchez-Moya, Y., Arche, A., López-Gómez, J., and Olaiz, A. 2009. Oblique strain partitioning and transpression on an inverted rift: The Castilian Branch of the Iberian Chain. *Tectonophysics*, ***470***(3-4), 224-242, https://doi.org/10.1016/j.tecto.2008.11.003.

Deer, W.A., FRS, Howie, R.A., and Zussman, J. 2013. *An Introduction to the Rock-Forming Minerals.* Mineralogical Society of Great Britain and Ireland. https://doi.org/10.1180/dhz.

Deutsch, C., and Tran, T. 2002. FLUVSIM: a program for object-based stochastic modeling of fluvial depositional systems. *Computers & Geosciences*, ***28***(4), 525-535.

di Primio, R., and Neumann, V. 2008. HPHT reservoir evolution: a case study from Jade and Judy fields, Central Graben, UK North Sea. *International Journal of Earth Sciences*, ***97***, 1101-1114, https://doi.org/10.1007/s00531-007-0206-y.

Donselaar, M.E., and Overeem, I. 2008. Connectivity of fluvial point-bar deposits: An example from the Miocene Huesca fluvial fan, Ebro Basin, Spain. *AAPG Bulletin*, ***92***(9), 1109-1129.

Dowey, P.J., Hodgson, D.M., and Worden, R.H. 2012. Pre-requisites, processes, and prediction of chlorite grain coatings in petroleum reservoirs: a review of subsurface examples. *Marine and Petroleum Geology*, ***32***, 63-75, https://doi.org/10.1016/j.marpetgeo.2011.11.007.

Dowey, P.J., Worden, R.H., Utley, J., and Hodgson, D.M. 2017. Sedimentary controls on modern sand grain coat formation. *Sedimentary Geology*, ***353***, 46-63, https://doi.org/10.1016/j.sedgeo.2017.03.001.

Du Bernard, X., Eichhubl, P., and Aydin, A. 2002. Dilation bands: A new form of localized failure in granular media. *Geophysical Research Letters*, ***29***(24), 2176-2179, https://doi.org/10.1029/2002GL015966.

Duteil, T., Bourillot, R., Grégoire, B., Virolle, M., Brigaud, B., Nouet, J., Braissant, O., Portier, E., Féniès, H., and Patrier, P. 2020. Experimental formation of clay-coated sand grains using diatom biofilm exopolymers. *Geology*, ***48***(10), 1012-1017, https://doi.org/10.1130/G47418.1.

Dutta, P.K., and Suttner, L.J. 1986. Alluvial sandstone composition and paleoclimate; II, Authigenic mineralogy. *Journal of Sedimentary Research*, ***56***(3), 346-358, https://doi.org/10.1306/212F890E-2B24-11D7-8648000102C1865D.

Dutton, S.P. 2008. Calcite cement in Permian deep-water sandstones, Delaware Basin, west Texas: Origin, distribution, and effect on reservoir properties. *AAPG Bulletin*, ***92***(6), 765-787.

Dutton, S.P., Hutton, M.E., Ambrose, W.A., Childers, A.T., and Loucks, R.G. 2018. Preservation of reservoir quality by chlorite coats in deep Tuscaloosa sandstones, Central Louisiana, USA. *Gulf Coast Assoication of Geological Socities*, ***7***, 46-58.

Dutton, S.P., Loucks, R.G., and Day-Stirrat, R.J. 2012. Impact of regional variation in detrital mineral composition on reservoir quality in deep to ultradeep lower Miocene sandstones, western Gulf of Mexico. *Marine and Petroleum Geology*, ***35***(1), 139-153.

Ehrenberg, S. 1990. Relationship between diagenesis and reservoir quality in sandstones of the Garn Formation, Haltenbanken, mid-Norwegian continental shelf. *AAPG Bulletin*, ***74***(10), 1538-1558, https://doi.org/10.1306/0C9B2515-1710-11D7-8645000102C1865D.

Ehrenberg, S. 1993. Preservation of anomalously high porosity in deeply buried sandstones by grain-coating chlorite: examples from the Norwegian continental shelf. *AAPG Bulletin*, ***77***, 1260-1286, https://doi.org/10.1306/BDFF8E5C-1718-11D7-8645000102C1865D.

Ehrenberg, S. 1995. Measuring sandstone compaction from modal analyses of thin sections; how to do it and what the results mean. *Journal of Sedimentary Research*, **65**(2a), 369-379.

Ehrenberg, S., and Jakobsen, K. 2001. Plagioclase dissolution related to biodegradation of oil in Brent Group sandstones (Middle Jurassic) of Gullfaks Field, northern North Sea. *Sedimentology*, ***48***(4), 703-721, https://doi.org/10.1046/j.1365-3091.2001.00387.x.

Einsele, G. 2000. Sedimentary basins: evolution, facies, and sediment budget: Berlin, Springer, 788 p.

Emery, D., Myers, K., and Young, R. 1990. Ancient subaerial exposure and freshwater leaching in sandstones. *Geology*, ***18***(12), 1178-1181.

Evans, D., Graham, C., Armour, A., Grahman, C., and Bathurst, P. 2003. The Millennium Atlas: Petroleum Geology of the Central and Northern North Sea. The Geological Society. *Millennium Atlas Co. Ltd., United Kingdom.*

Farquhar, S., Pearce, J., Dawson, G., Golab, A., Sommacal, S., Kirste, D., Biddle, D., and Golding, S. 2015. A fresh approach to investigating CO2 storage: experimental CO2–water–rock interactions in a low-salinity reservoir system. *Chemical Geology*, ***399***, 98-122.

Fitch, F., Miller, J., and Thompson, D. 1966. The palaeogeographic significance of isotopic age determinations on detrital micas from the Triassic of the Stockport-Macclesfield District, Cheshire, England. *Palaeogeography, Palaeoclimatology, Palaeoecology*, **2**, 281-312.

Flett, M., Gurton, R., and Weir, G. 2007. Heterogeneous saline formations for carbon dioxide disposal: Impact of varying heterogeneity on containment and trapping. *Journal of Petroleum Science and Engineering*, ***57***(1-2), 106-118.

Folk, R.L. 1980. *Petrology of sedimentary rocks.* Hemphill publishing company.

Folk, R.L., and Ward, W.C. 1957. Brazos River bar [Texas]; a study in the significance of grain size parameters. *Journal of Sedimentary Research*, ***27***(1), 3-26, https://doi.org/10.1306/74D70646-2B21-11D7-8648000102C1865D.

Fossen, H., and Bale, A. 2007. Deformation bands and their influence on fluid flow. *AAPG Bulletin*, ***91***(12), 1685-1700, https://doi.org/10.1306/07300706146.

Fossen, H., and Hesthammer, J. 1997. Geometric analysis and scaling relations of deformation bands in porous sandstone. *Journal of structural geology*, ***19***(12), 1479-1493, https://doi.org/10.1016/S0191-8141(97)00075-8.

Fossen, H., Schultz, R.A., Shipton, Z.K., and Mair, K. 2007. Deformation bands in sandstone: a review. *Journal of the Geological Society*, ***164***(4), 755-769, https://doi.org/10.1144/0016-76492006-036.

Franzel, M. (2022). *Correlation and development of fluvial systems: implications for three-dimensional facies models: PhD dissertation, Durham University.*

Franzel, M., Jones, S., Jermyn, I.H., Allen, M., and McCaffrey, K. (2019). Statistical Characterisation of Fluvial Sand Bodies: Implications for Complex Reservoir Models. In Petroleum Geostatistics 2019 (Vol. 2019, No. 1, pp. 1-5). European Association of Geoscientists & Engineers. https://doi.org/10.3997/2214-4609.201902215.

Franzel, M., Jones, S.J., Meadows, N., Allen, M.B., McCaffrey, K., and Morgan, T. 2021. Basin-scale fluvial correlation and response to the Tethyan marine transgression: An example from the Triassic of central Spain. *Basin Research*, ***33***(1), 1-25, https://doi.org/10.1111/bre.12451.

Friend, P., Slater, M., and Williams, R. 1979a. Vertical and lateral building of river sandstone bodies, Ebro Basin, Spain. *Journal of the Geological Society*, ***136***(1), 39-46.

Friend, P., Slater, M., and Williams, R. 1979b. Vertical and lateral building of river sandstone bodies, Ebro Basin, Spain. *Journal of the Geological Society*, ***136***, 39-46, https://doi.org/10.1144/gsjgs.136.1.0039.

Garcia, A., Morad, S., De Ros, L., and Al-Aasm, I. 1998. Paleogeographical, paleoclimatic and burial history controls on the diagenetic evolution of Lower Cretaceous Serraria sandstones in Sergipe-Alagoas Basin, NE Brazil. In Morad, S. (eds) Carbonate cementation in sandstones: International Association of Sedimentologists Special Publication, **26**, 107-140.

Garcia, S., Rosenbauer, R.J., Palandri, J., and Maroto-Valer, M.M. 2012. Sequestration of non-pure carbon dioxide streams in iron oxyhydroxide-containing saline repositories. *International Journal of Greenhouse Gas Control*, ***7***, 89-97.

Gaus, I. 2010. Role and impact of CO2–rock interactions during CO2 storage in sedimentary rocks. *International Journal of Greenhouse Gas Control*, ***4***(1), 73-89.

Gibling, M.R. 2006. Width and thickness of fluvial channel bodies and valley fills in the geological record: a literature compilation and classification. *Journal of Sedimentary Research*, ***76***, 731-770.

Gibson-Poole, C., Svendsen, L., Underschultz, J., Watson, M., Ennis-King, J., Van Ruth, P., Nelson, E., Daniel, R., and Cinar, Y. 2008. Site characterisation of a basin-scale CO2 geological storage system: Gippsland Basin, southeast Australia. *Environmental Geology*, ***54***(8), 1583-1606.

Gier, S., Worden, R.H., Johns, W.D., and Kurzweil, H. 2008. Diagenesis and reservoir quality of Miocene sandstones in the Vienna Basin, Austria. *Marine and Petroleum Geology*, ***25***, 681-695, https://doi.org/10.1016/j.marpetgeo.2008.06.001.

Giles, M., Indrelid, S., Beynon, G., Amthor, J., Worden, R., and Morad, S. 2000. The origin of large-scale quartz cementation: evidence from large data sets and coupled heat-fluid mass transport modelling. In Worden, R.H. and Morad, S. (eds) Quartz cementation in sandstones: International Association of Sedimentologists Special Publication, **29**, 21-38.

Gilfillan, S., Lollar, B.S., Holland, G., Blagburn, D., Stevens, S., Schoell, M., Cassidy, M., Ding, Z., Zhou, Z., and Lacrampe-Couloume, G. 2009. Solubility trapping in formation water as dominant CO2 sink in natural gas fields. *Nature*, ***458***(7238), 614-618.

Girard, J.P. 1998. Carbonate Cementation in the Middle Jurassic Oseberg Reservoir Sandstone, Oseberg Field, Norway: A Case of Deep Burial–High Temperature Poikilotopic Calcite. *Carbonate Cementation in Sandstones: Distribution Patterns and Geochemical Evolution*, 285-307.

Glennie, K.W. 1998. *Petroleum geology of the North Sea: Basic concepts and recent advances, 4th edn.* Blackwell Science, Oxford.

Gluyas, J., and Cade, C.A. 1997. Prediction of porosity in compacted sands. In Kupecz, J., Gluyas, J.G., and Bloch, S. (eds) Reservoir Quality Prediction in Sandstones and Carbonates. AAPGMemoir, **69**, 19-28.

Gluyas, J., and Coleman, M. 1992. Material flux and porosity changes during sediment diagenesis. *Nature*, ***356***(6364), 52-54.

Gluyas, J., Robinson, A., Emery, D., Grant, S., and Oxtoby, N. (1993). The link between petroleum emplacement and sandstone cementation. Geological society, London, petroleum geology conference series.

Gluyas, J.G., and Bagudu, U. 2020. The endurance CO2 storage site, blocks 42/25 and 43/21, UK North Sea. *Geological Society, London, Memoirs*, ***52***(1), 163-171, https://doi.org/10.1144/M52-2019-47.

Goldsmith, P.J., Hudson, G., and Van Veen, P. 2003. Triassic. *In: Evans D., Graham, C., Armour, A. & Bathurst, P. (eds) The Millennium Atlas: Petroleum Geology of the Central and Northern North Sea. Geological Society*, *London*, 105-127.

Goldsmith, P.J., Rich, B., and Standring, J. 1995. Triassic correlation and stratigraphy in the south Central Graben, UK North Sea. *Geological Society, London, Special Publications*, ***91***, 123-143, https://doi.org/10.1144/GSL.SP.1995.091.01.07.

Goodarzi, S., Settari, A., Zoback, M., and Keith, D. 2015. Optimization of a CO2 storage project based on thermal, geomechanical and induced fracturing effects. *Journal of Petroleum Science and Engineering*, ***134***, 49-59, https://doi.org/10.1016/j.petrol.2015.06.004.

Gordon, J.B., Sanei, H., and Pedersen, P.K. 2022. Secondary porosity development in incised valley sandstones from two wells from the Flemish Pass area, offshore Newfoundland. *Marine and Petroleum Geology*, ***140***, 105644.

Gowers, M.B., and Sæbøe, A. 1985. On the structural evolution of the Central Trough in the Norwegian and Danish sectors of the North Sea. *Marine and Petroleum Geology*, ***2***, 298-318, https://doi.org/10.1016/0264-8172(85)90026-1.

Grant, N.T., Middleton, A.J., and Archer, S. 2014. Porosity trends in the Skagerrak Formation, Central Graben, United Kingdom Continental Shelf: The role of compaction and pore pressure history. *AAPG Bulletin*, ***98***, 1111-1143, https://doi.org/10.1306/10211313002.

Gray, E., Hartley, A., and Howell, J. 2019. The influence of stratigraphy and facies distribution on reservoir quality and production performance in the Triassic Skagerrak Formation of the UK and Norwegian Central North Sea. *Geological Society, London, Special Publications*, https://doi.org/10.1144/sp494-2019-68.

Greenwood, P., and Habesch, S. 1997. Diagenesis of the Sherwood Sandstone Group in the southern East Irish Sea Basin (Blocks 110/13, 110/14 and 110/15): constraints from preliminary isotopic and fluid inclusion studies. *Geological Society, London, Special Publications*, ***124***(1), 353-371.

Griffiths, J., Worden, R.H., Wooldridge, L.J., Utley, J.E.P., and Duller, R.A. 2018. Detrital clay coats, clay minerals, and pyrite: a modern shallow-core analogue for ancient and deeply buried estuarine sandstones. *Journal of Sedimentary Research*, ***88***(10), 1205-1237, https://doi.org/10.2110/jsr.2018.56.

Güven, N. 2001. Mica structure and fibrous growth of illite. *Clays and Clay Minerals*, ***49***(3), 189-196.

Haile, B.G., Hellevang, H., Aagaard, P., and Jahren, J. 2015. Experimental nucleation and growth of smectite and chlorite coatings on clean feldspar and quartz grain surfaces. *Marine and Petroleum Geology*, ***68***, 664-674.

Han, W., Hong, H., Yin, K., Churchman, G., Li, Z., Chen, T., and Christidis, G. 2014. Pedogenic alteration of illite in subtropical China. *Clay Minerals*, ***49***(3), 379-390.

Han, W.S., McPherson, B.J., Lichtner, P.C., and Wang, F.P. 2010. Evaluation of trapping mechanisms in geologic CO2 sequestration: Case study of SACROC northern platform, a 35-year CO2 injection site. *American Journal of Science*, ***310***(4), 282-324, https://doi.org/10.2475/04.2010.03.

Hansen, H.N., Løvstad, K., Müller, R., and Jahren, J. 2017. Clay coating preserving high porosities in deeply buried intervals of the Stø Formation. *Marine and Petroleum Geology*, ***88***, 648-658.

Hardman, M., Buchanan, J., Herrington, P., and Carr, A. (1993). Geochemical modelling of the East Irish Sea Basin: its influence on predicting hydrocarbon type and quality. Geological Society, London, Petroleum Geology Conference series.

Harris, N.B. 1989. Diagenetic quartzarenite and destruction of secondary porosity: An example from the Middle Jurassic Brent sandstone of northwest Europe. *Geology*, ***17***(4), 361-364, https://doi.org/10.1130/0091-7613(1989)017<0361:DQADOS>2.3.CO;2.

Harris, N.B. 2006. Low-porosity haloes at stylolites in the feldspathic Upper Jurassic Ula sandstone, Norwegian North Sea: an integrated petrographic and chemical mass-balance approach. *Journal of Sedimentary Research*, ***76***(3), 444-459, https://doi.org/10.2110/jsr.2006.040.

Harwood, J., Aplin, A.C., Fialips, C.I., Iliffe, J.E., Kozdon, R., Ushikubo, T., and Valley, J.W. 2013. Quartz Cementation History of Sandstones Revealed By High-Resolution Sims Oxygen Isotope Analysis. *Journal of Sedimentary Research*, ***83***, 522-530, https://doi.org/10.2110/jsr.2013.29.

Heald, M., and Larese, R. 1974. Influence of coatings on quartz cementation. *Journal of Sedimentary Research*, ***44***, 1269-1274.

Heald, M.T. 1955. Stylolites in sandstones. *The journal of geology*, ***63***(2), 101-114.

Heinemann, N., Alcalde, J., Miocic, J.M., Hangx, S.J., Kallmeyer, J., Ostertag-Henning, C., Hassanpouryouzband, A., Thaysen, E.M., Strobel, G.J., and Schmidt-Hattenberger, C. 2021. Enabling large-scale hydrogen storage in porous media–the scientific challenges. *Energy & Environmental Science*, ***14***(2), 853-864, https://doi.org/10.1039/D0EE03536J.

Henares, S., Caracciolo, L., Cultrone, G., Fernández, J., and Viseras, C. 2014. The role of diagenesis and depositional facies on pore system evolution in a Triassic outcrop analogue (SE Spain). *Marine and Petroleum Geology*, ***51***, 136-151, https://doi.org/10.1016/j.marpetgeo.2013.12.004.

Henares, S., Caracciolo, L., Viseras, C., Fernández, J., and Yeste, L.M. 2016. Diagenetic constraints on heterogeneous reservoir quality assessment: A Triassic outcrop analog of meandering fluvial reservoirs. *AAPG Bulletin*, ***100***(9), 1377-1398, https://doi.org/10.1306/04041615103.

Henares, S., Donselaar, M.E., and Caracciolo, L. 2020. Depositional controls on sediment properties in dryland rivers: Influence on near-surface diagenesis. *Earth-Science Reviews*, ***208***, 103297.

Hillier, S. 1994. Pore-lining chlorites in siliciclastic reservoir sandstones: electron microprobe, SEM and XRD data, and implications for their origin. *Clay Minerals*, ***29***(4), 665-679.

Hirst, J. 1992. Variations in alluvial architecture across the Oligo-Miocene Huesca fluvial system, Ebro Basin, Spain.

Hodgson, N., Farnsworth, J., and Fraser, A. 1992. Salt-related tectonics, sedimentation and hydrocarbon plays in the Central Graben, North Sea, UKCS. *Geological Society, London, Special Publications*, ***67***, 31-63, https://doi.org/10.1144/GSL.SP.1992.067.01.03.

Hornibrook, E.R., and Longstaffe, F.J. 1996. Berthierine from the lower cretaceous Clearwater formation, Alberta, Canada. *Clays and Clay Minerals*, ***44***(1), 1-21.

Hornung, J., and Aigner, T. 1999. Reservoir and aquifer characterization of fluvial architectural elements: Stubensandstein, Upper Triassic, southwest Germany. *Sedimentary Geology*, ***129***(3-4), 215-280.

Houseknecht, D.W. 1987. Assessing the relative importance of compaction processes and cementation to reduction of porosity in sandstones. *AAPG Bulletin*, ***71***, 633-642, https://doi.org/10.1306/9488787F-1704-11D7-8645000102C1865D.

Houseknecht, D.W. 1988. Intergranular pressure solution in four quartzose sandstones. *Journal of Sedimentary Research*, ***58***, 228-246, https://doi.org/10.1306/212F8D64-2B24-11D7-8648000102C1865D.

Houseknecht, D.W., and Ross Jr, L.M. 1992. Clay minerals in Atokan deep-water sandstone facies, Arkoma basin: origins and influence on diagenesis and reservoir quality. In Houseknecht, D.W. and Pittman, E.D. (eds) Origin, Diagenesis, and Petrophysics of Clay Minerals in Sandstones: SEPM, Special Publication, **47**, 227-240.

Hovorka, S.D., Doughty, C., Benson, S.M., Pruess, K., and Knox, P.R. 2004. The impact of geological heterogeneity on CO2 storage in brine formations: a case study from the Texas Gulf Coast. *Geological Society, London, Special Publications*, ***233***(1), 147-163, https://doi.org/10.1144/GSL.SP.2004.233.01.10.

Howell, J.A., Martinius, A.W., and Good, T.R. 2014. The application of outcrop analogues in geological modelling: a review, present status and future outlook. *Geological Society, London, Special Publications*, ***387***, 1-25, https://doi.org/10.1144/SP387.12.

Huffman, C., Apaydin, O.G., Ma, Y.Z., Dubois, D.P., Iwere, F.O., and Luneau, B.A. (2005). Critical parameters in static and dynamic modeling of tight fluvial sandstones. SPE Annual Technical Conference and Exhibition.

Humphreys, B., Kemp, S., Lott, G., Dharmayanti, D., and Samsori, I. 1994. Origin of grain-coating chlorite by smectite transformation: an example from Miocene sandstones, North Sumatra back-arc basin, Indonesia. *Clay Minerals*, ***29***(4), 681-692, https://doi.org/10.1180/claymin.1994.029.4.21.

Humphreys, B., Smith, S., and Strong, G. 1989. Authigenic chlorite in late Triassic sandstones from the Central Graben, North Sea. *Clay Minerals*, ***24***(2), 427-444, https://doi.org/10.1180/claymin.1989.024.2.17.

Hurst, A., and Nadeau, P.H. 1995. Clay microporosity in reservoir sandstones: an application of quantitative electron microscopy in petrophysical evaluation. *AAPG Bulletin*, ***79***(4), 563-573, https://doi.org/10.1306/8D2B1598-171E-11D7-8645000102C1865D.

Isaksen, G.H. 2004. Central North Sea hydrocarbon systems: Generation, migration, entrapment, and thermal degradation of oil and gas. *AAPG Bulletin*, ***88***, 1545-1572, https://doi.org/10.1306/06300403048.

Issautier, B., Viseur, S., Audigane, P., and Le Nindre, Y.-M. 2014. Impacts of fluvial reservoir heterogeneity on connectivity: Implications in estimating geological storage capacity for CO2. *International Journal of Greenhouse Gas Control*, ***20***, 333-349, https://doi.org/10.1016/j.ijggc.2013.11.009.

Jackson, D., Johnson, H., and Smith, N. 1997. Stratigraphical relationships and a revised lithostratigraphical nomenclature for the Carboniferous, Permian and Triassic rocks of the offshore East Irish Sea Basin. *Geological Society, London, Special Publications*, ***124***(1), 11-32.

Jackson, D., and Mulholland, P. (1993). Tectonic and stratigraphic aspects of the East Irish Sea Basin and adjacent areas: contrasts in their post-Carboniferous structural styles. Geological Society, London, Petroleum Geology Conference series.

Jackson, D., Mulholland, P., Jones, S., and Warrington, G. (1987). The geological framework of the East Irish Sea basin. Conference on petroleum geology of North West Europe. 3.

Jahren, J., and Aagaard, P. 1989. Compositional variations in diagenetic chlorites and illites, and relationships with formation-water chemistry. *Clay Minerals*, ***24***(2), 157-170.

Jeans, C., Wray, D., Merriman, R., and Fisher, M. 2000. Volcanogenic clays in Jurassic and Cretaceous strata of England and the North Sea Basin. *Clay Minerals*, ***35***(1), 25-55.

Johnson, H., and Lott, G.K. 1993. *2. Cretaceous of the Central and Northern North Sea.* In: Knox, R. W. O'B. & Cordey, W. G. (eds) Lithostratigraphic nomenclature of the UK North Sea. British Geological Survey, Nottingham.

Johnson, J.W., Nitao, J.J., Steefel, C.I., and Knauss, K.G. (2001). Reactive transport modeling of geologic CO2 sequestration in saline aquifers: the influence of intra-aquifer shales and the relative effectiveness of structural, solubility, and mineral trapping during prograde and retrograde sequestration. First national conference on carbon sequestration.

Jones, A.D., Auld, H.A., Carpenter, T.J., Fetkovich, E., Palmer, I.A., Rigatos, E.N., and Thompson, M.W. 2005. Jade Field: an innovative approach to high-pressure, high-temperature field development. In Dore´, A.G. and Vining, B.A. (eds) Petroleum Geology: North-West Europe and Global Perspectives - Proceedings of the 6th Petroleum Geology Conference. Geological Society, London, 269-283, https://doi.org/10.1144/0060269.

Jones, N., and Ambrose, K. 1994. Triassic sandy braidplain and aeolian sedimentation in the Sherwood Sandstone Group of the Sellafield area, west Cumbria. *Proceedings of the Yorkshire Geological Society*, ***50***(1), 61-76.

Kampman, N., Bickle, M., Wigley, M., and Dubacq, B. 2014. Fluid flow and CO2–fluid–mineral interactions during CO2-storage in sedimentary basins. *Chemical Geology*, ***369***, 22-50.

Kazerouni, A.M., Poulsen, M.L., Friis, H., Svendsen, J.B., and Hansen, J.P. 2013. Illite/smectite transformation in detrital glaucony during burial diagenesis of sandstone: A study from Siri Canyon–Danish North Sea. *Sedimentology*, ***60***(3), 679-692.

Keating, E.H., Fessenden, J., Kanjorski, N., Koning, D.J., and Pawar, R. 2010. The impact of CO2 on shallow groundwater chemistry: observations at a natural analog site and implications for carbon sequestration. *Environmental Earth Sciences*, ***60***(3), 521-536, https://doi.org/10.1007/s12665-009-0192-4.

Keller, T., Bayes, R., Auld, H., and Lines, M. 2005. Judy Field: rejuvenation through a second phase of drilling. In Dore´, A.G. and Vining, B.A. (eds) Petroleum Geology: North-West Europe and Global Perspectives - Proceedings of the 6th Petroleum Geology Conference. Geological Society, London, 651-661, https://doi.org/10.1144/0060651.

Keogh, K.J., Martinius, A.W., and Osland, R. 2007. The development of fluvial stochastic modelling in the Norwegian oil industry: A historical review, subsurface implementation and future directions. *Sedimentary Geology*, ***202***(1-2), 249-268.

Kim, Y., and Lee, Y.I. 2004. Origin of quartz cement in the Lower Ordovician Dongjeom formation, Korea. *Journal of Asian Earth Sciences*, ***24***(3), 327-335.

Knipe, R., Cowan, G., and Balendran, V. (1993). The tectonic history of the East Irish Sea Basin with reference to the Morecambe Fields. Geological Society, London, Petroleum Geology Conference series.

Knox, R.W.O.B., and Holloway, S. 1992. 1. Paleogene of the Central and Northern North Sea. *In: Knox, R. W. O'B. & Cordey, W. G. (eds) Lithostratigraphic nomenclature of the UK North Sea. British Geological Survey, Nottingham.*

Koneshloo, M., Aryana, S.A., and Hu, X. 2018. The impact of geological uncertainty on primary production from a fluvial reservoir. *Petroleum Science*, ***15***(2), 270-288.

Korus, J.T., and Joeckel, R. 2022. Sandstone-body geometry and hydrostratigraphy of the northern High Plains Aquifer system, USA. *Quarterly Journal of Engineering Geology and Hydrogeology*, ***55***(3), https://doi.org/10.1144/qjegh2021-171.

Kozeny, J. 1927. Uber kapillare Leitung der Wassers im Boden. *Royal Academy of Science, Vienna, Proc. Class I*, ***136***, 271-306.

Kupecz, J.A., Gluyas, J., and Bloch, S. 1997. Reservoir quality prediction in sandstones and carbonates: An overview.

Labourdette, R., and Jones, R.R. 2007. Characterization of fluvial architectural elements using a three-dimensional outcrop data set: Escanilla braided system, South-Central Pyrenees, Spain. *Geosphere*, ***3***(6), 422-434, https://doi.org/10.1130/GES00087.1.

Lai, J., Wang, G., Ran, Y., Zhou, Z., and Cui, Y. 2016. Impact of diagenesis on the reservoir quality of tight oil sandstones: The case of Upper Triassic Yanchang Formation Chang 7 oil layers in Ordos Basin, China. *Journal of Petroleum Science and Engineering*, ***145***, 54-65, https://doi.org/10.1016/j.petrol.2016.03.009.

Lai, J., Wang, G., Wang, Z., Chen, J., Pang, X., Wang, S., Zhou, Z., He, Z., Qin, Z., and Fan, X. 2018. A review on pore structure characterization in tight sandstones. *Earth-Science Reviews*, ***177***, 436-457, https://doi.org/10.1016/j.earscirev.2017.12.003.

Lala, A.M.S., and El-Sayed, N.A. 2017. Controls of pore throat radius distribution on permeability. *Journal of Petroleum Science and Engineering*, ***157***, 941-950, https://doi.org/10.1016/j.petrol.2017.08.005.

Land, L., and Milliken, K. 2000. Regional loss of SiO_2 and $CaCO_3$, and gain of K_2O during burial diagenesis of Gulf Coast mudrocks, USA. In Worden, R.H. and Morad, S. (eds) Quartz cementation in sandstones. International Association of Sedimentologists Special Publication, **29**, 183-197.

Land, L.S. 1980. The isotopic and trace element geochemistry of dolomite: the state of the art.

Land, L.S. 1997. Mass transfer during burial diagenesis in the Gulf of Mexico sedimentary basin: an overview. https://doi.org/10.2110/pec.97.57.0029.

Lander, R.H., and Bonnell, L.M. 2010. A model for fibrous illite nucleation and growth in sandstones. *AAPG Bulletin*, ***94***(8), 1161-1187.

Lander, R.H., Larese, R.E., and Bonnell, L.M. 2008. Toward more accurate quartz cement models: The importance of euhedral versus noneuhedral growth rates. *AAPG Bulletin*, ***92***, 1537-1563, https://doi.org/10.1306/07160808037.

Lander, R.H., and Walderhaug, O. 1999. Predicting porosity through simulating sandstone compaction and quartz cementation. *AAPG Bulletin*, ***83***(3), 433-449.

Lanson, B., Beaufort, D., Berger, G., Bauer, A., Cassagnabere, A., and Meunier, A. 2002. Authigenic kaolin and illitic minerals during burial diagenesis of sandstones: a review. *Clay Minerals*, ***37***(1), 1-22.

Larue, D.K., and Hovadik, J. 2006. Connectivity of channelized reservoirs: a modelling approach. *Petroleum Geoscience*, ***12***(4), 291-308, https://doi.org/10.1144/1354-079306-699.

Lasaga, A.C. 1984. Chemical kinetics of water-rock interactions. *Journal of Geophysical Research: Solid Earth*, ***89***(B6), 4009-4025, https://doi.org/10.1029/JB089iB06p04009.

Lawan, A.Y., Worden, R.H., Utley, J.E., and Crowley, S.F. 2021. Sedimentological and diagenetic controls on the reservoir quality of marginal marine sandstones buried to moderate depths and temperatures: Brent Province, UK North Sea. *Marine and Petroleum Geology*, ***128***, 104993.

Leeder, M. 1973. Fluviatile fining-upwards cycles and the magnitude of palaeochannels. *Geological Magazine*, ***110***, 265-276, https://doi.org/10.1017/S0016756800036098.

Li, M., Zhu, R., Lou, Z., Yin, W., Hu, Z., Zhu, H., and Jin, A. 2019. Diagenesis and its impact on the reservoir quality of the fourth member of Xujiahe Formation, Western Sichuan Depression, China. *Marine and Petroleum Geology*, ***103***, 485-498.

Li, Z., Wu, S., Xia, D., Zhang, X., and Huang, M. 2017. Diagenetic alterations and reservoir heterogeneity within the depositional facies: A case study from distributary-channel belt sandstone of Upper Triassic Yanchang Formation reservoirs (Ordos Basin, China). *Marine and Petroleum Geology*, ***86***, 950-971.

Lianbo, Z., and Xiang-Yang, L. 2009. Fractures in sandstone reservoirs with ultra-low permeability: A case study of the Upper Triassic Yanchang Formation in the Ordos Basin, China. *AAPG Bulletin*, ***93***(4), 461-477, https://doi.org/10.1306/09240808047.

Longiaru, S. 1987. Visual comparators for estimating the degree of sorting from plane and thin section. *Journal of Sedimentary Research*, ***57***(4).

López-Gómez, J., and Arche, A. 1992. Paleogeographical significance of the Röt (Anisian, Triassic) Facies (marines clays, muds and marls fm.) in the Iberian Ranges, eastern Spain. *Palaeogeography, Palaeoclimatology, Palaeoecology*, ***91***(3-4), 347-361, https://doi.org/10.1016/0031-0182(92)90076-H.

López-Gómez, J., and Arche, A. 1993. Sequence stratigraphic analysis and paleogeographic interpretation of the Buntsandstein and Muschelkalk facies (Permo-Triassic) in the SE Iberian Range, E Spain. *Palaeogeography, Palaeoclimatology, Palaeoecology*, ***103***(3-4), 179-201.

Lowe, D.R. 1975. Water escape structures in coarse-grained sediments. *Sedimentology*, ***22***(2), 157-204.

Lu, J., Wilkinson, M., Haszeldine, R.S., and Boyce, A.J. 2011. Carbonate cements in Miller field of the UK North Sea: a natural analog for mineral trapping in CO 2 geological storage. *Environmental Earth Sciences*, ***62***(3), 507-517.

Lundegard, P.D. 1992. Sandstone porosity loss; a" big picture" view of the importance of compaction. *Journal of Sedimentary Research*, ***62***, 250-260, https://doi.org/10.1306/D42678D4-2B26-11D7-8648000102C1865D.
Luquot, L., Andreani, M., Gouze, P., and Camps, P. 2012. CO2 percolation experiment through chlorite/zeolite-rich sandstone (Pretty Hill Formation–Otway Basin–Australia). *Chemical Geology*, ***294***, 75-88, https://doi.org/10.1016/j.chemgeo.2011.11.018.
Ma, B., Cao, Y., Eriksson, K.A., Jia, Y., and Gill, B.C. 2017. Depositional and diagenetic controls on deeply-buried Eocene sublacustrine fan reservoirs in the Dongying Depression, Bohai Bay Basin, China. *Marine and Petroleum Geology*, ***82***, 297-317, https://doi.org/10.1016/j.marpetgeo.2017.02.014.
Maast, T.E., Jahren, J., and Bjørlykke, K. 2011. Diagenetic controls on reservoir quality in Middle to Upper Jurassic sandstones in the South Viking Graben, North Sea. *AAPG Bulletin*, ***95***, 1937-1958, https://doi.org/10.1306/03071110122.
Mahmic, O., Dypvik, H., and Hammer, E. 2018. Diagenetic influence on reservoir quality evolution, examples from Triassic conglomerates/arenites in the Edvard Grieg field, Norwegian North Sea. *Marine and Petroleum Geology*, ***93***, 247-271, https://doi.org/10.1016/j.marpetgeo.2018.03.006.
Makowitz, A., and Milliken, K.L. 2003. Quantification of brittle deformation in burial compaction, Frio and Mount Simon Formation sandstones. *Journal of Sedimentary Research*, ***73***(6), 1007-1021.
Mallon, A., and Swarbrick, R. 2002. A compaction trend for non-reservoir North Sea Chalk. *Marine and Petroleum Geology*, ***19***, 527-539.
Mallon, A., and Swarbrick, R. 2008. Diagenetic characteristics of low permeability, non-reservoir chalks from the Central North Sea. *Marine and Petroleum Geology*, ***25***, 1097-1108.
Mao, S., Bao, Z., Wang, X., Gao, Y., Song, J., Wang, Z., Liu, W., Zhang, L., Wei, M., and Bao, Y. 2019. Origin of carbonate cements and reservoir evolution of tight sandstone in the Upper Triassic Yanchang Formation, Ordos Basin, China. *Australian Journal of Earth Sciences*, ***66***(8), 1175-1194, https://doi.org/10.1080/08120099.2019.1596981.
Marchand, A., Haszeldine, R., Macaulay, C., Swennen, R., and Fallick, A. 2000. Quartz cementation inhibited by crestal oil charge: Miller deep water sandstone, UK North Sea. *Clay Minerals*, ***35***(1), 201-210, https://doi.org/10.1180/000985500546585.
Marchand, A.M., Haszeldine, R.S., Smalley, P.C., Macaulay, C.I., and Fallick, A.E. 2001. Evidence for reduced quartz-cementation rates in oil-filled sandstones. *Geology*, ***29***(10), 915-918.
Marchand, A.M., Smalley, P.C., Haszeldine, R.S., and Fallick, A.E. 2002. Note on the importance of hydrocarbon fill for reservoir quality prediction in sandstones. *AAPG Bulletin*, ***86***, 1561-1571.
Marsh, J., Jones, S., Meadows, N., and Gluyas, J. 2022. Petrographic and diagenetic investigation of the distal Triassic 'Budleighensis' fluvial system in the Solway and Carlisle Basins for potential CO2 storage. *Petroleum Geoscience*, ***28***(3), https://doi.org/10.1144/petgeo2021-065.
Martin, K.R., Baker, J.C., Hamilton, P.J., and Thrasher, G.P. 1994. Diagenesis and reservoir quality of Paleocene sandstones in the Kupe South field, Taranaki Basin, New Zealand. *AAPG Bulletin*, ***78***(4), 624-643.
Matlack, K.S., Houseknecht, D.W., and Applin, K.R. 1989. Emplacement of clay into sand by infiltration. *Journal of Sedimentary Research*, ***59***, 77-87, https://doi.org/10.1306/212F8F21-2B24-11D7-8648000102C1865D.
Matter, J.M., and Kelemen, P.B. 2009. Permanent storage of carbon dioxide in geological reservoirs by mineral carbonation. *Nature Geoscience*, ***2***(12), 837-841.

Mazzullo, S. 1992. Geochemical and neomorphic alteration of dolomite: a review. *Carbonates and evaporites*, ***7***(1), 21-37.
McBride, E., Picard, M.D., and Folk, R. 1994. Oriented concretions, Ionian Coast, Italy; evidence of groundwater flow direction. *Journal of Sedimentary Research*, ***64***(3a), 535-540.
McBride, E.F. 1989. Quartz cement in sandstones: a review. *Earth-Science Reviews*, ***26***, 69-112, https://doi.org/10.1016/0012-8252(89)90019-6.
McIntosh, J.A., Tabor, N.J., and Rosenau, N.A. 2021. Mixed-layer illite-smectite in pennsylvanian-aged paleosols: Assessing sources of illitization in the illinois basin. *Minerals*, ***11***(2), 108.
McKay, J., Longstaffe, F., and Plint, A. 1995. Early diagenesis and its relationship to depositional environment and relative sea-level fluctuations (Upper Cretaceous Marshybank Formation, Alberta and British Columbia). *Sedimentology*, ***42***(1), 161-190.
McKie, T. 2011. Architecture and behavior of dryland fluvial reservoirs, Triassic Skagerrak Formation, central North Sea. In Davidson, S., North, C., and Leleu, S. (eds) From River to Rock Record. SEPM Special Publication, **97**, 189-214, https://doi.org/doi.org/10.2110/sepmsp.097.189.
McKie, T. 2014. Climatic and tectonic controls on Triassic dryland terminal fluvial system architecture, central North Sea. In Martinius, A.W., Ravnas, R., Howell, J.A., Steel, R.J., and Wonham, J.P. (eds) From Depositional Systems to Sedimentary Successions on the Norwegian Continental Margin. International Association of Sedimentologists Special Publications, **46**, 19-58, https://doi.org/10.1002/9781118920435.ch2.
McKie, T., and Audretsch, P. 2005. Depositional and structural controls on Triassic reservoir performance in the Heron Cluster, ETAP, Central North Sea. *Geological Society, London, Petroleum Geology Conference series*, ***6***, 285-297, https://doi.org/10.1144/0060285.
McKie, T., Jolley, S., and Kristensen, M. 2010. Stratigraphic and structural compartmentalization of dryland fluvial reservoirs: Triassic Heron Cluster, Central North Sea. *Geological Society, London, Special Publications*, ***347***, 165-198, https://doi.org/10.1144/SP347.11.
McKie, T., and Shannon, P. 2011. Comment on "the Permian–Triassic transition and the onset of Mesozoic sedimentation at the northwestern peri Tethyan domain scale: palaeogeographic maps and geodynamic implications". *Palaeogeography, Palaeoclimatology, Palaeoecology*, ***311***, 136-143.
McKie, T., and Williams, B. 2009. Triassic palaeogeography and fluvial dispersal across the northwest European Basins. *Geological Journal*, ***44***, 711-741.
McKinley, J.M., Atkinson, P.M., Lloyd, C.D., Ruffell, A.H., and Worden, R. 2011. How porosity and permeability vary spatially with grain size, sorting, cement volume, and mineral dissolution in fluvial Triassic sandstones: the value of geostatistics and local regression. *Journal of Sedimentary Research*, ***81***(12), 844-858.
Mckinley, J.M., Worden, R.H., and Ruffell, A.H. 2003. Smectite in sandstones: a review of the controls on occurrence and behaviour during diagenesis. In Worden, R.H. and Morad, S. (eds) Int. Assoc. Sedimentol. Spec. Publ, **34**, 109-128.
Meadows, N., and Beach, A. (1993). Controls on reservoir quality in the Triassic Sherwood Sandstone of the Irish Sea. Geological Society, London, Petroleum Geology Conference Series.
Meadows, N.S., and Beach, A. 1993a. Structural and climatic controls on facies distribution in a mixed fluvial and aeolian reservoir: the Triassic Sherwood Sandstone in the Irish Sea. *Geological Society, London, Special Publications*, ***73***(1), 247-264.

Mediato, J.F., García-Crespo, J., Izquierdo, E., García-Lobón, J.L., Ayala, C., Pueyo, E.L., and Molinero, R. 2017. Three-dimensional reconstruction of the Caspe geological structure (Spain) for evaluation as a potential CO2 storage site. *Energy Procedia*, ***114***, 4486-4493, https://doi.org/10.1016/j.egypro.2017.03.1608.

Medici, G., Boulesteix, K., Mountney, N., West, L., and Odling, N. 2015. Palaeoenvironment of braided fluvial systems in different tectonic realms of the Triassic Sherwood Sandstone Group, UK. *Sedimentary Geology*, ***329***, 188-210.

Medici, G., West, L., and Mountney, N. 2018. Characterization of a fluvial aquifer at a range of depths and scales: the Triassic St Bees Sandstone Formation, Cumbria, UK. *Hydrogeology Journal*, ***26***(2), 565-591, https://doi.org/10.1007/s10040-017-1676-z.

Medici, G., West, L.J., and Mountney, N.P. 2019. Sedimentary flow heterogeneities in the Triassic UK Sherwood Sandstone Group: Insights for hydrocarbon exploration. *Geological Journal*, ***54***(3), 1361-1378.

Metz, B., Davidson, O., De Coninck, H., Loos, M., and Meyer, L. 2005. *IPCC special report on carbon dioxide capture and storage.* Cambridge: Cambridge University Press.

Miall, A. 2014. The facies and architecture of fluvial systems. In Miall, A. (eds) Fluvial depositional systems, 9-68, Springer.

Miall, A.D. 1985. Architectural-element analysis: a new method of facies analysis applied to fluvial deposits. *Earth-Science Reviews*, ***22***(4), 261-308.

Miall, A.D. 1988. Reservoir heterogeneities in fluvial sandstones: lessons from outcrop studies. *AAPG Bulletin*, ***72***(6), 682-697.

Miall, A.D. 1996. *The geology of fluvial deposits: sedimentary facies, basin analysis, and petroleum geology.* Springer.

Miruo, L., Yanzhong, W., Yingchang, C., Shuping, W., Qiangwang, X., and Xiuyu, D. 2020. Sources of Ca2+ in the major carbonate cements in Eocene sandstones and conglomerates: evidence from Sr isotopes, Sr/Ca ratios, and rare-earth elements. *Marine and Petroleum Geology*, ***120***, 104568.

Mitten, A., Mullins, J., Pringle, J., Howell, J., and Clarke, S. 2020. Depositional conditioning of three dimensional training images: improving the reproduction and representation of architectural elements in sand-dominated fluvial reservoir models. *Marine and Petroleum Geology*, ***113***, 104156, https://doi.org/10.1016/j.marpetgeo.2019.104156.

Mjøs, R., Walderhaug, O., Prestholm, E., Marzo, M., and Puigdefabregas, C. 1993. Crevasse splay sandstone geometries in the Middle Jurassic Ravenscar Group of Yorkshire, UK. *Alluvial Sedimentation. International association of Sedimentologists, special publication*, ***17***, 167-184.

Molenaar, N., Cyziene, J., and Sliaupa, S. 2007. Quartz cementation mechanisms and porosity variation in Baltic Cambrian sandstones. *Sedimentary Geology*, ***195***(3-4), 135-159, https://doi.org/10.1016/j.sedgeo.2006.07.009.

Molenaar, N., Cyziene, J., Sliaupa, S., and Craven, J. 2008. Lack of inhibiting effect of oil emplacement on quartz cementation: Evidence from Cambrian reservoir sandstones, Paleozoic Baltic Basin. *Geological Society of America Bulletin*, ***120***(9-10), 1280-1295, https://doi.org/10.1130/B25979.1.

Moore, C.H. 1989. *Carbonate diagenesis and porosity.* Developments in sedimentology, 46, Amsterdam, Elsevier.

Morad, S. 1998. Carbonate Cementation in Sandstones: Distribution Patterns and Geochemical Evolution. In Morad, S. (eds) Carbonate cementation in sandstones: International Association of Sedimentologists Special Publication, **26**, 1-26.

Morad, S. 2009. *Carbonate cementation in sandstones: distribution patterns and geochemical evolution.* John Wiley & Sons. **72**.

Morad, S., Al-Ramadan, K., Ketzer, J.M., and De Ros, L.F. 2010. The impact of diagenesis on the heterogeneity of sandstone reservoirs: A review of the role of depositional facies and sequence stratigraphy. *AAPG Bulletin*, ***94***, 1267-1309, https://doi.org/10.1306/04211009178.

Morad, S., Al-Aasm, I., Longstaffe, F., Marfil, R., Ros, L.d., Johansen, H., and Marzo, M. 1995. Diagenesis of a mixed siliciclastic/evaporitic sequence of the Middle Muschelkalk (Middle Triassic), the Catalan Coastal Range, NE Spain. *Sedimentology*, ***42***(5), 749-768.

Morad, S., De Ros, L., Nystuen, J., and Bergan, M. 1998. Carbonate diagenesis and porosity evolution in sheet-flood sandstones: evidence from the Middle and Lower Lunde Members (Triassic) in the Snorre Field, Norwegian North Sea.

Morad, S., Ismail, H.B., De Ros, L., Al-Aasm, I., and Serrhini, N.E. 1994. Diagenesis and formation water chemistry of Triassic reservoir sandstones from southern Tunisia. *Sedimentology*, ***41***, 1253-1272.

Morad, S., Ketzer, J., and De Ros, L.F. 2000. Spatial and temporal distribution of diagenetic alterations in siliciclastic rocks: implications for mass transfer in sedimentary basins. *Sedimentology*, ***47***, 95-120, https://doi.org/10.1046/j.1365-3091.2000.00007.x.

Moraes, M.A., and De Ros, L.F. 1990. Infiltrated clays in fluvial Jurassic sandstones of Recôncavo Basin, northeastern Brazil. *Journal of Sedimentary Research*, ***60***(6), 809-819, https://doi.org/10.1306/212F928C-2B24-11D7-8648000102C1865D.

Moraes, M.A., and De Ros, L.F. 1992. Depositional, Infiltrated and Authigenic Clays in Fluvial Sandstones of the Jurassic Sergi Formation, Recôncavo Basin, Northeastern Brazil. In Houseknecht, D.W., Pittman, E.D., and Keller, W.D.F. (eds) Origin, Diagenesis, and Petrophysics of Clay Minerals in Sandstones: SEPM, Special Publication, **47**, 197-208.

Morgan, T., Jones, S., Morris, J., Meadows, N., and Butler, M. (2010). Chemostratigraphy of the Middle Triassic, Central Iberian Basin–An Analogue for the Triassic Central Graben, North Sea. In 72nd EAGE Conference and Exhibition incorporating SPE EUROPEC 2010 (pp. cp-161). European Association of Geoscientists & Engineers.

Mouritzen, C., Farris, M.A., Morton, A., and Matthews, S. 2017. Integrated Triassic stratigraphy of the greater Culzean area, UK central North Sea. *Petroleum Geoscience*, ***24***, 197-207, https://doi.org/10.1144/petgeo2017-039.

Mozley, P.S. 1989. Relation between depositional environment and the elemental composition of early diagenetic siderite. *Geology*, ***17***(8), 704-706.

Mozley, P.S., and Davis, J.M. 1996. Relationship between oriented calcite concretions and permeability correlation structure in an alluvial aquifer, Sierra Ladrones Formation, New Mexico. *Journal of Sedimentary Research*, ***66***(1), 11-16.

Munz, I.A., Brandvoll, Ø., Haug, T., Iden, K., Smeets, R., Kihle, J., and Johansen, H. 2012. Mechanisms and rates of plagioclase carbonation reactions. *Geochimica et Cosmochimica Acta*, ***77***, 27-51, https://doi.org/10.1016/j.gca.2011.10.036.

Nadeau, P. 2000. The Sleipner Effect: a subtle relationship between the distribution of diagenetic clay, reservoir porosity, permeability, and water saturation. *Clay Minerals*, ***35***(1), 185-200, https://doi.org/10.1180/000985500546576.

Naylor, H., Turner, P., Vaughan, D., and Fallick, A. 1989. The Cherty Rock, Elgin: A petrographic and isotopic study of a Permo-Triassic calcrete. *Geological Journal*, ***24***(3), 205-221, https://doi.org/10.1002/gj.3350240305.

Needham, S.J., Worden, R.H., and McIlroy, D. 2005. Experimental production of clay rims by macrobiotic sediment ingestion and excretion processes. *Journal of Sedimentary Research*, ***75***(6), 1028-1037, https://doi.org/10.2110/jsr.2005.078.

Nelson, C.S., and Smith, A.M. 1996. Stable oxygen and carbon isotope compositional fields for skeletal and diagenetic components in New Zealand Cenozoic nontropical carbonate sediments and limestones: a synthesis and review. *New Zealand Journal of Geology and Geophysics*, ***39***(1), 93-107, https://doi.org/10.1080/00288306.1996.9514697.

Nelson, P.H. 2009. Pore-throat sizes in sandstones, tight sandstones, and shales. *AAPG Bulletin*, ***93***(3), 329-340, https://doi.org/10.1306/10240808059.

Newell, A.J. 2018. Rifts, rivers and climate recovery: A new model for the Triassic of England. *Proceedings of the Geologists' Association*, ***129***(3), 352-371.

Newell, A.J., and Shariatipour, S.M. 2016. Linking outcrop analogue with flow simulation to reduce uncertainty in sub-surface carbon capture and storage: an example from the Sherwood Sandstone Group of the Wessex Basin, UK. *Geological Society, London, Special Publications*, ***436***(1), 231-246.

Nguyen, B.T., Jones, S.J., Goulty, N.R., Middleton, A.J., Grant, N., Ferguson, A., and Bowen, L. 2013. The role of fluid pressure and diagenetic cements for porosity preservation in Triassic fluvial reservoirs of the Central Graben, North Sea. *AAPG Bulletin*, ***97***, 1273-1302, https://doi.org/10.1306/01151311163.

Nguyen, D.T., Horton, R.A., and Kaess, A.B. 2018. Diagenesis, plagioclase dissolution and preservation of porosity in Eocene and Oligocene sandstones at the Greeley oil field, southern San Joaquin basin, California, USA. *Geological Society, London, Special Publications*, ***435***, 265-282, https://doi.org/10.1144/sp435.14.

Nichols, G. 2009. *Sedimentology and stratigraphy.* John Wiley & Sons.

O'Neill, S.R., Jones, S.J., Kamp, P.J., Swarbrick, R.E., and Gluyas, J.G. 2018. Pore pressure and reservoir quality evolution in the deep Taranaki Basin, New Zealand. *Marine and Petroleum Geology*, ***98***, 815-835, https://doi.org/10.1016/j.marpetgeo.2018.08.038.

Odin, G.S., and Matter, A. 1981. De glauconiarum origine. *Sedimentology*, ***28***(5), 611-641.

Oelkers, E.H., Bjorkum, P.A., and Murphy, W.M. 1996. A petrographic and computational investigation of quartz cementation and porosity reduction in North Sea sandstones. *American Journal of Science*, ***296***(4), 420-452, https://doi.org/10.2475/ajs.296.4.420.

Okunuwadje, S.E., Bowden, S.A., and Macdonald, D.I. 2020. Diagenesis and reservoir quality in high-resolution sandstone sequences: An example from the Middle Jurassic Ravenscar sandstones, Yorkshire CoastUK. *Marine and Petroleum Geology*, ***118***, 104426.

Olivarius, M., Weibel, R., Hjuler, M.L., Kristensen, L., Mathiesen, A., Nielsen, L.H., and Kjøller, C. 2015. Diagenetic effects on porosity–permeability relationships in red beds of the Lower Triassic Bunter Sandstone Formation in the North German Basin. *Sedimentary Geology*, ***321***, 139-153, https://doi.org/10.1016/j.sedgeo.2015.03.003.

Oluwadebi, A.G., Taylor, K.G., and Dowey, P.J. 2018. Diagenetic controls on the reservoir quality of the tight gas Collyhurst Sandstone Formation, Lower Permian, East Irish Sea Basin, United Kingdom. *Sedimentary Geology*, ***371***, 55-74, https://doi.org/10.1016/j.sedgeo.2018.04.006.

Osborne, M.J., and Swarbrick, R.E. 1997. Mechanisms for generating overpressure in sedimentary basins: a reevaluation. *AAPG Bulletin*, ***81***, 1023-1041, https://doi.org/10.1306/522B49C9-1727-11D7-8645000102C1865D.

Osborne, M.J., and Swarbrick, R.E. 1999. Diagenesis in North Sea HPHT clastic reservoirs consequences for porosity and overpressure prediction. *Marine and Petroleum Geology*, ***16***, 337-353.

Owen, G., and Moretti, M. 2011. Identifying triggers for liquefaction-induced soft-sediment deformation in sands. *Sedimentary Geology*, ***235***(3-4), 141-147.

Oye, O.J., Aplin, A.C., Jones, S.J., Gluyas, J.G., Bowen, L., Harwood, J., Orland, I.J., and Valley, J.W. 2020. Vertical effective stress and temperature as controls of quartz cementation in sandstones: Evidence from North Sea Fulmar and Gulf of Mexico

Wilcox sandstones. *Marine and Petroleum Geology*, ***115***, 104289, https://doi.org/10.1016/j.marpetgeo.2020.104289.
Oye, O.J., Aplin, A.C., Jones, S.J., Gluyas, J.G., Bowen, L., Orland, I.J., and Valley, J.W. 2018. Vertical effective stress as a control on quartz cementation in sandstones. *Marine and Petroleum Geology*, ***98***, 640-652, https://doi.org/10.1016/j.marpetgeo.2018.09.017.
Pacheco, F., Harrison, M., Chatterjee, S., Ishinaga, K., Ishii, S., Mills, W., Vargas, N., Paul, S., and Roy, P. 2019. Integrated sedimentological and seismic reservoir characterization studies as inputs into a Lower Cretaceous reservoir geomodel, offshore Abu Dhabi. *First Break*, ***37***(10), 73-84, https://doi.org/10.3997/1365-2397.2019027.
Palandri, J.L., and Kharaka, Y.K. 2005. Ferric iron-bearing sediments as a mineral trap for CO2 sequestration: Iron reduction using sulfur-bearing waste gas. *Chemical Geology*, ***217***(3-4), 351-364.
Palandri, J.L., Rosenbauer, R.J., and Kharaka, Y.K. 2005. Ferric iron in sediments as a novel CO2 mineral trap: CO2–SO2 reaction with hematite. *Applied Geochemistry*, ***20***(11), 2038-2048.
Pan, P., Wu, Z., Feng, X., and Yan, F. 2016. Geomechanical modeling of CO2 geological storage: A review. *Journal of Rock Mechanics and Geotechnical Engineering*, ***8***(6), 936-947, https://doi.org/10.1016/j.jrmge.2016.10.002.
Paxton, S., Szabo, J., Ajdukiewicz, J., and Klimentidis, R. 2002. Construction of an intergranular volume compaction curve for evaluating and predicting compaction and porosity loss in rigid-grain sandstone reservoirs. *AAPG Bulletin*, ***86***, 2047-2067, https://doi.org/10.1306/61EEDDFA-173E-11D7-8645000102C1865D.
Pay, M., Astin, T., and Parker, A. 2000. Clay mineral distribution in the Devonian-Carboniferous sandstones of the Clair Field, west of Shetland, and its significance for reservoir quality. *Clay Minerals*, ***35***(1), 151-162.
Pittman, E.D., and Larese, R.E. 1991. Compaction of lithic sands: experimental results and applications. *AAPG Bulletin*, ***75***(8), 1279-1299.
Pittman, E.D., Larese, R.E., and Heald, M.T. 1992. Clay coats: occurrence and relevance to preservation of porosity in sandstones. In Houseknecht, D.W. and Pittman, E.D. (eds) Origin, diagenesis, and petrophysics of clay minerals in sandstones: SEPM Special Publication, **47**, 241–264, https://doi.org/10.2110/pec.92.47.0241.
Pranter, M.J., Hewlett, A.C., Cole, R.D., Wang, H., and Gilman, J. 2014. Fluvial architecture and connectivity of the Williams Fork Formation: use of outcrop analogues for stratigraphic characterization and reservoir modelling. *Geological Society, London, Special Publications*, ***387***(1), 57-83, https://doi.org/10.1144/SP387.1.
Pranter, M.J., and Sommer, N.K. 2011. Static connectivity of fluvial sandstones in a lower coastal-plain setting: An example from the Upper Cretaceous lower Williams Fork Formation, Piceance Basin, Colorado. *AAPG Bulletin*, ***95***(6), 899-923, https://doi.org/10.1306/12091010008.
Primmer, T.J., Cade, C.A., Evans, J., Gluyas, J.G., Hopkins, M.S., Oxtoby, N.H., Smalley, P.C., Warren, E.A., and Worden, R.H. 1997. Global patterns in sandstone diagenesis: their application to reservoir quality prediction for petroleum exploration.
Pueyo, E.L., Calvin, P., Casas, A.M., Oliva-Urcia, B., Klimowitz, J., García-Lobón, J.L., Rubio, F.M., Ibarra, P.I., Martínez-Durán, P., and Rey-Moral, M.C. 2012. A research plan for a large potential CO2 reservoir in the Southern Pyrenees. *Geotemas*, ***13***, 1970-1973.
Puig, J.M., Cabello, P., Howell, J., and Arbués, P. 2019. Three-dimensional characterisation of sedimentary heterogeneity and its impact on subsurface flow behaviour through the braided-to-meandering fluvial deposits of the Castissent Formation (late Ypresian, Tremp-Graus Basin, Spain). *Marine and Petroleum Geology*, ***103***, 661-680.

Pyrcz, M.J., Boisvert, J.B., and Deutsch, C.V. 2009. ALLUVSIM: A program for event-based stochastic modeling of fluvial depositional systems. *Computers & Geosciences*, ***35***(8), 1671-1685.

Rahman, M.J.J., and Worden, R.H. 2016. Diagenesis and its impact on the reservoir quality of Miocene sandstones (Surma Group) from the Bengal Basin, Bangladesh. *Marine and Petroleum Geology*, ***77***, 898-915, https://doi.org/10.1016/j.marpetgeo.2016.07.027.

Ramón, J., and Cross, T. 1997. Characterization and prediction of reservoir architecture and petrophysical properties in fluvial channel sandstones, middle Magdalena Basin, Colombia. *CT&F-Ciencia, Tecnología y Futuro*, ***1***(3), 19-46.

Raza, A., Gholami, R., Rezaee, R., Rasouli, V., and Rabiei, M. 2019. Significant aspects of carbon capture and storage–A review. *Petroleum*, ***5***(4), 335-340, https://doi.org/10.1016/j.petlm.2018.12.007.

Raza, A., Rezaee, R., Gholami, R., Bing, C.H., Nagarajan, R., and Hamid, M.A. 2016. A screening criterion for selection of suitable CO2 storage sites. *Journal of Natural Gas Science and Engineering*, ***28***, 317-327.

Rezaee, M., and Lemon, N. 1996. Influence of depositional environment on diagenesis and reservoir quality: Tirrawarra sandstone reservoir, southern Cooper Basin, Australia. *Journal of Petroleum Geology*, ***19***, 369-391, https://doi.org/10.1111/j.1747-5457.1996.tb00445.x.

Richards, P.C., Lott, G.K., Johnson, H., Knox, R.W.O., and Riding, J.B. 1993. *3. Jurassic of the Central and Northern North Sea.* In: Knox, R. W. O'B. & Cordey, W. G. (eds) Lithostratigraphic nomenclature of the UK North Sea. British Geological Survey, Nottingham.

Ringrose, P., Mathieson, A., Wright, I., Selama, F., Hansen, O., Bissell, R., Saoula, N., and Midgley, J. 2013. The In Salah CO2 storage project: lessons learned and knowledge transfer. *Energy Procedia*, ***37***, 6226-6236, https://doi.org/10.1016/j.egypro.2013.06.551.

Ringrose, P.S. 2018. The CCS hub in Norway: some insights from 22 years of saline aquifer storage. *Energy Procedia*, ***146***, 166-172, https://doi.org/10.1016/j.egypro.2018.07.021

Rochelle, C.A., Czernichowski-Lauriol, I., and Milodowski, A. 2004. The impact of chemical reactions on CO2 storage in geological formations: a brief review. *Geological Society, London, Special Publications*, ***233***(1), 87-106.

Rutqvist, J., Vasco, D.W., and Myer, L. 2010. Coupled reservoir-geomechanical analysis of CO2 injection and ground deformations at In Salah, Algeria. *International Journal of Greenhouse Gas Control*, ***4***(2), 225-230, https://doi.org/10.1016/j.ijggc.2009.10.017.

Saigal, G., and Bjørlykke, K. 1987. Carbonate cements in clastic reservoir rocks from offshore Norway—relationships between isotopic composition, textural development and burial depth. *Geological Society, London, Special Publications*, ***36***(1), 313-324, https://doi.org/10.1144/GSL.SP.1987.036.01.22.

Salas, R., Guimerà, J., Mas, R., Martín-Closas, C., and Melendez, A. 2001. Evolution of the Mesozoic central Iberian Rift System and its Cainozoic inversion (Iberian chain). *Peri-Tethys Memoir*, ***6***, 145-185.

Salem, A.M., Ketzer, J., Morad, S., Rizk, R.R., and Al-Aasm, I. 2005. Diagenesis and reservoir-quality evolution of incised-valley sandstones: evidence from the Abu Madi gas reservoirs (Upper Miocene), The Nile Delta Basin, Egypt. *Journal of Sedimentary Research*, ***75***(4), 572-584.

Salem, A.M., Morad, S., Mato, L.F., and Al-Aasm, I. 2000. Diagenesis and reservoir-quality evolution of fluvial sandstones during progressive burial and uplift: Evidence from the Upper Jurassic Boipeba Member, Recôncavo Basin, Northeastern Brazil. *AAPG*

Bulletin, ***84***, 1015-1040, https://doi.org/10.1306/A9673B9E-1738-11D7-8645000102C1865D.
Sathar, S., and Jones, S. 2016. Fluid overpressure as a control on sandstone reservoir quality in a mechanical compaction dominated setting: Magnolia Field, Gulf of Mexico. *Terra nova*, ***28***(3), 155-162, https://doi.org/10.1111/ter.12203.
Sathar, S., Worden, R.H., Faulkner, D.R., and Smalley, P.C. 2012. The Effect of Oil Saturation On the Mechanism of Compaction In Granular Materials: Higher Oil Saturations Lead To More Grain Fracturing and Less Pressure Solution. *Journal of Sedimentary Research*, ***82***, 571-584, https://doi.org/10.2110/jsr.2012.44.
Sayem, A.S.M., Rahman, M.J.J., Abdullah, R., and Azim, K.R. 2022. Diagenetic history of the Miocene Surma Group sandstones from the Eastern Fold Belt of the Bengal Basin. *Journal of Asian Earth Sciences: X*, ***7***, 100098.
Schmid, S., Worden, R.H., and Fisher, Q.J. 2004. Diagenesis and reservoir quality of the Sherwood Sandstone (Triassic), Corrib Field, Slyne Basin, west of Ireland. *Marine and Petroleum Geology*, ***21***, 299-315, https://doi.org/10.1016/j.marpetgeo.2003.11.015.
Schmidt, V., and McDonald, D.A. 1979. The role of secondary porosity in the course of sandstone diagenesis. In Scholle, P.A. and Schluger, P.R. (eds) In Aspects of Diagenesis: SEPM Special Publication, **26**, 175-207.
Schneider, F., and Wolf, S. 2000. Quantitative HC potential evaluation using 3D basin modelling: application to Franklin structure, Central Graben, North Sea, UK. *Marine and Petroleum Geology*, ***17***(7), 841-856, https://doi.org/10.1016/S0264-8172(99)00060-4.
Sclater, J.G., and Christie, P.A. 1980. Continental stretching: An explanation of the post-Mid-Cretaceous subsidence of the central North Sea Basin. *Journal of Geophysical Research: Solid Earth*, ***85***, 3711-3739.
Scorgie, J.C., Worden, R., Utley, J., and Roche, I.P. 2021. Reservoir quality and diagenesis of Triassic sandstones and siltstones from arid fluvial and playa margin environments: A study of one of the UK's earliest producing oilfields. *Marine and Petroleum Geology*, ***131***, 105154, https://doi.org/10.1016/j.marpetgeo.2021.105154.
Seedhouse, J., and Racey, A. 1997. Sealing capacity of the Mercia Mudstone Group in the East Irish Sea Basin: implications for petroleum exploration. *Journal of Petroleum Geology*, ***20***(3), 261-286.
Seifert, D., and Jensen, J. 2000. Object and pixel-based reservoir modeling of a braided fluvial reservoir. *Mathematical geology*, ***32***(5), 581-603.
Shafeen, A., Croiset, E., Douglas, P., and Chatzis, I. 2004. CO2 sequestration in Ontario, Canada. Part I: storage evaluation of potential reservoirs. *Energy conversion and management*, ***45***(17), 2645-2659, https://doi.org/10.1016/j.enconman.2003.12.003.
Shammari, S., Franks, S., and Soliman, O. (2011). Depositional and Facies Controls on Infiltrated/Inherited Clay Coatings: Unayzah Sandstones, Saudi Arabia. AAPG Annual Convention and Exhibition, Houston, Texas, USA (2011).
Sharp, J.M., Shi, M., and Galloway, W.E. 2003. Heterogeneity of fluvial systems—Control on density-driven flow and transport. *Environmental & Engineering Geoscience*, ***9***(1), 5-17, https://doi.org/https://doi.org/10.2113/9.1.5.
Sheldon, H.A., Wheeler, J., Worden, R.H., and Cheadle, M.J. 2003. An analysis of the roles of stress, temperature, and pH in chemical compaction of sandstones. *Journal of Sedimentary Research*, ***73***(1), 64-71, https://doi.org/10.1306/070802730064.
Shelukhina, O., El-Ghali, M.A., Abbasi, I.A., Hersi, O.S., Farfour, M., Ali, A., Al-Awah, H., and Siddiqui, N.A. 2021. Origin and control of grain-coating clays on the development of quartz overgrowths: example from the lower Paleozoic Barik Formation sandstones,

Huqf region, Oman. *Arabian Journal of Geosciences*, ***14***(3), 1-20, https://doi.org/10.1007/s12517-021-06541-5.
Shepherd, M. 2009. Braided fluvial reservoirs. *In M. Shepherd, Oil field production geology: AAPG Memoir*, ***91***, 273-277.
Singh, M., Chaudhuri, A., Soltanian, M.R., and Stauffer, P.H. 2021. Coupled multiphase flow and transport simulation to model CO2 dissolution and local capillary trapping in permeability and capillary heterogeneous reservoir. *International Journal of Greenhouse Gas Control*, ***108***, 103329, https://doi.org/10.1016/j.ijggc.2021.103329.
Smith, R., Hodgson, N., and Fulton, M. 1993. Salt control on Triassic reservoir distribution, UKCS central North Sea. *Geological Society, London, Petroleum Geology Conference series*, ***4***, 547-557, https://doi.org/10.1144/0040547.
Smithson, T. 2016. HPHT wells. *Oilfield Review*, https://www.slb.com/-/media/files/oilfield-review/defining-hpht.ashx.
Song, Y., Jun, S., Na, Y., Kim, K., Jang, Y., and Wang, J. 2022. Geomechanical Challenges during Geological CO2 Storage: A Review. *Chemical Engineering Journal*, 140968, https://doi.org/10.1016/j.cej.2022.140968.
Sopeña, A., López, J., Arche, A., Pérez-Arlucea, M., Ramos, A., Virgili, C., and Hernando, S. 1988. Permian and Triassic rift basins of the Iberian Peninsula. In Manspeizer, W. (eds) Triassic-Jurassic Rifting, Developments in Geotectonics, **22**, 757-786, Elsevier, https://doi.org/10.1016/B978-0-444-42903-2.50036-1.
Souza, R.S., De Ros, L.F., and Morad, S. 1995. Dolomite diagenesis and porosity preservation in lithic reservoirs: Carmópolis Member, Sergipe-Alagoas Basin, northeastern Brazil. *AAPG Bulletin*, ***79***(5), 725-747, https://doi.org/10.1306/8D2B1B88-171E-11D7-8645000102C1865D.
Środoń, J. 1999. Use of clay minerals in reconstructing geological processes: recent advances and some perspectives. *Clay Minerals*, ***34***(1), 27-37, https://doi.org/10.1180/000985599546046.
Steel, R., and Ryseth, A. 1990. The Triassic—Early Jurassic succession in the northern North Sea: megasequence stratigraphy and intra-Triassic tectonics. *Geological Society, London, Special Publications*, ***55***, 139-168, https://doi.org/10.1144/GSL.SP.1990.055.01.07.
Storvoll, V., Bjørlykke, K., Karlsen, D., and Saigal, G. 2002. Porosity preservation in reservoir sandstones due to grain-coating illite: a study of the Jurassic Garn Formation from the Kristin and Lavrans fields, offshore Mid-Norway. *Marine and Petroleum Geology*, ***19***, 767-781, https://doi.org/10.1016/S0264-8172(02)00035-1.
Stricker, S. 2016. Influence of fluid pressure on the diagenesis of clastic sediments: PhD dissertation, Durham University.
Stricker, S., and Jones, S.J. 2016. Enhanced porosity preservation by pore fluid overpressure and chlorite grain coatings in the Triassic Skagerrak, Central Graben, North Sea, UK. *Geological Society, London, Special Publications*, ***435***, 321-341, https://doi.org/10.1144/SP435.4.
Stricker, S., Jones, S.J., and Grant, N.T. 2016a. Importance of vertical effective stress for reservoir quality in the Skagerrak Formation, Central Graben, North Sea. *Marine and Petroleum Geology*, ***78***, 895-909.
Stricker, S., Jones, S.J., Meadows, N., and Bowen, L. 2018. Reservoir quality of fluvial sandstone reservoirs in salt-walled mini-basins: an example from the Seagull field, Central Graben, North Sea, UK. *Petroleum Science*, ***15***, 1-27, https://doi.org/10.1007/s12182-017-0206-x.
Stricker, S., Jones, S.J., Sathar, S., Bowen, L., and Oxtoby, N. 2016b. Exceptional reservoir quality in HPHT reservoir settings: examples from the Skagerrak Formation of the

Heron Cluster, North Sea, UK. *Marine and Petroleum Geology*, ***77***, 198-215, https://doi.org/10.1016/j.marpetgeo.2016.02.003.
Strong, G., and Pearce, J. 1995. Carbonate spheroids in Permo-Triassic sandstones of the Sellafield area, Cumbria. *Proceedings of the Yorkshire Geological Society*, ***50***(3), 209-211.
Stuart, J.Y., Mountney, N.P., McCaffrey, W.D., Lang, S.C., and Collinson, J.D. 2014. Prediction of channel connectivity and fluvial style in the flood-basin successions of the Upper Permian Rangal coal measures (Queensland). *AAPG Bulletin*, ***98***(2), 191-212.
Suárez, I., Zapatero, M., Martínez, R., and Marina, M. 2009. Synthesis of the exploration of formations with a potential of CO2 storage: Intermediate Depression and Madrid Basin. *Energy Procedia*, ***1***(1), 2709-2715, https://doi.org/10.1016/j.egypro.2009.02.040.
Sun, Z.X., Sun, Z.L., Yao, J., Wu, M.L., Liu, J.R., Dou, Z., and Pei, C.r. 2014. Porosity preservation due to authigenic chlorite coatings in deeply buried Upper Triassic Xujiahe Formation sandstones, Sichuan Basin, western China. *Journal of Petroleum Geology*, ***37***(3), 251-267, https://doi.org/10.1111/jpg.12582.
Surdam, R.C., Boese, S.W., and Crossey, L.J. 1984. The chemistry of secondary porosity. In McDonald, D.A. and Surdam, R.C. (eds) Clastic Diagenesis: Tulsa, OK, AAPG Memoir, **37**, 127-150.
Swarbrick, R., Osborne, M., Grunberger, D., Yardley, G., Macleod, G., Aplin, A., Larter, S., Knight, I., and Auld, H. 2000. Integrated study of the Judy Field (Block 30/7a)—an overpressured Central North Sea oil/gas field. *Marine and Petroleum Geology*, ***17***, 993-1010, https://doi.org/10.1016/S0264-8172(00)00050-7.
Tang, L.-X., Gluyas, J., Jones, S., and Bowen, L. 2018a. Diagenetic and geochemical studies of the Buchan Formation (Upper Devonian) in the Central North Sea. *Petroleum Science*, ***15***, 211-229, https://doi.org/10.1007/s12182-018-0232-3.
Tang, L., Gluyas, J., and Jones, S. 2018. Porosity preservation due to grain coating illite/smectite: evidence from Buchan Formation (Upper Devonian) of the Ardmore Field, UK North Sea. *Proceedings of the Geologists' Association*, ***129***, 202-214, https://doi.org/10.1016/j.pgeola.2018.03.001.
Tang, Z., Parnell, J., and Longstaffe, F.J. 1997. Diagenesis of analcime-bearing reservoir sandstones; the Upper Permian Pingdiquan Formation, Junggar Basin, Northwest China. *Journal of Sedimentary Research*, ***67***(3), 486-498, https://doi.org/10.1306/D42685A4-2B26-11D7-8648000102C1865D.
Taylor, K.G., Gawthorpe, R.L., Curtis, C.D., Marshall, J.D., and Awwiller, D.N. 2000. Carbonate cementation in a sequence-stratigraphic framework: Upper Cretaceous sandstones, Book Cliffs, Utah-Colorado. *Journal of Sedimentary Research*, ***70***(2), 360-372.
Taylor, K.G., and Machent, P.G. 2011. Extensive carbonate cementation of fluvial sandstones: An integrated outcrop and petrographic analysis from the Upper Cretaceous, Book Cliffs, Utah. *Marine and Petroleum Geology*, ***28***(8), 1461-1474.
Taylor, T.R., Giles, M.R., Hathon, L.A., Diggs, T.N., Braunsdorf, N.R., Birbiglia, G.V., Kittridge, M.G., Macaulay, C.I., and Espejo, I.S. 2010. Sandstone diagenesis and reservoir quality prediction: Models, myths, and reality. *AAPG Bulletin*, ***94***, 1093-1132, https://doi.org/10.1306/04211009123.
Taylor, T.R., Kittridge, M.G., Winefield, P., Bryndzia, L.T., and Bonnell, L.M. 2015. Reservoir quality and rock properties modeling – Triassic and Jurassic sandstones, greater Shearwater area, UK Central North Sea. *Marine and Petroleum Geology*, ***65***, 1-21, https://doi.org/10.1016/j.marpetgeo.2015.03.020.

Teletzke, G.F., and Lu, P. 2013. Guidelines for reservoir modeling of geologic CO2 storage. *Energy Procedia*, ***37***, 3936-3944, https://doi.org/10.1016/j.egypro.2013.06.292.

Thanh, H.V., and Sugai, Y. 2021. Integrated modelling framework for enhancement history matching in fluvial channel sandstone reservoirs. *Upstream Oil and Gas Technology*, ***6***, 100027.

Thomson, A. 1979. Preservation of porosity in the deep Woodbine/Tuscaloosa trend, Louisiana. *Transactions of the Gulf Coast Association of Geological Societies*, ***29***, 396-403.

Thomson, A., and Stancliffe, R.J. 1990. Diagenetic controls on reservoir quality, eolian Norphlet Formation, south State Line field, Mississippi. In (eds) Sandstone petroleum reservoirs, 205-224, Springer.

Tyler, N., and Finley, R.J. 1991. Architectural Controls on the Recovery of Hydrocarbons From Sandstone Reservoirs. *In: Miall, A. D. & Tyler, N. (eds) The Three Dimensional Facies Architecture of Terrigenous Clastic Sediments and its Implications for Hydrocarbon Discovery and Recovery. Society for Sedimentary Geology, Concepts in Sedimentology and Paleontology*, ***3***, 1-5.

Ulmer-Scholle, D.S., Scholle, P.A., Schieber, J., and Raine, R.J. 2014. *A color guide to the petrography of sandstones, siltstones, shales and associated rocks.* American Association of Petroleum Geologists. https://doi.org/10.1306/M1091304.

van der Meer, L.B., Hofstee, C., and Orlic, B. 2009. The fluid flow consequences of CO2 migration from 1000 to 600 metres upon passing the critical conditions of CO2. *Energy Procedia*, ***1***(1), 3213-3220, https://doi.org/10.1016/j.egypro.2009.02.105.

Van Toorenenburg, K., Donselaar, M., Noordijk, N., and Weltje, G.J. 2016. On the origin of crevasse-splay amalgamation in the Huesca fluvial fan (Ebro Basin, Spain): Implications for connectivity in low net-to-gross fluvial deposits. *Sedimentary Geology*, ***343***, 156-164.

Verhagen, I.T.E., Crisóstomo-Figueroa, A., Utley, J.E.P., and Worden, R.H. 2020. Abrasion of detrital grain-coating clays during sediment transport: Implications for diagenetic clay coats. *Sedimentary Geology*, ***403***, 105653, https://doi.org/10.1016/j.sedgeo.2020.105653.

Vevle, M.L., Skorstad, A., and Vonnet, J. 2018. Recent developments in object modelling opens new era for characterization of fluvial reservoirs. *First Break*, ***36***(6), 85-89.

Virolle, M., Brigaud, B., Bourillot, R., Féniès, H., Portier, E., Duteil, T., Nouet, J., Patrier, P., Beaufort, D., and Hendry, J. 2019. Detrital clay grain coats in estuarine clastic deposits: origin and spatial distribution within a modern sedimentary system, the Gironde Estuary (SW France). *Sedimentology*, ***66***, 859-894, https://doi.org/10.1111/sed.12520.

Virolle, M., Brigaud, B., Luby, S., Portier, É., Féniès, H., Bourillot, R., Patrier, P., and Beaufort, D. 2019. Influence of sedimentation and detrital clay grain coats on chloritized sandstone reservoir qualities: Insights from comparisons between ancient tidal heterolithic sandstones and a modern estuarine system. *Marine and Petroleum Geology*, ***107***, 163-184, https://doi.org/10.1016/j.marpetgeo.2019.05.010.

Virolle, M., Féniès, H., Brigaud, B., Bourillot, R., Portier, E., Patrier, P., Beaufort, D., Jalon-Rojas, I., Derriennic, H., and Miska, S. 2020. Facies associations, detrital clay grain coats and mineralogical characterization of the Gironde estuary tidal bars: A modern analogue for deeply buried estuarine sandstone reservoirs. *Marine and Petroleum Geology*, ***114***, https://doi.org/10.1016/j.marpetgeo.2020.104225.

Walderhaug, O. 1990. A fluid inclusion study of quartz-cemented sandstones from offshore mid-Norway; possible evidence for continued quartz cementation during oil emplacement. *Journal of Sedimentary Research*, ***60***(2), 203-210, https://doi.org/10.1306/212F9151-2B24-11D7-8648000102C1865D.

Walderhaug, O. 1994a. Temperatures of quartz cementation in Jurassic sandstones from the Norwegian continental shelf; evidence from fluid inclusions. *Journal of Sedimentary Research*, ***64***, 311-323, https://doi.org/10.1306/D4267D89-2B26-11D7-8648000102C1865D.

Walderhaug, O. 1994b. Precipitation rates for quartz cement in sandstones determined by fluid-inclusion microthermometry and temperature-history modeling. *Journal of Sedimentary Research*, ***64***, 324-333, https://doi.org/10.2110/jsr.64.324.

Walderhaug, O. 1996. Kinetic modeling of quartz cementation and porosity loss in deeply buried sandstone reservoirs. *AAPG Bulletin*, ***80***, 731-745, https://doi.org/10.1306/64ED88A4-1724-11D7-8645000102C1865D.

Walderhaug, O. 2000. Modeling quartz cementation and porosity in Middle Jurassic Brent Group sandstones of the Kvitebjørn field, northern North Sea. *AAPG Bulletin*, ***84***(9), 1325-1339, https://doi.org/10.1306/A9673E96-1738-11D7-8645000102C1865D.

Walderhaug, O., Eliassen, A., and Aase, N.E. 2012. Prediction of permeability in quartz-rich sandstones: examples from the Norwegian continental shelf and the Fontainebleau sandstone. *Journal of Sedimentary Research*, ***82***(12), 899-912, https://doi.org/10.2110/jsr.2012.79.

Walderhaug, O., Lander, R., Bjørkum, P., Oelkers, E., Bjørlykke, K., Nadeau, P., Worden, R., and Morad, S. 2000. Modelling quartz cementation and porosity in reservoir sandstones: examples from the Norwegian continental shelf. *International Association of Sedimentologists Special Publications*, ***29***, 39-49.

Walker, T.R., Waugh, B., and Grone, A.J. 1978. Diagenesis in first-cycle desert alluvium of Cenozoic age, southwestern United States and northwestern Mexico. *Geological Society of America Bulletin*, ***89***(1), 19-32.

Wang, J., Cao, Y., Liu, K., Liu, J., Xue, X., and Xu, Q. 2016. Pore fluid evolution, distribution and water-rock interactions of carbonate cements in red-bed sandstone reservoirs in the Dongying Depression, China. *Marine and Petroleum Geology*, ***72***, 279-294, https://doi.org/10.1016/j.marpetgeo.2016.02.018.

Wang, J., Cao, Y., Xiao, J., Liu, K., and Song, M. 2019. Factors controlling reservoir properties and hydrocarbon accumulation of the Eocene lacustrine beach-bar sandstones in the Dongying Depression, Bohai Bay Basin, China. *Marine and Petroleum Geology*, ***99***, 1-16, https://doi.org/10.1016/j.marpetgeo.2018.09.022.

Wang, Z., Luo, X., Lei, Y., Zhang, L., Shi, H., Lu, J., Cheng, M., Liu, N., Wang, X., and He, Y. 2020. Impact of detrital composition and diagenesis on the heterogeneity and quality of low-permeability to tight sandstone reservoirs: An example of the Upper Triassic Yanchang Formation in Southeastern Ordos Basin. *Journal of Petroleum Science and Engineering*, ***195***, 107596, https://doi.org/10.1016/j.petrol.2020.107596.

Warren, E.A., and Pulham, A.J. 2001. Anomalous porosity and permeability preservation in deeply buried Tertiary and Mesozoic sandstones in the Cusiana field, Llanos Foothills, Colombia. *Journal of Sedimentary Research*, ***71***(1), 2-14, https://doi.org/10.1306/081799710002.

Weber, K. (1980). Influence on fluid flow of common sedimentary structures in sand bodies. SPE Annual Technical Conference and Exhibition, Texas, USA.

Wells, M., Hirst, P., Bouch, J., Whear, E., and Clark, N. 2015. Deciphering multiple controls on reservoir quality and inhibition of quartz cement in a complex reservoir: Ordovician glacial sandstones, Illizi Basin, Algeria. *Geological Society, London, Special Publications*, ***435***, 343-372, https://doi.org/10.1144/SP435.6.

Wethington, C., Pashin, J., Wethington, J., Esposito, R., and Riestenberg, D. 2022. Mudstone Baffles and Barriers in Lower Cretaceous Strata at a Proposed CO2 Storage Hub in Kemper County, Mississippi, United States. *Frontiers in Energy Research*, 879.

Wilkinson, M., Darby, D., Haszeldine, R.S., and Couples, G.D. 1997. Secondary porosity generation during deep burial associated with overpressure leak-off: Fulmar Formation, United Kingdom Central Graben. *AAPG Bulletin*, ***81***(5), 803-813, https://doi.org/10.1306/522B484D-1727-11D7-8645000102C1865D.

Wilkinson, M., and Haszeldine, R.S. 2002. Fibrous illite in oilfield sandstones–a nucleation kinetic theory of growth. *Terra nova*, ***14***(1), 56-60.

Wilkinson, M., and Haszeldine, R.S. 2011. Oil charge preserves exceptional porosity in deeply buried, overpressured, sandstones: Central North Sea, UK. *Journal of the Geological Society*, ***168***, 1285-1295, https://doi.org/10.1144/0016-76492011-007.

Wilkinson, M., Haszeldine, R.S., Morton, A., and Fallick, A.E. 2014. Deep burial dissolution of K-feldspars in a fluvial sandstone, Pentland Formation, UK Central North Sea. *Journal of the Geological Society*, ***171***, 635-647.

Wilson, M. 1982. Origins of clays controlling permeability in tight gas sands. *Journal of Petroleum Technology*, ***34***(12), 2871-2876, https://doi.org/10.2118/9843-PA.

Wilson, M.D. 1992. Inherited grain-rimming clays in sandstones from eolian and shelf environments: their origin and control on reservoir properties. In Houseknecht, D.W. and Pittman, E.D. (eds) Origin, Diagenesis and Petrophysics of Clay Minerals in Sandstones. SEPM Special Publication, **47**, 209–225, https://doi.org/10.2110/pec.92.47.0209.

Wilson, M.D., and Pittman, E.D. 1977. Authigenic clays in sandstones; recognition and influence on reservoir properties and paleoenvironmental analysis. *Journal of Sedimentary Research*, ***47***, 3-31, https://doi.org/10.1306/212F70E5-2B24-11D7-8648000102C1865D.

Wolela, A.M., and Gierlowski-Kordesch, E.H. 2007. Diagenetic history of fluvial and lacustrine sandstones of the Hartford Basin (Triassic–Jurassic), Newark Supergroup, USA. *Sedimentary Geology*, ***197***, 99-126, https://doi.org/10.1016/j.sedgeo.2006.09.006.

Wooldridge, L.J., Worden, R., Griffiths, J., Thompson, A., and Chung, P. 2017a. Biofilm origin of clay-coated sand grains. *Geology*, ***45***, 875-878, https://doi.org/10.1130/G39161.1

Wooldridge, L.J., Worden, R.H., Griffiths, J., and Utley, J.E.P. 2017b. Clay-Coated Sand Grains In Petroleum Reservoirs: Understanding Their Distribution Via A Modern Analogue. *Journal of Sedimentary Research*, ***87***, 338-352, https://doi.org/10.2110/jsr.2017.20.

Wooldridge, L.J., Worden, R.H., Griffiths, J., and Utley, J.E.P. 2019b. How To Quantify Clay-Coat Grain Coverage in Modern and Ancient Sediments. *Journal of Sedimentary Research*, ***89***, 135-146, https://doi.org/10.2110/jsr.2019.6.

Wooldridge, L.J., Worden, R.H., Griffiths, J., Utley, J.E.P., and Sheldon, N. 2019a. Clay-coat diversity in marginal marine sediments. *Sedimentology*, https://doi.org/10.1111/sed.12538.

Worden, R., Griffiths, J., Wooldridge, L., Utley, J., Lawan, A.Y., Muhammed, D., Simon, N., and Armitage, P. 2020. Chlorite in sandstones. *Earth-Science Reviews*, ***204***, 103105, https://doi.org/10.1016/j.earscirev.2020.103105.

Worden, R., and Morad, S. 2003. Clay minerals in sandstones: controls on formation, distribution and evolution. In Worden, R.H. and Morad, S. (eds) Clay mineral cements in sandstones. International Association of Sedimentologists Special Publication, **34**, 3-41, https://doi.org/10.1002/9781444304336.ch1.

Worden, R.H. 2006. Dawsonite cement in the Triassic Lam Formation, Shabwa Basin, Yemen: a natural analogue for a potential mineral product of subsurface CO2 storage for greenhouse gas reduction. *Marine and Petroleum Geology*, ***23***(1), 61-77.

Worden, R.H., Armitage, P.J., Butcher, A.R., Churchill, J.M., Csoma, A.E., Hollis, C., Lander, R.H., and Omma, J.E. 2018a. Petroleum reservoir quality prediction: overview and contrasting approaches from sandstone and carbonate communities. *Geological Society, London, Special Publications*, ***435***, 1-31, https://doi.org/10.1144/sp435.21.

Worden, R.H., Bukar, M., and Shell, P. 2018b. The effect of oil emplacement on quartz cementation in a deeply buried sandstone reservoir. *American Association of Petroleum Geologists Bulletin*, ***102***, 49-75, https://doi.org/10.1306/02071716001.

Worden, R.H., and Burley, S.D. 2003. Sandstone Diagenesis: The Evolution of Sand to Stone. In (eds) Sandstone Diagenesis, 1-44, https://doi.org/10.1002/9781444304459.ch.

Worden, R.H., Mayall, M., and Evans, I.J. 2000. The effect of ductile-lithic sand grains and quartz cement on porosity and permeability in Oligocene and lower Miocene clastics, South China Sea: prediction of reservoir quality. *AAPG Bulletin*, ***84***, 345-359, https://doi.org/10.1306/C9EBCDE7-1735-11D7-8645000102C1865D.

Worden, R.H., and Morad, S. 2000. Quartz cementation in oil field sandstones: a review of the key controversies. In Worden, R.H. and Morad, S. (eds) Quartz cementation in sandstones. International Association of Sedimentologists Special Publication, **29**, 1-20, https://doi.org/10.1002/9781444304237.ch1.

Worden, R.H., and Morad, S. 2000. Quartz Cementation in Oil Field Sandstones: A Review of the Key Controversies. In (eds) Quartz Cementation in Sandstones, 1-20, https://doi.org/10.1002/9781444304237.

Worden, R.H., Needham, S.J., and Cuadros, J. 2006. The worm gut; a natural clay mineral factory and a possible cause of diagenetic grain coats in sandstones. *Journal of Geochemical Exploration*, ***89***, 428-431, https://doi.org/10.1016/j.gexplo.2005.12.011.

Worden, R.H., and Smith, L.K. 2004. Geological sequestration of CO2 in the subsurface: lessons from CO2 injection enhanced oil recovery projects in oilfields. *Geological Society, London, Special Publications*, ***233***(1), 211-224.

Wu, C., Bhattacharya, J.P., and Ullah, M.S. 2015. Paleohydrology and 3D facies architecture of ancient point bars, Ferron Sandstone, Notom Delta, south-central Utah, USA. *Journal of Sedimentary Research*, ***85***, 399-418, https://doi.org/10.2110/jsr.2015.29.

Wu, C., Ullah, M.S., Lu, J., and Bhattacharya, J.P. 2016. Formation of point bars through rising and falling flood stages: Evidence from bar morphology, sediment transport and bed shear stress. *Sedimentology*, ***63***, 1458-1473, https://doi.org/10.1111/sed.12269.

Xi, K., Cao, Y., Jahren, J., Zhu, R., Bjørlykke, K., Zhang, X., Cai, L., and Hellevang, H. 2015. Quartz cement and its origin in tight sandstone reservoirs of the Cretaceous Quantou formation in the southern Songliao basin, China. *Marine and Petroleum Geology*, ***66***, 748-763, https://doi.org/10.1016/j.marpetgeo.2015.07.017.

Xia, C., Wilkinson, M., and Haszeldine, S. 2020. Petroleum emplacement inhibits quartz cementation and feldspar dissolution in a deeply buried sandstone. *Marine and Petroleum Geology*, ***118***, 104449, https://doi.org/10.1016/j.marpetgeo.2020.104449.

Xia, H., Perez, E.H., and Dunn, T.L. 2020. The impact of grain-coating chlorite on the effective porosity of sandstones. *Marine and Petroleum Geology*, ***115***, 104237, https://doi.org/10.1016/j.marpetgeo.2020.104237.

Xue, X., Liu, Z., Jiang, Z., Zhang, J., and Yang, T. 2021. Static connectivity of fluvial reservoirs and their temporal evolution: An example from densely drilled subsurface data in the Sanzhao Sag, Songliao Basin. *Marine and Petroleum Geology*, ***134***, 105327, https://doi.org/10.1016/j.marpetgeo.2021.105327.

Yaliz, A., and Chapman, T. 2003. The Lennox oil and gas field, block 110/15, East Irish Sea. *Geological Society, London, Memoirs*, ***20***(1), 87-96.

Yan, Y., Zhang, L., Luo, X., Liu, K., Yang, B., and Jia, T. 2022. Simulation of ductile grain deformation and the porosity loss predicted model of sandstone during compaction based on grain packing texture. *Journal of Petroleum Science and Engineering*, ***208***, 109583.

Yang, L., Xu, T., Feng, G., Liu, K., Tian, H., Peng, B., and Wang, C. 2017. CO2-induced geochemical reactions in heterogeneous sandstone and potential conditions causing the tight cementation. *Applied Geochemistry*, ***80***, 14-23, https://doi.org/10.1016/j.apgeochem.2017.03.003.

Yanzhong, W., Nianmin, Z., Xu, C., Yingchang, C., Guanghui, Y., Gluyas, J.G., and Miruo, L. 2020. Geologic CO2 storage in arkosic sandstones with CaCl2-rich formation water. *Chemical Geology*, ***558***, 119867, https://doi.org/10.1016/j.chemgeo.2020.119867.

Yardley, G., and Swarbrick, R. 2000. Lateral transfer: A source of additional overpressure? *Marine and Petroleum Geology*, ***17***(4), 523-537, https://doi.org/10.1016/S0264-8172(00)00007-6.

Yeste, L.M., Varela, A.N., Viseras, C., Mcdougall, N.D., and García-García, F. 2020. Reservoir architecture and heterogeneity distribution in floodplain sandstones: Key features in outcrop, core and wireline logs. *Sedimentology*, ***67***(7), 3355-3388, https://doi.org/10.1111/sed.12747.

Yu, L., Wu, K., Liu, L., Liu, N., Ming, X., and Oelkers, E.H. 2020. Dawsonite and ankerite formation in the LDX-1 structure, Yinggehai basin, South China sea: An analogy for carbon mineralization in subsurface sandstone aquifers. *Applied Geochemistry*, ***120***, 104663.

Yuan, G., Cao, Y., Gluyas, J., Li, X., Xi, K., Wang, Y., Jia, Z., Sun, P., and Oxtoby, N.H. 2015. Feldspar dissolution, authigenic clays, and quartz cements in open and closed sandstone geochemical systems during diagenesis: Typical examples from two sags in Bohai Bay Basin, East China. *AAPG Bulletin*, ***99***(11), 2121-2154, https://doi.org/10.1306/07101514004.

Appendix A

Skagerrak petrographic data

Abbreviations

Q: Quartz

F: Feldspar

L: Lithic rock fragment

M: Mica

CM: Clay matrix

HM: Heavy mineral

CB: Carbonate cement

Py: Pyrite

GC: Grain coating clay

Fo: Feldspar overgrowth

Qo: Quartz overgrowth

Bi: Bitumen

Interg. Poro: Intergranular porosity

Sec. poro: Secondary (dissolution) porosity

Av GS: Average grain size

He poro: Helium porosity

KH: Measured permeability

Micropor: Microporosity

Tclay: Total clay

IGV: Intergranular volume

COPL: Porosity loss due to compaction

CEPL: Porosity loss due to cementation

Judy field (well 30/7a-7)

															Thin section porosity											
Depth	Depth	Facies	Q	F	L	M	CM	HM	CB	Py	GC	Fo	Qo	Bi	Interg. poro	Sec. poro	Total porosity	Av. GS	Sorting (F &W)	He poro	KH	Micropor	Tclay	IGV	COPL	CEPL
(ft)	(m)		(%)	(%)	(%)	(%)	(%)	(%)	(%)	(%)	(%)	(%)	(%)	(%)	(%)	(%)	(%)	(mm)		(%)	(mD)	(%)	(%)	(%)	(%)	(%)
11291.25	3441.57	LEFC	43	29.7	2.4	1.6	3.8				7.3		1.8	0.7	7.7	2	9.7	0.098	0.41	24.1	43	14.4	11.1	21.3	30.1	6.8
11303.8	3445.40	LEFC	24	42.7	1.3	5.7	1.3	0.3			10	0.3	1.6	0.7	10	2	12	0.089	0.36	25.7	18	13.7	11.3	23.9	27.7	9.1
11308.82	3446.93	LEFC	30.3	38	0.3	6.3	2.3			2.1	9		1	0.7	9.7	0.3	10	0.088	0.41	25.4	20	15.4	11.3	24.8	26.9	9.4
11309.82	3447.23	LEFC	35.3	32.3	0.3	6.7	3			1	6	0.3	0.5		12.7	1.7	14.4	0.093	0.36	21.5	27	7.1	9	23.5	28.1	5.6
11318	3449.73	SF	28.4	23.3	1	12	31.7	0.7		0.3	1		0.3		0.7	0.6	1.3	0.086	0.44	19.1	0.32	17.8	32.7	34		
11320.08	3450.36	FL					100				0							0.061		11.7	0.05	11.7	100			
11324.4	3451.68	SF	28.3	32	0.3	4.7	21.7	0.7	0.7	0.7	4		1.7		5	0.3	5.3	0.086	0.38	15.6	0.33	10.3	25.7	33.8		
11326	3452.16	SF	38.7	28.3	1.6	4.4	19.6			0.7	3.3		0.3	1.2	1.6	0.3	1.9	0.092	0.38	18.1	0.23	16.2	22.9	26.7		
11328.68	3452.98	FL	3	1	1		69.7		21.3		0					4	4	0.062		12.8	0.12	8.8	69.7			
11331.17	3453.74	LEFC	31.6	26.3	0.3	7.3	12.4			0.3	7.6		0.3		8.3	5.6	13.9	0.083	0.38	23.7	9.7	9.8	20	28.9		
11335.08	3454.93	LEFC	33.3	37.4	0	2.7	3.6				6.7		1.7	0.6	12.3	1.7	14	0.092	0.33	25.7	45	11.7	10.3	24.9	26.8	6.6
11338.42	3455.95	LEFC	39.6	30		8	2.6				5		1.3		12.3	1	13.3	0.097	0.36	26.2	53	12.9	7.6	21.2	30.2	4.4
11345.58	3458.13	LEFC	45	18.7	1.7	7.3	2			1	10		1.3	0.3	11.3	1.4	12.7	0.094	0.39	25.9	68	13.2	12	25.9	25.8	9.4
11348	3458.87	SF	25.7	26.7	4.4	13.7	18.2			0.6	9.3			0.3	0.3	0.6	0.9	0.078	0.36	15.7	0.32	14.8	27.5	28.7		
11352	3460.09	FL	7.3			6.3	84				0			0.3		2	2	0.061		10	0.06	8	84			
11353	3460.39	FL	7.3	2		2.3	87.7				0					0.6	0.6	0.063		18.9	0.45	18.3	87.7			
11354	3460.70	FL					100				0							0.062		10.9	0.19	10.9	100			
11356.92	3461.59	SF	29.3	28.7		7.3	24.7			0.7	5				2.3	2	4.3	0.078	0.39	17.4	0.37	13.1	29.7	32.7		
11360.08	3462.55	SF	30	20.3	11	19.6	9.3			1.3	7.3				0.3	0.9	1.2	0.077	0.37	6.9	0.01	5.7	16.6	18.2	32.8	5.8
11363.5	3463.59	FL			1		61		38		0							0.059		13.2	0.51	13.2	61			
11365.25	3464.13	FL	3			1	91				0			3		2	2	0.061		11.1	0.04	9.1	91			
11365.75	3464.28	FL	12	9	10	4.7	62		1.3	0.3	0		0.3	0.3			0	0.062		15.8	0.47	15.8	62			

															Thin section porosity											
Depth	Depth	Facies	Q	F	L	M	CM	HM	CB	Py	GC	Fo	Qo	Bi	Interg. poro	Sec. poro	Total porosity	Av. GS	Sorting (F &W)	He poro	KH	Micropor	Tclay	IGV	COPL	CEPL
(ft)	(m)		(%)	(%)	(%)	(%)	(%)	(%)	(%)	(%)	(%)	(%)	(%)	(%)	(%)	(%)	(%)	(mm)		(%)	(mD)	(%)	(%)	(%)	(%)	(%)
11368.67	3465.17	LEFC	39	19.7	3	5.6	11.3			0.3	17.4		1		1.3	1.3	2.6	0.095	0.34	18.4	1.6	15.8	28.7	31.3		
11371.67	3466.09	LEFC	33	38		2.6	6			0.3	10.3		0.3		5.6	3.9	9.5	0.092	0.32	23.9	6.8	14.4	16.3	22.5	29.0	7.7
11433	3484.78	LEFC	25.6	38.3		6.3	2.7			0.7	8		4.7		10.7	3	13.7	0.097	0.37	25	48	11.3	10.7	26.8	24.9	10.1
11436.17	3485.74	LEFC	27.3	34.3	9.6	5	4.6			0.7	5.6		1	0.3	10	1.6	11.6	0.09	0.37	23.6	42	12	10.2	22.2	29.3	5.4
11439.17	3486.66	LEFC	28	37.3		13.6	7.7			0.9	4			0.7	5.3	2.3	7.6	0.073	0.35	12.6	5.9	5	11.7	18.6	32.4	3.8
11440.2	3486.97	LEFC	20	2	13.6	0.7	32.7		30		0.3		0.3	0.3			0	0.095	0.61	2.3	0.01	2.3	33			
11442	3487.52	LEFC	34.3	27	10.8	2.6	0.7	0.3		0.7	5.6		2.7	0.6	11.7	3	14.7	0.101	0.39	25.9	85	11.2	6.3	22	29.5	6.8
11443	3487.83	LEFC	40	19.3	12	3	1.6			1.6	11	0.3	3.3		6.3	1.6	7.9	0.102	0.40	26.4	141	18.5	12.6	24.1	27.5	11.7
11447	3489.05	FL					100				0							0.059		11.3	0.04	11.3	100			
11452	3490.57	FL	17.7	7	0	10.3	55.7				6.3			2		0.9	0.9	0.063		11.7	0.11	10.8	62			
11453.18	3490.93	SF	30.7	41.6	1.7	5.6	1				9.7		1		8.7		8.7	0.085	0.40	22.6	11	13.9	10.7	20.4	30.9	7.4
11455.5	3491.64	FL	4.3	0.7			95				0							0.061		11.5	0.24	11.5	95			
11457	3492.09	SF	32.3	16.7	0.3	10.6	36.4			0.7	0.3			0.7		2	2	0.069	0.45	18	0.72	16	36.7	38.1		
11465.25	3494.61	SF	35.3	10.7	0.7	5.7	37.6				9.3					0.7	0.7	0.065	0.45	12.1	0.47	11.4	46.9			
11468.33	3495.55	SF	44.7	18	4.3	1.3	0			0.3	6.6		3.8		18.7	2.3	21	0.144	0.32	23.5	166	2.5	6.6	29.4	22.1	8.3
11471.17	3496.41	FL	3				97				0							0.058					97			
11472.67	3496.87	SF	34	23.3	10.0	5.0	25				0.6		0.3		0.3	1.6	1.9	0.138	0.37	17.3	1.2	15.4	25.6	26.2		
11473.75	3497.20	SF	41.3	17.7	4.7	5.9	1.2	0.3		1.6	8		2	0.3	12	5	17	0.122	0.33	23.3	27	6.3	9.2	25.1	26.6	8.7
11479	3498.80	FL	1				99				0							0.061		10.5	0.11	10.5	99			
11480	3499.10	LEFC	34	19	3.6	12.7	27.7			1	0.3				0.3	1.3	1.6	0.074	0.41	18.1	3.1	16.5	28	29.3		
11490.93	3502.44	LEFC	41.7	20	5.3	3.6	1.1	0.3		1.3	5.2	0.7	4.2		13.6	3	16.6	0.135	0.30	21.9	52	5.3	6.3	26.1	25.6	8.5
11496	3503.98	HEFC	31.4	22	8.9	4.3	0			1	8.3	0.3	4	0.3	17	2.4	19.4	0.145	0.37	25.3	269	5.9	8.3	30.9	20.4	11.1

															Thin section porosity											
Depth	**Depth**	**Facies**	**Q**	**F**	**L**	**M**	**CM**	**HM**	**CB**	**Py**	**GC**	**Fo**	**Qo**	**Bi**	**Interg. poro**	**Sec. poro**	**Total porosity**	**Av. GS**	**Sorting (F &W)**	**He poro**	**KH**	**Micropor**	**Tclay**	**IGV**	**COPL**	**CEPL**
(ft)	**(m)**		**(%)**	**(%)**	**(%)**	**(%)**	**(%)**	**(%)**	**(%)**	**(%)**	**(%)**	**(%)**	**(%)**	**(%)**	**(%)**	**(%)**	**(%)**	**(mm)**		**(%)**	**(mD)**	**(%)**	**(%)**	**(%)**	**(%)**	**(%)**
11498.4	3504.71	HEFC	38.3	26.7	6.3	3	5		0.3	0.3	5.3	0.7	4.3		6.7	3	9.7	0.125	0.36	24.7	67	15	10.3	22.6	28.9	7.7
11503.7	3506.33	HEFC	35.5	22.3	10.3	2	1.9	0.3		1	4.7		3.7	0.3	12	6	18	0.165	0.37	26	539	8	6.6	23.6	28.0	7.0
11505.17	3506.78	HEFC	32.6	18.4	12.6	2	1.3		8.3	0.9	5.3	0.3	3		10	5.3	15.3	0.158	0.42	17.9	14	2.6	6.6	29.1	22.4	13.8
11507.2	3507.39	HEFC	30	46.7	0.3	5.6	0.3			1	5.3		2		7.7	1	8.7	0.122	0.43	23.1	48	14.4	5.6	16.3	34.3	5.5
11508	3507.64	LEFC	38	27.6	6.3	3.7	6.7			0.3	11.3	0.3	1.3		2.7	1.7	4.4	0.097	0.31				18	22.6	28.9	9.4
11511	3508.55	LEFC	28	17.7	10.7	12.6	12.1			0.7	11.3		1	2	1.3	2.6	3.9	0.088	0.39	21.4	4.2	17.5	23.4	28.4		
11513.58	3509.34	HEFC	38.3	15	7	9.3	19.6			1	2.7	0.3	0.7		2.4	3.7	6.1	0.15	0.38				22.3	26.7		
11517	3510.38	HEFC	42.7	19	4.3	1.3	2		6	0.3	6.6		3.8		9.7	4.3	14	0.12	0.37	25.1	59	11.1	8.6	28.4	23.2	12.8
11522.67	3512.11	HEFC	33.7	20.3	11.7	5	0.7	0.3		1	8.3		3		12.3	3.7	16	0.118	0.37	24.7	95	8.7	9	25.3	26.4	9.1
11525.75	3513.05	LEFC	33	18.6	12.3	9.4	1.7			0.7	8.4		1		10.3	4.6	14.9	0.107	0.34	24.5	59	9.6	10.1	22.1	29.4	7.1
11531.58	3514.83	LEFC	40.3	19.7	10.3	6	1.4			1	5		0.3		12.6	3.3	15.9	0.083	0.43	26.7	132	10.8	6.4	20.3	31.0	4.3
11548	3519.83	FL	5			1	94											0.059		18.9	0.005	18.9	94			

Jade field (well 30/2c-4)

															Thin section porosity											
Depth (ft)	Depth (m)	Facies	Q (%)	F (%)	L (%)	M (%)	CM (%)	HM (%)	CB (%)	Py (%)	GC (%)	Fo (%)	Qo (%)	Bi (%)	Interg. poro (%)	Sec. poro (%)	Total porosity (%)	Av. GS (mm)	Sorting (F &W)	He poro (%)	KH (mD)	Micropor (%)	Tclay (%)	IGV (%)	COPL (%)	CEPL (%)
15585.58	4750.48	FL	12	1.3	0	2.3	80.4		3.3		0		0.3			0.3	0.3	0.061		8.5		8.2	80.4			
15590.08	4751.86	FL	13.3	0.7		1	85				0						0	0.062		7.8	0.005	7.8	85			
15592.17	4752.49	SF	30.3	31.3	0.6	4.6	31				0.7		0.3	0.3	0.3	0.6	0.9	0.092	0.44	14.8	0.34	13.9	31.7	32.6		
15595.08	4753.38	FL	27.7	10	0.3	0.7	60.4			0.7	0			0.3			0	0.065		8.1		8.1	60.4			
15596.08	4753.69	FL	22.3	2.3	0	0	75.3				0						0	0.063		8.1		8.1	75.3			
15599	4754.58	SF	29	13	0	2.3	14.3		36.3	0.3	4.3			0.3			0	0.063		8.8	0.025	8.8	18.6			
15602	4755.49	SF	34	18.7	1.6	2.6	33.6		5.3	1.3	2.6					0.3	0.3	0.138	0.63	7.6	0.019	7.3	36.2	42.8		
15606	4756.71	SF	29.6	12	0.3	4.3	31		18.7	1	2.3					0.7	0.7	0.131	0.59	9.8	0.02	9.1	33.3			
15608	4757.32	SF	36.4	18	1.3	2.7	27.4		9.7	0.3	3.3		0.3	0.3		0.3	0.3	0.144	0.51	16	0.499	15.7	30.7	41.3		
15612	4758.54	HEFC	42.7	25.5	4.5	5.4	0				6.3		2.3	0.3	11.7	1.3	13	0.152	0.42	23.3	124	10.3	6.3	20.6	30.7	6.2
15614.17	4759.20	HEFC	45.3	18.3	2.3	1	0.7				4.8	0.3	6	0.3	19.7	1.3	21	0.259	0.47	25.4	890	4.4	5.5	31.8	19.4	9.2
15617.08	4760.09	HEFC	39.4	28.4	2	1.3	0		0.3		2.3	0.3	5	0.7	19	1.3	20.3	0.245	0.46	22	692	1.7	2.3	27.6	24.0	6.5
15621.05	4761.30	HEFC	42	27.3	3.6	0.6	0.6			0.3	1.7		4.3		18.7	1	19.7	0.32	0.62	23.4	842	3.7	2.3	25.6	26.1	4.7
15625	4762.50	HEFC	48.7	18.6	1.7	4.4	1.6			0.3	3.7		6	0.7	11.6	2.7	14.3	0.245	0.71	19.9	355	5.6	5.3	23.9	27.7	7.7
15625.08	4762.52	HEFC	54.7	20.3	6	0.3	5		9		0.7	0.7	0.7	0.3	1	1.3	2.3	0.332	0.63				5.7	17.4	33.4	7.6
15626	4762.80	SF	27.6	17.6	0.3	3.3	26.7		22	0.6	1.3	0.3	0.3				0	0.095	0.50	6.5	0.004	6.5	28			
15630.5	4764.18	SF	35.4	28	2	0.7	22.3				7		2.3	0.3	2		2	0.140	0.56	12.2	0.122	10.2	29.3	33.9		
15633	4764.94	HEFC	41.3	27	0.3	1	9		11.3		6		1.7	0.3	1.3	0.7	2	0.125	0.50	12.5	0.106	10.5	15	29.6	21.9	15.1
15636	4765.85	FL	10.3	8.3	0	3.3	59		18		0			0.3			0	0.064		6.5	0.006	6.5	59			
15638.33	4766.56	FL	9.3			2	75.3		13		0			0.3			0	0.063		5.6	0.01	5.6	75.3			
15643	4767.99	FL	21	6.7	0.3	1.7	70.3				0						0	0.110		6.8	0.005	6.8	70.3			
15644.9	4768.57	HEFC	49.6	18.7	0.6	0.7	0.7				5.3	0.3	4.5		18	1.6	19.6	0.22	0.42	24.4	670	4.8	6	28.8	22.8	7.8

															Thin section porosity											
Depth (ft)	**Depth (m)**	**Facies**	**Q (%)**	**F (%)**	**L (%)**	**M (%)**	**CM (%)**	**HM (%)**	**CB (%)**	**Py (%)**	**GC (%)**	**Fo (%)**	**Qo (%)**	**Bi (%)**	**Interg. poro (%)**	**Sec. poro (%)**	**Total porosity (%)**	**Av. GS (mm)**	**Sorting (F &W)**	**He poro (%)**	**KH (mD)**	**Micropor (%)**	**Tclay (%)**	**IGV (%)**	**COPL (%)**	**CEPL (%)**
15650.08	4770.14	HEFC	42.2	20	2.3	8.3	0.3		0.3		2.3		7.3	0.3	13.8	2.9	16.7	0.216	0.54	19.9	279	3.2	2.6	24.3	27.3	7.4
15656.2	4772.01	HEFC	38	26.3	3	1	0				3.3		4.2	0.3	21.3	2.6	23.9	0.211	0.52	25.3	1150	1.4	3.3	29.1	22.4	6.1
15660	4773.17	HEFC	45.6	20.3	0.3	3.3	0		1.3		1.3		6.2		16.3	3.4	19.7	0.221	0.42	23	1050	3.3	1.3	25.1	26.6	6.5
15661	4773.47	FL	8.3	1.3	0.3	2.3	81.3		4	0.3	0			0.3			0	0.062		6.6	0.005	6.6	81.3			
15664	4774.39	SF	27.7	38	0.3	3.3	21		0.7	0.3	2.4			1	2	1.2	3.2	0.099	0.36	12.2	0.025	9	23.4	27.4		
15668	4775.61	HEFC	32	39.3	0.7	6	0.3		7.7	0.3	1.3	0.3	2.7		4.3	3.3	7.6	0.158	0.42				1.6	16.9	33.8	8.1
15671	4776.52	HEFC	29.3	37.3	1.7	3	0		3.3		8.3		2.7	0.7	12.7	1	13.7	0.145	0.39	25.9	167	12.2	8.3	27.7	23.9	11.4
15671.5	4776.67	FL	5	2.7	0	5	85.4		1.7		0						0	0.057		11.2	0.039	11.2	85.4			
15676.2	4778.11	HEFC	27	34.4	0	4.6	2		4.3	0.7	2.7	0.3	6.3		15.3	2.4	17.7	0.163	0.49	23.3	529	5.6	4.7	31.6	19.6	11.5
15681	4779.57	HEFC	19.3	6.3	2	0.3	27.9		41.7	0.3	1.3	0.3	0.3	0.3			0	0.263	0.67	4.9	0.038	4.9	29.2			
15682	4779.87	FL	0.7	0	0	0	97.6		1.7		0						0	0.051		6.7	0.017	6.7	97.6			
15685	4780.79	HEFC	40.3	17.6	11.7	2.6	2		1	1.6	4.7		4	9	4	1.6	5.6	0.196	0.39	16.7	1.13	11.1	6.7	26.3	25.4	15.1
15688	4781.70	HEFC	24.3	29	2.4	2.3	0		29	0.6	3	0.3	3		1.7	1.7	3.4	0.198	0.36	23.2	273	19.8	3	37.6	11.9	31.6
15696	4784.14	HEFC	28.7	38	2	2	5.6		0.7	1.7	5.3	0.3	1.6	10.7	2.3	1	3.3	0.159	0.37	21.9	4.73	18.6	10.9	28.2	23.4	15.6
15697.17	4784.50	HEFC	24.3	18	5.7	1.3	4.7		42.7	0.6	1.3						0	0.216	0.64	13.3	2.6	13.3	6			
15698	4784.75	HEFC	36.6	26	4.6	4	3.6		12		6.3	0.3	2.3		3.3	1	4.3	0.152	0.41	11.5	8.69	7.2	9.9	27.8	23.8	15.9
15699.92	4785.34	FL	14.7	4.3	0	4.3	69.4		7		0	0.3					0	0.077		8		8	69.4			
15703.5	4786.43	FL	22.6	13	0	4.7	56.7		0.3		0			2	0.3		0.3	0.066		11.5	0.059	11.2	56.7			
15706.08	4787.21	FL	8.7	4.3	0.7	2	83.7		0.7		0						0	0.062		5.2	0.005	5.2	83.7			
15707.33	4787.59	SF	40	18.3	3.6	3	20			0.6	7	0.3	2.3		3	1.3	4.3	0.161	0.48	15.8	1.03	11.5	27	33.2		
15714.95	4789.92	HEFC	42.3	20.7	0.3	0.3	1.3		34.7		0.3						0.3	0.238	0.47	6.2	2.07	5.9	1.3	36.3	13.7	30.2
15718.25	4790.92	HEFC	37	25.6	5	1.6	0.3				2.7	0.7	6		15.4	5.7	21.1	0.183	0.43	24.7	614	3.6	3	25.1	26.6	6.9

															Thin section porosity											
Depth (ft)	**Depth (m)**	**Facies**	**Q (%)**	**F (%)**	**L (%)**	**M (%)**	**CM (%)**	**HM (%)**	**CB (%)**	**Py (%)**	**GC (%)**	**Fo (%)**	**Qo (%)**	**Bi (%)**	**Interg. poro (%)**	**Sec. poro (%)**	**Total porosity (%)**	**Av. GS (mm)**	**Sorting (F &W)**	**He poro (%)**	**KH (mD)**	**Micropor (%)**	**Tclay (%)**	**IGV (%)**	**COPL (%)**	**CEPL (%)**
15719.17	4791.20	FL	17.7	5.6	0	1	75				0			0.3			0	0.064					75			
15723	4792.37	SF	38.7	23	1.9	0.3	25.3		0.3	1.7	6.6			0.7		1.3	1.3	0.119	0.51	8.8	0.058	7.5	31.9	34.6		
15727	4793.59	FL	17	8.5	0	2.6	53.3			0.3	3			15		0.3	0.3	0.062					56.3			
15737	4796.64	HEFC	38	23.3	3	1.3	5.9		1.3	2.6	4		4.3	12.3	3.3	0.7	4	0.17	0.56	9.4	0.188	5.4	9.9	33.7	17.0	20.3
15740	4797.55	HEFC	32.3	36.7	8	4	3.6		0.7		4.7		1	6.3	1.7	1	2.7	0.18	0.58	16.9	1.77	14.2	8.3	18	32.9	8.5
15745.08	4799.10	HEFC	38.4	17	8.6	2.3	0		10		3.7	1.3	2.7		10.7	5.3	16	0.286	0.52	20.6	682	4.6	3.7	28.4	23.2	13.6
15748.18	4800.05	HEFC	39.7	17.5	7.2	2.3	0.3			0.7	4	0.3	7	1	15.8	4.2	20	0.274	0.56	23	1134	3	4.3	29.1	22.4	10.1
15750.5	4800.75	FL	6.7	2.7	17.3	0.3	71		2		0						0	0.052					71			
15753.83	4801.77	FL	4	0	0	0.3	95.7				0						0	0.059					95.7			
15758	4803.04	FL	18	0.7	0.6	2	78				0			0.7			0	0.061					78			
15761.83	4804.21	FL	25.7	6.3	0.7	5.3	62				0						0	0.075		7.4	0.012	7.4	62			
15763	4804.56	FL					100				0						0	0.057		6.2	0.012	6.2	100			
15777.3	4808.92	FL					80		20		0						0	0.058		3.7	0.004	3.7	80			
15778	4809.13	FL	2.3	0	0	0.3	97.3				0						0	0.057		6.3	0.014	6.3	97.3			
15791	4813.10	FL	0	0	0	0	100				0						0	0.052					100			
15792.5	4813.55	SF	33.6	42.3	3.3	6.3	3.6				4	0.3	4.3	0.3	0	2	2	0.186	0.38	13.4	2.35	11.4	7.6	12.5	37.1	5.6

Appendix B

Clay coat quantification technique

Chlorite coat coverage (%):

$$\frac{\textit{Sum of chlorite coated lengths}}{\textit{Grain circumference} - \textit{Sum of grain contact length}} * 100$$

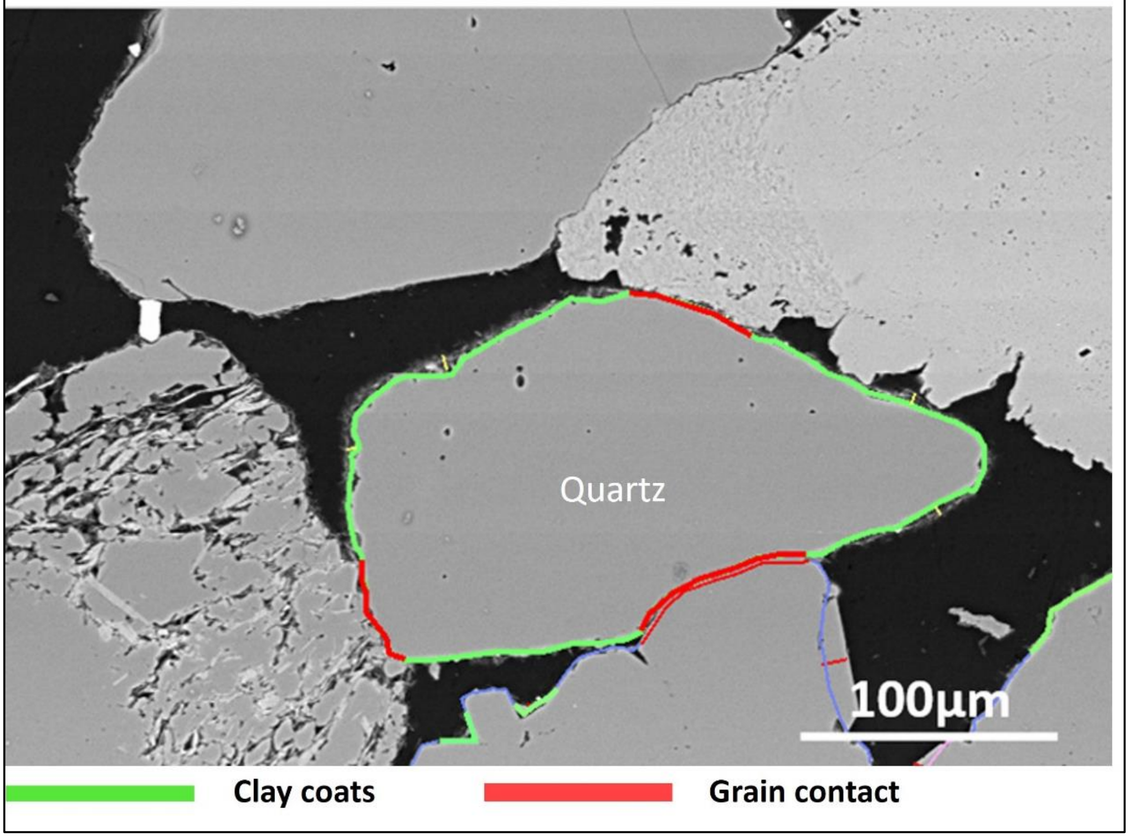

Figure B.1: Clay coat quantification technique used in this study. This technique follows the method of Dutton et al. (2018). For each detrital quartz grain, we measured (1) the grain circumference, (2) the lengths of any parts of the grain that are in contact with other grains and thus not available for clay coating and (3) the lengths of chlorite coatings on the grain surface. Chlorite coat coverage was then calculated using the equation above.

Appendix C

Quartz cement modelling parameters and algorithms used in the study

Judy field (well 30/7a-7)

Field	Formation	Well	Depth	D		Q	f	V	A_0	C		A	Q_0	Facies
			(ft)	(mm)	(cm)	(%)	(fraction)	(cm^3)	(cm^2/cm^3)	(%)	(fraction)	(cm^2/cm^3)	(%)	
Judy	Judy	30/7a-7	11291.3	0.098	0.0098	43	0.43	1	262.5	78.5	0.785	56.4	1.8	Fluvial channel
Judy	Judy	30/7a-7	11303.8	0.089	0.0089	24	0.24	1	162	95.3	0.953	7.6	1.6	Fluvial channel
Judy	Judy	30/7a-7	11309.8	0.093	0.0093	35.3	0.353	1	227	96	0.96	9.1	0.5	Fluvial channel
Judy	Judy	30/7a-7	11335.1	0.0917	0.00917	33.3	0.333	1	217.9	93	0.93	15.3	1.7	Fluvial channel
Judy	Judy	30/7a-7	11338.4	0.0968	0.00968	39.6	0.396	1	245.5	91	0.91	22.1	1.3	Fluvial channel
Judy	Judy	30/7a-7	11442	0.101	0.0101	34.3	0.343	1	203	98	0.98	4.1	2.7	Fluvial channel
Judy	Judy	30/7a-7	11490.9	0.135	0.0135	41.7	0.417	1	185	92.7	0.927	13.5	4.2	Fluvial channel
Judy	Judy	30/7a-7	11496	0.145	0.0145	31.4	0.314	1	130.4	80.4	0.804	25.6	4.0	Fluvial channel
Average values used in the modelling				**0.11**	**0.011**	**35.3**	**0.353**			**91**	**0.91**		**2.2**	

Jade field (well 30/2c-4)

Field	Formation	Well	Depth	D		Q	f	V	A_0	C		A	Q_0	Facies
			(ft)	(mm)	(cm)	(%)	(fraction)	(cm^3)	(cm^2/cm^3)	(%)	(fraction)	(cm^2/cm^3)	(%)	
Jade	Joanne	30/2c-4	15612	0.152	0.0152	42.7	0.427	1	169.1	69	0.69	52.4	2.3	Fluvial channel
Jade	Joanne	30/2c-4	15614.2	0.259	0.0259	45.3	0.453	1	104.9	50	0.5	52.4	6.0	Fluvial channel
Jade	Joanne	30/2c-4	15617.1	0.245	0.0245	39.4	0.394	1	96.6	36.2	0.362	61.6	5.0	Fluvial channel
Jade	Joanne	30/2c-4	15621.1	0.3195	0.03195	42	0.42	1	78.8	30.2	0.302	55.0	4.3	Fluvial channel
Jade	Joanne	30/2c-4	15625	0.245	0.0245	48.7	0.487	1	119	40	0.4	71.6	6.0	Fluvial channel
Jade	Joanne	30/2c-4	15644.9	0.219	0.0219	49.6	0.496	1	135.6	60	0.6	54.2	4.5	Fluvial channel
Jade	Joanne	30/2c-4	15650.1	0.216	0.0216	42.2	0.422	1	115.1	17	0.17	95.5	7.3	Fluvial channel
Jade	Joanne	30/2c-4	15656.2	0.211	0.0211	38	0.38	1	107.9	36.8	0.368	68.2	4.2	Fluvial channel
Jade	Joanne	30/2c-4	15660	0.221	0.0221	45.6	0.456	1	124	27	0.27	90.5	6.2	Fluvial channel
Jade	Joanne	30/2c-4	15671	0.145	0.0145	29.3	0.293	1	121.1	60.2	0.602	48.2	2.7	Fluvial channel
Jade	Joanne	30/2c-4	15676.2	0.163	0.0163	27	0.27	1	99.2	36	0.36	63.5	6.3	Fluvial channel
Jade	Joanne	30/2c-4	15718.3	0.183	0.0183	37	0.37	1	121	17.3	0.173	100.3	6.0	Fluvial channel
Jade	Joanne	30/2c-4	15748.2	0.274	0.0274	39.7	0.397	1	87	15.9	0.159	73.2	7.0	Fluvial channel
Average values used in the modelling				**0.22**	**0.022**	**40.5**	**0.405**			**38**	**0.38**		**5.2**	

Principle functions:

Q = Point counted quartz clasts

$A_0 = 6fV / D$

$V_{q2} = \phi_o - (\phi_o - V_{q1}) \exp - MaA_0 / \rho\phi_0 bc \ln 10(10^{bT_2} - 10^{bT_1})$

$A = (1 - C)6fV / D$

Where:

A_0 = Cumulative surface area of quartz clasts prior to clay coatings and quartz cementation per cubic centimeter of sandstone

A = Cumulative surface area of quartz clasts after clay coatings and prior to quartz cementation per cubic centimeter of sandstone

C = fraction of quartz grain surface coated by clay (i.e., clay coat coverage)

f = Volume fraction of quartz clasts

V = Sample volume (or unit volume)

D = Quartz grain size (or diameter of grains)

V_{q2} is the amount of quartz cement (cm^3) precipitated from time T_1 to T_2

V_{q1} is the amount of quartz cement present at time T_1

ρ = Density of quartz (2.65 g/cm^3)

M = Molar mass of quartz (60.09 g/mole)

ϕ = Porosity at the start of quartz cementation

a = 1.98 × 10-22 mol/cm^2s

b = 0.022/°C

Q_0 = Point counted quartz cement volume

Detailed description of algorithms used for quartz cement modelling can be found in chapter 1 (section 1.3.6) and Walderhaug 1994a, 1994b, 1996 and Walderhaug et al. 2000.

Appendix D

Kozeny permeability data derived using Kozeny equation.

(See Walderhaug et al. 2012 for further details).

JUDY SANDSTONE MEMBER (30/7a-7)									
Depth	**Facies**	**Grain size**	**Measured permeability**	**Helium porosity**	**Constant**	**P^3**	**D^2**	**(100-P)^2**	**Kozeny permeability**
(ft)		**(mm)**	**(mD)**	**(%)**					**(mD)**
11291.25	LEFC	0.098	43	24.1	8000	13997.5210	0.0096	5760.8	186.7
11303.8	LEFC	0.089	18	25.7	8000	16974.5930	0.0079	5520.5	194.8
11308.82	LEFC	0.088	20	25.4	8000	16387.0640	0.0077	5565.2	182.4
11309.82	LEFC	0.093	27	21.5	8000	9938.3750	0.0086	6162.3	111.6
11318	SF	0.086	0.32	19.1	8000	6967.8710	0.0074	6544.8	63.0
11320.08	FL	0.061	0.05	11.7	8000	1601.6130	0.0037	7796.9	6.1
11324.4	SF	0.086	0.33	15.6	8000	3796.4160	0.0074	7123.4	31.5
11326	SF	0.092	0.23	18.1	8000	5929.7410	0.0085	6707.6	59.9
11328.68	FL	0.062	0.12	12.8	8000	2097.1520	0.0038	7603.8	8.5
11331.17	LEFC	0.083	9.7	23.7	8000	13312.0530	0.0069	5821.7	126.0
11335.08	LEFC	0.092	45	25.7	8000	16974.5930	0.0085	5520.5	208.2
11338.42	LEFC	0.097	53	26.2	8000	17984.7280	0.0094	5446.4	248.6
11345.58	LEFC	0.094	68	25.9	8000	17373.9790	0.0088	5490.8	223.7
11348	SF	0.078	0.32	15.7	8000	3869.8930	0.0061	7106.5	26.5
11351	FL	0.061	0.06	10	8000	1000.0000	0.0037	8100.0	3.7
11353	FL	0.063	0.45	18.9	8000	6751.2690	0.0040	6577.2	32.6
11354	FL	0.062	0.19	10.9	8000	1295.0290	0.0038	7938.8	5.0
11356.92	SF	0.077	0.37	17.4	8000	5268.0240	0.0059	6822.8	36.6
11360.08	SF	0.077	9.2	6.9	8000	328.5090	0.0059	8667.6	1.8
11362.42	FL		0.01		8000	0.0000	0.0000	10000.0	0.0
11363.5	FL	0.059	0.51	13.2	8000	2299.9680	0.0035	7534.2	8.5
11365.25	FL	0.061	0.04	11.1	8000	1367.6310	0.0037	7903.2	5.2
11365.75	FL	0.062	0.47	15.8	8000	3944.3120	0.0038	7089.6	17.1
11368.67	LEFC	0.095	1.6	18.4	8000	6229.5040	0.0090	6658.6	67.5
11371.67	LEFC	0.092	6.8	23.9	8000	13651.9190	0.0085	5791.2	159.6
11433	LEFC	0.097	48	25	8000	15625.0000	0.0094	5625.0	209.1
11436.17	LEFC	0.090	42	23.6	8000	13144.2560	0.0081	5837.0	145.9
11439.17	LEFC	0.073	5.9	12.6	8000	2000.3760	0.0053	7638.8	11.2
11440.2	LEFC	0.095	0.01	2.3	8000	12.1670	0.0090	9545.3	0.1
11442	LEFC	0.101	85	25.9	8000	17373.9790	0.0102	5490.8	258.2
11443	LEFC	0.102	141	26.4	8000	18399.7440	0.0104	5417.0	282.7
11447	FL	0.059	0.04	11.3	8000	1442.8970	0.0035	7867.7	5.1
11452	FL	0.063	0.11	11.7	8000	1601.6130	0.0040	7796.9	6.5
11453.18	SF	0.085	11	22.6	8000	11543.1760	0.0072	5990.8	111.4
11455.5	FL	0.061	0.24	11.5	8000	1520.8750	0.0037	7832.3	5.8

JUDY SANDSTONE MEMBER (30/7a-7)									
Depth	**Facies**	**Grain size**	**Measured permeability**	**Helium porosity**	**Constant**	**P^3**	**D^2**	**(100-P)^2**	**Kozeny permeability**
(ft)		**(mm)**	**(mD)**	**(%)**					**(mD)**
11457	SF	0.069	0.72	18	8000	5832.0000	0.0048	6724.0	33.0
11465.25	SF	0.065	0.47	12.1	8000	1771.5610	0.0042	7726.4	7.7
11468.33	SF	0.144	166	23.5	8000	12977.8750	0.0207	5852.3	367.9
11471.17	FL	0.058			8000	0.0000	0.0034	10000.0	
11472.67	SF	0.138	1.2	17.3	8000	5177.7170	0.0190	6839.3	115.3
11473.75	SF	0.122	27	23.3	8000	12649.3370	0.0149	5882.9	256.0
11479	FL	0.061	0.11	10.5	8000	1157.6250	0.0037	8010.3	4.3
11481	LEFC	0.074	3.1	18.1	8000	5929.7410	0.0055	6707.6	38.7
11490.93	LEFC	0.135	52	21.9	8000	10503.4590	0.0182	6099.6	251.1
11496	HEFC	0.145	269	25.3	8000	16194.2770	0.0210	5580.1	488.1
11498.4	HEFC	0.125	67	24.7	8000	15069.2230	0.0156	5670.1	332.2
11503.7	HEFC	0.165	539	26	8000	17576.0000	0.0272	5476.0	699.1
11505.17	HEFC	0.158	14	17.9	8000	5735.3390	0.0250	6740.4	169.9
11507.2	HEFC	0.122	48	23.1	8000	12326.3910	0.0149	5913.6	248.2
11508	LEFC	0.097			8000	0.0000	0.0094	10000.0	
11511	LEFC	0.088	4.2	21.4	8000	9800.3440	0.0077	6178.0	98.3
11513.58	HEFC	0.150			8000	0.0000	0.0225	10000.0	
11517	HEFC	0.120	59	25.1	8000	15813.2510	0.0144	5610.0	324.7
11522.67	HEFC	0.118	95	24.7	8000	15069.2230	0.0139	5670.1	296.0
11525.75	LEFC	0.107	59	24.5	8000	14706.1250	0.0114	5700.3	236.3
11531.58	LEFC	0.083	132	26.7	8000	19034.1630	0.0069	5372.9	195.2
11548	FL	0.059	0.005	18.9	8000	6751.2690	0.0035	6577.2	28.6

JOANNE SANDSTONE MEMBER (30/2c-4)									
Depth	**Facies**	**Grain size**	**Measured permeability**	**Helium porosity**	**Constant**	**P^3**	**D^2**	**100-P^2**	**Kozeny permeability**
(ft)		**(mm)**	**(mD)**	**(%)**					**(mD)**
15585.58	FL	0.061		8.5	8000	614.13	0.0037	8372.3	2.2
15590.08	FL	0.062	0.005	7.8	8000	474.55	0.0038	8500.8	1.7
15592.17	SF	0.092	0.34	14.8	8000	3241.79	0.0085	7259.0	30.2
15595.08	FL	0.065		8.1	8000	531.44	0.0042	8445.6	2.1
15596.08	FL	0.063		8.1	8000	531.44	0.0040	8445.6	2.0
15599	SF	0.063	0.025	8.8	8000	681.47	0.0040	8317.4	2.6
15602	SF	0.138	0.019	7.6	8000	438.98	0.0190	8537.8	7.8
15606	SF	0.131	0.02	9.8	8000	941.19	0.0172	8136.0	15.9
15608	SF	0.144	0.499	16	8000	4096.00	0.0207	7056.0	96.3
15612	HEFC	0.152	124	23.3	8000	12649.34	0.0231	5882.9	397.4
15614.17	HEFC	0.259	890	25.4	8000	16387.06	0.0671	5565.2	1580.2
15617.08	HEFC	0.245	692	22	8000	10648.00	0.0600	6084.0	840.4
15621.05	HEFC	0.32	842	23.4	8000	12812.90	0.1024	5867.6	1788.9
15625	HEFC	0.245	355	19.9	8000	7880.60	0.0600	6416.0	589.8
15625.08	HEFC	0.332			8000	0.00	0.1102	10000.0	0.0
15626	SF	0.095	0.004	6.5	8000	274.63	0.0090	8742.3	2.3
15630.5	SF	0.140	0.122	12.2	8000	1815.85	0.0196	7708.8	36.9
15633	HEFC	0.125	0.106	12.5	8000	1953.13	0.0156	7656.3	31.9
15636	FL	0.064	0.006	6.5	8000	274.63	0.0041	8742.3	1.0
15638.33	FL	0.063	0.01	5.6	8000	175.62	0.0040	8911.4	0.6
15643	FL	0.110	0.005	6.8	8000	314.43	0.0121	8686.2	3.5
15644.9	HEFC	0.22	670	24.4	8000	14526.78	0.0484	5715.4	984.1
15650.08	HEFC	0.216	279	19.9	8000	7880.60	0.0467	6416.0	458.4
15656.2	HEFC	0.211	1150	25.3	8000	16194.28	0.0445	5580.1	1033.7
15660	HEFC	0.221	1050	23	8000	12167.00	0.0488	5929.0	801.8
15661	FL	0.062	0.005	6.6	8000	287.50	0.0038	8723.6	1.0
15664	SF	0.099	0.025	12.2	8000	1815.85	0.0098	7708.8	18.5
15668	HEFC	0.158			8000	0.00	0.0250	10000.0	0.0
15671	HEFC	0.145	167	25.9	8000	17373.98	0.0210	5490.8	532.2
15671.5	FL	0.057	0.039	11.2	8000	1404.93	0.0032	7885.4	4.6
15676.2	HEFC	0.163	529	23.3	8000	12649.34	0.0266	5882.9	457.0
15681	HEFC	0.263	0.038	4.9	8000	117.65	0.0692	9044.0	7.2
15682	FL	0.051	0.017	6.7	8000	300.76	0.0026	8704.9	0.7
15685	HEFC	0.196	12.1	16.7	8000	4657.46	0.0384	6938.9	206.3

JOANNE SANDSTONE MEMBER (30/2c-4)									
Depth	**Facies**	**Grain size**	**Measured permeability**	**Helium porosity**	**Constant**	**P^3**	**D^2**	**100-P^2**	**Kozeny permeability**
(ft)		**(mm)**	**(mD)**	**(%)**					**(mD)**
15688	HEFC	0.198	273	23.2	8000	12487.17	0.0392	5898.2	664.0
15696	HEFC	0.159	4.73	21.9	8000	10503.46	0.0253	6099.6	348.3
15697.17	HEFC	0.216	2.6	13.3	8000	2352.64	0.0467	7516.9	116.8
15698	HEFC	0.152	8.69	11.5	8000	1520.88	0.0231	7832.3	35.9
15699.92	FL	0.077		8	8000	512.00	0.0059	8464.0	2.9
15703.5	FL	0.066	0.059	11.5	8000	1520.88	0.0044	7832.3	6.8
15706.08	FL	0.062	0.005	5.2	8000	140.61	0.0038	8987.0	0.5
15707.33	SF	0.161	1.03	15.8	8000	3944.31	0.0259	7089.6	115.4
15714.95	HEFC	0.238	2.07	6.2	8000	238.33	0.0566	8798.4	12.3
15718.25	HEFC	0.183	614	24.7	8000	15069.22	0.0335	5670.1	712.0
15719.17	FL	0.064			8000	0.00	0.0041	10000.0	0.0
15723	SF	0.119	0.058	8.8	8000	681.47	0.0142	8317.4	9.3
15727	FL	0.062			8000	0.00	0.0038	10000.0	0.0
15737	HEFC	0.17	0.188	9.4	8000	830.58	0.0289	8208.4	23.4
15740	HEFC	0.18	1.77	16.9	8000	4826.81	0.0324	6905.6	181.2
15745.08	HEFC	0.286	682	20.6	8000	8741.82	0.0818	6304.4	907.4
15748.18	HEFC	0.274	1134	23	8000	12167.00	0.0751	5929.0	1232.5
15750.5	FL	0.052			8000	0.00	0.0027	10000.0	0.0
15753.83	FL	0.059			8000	0.00	0.0035	10000.0	0.0
15758	FL	0.061			8000	0.00	0.0037	10000.0	0.0
15761.83	FL	0.075	0.012	7.4	8000	405.22	0.0056	8574.8	2.1
15775	FL	0.057	0.012	6.2	8000	238.33	0.0032	8798.4	0.7
15781.92	FL	0.058	0.004	3.7	8000	50.65	0.0034	9273.7	0.1
15784.5	FL	0.057	0.014	6.3	8000	250.05	0.0032	8779.7	0.7
15791	FL	0.052			8000	0.00	0.0027	10000.0	0.0
15792.5	SF	0.186	2.35	13.4	8000	2406.10	0.0346	7499.6	88.8

$$k = 8000 \frac{P^3}{(100\text{-}P)^2} D^2$$

K = Kozeny permeability

P = Helium porosity (%)

D = Grain size (mm)

8000 = Constant

Appendix E

St Bees petrographic data

Abbreviations

Q: Quartz

F: Feldspar

L: Lithic rock fragment

M: Mica

CM: Clay matrix

HM: Heavy mineral

CB: Carbonate cement

Hmt: Hematite

PF: Pore filling clay

GC: Grain coating clay

Fo: Feldspar overgrowth

Qo: Quartz overgrowth

Interg. Poro: Intergranular porosity

Sec. poro: Secondary (dissolution) porosity

GS: Average grain size

PFD: Ductile grains (pseudomatrix + ductile mica grains)

IGV: Intergranular volume

COPL: Porosity loss due to compaction

CEPL: Porosity loss due to cementation

South Head

								Authigenic clays					Porosity							
Sample	**Q**	**F**	**L**	**M**	**CM**	**HM**	**CB**	**PF**	**GC**	**Hmt**	**Fo**	**Qo**	**Interg. Poro**	**Sec. poro**	**Total porosity**	**GS**	**PFD**	**IGV**	**CEPL**	**COPL**
	(%)	(%)	(%)	(%)	(%)	(%)	(%)	(%)	(%)	(%)	(%)	(%)	(%)	(%)	(%)	(mm)	(%)	(%)	(%)	(%)
LS4	22.3	17.7	0	4.6	48.6		0.3	0	4.7	1			0.3	0.3	0.6	0.051		54.9	44.8	
LS5	48	37	0.3	0.7	4.3			0	7.7				1	1	2	0.095	5	13	7.6	36.8
LS6	40.3	41.3	0.3	1	3.3			0	11	2		0.3	0.3	0	0.3	0.087	6.3	16.9	11.0	33.8
LS7	24.3	4	0	2.3	69.3			0					0	0	0	0.108	2.3	69.3	45.0	
LS8	44.7	22.3	3	0	0.3	0.3		1.3	7	0.3		6.7	10.3	3.6	13.9	0.166	1.9	25.9	11.6	25.8
LS9	39	24	1.3	0.3	0.3			0.7	8			9.3	13.7	3.3	17	0.173	1.3	32	14.8	19.1
LS10	42.4	27	1.3	0.3	4			0.7	10.7	0.3		3	8	2.3	10.3	0.131	5.3	26.7	14.0	25.0
LS11	36	23.3	1	0				0.7	8.7	0.3		9.3	17.7	3	20.7	0.167	1	36.7	16.5	13.1
LS12	38.3	28.3	1	0	2			0.7	5.7	0.7		5.7	14	3.6	17.6	0.163	3.4	28.8	11.4	22.8
LS13	37.9	31	0.7	0.3	4			0.3	10.7			3.3	9.7	2	11.7	0.111	4.6	28	14.0	23.6
LS14	38.7	34	0.7	0.7	4.7			0	4.7	0.7	0.3	2	10.7	3	13.7	0.116	6.1	23.1	8.9	28.5
LS15	38.3	37.3	0	2.3	5			0	6.3	0.3		1.3	7	2	9	0.119	7.6	19.9	8.9	31.3
LS16	41	34	0	0.7	2			0	6.7	0.3		1.7	12.3	1.3	13.6	0.127	3	23	7.6	28.6
LS17	49	21.3	0.3	0	1			0	9.7	0.7		3.3	12.7	2	14.7	0.152	1.7	27.4	11.1	24.2
LS18	53.3	15.3	0.7	0.7		0.3		0	6.7	1.3		3.3	15.3	3	18.3	0.150	2	26.6	8.5	25.1
LS19	40	29.7	0.3	1	12			0	7.3	0.3		2.7	5.3	1.3	6.6	0.143	13.3	27.6	36.4	
LS20	49	21	0.3	1	0.6			0.3	6.7	0.3		3.3	12.7	4.7	17.4	0.166	2.2	23.9	8.1	27.7
LS21	53	24	0.7	0.3	1.7			0.3	7.7	0.7		1.7	9	1	10	0.128	3	21.1	8.4	30.3
LS22	49.3	19.7	0.7	0.3	3		1.7	0.3	10.3	0.7		1.7	11.3	1	12.3	0.166	4.3	29	13.7	22.5
LS23	44	27	2	0				0	10.3	0.3		2	13.3	1	14.3	0.161	0.3	25.9	9.4	25.8
LS24	47	26	0.7	1.4	2.6			0.3	7.3	0.7		2.3	10	1.7	11.7	0.124	5	23.2	9.5	28.4
LS25	45.7	30	0	1	4			0	7	0.3		1	10	1	11	0.099	5.3	22.3	8.7	29.2
LS26	45	29.7	0.7	1.7	2.3			0	8.3	0.7		1	9.3	1.3	10.6	0.114	4.7	21.6	8.6	29.8

								Authigenic clays					Porosity							
Sample	**Q**	**F**	**L**	**M**	**CM**	**HM**	**CB**	**PF**	**GC**	**Hmt**	**Fo**	**Qo**	**Interg. Poro**	**Sec. poro**	**Total porosity**	**GS**	**PFD**	**IGV**	**CEPL**	**COPL**
	(%)	(%)	(%)	(%)	(%)	(%)	(%)	(%)	(%)	(%)	(%)	(%)	(%)	(%)	(%)	(mm)	(%)	(%)	(%)	(%)
LS27	37	32.9	1	0.6	1			0.3	13.7	1		2	7.7	2.7	10.4	0.120	2.9	25.7	13.3	26.0
LS28	38.7	33	0.3	0.6	1			0.7	10	1.7		1	10.7	2.3	13	0.115	4	25.1	10.6	26.6
LS36	41.4	32	0.3	0.7	0.7			0	7.7	1		4.7	10.7	1	11.7	0.147	2.4	24.8	10.3	26.9
LS37	49	20	0.3	0	0.3			1	9	0.3		5	11.7	3.3	15	0.195	1.6	27.3	11.8	24.3
LS38	41	27	1.3	0.3			0.3	0	9			3	17	1	18	0.187	0.3	29.3	9.6	22.2
LS39	45.3	21.7	1.3	0				0	9.3	0.7		4	17.3	0.3	17.6	0.207	0.7	31.3	11.2	19.9
LS40	43	33.7	0	0.3			2.6	0	8.7	0.3		1.7	9	0.7	9.7	0.159	0.6	22.3	9.4	29.2
LS41	41.7	34.7	2.7	1.7	1			0.3	6.3	1.3		0.7	8.7	1	9.7	0.139	4.3	18.3	6.5	32.7
LS42	40.7	25.3	0.7	1.3	0.3		2	0.7	11	0.3		1.3	13	3.3	16.3	0.171	2.6	28.6	12.0	23.0
LS42.1	48.3	22.3	1	0.6				0.3	10	0.3	0.3	2.7	11.7	2.3	14	0.187	1.2	25.3	10.0	26.4
LS43	52	21.3	3	0.3	0.7			0.3	5.7		0.3	3.3	11.7	1.3	13	0.201	1.3	22	7.3	29.5
LS44	44	27	1.6	0	0.3		0.3	0	9.7	0.7		2.7	12.7	1	13.7	0.184	1	26.4	10.2	25.3
LS45	38.7	11.7	8.3	5.3	24.7	0.3		1.3	2.3		0.3	2	4.7	0.3	5	0.146	31.3	35.3	39.0	
LS46	41.3	21.7	1	0.6	7.3			1	6.3	1		3.3	9.3	3	12.3	0.180	9.9	28.2	14.5	23.4
LS47	29.7	37	6.4	0.7				0	8	1		3	11.3	3	14.3	0.167	1.7	23.3	8.6	28.3
LS48	44.7	25.3	1	2	3			0.3	7			4	10	2.7	12.7	0.186	5.3	24.3	10.4	27.3
LS49	44	22.3	3					0.3	8	0.3	0.7	6	14	1.3	15.3	0.187	0.6	29.3	11.9	22.2
LS50	42	22.7	4.6	0.6	2			1	9	1		4.3	11.3	1.3	12.6	0.174	4.6	28.6	13.3	23.0

Fleswick Bay (Cross-section)

								Authigenic clays					Porosity							
Sample	**Q**	**F**	**L**	**M**	**CM**	**HM**	**CB**	**PF**	**GC**	**Hmt**	**Fo**	**Qo**	**Interg. Poro**	**Sec. poro**	**Total porosity**	**GS**	**PFD**	**IGV**	**CEPL**	**COPL**
	(%)	(%)	(%)	(%)	(%)	(%)	(%)	(%)	(%)	(%)	(%)	(%)	(%)	(%)	(%)	(mm)	(%)	(%)	(%)	(%)
F01	50.6	14.7	4.3	0			1.3	0	7.3	0.3		3	15.3	3	18.3	0.214	0.3	27.2	9.0	24.5
F02	49.3	15.3	4.4	0.6			7.3	0.7	8.7	0.7		2.3	9.7	1	10.7	0.199	2	29.4	15.3	22.1
F03	42.6	21.3	4.3	0.7			2.4	0.7	7.7			4	12.7	3.7	16.4	0.211	1.4	27.5	11.2	24.1
FA	11	2.3	0	9	77.3		0.3	0					0	0	0	0.174	9	77.6	45.0	
F1B	44	24	1.3	0.6				0	8.7	1		3.3	15.7	1.3	17	0.181	1.6	28.7	10.0	22.9
F1M	43	26.7	1.7	1	0.3			1	9			7	9	1.3	10.3	0.216	2.3	26.3	12.9	25.4
F1T	50	20.7	9.3	0.7	0.3			0.3	3.7	0		1.3	12	1.7	13.7	0.179	1.3	17.6	14.3	
F2	19.3	16	0.3	6.7	50.6	0.3		0.7	4	0.6		1.3	0	0	0	0.099		57.2	45.0	
F3	31.7	31.7	0	2.7	15		0.3	1.3	13	1		1.7	1	0.7	1.7	0.108	20	33.3	43.6	
X1	38.3	30.7	4.4	0.3	1.3		2	0	3.7	1		4	13	1.3	14.3	0.182	2.6	25.0	8.8	26.7
X2	45	21.3	3	0	0.3			0	6.7			3.7	17.7	2.3	20	0.203	0.3	28.4	8.2	23.2
X3	41.7	23	2	0.3	0.7			0.7	8	0.7		4	16.7	2.3	19	0.193	2.4	30.8	11.2	20.5
X4	33.4	24.3	4.3	0	0.7		1	0.3	9.7	0.7		4	13.7	8	21.7	0.183	1.7	30.1	12.9	21.3
X5	44.6	18	3.7	0				0	7			5	18	3.6	21.6	0.212	0	30.0	9.4	21.4
X6	52.7	19.7	2.3	0				0	6.7	0.3		4.3	11	3	14	0.186	0.3	22.3	8.0	29.2
X7	43.6	23	2	0	0.7			0	8.3			4.7	14	3.7	17.7	0.179	0.7	27.7	10.4	23.9
X8	46.6	15.3	3.4	0.3				0.3	8.7			5.3	19	1	20	0.191	0.6	33.3	11.8	17.5
X9	37	30.7	0	4	0.3			0.7	9	2		2.3	10.7	3.3	14	0.143	7	25.0	10.5	26.7
X10	35	27	4	1	8.3		3	0.3	11	0.3		2.3	4.3	2	6.3	0.165	9.9	29.5	19.7	22.0
X11	47	26.7	1.7	0.3				0.3	4.3	1		2	13.3	3.3	16.6	0.165	1.6	20.9	5.3	30.5
Z1	30	30	0	4	10.7		7	0	11.7	2		1.7	1.3	1.7	3	0.094	16.7	27.4	42.9	
Z2	34.7	25.7	2.4	0			10.3	1	10.7	1	0.6	3.3	7.7	2.7	10.4	0.172	2	34.6	22.6	15.9

								Authigenic clays					Porosity							
Sample	**Q**	**F**	**L**	**M**	**CM**	**HM**	**CB**	**PF**	**GC**	**Hmt**	**Fo**	**Qo**	**Interg. Poro**	**Sec. poro**	**Total porosity**	**GS**	**PFD**	**IGV**	**CEPL**	**COPL**
	(%)	(%)	(%)	(%)	(%)	(%)	(%)	(%)	(%)	(%)	(%)	(%)	(%)	(%)	(%)	(mm)	(%)	(%)	(%)	(%)
Z3	40	19	3.9	0	2.3			1.7	9.3	0.7		5.3	16	1.6	17.6	0.166	4.7	35.3	16.4	15.0
Z4	38	25	4.7	1	0.3		4.7	0.3	6.3	0.3	0.7	5	12.3	1.3	13.6	0.186	1.9	29.9	13.8	21.5
Z5	40	29	3.3	0	0.3			0	6.7	1		2	16.3	1.3	17.6	0.172	1.3	26.3	7.5	25.4
Z5.1	37.4	33.7	1	0.3				0	12.7			1.3	13	0.7	13.7	0.147	0.3	27.0	10.5	24.7
Z5.2	41.6	24.6	1	1	4			1.3	7	0.7	0.3	2.7	15	0.7	15.7	0.166	7	31.0	12.8	20.3
Z5.3	37.4	31	1.7	0.3				0.3	6.7			4.3	15.7	2.6	18.3	0.181	0.6	27.0	8.5	24.7
Z5.4	38.3	23.3	3	0				1	6.7			3.7	22	2	24	0.171	1	33.4	9.4	17.4
Z5.5	35	34.3	2	1.7				1.7	9	0.7		3	10.7	2	12.7	0.147	4.1	25.1	10.6	26.6
Z5.6	39	28	4	0.3		0.3	1.3	0.3	10.3	0.7		4	9.3	2.3	11.6	0.163	1.3	25.9	12.3	25.8
Z5.7	16	3.3	0	9	71.7			0							0	0.106	9	71.7	45.0	
Z6	35	42.3	0.7	1.6			0.6	1	6.7	2.6		1.3	6.3	1.7	8	0.120	5.2	18.5	8.2	32.5
Z7	26	38	0.3	5	14		1.7	6	0.6	0.3		2	4.3	1.7	6	0.131	25.3	28.9	38.3	
Z8	13	5.3	0	3	78			0	0.3			0.3	0	0	0	0.089	3	78.6	45.0	

Fleswick Bay (Longitudinal section)

								Authigenic clays					Porosity							
Sample	**Q**	**F**	**L**	**M**	**CM**	**HM**	**CB**	**PF**	**GC**	**Hmt**	**Fo**	**Qo**	**Interg. Poro**	**Sec. poro**	**Total porosity**	**GS**	**PFD**	**IGV**	**CEPL**	**COPL**
	(%)	(%)	(%)	(%)	(%)	(%)	(%)	(%)	(%)	(%)	(%)	(%)	(%)	(%)	(%)	(mm)	(%)	(%)	(%)	(%)
A1	34.3	26.3	2	0.3		0.3		0	7	1	0.3	5	19.3	4	23.3	0.159	1.3	32.6	10.9	18.4
A2	50.6	20.7	5.3	0.3	0		4.7	0	3.3	1		5.3	8.7	0	8.7	0.180	1.3	23.0	10.2	28.6
A2X	42.3	21.7	4	0.3	1.4			0.7	6.7	0.3		7	14	1.6	15.6	0.186	2.7	30.1	12.7	21.3
A2.1	42.3	26	3.7	1.7	0.6			1	5.3	1		4	12.6	1.7	14.3	0.176	4.3	24.5	8.7	27.2
A3	46.7	19.3	7.3		0.7	0.3		0.7	9.3	1	0.3	4.7	8.7	1	9.7	0.149	2.4	25.4	12.3	26.3
A4	56.3	22	10.6	5.3	0.6			0	2.7		0.3	1.3	0.3	0.3	0.6	0.160	5.9	5.2	2.8	42.0
A5	45	23.3	5.3	2	0.7			0	5.7	1		3.7	10	3.3	13.3	0.156	3.7	21.1	7.7	30.3
A6	40.6	31.7	5	1	2		0.7	0.3	3.7	0.7	0.7	0.3	9	4.3	13.3	0.145	4	17.4	5.6	33.4
A7	43.7	21.3	7	0.3	0.3			0	4.7			3.3	18.3	1	19.3	0.190	0.6	26.6	6.2	25.1
0-0-0-1	39	21	4.7	0.6	3			0.7	7	1		4.3	16	2.4	18.4	0.180	5.3	32.0	12.9	19.1
0-0-1	41	22.7	5.3					0.3	4.7	0.7		3.7	17	4.4	21.4	0.179	1	26.4	7.0	25.3
0-1	45	29.7	3	1			2.3	0	5	0.3		1	8.7	4	12.7	0.137	1.3	17.3	5.7	33.5
0-2	49.3	38	1.3	0	0.3		0	0	5.7	1		1.7	2.3	0.3	2.6	0.145	1.3	11.0	5.4	38.2
0-3	44.3	37.3	1.4	0.3	0		0.7	0	4			0.7	9.7	1.7	11.4	0.153	0.3	15.1	3.5	35.2
0-4	28.3	14.3	0.6	1.6	44.4		7.3	0				1.3	1.3	0.7	2	0.115	46	54.3		
0-5	41	22.7	1.7	0			7.3	0.3	7.7	0.7		4	10.7	4	14.7	0.168	1	30.7	15.9	20.6
0-6	40.7	25.3	3.7	0.3	0.3		2	1	6	1.6	0.7	4	11.7	2.7	14.4	0.168	3.2	27.3	11.8	24.3
0-7	41.7	32.3	3	0.7	1		1.4	0.3	8	0.3	0.3	2.7	6.7	1.7	8.4	0.154	2.3	20.7	9.7	30.6
B1	43.6	25.7	3.7	0.3	3		1	0.3	2.3	0.3		4	12	3.6	15.6	0.194	3.9	22.9	7.8	28.7
B2	39.6	24.6	4.9	0.3	1		4.3	0	5	0.7	0.3	3.3	12.7	3	15.7	0.188	2	27.3	11.0	24.3
B3	43	39	1.3	0	0.7		1	0.3	3.7	0.3		1.7	7	2	9	0.133	1.3	14.7	5.0	35.5
B4	44	32.7	1.6	3.7	0.7		3	0	4.3	0.3		1	6.7	2.3	9	0.125	4.7	16.0	6.1	34.5
B4.1	25.3	6.3	0.3	2.6	61.3		2	0				0.3	1	0.7	1.7	0.110	2.6	64.6		

								Authigenic clays					Porosity							
Sample	**Q**	**F**	**L**	**M**	**CM**	**HM**	**CB**	**PF**	**GC**	**Hmt**	**Fo**	**Qo**	**Interg. Poro**	**Sec. poro**	**Total porosity**	**GS**	**PFD**	**IGV**	**CEPL**	**COPL**
	(%)	(%)	(%)	(%)	(%)	(%)	(%)	(%)	(%)	(%)	(%)	(%)	(%)	(%)	(%)	(mm)	(%)	(%)	(%)	(%)
B5	44.6	17.3	4.3	0.3	0.3		9.7	0	2.3	0.3	0.7	9	8	3	11	0.198	0.9	30.3	17.6	21.1
B5.1	37.4	28.6	10.4	1.3	3		1	0.7	4.3	0.3		3.7	6	3.3	9.3	0.148	5.3	19.0	8.8	32.1
B6	44.4	26.4	2.4	1.6	2		2.6	0.3	5.3			3.3	9.3	2.3	11.6	0.147	3.9	22.8	9.6	28.8
B7	49	16	4	1	1		2.3	0.3	7.7	0.3		6	11	1.3	12.3	0.182	2.6	28.6	13.6	23.0
B8	42.4	18.3	7	0.3	0.3		3.7	0	5.7	0.3		2	18	2	20	0.198	0.9	30.0	9.4	21.4
C1	46.3	14.7	6.6	0.3			3.3	0	6.7	0.3		4	14.7	3	17.7	0.214	0.6	29.0	11.1	22.5
C2	41.7	39	2.3	3	0		0.7	0	4.7	0.3		1	4.3	3	7.3	0.122	3.3	11.0	4.1	38.2
C3	45.7	39.3	0	0.3	0		1	0	5.3	0.7	0.3	0.7	4.3	2.3	6.6	0.133	1	12.3	5.0	37.3
C4	45.7	27	2	1.3	0	0	5.7	0	3.7	0.7		3	8.3	2.7	11	0.169	2	21.4	9.2	30.0
C4.1	44	30.3	3.6	1	0		3	0	9.7	1.3		1.3	5	0.7	5.7	0.121	2.3	20.3	10.6	31.0
C5	36.3	9.3	4.4	6.6	30		4.7	2.3	1.7	0.3		1.3	2	1	3	0.120	39.2	42.3		
C6	37	18.7	6.7	2.7	1.7	0.3	2	0.7	8	1.7		5.7	12.7	2.3	15	0.164	6.8	32.5	16.1	18.5
C7	38.3	21.6	5.7	0.3	0.3		6	0.3	6.3	1		6	10.3	3.6	13.9	0.177	1.9	30.2	15.7	21.2
C8	37	17	9	0.3	1		6	0	4	1.3		7.3	13.3	3.7	17	0.204	2.6	32.9	16.1	18.0
C9	47	30.3	2.3	0.3	0		2	0	1.7	0.3		2.7	12	1.3	13.3	0.179	0.6	18.7	4.5	32.3
F12	41	28	4.6	1			4.7	0	4.7		0.3	2	11.7	2	13.7	0.157	1	23.4	8.4	28.2
F13	51.7	22.3	3.4	0			3	0	3.3		0.3	0.7	12.3	3	15.3	0.153	0	19.6	5.0	31.6
F15	45.3	33	2	0			3	0	4.3	0.3		1.3	7	3.7	10.7	0.152	0.3	15.9	5.8	34.6
F16	47	29	2	0		0.3		0.3	2.3	0.7		1.7	14.3	2.3	16.6	0.210	1	19.3	3.4	31.8
F17	46.3	31	1.3	0.3			3.3	0	5.3	1		0.7	8.3	2.3	10.6	0.190	1.3	18.6	7.0	32.4
F18	46	36.7	1	0.3				0.3	3	1		1.3	6	4.3	10.3	0.169	1.6	11.6	3.5	37.8
F19	48	28	2	1	1	0.3	5.3	0	3.3	0.7		1.3	7.3	1.7	9	0.136	2.7	18.9	7.9	32.2
F20	44.3	43.7	0	1			1.3	0	2.3			0.7	5	1.7	6.7	0.120	1	9.3	2.6	39.4

								Authigenic clays					Porosity							
Sample	**Q**	**F**	**L**	**M**	**CM**	**HM**	**CB**	**PF**	**GC**	**Hmt**	**Fo**	**Qo**	**Interg. Poro**	**Sec. poro**	**Total porosity**	**GS**	**PFD**	**IGV**	**CEPL**	**COPL**
	(%)	(%)	(%)	(%)	(%)	(%)	(%)	(%)	(%)	(%)	(%)	(%)	(%)	(%)	(%)	(mm)	(%)	(%)	(%)	(%)
F21	43.3	39.7	0	0			2.3	0	4	2		1.7	6.7	0.3	7	0.126	2	16.7	6.6	34.0
F22	44.4	28.7	2	0			2.3	0.3	6	1		1.7	10.3	3.3	13.6	0.151	1.3	21.6	7.9	29.8
E6	45.3	28.3	2.1	0.3			4.3	0	3.7	1.3		3.3	10.7	0.7	11.4	0.188	1.6	23.3	9.0	28.3
E7	47	19.6	3.4	0.3			7.3	0	3	0.7	0.3	3.7	11	3.7	14.7	0.188	1	26.0	11.1	25.7
E8	48.3	25.7	5.3	0.7			4.3	0	2	0.7		2.7	7.3	3	10.3	0.165	1.4	17.0	6.4	33.7
E11	51	21	1.2	0.3			6.7	0	3.7			3	8.3	4.7	13	0.208	0.3	21.7	9.4	29.8
E12	40.7	26	2.6	0			5	0	6	0.3		3	13	3.3	16.3	0.200	0.3	27.3	10.8	24.3
E13	38.3	36.3	2.7	3.3			3.3	0	6	2.3			3.7	4	7.7	0.134	5.6	15.3	7.5	35.1
E14	43.3	32.3	0.3	0.3			2	0.3	5.3	0.7		2.7	10.3	2.3	12.6	0.156	1.3	21.3	7.7	30.1

Birkham's Quarry

								Authigenic clays					Porosity							
Sample	**Q**	**F**	**L**	**M**	**CM**	**HM**	**CB**	**PF**	**GC**	**Hmt**	**Fo**	**Qo**	**Interg. Poro**	**Sec. poro**	**Total porosity**	**GS**	**PFD**	**IGV**	**CEPL**	**COPL**
	(%)	(%)	(%)	(%)	(%)	(%)	(%)	(%)	(%)	(%)	(%)	(%)	(%)	(%)	(%)	(mm)	(%)	(%)	(%)	(%)
S1	46.7	29.7	0.7	0			2	1.3	8.7	0.7		0.7	7	2.6	9.6	0.132	2	20.4	9.3	30.9
S2	50.7	31.4	0.3	0.3			1.6	0.3	6.3	1		1.7	5.7	0.7	6.4	0.134	1.6	16.6	7.2	34.1
S3	47.4	22	3	0			1.7	0.7	6.7	3		2.7	11	1.7	12.7	0.169	3.7	25.8	11.0	25.9
S4	47.3	28.6	0.3	0			3	1.3	7	1		1.3	8.7	0.7	9.4	0.123	2.3	22.3	9.6	29.2
S4.1	49.7	23	1	0	1			0.7	8	4.5		2.3	8.7	1	9.7	0.176	6.2	25.2	12.1	26.5
SA	19.7	5.3	0	0.7	72.7			0		1			0.3		0.3	0.084	0.7	74.0	44.8	
S5	38	26	0	4.3	20.7			0	4.7	2		0.3	3	1	4	0.074	27	30.7	40.6	
S6	45.7	16	0.3	4.4	22.3		3.7	0	4.7	0.3		0.3	2.3		2.3	0.088	27	33.6	41.9	
S7	46.6	28	0	0			0.3	1	8.7	1.7		2.3	10.3	1	11.3	0.129	2.7	24.3	10.2	27.3
S8	51.6	21	0.3	0.3			2	1	8.3	3.7		1.7	9.3	0.7	10	0.142	5	26.0	12.4	25.7
S8.1	38.7	45.7	0.7	1.6				0	5.3	1.3		0.3	4.3	2	6.3	0.093	2.9	11.2	4.3	38.1
S9	46.6	27.3	4	0				0	7.3	1		2.7	8.7	2.3	11	0.156	1	19.7	7.5	31.5
S10	37.3	31.4	1.3	1.3				0.3	9.3	0.7		5.3	12.3	0.7	13	0.162	2.3	27.9	11.9	23.7
S11	27.7	16.3	0	0.7	35.7			0	17.3	1.3		0.3	0.3	0.3	0.6	0.063	37.7	54.9	44.8	
S12	30.5	26	0	1	10		0.7	0	24.7	4.3		0.7	1.3	0.7	2	0.074	15.3	41.7	43.6	
S13	45.3	27	1.4	0.7	3			0	9	4		1.3	6.7	1.7	8.4	0.123	7.7	24.0	12.5	27.6
S14	46.4	26.7	2.4	5.7	11			0	2			3	2.7	0.3	3	0.152	16.7	18.7	38.5	
S15	45	26.7	1.9	1.3				0	11	1		1	8.7	3.3	12	0.138	2.3	21.7	9.1	29.8
S16	30.6	20	0	1	42		0.3	0	2.7				2	1.3	3.3	0.093	43	47.0	43.1	
S17	33.3	10.6	0	0.3	51			0.3	3.3	0.3		0.3	0	0.3	0.3	0.071		55.2	45.0	
S18	44.7	24.3	4	0.3				0	5.7			2	17.7	1.3	19	0.199	0.3	25.4	5.7	26.3
S19	36	42.3	0.7	0.3				1	5			0.7	11.7	2.3	14	0.126	1.3	18.4	4.5	32.6
S20	41.3	32.7	2.3	0.6				0	7.3	0.6		1.3	11.7	2	13.7	0.169	1.2	20.9	6.4	30.5

								Authigenic clays						Porosity						
Sample	**Q**	**F**	**L**	**M**	**CM**	**HM**	**CB**	**PF**	**GC**	**Hmt**	**Fo**	**Qo**	**Interg. Poro**	**Sec. poro**	**Total porosity**	**GS**	**PFD**	**IGV**	**CEPL**	**COPL**
	(%)	(%)	(%)	(%)	(%)	(%)	(%)	(%)	(%)	(%)	(%)	(%)	(%)	(%)	(%)	(mm)	(%)	(%)	(%)	(%)
S21	43.3	24	1.3	0				0.7	8			3	17.3	2.3	19.6	0.193	0.7	29.0	9.1	22.5
S22	45	29	2	0.3	1	0.3		0	5.7	1		2.3	11.7	1.7	13.4	0.163	2.3	21.7	7.0	29.8
S23	46	23	1.7	0				1.3	9.7			3	13	2.3	15.3	0.145	1.3	27.0	10.5	24.7

Saltom Bay

								Authigenic clays					Porosity							
Sample	**Q**	**F**	**L**	**M**	**CM**	**HM**	**CB**	**PF**	**GC**	**Hmt**	**Fo**	**Qo**	**Interg. Poro**	**Sec. poro**	**Total porosity**	**GS**	**PFD**	**IGV**	**CEPL**	**COPL**
	(%)	(%)	(%)	(%)	(%)	(%)	(%)	(%)	(%)	(%)	(%)	(%)	(%)	(%)	(%)	(mm)	(%)	(%)	(%)	(%)
SB1	34.3	28	0.3	0	0.3			0.3	15.3	0.7		4	14.7	2	16.7	0.140	1.3	35.3	17.5	15.0
SB2	44.3	35.3	0.3	1				0	7	1.3		0.7	8.3	1.7	10	0.105	2.3	17.3	6.0	33.5
SB3	26.3	6	0.3	1.3	63.6			0	0.7			0.3	0.7	0.7	1.4	0.098	1.3	65.3	44.5	
SB4	46.3	18	1	0.3				0.3	10	2.7		6.3	13.3	1.7	15	0.125	3.3	32.6	15.7	18.4
SB4.1	41.3	31.7	0.7	0.3	3			0.7	9			1.7	9	2.3	11.3	0.118	4	23.4	10.3	28.2
SB5	37	31.3	0.3	1.7	0.3		1	0.3	9.7	0.3		3.3	11.7	3	14.7	0.109	2.6	26.6	11.2	25.1
SB6	40	27	0.7	0.7	2.3		0.3	0.3	9.7	0.3		6	10.3	2.3	12.6	0.091	3.6	29.2	14.7	22.3
SB7	34.3	23	0	2	16		15.3	0	3.7	3.7		0.3	1.3	0.3	1.6	0.083	21.7	40.3	43.5	
SB8	30.3	25	0.3	3	15		17.7	0.3	4.7	1.3		0.3	1	1	2	0.077	19.6	40.3	43.9	
SB9	37	38.6	1	1	3.3			0	5.3	1.7			8.7	3.3	12	0.116	6	19	7.0	32.1
SB9.1	11	3.7	0	0	52.3		21	0	1.3	8.7			0.3	1.3	1.6	0.079	0	83.6	44.8	
SB10	32.3	30	0.6	0.3	17.3		0.3	0	4.3	4		2	5.7	3	8.7	0.084	21.6	33.6	37.4	
SB11	37	32.3	0.7	1.7	2.3			0.7	4.3	2		2	12.7	4.3	17	0.109	6.7	24	8.2	27.6
SB12	39.4	25.7	0.7	0.7	0.6			0.7	12.3	0.3		4	14	1.7	15.7	0.109	2.3	31.9	14.5	19.2
SB13	34	38.7	1	0.3	1.4			0.7	8	1.7		5	7.3	2	9.3	0.116	4.1	24.1	12.2	27.5
SB14	38.3	38.7	1	0.3	3.4			0.3	7.7	1.3		4	4.3	0.7	5	0.106	5.3	21	11.6	30.4
SC01	30.3	25	0.3	3	15		17.7	0.3	4.7	1.3		0.3	1	1	2	0.077	19.6	40.3	43.9	
SC1	39	28.7	1.3	0.7	0.7			0	5.7	1		5.3	15.3	2.3	17.6	0.166	2.4	28	9.7	23.6
SC2	40	32	0.7	0				0	6.3	0.7		4.3	12.7	3.3	16	0.135	0.7	24	8.2	27.6

							Authigenic clays					Porosity							
Sample	**Q**	**F**	**L**	**M**	**CM**	**HM**	**CB**	**PF**	**GC**	**Hmt**	**Fo**	**Qo**	**Interg. Poro**	**Sec. poro**	**Total porosity**	**GS**	**PFD**	**IGV**	**CEPL**	**COPL**
	(%)	(%)	(%)	(%)	(%)	(%)	(%)	(%)	(%)	(%)	(%)	(%)	(%)	(%)	(%)	(mm)	(%)	(%)	(%)	(%)
SC3	31	39.7	1	0.6	6.7		2	0.7	5.7	0.3	0.3	5	5.3	1.7	7	0.127	8.3	26	15.4	25.7
SC4	38.3	37.7	0.3	1.3	4.7		1	0.7	4.7	1.3		2.3	6.7	1	7.7	0.110	8	21.4	10.3	30.0
SC5	33.4	38.6	0.7	0	1.7			0.7	7.7	2		2.7	10	2.7	12.7	0.099	4.4	24.8	10.8	26.9
SC6	24	30.7	0	3.7	28.4		3.3	0	1.3	4		1.3	2	1.3	3.3	0.077	36.1	40.3	42.8	
SC7	25	43.3	0.3	2.3	4			0.7	8	2.7		1.3	10	2.3	12.3	0.098	9.7	26.7	12.5	25.0
SC8	33	29.6	1	0	0.3			0	8	2.3	0.7	5.3	17.7	2	19.7	0.130	2.6	34.3	13.9	16.3
SC9	40	33	0.3	1	2	0.3		0	11	1		2	8	1.3	9.3	0.109	4	24	11.6	27.6

Appendix F

SEM images and SEM-EDX data

Skagerrak Formation

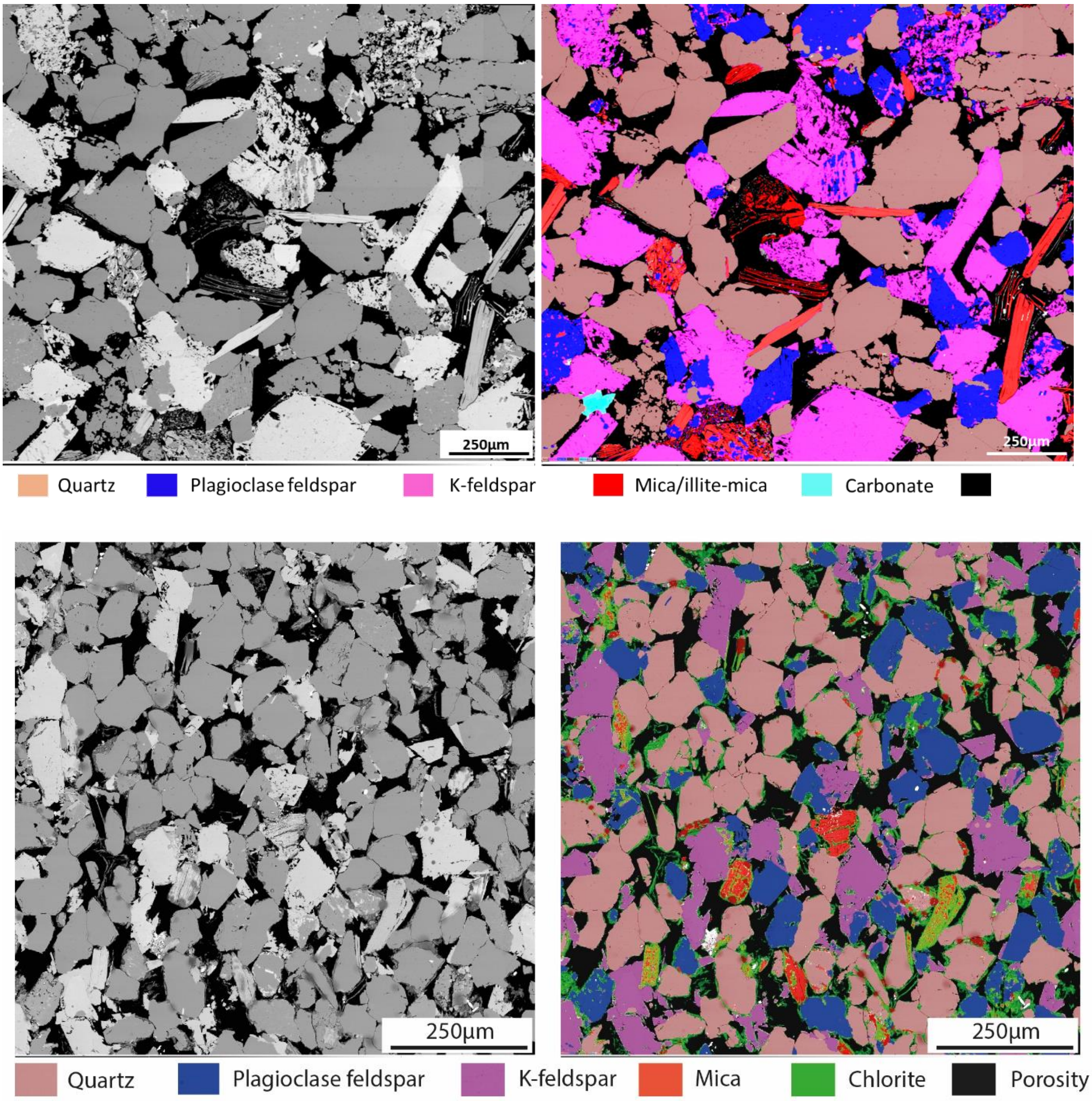

Figure F.1: BSE images of selected Skagerrak Formation sandstones and their corresponding phase maps (Upper image: sample from well 30/2c-4 (Jade field), 15,650.1 ft MD; Lower image: sample from well 30/7a-7 (Judy field), 11,335.1 ft MD).

BSE

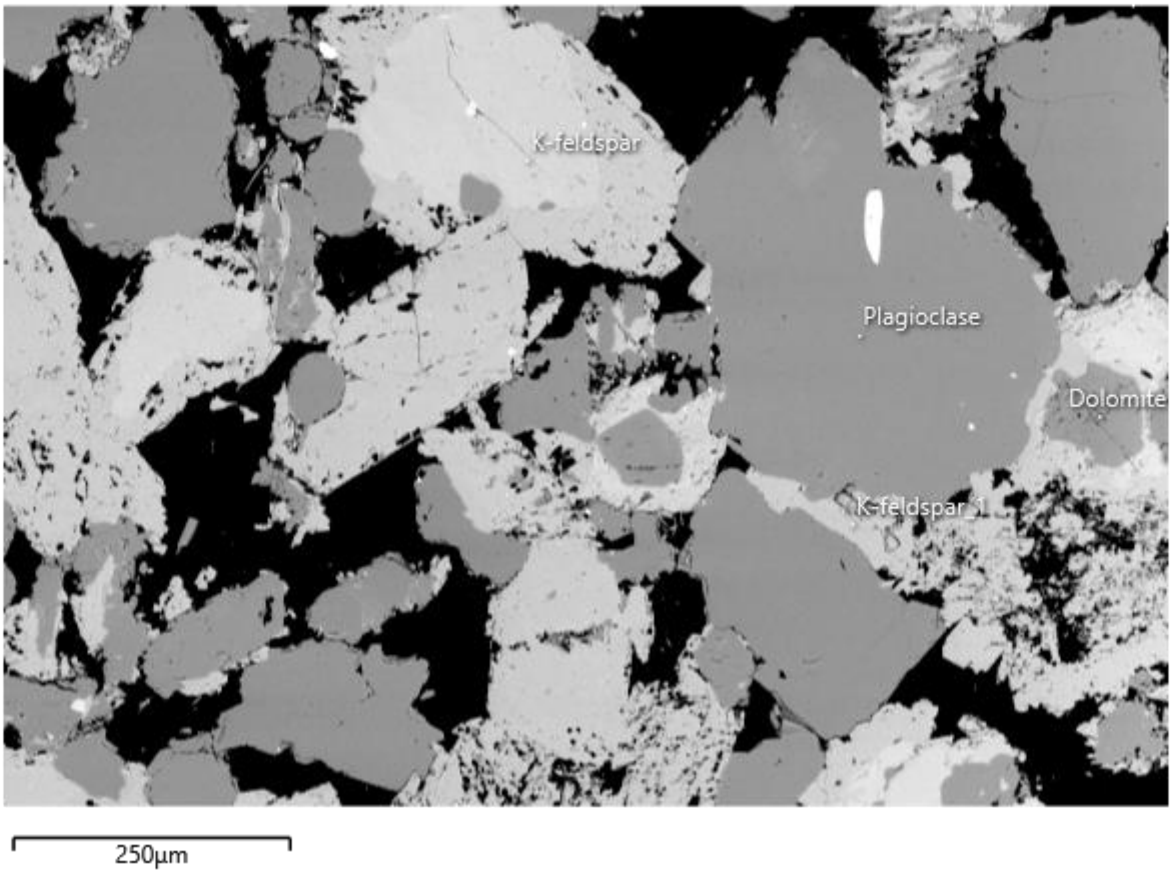
K-feldspar
Plagioclase
Dolomite
K-feldspar_1
250µm

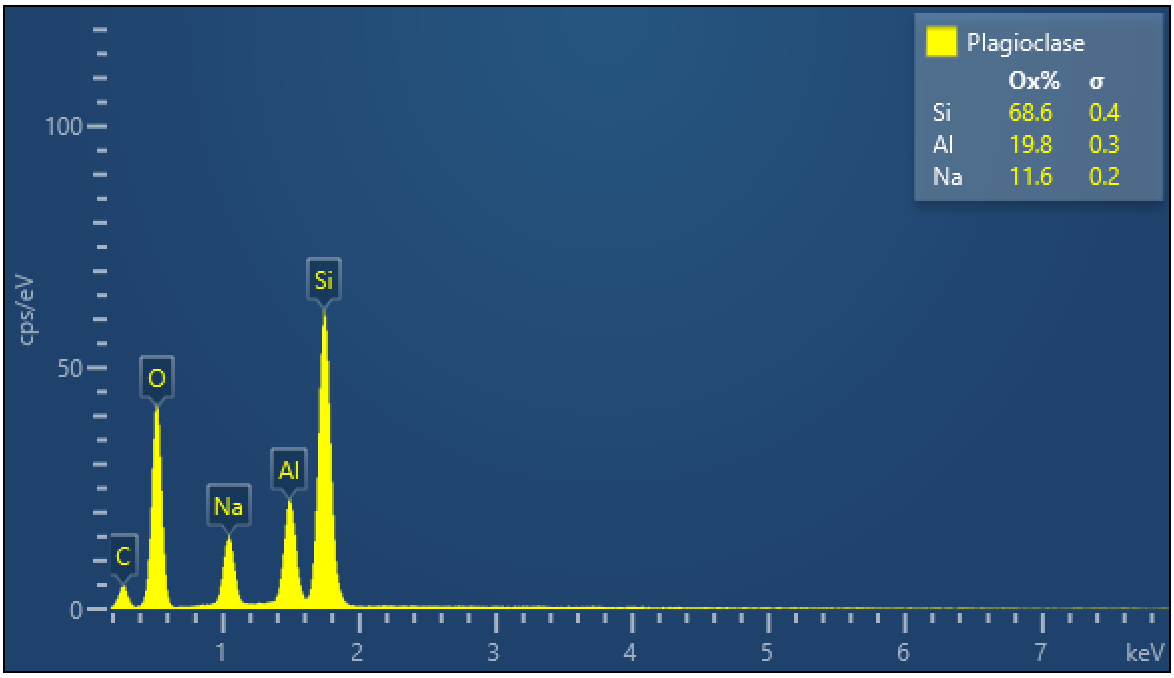
Plagioclase
Ox% σ
Si 68.6 0.4
Al 19.8 0.3
Na 11.6 0.2
Si
O
Al
Na
C
cps/eV
100
50
0
1
2
3
4
5
6
7
keV

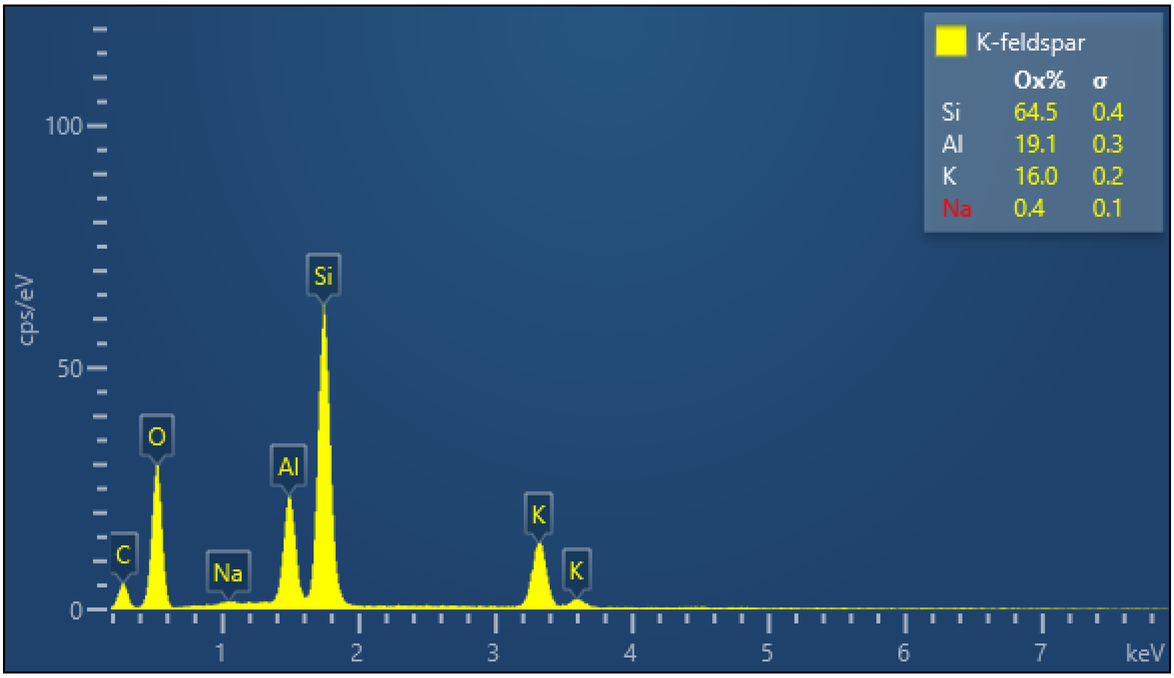
K-feldspar
Ox% σ
Si 64.5 0.4
Al 19.1 0.3
K 16.0 0.2
Na 0.4 0.1
cps/eV
100
50
0
C
O
Na
Al
Si
K
K
1
2
3
4
5
6
7
keV

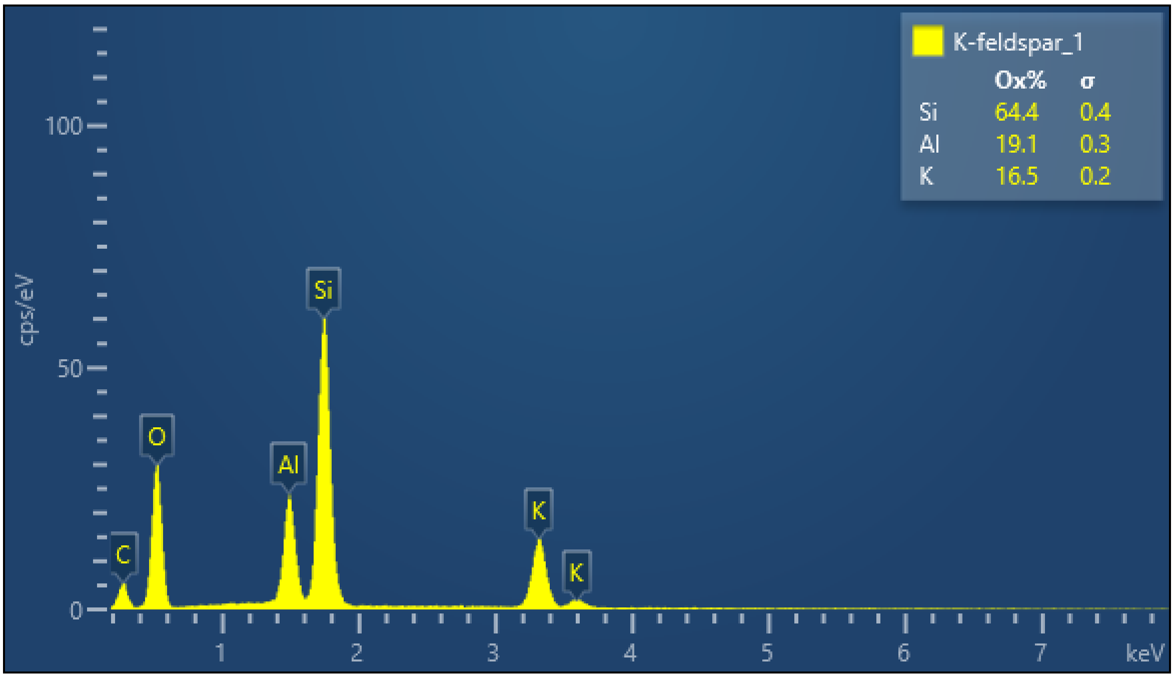
K-feldspar_1
Ox% σ
Si 64.4 0.4
Al 19.1 0.3
K 16.5 0.2
cps/eV
100
50
0
C
O
Al
Si
K
K
1
2
3
4
5
6
7
keV

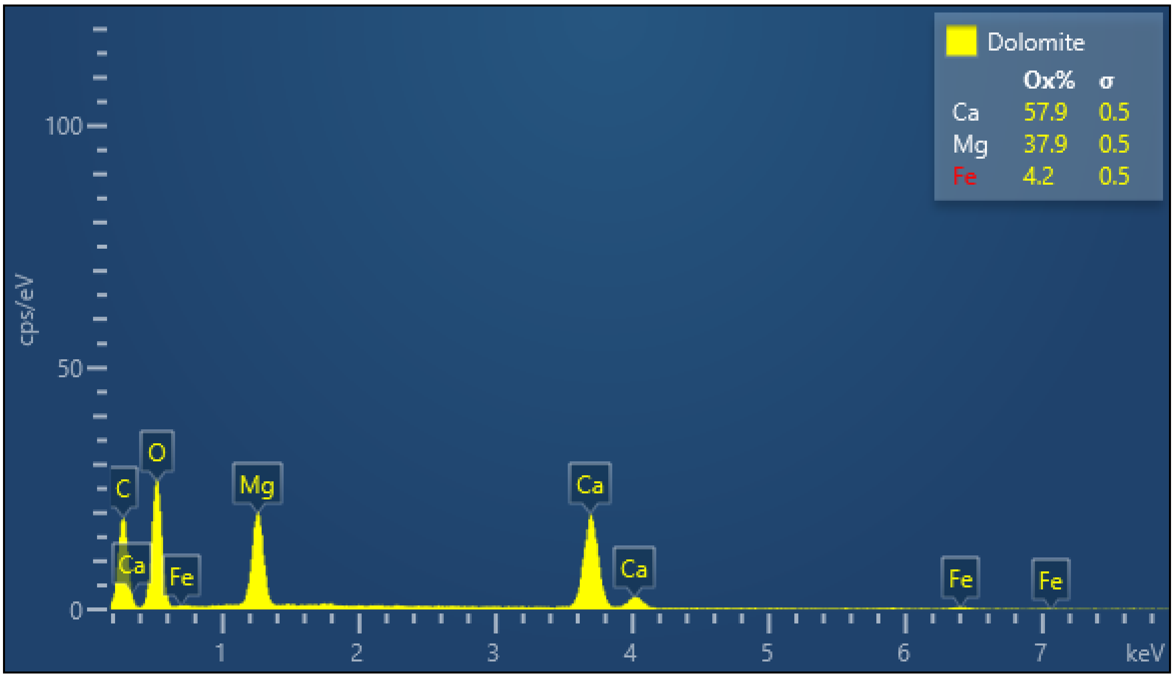

Figure F.2: SEM-EDX analysis of detrital plagioclase feldspar, K-feldspar and dolomite, and their EDX spectra. Sample from well 30/2c-4 (Jade field), 15,745 ft MD.

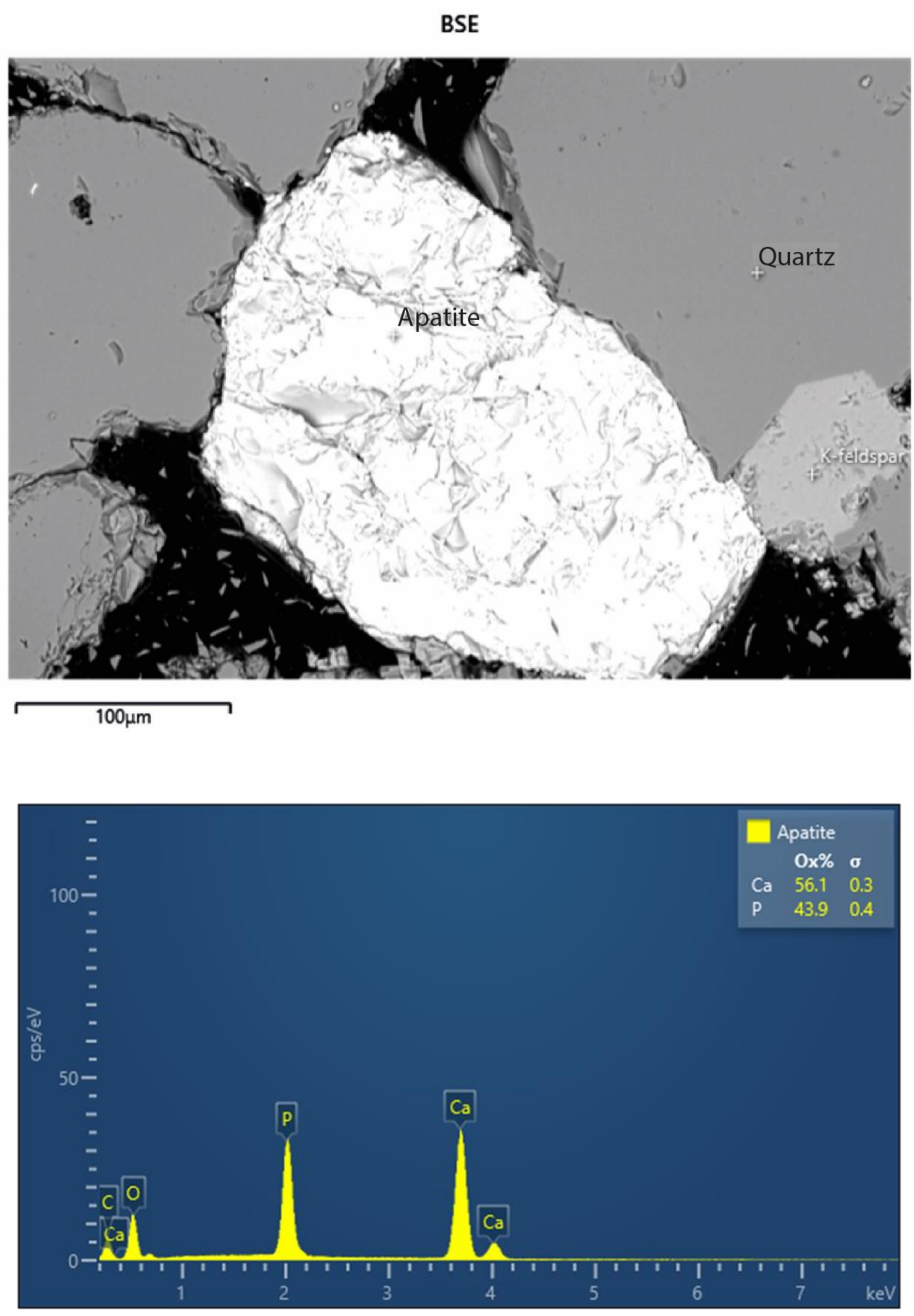

Figure F.3: BSE image of apatite and its EDX spectrum. Sample from well 30/2c-4 (Jade field), 15,748.2 ft MD.

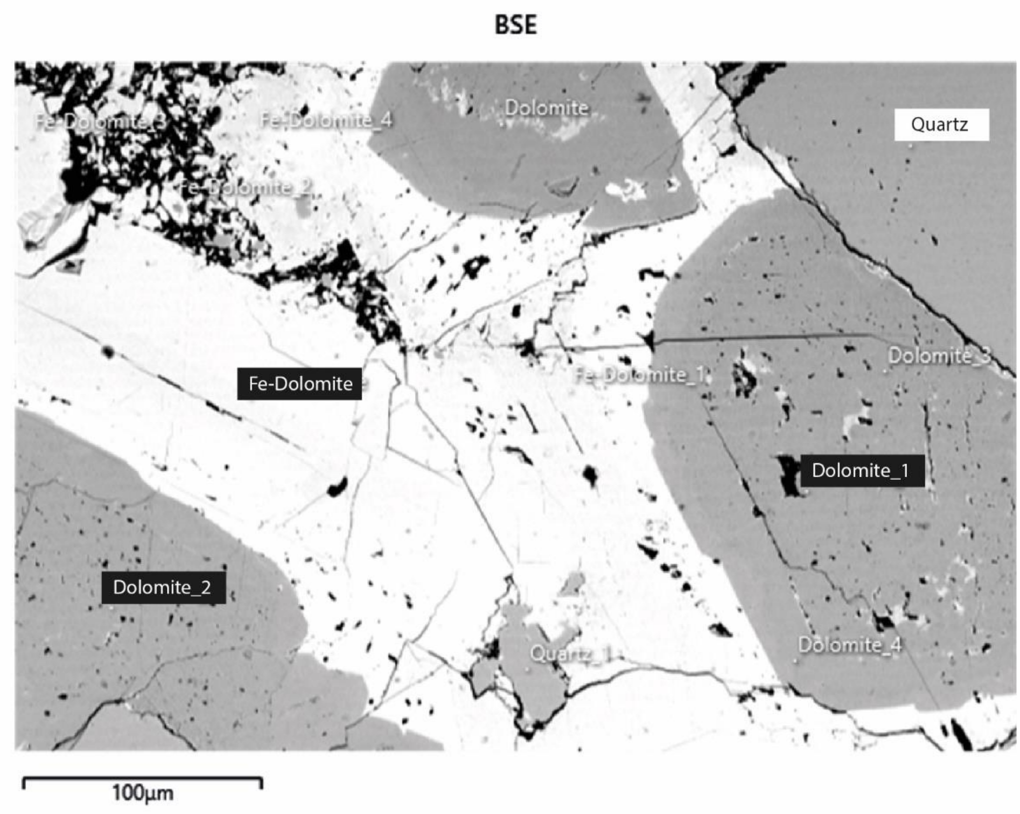
BSE
Fe-Dolomite_3
Fe-Dolomite_4
Dolomite
Quartz
Fe-Dolomite_2
Fe-Dolomite
Fe-Dolomite_1
Dolomite_3
Dolomite_1
Dolomite_2
Quartz_1
Dolomite_4
100µm

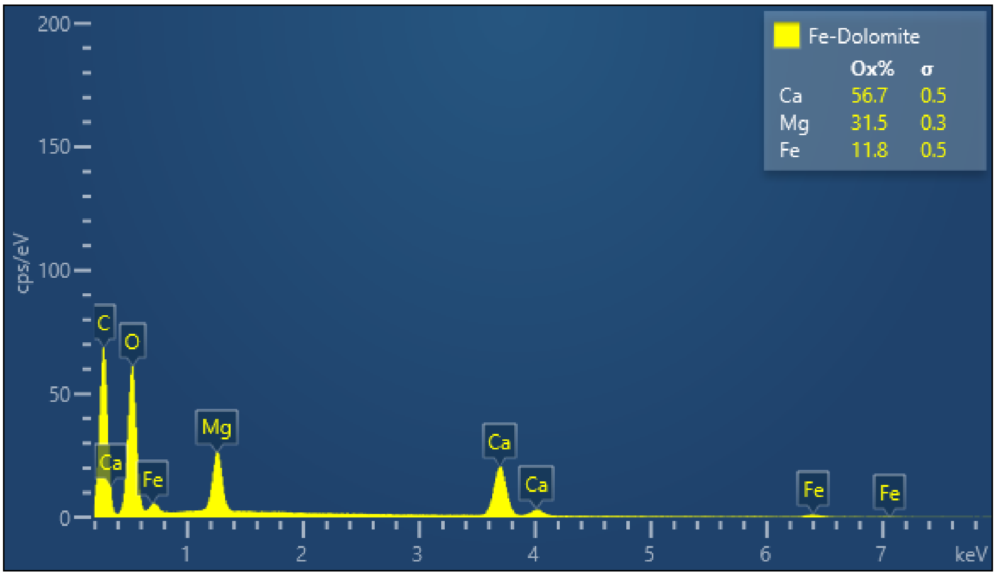
Fe-Dolomite
Ox% σ
Ca 56.7 0.5
Mg 31.5 0.3
Fe 11.8 0.5
cps/eV
200
150
100
50
0
C
O
Ca
Fe
Mg
Ca
Ca
Fe
Fe
1
2
3
4
5
6
7
keV

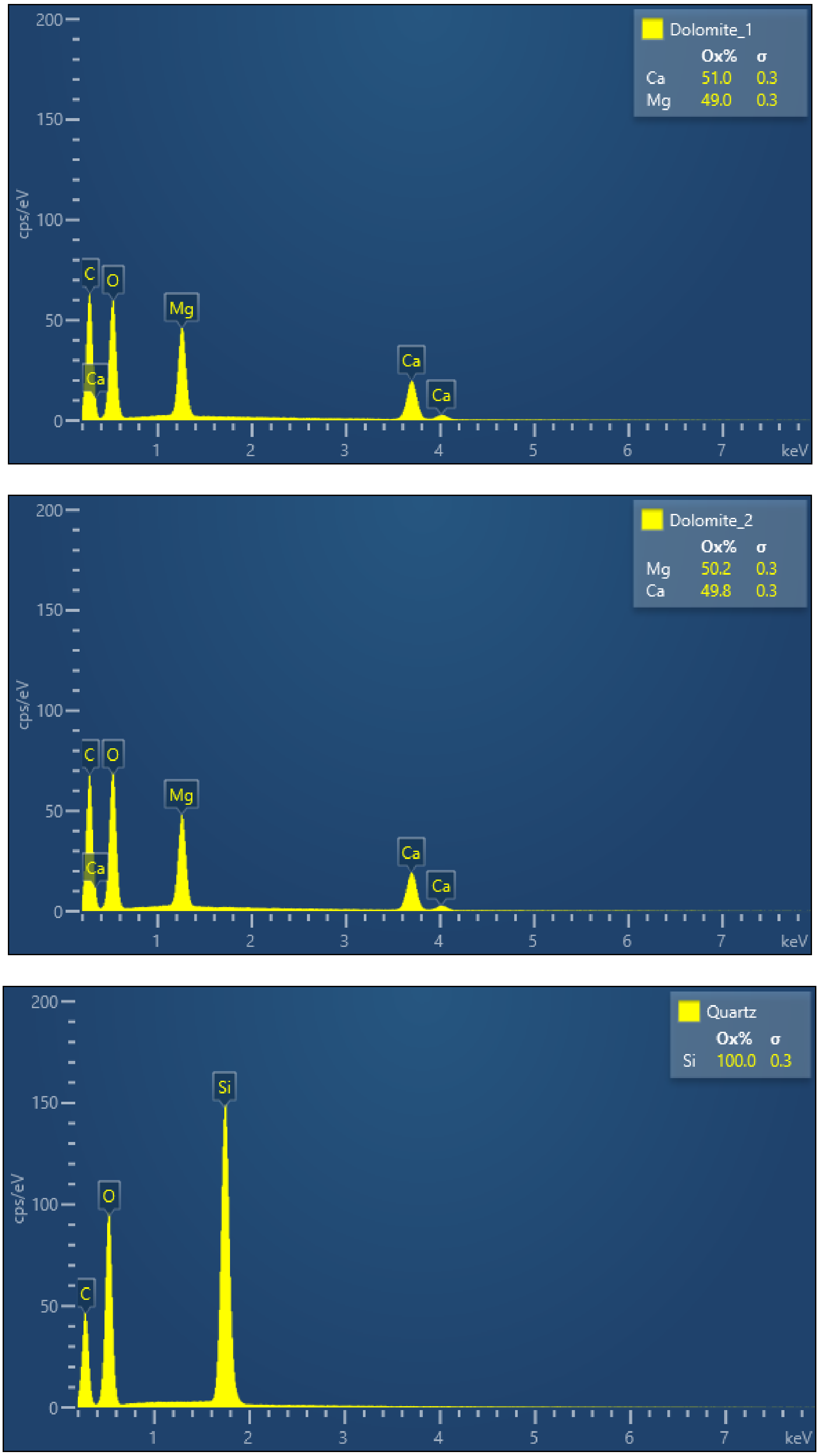

Figure F.4: SEM-EDX analysis of ferroan dolomite, non-ferroan dolomite and detrital quartz, and their EDX spectra. Sample from well 30/2c-4 (Jade field), 15,681 ft MD.

St Bees sandstone

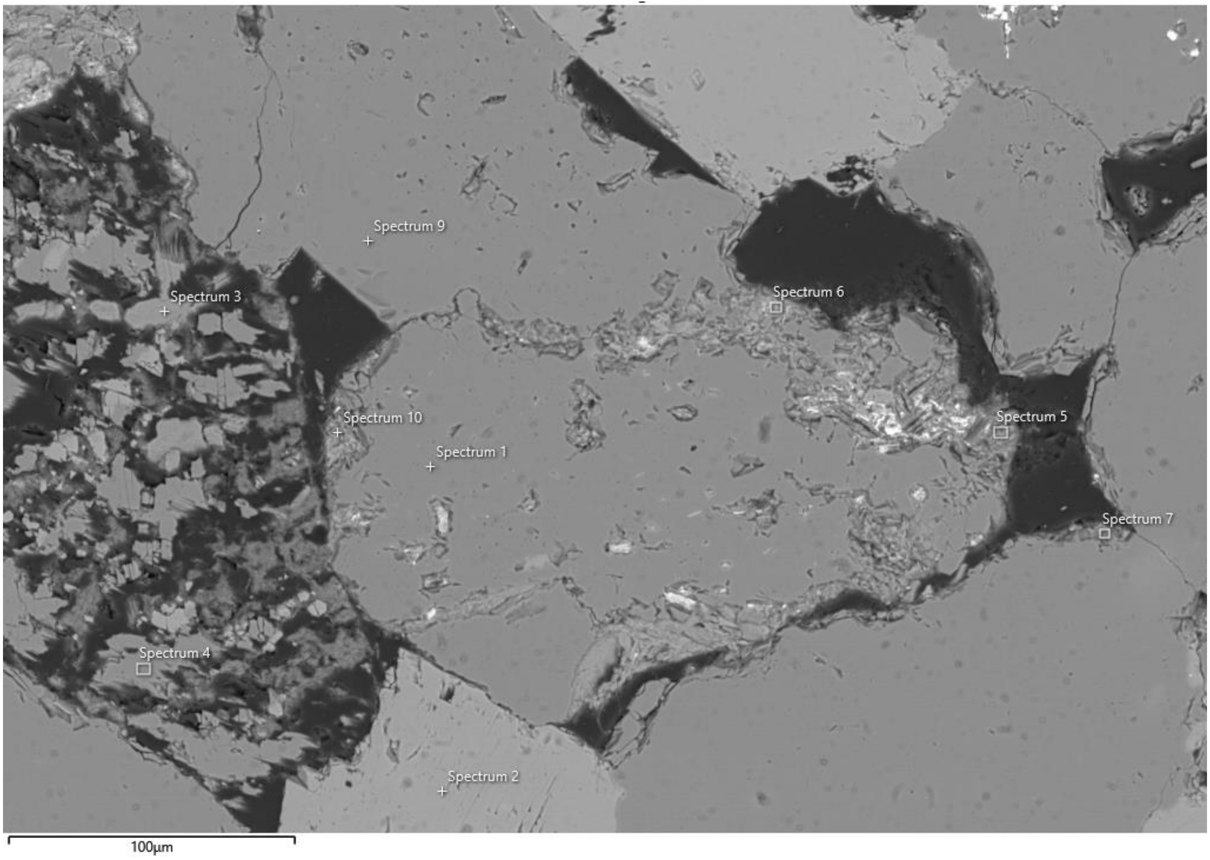

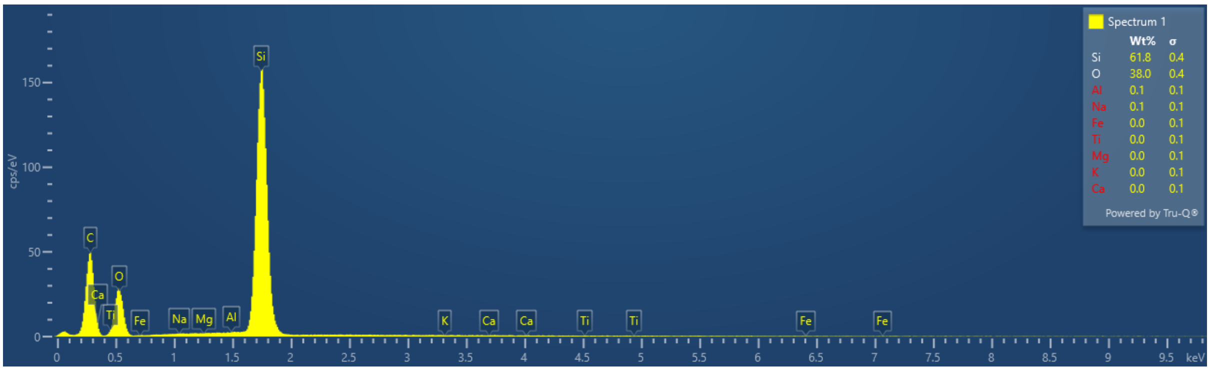

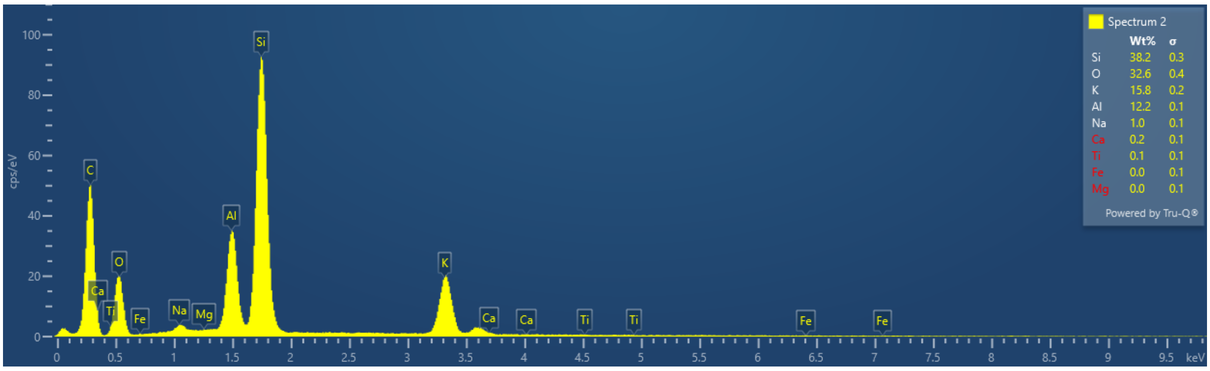

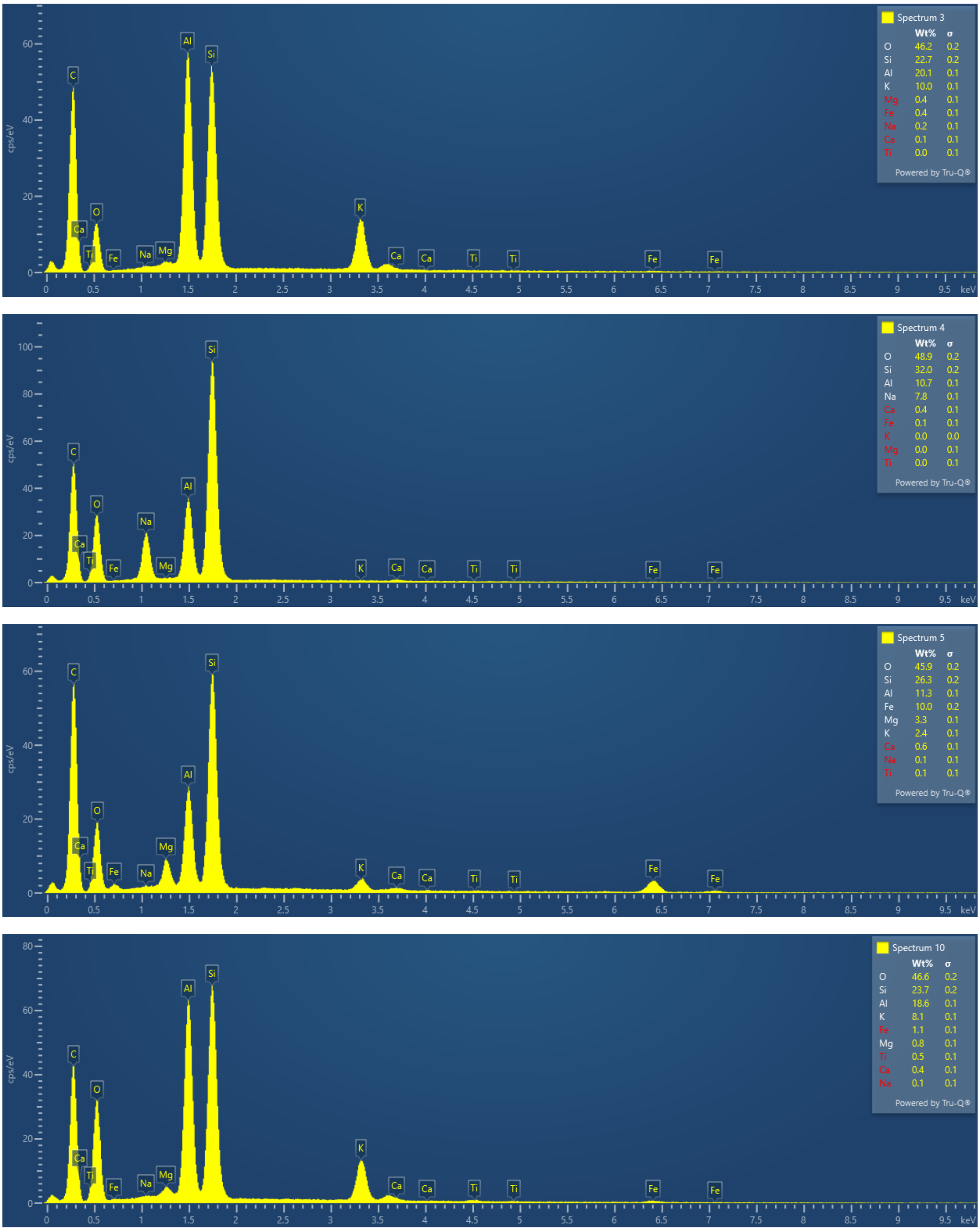

Figure F.5: SEM-EDX analysis of quartz, K-feldspar, plagioclase feldspar, chlorite and illite and their EDX spectra. (Spectrum 1: Quartz; Spectrum 2: K-feldspar; Spectrum 3: K-feldspar; Spectrum 4: Plagioclase feldspar (Note: the dissolved feldspar grain with spectra 3 and 4 represents albitized K-feldspar); Spectrum 5: Chlorite; Spectrum 10: Illite).

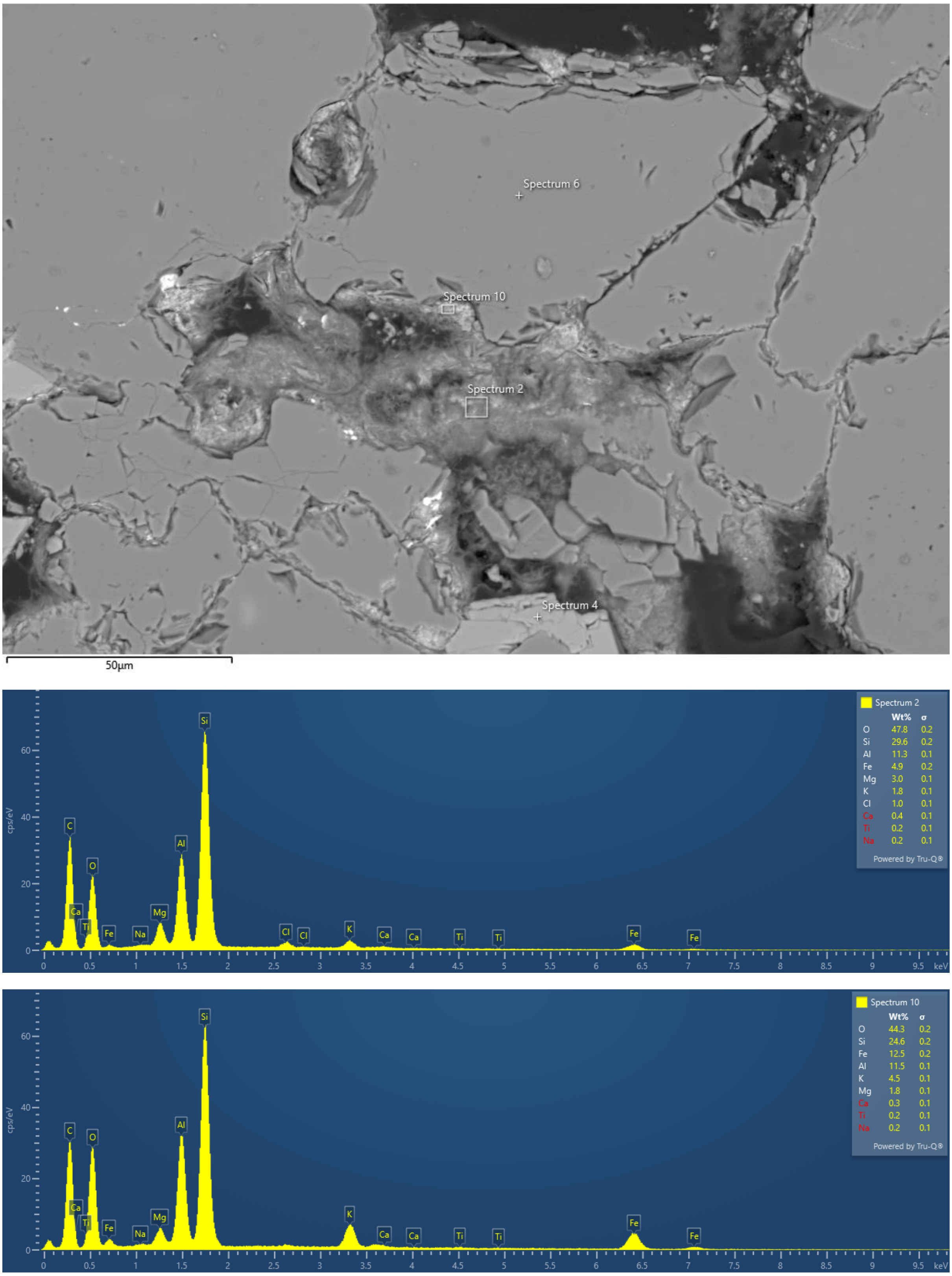

Figure F.6: BSE image of chlorite and its EDX spectrum (Spectrum 2: Grain coating chlorite; Spectrum 10: Pore-filling chlorite).

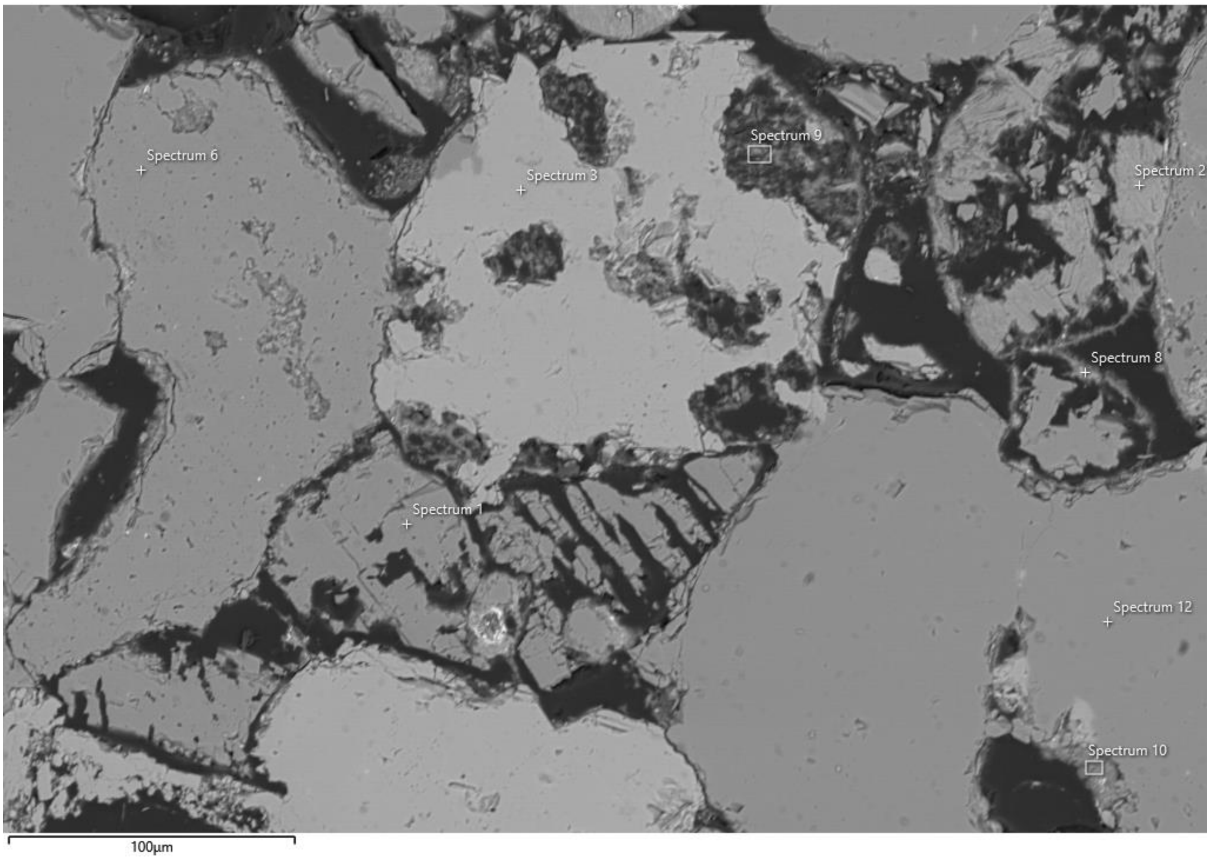
Spectrum 6
Spectrum 3
Spectrum 9
Spectrum 2
Spectrum 8
Spectrum 1
Spectrum 12
Spectrum 10
100µm

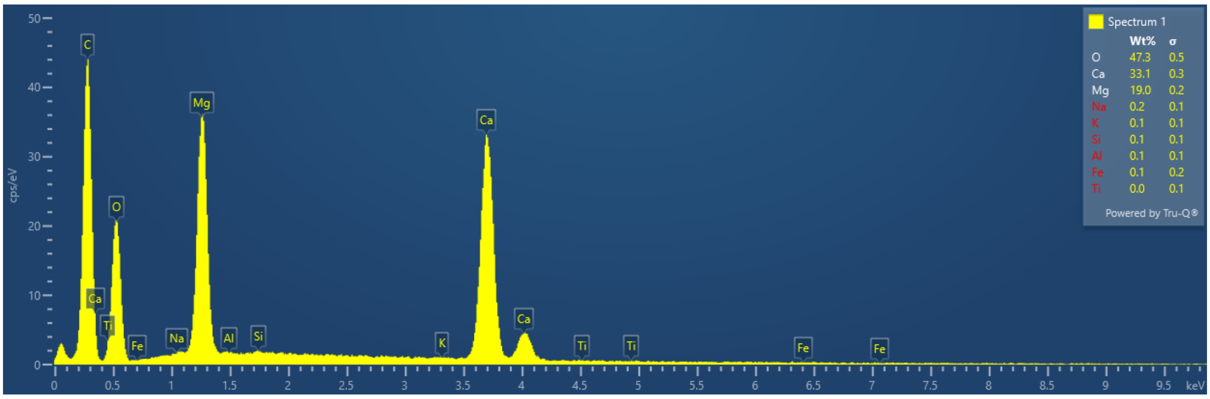
Spectrum 1
Wt% σ
O 47.3 0.5
Ca 33.1 0.3
Mg 19.0 0.2
Na 0.2 0.1
K 0.1 0.1
Si 0.1 0.1
Al 0.1 0.1
Fe 0.1 0.2
Ti 0.0 0.1
Powered by Tru-Q®
cps/eV
keV

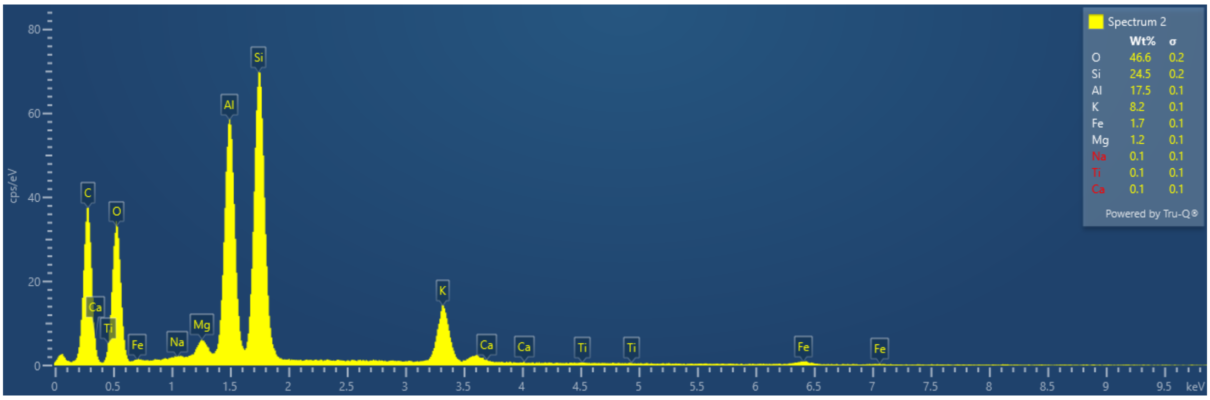
Spectrum 2
Wt% σ
O 46.6 0.2
Si 24.5 0.2
Al 17.5 0.1
K 8.2 0.1
Fe 1.7 0.1
Mg 1.2 0.1
Na 0.1 0.1
Ti 0.1 0.1
Ca 0.1 0.1
Powered by Tru-Q®
cps/eV
keV

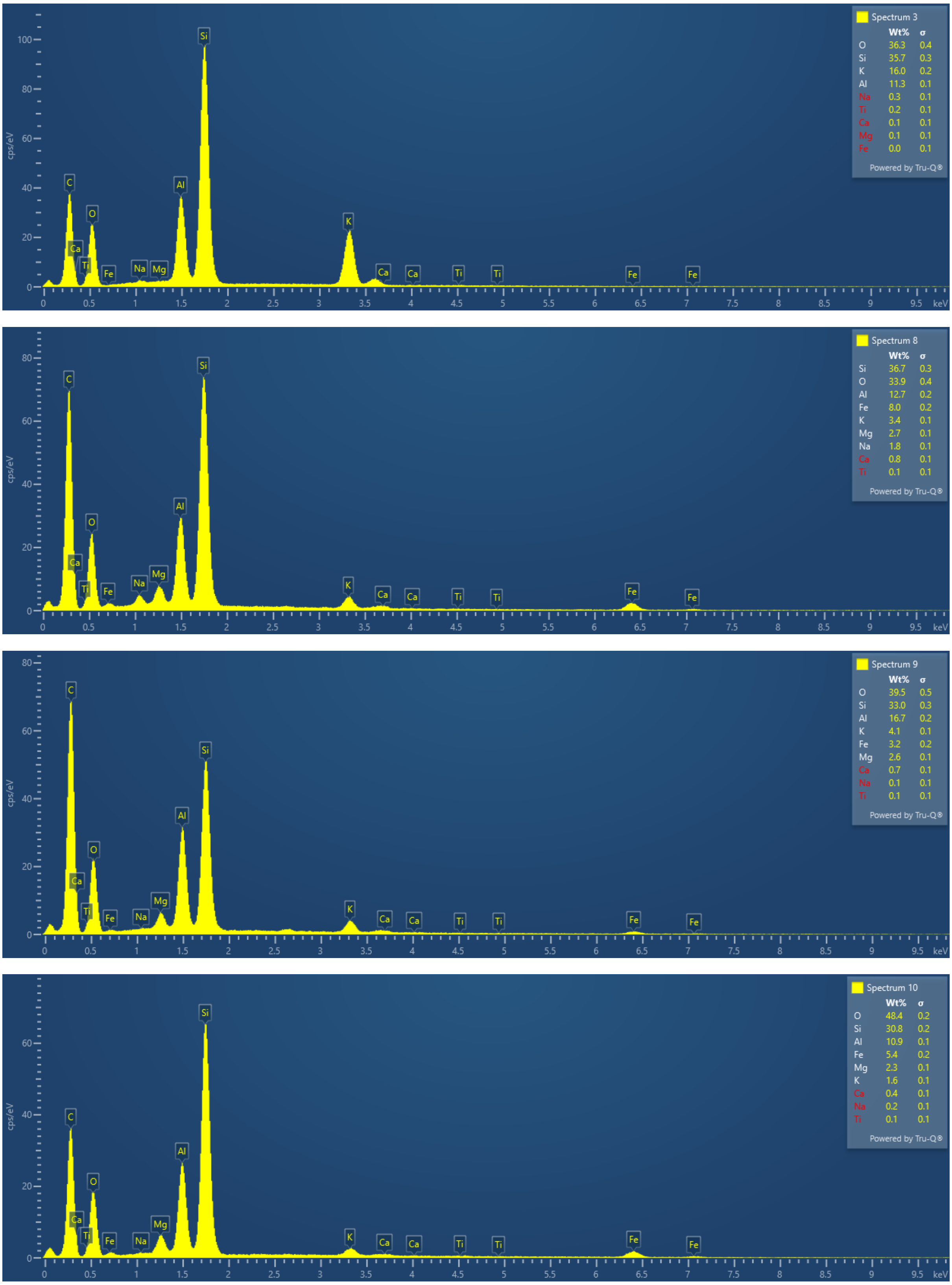

Figure F.7: SEM-EDX analysis of dolomite, mica, K-feldspar, and mixture of illite and chlorite and their EDX spectra (Spectrum 1: Dolomite; Spectrum 2: Mica; Spectrum 3: K-feldspar; Spectrum 8: Mixture of illite and chlorite; Spectrum 9: Mixture of illite and chlorite; Spectrum 10: Chlorite).